EPSRC Engineering Doctorate Program

University of Wales

E. V. Stevenson

Doctorate Thesis

The Design and Evaluation of Building Integrated Thermal Cladding.

March 2007

Academic Supervisors
Mr D Alexander
Dr Phil Jones

Industrial Supervisor
Mr B Jones

Theme Leader
Mr P Jones

Acknowledgements

I would like to acknowledge the help and support I received during the course of this project.

The project was funded by EPSRC and Corus Group.

Within Corus Group, I would particularly like to thank Ian Clarke, Vernon John, Bryan Jones, Paul Jones and Chris Ponting for their advice and support.

Within Cardiff University I would like to thank Don Alexander, Phil Jones and members of the Science Group within the Welsh School of Architecture who supplied advice and equipment.

Within University of Wales Swansea I would like to thank Mark Evans for his help in understanding factorial experiments.

Within ECM^2 I would like to thank Tracey Mayes, Clive Broome and Adrian Jickells for finding space for my experiments. Many thanks to Mike for his advice and his ability to transform my ideas into technical drawings! Many thanks to Terry, Mark, Peter and Richard for helping to transform the technical drawings into reality and for a ready supply of spanners!

Thanks are also due to my fellow Engineering Doctorate students as well as Norman, Gareth and Tracey who spent many hours on 'scaffolding cover' with mobile phone at the ready in case an ambulance was required!

I would also like to thank Alex Gater for adapting the Fortran code and Dave Thomson for his advice on adhesives and sealants.

Of course, this work could never have been completed without the support of my family and friends. Thanks to Mum and Dad for getting me here in the first place (especial thanks to Dad who might finally get a break from helping me with my maths). Thanks to Tracey, Brian, Ria and Angela for moral support. Last, but definitely not least, all my love and gratitude to Andy for putting up with this dominating the last four years!

Declaration and Statements

DECLARATION

This work has not previously been accepted in substance for any degree and is not concurrently submitted in candidature for any degree.

Signed…….(candidate) Date……

STATEMENT 1

This thesis is being submitted in partial fulfilment of the requirements for the degree of Eng D.

Signed…….(candidate) Date……

STATEMENT 2

This thesis is the result of my own independent work/investigation, except where otherwise stated. Other sources are acknowledged by explicit references.

Signed…….(candidate) Date……

STATEMENT 3

I hereby give consent for my thesis, if accepted, to be available for photocopying and for inter-library loan, and for the title and summary to be made available to outside organisations.

Signed…….(candidate) Date……

STATEMENT 4

I hereby give consent for my thesis, if accepted, to be available for photocopying and for inter-library loans after expiry of a bar on access approved by the Graduate Development Committee.

Signed…….(candidate) Date……

Table of Contents

Nomenclature

Abbreviations

A	Area (m^2)
A_c	cross sectional area (m^2)
Al	Albedo
AR	aspect ratio
b	depth of duct (m) or separation of parallel plates (m)
B	building volume (m^3)
c_p	specific heat capacity (J kg^{-1} K^{-1})
C	cloud cover
C_d	Coefficient of discharge
Cp	pressure coefficient
Cr	radiation coefficient
d	diameter of orifice (m)
	thickness of material (m)
D	tube diameter (m)
D_e	equivalent diameter (m)
D_h	hydraulic diameter (m)
E	solar irradiance (W m^{-2})
	electrical energy
E’	solar irradiance (kJ m^{-2} h^{-1})
Ediff	diffuse irradiance (W m^{-2})
Edir	direct irradiance (W m^{-2})
Eg	global irradiance (W m^{-2})
f	friction factor
F’	efficiency factor of the solar air heater
F_R	collector heat removal factor
g	acceleration due to gravity (m s^{-2})
	glass surface
Gr	Grashof number
h	heat transfer coefficient (W m^{-2} K^{-1})
	hourly
h’	heat transfer coefficient (kJ h^{-1} m^{-2} K^{-1})

H	height of duct (m)
I	pressure loss coefficient
k	thermal conductivity (W m^{-1} K^{-1})
k’	thermal conductivity (kJ h^{-1} m^{-1} K^{-1})
K	area compensation factor
K_{cov}	equivalent heat transfer coefficient of the cover system (W m^{-2} K^{-1})
l	total flow path (m)
L	duct length (m)
L^+	dimensionless length
LW	long wave radiation (W m^{-2})
m	mass (kg)
$\dot{m}$	mass flow rate (kg s^{-1})
$\dot{m}$'	mass flow rate (kg h^{-1})
$\dot{M}$	mass flow rate per unit area (kg s^{-1} m^{-2})
N	inward flowing fraction of solar irradiation
Nu	Nusselt number
Δp	change in pressure (Pa)
p	pressure (Pa)
	absorbing plate
P	Perimeter (m)
P_{fan}	fan pumping power (W)
P_{flow}	flow pumping power (W)
Pr	Prandtl number
q	heat flux at duct wall (W m^{-2})
	power output (W m^{-2})
Q	Solar heat gain (W)
	power (W)
$\dot{Q}$	volume flow rate (m^3 s^{-1})
R	roughness (m)
	reflectivity
	thermal resistance
Ra	Rayleighs number
Re	Reynolds number

RMSE root mean square error

s stratification parameter (=0.5 for linear temperature gradient)

S solar radiation absorbed (W m^{-2})

SHGC solar heat gain coefficient

t time (s)

T Temperature (^oC)

T' Temperature (K)

$\overline{T}$ Mean temperature (^oC)

$\overline{T}$' Mean temperature (K)

U heat loss coefficient (W m^{-2} K^{-1})

U' heat loss coefficient (kJ h^{-1} m^{-2} K^{-1})

V flow velocity in duct (m s^{-1})

$\overline{V}$ mean flow velocity in duct (m s^{-1})

v wind velocity (m s^{-1})

v' wind velocity (m h^{-1})

W duct width (m)

y distance from the point to the bottom of the collector (m)

Greek

α absorptivity

solar altitude (^{o})

β coefficient of proportionality

volume coefficient of thermal expansion

ratio of orifice diameter to tube diameter

γ thermal gradient = 0.5 for linear

Δp difference in pressure (Pa)

ΔT difference in temperature (^{o}C or K)

ε emissivity

expansion factor

η efficiency

θ solar incident angle (^{o})

κ isentropic exponent

μ dynamic viscosity (N s m^{-2})

μ'	dynamic viscosity (kg m^{-1} h^{-1})
ν	kinematic viscosity [=μ/ρ] (m^2 s^{-1})
ρ	density (kg m^{-3})
σ	Stefan-Boltzmann constant (5.67E-8 W m^{-2} K^{-4})
σ'	Stefan-Boltzmann constant (2.04E-7 kJ h^{-1} m^{-2} K^{-4})
τ	transmissivity
ϕ	tilt angle (^{o})
$(\tau\alpha)_e$	effective transmittance-absorptance product

Summary

The project aim was to investigate the potential of a large scale, inexpensive, solar thermal façade in the UK climate. Profiled steel cladding was utilised as a solar absorber, with the channels used to form a series of parallel ducts when covered by a glass surface. Air was considered to flow through the ducts in two modes; forced or buoyant convection.

The factors affecting air flow were investigated in a laboratory experiment. The factors affecting solar heat transfer to the air were investigated using prototypes in field conditions. Three models for forced convection and two for buoyant were found in the literature. These were developed and compared against the experimental results to establish appropriate design models.

The design models were used to optimise the duct geometry for three desirable outputs; mass flow, temperature output or power output. Optimal duct geometry was found to depend on the flow mode assumed. In addition, the optimal geometry also depended on the required output. Thus it was determined that an optimal hybrid system which could switch modes as required, could not be configured; the function and utility of the system must be decided at the design stage and not reconfigured afterwards.

The annual performance of a building-scale south facing façade fitted with such a system (optimised for power output) was modelled for forced and buoyant convection modes. It was found that both flow modes had the potential to generate significant amounts of heat energy which could be used, for instance, to preheat ventilation air. The buoyant system also showed the potential for the generation of significant natural ventilation. However the forced convection system would have the advantage of being more controllable, have a better seasonal distribution of performance and have a greater potential for higher air exit temperatures to be achieved in winter.

1 Introduction

The continuing consumption of fossil fuels at current trends faces several problems. The rising costs of fossil fuels are a symptom of rising demands, political instability in many areas where known oil reserves remain, rising costs of exploration as well as the costs of recovering fossil fuels from less accessible areas. For the United Kingdom (UK) the prospect of becoming a net energy importer at a time of rising fossil fuel prices has also been a significant concern. Such issues led to the 2003 white paper 'Our Energy Future – Creating a Low Carbon Economy' [1].

In addition there is growing concern over the effect of fossil fuels on global warming. The Intergovernmental Panel on Climate Change has concluded that 'most of the observed warming over the last fifty years is likely to have been due to the increase in greenhouse gas concentrations' [2]. The financial cost of global damage of carbon emissions has been estimated as £70 per tonne of carbon (tC) [3].

These environmental and financial concerns have been reinforced by a selection of International, European and National legislation aimed at reducing carbon emissions. These include:

- The Kyoto Protocol of 1997 which became legally binding on its 128 parties on 16 February 2005.
- The EU Energy Performance of Buildings Directive 2002, which aims to save 45 MtC by 2010 across the European Union.
- The UK Climate Change Levy 2001, Renewables Obligation 2002 and Energy Efficiency Commitment 2002.

Analysis of UK energy consumption has shown that transport and domestic energy are the fastest growing sectors [4]. It has also shown that space and water heating account for more than fifty percent of non-transport energy use [5]. These trends have been reflected in other countries also. This makes heating a key area to reduce fossil fuel consumption. This could be achieved by energy efficiency measures (e.g. increased insulation) and by the use of renewable energy. Both methods of tackling the problem are suggested in EU Energy Performance of Buildings Directive [6]. In the UK, the main vehicle for implementing the directive is through the Part L Building Regulations

[7-10] which recommend that 10% of a buildings' energy should be met by low or zero carbon emission sources. People who are concerned about the increased costs of constructing a building which meets environmental targets have often overlooked the fact that 75-90% of a building's operational and maintenance costs have been determined once the design is completed. Figure 1.1 shows that although a 'green' building may cost slightly more initially, the overall costs throughout the lifetime of the building are dramatically reduced. This fact needs to be emphasised in a market where the capital costs are often the only figures considered [11].

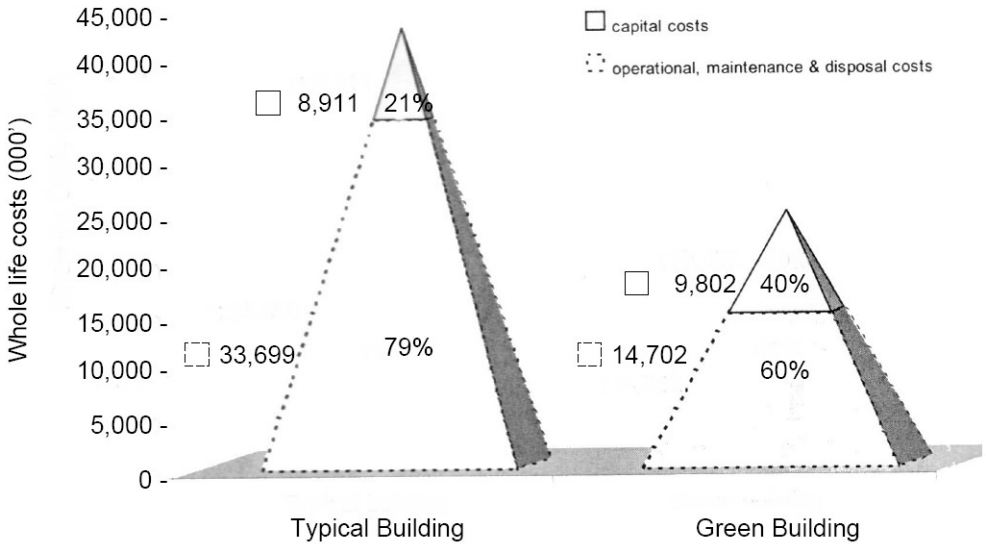

Figure 1.1. Whole life costs comparison [11]

The Microgeneration Strategy [12] is specifically advocating the use of small-scale, low carbon sources of energy. Solar energy is such a source, which is especially suited to buildings. Some existing methods of using solar energy in a building include:

- Photovoltaics (PV) – these can be installed in small sections, or as entire façades / roofs. The cost of a PV installation (£6,000 per kWpeak [13]) generally inhibits large scale use.
- Solar water heating systems – these are highly efficient, and independent trials have shown that around 60% of residential hot water could be met using them [14]. However, they tend to be installed in small sections (prices start around £2,000 [13]) and some customers have reservations about the possibility of leaks.

- Solar air heating systems - systems utilising glazed façades have been described by Jones [15] in his design for a ‘solar office’. The façade is expected to assist with heating the building in the winter and ventilating the building in summer.

One of the methods through which energy is being saved, is by cutting down air infiltration to buildings. This is effectively ‘accidental’ ventilation through cracks between windows and their frames etc. Although it is important to reduce this uncontrollable air flow, it is also important to retain adequate controlled ventilation for the occupants of a building. The revised building regulations [16] recommend that at least 10 l s^{-1} of outdoor air is supplied per person. Solar air heating may have a place in pre-heating ventilation air being fed into a building in preference to using fossil fuels to heat the building after cold air has been admitted.

In summary, there are several drivers for the use of renewable energy systems in buildings. Heating has been identified as a major area where the use of fossil fuels could be reduced, in favour of energy efficiency and renewable energy. Solar air heaters have potential to be integrated into the building and provide useful heat all year round, and particularly to ensure that ventilation is not sacrificed for energy efficiency.

In 2006, 8.5 million m^2 of profiled wall-cladding was sold in the United Kingdom [17]. Of this total approximately 5.3 million m^2 was used in a position with potential for solar energy capture, e.g. east, south or west facing walls. The average insolation level for the United Kingdom has been calculated as 2.4 kWh m^{-2} day^{-1} [18]. Thus, annually, the solar energy falling on one years production of precoated coil can be estimated at over 12.7 GWh. This indicates the potential which exists for significant building integrated solar energy.

1.1 Aims

The aim of this project is to investigate the potential for collecting solar heat in UK climate conditions through a relatively inexpensive, building integrated system utilizing covered profiled steel. A subsidiary aim will be to develop a simple design model

which could easily be used in industry to predict the performance of the system. Questions to be considered during this investigation are:

- Can covered profile sheet produce useful energy?
- Is the flow resistance small enough to allow use as a natural ventilated system?
- Can high enough temperatures be generated to provide heating?
- What factors will influence the heat performance?

This aim of the project will be met by carrying out the following objectives:

- Carry out a literature survey on solar air heaters, particularly in relation to predicting and optimising their performance.
- Use the information from the literature survey to predict suitable dimensions for full size prototypes. The prototype dimensions should be:
  - appropriate to ensure that the outputs of interest are likely to be measurable.
  - include enough variation to give indications of performance for different geometries.
  - feasible to build.
- Evaluate the flow characteristics of the system in the laboratory, in order to evaluate alternative theories on the relationship of pressure drop along the length of the duct to the duct geometry. This will be of significant importance in modelling ventilation systems, but also of concern in forced flow.
- Evaluate the heat transfer characteristics of the system in a field test to provide real life data on solar potential. This will also;
  - Demonstrate the potential for solar energy capture.
  - Demonstrate that the system is robust and would not be damaged in stagnant conditions.
- Develop and test models for forced and buoyant air flow in solar air heaters, to ensure a full understanding of the significant factors. The results of the model will be compared against the data from the prototypes to show that they are adequate at predicting the air exit temperature and power output of the duct.
- Choose the numerical design model which most accurately predicts the measured results from the outdoor prototypes. The chosen design model will be used to optimise the air heater geometry for forced and buoyant air flow.

- Use the design model to predict the annual output of the optimised system in Cardiff weather conditions.

1.2 Thesis Structure

To achieve the objectives stated above, several experiment and analysis phases are required. The experimental method for each phase is described in the relevant chapter.

The thesis is structured in the following way:

Chapter 2 contains the literature survey. This reviews suitable materials for solar air heaters bearing in mind practical and aesthetic considerations. The pros and cons of existing commercial solar air heaters are considered. Existing models which have been developed to predict the performance of a solar air heater, or which appear to be readily adaptable are also examined. Methods which have been utilised to optimise the heat transfer and overall performance of solar air heaters are also examined.

Chapter 3 covers the investigation of surface friction and its effect on the pressure drop across the length of a duct formed from covered profiled sheet. For forced convection solar air heaters this can affect the pumping power required to drive the system. For natural convection solar air heaters this will affect the air mass flow. The chapter begins with the experimental method – including the design and construction of the air movement experiment (referred to as Experiment 1). The results of the experiment and their relationship to alternate definitions of the friction factor are discussed. It concludes by suggesting the most appropriate definition for the friction factor for use in the models of the proposed device.

Chapter 4 covers the investigation of heat transfer within the device, from incoming solar energy to output air. The chapter begins with a discussion of the mechanisms operating within the solar air heater under forced convection. These are used to form a mathematical model to describe the system. Subsequently the experimental method – including the design and construction of the experiment (referred to as Experiment 2) to verify this model is considered. Experimental results obtained during forced

convection, buoyant convection and when the system was left in a stagnant condition are presented with some discussion. The correlation between the results predicted by the model, and the results obtained from the experiment is considered.

Chapter 5 utilises design models. The model developed in Chapter 4 is not suitable since it depends on measured values. However, suitable models to predict the behaviour of the model under forced convection and buoyant convection were previously identified in the literature survey. These results are analysed, and methods of improving the design models to better predict the measured performance are considered. Finally the most appropriate models for forced convection the most appropriate model for buoyant convection are identified and their accuracy is discussed.

Chapter 6 considers the optimisation of a solar duct using the best design models. The chapter begins with an analysis of the effect of changing the reflectivity of the absorbing surface. A reflectivity experiment which can compare the reflectivity of black and silver coloured absorbing surfaces is described. The results from the experiment are used to consider the effect of absorbing surface reflectivity changes on the output of the system. This is followed by a factorial analysis (based on the design models identified in chapter 5) to consider how the geometry of the duct could be optimised for exit air temperature and net power output under forced and buoyant convection.

Chapter 7 considers the application of the optimal solar ducts so developed on a large area (~200 m^2) south facing façade in Cardiff weather conditions. The predicted air exit temperature, net power output and air mass flow for a 200m^2 façade area over a year are presented.

Chapter 8 concludes the thesis, and summarises the findings.

Appendix A contains further details of the mathematical models identified in the literature survey.

Appendix B contains information on fluid dynamics relevant to the experimental work in Chapters 3 and 4 and the design model development in Chapter 5.

Appendix C contains information on thermodynamics relevant to the experimental work in Chapter 4 and the design model development in Chapter 5.

Appendix D contains information on the measurement of air mass flow relevant to the experimental work in Chapters 3 and 4.

Appendix E contains information on solar angle calculations relevant to the experimental work in Chapter 4 and the design model development in Chapter 5.

Appendix F contains error propagation calculations for the model described in Chapter 4.

Appendix G contains data required for the design model development in Chapter 5.

Appendix H contains the procedure followed for each of the design models in Chapter 5.

Appendix I contains data generated during the geometry optimisation calculations in Chapter 7.

When information from the Appendices is referred to in the main text, the Appendix will be named (e.g. referring to laminar flow as described in Appendix C). When an equation is referred to from an Appendix, the equation will be named (e.g. C13 would refer to equation 13 from Appendix C).

1.3 References

1. DTI, *Our Energy Future - Creating A Low Carbon Economy,* 2003, Department for Trade and Industry: London.
2. IPCC, *Climate Change 2001: The Scientific Basis,* 2001, Intergovernmental Panel on Climate Change.
3. DEFRA. *Climate Change: the cost of carbon.* 2006 22nd February 2006 [cited 27th March 2006]; http://www.defra.gov.uk/environment/climatechange/carboncost/index.htm.
4. *Indigenous fuel production down; consumption rose in 2004.* Energy World, 2004(323): p. 20.

5. DTI, *Energy Consumption in the United Kingdom*, 2004, Department for Trade and Industry.
6. European Parliament, *Directive 2002/91/EC of the European Parliament and of the Council of 16 December 2002 on the Energy Performance of Buildings*. 2002. p. LI65-LI71.
7. Office of the Deputy Prime Minister, *The Building Regulations: L2A Conservation of Fuel and Power (New buildings other than dwellings)*. 2006: Department for Communities and Local Government,.p.1- 36; 13 978 1 85946 219 5.
8. Office of the Deputy Prime Minister, *The Building Regulations: L2B Conservation of Fuel and Power (Work in existing buildings that are not dwellings)*. 2006: Department for Communities and Local Government,.p.1- 36; 13 978 1 85946 220 1.
9. Office of the Deputy Prime Minister, *The Building Regulations: L1A Conservation of Fuel and Power in new dwellings* Vol. 2006. 2006: Department for Communities and Local Government,.p.1- 35; 13 978 1 85946 217 1.
10. Office of the Deputy Prime Minister, *The Building Regulations: L1B Conservation of Fuel and Power in existing dwellings*. Vol. 2006. 2006: Department for Communities and Local Government,.p.1- 31; 13 978 1 85946 218 8.
11. Cheng, J., et al. *Towards Green and Intelligent Buildings: The Economic and Environmental Impact - a UK Perspective*. in *Conference for Postgraduate Researchers of the Built and Natural Environment (PRoBE)*. 2005. Glasgow Caledonian University, Glasgow, UK: Glasgow Caledonian University.
12. DTI, *Our Energy Challenge: Power from the people - Microgeneration Strategy*, DTI/Pub 8243/1k/03/06/NP, 2006, DTI.
13. DTI. *Renewables Explained: Solar - What can I do?* [cited 27th March 2006]; http://www.dti.gov.uk/renewables/renew_1.3.4.htm.
14. Hawkins, E., *Solar heating gets hotter*. Energy in Buildings & Industry, 2004: p. 32.
15. Jones, D.L., *The Solar Office: A Solar Powered Building with a Comprehensive Energy Strategy*, in *European Directory of Sustainable and Energy Efficient Building*, O. Lewis and J. Goulding, Editors. 1999, James & James: London. 8 - 13.
16. Office of the Deputy Prime Minister, *The Building Regulations: F Ventilation*. 2006: Department for Communities and Local Government,.p.1- 53; 13 978 1 85946 205 8.
17. Peacock, G., *Personal Communication: E-mail regarding sales of profiled wall cladding*, to E.V. Stevenson, 2007: Shotton.
18. Whitlock, C.E. and et al. *Release 3 NASA Surface Meteorology and Solar Energy Data Set for Renewable Energy Industry Use. 26th Annual Conference of the Solar Energy Society of Canada, 21-24th October 2000.* [cited 29th October 2004]; http://www.apricus-solar.com/insolation_levels_europe.htm.

2 Literature Survey

2.1 Introduction

This investigation is concerned with building integrated, solar air heating systems. Such a system requires a solar absorbing material to collect heat, a heat transfer medium (i.e. air) and a cover to retain the air. The heated air can be fed into a building to provide pre-heated ventilation air, reducing the fossil fuel consumption while attaining comfort for the occupants.

To develop a satisfactory solar air heating system, the thermal and physical behaviour of the proposed system must be understood. A literature survey has been carried out to identify existing solar air heaters and to assess the investigations which have already been undertaken into solar air heaters.

2.2 Requirements of a thermal solar system

2.2.1 Materials

The British Standard 'Thermal Solar Systems and Components – Solar Collectors' [1] suggests several requirements which are appropriate for solar collector materials:

- Non-combustible
- Able to withstand the maximum temperature which may occur at stagnation temperature, and the thermal shocks which may occur during the summer period.
- Resistant to UV- radiation
- Resistant to the mechanical loads resulting from heating and cooling
- Resistant to environmental stress from the factors such as rain, snow, hail, wind, humidity, condensate and pollutants.
- Able to withstand corrosion under normal operating conditions

Suitable materials need to be considered for the solar absorber and the cover. A method of joining these two elements in a system also needs to be considered.

2.2.1.1 Solar Absorber

An aim of the project is to investigate the potential of a building integrated system utilizing profiled steel in UK conditions. Profiled steel is a widely accepted construction product which is readily available. The Corus Colorcoat® Cladding system is an example of such a product. Colorcoat® cladding consists of a steel substrate with a metallic coating, pre-treatment, and a primer on both sides, with a paint topcoat and reverse side (commonly referred to as the backing coat). There are different metallic and organic coatings for particular applications [2]. The product selected for this application was Colorcoat Armacor® which is known to have good resistance to UV radiation and high temperatures. The black version was selected as it has the lowest reflection of the available colours [3].

The strength of the final profiled sheet will depend on the strength of the steel substrate used. The required strength of the steel used in constructing the solar façade would depend on whether the glass was being affixed to the Armacor®, or through the Armacor® to the supporting frame.

2.2.1.2 Transparent Covers

Glass or transparent plastic are generally used to cover solar collectors. Glass and tempered glass are generally considered to be durable. Plastics and coated glass are generally found to be less resistant to UV radiation and temperature variations. The degradation of these materials can affect the collector performance [1]. Glass has a high transmittance for solar radiation with a lower transmittance for longer wavelength (re-radiated) energy. In this way it allows the solar irradiance to reach the solar absorber, but inhibits the loss of re-radiated energy from the duct.

The standard factory dimension of float glass is 3.2 by 6 m [4]. However, the maximum size of glass which can be readily handled is dependent on its thickness. Panels of 6mm float glass can be as large as 4.55m x 3.15m; however, the maximum panel size for 3mm float glass is 2.4m x 1.3m [5]. Since float glass is already used in

façades and other construction applications, the procedures for its use as a construction material are already established.

However, the appropriateness of glass as a material for the building has to be considered. In school playgrounds or factory areas where fork lift trucks are working, it is advisable to restrict the use of more fragile cladding materials to above first floor height [6]. In many buildings, a solar air heating façade on the ground floor would be impractical due to shadows anyway.

2.2.1.3 Interaction of Materials

A practical product using this approach would need to ensure a safe and effectively sealed joint between the glass covering and profiled sheeting.

According to Hughes [6] UK temperatures on roof surfaces can range from -30 ^{o}C in the winter to over 80 ^{o}C in the summer. During clear days in spring and autumn it is possible to have diurnal temperature changes of 60 ^{o}C or more. Such temperature changes cause movement in the construction materials due to thermal expansion.

An unrestrained piece of steel 3 m long has been found to expand by between 0.9 and 1.05 mm under a 30 ^{o}C change in temperature. Under the same circumstances glass has been found to expand by 0.95 mm [6]. The similarity in the linear thermal expansion of the two materials would appear to be useful since the glass and the metal will be in parallel. However, the glass is likely to be at a lower temperature than the metal, and is therefore unlikely to expand to the same extent.

There are two potential methods for attaching these two materials; mechanical fasteners and adhesives.

If the glass is attached to a frame behind the cladding using mechanical fasteners which penetrate the cladding, elongated clearance holes will have to be sized and positioned to allow for movement of the fixing due to the difference in thermal

expansion of the two materials. There may be air leakage through these holes which may affect the energy efficiency of the system.

If an adhesive is used to attach the glass directly to the cladding, it will have to be selected to allow for some movement within the joint. The dimensions of the materials (i.e. the length and width of the steel cladding and glass panels) can be limited to ensure that the movement of the joint is within the tolerance of the adhesive. One-part silicone (high modulus) has a maximum tolerated movement of 20 % of the joint width. If this is not adequate, one-part silicone (low modulus) has a maximum tolerated movement of 50 % of the joint width. Both sealants have an expected service life of up to 20 years [7].

The silicone sealant can accommodate movement resulting from temperature changes, moisture, shrinkage of construction materials, sound, wind and other vibrations. It has even been found to reduce the resulting damage in small to medium-scale earthquakes [8].

Due to its relative simplicity, the adhesive approach will be considered to be the most appropriate.

2.2.1.4 Aesthetics

Munari-Probst et al [9] have carried out a European survey on the aesthetics of solar thermal collectors.

Initially a series of photos of existing solar thermal solutions on buildings were rated by Architects, Engineers and Façade manufacturers. The responses by the architects were split into three geographical areas (North Europe, Central Europe and South Europe). Figure 2.1 shows the photos and the ratings.

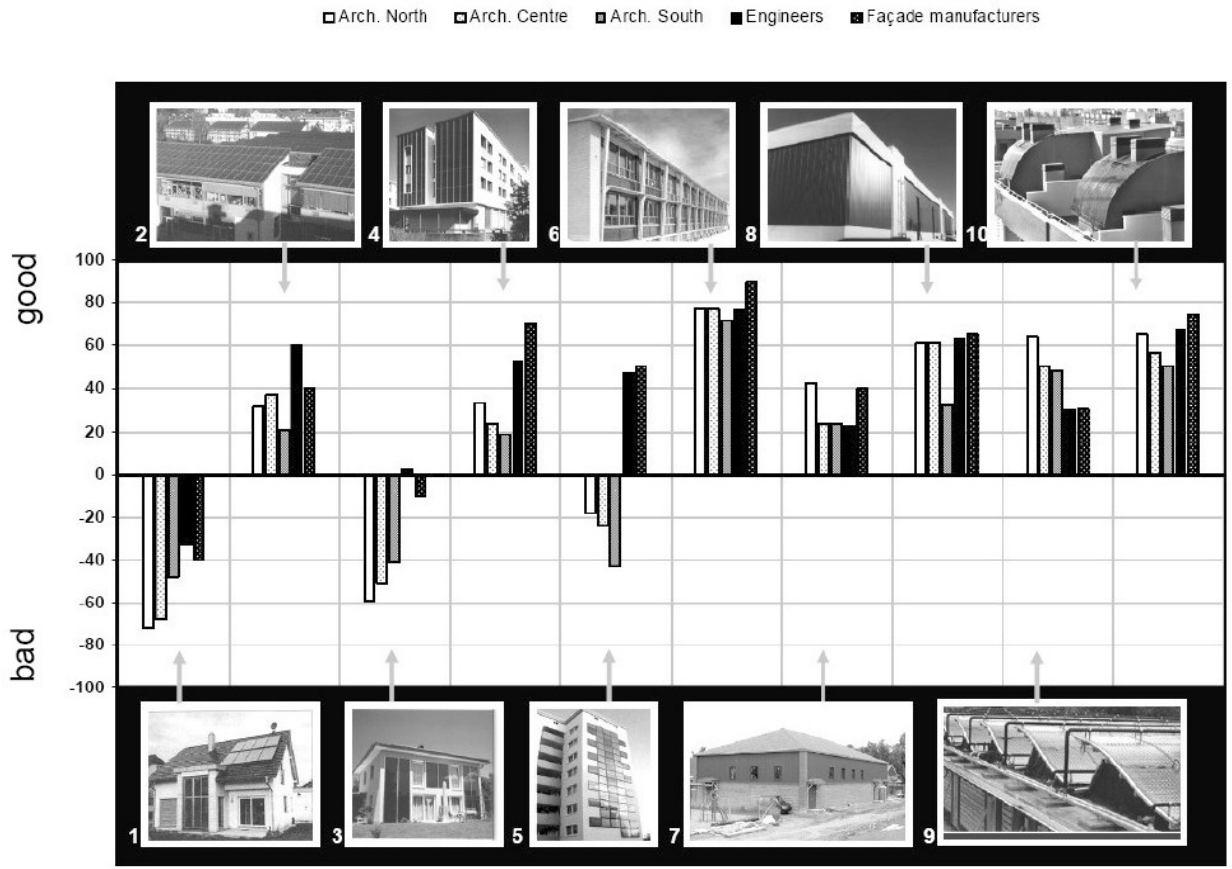

Figure 2.1. Survey of existing solar thermal installations [9]

The researchers were surprised to find that the dark colour of the solar elements was not considered as a negative factor by the architects. The size, shape, finishing and attention to detail were considered at least as important.

Some guidelines which were derived from Munari-Probst's questionnaires [9] were:

- The position and dimensions of the solar system should make sense in respect of the whole building – not just with respect to the façade exposed to solar energy (i.e. south facing façades should not be distinct from the rest of the building).
- The module size of the solar system should make sense in respect to the whole building (this can be particularly related to window grids)
- The colours and materials of the solar systems should be in context with the building
- When the solar element is integrated into the building as a construction element it is less intrusive.

In an attempt to find out preferences for future systems, questions relating to shape/size, surface texture and colour were also asked. Preferences on unglazed solar collectors were sought; therefore the most options were related to metal cladding systems.

When asked to compare plank style (Figure 2.2) and cassette style (Figure 2.3) cladding systems for future integrated solar elements, both were considered a valuable approach, although the plank system was considered to be more flexible – particularly by engineers.

Figure 2.2. Illustration of plank style cladding [9]

Figure 2.3. Illustration of cassette style cladding [9]

When considering texturing and finishing, the respondents tended to prefer traditional flat or profiled systems compared to more modern collectors based on embossed square shapes. Respondents unanimously preferred matt to a polished appearance. This would be a difficult requirement to meet using a glazed solar air heater, since the transmissivity of frosted glass is significantly lower than that of clear float glass. However, glass façades on buildings are popular and command a premium, so the requirement for matt surfaces does not appear to be universal.

Although the dark colours associated with solar elements were not considered a disadvantage on assessment of current systems, only 50 % of architects would be satisfied by a colour palette of 10 to 20 colours for future systems. A colour palette of up to 40 colours would be required to satisfy the majority of architects. If a very limited colour palette was going to be available, grey was considered to be an essential colour, followed by blues and reds. Greens, browns and yellows were less favoured. More importantly, architects wanted a range of shades of a colour (from light to dark) [9]. This could require the development of light coloured paints with lower solar reflectance.

2.2.1.5 Additional Costs

It has been assumed that profiled steel cladding is included in the base cost of a building. However, there would be additional costs to integrate a solar air heating system with the building façade. The scope of this project does not include the ducting which would be required within the building.

Glass

Griffiths [5] indicates the cost of float glass to vary from £28.79 m^{-2} (3mm thick) to £42.31 m^{-2} (6mm thick).

Silicone Sealant

The additional cost of silicone sealant depends on the thickness of the bead used to join the glass to the façade. A 6mm thick bead (which costs £0.44 per linear metre [10]) would be considered adequate assuming:

- wind load does not exceed 1.5kPa
- 6mm float glass with a maximum panel size of 2 m x 1 m
- each bead stretches the full length of the glass panel
- each bead is separated from the next by a distance of 0.2 m (Figure 2.4).

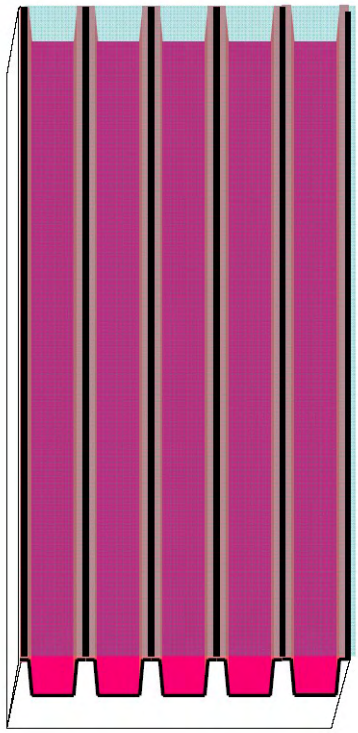

Figure 2.4. Glass Panel with Sealant Beads

One meter squared of glass would require six linear metres of sealant. The sealant would cost £2.65 per m^2 of glass.

Labour

It is difficult to estimate an accurate cost for the labour of assembling the system. The cost would depend on the assembly process. The system could be assembled as a cassette in a factory to be used on a building site at a later date. This would incur less labour, but higher equipment costs. Alternatively the system could be built in layers on site (i.e. assemble profiled steel layer, then the glazing layer).

2.3 Commercial Solar Air Heating Products

2.3.1 Solarwall® / InSpire™ Wall System [11, 12]

Conserval Engineering and ATAS International sell a solar air heating product. It is known as Solarwall® [12] when sold by Conserval Engineering and as InSpire™ [11] Wall when sold by ATAS International. The system consists of an aspirated dark-coloured, profiled metal cladding which is mounted onto the south face of a building. The schematic in Figure 2.5 illustrates how it works. The dark-coloured metal cladding is heated by solar radiation. A fan creates a negative pressure in the gap between the cladding and the inner wall. Outside air is drawn through the holes in the cladding where it is heated. The air in the cavity rises to a plenum at the top of the wall. The incoming warm air is transported into the building through a duct. The system also claims to reduce heat loss during the winter. In the summer the system can be bypassed, and the hot air can be ventilated through holes at the top of the cladding [12].

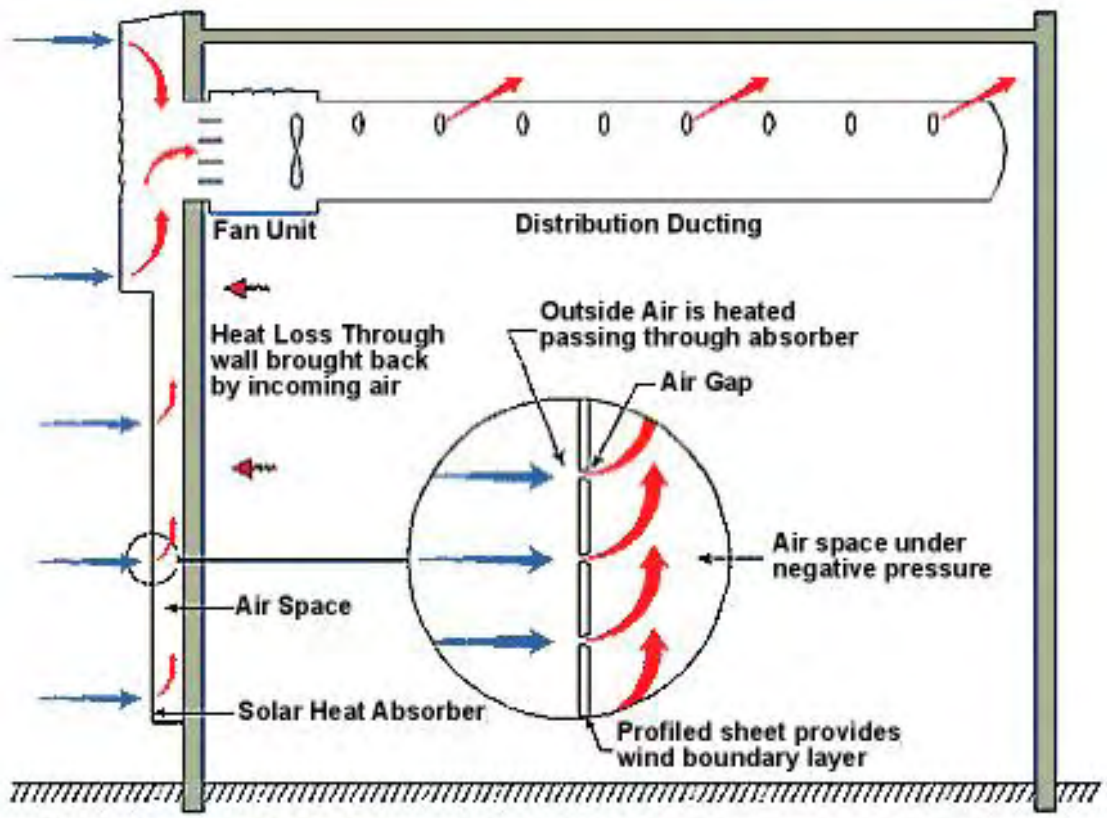

Figure 2.5. Schematic of Solarwall system [12]

Conserval Engineering and ATAS International claim that the system is highly efficient. However, it is only available in dark colours and is not available as a passive system. An example of the system is shown in Figure 2.6.

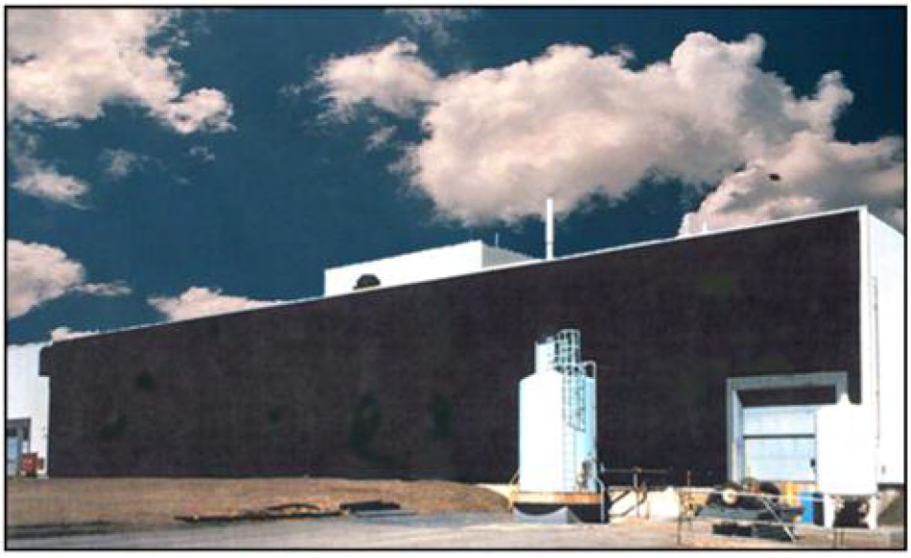

Figure 2.6. InSpire Wall - General Motors, Ontario, Canada [11]

2.3.2 Solar-Luft Systeme

Grammer have developed a solar air collector in conjunction with the Fraunhofer-Institut for solar energy systems in Freiburg. Air traverses through parallel channels made from U-shaped aluminium profiles [13]. This is considered the 'Mercedes' of air collectors in Germany (priced at €350 ~ 650 / m^2). It can run as a passive (Figure 2.7) or fan-driven system, and can incorporate photovoltaic cells (Figure 2.8).

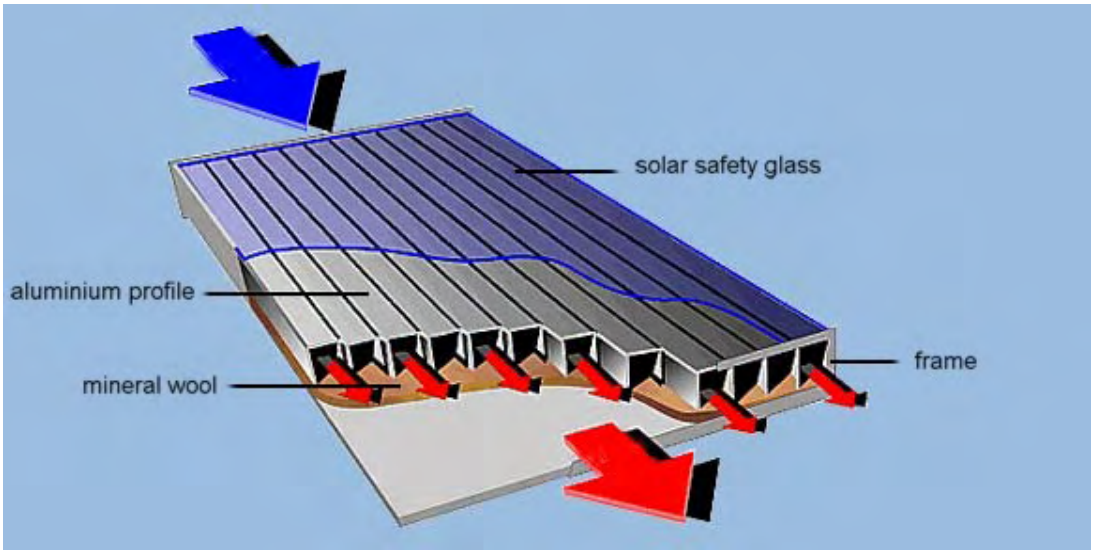

Figure 2.7. Solar-Luft - passive system [13]

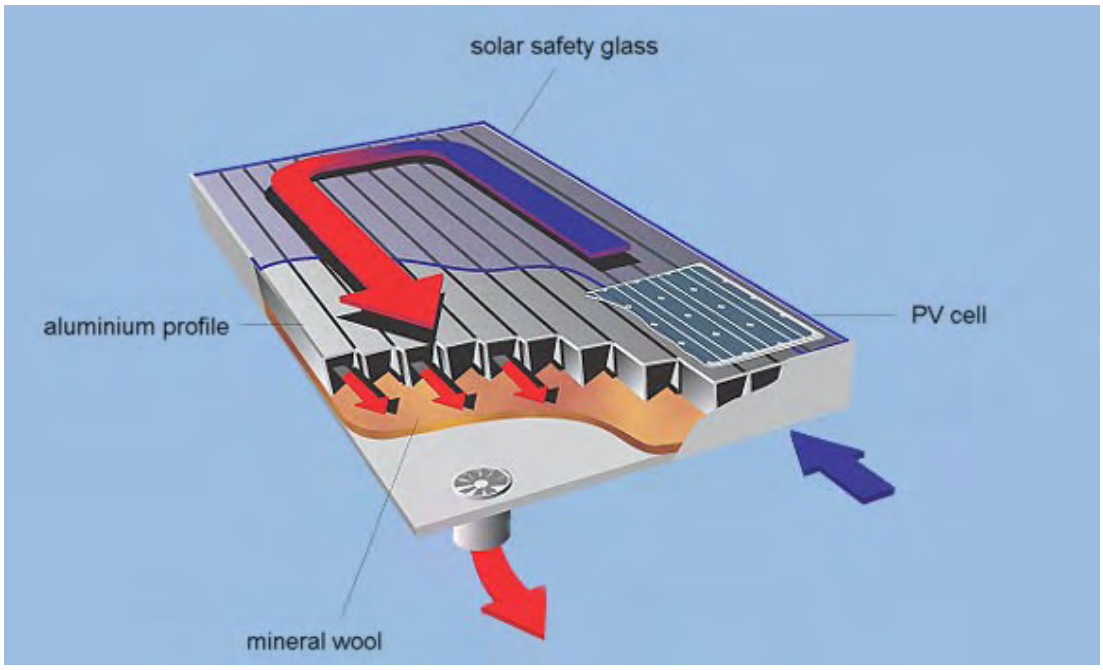

Figure 2.8. Solar-Luft - driven system [13]

However a schematic (Figure 2.9) from Shankland's paper [14] indicates that the system is only implemented on part of one façade. This type of installation runs contrary to the design advice by Munari-Probst [9] discussed earlier in this chapter.

Figure 2.9. Solaf-Luft system on Brocks Hill Millenium Park Environment Centre [14]

2.3.3 Nuaire Sunwarm

Nuaire provides a solar air heating system called Sunwarm [15]. This system is suitable for year round use as it incorporates a facility to draw air from the attic area when there isn't enough solar energy available to heat outside air. In warm weather, the system can be used to draw cool outside air into the building, and to heat water instead of air. Figure 2.10 illustrates how the system would work on a cold day, when air would be drawn through the panels on the roof. The warmed air would then be fed into the building, or used to heat water.

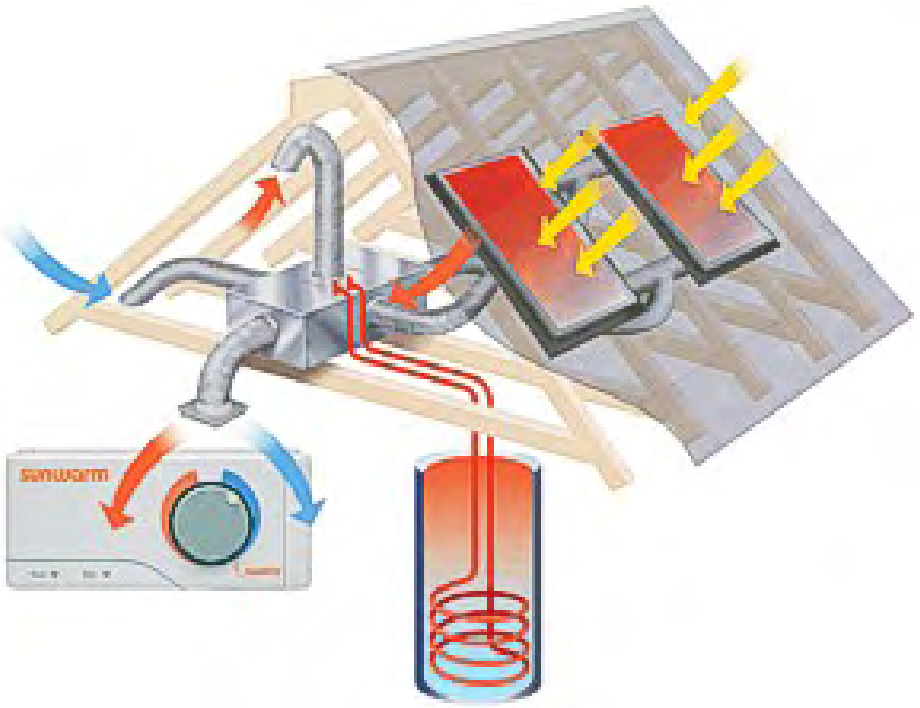

Figure 2.10. Schematic of Sunwarm system [15]

An example of a building with the Sunwarm system installed is shown in Figure 2.11, which shows that the absorber panel is a separate panel and not integrated into the roof.

Figure 2.11. Sunwarm installation [15]

2.3.4 Sun Lizard

The Sun Lizard [16] is a roof mounted air heating system which has been developed by BHP steel, the University of South Australia and the South Australian Housing Trust. Again, this is not an integrated system, and involves two roof mounted panels – one to heat the air and a PV panel to power the fans as shown in Figure 2.12.

Figure 2.12. Sun Lizard unit [16]

2.3.5 Comparison with proposed system

The Solar-Luft, Sunwarm and Sun Lizard solar air heaters described in this section have one main point in common – the designers have concentrated on high efficiency over a small area, which may have benefits for retrofit situations. However, such modular systems give rise to the aesthetic concerns raised in Section 2.2.1.4.

The Solar Wall® / InSpire Wall™ system does cover the entire façade but is only available in dark colours, and as a fan driven system.

The proposed system will utilise the building fabric, thereby reducing costs, and allowing the whole façade to be covered. The potential of the system to run passively will be considered, as will its sensitivity to light coloured absorbing surfaces.

2.4 Models describing Solar Air Heating Systems

This section will describe several mathematical models which have been developed for solar air heating systems. This will be preceded by an introduction to heat transfer.

More details on the models (including equations used) can be found in Appendix A. Terms relating to fluid dynamics can be found in Appendix B. Similarly terms relating to thermodynamics can be found in Appendix C. Equations labelled as (B..) or (C..) can be found in appendices B and C. Nomenclature has been changed from the original papers to allow consistency throughout the report.

2.4.1 Modes of Heat Transfer

There are three modes of heat transfer: conduction, radiation and convection.

Radiation is the transfer of heat without a medium, and is the form of heat transfer from the sun to the absorbing surface of the solar air heater.

Convection is the transfer of heat by a fluid, and is the major form of heat transfer within a fluid or between a fluid and a solid. This is the mechanism which allows the air in the heater to absorb heat from the solar absorber surface. The heat loss from the solar absorber to the air (due to convection) depends on the area of the material (A) and the convective heat transfer coefficient (h_c). The convective heat transfer coefficient in a duct is related to the Nusselt number (Nu) through the relationship [17]:

$$h_c = \frac{kNu}{D_h} \qquad \text{C2}$$

The Nusselt number is different depending on the situation. Significant effort has gone into identifying suitable Nusselt calculations for boundary cases [18]. Ong [19], Yeh and Lin [20] and Ho and Loveday [21] have used Nusselt number calculations which assume that the duct is two parallel plates, with one surface experiencing uniform heat flux, while the other surface is adiabatic. This is appropriate for systems

where the topmost surface is the solar absorbing surface (which can be assumed to receive uniform heat flux) with the air travelling underneath. The top surface absorbs and re-radiates heat to the air and surfaces below it. The radiative transfer from the top surface causes the temperature of the bottom surface to increase (no longer adiabatic), but this is considered to be a minor discrepancy. Glazed systems where the heat is transmitted through a cover to the absorbing plate (which is insulated) are further from this scenario, and therefore Nusselt numbers based on this assumption may no longer apply.

Conduction is the transfer of heat from molecule to molecule within a substance and is the major form of heat transfer within a solid. The heat flow rate (q) due to conduction is dependent on the thermal conductivity (k), area of the material (A), the distance it travels through the material (d) and the initial (T_1) and final (T_2) temperatures and can be described by the following equation [22]:

$$q = \frac{k}{d}(T_1 - T_2) \qquad \text{C1}$$

2.4.2 Ong [19, 23]

Ong indicated the heat transfers occurring between two parallel plates and derived a thermal network from this which is illustrated in Figure 2.13.

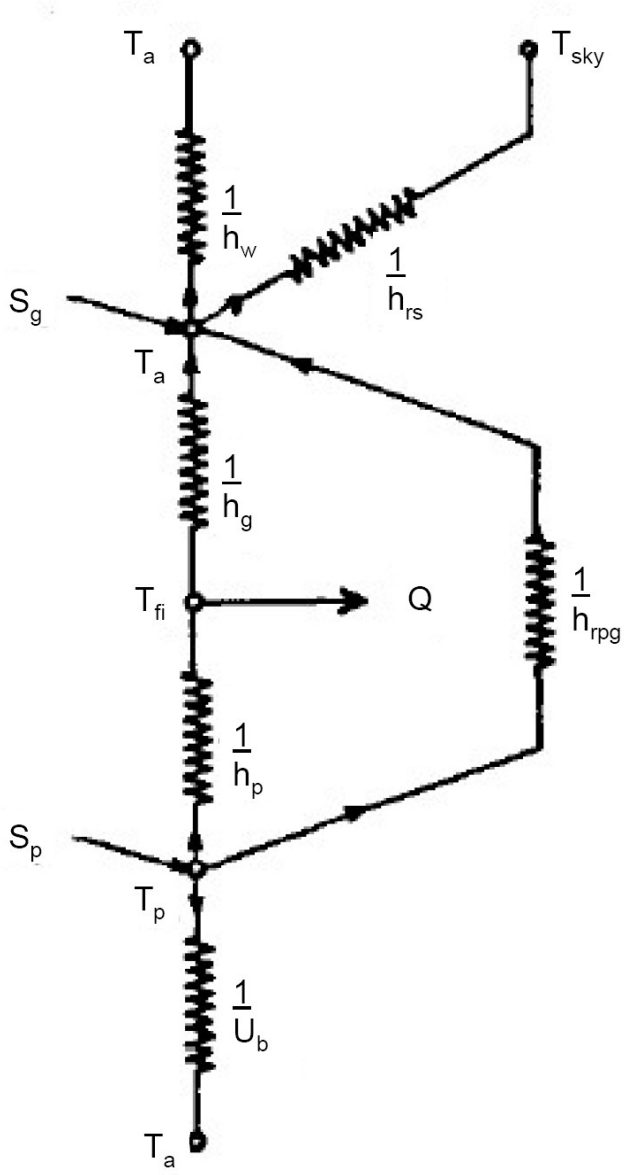

Figure 2.13. Representation of the thermal network for a solar air collector [19]

The thermal network shown in Figure 2.13 represents the scenario where solar irradiation is transmitted through the glass (surface 'g') to the absorbing surface (surface 'p'). Heat balance equations are derived for the two surfaces and for the fluid. The three heat balance equations are then represented as matrices, where the mean temperature can be determined by matrix inversion.

Ong considered that the fluid could obtain heat from the glass plate and the absorbing plate (the sides of the duct were ignored). Ong analysed the performance of a variety of definitions of the Nusselt number (related to the heat transfer coefficient by equation C2). He found several derivations of the Nusselt number which were suitable for specific circumstances and selected Nusselt's definition (C6) for use in the entry length region.

The model assumes that the fluid temperature gradient is linear. Such assumptions are only valid for short ducts. However, a long collector can be analysed as a series of ducts less than 1m long.

Solar radiation absorbed by the transparent surface is given by:

$$S_g = \alpha_g E \qquad 2.1$$

Solar radiation absorbed by the absorbing plate below the transparent surface is given by:

$$S_p = \tau_g \alpha_p E \qquad 2.2$$

This does not account for any variation in transmission or absorption due to incident angle of the solar irradiation. Nor does it account for any variation in the behaviour of diffuse or direct solar irradiation.

Although his original paper focussed on forced convection, Ong enhanced his model [23] in 2003 to account for buoyant air movement. Ong did not have any experimental data to validate his original matrix inversion model. However, he did use experimental data which had been reported by Hirunlabh et al [24] to partially validate his buoyant model [23]. Full validation was not possible since the exit air from Hirunlabh's solar chimney mixed with the ambient air, causing an unusual temperature gradient which Ong could not replicate with his model.

2.4.3 Yeh & Lin [20]

Yeh & Lin also analysed a glazed solar air collector. Yeh used the Hottel-Whillier-Bliss (efficiency) equation (C36) as the basis of his calculations. The useful heat passed to the fluid was considered. This required the Nusselt number (C12) derived

from Kay's [25] work on fully developed turbulent flow with one side heated and the other side insulated. Heat loss from the collector was also analysed and included Klein's [26] empirical equation for the heat loss through the top surface. An equation was constructed which showed the energy balance in the system. This was rearranged to derive the temperature of the absorbing plate or the fluid. The mean temperature was found by integrating the temperature from the entry to the exit of the duct.

Assuming that the collector geometry, material properties and weather conditions are known, initial estimates of temperatures could be used to carry out initial calculations. These calculations can be used to obtain values for the mean fluid and mean plate temperatures. The procedure is repeated until the variance between iterations is excluded from the temperatures; then the final efficiency can be calculated. This analysis technique was validated against a physical experiment at flow rates of 0.0107, 0.0161 and 0.0214 kg s^{-1}. It was found to give a better correlation for lower air mass flow rates.

This model has not been developed for the analysis of buoyant flows.

2.4.4 Ho and Loveday [21]

Ho and Loveday developed their model for a system with a multi-layered polycarbonate glazing. Like Ong [19], they carried out an energy balance at the top surface, at the fluid and at the bottom surface. These energy balances differed from Ong's since Ho and Loveday have assumed that the top surface does not absorb any solar irradiation. However, they have used polycarbonate as their top surface and have accounted for natural convection within the polycarbonate partitions. Ho and Loveday's equations also include the factor K to compensate for the area difference caused by the profile of the absorber surface. Since their glazing cover is suspended 0.1m above the top surface of the profiled steel, their system more closely approximates the assumption of parallel plates.

Instead of arranging the energy balance equations to be solved by the matrix inversion technique; Ho and Loveday arrange them to be solved explicitly.

It is assumed that the convection heat coefficient for the inner cover surface is the same as that for the absorber surface. Again the Nusselt number (C12) has been derived from Kays work [27] on fully developed turbulent flow with one side heated and the other side insulated.

This model was validated through experimental testing. An advantage of this model over Ong's is that it can accommodate different ambient temperatures at the front and rear of the collector.

This model has not been developed for the analysis of buoyant flows.

2.4.5 Guan [28]

The model used by Delahaye et al [29], is described by Guan in his thesis. Although Delahaye et al considered three types of solar collector, only the model for analysing the glazed solar collector is considered here.

The definition of absorbed solar power is similar to Ong's, and does not account for solar incident angle or the different behaviour of direct and diffuse solar irradiation. However, unlike Ong's model, it does not allow for any solar absorption by the glazing.

An equation to describe the energy balance of the absorbing plate, was combined with the formula for the mass of the absorber. This enabled the thermal mass of the system to be incorporated into the model.

This model was operated inside a Matlab environment, and as such was able to incorporate a more complicated structure. The duct was considered as several segments. In addition the system incorporated two definitions of the Nusselt number: one for laminar and one for turbulent flow. It also calculated a mixture of these Nusselt numbers to cover the transition area. The actual Nusselt numbers were taken

from Pottler [30]. For laminar air flows, the Nusselt number was able to take account of the heat transfer coefficient from both the absorbing plate and the glazing plate.

Even such a complex model had limitations:

- It was based on experimental measurements with their associated errors (e.g. 5% error in air mass flow calculations, 1K error in temperature measurements).
- It was based on theory which was optimised for air mass flows of 0.025 to 0.083 kg s^{-1}, and was less reliable for lower flow rates.
- Each slice of the duct was considered as a separate entity

As a result of these limitations, the model tended to underestimate the temperature at the bottom of the duct and overestimate at the top.

This model was not developed for the analysis of buoyant flows.

2.4.6 Brinkworth et al [31-35] & Sandberg and Moshfegh [36-40]

Brinkworth et al [31-35] & Sandberg and Moshfegh [36-40] have both carried out considerable work on the cooling of photovoltaic façades attached to buildings. Although this work was not aimed to design a model to predict the behaviour of a solar air heater, the scenarios are similar. In particular, these models generally pay close attention to the buoyant movement of air, which is not always accounted for in solar air heater models. However, solar incident angle and the different behaviours of direct and diffuse solar irradiation are not included in these models since that is not relevant to their original aim.

Sandberg and Moshfegh's work has mainly involved a computational fluid dynamics (CFD) model, which is beyond the scope of a simple Microsoft Excel based model. However, the work of both teams has culminated in a joint paper between Brinkworth and Sandberg [41] which describes a model for buoyantly induced flow in ducts.

The driving forces for air movement are considered to be buoyancy and wind, while resistances are considered to be wall friction and other hydraulic restrictions.

The basic model has been validated for vertical smooth-walled ducts without obstructions or wind effects where the ratio of length to hydraulic diameter (L/D_h) is between 5 and 30, the correlation still holds (but not as tightly) for L/D_h up to 50.

Brinkworth et al [35] had previously reported their findings on the heat transfer part of the model. They derived their Nusselt number (C18) from the work of Kakac et al [18] relating to parallel-plate ducts.

2.4.7 Summary of Models

Four models for forced convection have been described in the literature; however, the Guan [28] model is outwith the scope of this investigation. The Ong [19], Yeh & Lin [20] and Ho & Loveday [21] models will be considered in Chapter 5. Ong [23] and Brinkworth [31-35, 41] have proposed models suitable for buoyant convection. Both models will be considered in Chapter 5.

2.5 Improving Solar Air Heating Efficiency

Many factors can affect the solar air heating efficiency, such as: the geometry, the configuration and the extension of the air flow path. These factors will be considered in this section

2.5.1 Solar Air Heating Geometry

2.5.1.1 Hollands and Shewen [42]

Hollands and Shewen [42] considered the collector as two parallel plates. The top surface was the (opaque) absorbing plate and the bottom surface was considered to be adiabatic. Since the top surface was opaque the only source of temperature increase available to the bottom plate was from radiative transfer from the absorbing plate.

They concluded that reducing the duct spacing would increase the pressure drop across the duct, thereby increasing the fan pumping power requirements. However,

by reducing the distance travelled by the air in the collector the pressure drop could be reduced. By reducing the distance travelled by the air, they also would benefit from the higher convective heat transfer coefficient which is experienced within the entrance length of the duct; in a short duct, this entrance length becomes a significant proportion of the total. Since they could not expect to heat the air significantly in a short duct, they suggested that a long collector could be constructed with multiple air entrances and exits along the length (Figure 2.14). This allowed the air leaving one section to be fed back into the collector at a later stage to collect more heat.

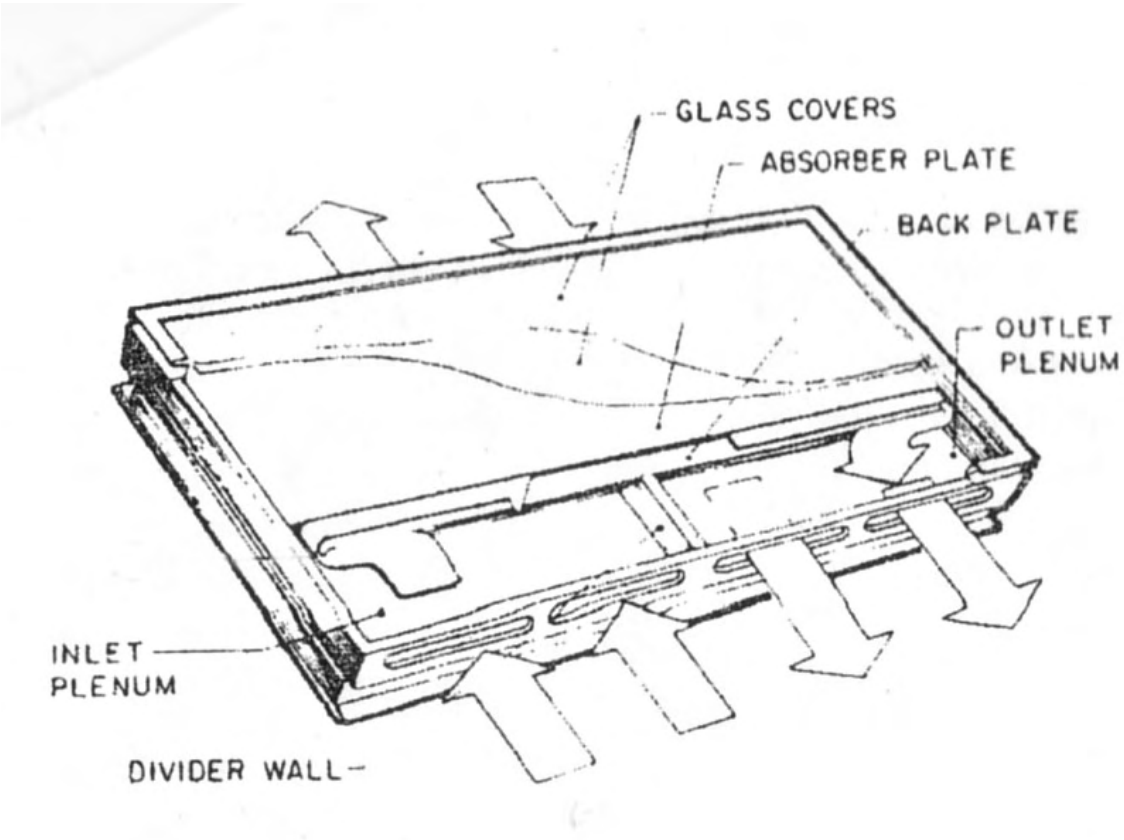

Figure 2.14. Collector proposed by Hollands and Shewen [42]

2.5.1.2 Sandberg and Moshfegh [36-38, 40]

Sandberg and Moshfegh examined the scenario where the temperature of photovoltaic cells increased during exposure to sunlight. The increased temperature behind the PV cells can induce natural convection which can be used to cool the PV cells, thereby

improving their electrical efficiency. Although this scenario is more concerned with cooling the PV cells than obtaining heat for use in a building, some of the findings are relevant.

An experimental geometry assessment [38] was used to verify a CFD model [37]. The CFD model can give more detailed output than an average plate or fluid temperature. A temperature profile was produced which indicated that the fluid undergoes a temperature gradient within a few centimetres of the unheated wall. The output fluid temperature shows a jump when the input power was increased from 20 to 200 W m^{-2}, but did not increase significantly when the input power was increased to 400 W m^{-2}.

Analysis of 0.21, 0.23 and 0.25 m plate spacings indicated that decreasing the plate spacing:

- reduces the relative flow rate (due to increased frictional resistance from channel walls)
- increases the outlet air temperature

It was found that changing the duct spacing changed the ratio of convection / radiation power exchange: increasing the duct spacing increased the proportion of convection heat transfer and decreased the radiation heat exchange between the surface boundaries. Further work by Sandberg and Moshfegh [36] reinforced this finding.

Sandberg and Moshfegh continued their work by analysing the air collector geometry – in particular the positioning of the solar cell modules and restriction of the outlet. It was found that if the outlet was left unrestricted, the flow rate increased and became turbulent. For a given heat input the flow rate could be maximised by increasing the height of the air gap until a balance between friction and buoyancy forces was obtained.

2.5.2 Solar Air Heater Configuration

2.5.2.1 Ong [19]

Ong used his matrix inversion model to compare the performance of four types of solar air collector:

Type 1 - Single Channel with single air flow between top glass and bottom absorbing plate

Type 2 - Single Channel with single air flow between top opaque absorbing plate and bottom insulated plate

Type 3 – Double Channel with no air flow between glass and absorbing plate, but with air flow between absorbing plate and backing plate

Type 4 – Double Channel with air flow between glass plate and absorbing plate and between absorbing plate and backing plate

All four ducts were 10m long and 0.254 m wide. The spacing between each pair of plates was 0.0254 m. The assumed weather conditions were: T_a= 27 ^oC, wind velocity of 1 m s^{-1} and solar irradiation of 700 W m^{-2}. Ong deduced that each collector type had a higher efficiency for air mass flows of 0.04 kg s^{-1} compared to 0.004 kg s^{-1}. The air mass flows were assumed to be induced using a fan. He also indicated the efficiency ranking by type (best first) was Type 4, Type 3, Type 1 and Type 2. However, Types 3 and 1 produced output air at the highest temperatures.

2.5.2.2 Yeh et al [20, 43, 44]

Yeh et al used a combination of experimental and analytical modelling to determine the optimum position of an insulating vertical barrier in the air heater to form two subcollectors (Figure 2.15). The air flows up the first channel and returns by the second channel (fan induced flow).

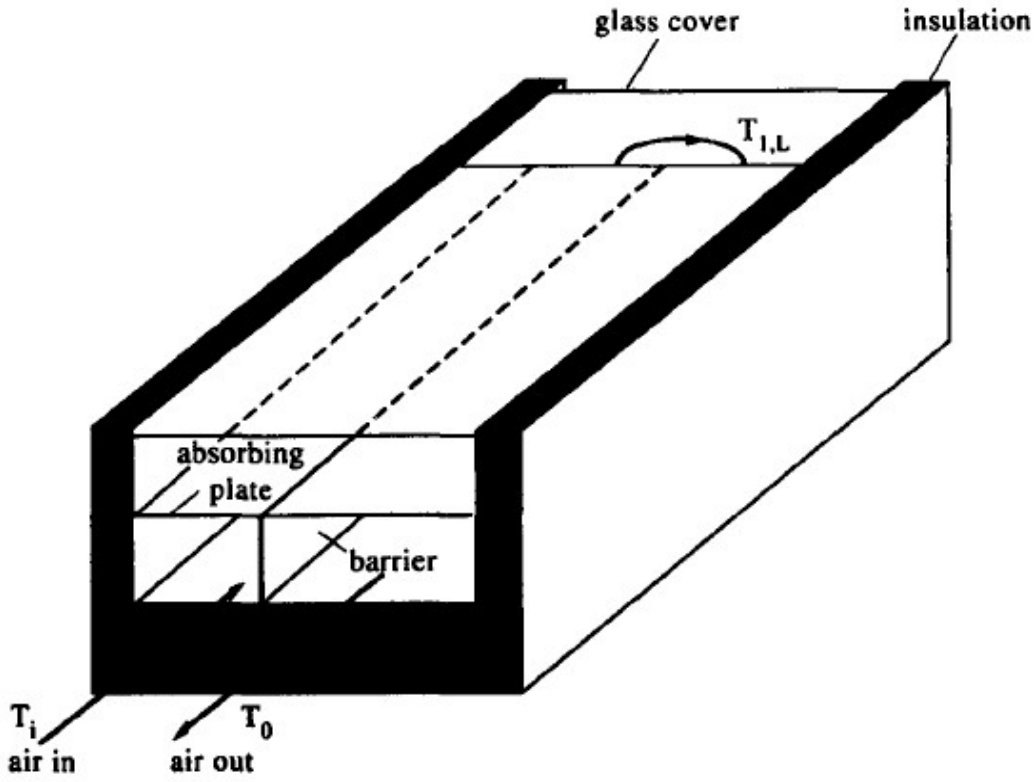

Figure 2.15. Solar air heater with a dividing barrier [20]

The following ratios of W1/W were examined: 1/6, 1/5, 1/4, 1/3, 1/2, 2/3, 3/4, 4/5, 5/6 and 1/1 for three mass flow rates (0.0107, 0.0161, 0.0214 kg s^{-1}). It was found that the optimum ratio of W_1/W is 1/2.

In a later paper, Yeh et al [43] used a similar methodology to analyse a collector with two covers and where the air flow occurred above and below the absorber plate. Allowing air to flow above and below the absorber plate will increase the heat transfer area and should lead to improved thermal performance. Physical and theoretical analysis found that the optimum split of the mass flow between the upper and lower ducts was 50:50.

Yeh et al also considered a collector divided into multiple sub-collectors formed by fins (barriers) with the flow further disrupted by baffles [44]. This was analysed with a similar methodology as before.

They concluded that collector efficiency improved if air flow took place over the absorber plate rather than under; however, in this case a second cover plate was required to reduce heat loss from the top of the solar air heater.

Increasing the aspect ratio (L/W) of the collector improved the collector efficiency. This was linked to the decreasing cross sectional area of the air duct and resulting increased air flow velocity and convective heat transfer rate from the surface of the absorbing plate. Alternatively, inserting fins and baffles can increase the heat transfer area and produce air turbulence improving the collector efficiency. However both these options require higher production costs and fan power (leading to higher operation costs) and potentially affecting their economic viability.

2.5.2.3 Delahaye et al [29]

Delahaye et al [29] have looked at the optimization of a solar air heater incorporating Fischer Profil steel cladding. Their practical work involved building three 8 m high solar air heating prototypes (Figure 2.16):

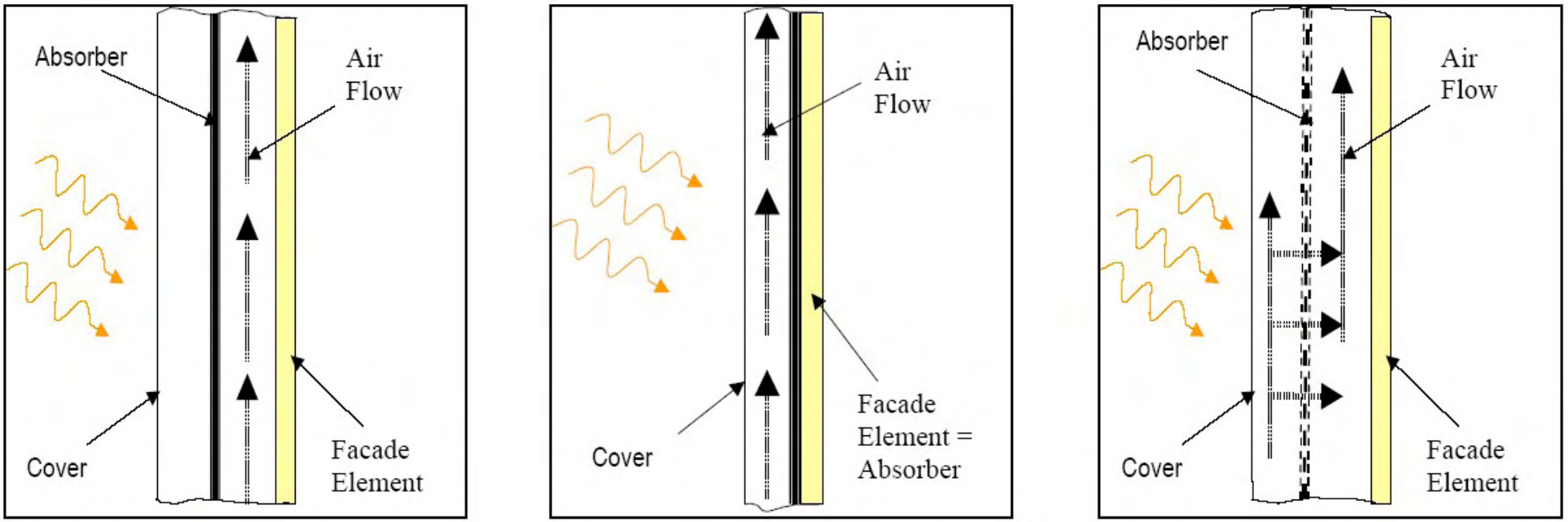

Figure 2.16. Schematic illustrating under flow, over flow and permeable solar air heaters [29]

1. with the air traveling under the absorbing material
2. with the air traveling over the absorbing material but under the cover
3. with the air being drawn through perforations in the absorbing material

The solar absorber was steel painted with Type M40 Li solar paint from Co. Transfer-Electric. The duct cover was 3 mm Makrolon (Perspex), which was attached mechanically to wooden spacers, which were attached to the absorber. The resulting duct depth was 100 mm between the cover and the absorbing material. The over flow prototype suffered from high levels of air leakage – this has been attributed to the different coefficients of expansion between the Makrolon, the steel and the wooden strips. The system was tested under natural convection and forced flow rates up to 0.033 kg s^{-1} m^{-2}. It was concluded that the under flow collector gave the best thermal performance. The system has been costed at 20-32 Euro m^{-2}. A computer simulation indicated that pay back could be expected within 3 to 5 years based on:

- the weather conditions for a south facing façade in Wurzburg, Germany
- heating costs of 50 Euro/MWh.
- under flow system predicted yield 444 k Wh m^{-2} per annum
- over flow system predicted yield 392 k Wh m^{-2} per annum
- permeable system predicted yield 419 k Wh m^{-2} per annum [29].

2.5.2.4 Brinkworth and Sandberg [41]

Brinkworth and Sandberg used their model to investigate the effect of obstructions at the entry and exit. They found that standard industrial netting which is often used to exclude colonization by birds and insects (mesh 1.7 mm, thread diameter = 0.25 mm, corresponding to an area ratio or porosity of 73 %) has a higher than expected impact on the pressure drop. In fact it causes a more significant pressure drop than an inlet restricted to 25 % of its original area. Analysis of hooded outlets (90^o bend to prevent rain ingress) has indicated that the opening area should be at least twice the area of the duct to avoid excessive losses.

2.5.3 Extension of the Air Flow Path

2.5.3.1 Matrawy [45]

Matrawy investigated a multiple flow air collector. This design was similar to that investigated by Yeh [20], but with additional equispaced fins/vanes. Matrawy also used a similar model to Yeh [20] to analyse the benefits of using vanes to form subcollectors. It was found that increasing the number of vanes beyond 10 gave no significant increase to the collector efficiency. A duct depth of 0.04 – 0.06 m was found to be suitable for satisfying a low pressure drop with an appropriate efficiency of the collector.

The importance of depth as a design factor was emphasised with the following points:

- the convective heat transfer coefficient decreases as depth increases (related to the increased air velocity at the smaller depth)
- the area of the metal vanes (which increase the heat transfer to the flowing air) increases as the depth increases
- less heat is conducted to the back plate as the depth increases
- the pressure drop through the collector decreases as depth increases.

2.5.3.2 Kurtbas and Durmus [46]

Kurtbas and Durmus investigated the effects of positioning four barriers in the air flow of the duct to ensure that the air had to take an undulatory path to the exit, thereby extending the flow path. He also investigated the effects of the surface texture of the absorber as shown in Figure 2.17.

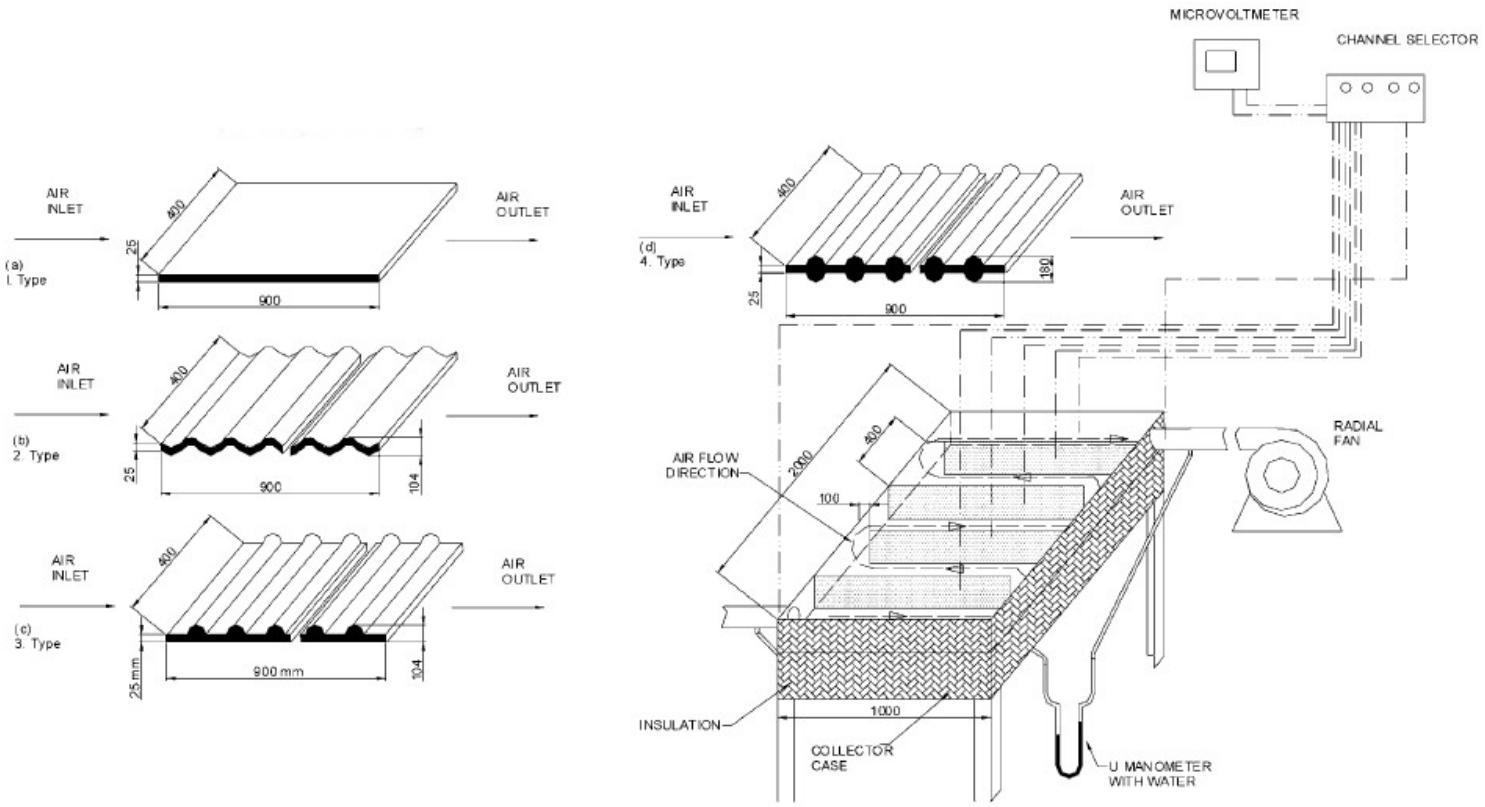

Figure 2.17. Kurtbas and Durmus Experimental Layout [46]

Within a collector 2 m long and 1 m wide, they investigated the following

Type 1 five sections - flat plate gap rising from 25 mm to 180 mm above flat plate

Type 2 five sections - undulating plate 25 mm above flat plate

Type 3 five sections - flat bottom surface with ridges on top surface 25 mm above flat plate

Type 4 five sections - ridges on both surfaces 25 mm above flat plate

Type 5 was a control where the air was allowed to travel directly from entry to exit (no barriers)

The collector efficiency (η) can be calculated from the ratio of solar heat gain (Q) to solar irradiation (E) over the area of the collector (A):

$$\eta = \frac{Q}{EA} \qquad \text{C35}$$

Maximum efficiency for each geometry type was:

Type 1 29.2 %

Type 2 44.3 %

Type 3 60.4 %

Type 4 67.0 %

Type 5 16.0 %

These efficiencies were obtained at a mass flow of 0.028 kg s^{-1}, lower efficiencies were found for lower air mass flows. These efficiencies indicate that extending the flow line of the air is beneficial. Introducing obstructions to the air flow is thought to cause an extension of the flow line as well as introducing swirl and secondary flows, thereby increasing the heat transfer coefficient. However, the pressure drop increased from approximation 1.5 to 4 Pa by introducing the increased flow path and surface obstructions. This would have a significant effect on a passive system.

2.5.4 Integration of Photovoltaic and Solar Thermal Collectors

Hegazy's [47] main interest was the integration of photovoltaic and solar thermal technology for the maximum combined efficiency. He investigated the relative

positioning of the absorber plate and the photovoltaic cells to achieve the best combined performance (Figure 2.18).

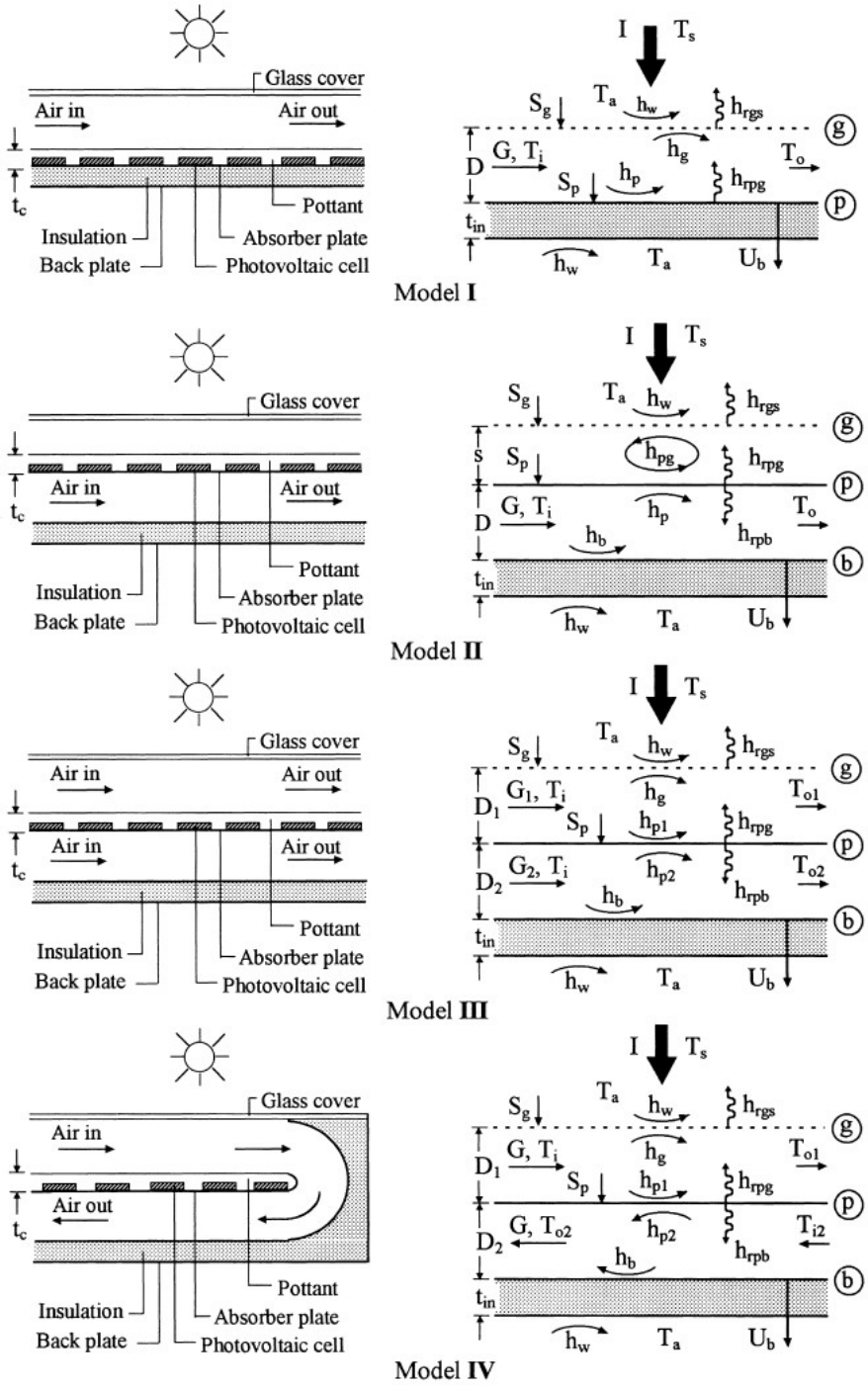

Figure 2.18. Relative positioning of photovoltaic and thermal absorbers [47]

He also considered the implications of powering the solar thermal fans, with electrical power from the photovoltaic cells. He assumed that the fan efficiency was 74 %, and that of the electrical motor was 90 %. From this the calculation of instantaneous power required for circulating a certain amount of air (P_{fan}) became:

$$P_{fan} = \frac{P_{flow}}{\eta_{fan}\eta_{motor}} = 1.5P_{flow} \qquad 2.3$$

Where P_{flow} was the flow pumping power which is dependent on collector geometry.

Hegazy believed that the fan power should be supplied from storage batteries supplied by the PVs. Assuming the following energy losses:

- 10 % in the batteries
- 5 % charge regulator
- 15 % inverter
- 2.5 % cabling

Then approximately 70 % of the PV energy is stored. However, only 80 % of this stored energy can be recalled from the batteries. Thus only 56 % of the PV power is useful. The net available electrical energy can be determined as the useful PV power minus the fan pumping power.

Hegazy found that the combined efficiency of Type 1 was poor compared to the other models which were similar to each other.
It also indicates that the PV could afford to run the fans:

- where $\dot{M}$ <= 0.02 kg s^{-1} m^{-2} for Models I and II
- where $\dot{M}$ <= 0.025 kg s^{-1} m^{-2} for Model IV
- where $\dot{M}$ < 0.035 kg s^{-1} m^{-2} for Model III

Since it would be disadvantageous to pump high flow rates through the collector in the periods of low solar irradiation (E < 400 W m^{-2}), particularly during the two hour interval after sunrise and before sunset power savings could be made during these two periods. This could amount to 25% of the daily fan power requirements.

2.5.5 Other Methods

Hachemi's [48] literature survey mentions methods which have been investigated with the aim of improving the energy efficiency of solar air heaters. These include

the packing of the air space with iron filings by Yeh and Ting [49] which improved the heat transfer, but caused increased electricity consumption by the fan powering the air flow. Slit and expanded aluminium foil matrices [50] assessed by Chiou et al and blackened wire screen matrices [51] were both found to improve the thermal performance of the collector.

Hachemi [48] focused his analysis on the effects of selective (transmits heat mostly by convection) and non selective (transmits heat mostly by radiation) absorber plates. He found a slight benefit from the selective absorber plate when loss mass flow rates were used.

2.5.6 Solar Efficiency Conclusions

It has been established that reducing the spacing between the duct plates improves the heat transfer coefficient between the absorber plate and the air. However, this also increases the pressure drop along the duct – reducing the chance of the system being driven by buoyant flow, or increasing the electricity requirements of the fans if forced convection has been arranged.

Introducing iron filings to the air space increased the heat transfer area, and was found to improve heat transfer but also increased the pressure drop along the duct.

Dividing the air channel with vanes, fins and/or baffles induce turbulent flow and increase the flow path that the air takes through the duct. This increases the air output temperature from the duct. However, these alterations tend to increase the pressure drop across the duct and also increase the cost of manufacturing the air collector system.

Introducing a second air flow channel, so that there is air flow along both sides of the absorbing surface increases the heat transfer area, and overall efficiency of the system. Again, this extra engineering increases the manufacturing cost.

This section indicates that optimising the duct geometry to maximise the efficiency without causing an unnecessary resistance for the air flow will be the most economic way optimising the system.

2.6 Conclusion

Engineers have tended to concentrate on developing small, high efficiency solar air heating systems. However, architects are strongly influenced by the concept of a solar heating system 'making sense with respect to whole building'. This indicates that systems which entirely clothe a building or which can be incorporated into the overall building design would be more widely accepted. Other aesthetic points which have been made are:

- solar elements should be made available in a range of colours and shades.
- matt surfaces are preferred.

Assessment of the materials typically used in solar air heaters indicates that black Colorcoat Armacor® will be suitable as an absorber plate and that glass will make a suitable solar transmitting cover. These materials will be used for the prototypes (Figure 2.19) discussed in Chapters 4 and 5. In order to design a suitably dimensioned solar air heater, a design model will be required to assess likely performance depending on geometry at prospective sites.

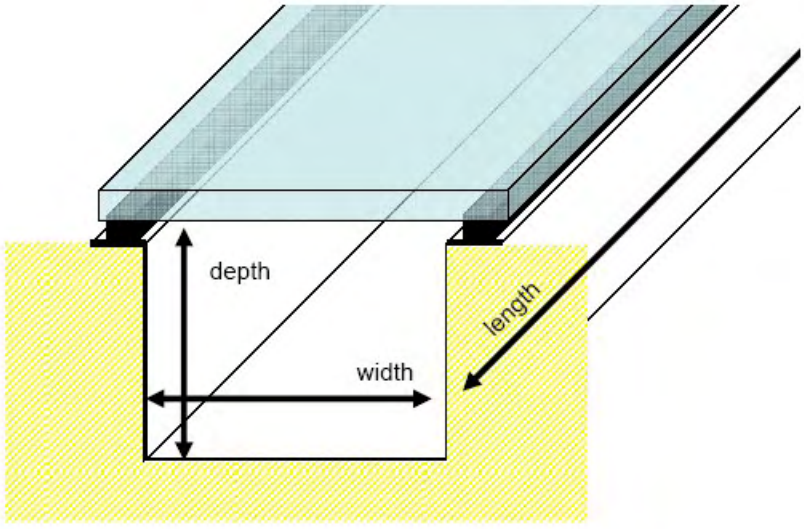

Figure 2.19. Illustration of solar collector structure

Three models for forced convection and two models for buoyant convection were found in the literature, and will be assessed as part of the project.

The most cost effective method of improving efficiency appears to be to optimise the geometry. A few key findings have been found from the literature:

- The convective heat transfer coefficient is higher within the entrance length of the duct, and when the duct spacing is reduced. However, reducing the duct spacing increases the required fan pumping power.
    - The methods suggested to increase the heat transfer (i.e. adding vanes to form sub-collectors, adding barriers to increase the air flow path, or packing the air space with iron filings) all increase the required fan pumping power.
- The efficiency can be increased by utilising a double channel with air flow in both channels; however, this is more expensive to build.

If increasing air output temperature is considered more important than collector efficiency, increasing the air path distance is effective.

This information leads to the final concept of air solar collector to be tested and optimised in the project. The duct will be formed from black Armacor Colorcoat® covered with float glass. The geometry parameters which will be optimised are: length, width, depth and tilt angle.

2.7 References

1. British Standards Institution, *Thermal Solar Systems and Components - Solar Collectors: Part 1 - general Requirements*, BS EN ISO 12975-1, 2000, British Standards Institution:
2. Corus Construction Centre. *Corus Colors - Overview of Products*. [cited 6th May 2003]; http://www.corusconstruction.com/.
3. Maxted, J., *Personal Communication: E-mail regarding heat absorption of Colorcoat Armacor*, to E.V. Stevenson, 2006: Liverpool.
4. Borch, I.T., et al., *Skins for Buildings: The Architect's Materials Sample Book*. 2004, Amsterdam: BIS Publishers,.p.1- 313-348; 90 6369 042 8.

5. *Griffiths: Complete Building Price Book 2006*. 52nd ed. 2006: Franklin + Andrews Ltd; 1 901 856 16 X.
6. Hughes, M.J., *Weathertightness: A Physicist's View*. Structural Survey, 1993/4. **12**(1): p. 7-10.
7. Sika, *Product Data Sheet: Elastosil® SG-20: High Performance 1-Part Silicone Sealant and Adhesive for Glass Facades*, 02 05 01 14 001 0 000001, 2004, Sika:
8. Sika, *Engineering Silicones: Elastosil*

Sika Facade Systems: All-round Expertise Guarantees Success, 2006, Sika:

9. Munari-Probst, M., C. Roecker, and A. Scheuler. *Architectural Integration of Solar Thermal Collectors: Results of a European Survey*. in *ISES 2005 Solar World Congress*. 2005. Orlando, Florida, USA: International Solar Energy Society.
10. Richards, J., *Cost of Sikasil SG20*, to E.V. Stevenson, 2007: Welwyn Garden City.
11. ATAS International. *InSpire Wall System*. [cited 2nd July 2006]; http://www.atas.com/inspirewall/#How.
12. Solarwall. *The Solarwall Solar Heating System*. [cited 16th May 2003]; www.solarwall.com/system.html.
13. *Solar Luft Systeme*. 2006 [cited 2nd July 2006]; http://grammer-solar.de/solarluft/sls/kollektor.shtml.
14. Shankland, N.J., P. Reeve, and W. Dotzler. *A ventilated photovoltaic and solar-air collector for space and water heating*. [cited 3rd January 2007]; www.cibse.org/pdfs/ventilatedpv.pdf.
15. Nuaire. *Sunwarm breathing sunshine into homes*. [cited 12th January 2007]; http://www.sunwarm.com/information.shtml.
16. *Putting the Greenhouse to Work*. Steel Edge, 2004(15): p. 6.
17. ASHRAE, *2005 ASHRAE Handbook: Fundamentals, SI Edition*, ed. R.a.A.C.E. American Society of Heating, Inc. 2005, Atlanta: ASHRAE; 1-931862-71-0.
18. Kakac, S., R.K. Shah, and W. Aung, *Handbook of Single-Phase Convective Heat Transfer*. 1987, New York: John Wiley & Sons; 0-471-81702-3.
19. Ong, K.S., *Thermal performance of solar air heaters: Mathematical model and solution procedure*. Solar Energy, 1995. **55**(2): p. 93-109.
20. Yeh, H.-M. and T.-T. Lin, *Efficiency Improvement of Flat-Plate Solar Air Heaters*. Energy, 1996. **21**(6): p. 435-443.
21. Ho, K.T.K. and D.L. Loveday, *Covered profiled steel cladding as an air heating solar collector: laboratory testing, modelling and validation*. Energy and Buildings, 1997. **26**: p. 293-301.
22. British Standards Institution, *Thermal insulation for building equipment and industrial installations - Calculation Rules*, BS EN ISO 12241, 1998, British Standards Institution:
23. Ong, K.S., *A mathematical model of a solar chimney*. Renewable Energy, 2003. **28**: p. 1047-1060.
24. Hirunlabh, J., et al., *Study of natural ventilation of houses by a metallic solar wall under tropical climate*. Renewable Energy, 1999. **18**: p. 109-119.
25. Kays, W.M., *Convective heat and mass transfer*. 1996, New York: McGraw & Hill;
26. Klein, S.A., *Calculation of flat-plate collector loss coefficients*. Solar Energy, 1979. **17**(1): p. 79-80.

27. Kays, W.M., *Convective heat and mass transfer*. 1966, New York: McGraw & Hill;
28. Guan, C.N. *Dynamic Models of Solar Air Collector* 2006: Master of Science in Energy Systems; Department of Applied Sciences at Aachen University.
29. Delahaye, A., et al. *Solar Air Collector - Development and Optimization of Existing Elements for Facades*. in *ISES 2005 Solar World Congress*. 2005. Orlando, Florida, USA: International Solar Energy Society.
30. Pottler, K., *Energetische Optimierung von Solar-Luft-Kollektoren.* 2000: Frankfurt. Chapter 2.4.1.
31. Brinkworth, B.J., *A procedure for the routine calculation of laminar free and mixed convection in inclined ducts.* International Journal of Heat and Fluid Flow, 2000. **21**: p. 456-462.
32. Brinkworth, B.J., *Estimation of flow and heat transfer for the design of PV cooling ducts.* Solar Energy, 2000. **69**(5): p. 413-420.
33. Brinkworth, B.J., *Coupling of Convective and Radiative Heat Transfer in PV Cooling Ducts.* Transactions of American Society of Mechanical Engineers: Journal of Solar Energy Engineering, 2002. **124**: p. 250-255.
34. Brinkworth, B.J., et al., *Thermal regulation of photovoltaic cladding.* Solar Energy, 1997. **61**(3): p. 169-178.
35. Brinkworth, B.J., R.H. Marshall, and Z. Ibarahim, *A Validated Model of Naturally Ventilated PV Cladding.* Solar Energy, 2000. **69**: p. 67-81.
36. Moshfegh, B. and M. Sandberg, *Flow and heat transfer in the air gap behind photovoltaic panels.* Renewable and Sustainable Energy Reviews, 1998. **2**: p. 287-301.
37. Moshfegh, B. and M. Sandbergh. *Investigation of fluid flow and heat transfer in a vertical channel heated from one side by PV elements: Part 1 Numerical study*. in *WREC (World Renewable Energy Congress) IV*. 1996.
38. Moshfegh, B. and M. Sandbergh. *Investigation of fluid flow and heat transfer in a vertical channel heated from one side by PV elements: Part II Experimental study*. in *WREC (World Renewable Energy Congress) IV*. 1996.
39. Moshfegh, B., et al. *Analysis of fluid flow and heat transfer within the photovoltaic facade on the ELSA Building JRC ISPRA*. in *13th European Photovoltaic Solar Energy Conference*. 1995.
40. Sandberg, M. and B. Moshfegh, *Buoyancy-induced air flow in photovoltaic facades: Effect of geometry of the air gap and location of the solar cell modules.* Building and Environment, 2002. **37**: p. 211-218.
41. Brinkworth, B.J. and M. Sandberg, *A validated procedure for determining the buoyancy-induced flow in ducts.* Building Services Engineering Research & Technology, 2005. **26**(1): p. 35-48.
42. Hollands, K.G.T. and E.C. Shewen, *Optimization of flow passage geometry for air-heating, plate-type solar collectors.* Journal of Solar Energy Engineering, 1981. **103**: p. 323-330.
43. Yeh, H.-M., C.-D. Ho, and J.-Z. Hou, *The improvement of collector efficiency in solar air heaters by simultaneously air flow over and under the absorbing plate.* Energy, 1999. **24**: p. 857-871.
44. Yeh, H.-M., C.-D. Ho, and C.-Y. Lin, *Effect of collector aspect ratio on the collector efficiency of upward type baffled solar air heaters.* Energy Conversion and Management, 2000. **41**: p. 971-981.
45. Matrawy, K.K., *Theoretical analysis for an air heater with a box-type absorber.* Solar Energy, 1998. **63**(3): p. 191-198.

46. Kurtbas, I. and A. Durmus, *Efficiency and exergy analysis of a new solar air heater.* Renewable Energy, 2004. **29**: p. 1489-1501.
47. Hegazy, A.A. *Comparative Study of the Performances of Four Photovoltaic/Thermal Solar Air Collectors.* in *Energy Conversion and Management.* 2000.
48. Hachemi, A., *Theoretical and experimental study of efficiency factor, heat transfer and thermal heat loss coefficients in solar air collectors with selective and nonselective absorbers.* International Journal of Energy Research, 1999. **23**: p. 675-682.
49. Yeh, H.M. and Y.C. Ting, *Efficiency of solar air heaters packed with iron filings.* Energy, 1988. **13**(7): p. 543-547.
50. Chiou, J.P., M.M. El-Wakil, and J.A. Duffie, *A slit and expanded aluminium-foil matrix solar collector.* Solar Energy, 1995. **9**(2): p. 73-80.
51. Hamid, Y.H. and W.A. Beckman, *Performance of air-cooled radiatively heated screen matrices.* Transactions of American Society of Mechanical Engineers: Journal Engineering Power, 1971: p. 221-224.

3 Experiment 1: Air Mass Flow

The system being modelled has two interacting outputs: air mass flow and increased air temperature. As the temperature difference between entry and exit air increases, an increase in air mass flow can be expected. Although air temperature can be measured readily, the low levels of air mass flow expected to arise from buoyancy will be difficult to measure accurately.

Important to understanding the airflow characteristics is the pressure loss associated with the surface friction. A system with high friction will not be able to generate much flow through buoyancy, and can be costly to force air through. This first experiment will focus on friction and pressure loss in the duct system.

A first stage in simplifying the problem, is to separate the interaction between air temperature and air mass flow. If the system is kept out of direct sunlight and away from any sources of heat, the air temperature will remain constant along the length of the duct. This will also remove any source of air movement through buoyancy. If a controlled air mass flow is created, the pressure difference across the length of a duct can be measured accurately. The pressure difference can be calculated using the Darcy-Weisbach equation [1]:

$$\Delta p = \rho f \frac{L}{D_h} \frac{V^2}{2} \qquad \text{B15}$$

Where:

Δp is the difference in pressure (Pa)

ρ is the air density (kg m^{-3})

f is the friction factor

L is the length of the duct (m)

V is the air flow velocity (m s^{-1})

D_h is the hydraulic diameter which is calculated from $D_h = \frac{4A_c}{P_w}$ B1

A_c is the cross sectional area (m^2)

P_w is the wetted perimeter (m)

The Darcy Weisbach equation and the hydraulic diameter are discussed in Appendix B sections B9 and B2. The experimental results will be used to identify the most appropriate version of friction factor for use in the model. The candidates include:

1) the version which Brinkworth et al [2] derived from the work of Hollands and Shewen [3] which will be referred to as the Brinkworth friction factor (f_{Br}):

$$f = f_o + \frac{f_1}{\left(\frac{L}{D_h}\right)} + \frac{f_2}{\mathrm{Re}^n} \qquad 3.1$$

Where Re is the Reynolds number.

2) the version given in ASHRAE Fundamentals 1989 [4] which will be referred to as the ASHRAE friction factor (f_{ASH}):

$$f' = 0.11\left(\frac{R}{D_h} + \frac{68}{\mathrm{Re}}\right)^{0.25} \qquad B16$$

If f' ≥ 0.018: f=f'

If f' < 0.018: f= 0.85*f' + 0.0028

Where R is the surface roughness.

3) Churchill's friction factor (f_{Ch}) [1]:

$$f = 8\left[\left(\frac{8}{\mathrm{Re}}\right)^{1/2} + \frac{1}{(A+B)^{1.5}}\right]^{1/12} \qquad B17$$

where:

$$A = \left[2.457 \ln\left(\frac{1}{\left(\frac{7}{\mathrm{Re}}\right)^{0.9} + \frac{0.27R}{D_h}}\right)\right]^{16} \qquad B17a$$

$$B = \left(\frac{37530}{\mathrm{Re}}\right)^{16} \qquad B17b$$

3.1 Experiment Design

The experiment design is shown schematically in Figure 3.1 with a photograph of the equipment in Figure 3.2. The details of various aspects of this experiment are explained in the following sections, but in summary:

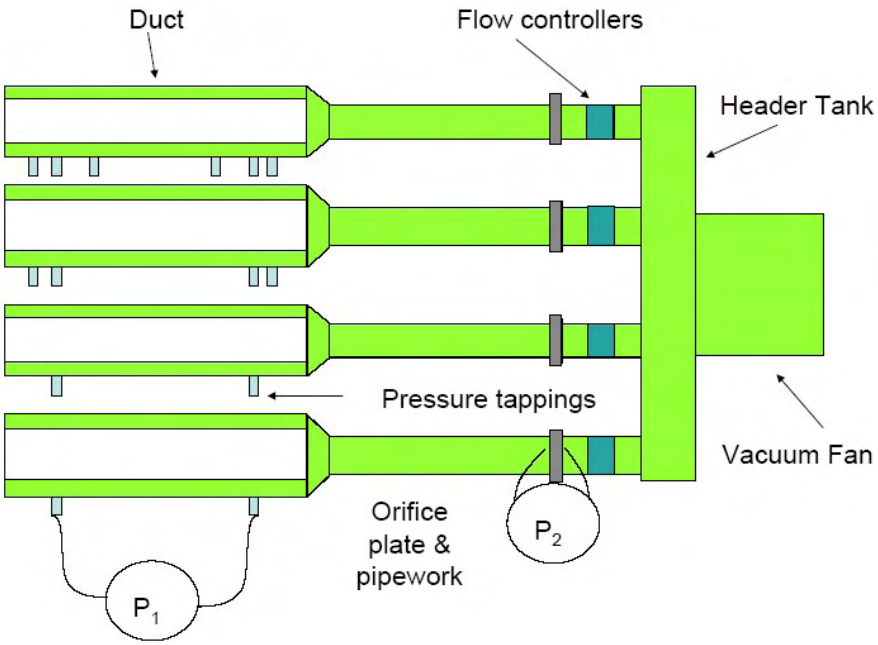

Figure 3.1. Schematic of pressure experiment

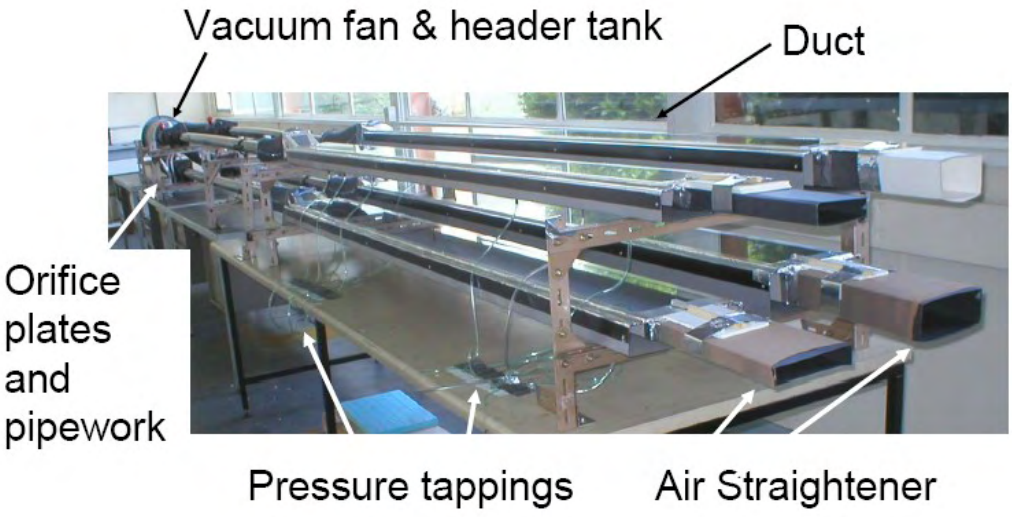

Figure 3.2. Overview of pressure test experiment

A vacuum fan pulls air through four prototype ducts. The air mass flow in each duct is controlled by ball valves, and monitored from the pressure drop across an orifice plate. The pressure drop across the length of the prototype duct is monitored for various flow rates representing a range of practical flows and compared to the predicted values.

3.1.1 Prototype Ducts

In order to undertake such measurements a number of prototype ducts were constructed using black Colorcoat Armacor® covered with float glass. Initial calculations of the likely pressure drop along the length of ducts of different geometry were made. This was to indicate the duct geometry from which measurable pressure drops could be obtained at an air mass flow of 0.01 kg s^{-1}. This flow rate was selected as it would provide a sensible rate of ventilation to the occupants: this air mass flowing through a series of 0.15m wide ducts occupying a 10m stretch of façade would produce 387 l s^{-1} which would meet the ventilation requirements of 38 people within the building, using the guidelines in the Part F building regulations [5]. This choice was backed up by the work of Hollands and Shewen [3] which took place at an air mass flow of 0.01 kg s^{-1}.

The duct length was limited to 2.4m by the maximum blank size that could be obtained for forming the duct. The Darcy-Weisbach equation was used in conjunction with the friction factor given in ASHRAE Fundamentals 1989 [4] to calculate the expected pressure drop for 2.4m long ducts with different width/depth combinations. The maximum width/depth combination was determined by the minimum pressure drop which would be measurable at an air mass flow of 0.01 kg s^{-1}. The other dimensions were chosen to demonstrate the influence of reducing the width and depth separately. Duct A is narrow and shallow, duct B is narrow and deep, duct C is wide and shallow and duct D is wide and deep. The duct dimensions are shown in Table 3.1.

Table 3.1 Actual Prototype Duct Dimensions

	Length (m)	Width (m)	Depth (m)
A	2.4	0.1	0.034
B	2.4	0.1	0.063
C	2.4	0.15	0.033
D	2.4	0.15	0.063

The glass was attached to the prototype ducts using Elastosil SG 20, which is an engineering silicone sealant designed for structural glazing [6]. The joints between the glass and the duct were also covered with tape to block off any small leaks that may be present in the joint between the duct and the glass, see Figure 3.3.

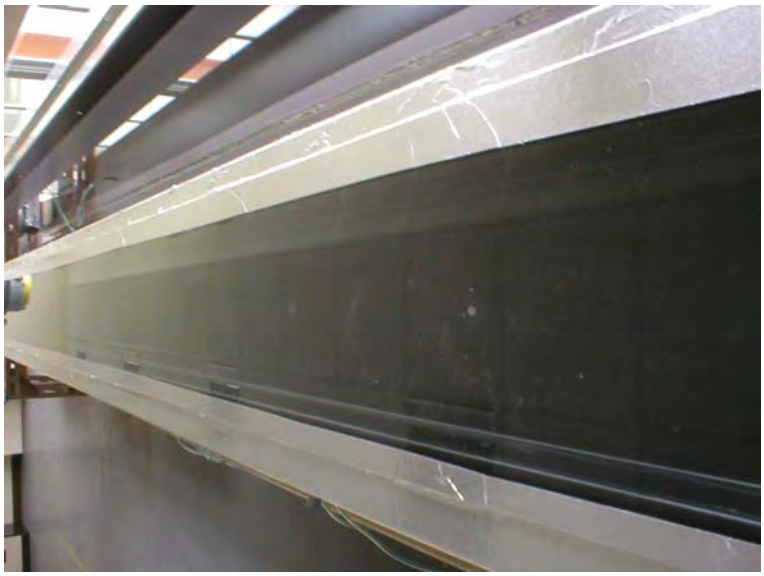

Figure 3.3. Glass joined to prototype duct

In order to reduce the effect of the sharp inlet and outlet geometry of the test structure, flow straighteners were added to each end. The flow straighteners were constructed from drinking straws (Figure 3.4).

Figure 3.4. Flow straightening cassette for exit of duct

Edge effects are expected to dominate the entry and exit ends of the duct; however, they are not expected to extend beyond a length equivalent to six times the depth of the duct. For the shallow ducts, no measurement was taken within 0.23 m of the entry or exit. For the deeper ducts, no measurements were taken within 0.41 m of the entry or exit.

3.1.2 Source of Air Mass Flow

The source of the air mass flow is a vacuum fan, which is attached to a header tank. This allows air to be pulled through four separate ducts at the same time. The air mass flow generated by the vacuum fan is controlled by a ball valve attached to each duct. The air mass flow through each duct is measured indirectly by measuring the pressure difference across an orifice plate. The translation between this pressure difference and the calculated air mass flow is described in Appendix D.

Since fans generate turbulence in a fluid, the vacuum fan is positioned at the opposite end of the system from the sensitive pressure difference measurements.

Since the target air mass flow is 0.01 kg s^{-1}, and four ducts are being assessed at the one time, the vacuum fan must be capable of generating an air mass flow greater than 0.04 kg s^{-1}. It must also be capable of coping with the intended pressure drop across the orifice plate. This was calculated in Appendix D to be 738 Pa.

In general, fans are not designed to accommodate such a low mass flow across a relatively high pressure drop. A suitable fan was identified; model V5HK-T 1-2 manufactured by Eastern Air Devices in United States. Unfortunately, there were delivery and cost issues which prevented this fan from being used for the experiment. A cheaper, more accessible product had to be found.

A brief experiment with a vacuum cleaner indicated that such a product was suitable. A cylinder vacuum cleaner had the added advantage that the header tank could be made out of the cylinder. Flexy pipe was used to connect the four ducts to the header tank.

There were concerns that the vacuum motor might overheat since it might not be receiving the throughput of air that it was designed for. This was because an inlet of 50 mm diameter was being replaced by four pipes which were restricted by 22 mm orifice plates (two of which would be further restricted by ball valves when the experiment was underway). For this reason, twelve 10 mm diameter holes were drilled in the casing. The modified vacuum source can be seen in Figure 3.5.

Figure 3.5. Modified vacuum source

3.1.3 Control of Air Mass Flow

The mass flow rate of air is controlled by ball valves (Figure 3.6). The mass flow rate of air is calculated from the pressure difference across an orifice plate (described in Appendix D). The pressure difference is measured using a Furness FL-1 pressure gauge which has a resolution of ±5 Pa (Figure 3.7). The output of the pressure gauge is a voltage, which is read using a voltmeter (Figure 3.8). The air mass flow was checked manually at two minute intervals.

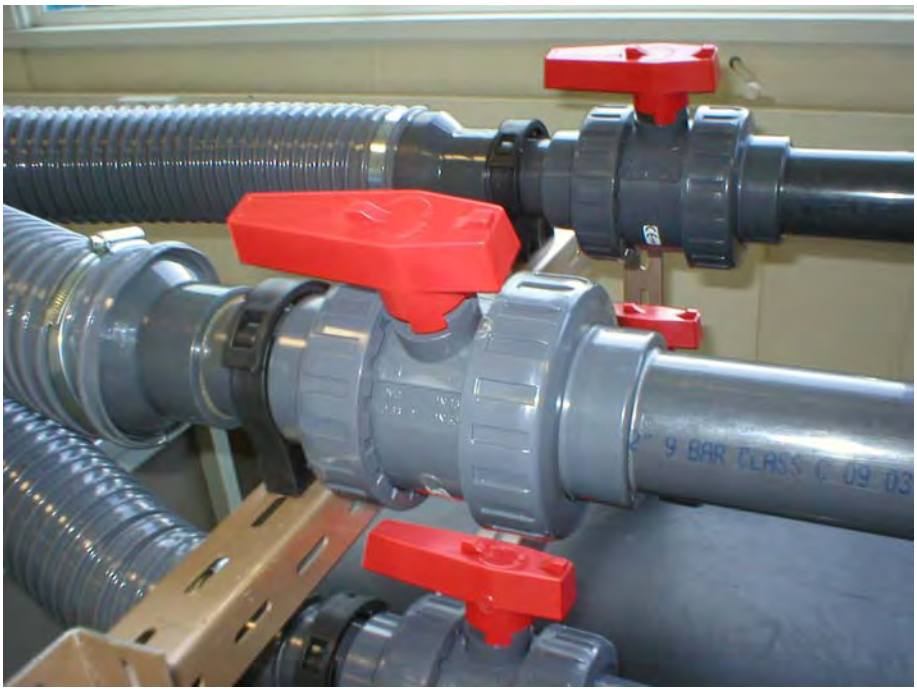

Figure 3.6. Closeup of ball valve controls

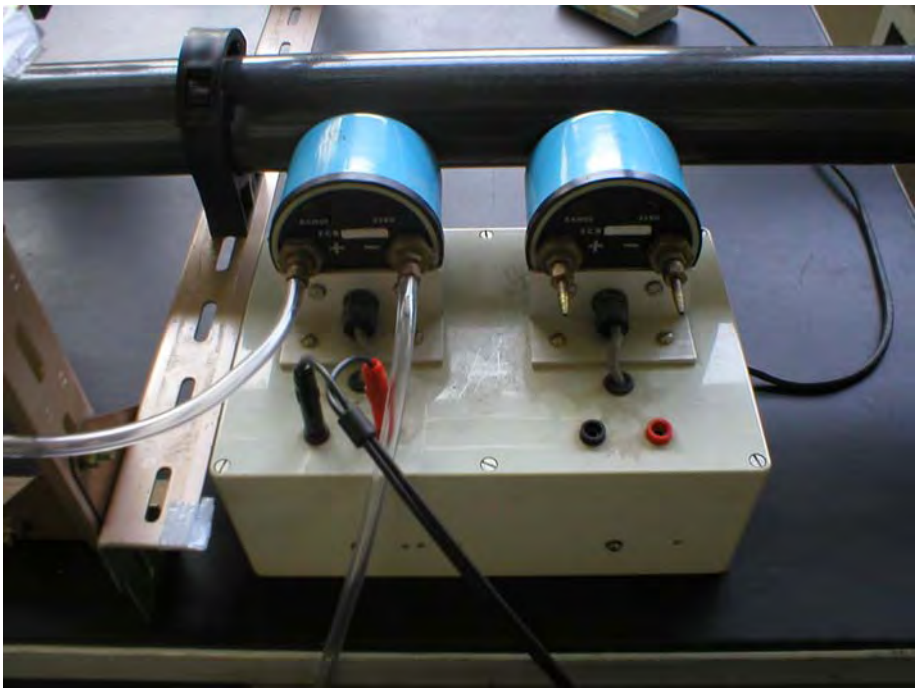

Figure 3.7. Orifice plate pressure gauges

Figure 3.8. Voltmeter to read pressure gauge from orifice pressure gauge

3.1.4 Pressure Measurements Across the Length of the Duct

Pressure tappings were inserted flush with the base surface of the ducts at intervals along the length. The pressure tappings were connected to a KAL 84 pressure indicator (Figure 3.9) which displays the pressure in Pa. The KAL 84 has an uncertainty of

±(0.25% display + 0.09) Pa when measuring in the range between 0 and ±200 Pa. The pressure difference was checked manually at two minute intervals.

Figure 3.9. Sensitive pressure gauge

The arrangement of pressure tappings was dependent on the duct geometry. Ducts with larger hydraulic diameters have smaller pressure drops, and require as large a distance between the pressure tappings as possible without entering the entry or exit zones. The ducts with smaller hydraulic diameters could have additional pressure tappings inserted. All ducts had pressure tappings separated by 1.58m to allow comparisons. The position of the pressure tappings are shown in Table 3.2, along with the hydraulic diameter of each duct.

Table 3.2 Pressure tapping positions

Duct	Distance from duct entrance (m)						Hydraulic diameter (m)
A	0.23	0.41	0.71	1.69	1.99	2.17	0.0507
B		0.41			1.99		0.0773
C	0.23	0.41			1.99	2.17	0.0541
D		0.41			1.99		0.0887

3.1.5 Confidence in Results

The experiments were repeated at least three times for each condition.

3.1.5.1 Air Mass Flow

An orifice plate was manufactured for each duct. Since the orifice plate is critical to measuring the air mass flow, it is essential that each orifice plate matches the specification stated in BS EN ISO 5167-1&2 [7, 8] and that any variation between the orifice plates is identified.

The flatness of the upstream face of the plate is considered acceptable when $Gap < 0.005(D-d)/2$ where Gap is the maximum gap between the plate and a straight edge of length D laid across any diameter of the plate [7]. Therefore, the maximum acceptable gap across a diameter is 0.16 mm. A dial test indicator has been used to check the variation in height along the surface of the orifice plates. The gaps across four representative diameters for each plate are: 0.08 mm, 0.08 mm, 0.03 mm and 0.05 mm.

The upstream face of the orifice plate is within specification if the surface roughness is less than one thousandth of the orifice diameter. This roughness must hold within the area facing the upstream pipe. For the orifice diameter being considered, this would require roughness to be less than 0.022 mm. The upstream orifice plate faces have a turned finish. The average surface roughness for a turned finish generally lies between 0.0004 and 0.0063 mm which matches this specification [9].

The diameter (d) of the orifice is acceptable if the measured diameter across four points of the plate (approximately 90^o intervals) are within 0.05 % of the mean value. The measurements taken and the calculations derived from them are shown in Table 3.3.

Table 3.3 Orifice diameter measurements and calculations

Orifice plate	#1	#2	#3	#4
Measurement 1 (mm)	21.97	21.96	21.96	21.97
Measurement 2 (mm)	21.96	21.98	21.97	21.96
Measurement 3 (mm)	21.98	21.96	21.96	21.96
Measurement 4 (mm)	21.97	21.98	21.96	21.97
Mean (mm)	21.97	21.97	21.96	21.96
Allowable deviation from mean (mm)	0.01	0.01	0.01	0.01

These measurements indicate that all four orifice plates are within specification. Therefore measurement of flow shall be made to 1.5% according to BS EN ISO 5167-1&2 2003 [7, 8].

3.1.5.2 Measurement Errors

The overall uncertainty for calculating the air mass flow was calculated to be 1.5% in Appendix D. The effect of this error on the pressure drop can be predicted using the Darcy-Weisbach equation (B15) in conjunction with the friction factor given in ASHRAE Fundamental 1989 (B16) [4]. The difference in pressure drop caused by 1.5% variation of the air mass flow has been calculated for each combination of duct geometry and length. This has been expressed in Pascals and as a percentage of the calculated pressure drop in Table 3.4.

The percentage errors were of the same order as the resolution of the pressure measurement equipment available, and so were not expected to affect the experiment unduly. The percentage errors for low flows on the larger ducts were high, these flows were not used for experimental work.

Table 3.4 Predicted error in measurements of pressure drop

Duct	Air mass flow (kg s^{-1})	Distance (m)	Error (Pa)	Error (%)
A	0.01	0.17	0.10	25.6
		0.3	0.11	15.9
		1.28	0.19	6.2
	0.001	1.58	0.09	138.6
	0.01		0.21	5.6
	0.018		0.43	4.1
	0.01	1.76	0.22	5.4
B	0.001	1.58	0.09	677.3
	0.01		0.11	15.2
	0.018		0.16	7.5
C	0.01	0.17	0.10	49.9
	0.001	1.58	0.09	286.1
	0.01		0.15	8.3
	0.018		0.25	5.0
	0.01	1.76	0.15	7.7
D	0.001	1.58	0.09	1631.6
	0.01		0.10	32.2
	0.018		0.12	13.6

3.2 Results

The correlation between the predicted and actual pressure drops was assessed for two aspects of the air mass flow:

- The effect of varying the length over which the pressure drop was measured
- The effect of varying the air mass flow for which the pressure drop was measured.

3.2.1 Pressure Difference for Varying Length

A constant mass flow of 0.01 kg s^{-1} was passed through ducts A and C while pressure drop measurements were taken over different lengths. For each set of measurements the mean pressure drop and the variance has been calculated. The friction factors were used to predict pressure drops for comparison with the measured results. The comparisons for duct A (0.1 x 0.034 m) and C (0.15 x 0.033 m) are shown respectively in Figure 3.10 and Figure 3.11, where the error bars represent the error relating to air mass flow calculations and the resolution of the measured pressure drop. The experiments were

repeated several times, on different days, this caused slight variations in the actual air mass flows through the duct. Only measurements which were carried out when the air mass flow was between 0.0095 and 0.0105 kg s^{-1} are shown in Figure 3.10 and Figure 3.11.

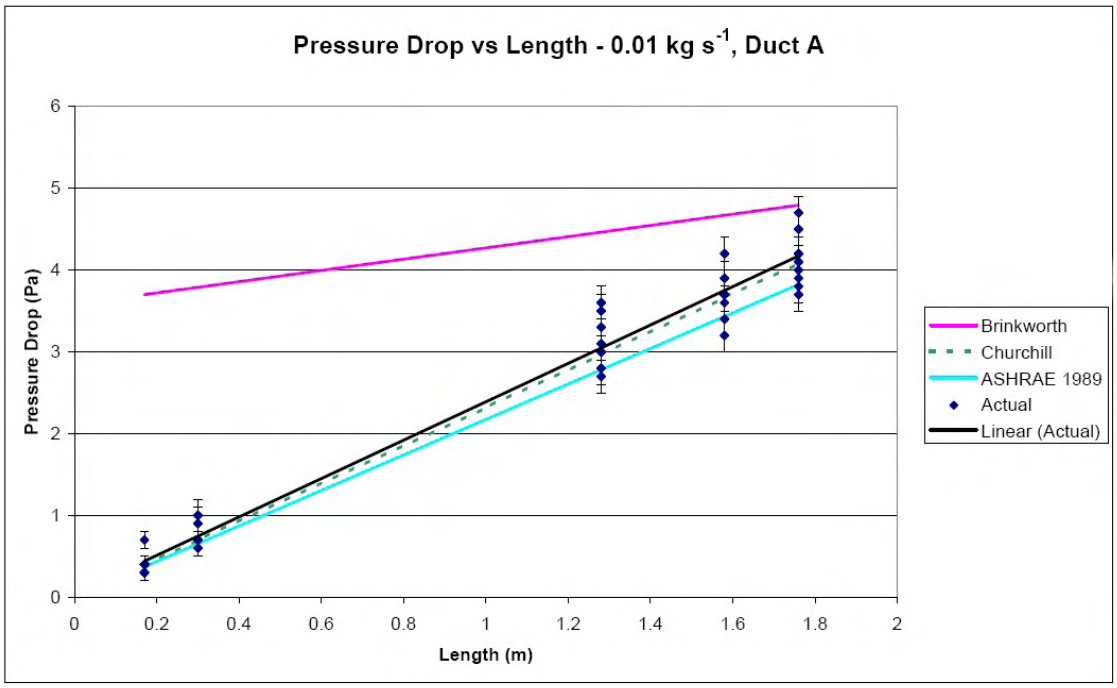

Figure 3.10. Pressure Drop vs Length - 0.01 kg s-1, Duct A

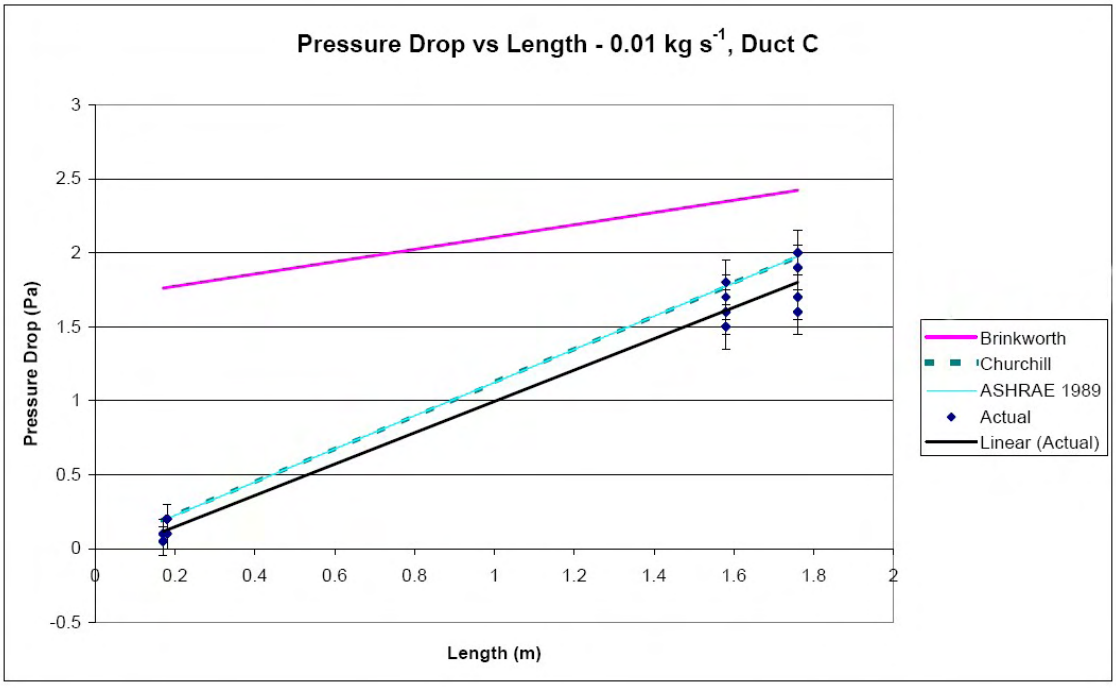

Figure 3.11. Pressure Drop vs Length - 0.01 kg s-1, Duct C

The accuracy of the model predictions in relation to the measured values can be considered in terms of the mean bias and the root mean square error (RMSE). The mean bias and RMSE values for all measurements relating pressure drop to distance travelled by the air can be seen in Table 3.5.

Table 3.5 Mean Bias and RMSE for models predicting the pressure drop

Distance (m)	Mean Bias (Pa)		RMSE (Pa)	
	Duct A	Duct C	Duct A	Duct C
Brinkworth	-1.81	-1.11	2.11	1.24
ASHRAE	0.07	-0.15	0.19	0.19
Churchill	0.59	0.15	0.71	0.25

From Table 3.5 it can be seen that the ASHRAE friction factor has the lowest mean bias and RMSE. This indicates that it is the most accurate model for predicting the pressure drop in these ducts. The apparent convergence of the three models for a duct length of 2 m is considered to be coincidental.

Two of the restrictions for the Brinkworth friction factor are:

- the flow shall be laminar (Re < 2300)
- L^+ must be greater than 0.04, where L^+ is the dimensionless length related to the Prandtl (Pr) and Grashof (Gr) numbers, calculated from:

$$L^+ = \left(\frac{48\,\mathrm{Pr}}{Gr} \right)^{0.5} \qquad \text{C19}$$

Table 3.6 shows the Reynolds number and dimensionless length L^+ for the experimental conditions in ducts A and C. It can be seen that neither requirement was met in this experiment.

Table 3.6 Values of Re and L^+ for Ducts A and C

Duct	A	C
Re	8214	6015
L^+	0.0058	0.0074

For the Brinkworth friction factor to be applicable, ducts A and C would have required different dimensions. If the air mass flow was going to be kept at 0.01 kg s^{-1}, longer

ducts would have been required. If the duct geometries were to be kept at the current dimensions, a lower air mass flow would be required. Alternatively if the duct length and air mass flows were to be kept at the current levels, the duct depth would have to be altered. The values required to meet the criteria for the Brinkworth friction factor are shown in Table 3.7.

Table 3.7 Criteria for Brinkworth friction factor relating to Ducts A and C

Duct	A	C
Min duct length for 0.01 kg s^{-1} (m)	16.67	13.02
Max air mass flow for 2.4 m long duct (kg s^{-1})	0.00144	0.00185
Max duct depth for 0.01 kg s^{-1} and 2.4 m long duct (m)	0.0028	0.0043

The restricted applicability of the Brinkworth friction factor is a disadvantage to its use in the model. The other disadvantage of the Brinkworth friction factor is that it would under predict the pressure drop per unit length for longer ducts. For geometry optimisation purposes, this could lead to the erroneous conclusion that longer ducts were advantageous. In practice it could lead to difficulties such as fan powers being under specified. For these reasons the Brinkworth friction factor will not be considered in the next part of the experiment, or used in the final model.

3.2.2 Pressure Difference for Varying Air Mass Flow

In the experiment the air mass flow could be varied between 0 and 0.02 kg s^{-1}. The pressure drop over 1.58 m length was measured for ducts A and C within this range of air mass flow. For ducts B and D, flows below 0.008 kg s^{-1} would result in a pressure drop which is below the resolution of the available equipment. Pressure drops were calculated using the Darcy –Weisbach equation for both the ASHRAE and Churchill friction factors.

The comparison between predicted and actual pressure drops is shown in (Figure 3.12).

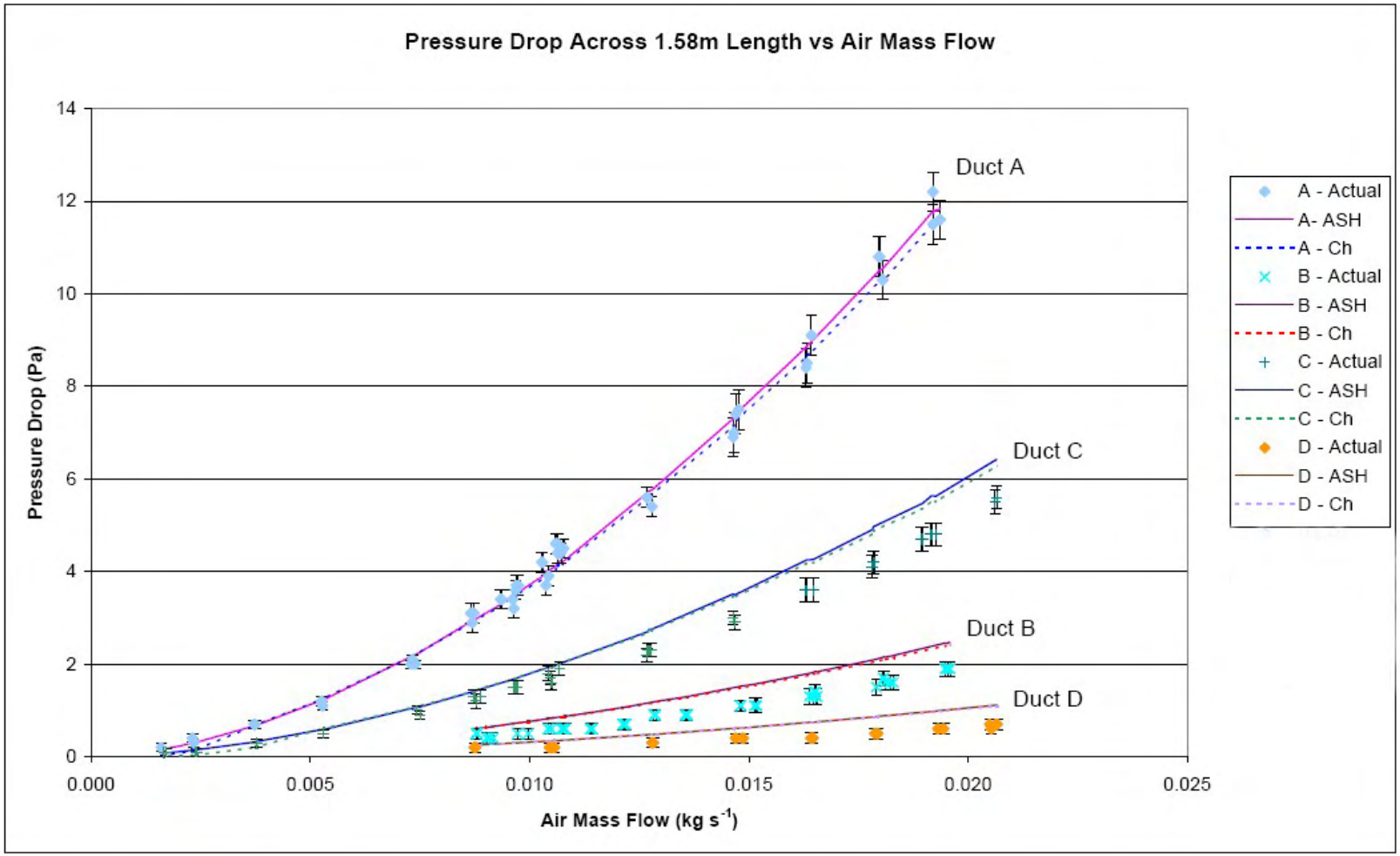

Figure 3.12. Pressure drop across 1.58m length vs Air mass flow

The error bars represent the errors attributable to the air mass flow calculation and the pressure drop measurement, as shown in Table 3.4.

As shown in Figure 3.12 there is a good correlation between the pressure drop predicted using both friction factors and the measured values for duct A (the duct with the smallest hydraulic diameter). However, the pressure drop is overestimated for ducts B, C and D. Although it is beneficial that the actual pressure loss be less than expected (so promoting greater passive flows or requiring less fan power), it is of interest to determine where the predictive theory is inadequate for these geometries, and where possible to tune the prediction equations.

The flows for the four ducts had Reynolds numbers ranging between 1,000 and 18,000 – indicating that the flow is mainly transitional. Flows in this area are not well understood and there are no well established models. The Darcy-Weisbach equation is accepted for turbulent flow, but unproven for transitional flow. This may account for the difference between predicted and measured pressure drop values.

In an attempt to improve the agreement between the predicted and actual results, parameters were adjusted to reduce the bias observed in ducts B, C and D without unduly affecting duct A. The aim was to make a global adjustment, rather than adjust for individual geometries. Parameters were varied by ±10% and the mean bias calculated. From this the percentage change required to achieve a mean bias of zero was calculated. After this percentage change had been applied the RMSE was calculated as a further indicator of fit between the actual and predicted results. Changes were assessed using mean bias and RMSE between 240 measured values and the corresponding predictions.

Potential candidates for the systematic error in the pressure drop calculations are:

- friction factor (f)
- roughness (R) which is used in both the ASHRAE friction factor (B16) and the Churchill friction factor (B17)
- hydraulic diameter (D_h) which is used in the Darcy-Weisbach equation (B15), the ASHRAE friction factor (B16) and the Churchill friction factor (B17).

Manufacturer's measurements of the surface roughness of Colorcoat Armacor® indicate a typical surface roughness of 3 μm ± 10 %. The effect of varying roughness within these limits only reduced the mean bias by 0.017% for the ASHRAE friction factor. This indicates that the roughness would have to be modified by 730% to attain a zero bias. Although roughness had a stronger effect on the Churchill friction factor, the effect was non-linear, and couldn't be used to adjust the mean bias to zero. Therefore, it appears that roughness is not a satisfactory correction factor.

Table 3.8 shows a comparison of the mean bias (%) and RMSE (%) for the variations in f and D_h. The effect of varying either of the friction factors by ± 10 % was considered; from this the percentage of the friction factor which would generate the lowest bias was calculated. The bias (%) and RMSE (%) for f_{ASH} -11.3 % and f_{CH} -5.8 % are shown in Table 3.8.

A similar process was carried out with D_h as its subject. From this the percentage of D_h which would generate the lowest bias was found to be D_h + 9.75 % for f_{ASH} and D_h +5 % for f_{CH}. The bias and RMSE for varying D_h in f_{ASH} and f_{CH} are shown in Table 3.8.

For a rectangular duct, it is possible to calculate the circular equivalent diameter (D_e) as an alternative to D_h. D_e is defined as [4]:

$$D_e = 1.3\frac{(ab)^{0.625}}{(a+b)^{0.25}} \qquad \text{B3}$$

where a and b refer to the duct section dimensions. The mean bias (%) and RMSE (%) for f_{ASH} and f_{CH} with D_e replacing D_h are shown in Table 3.8. The bias for D_e is high in comparison to the other factors considered; however the percentage of D_e which would generate the lowest bias was found. The bias (%) and RMSE (%) of D_e – 10.3 % for f_{ASH} and D_e -13.8 % for f_{CH} are shown in Table 3.8.

Table 3.8 Bias and RMSE for Factors Affecting the Pressure Drop Calculation

Duct	Duct ID									
	Mean Bias					RMSE				
	A	B	C	D	all	A	B	C	D	all
ASHRAE										
D_h	1.5	-41.4	-15.1	-63.7	-12.7	7.8	42.6	19.7	65.4	27.9
D_e	22.6	-23.3	19.5	-34.5	12.5	23.4	24.9	21.4	36.5	26.3
+9.75 % D_h	12.6	-25.5	-2.2	-45.3	0.0	14.3	27.0	11.5	47.2	22.0
-11.3 % f	12.6	-25.4	-2.1	-45.2	0.0	14.3	26.9	11.4	47.1	22.0
-10.3 % De	11.4	-41.2	7.8	-54.0	-0.2	13.3	42.4	12.8	55.8	26.5
Churchill										
D_h	6.0	-39.5	-1.1	-62.0	-6.2	18.9	40.9	32.3	63.5	34.2
De	28.6	-21.3	26.6	-32.4	16.5	27.8	23.1	32.1	34.4	31.7
+5 % Dh	11.4	-31.1	4.3	-52.1	-0.1	19.7	32.6	29.6	53.8	31.1
-5.8 % f	11.5	-31.5	4.8	-52.6	0.0	20.4	33.0	30.8	54.2	31.7
-13.8 % De	11.0	-46.7	13.3	60.1	0.0	19.6	48.0	27.8	61.7	34.2

The bias can be reduced to the same levels for both friction factors. However, the Churchill friction factor has higher RMSE values. For this reason the ASHRAE friction factor is considered to be the most suitable for use in the model.

For the ASHRAE friction factor, the bias could be reduced by either reducing f by 10.3 % or increasing D_h by 9.75 %. Both of these adjustments generate similar RMSE values. Dh + 9.75% has been chosen as the adjusting factor.

With this adjustment, the pressure drop of the ducts could be predicted to within 22 % across all four duct geometries, even though the flows were in the transition region. The comparison between actual pressure drop and that predicted using f_{ASH} with D_h + 9.75 % is shown in (Figure 3.13). The error bars on the actual values represent the errors related to air mass flow calculation and pressure readings. The error bars on the calculated values represent the errors inherent in the calculation. The adjusted friction factor shows better agreement across all cases. Although, at an error of 22 %, the predictive power is not high, it is considered sufficient to predict system performance and to distinguish between alternative geometries in an optimisation process.

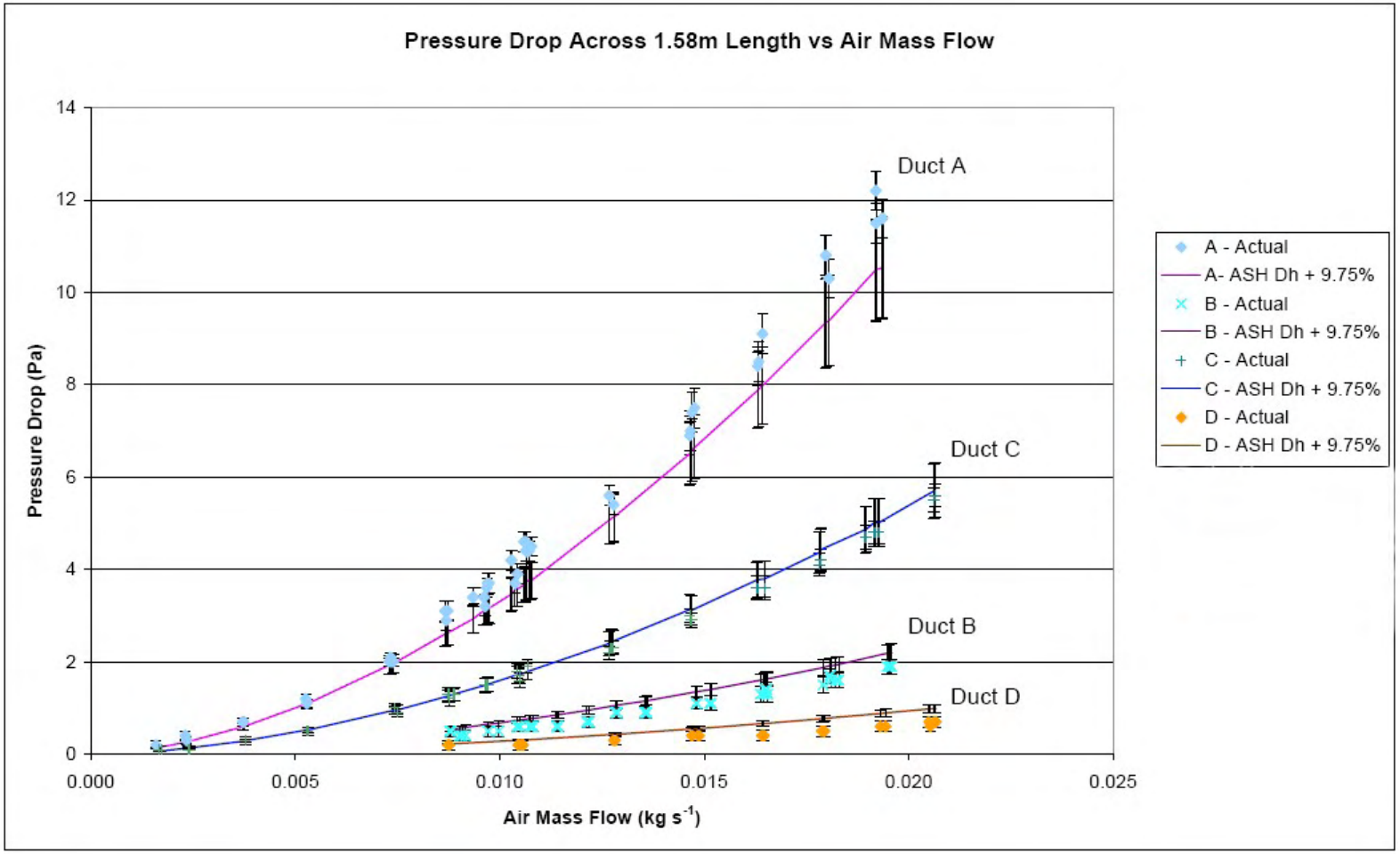

Figure 3.13. Pressure drop across 1.58m length vs air mass flow - adjusted friction factor

The agreement for ducts B and D is still poor. These ducts are deeper and require a significant increase in air mass flow to elicit a significant change in pressure drop.

3.3 Conclusion

Figure 3.10 and Figure 3.11 show disagreement between the measured results and the pressure losses predicted using Brinkworth's apparent friction factor. The apparent convergence of the two models for a duct length of 2 m is considered to be coincidental. Most importantly, the pressure drop per unit length is under predicted; this could lead to an erroneous conclusion that longer ducts were better. In comparison, the ASHRAE and Churchill friction factors provide a much better agreement, even though they are more commonly applied to much larger duct geometries and flows.

While the geometries of the prototype systems tested were not dissimilar to those of Brinkworth's, the flows were greater. At the flow rates considered here, the flow should be transitional to early turbulent – not laminar.

The pressure difference across the length of the duct was measured at mass flows as low as 0.002 kg s^{-1}. Even at these lower flows, the ASHRAE and Churchill friction factors are still more appropriate than Brinkworth's for the geometries considered. It was not possible to reliably measure, with the equipment available, pressure losses at flows low enough to be in the regime where Brinkworth's formulation would be appropriate.

The calculation of pressure drop due to surface friction in a prototype solar collector system was compared to measurements. For the larger duct dimensions, under the flow-rates considered, the ASHRAE friction factor was found to over estimate the system pressure drop. It was found that using the ASHRAE friction factor with an adjusted hydraulic diameter (increased by 9.75 %) gave a better match to the actual data for the geometries and flows considered, reducing the mean bias as well as the root mean square error in the predictions. Across the range of duct geometries and flow rates considered, pressure loss due to friction could be predicted to within 22%.

The ability to predict system pressure losses will be important to a passive air heating system, since a system with a low pressure drop per metre in length is more likely to operate without the assistance of a fan. Similarly the lower the pressure drop per metre in length, the lower the pumping power required to drive air through the system in a forced convection system.

The results from this chapter will be embedded in calculations in Chapters 5 and 6.

3.4 References

1. ASHRAE, *2005 ASHRAE Handbook: Fundamentals, SI Edition*, ed. R.a.A.C.E. American Society of Heating, Inc. 2005, Atlanta: ASHRAE; 1-931862-71-0.
2. Brinkworth, B.J., R.H. Marshall, and Z. Ibarahim, *A Validated Model of Naturally Ventilated PV Cladding.* Solar Energy, 2000. **69**: p. 67-81.
3. Hollands, K.G.T. and E.C. Shewen, *Optimization of flow passage geometry for air-heating, plate-type solar collectors.* Journal of Solar Energy Engineering, 1981. **103**: p. 323-330.
4. ASHRAE, *1989 ASHRAE Handbook: Fundamentals, SI Edition*, ed. R.a.A.C.E. American Society of Heating, Inc. 1989, Atlanta: ASHRAE; 0-910110-57-3.
5. Office of the Deputy Prime Minister, *The Building Regulations: F Ventilation.* 2006: Department for Communities and Local Government,.p.1- 53; 13 978 1 85946 205 8.
6. Sika, *Product Data Sheet: Elastosil® SG-20: High Performance 1-Part Silicone Sealant and Adhesive for Glass Facades,* 02 05 01 14 001 0 000001, 2004, Sika:
7. British Standards Institution, *Measurement of fluid flow by means of pressure differential devices inserted into circular cross-section conduits running full - Part 1: General principles and requirements,* BS EN ISO 5167-1, 2003, British Standards Institution:
8. British Standards Institution, *Measurement of fluid flow by means of pressure differential devices inserted into circular cross-section conduits running full - Part 2: Orifice Plates,* BS EN ISO 5167-2, 2003,
9. *Machinery's Handbook 24*. 1992, New York: Industrial Pressings Inc.p.1- 2543; 0-8311-2424-5.

4 Experiment 2: Air Heating

The aim of this chapter is to investigate the thermodynamic workings of the system in some detail. It also aims to obtain some empirical data in a semi-realistic setting with enough control to isolate parameters. Empirical data are required to evaluate the performance in winter and summer operation under forced convection. In addition summer operation under buoyant convection will be assessed. The duct being considered in the model is constructed of mild steel coated in a black polyurethane paint, with a float glass cover. The duct would be insulated to reduce heat loss.

The prototype ducts would be tested in real climatic conditions, on a site in South Wales.

4.1 Thermodynamic Model

In order to understand the thermodynamic system, a mathematical steady state model study of the heat flows in the system will be constructed. The thermodynamic model is considered in three sections:

- Input power
- Useful output power
- Power losses

4.1.1 Input Power (Q_{in})

Input power will be considered to be primary solar energy through the glazed panel. In order to calculate this, it is necessary to know the amount of direct and diffuse solar irradiation incident on the panel. The amount of solar irradiation which passes through the glass can then be calculated.

4.1.1.1 Solar irradiation incident on glazed panel

The diffuse irradiation incident on a vertical panel is a combination of diffuse solar irradiation (E_{vdiff}) and irradiation reflected from the ground (R_{vh}). The incident diffuse

irradiation can be calculated from direct and diffuse horizontal solar irradiation data (E_{hdir} and E_{hdiff}) in combination with the albedo (Al) using:

$$E_{vdiff} + R_{vh} = Al E_{hdir} + 0.5 E_{hdiff} \qquad 4.1$$

where 0.5 is the fraction of the diffuse solar irradiation visible to a vertical surface in relation to a horizontal one. A vertical surface is equivalent to a tilt angle (Σ) of 90^o.

If global vertical solar irradiation (E_{vg}) is measured, the vertical direct solar irradiation (E_{vdir}) is calculated by subtracting E_{vdiff} from E_{vg}. Alternatively, E_{vdir} can be calculated from [1]:

$$E_{vdir} = \frac{E_{hdir}}{\sin \alpha} \cos \theta \qquad E2$$

Where

E_{hdir} is the horizontal direct solar irradiation (calculated by subtracting E_{hdiff} from E_{hg}).

α = solar altitude (^{o})

θ = angle of incidence (^{o}).

The angles are shown in Figure 4.1.

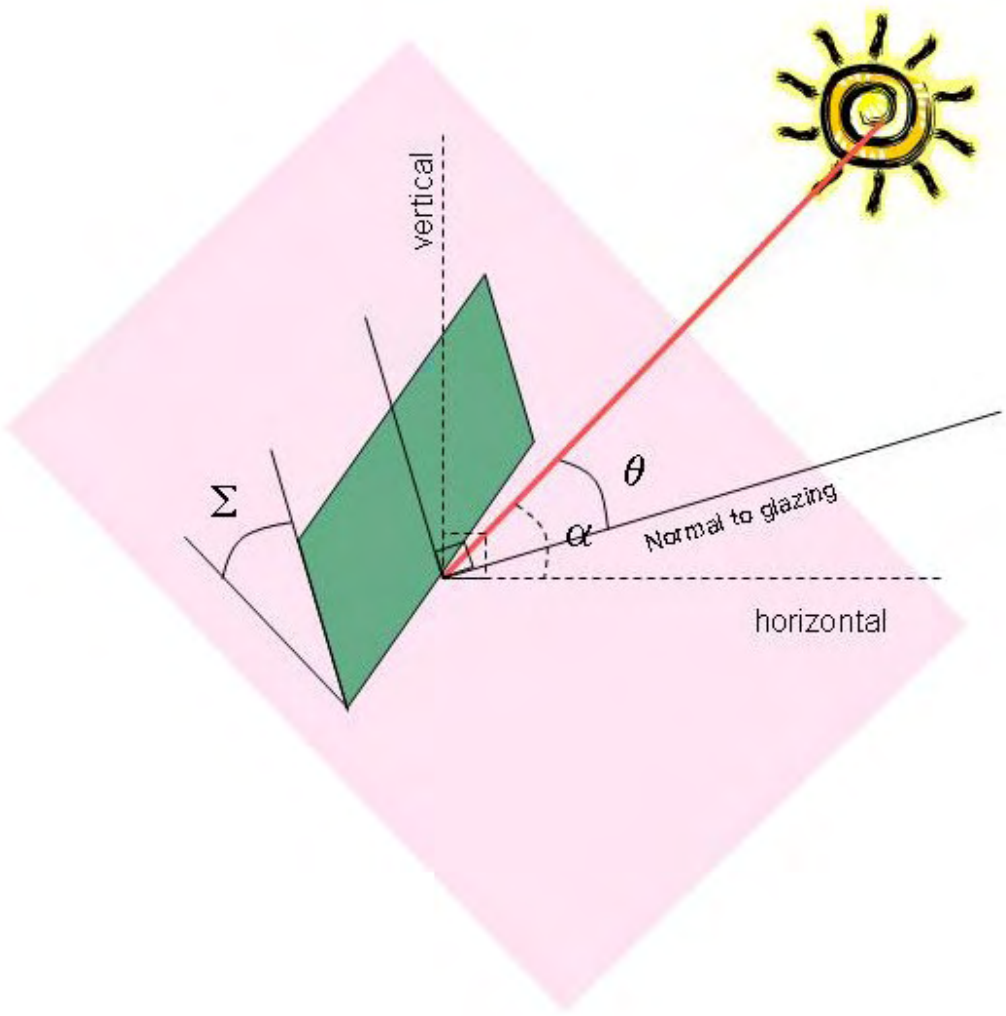

Figure 4.1. Representation of Solar Angles

α and θ can be calculated using the Fortran codes supplied by Muneer in his book 'Solar Radiation & Daylight Models' [2].

4.1.1.2 Solar irradiation transmitted through glazing

The Solar Heat Gain Coefficient (SHGC) is considered as two components: a) the solar irradiance which is transmitted directly through the glass, and b) solar gain which is re-emitted after it has been absorbed by the glass. Since the absorption and transmittance of the glass vary with the angle of incidence, the SHGC is also a function of the angle of

incidence [3]. Values of the SHGC at different incident angles, and for diffuse irradiation can be found in ASHRAE Fundamentals 2005 [3] for specific glazing systems.

The input power can be split into the direct solar heat gain, and the diffuse. The direct solar heat gain (Q_{dir}) is calculated from [3]:

$$Q_{dir} = A_g E_{vdir} SHGC_\theta \quad 4.2$$

Where

A_g is the collector area exposed to the solar irradiation

$SHGC_\theta$ is the angle dependent solar heat gain coefficient for direct solar irradiation.

The diffuse solar heat gain (Q_{diff}) is calculated from [3]:

$$Q_{diff} = A_g E_{vdiff} SHGC_{diff} \quad 4.3$$

Where $SHGC_{diff}$ is the solar heat gain coefficient for diffuse solar irradiation.

Therefore, input power (Q_{in}) is calculated from:

$$Q_{in} = Q_{dir} + Q_{diff} \quad 4.4$$

4.1.1.2.1 Solar Heat Gain Coefficient

The SHGC can be calculated for a specific scenario by following the procedure in this section.

The SHGC is related to the transmissivity (τ), absorptivity (α) and the inward flowing fraction of solar irradiation (N) of the glass [3]:

$$SHGC = \tau + N\alpha \quad 4.5$$

τ and α can be obtained from tables [3] for specific glazing systems.

N can be calculated from [3]:

$$N = \frac{U}{h_o} \quad 4.6$$

Where U is the thermal transmittance, and h_o is the heat transfer coefficient on the outer surface.

U can be calculated from [4]:

$$\frac{1}{U} = \frac{1}{h_i} + R + \frac{1}{h_o} \qquad 4.7$$

Where h_i is the heat transfer coefficient on the inner surface and R is the thermal resistance.

The heat transfer coefficient on the inner surface can be calculated from [4]:

$$h_i = h_{ci} + h_{ri} \qquad 4.8$$

Where h_{ci} is the heat transfer coefficient on the internal surface due to convection, and h_{ri} is the linearised heat transfer coefficient on the internal surface due to radiation.

h_{ci} can be calculated from [3]:

$$h_{ci} = \frac{kNu}{L} \qquad 4.9$$

Where k is the thermal conductivity of the material, Nu is the Nusselt number and L is the length of the surface.

The required Nusselt number depends on whether the air mass flow is laminar or turbulent.

Laminar Nusselt number for a pipe [3]:

$$Nu_{lam} = 1.86\left(\frac{\mathrm{Re}\,\mathrm{Pr}}{L/D_h}\right)^{1/3}\left(\frac{\mu}{\mu_{sur}}\right)^{0.14} \qquad C10$$

Where Re is the Reynolds number, Pr is the Prandtl number, D_h is the hydraulic diameter, μ is the dynamic viscosity of air.

Turbulent Nusselt number for a pipe [3]:

$$Nu_{turb} = \frac{\left(f_s/2\right)(\mathrm{Re}-1000)\mathrm{Pr}}{1+12.7\left(f_s/2\right)^{1/2}\left(\mathrm{Pr}^{2/3}-1\right)}\left[1+\left(\frac{D_h}{L}\right)^{2/3}\right]\left(\frac{T}{T_{sur}}\right)^{0.45} \qquad \text{C14}$$

Where T is the temperature of the air and f_s can be calculated from [3]:

$$f_s = \frac{1}{(1.58\ln \mathrm{Re}-3.28)^2} \qquad \text{C15}$$

and h_{ri} can be calculated from [4]:

$$h_{ri} = \frac{T'^4_1 - T'^4_2}{T'_1 - T'_2}\varepsilon\sigma \qquad 4.10$$

Where T'_1 is the glass temperature in Kelvin, T'_2 is the average temperature of the other three duct surfaces in Kelvin (Figure 4.2). ε is the emissivity of the glass and σ is the Stefan Boltzmann constant (5.67E-8 W m^{-2} K^{-4}).

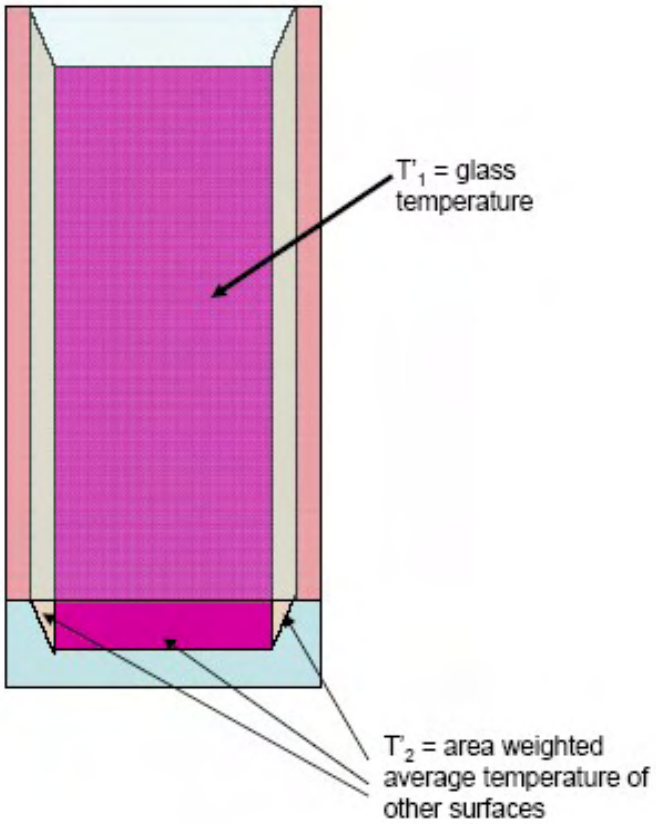

Figure 4.2. Representation of surface temperatures

The thermal resistance can be calculated from [4]:

$$R = \frac{d}{k} \qquad 4.11$$

Where d is the distance the heat travels through the material.

The heat transfer coefficient on the outer surface can be calculated from [4]:

$$h_o = h_{co} + h_{ro} \qquad 4.12$$

Where h_{co} is the heat transfer coefficient on the outer surface due to convection, and h_{ro} is the heat transfer coefficient on the outer surface due to radiation.

The heat transfer coefficient on the outer surface due to convection is due to wind. The heat transfer coefficient is affected by the combination of wind velocity (v) and the height of the surface (H). If $v*H \leq 8$ (C24) [4] the wind flow is considered to be laminar and the following equation is used to calculate h_{co} [4]:

$$h_{colam} = 3.96\sqrt{\frac{v}{H}} \qquad C25$$

otherwise the wind flow is considered to be turbulent and the following equation is used [4]:

$$h_{coturb} = 5.76\sqrt[5]{\frac{v^4}{H}} \qquad C26$$

The heat transfer coefficient on the outer surface due to radiation is calculated using the same form as equation 10; however, T'_s is replaced with the sky temperature (T_{sky}) in Kelvin [4]:

$$h_{ro} = \frac{T'^4_1 - T'^4_{sky}}{T'_1 - T'_{sky}}\varepsilon\sigma \qquad 4.10$$

Where T'_1 is the glass temperature in Kelvin.

A definition of the clear sky temperature (^oC) according to the thermal model HTB2 is [5]:

$$T_{sky} = \left(\frac{\frac{LW_v}{0.9}}{5.67^{-8}} \right)^{0.25} - 273.15 \qquad 4.13$$

where

$$LW_v = \frac{LW_h}{2} + 0.3457 * B\sigma\left(T_{amb} + 273.15\right)^4 + A - 8BC \qquad 4.14$$

where

$$LW_h = 222 + 4.94T_{amb} + \left(8.1 + 0.07T_{amb}\right)8C \qquad 4.15$$

$$A = 162 + 3.15T_{amb} \qquad 4.16$$

$$B = 0.09\left(1 - C\left(0.7067 + 0.00822T_{amb}\right)\right) \qquad 4.17$$

C = cloud cover on a scale of 0 = clear to 1 = overcast.

4.1.2 Useful Power Output (Q_{use})

Useful power output will be manifested as an increase in air temperature from inlet to outlet. Useful power output is calculated from [6]:

$$Q_{use} = \dot{m}c_p\left(T_{fo} - T_{fi}\right) \qquad 4.18$$

Where $\dot{m}$ is the air mass flow (kg s^{-1}), c_p is the specific heat capacity of air (J kg^{-1} K^{-1}), T_{fo} is the temperature of the air at outlet, and T_{fi} is the temperature of the air at inlet.

4.1.3 Power Losses (Q_{loss})

Heat can be lost from the system in several ways.

- Some of the direct irradiance will be reflected off the solar absorber and will be transmitted back through the glass. This will be discussed in Section 4.1.3.1.
- The solar irradiance which is not reflected out of the duct is absorbed by the duct surfaces. Some of the heat from these surfaces is transmitted to the air passing through the duct. This has been calculated as 'Useful Power Output' in Section 4.1.2. The remaining heat will be lost through conduction, convection and radiation from each of the duct outer surfaces. This will be discussed in Section 4.1.3.2.

The total heat loss is calculated as follows:

$$Q_{loss} = Q_R + Q_{front} + Q_{back} + Q_{left} + Q_{right} \quad 4.19$$

These losses are represented in Figure 4.3.

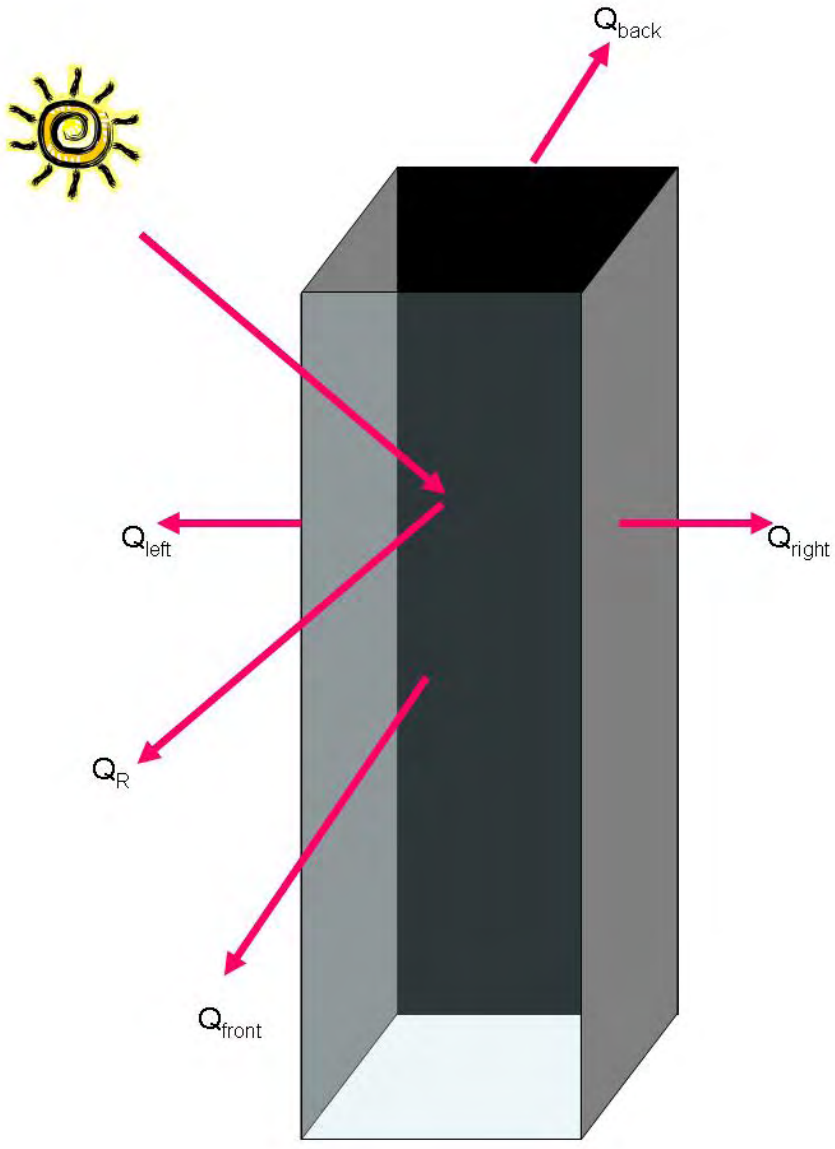

Figure 4.3. Representation of power losses from surfaces

4.1.3.1 Reflection

A proportion of solar irradiation is reflected off the glazed surface. This loss has already been accounted for in the calculation of the Solar Heat Gain Coefficient

(Section 4.1.1.2.1). The path of the solar irradiation from this point on is shown in Figure 4.4.

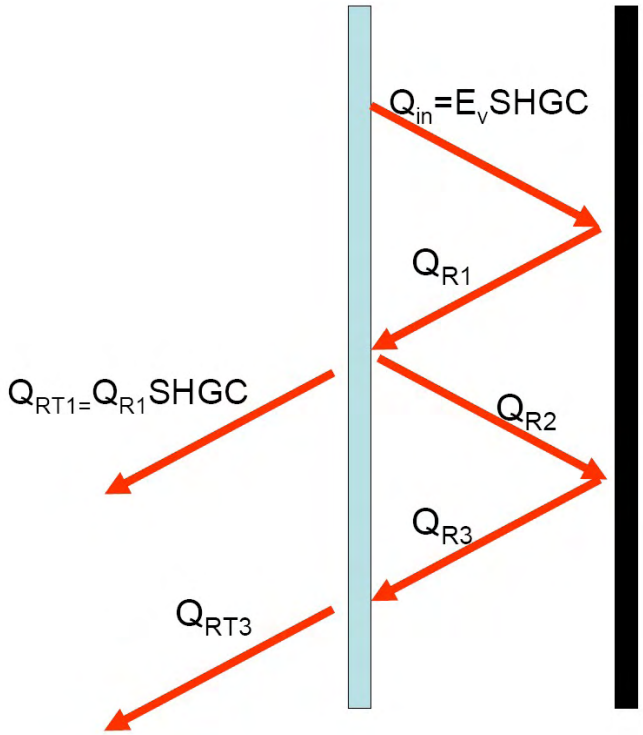

Figure 4.4. Path of heat loss through reflection

A proportion of the direct solar heat gain would be reflected from the solar absorber towards the glass. The spectral reflection would cause the solar heat gain to be diffuse rather than a direct beam. The proportion of the heat reflected back towards the glass cover is given by:

$$Q_{R1dir} = R_p Q_{dir} \qquad 4.20$$

Where R_p is the reflectivity of the paint on the absorber surface.

A proportion of this reflected heat (Q_{R1dir}) dependent on the diffuse reflectivity of the glass (R_{diff}) would be transmitted back out through the glass, this is approximated by:

$$Q_{RT1dir} = SHGC_{diff} Q_{R1} \qquad 4.21$$

However, a proportion of the reflected heat (Q_{R1dir}) would be reflected back towards the solar absorber. For direct solar irradiation the residual heat is small enough that further

losses can be ignored after three reflections and two sets of transmission losses. A similar procedure can be carried out for the diffuse solar irradiation, although the residual heat is small enough that further losses can be ignored after one reflection and one transmission loss. The total reflection loss (Q_R) is the sum of the three transmission losses:

$$Q_R = Q_{RT1dir} + Q_{RT3dir} + Q_{RT1diff} \qquad 4.22$$

4.1.3.2 Heat Loss from Surface

The outer surfaces lose heat through radiation, convection and conduction. This process has already been discussed in the calculation of the Solar Heat Gain Coefficient (Section 4.1.1.2.1).

The information on radiation, convection and conduction is combined to give a generic equation for the heat loss from a surface:

$$Q_{sur} = A\frac{T_{sur} - T_{amb}}{\frac{d}{k} + \frac{1}{h_c + h_r}} \qquad 4.23$$

This can be applied to each of the four duct surfaces.

4.1.3.3 Summary of Thermodynamic Model

The thermodynamic model is:

$$Q_{in} = Q_{use} + Q_{loss}$$

Where the input power (Q_{in}), useful power output (Q_{use}) and power loss (Q_{loss}) have been defined in the previous sections.

4.1.4 Requirements for Model Validation and for Obtaining Empirical Data

The model described above could predict the behaviour of a prototype from the following parameters:

Meteorological Data - Al, E_{vg}, E_{hg}, E_{hdiff}, C, *v*, T_{amb},

Duct/Material parameters (specified) – A (front, back and sides), H, L, $SHGC_{diff}$, $SHGC_{\theta}$, c_p, R_p, R_{diff}, ε_g, ε_p, k_g, k_p, k_{ins},

Duct/Material parameters (measured) - $\dot{m}$, T_{fo}, T_{fi}, T_{sur} (front, back and sides),

Constants – σ

4.2 Experiment Design

Experimental data are required to test the validity of this model. If it is valid, then it can help identify the relative importance of variables in the design of a duct. Once the experiment has been constructed it would also be useful to analyse its behaviour in different weather conditions. These should include:

- Winter – cold, variable day under forced convection. These conditions would indicate how the system operates as a ventilation preheater in winter.
- Winter – sunny day under forced convection. These conditions would indicate how the system operates as a ventilation preheater in winter.
- Summer – sunny day (forced convection). These conditions would indicate if the system has potential as a heat exchanger for water heating.
- Summer – sunny day (buoyant convection). These conditions would indicate how the system is likely to perform as a passive ventilation preheater.
- Summer – sunny day (stagnant). These conditions would indicate if there is any danger of part of the system reaching excessive temperatures under stagnant conditions.

The experiment design is shown schematically in Figure 4.5.

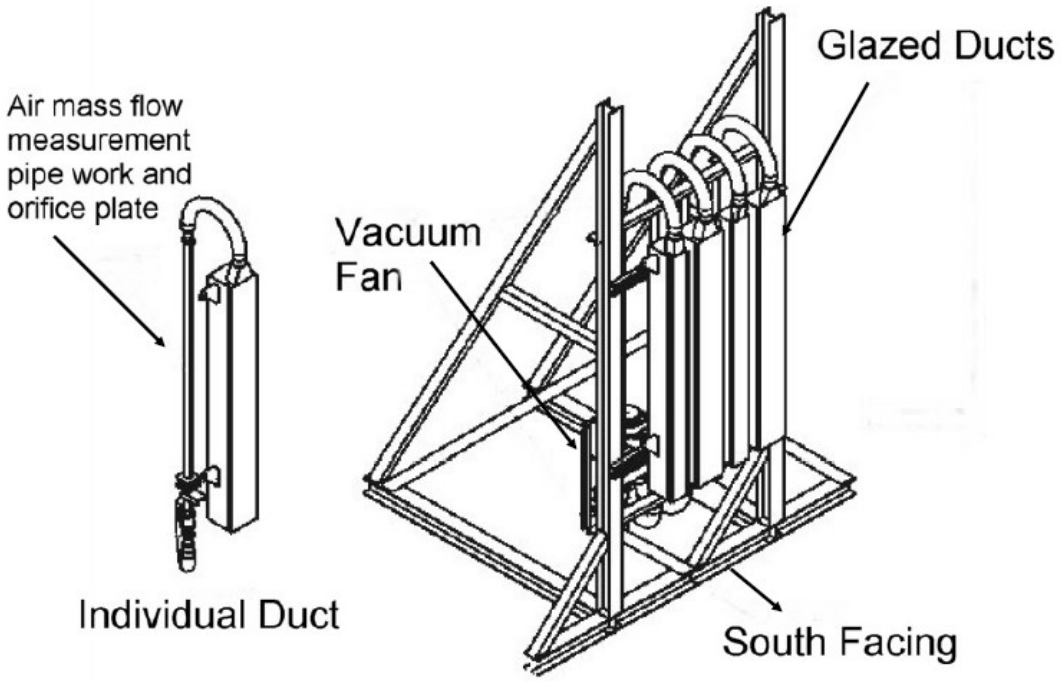

Figure 4.5. Experiment 2 Schematic

4.2.1 Location

A suitable location for the experiment was required. Ideally this would be in an enclosed, unoccupied area to prevent vandalism or accidental damage. It would also be south facing to obtain the most solar irradiation; with no obstructions to block or reflect solar irradiance. An enclosed, south facing area was found within the Corus weathering station in Port Talbot (latitude 51.34 ^{o}, longitude 3.45^{o}). Unfortunately a hill and some trees to the east blocked the early morning sun. The area was used as a weathering station by Corus, and had several metal frames holding painted and metal samples. Figure 4.6 shows the view from the experiment (taken with a fish eye lens). There were concerns that these reflections could affect the local albedo, and an ancillary measurement was required to verify this (Section 4.2.6.1). After assembly the exact orientation of the experiment was measured by observing solar shadows and found to be 7^{o} to the east of solar south. Compass confirmation was not possible due to interference from electricity lines overhead.

Figure 4.6. 180^{o} view from experiment

4.2.2 Prototype Construction

The ducts were manufactured as in Section 3.1.1, but with the addition of Isover Cladding Roll insulation to reduce the heat losses from back (160 mm thickness) and sides (38 mm thickness) of the duct. An outer skin made of mild steel was used to contain the insulation and support the ducts. The dimensions of the duct and of the system including the outer skin are shown in Table 4.1 and represented in Figure 4.7. The ducts have been identified with respect to their dimensions (i.e. N represents narrow, W represents wide, D represents deep and S represents shallow).

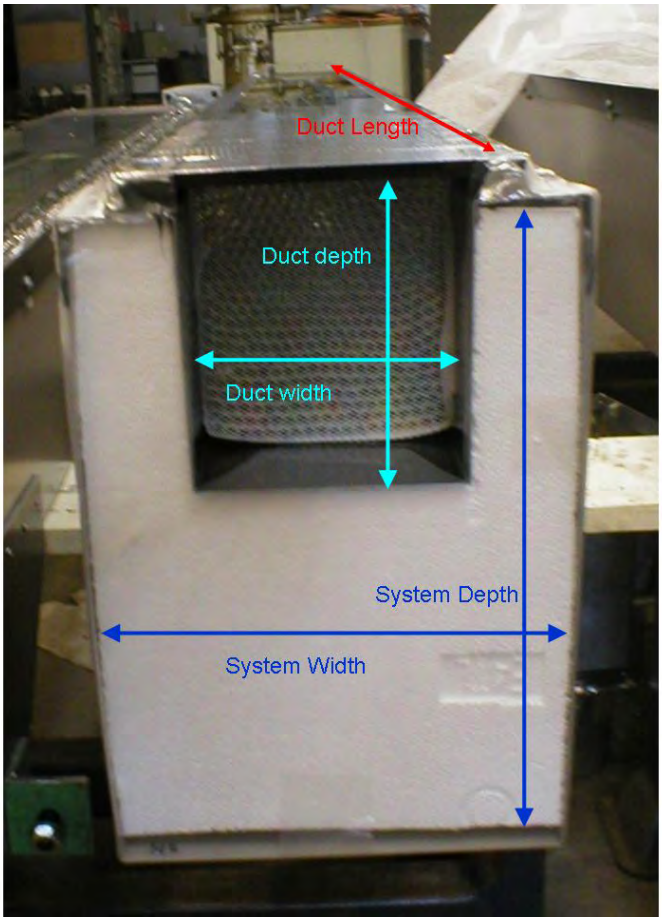

Figure 4.7. Schematic Showing Duct and System Dimensions

Table 4.1 Dimensions of ducts in Experiment 2

Duct ID	Duct		System		Length (m)
	Width (m)	Depth (m)	Width (m)	Depth (m)	
ND	0.101	0.1105	0.177	0.26	2.4
WD	0.208	0.1105	0.285	0.275	2.4
NS	0.101	0.0405	0.177	0.19	2.4
WS	0.2005	0.041	0.277	0.2	2.4

These width and depth dimensions are larger than the ducts used in Chapter 3, where a measurable pressure drop across the duct was required. In this experiment, a high pressure drop across the duct would inhibit buoyant flow.

The system length is 2.4 m as before; however, 20 cm from the bottom of the glass and 30 cm from the top of the glass was masked with reflective tape to protect the air

temperature thermocouples from solar irradiance, this gave an exposed glass length of 1.9 m. The ducts were attached to the frame separately to avoid one duct having an influence on its neighbour through heat conduction.

The assembled experiment is shown in Figure 4.8, with the position of pyranometers, anemometer, wind vane, ambient temperature, relative humidity sensor shown. Details of the individual meters are given in Section 4.2.5. The air temperature at the inlet and outlet of each duct was monitored. Full details of the temperature monitoring are given in Section 4.2.4. The sensors and thermocouples were connected to a Campbell Scientific Datalogger. Data from the sensors was collected at 5s intervals and averaged over a period of 5 minutes.

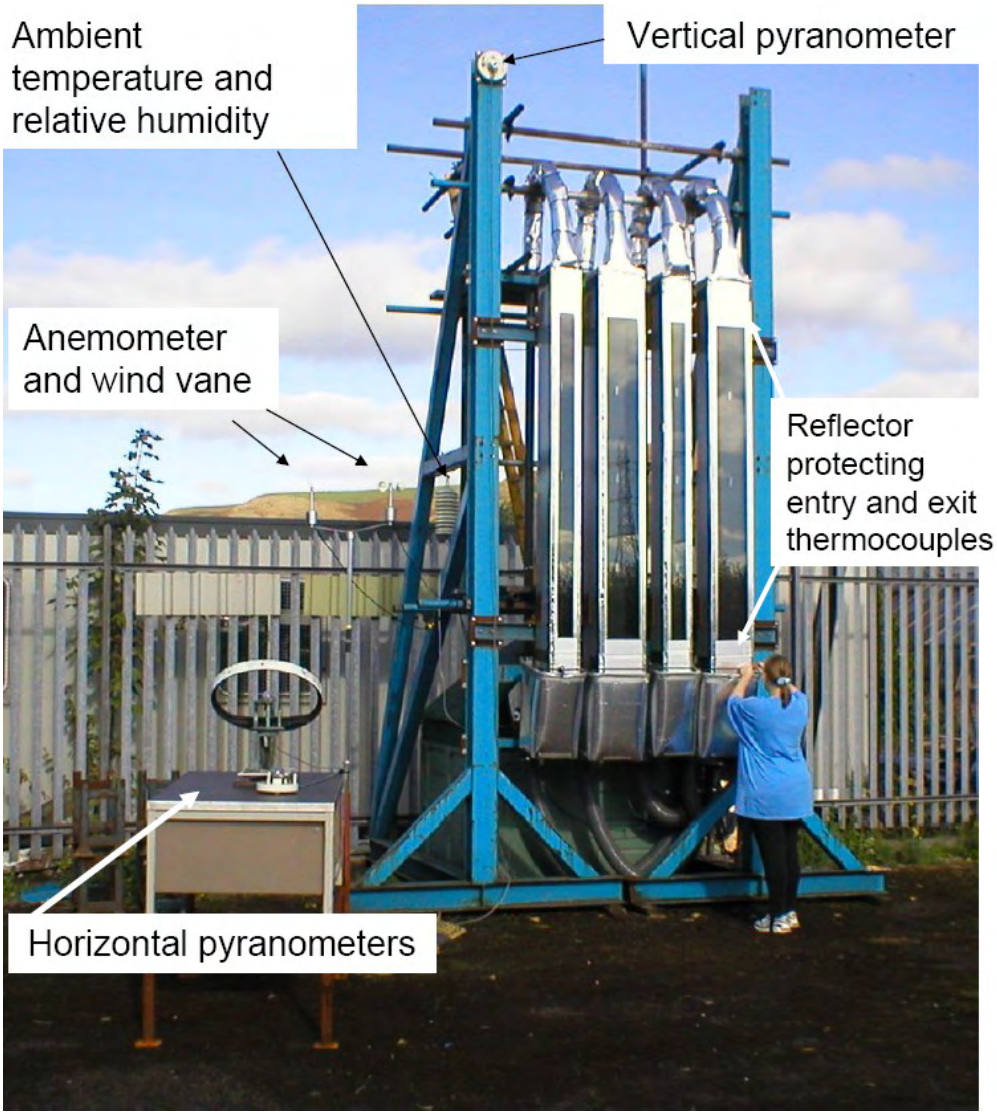

Figure 4.8. Overview of Experiment 2

Figure 4.9 shows the position of the individual ducts on the frame.

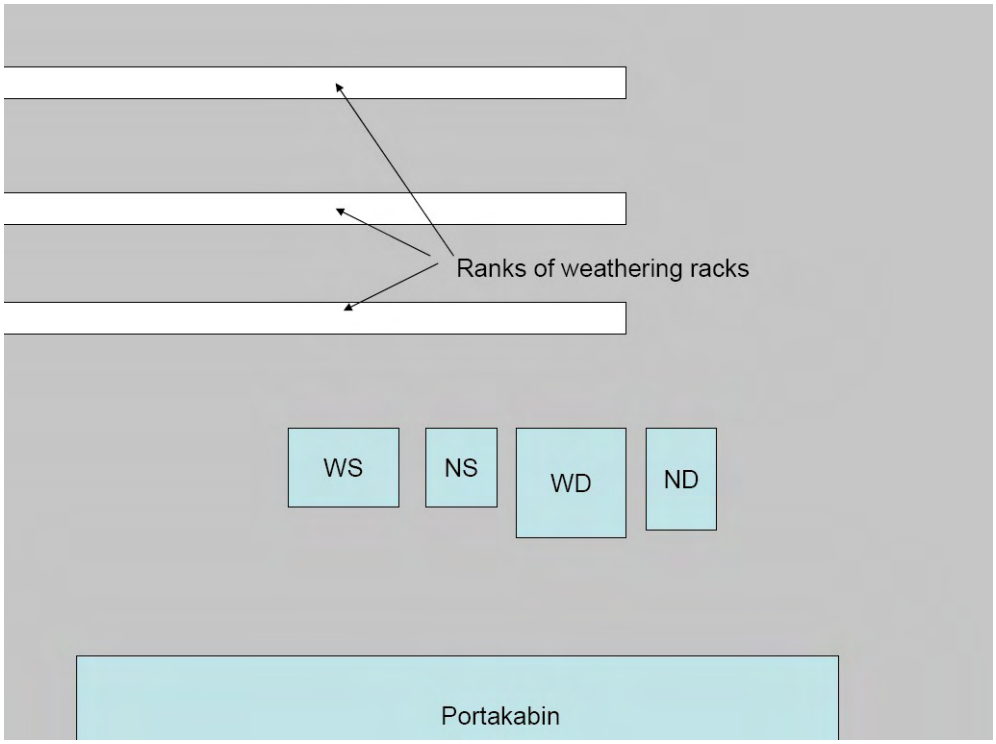

Figure 4.9. Experiment Layout

4.2.3 Air Mass Flow

As can be seen from Figure 4.5, the air mass flow is generated using a vacuum fan, and measured indirectly from the pressure drop over an orifice plate as in the previous experiment (Section 3.1). However, the additional effects of temperature and relative humidity on air density have been accounted for in the air mass flow calculations for this experiment. The pressure drop measurements (from which the air mass flow was calculated) were taken manually at hourly intervals.

The literature survey indicated that a typical air mass flow would be 0.01 kg s^{-1}. However, the air mass flow was set to 0.005 kg s^{-1} for this experiment. This was to ensure larger differences between the air entry temperature and the air exit temperature and so improved measurement accuracy.

4.2.4 Temperature Measurements

The temperature measurement points are indicated by asterisks in Figure 4.10. Each duct had one measurement taken at the following points:

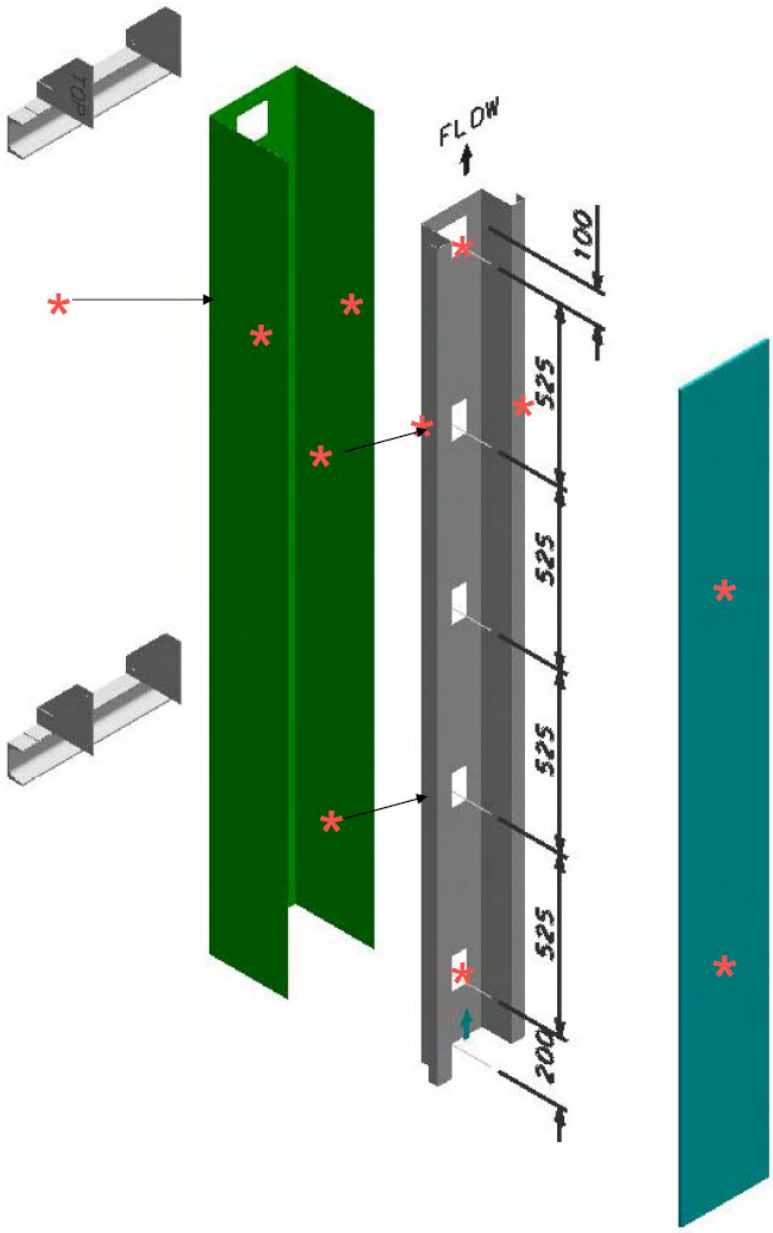

Figure 4.10. Illustration of duct design showing temperature measurement points

- Air temperature measurement at 0.2 m and 2.3 m from the air inlet.
- Temperature of the glass at 0.725 m and 1.775 m from the air inlet.

- Temperature of the solar absorbing duct rear at 0.725 m and 1.775 m from the air inlet.
- The temperature of the left and right sides of the solar absorbing duct at 0.725 m and 1.775 m from the air inlet.

These measurements used up 24 of the 29 available connections to the datalogger. It was only possible to take the following measurements from some of the ducts (discussed further in Section 4.2.6.3):

- The temperature of the left, rear and right of the outer skin at 1.775m from the air inlet.

PTFE sheathed, twisted Type T thermocouple wire was used to monitor all temperatures apart from ambient air temperature. The thermocouples were calibrated along with the ambient air temperature sensor (discussed in Section 4.2.6.2). This calibration indicated that the thermocouples used for measuring the air temperatures were accurate to 0.03 ^{o}C. The thermocouples used for measuring the temperatures of the metal duct surfaces were accurate to 0.31 ^{o}C.

As can be seen from Figure 4.10, the air temperature was measured on entering and exiting the duct. The air was measured at a distance of 2 cm from the metal surface of the duct. Each thermocouple was placed in a protective sheath (Figure 4.11). In addition reflective tape was placed over the surface of the glass to protect the thermocouple positions from solar irradiance.

Figure 4.11. Sheath to protect air temperature measurement thermocouple

For the glass surfaces, the thermocouple wires were kept in place using glass glue. The procedure for ensuring accurate glass temperature measurements is described in Section 4.2.7.1. For the opaque duct surfaces the thermocouple wires were kept in place using tape.

4.2.5 Meteorological Measurements

4.2.5.1 Solar Irradiance

Three Kipp and Zonen CM5 pyranometers which complies with the WMO specification for Class 1 have been used for the experiment.

The vertical pyranometer was mounted on the frame along with the experimental ducts. This was to ensure it received the same view of incoming solar irradiance as the ducts. The readings from this pyranometer were termed as global vertical irradiance (E_{vg}).

Two horizontal pyranometers were mounted on a table near the experimental rig. The unshaded pyranometer gave readings for global horizontal irradiance (E_{hg}). The third pyranometer had a shade positioned to protect it from direct solar irradiance and gave readings for diffuse horizontal irradiance (E_{hdiff}).

The sensitivity of the pyranometer can be affected by variations in temperature, irradiance, tilt angle and direction of radiation. The sensitivity of the pyranometer to temperature is shown in Figure 4.12 [7].

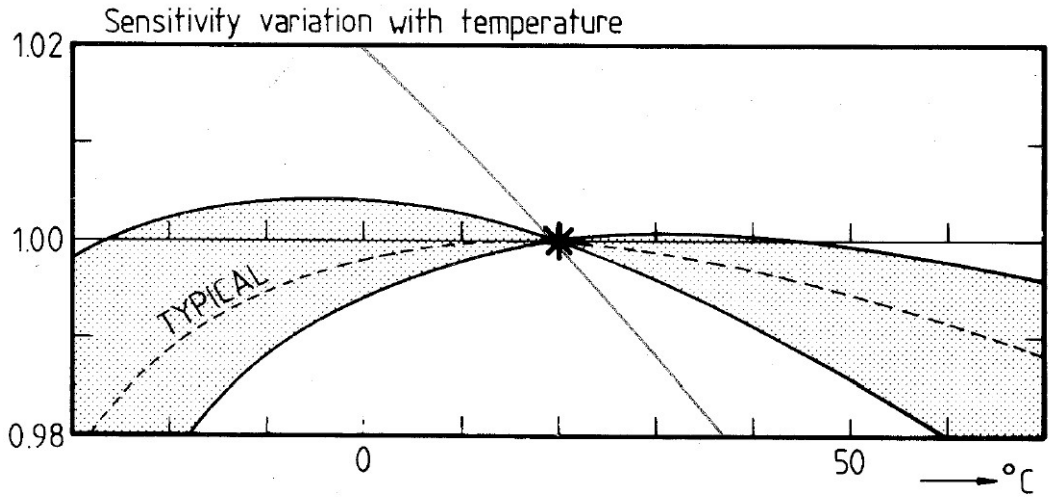

Figure 4.12. CM5 Pyranometer - sensitivity variation with temperature [7]

The seasonal outdoor temperature variation is unlikely to exceed -5°C to 30°C in its location. The maximum error attributable to the temperature variation would be -1% to +0.5%.

The sensitivity of the pyranometer to tilt is shown in Figure 4.13 [7].

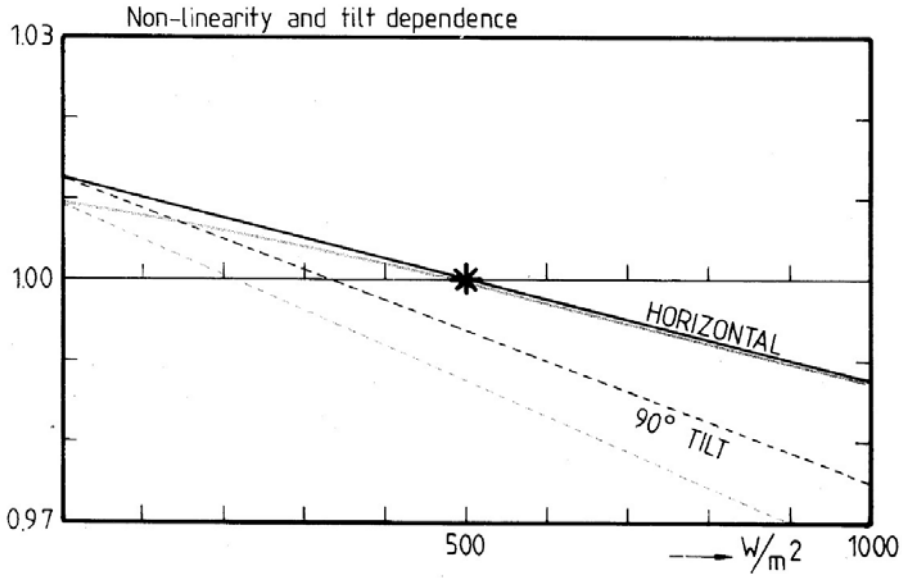

Figure 4.13. CM5 pryanometer sensitivity variation with tilt [7]

The vertical pyranometer was mounted at a 90^{o} tilt and is likely to have suffered an error from +1% at low solar irradiance, to -2% at high solar irradiance (~ 800 W m^{-2}). The horizontal pyranometers are likely to have suffered an error from +1% at low solar irradiance to -1% at high solar irradiance (~900 W m^{-2}).

Since the solar irradiance measurements suffer most through errors due to tilt and solar intensity, these errors are considered to be dominant. The measured solar irradiance is considered to have an error of ±1 % for the horizontal pyranometers and ±2 % for the vertical pyranometer.

4.2.5.2 Wind speed and Direction

The wind speed is monitored by an A100R anemometer which operates over a range of 0.2 to 75 m s^{-1}. The system is accurate to 1% of the reading for a range of 10 to 55 ms^{-1}. The accuracy below 10 m s^{-1} is 0.1 m s^{-1}. The number of rotations of the anemometer in a 5 minute period is monitored, and reported as a distance traversed in that time period. The average wind speed over the period is calculated by dividing the distance traversed by the 300 s time period [8].

The wind direction is measured by a 16 sector W200G windvane [9]. This assigns a compass direction (e.g. NNE, WSW…) to each sector. The direction of the windvane is monitored every 5 s. After a period of 5 minutes the number of times the anemometer has been pointing in a specific direction is totalled, this averaged output data is considered to be accurate to ±3^{o}. The prevailing wind direction is the one which shows the highest number of 'hits'. The windvane operates over a windspeed range of 0.3 to 75 m s^{-1}.

4.2.5.3 Ambient Temperature / Relative Humidity

The ambient air temperature was measured using a Vaisala HMP45A which incorporates a humidity monitor. The manufacturers have specified the relative humidity to be accurate to ±2 % in the range 0 to 90 % RH, and accurate to ±3 % in the range 90 to 100 % RH. The accuracy of the air temperature measurement is shown in Figure 4.14 [10].

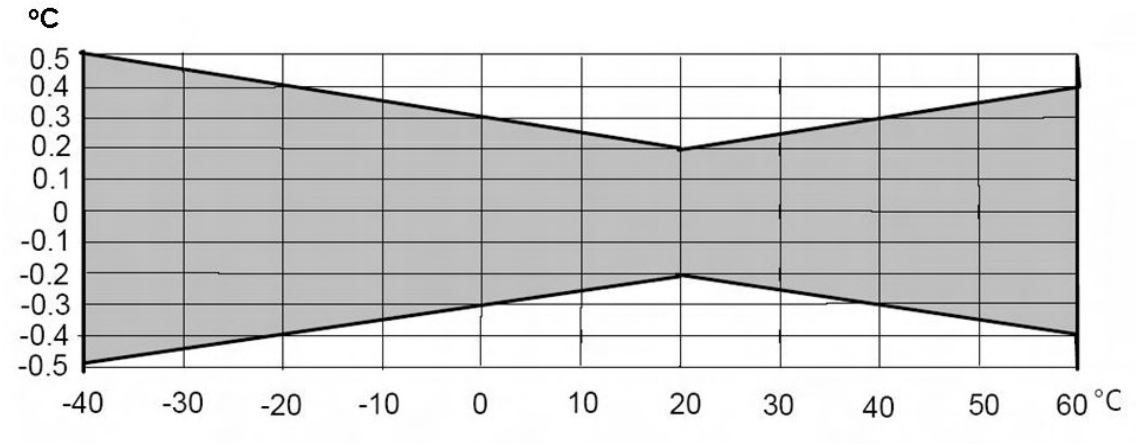

Figure 4.14. HMP45A-D Accuracy (Y-axis) over Temperature Measurement Range (X-axis)

4.2.6 Ancillary Experiments

Ancillary experiments were required to determine the albedo at the experiment site, calibrate the temperature sensors and make assumptions about the temperature in parts of the experiment which could not be monitored continuously.

4.2.6.1 Albedo Determination Experiment

The view from the top of the experiment (Figure 4.6) shows significant amounts of metal and a body of water are visible. This led to concerns that the ground albedo in this area may be higher than the generally accepted average value of 0.2 [3]. A pyranometer was suspended (facing downwards) approximately 4.5m above the ground, with the scaffolding covered by a matt black material. Its readings were compared with the data from another pyranometer facing upwards. A schematic of the experiment is shown in Figure 4.15.

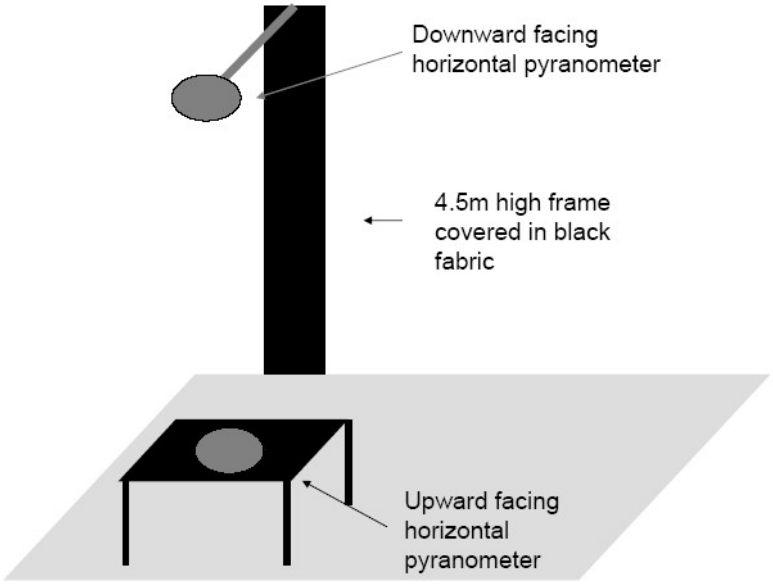

Figure 4.15. Schematic of albedo experiment

Data was taken from both pyranometers over the daylight periods of five days. The ratio of the downward facing irradiation to the upward facing irradiation is plotted in Figure 4.16. The average albedo was calculated to be 0.086 ± 0.026. This is actually lower than expected. This can be attributed to the dark mossy ground around the experiment, which outweighed the other factors. The value of the albedo is required to calculate the input power in the model described in Section 4.1.1.

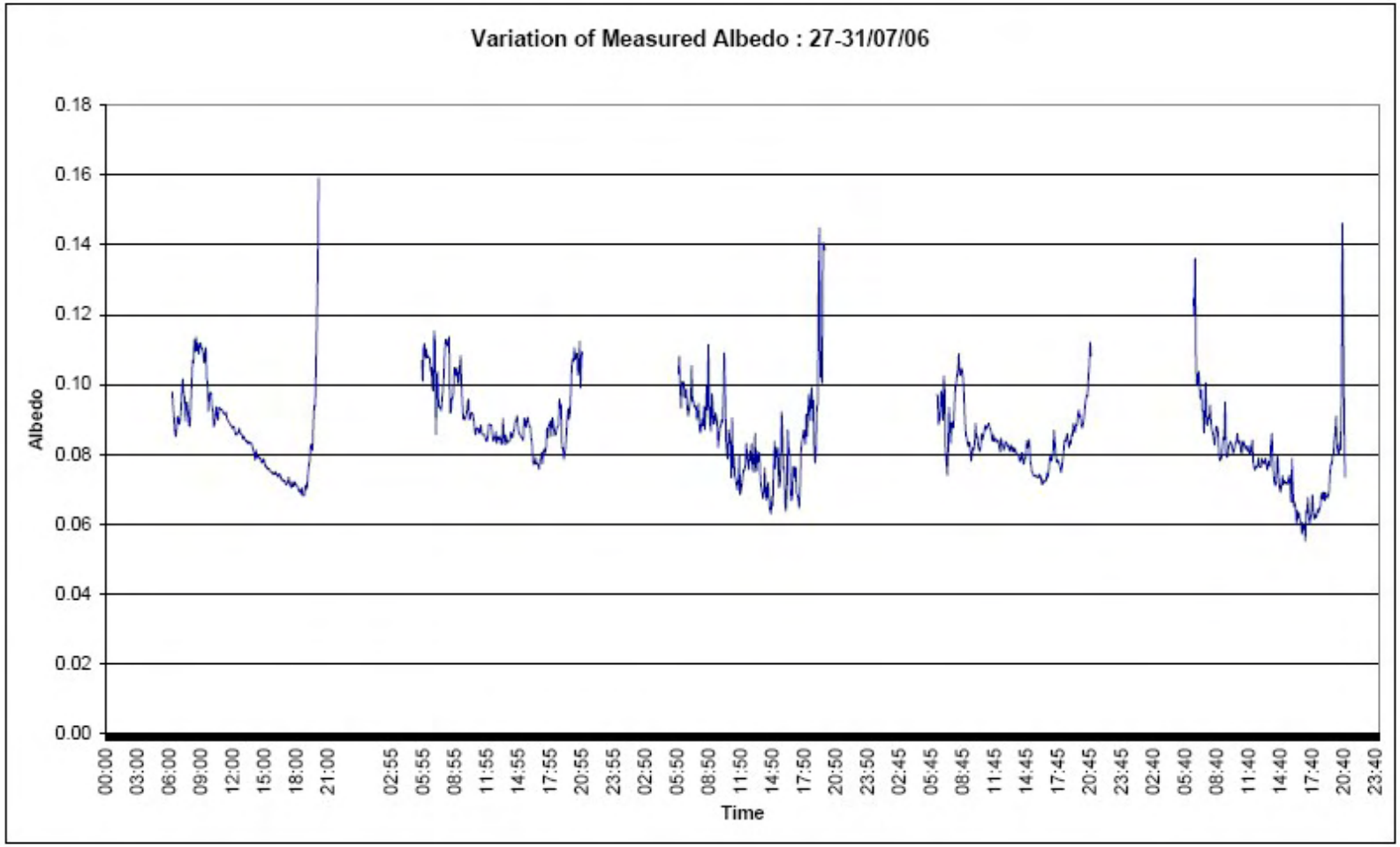

Figure 4.16. Variation of Measured Albedo: 27-31/07/06

4.2.6.2 Calibration of Temperature Measurements

Monitoring of the experiment requires air, metal and glass temperatures to be monitored accurately. Thermistors are widely regarded as being an accurate (±0.1 ^{o}C) temperature sensor; however, there were several disadvantages to their use in this experiment. Thermistors have a slower thermal response [11], are more expensive (particularly for the high number of temperature measurements required), have a smaller temperature range and are difficult to work with over long lengths. In addition there was a datalogger available which was suitable for all the meteorological inputs as well as large numbers of thermocouples. For this reason it was decided to use PTFE sheathed, twisted Type T (copper – constantan) thermocouple wire to monitor all temperatures apart from ambient air temperature. These thermocouples are suitable for measurements between -70 to 250 ^{o}C and are generally considered to have an accuracy of 1 ^{o}C [11]. However, this level of accuracy would not be acceptable for the measurements needed here. The ambient air sensor was included in this calibration to improve the accuracy.

The thermocouples and temperature sensor were wrapped in latex and held in a temperature controlled bath. Initially chilled water and ice were used to obtain a low temperature, then ice cubes were fed into the water to retain it. A temperature of 7.3 ± 0.1^{o}C (as indicated by the sensor on the bath) was kept for 30 minutes. The bath's temperature control was then used to hold the temperature steady at 20.0, 40.0, 60.0, and 27.0^{o}C for at least 30 minute intervals. Correction factors for each thermocouple were obtained from these results. After implementing the correction factor, the standard error for each thermocouple was calculated and listed in Table F5. Typically surface and air temperature could be taken to better than 0.1^{o}C after calibration; however, a few thermocouples were only accurate to 0.5^{o}C.

4.2.6.3 Error calculation for temperatures without thermocouples

The outer surface temperature of the ducts is relevant to heat loss calculations. However, only 5 thermocouples were available to measure the temperature of 12 outer surfaces over four ducts. The measurement of the outer surfaces was further complicated by the likelihood of solar irradiation on the outer surfaces affecting the

temperature readings of thermocouples placed between the metal outer surface and the insulation. Therefore the available sensors were placed where they were expected to provide the most useful information.

One thermocouple was used to measure the back surface of the duct ND. Two of the remaining four thermocouples were placed on outer surfaces of duct ND, ensuring that at least one duct had as complete a set of data as possible. One thermocouple was placed on the right (from the back) outermost surface of duct WD. The remaining thermocouple was placed on the left surface of duct WS. The position of the thermocouples are shown in Figure 4.17 where green represents thermocouples which were in place, and red represents place where thermocouples would have been placed, had there been enough thermocouples. The markings in the middle of the ducts represent the thermocouple on the back outer surface of each duct.

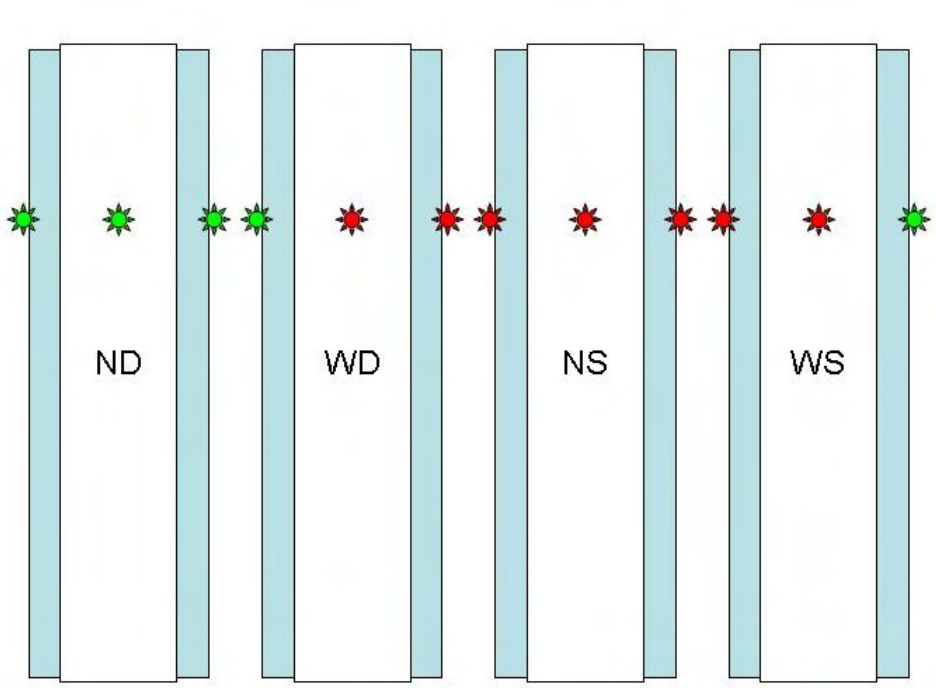

Figure 4.17. Schematic illustrating position of thermocouples on outer surface of ducts

After the experiment was complete, thermocouples were rearranged so that the positions which had not been previously monitored could be compared with the thermocouples which had been used to make assumptions about their temperature. The

average difference between the actual temperature reading and the temperature reading from the thermocouple used to make the assumptions was calculated over a seven day period in July. The results are shown in Table 4.2.

Table 4.2 Average difference between real and assumed temperature

Duct	Surface[c]	Average Difference (^{o}C)	Maximum Difference (^{o}C)
WD	Left	0.3[b]	0.5
	Back	0.7	9.2
NS	Left	2.9[b]	2.4
	Back	1.0[a]	6.9
	Right	0.8	4.5
WS	Back	1.1	7.0
	Right	0.6	3.2

[a] only averaged over 2 sunny days due to thermocouple failure
[b] only averaged over 1 sunny hour due to failure of control thermocouple
[c] left and right surface identified from rear of experiment

The average difference found between each position and the thermocouple which was used to predict its value was considered to be the standard error.

4.2.7 Experiment Issues

4.2.7.1 Glass Temperature

Measuring glass temperature requires more preparation than measuring the temperature of opaque surfaces. This is because the thermocouple can be affected by the solar irradiance transmitted through transparent materials. The MSc Thesis by George Papailiou on 'Measurement of Glass Temperature' [12] indicates that glass temperature measurement can be undertaken by:

- Applying 7mm diameter circular patch of copper foil to the top surface of the glass. N.B. patches should be at least 5 patch diameters from the edge of the glass and 10 patch diameters from each other.
- Placing the thermocouple under the centre of the patch.

Although the emissivity of the two materials is different (polished copper emissivity 0.03, glass 0.94 [84]), the small area of copper used should not significantly affect the measured glass temperature, particularly as the copper would quickly corrode and reach a higher emissivity (0.78 [84]).

The results from his experiments indicate that this method would give temperatures accurate to between 1.2 to 2.6 ^{o}C, the higher error has been assumed. The standard error for glass temperature measurements have added this general value to the error for the individual thermocouple found during calibration in Section 4.2.6.2.

4.2.7.2 Air Temperature Gradient

It was one aim of the experiment to monitor the air temperature gradient at five positions along the length of the ducts. This would add to the information available in the literature on the temperature gradient [14-16]. To this aim, five thermocouples with heat reflecting sheaths were placed in each duct to measure the air temperature gradient throughout the duct (Figure 4.11). The protective sheath consisted of copper tubing painted with a heat reflecting aluminium paint. This tube was attached to the main duct via a 1.5 cm thermal break of plastic tubing. In addition, the entry and exit thermocouple positions were protected from solar irradiance by placing reflective tape over the surface of the glass. Despite the sheaths, the middle three thermocouples were found to give temperature readings higher than the exit air temperature which was considered to be physically impossible. Therefore these were considered unreliable and not used in analysis.

The emissivity of glass is relatively high (0.94) [13], indicating that it will radiate heat towards the sheaths. The emissivity of copper should be low (0.03) [13], therefore heat should not be radiated from the copper sheath towards the thermocouple. There are four potential reasons for the failure of the sheaths to protect the thermocouple: the paint may not have been adequately reflective, corrosion may have increased the tube emissivity, the plastic tubing mounts may not have been adequately resistant to heat transfer, or there may not have been sufficient airflow through the tube.

4.2.7.3 Ambient Air Temperature

The ambient air temperature sensor is a Vaisala HMP45A which incorporates a humidity monitor. The difference in type of sensor could explain why the ambient temperature sensor was found to read approximately 1.1 ^{o}C lower than the thermocouples during the night when there was no interference from solar irradiation. A

correction factor for this was not possible since the ambient temperature sensor gave hotter readings than the shaded air entry thermocouples when it was exposed to solar irradiation (despite using the shading device provided by the manufacturer). Although it was positioned in an area where it was in shade until about mid afternoon, it could not be positioned in an area where it was shaded permanently. For these reasons the average air entry temperature seemed a more accurate representation of ambient air temperature. However, when the solar altitude was high (mid day in the summer months), it was found to interfere with the air entry temperature readings for ducts ND and WD. The air entry temperature of ducts NS and WS showed similar results to each other. Therefore an average of the two entry temperatures from the shallow ducts was used as the entry temperature for all four ducts and was also used to represent the ambient air temperature in the model.

4.2.7.4 Orifice Plate Corrosion

On removing the orifice plates they were found to have corroded. The principal issue from the corrosion was an alteration of the orifice diameter. The initial orifice plate diameter measurements had been taken with vernier callipers. However, this was not possible on the corroded plates, as any contact could have removed the corrosion and given a false reading. Photographs were taken of the orifice plates in their housings. Since the housing was made of aluminium and had not suffered any corrosion, this could be measured and other dimensions could be calculated from their proportions in relation to the housing. Although this did not give as accurate a result, it gave an indication of the new diameter. The results are shown in Table 4.3. The effect of the change in diameter on the air mass flow was estimated, and this is also shown in Table 4.3, and taken into consideration in the error propagation calculations in Appendix F. The final diameter was applied to all of the air mass flow calculations.

Table 4.3 Orifice Plate Diameter Measurements

Duct	Initial Diameter (mm)		Final Diameter (mm)		Effect on air mass flow
	average	Error	Average	Error	
ND	21.97	0.01	21.2	0.5	-0.5%
WD	21.97	0.01	21.2	0.4	-0.5%
NS	21.96	0.01	21.9	0.7	-0.1%
WS	21.96	0.01	20.9	0.5	-0.7%

4.3 Results

The experiment was operated in different weather conditions to achieve the sub tasks specified in Section 4.2. Consistently sunny weather conditions were required to evaluate the model. Dates for running the experiment were established by watching weather forecasts to identify such days. The experiments were started before direct solar irradiation was incident on the solar collectors (generally before 06:30) and allowed to stabilise for at least 30 minutes before readings were taken. The experiments were concluded after dusk, unless it had to be stopped for safety reasons (e.g. rain started and the fan had to be switched off). Several attempts to capture data for consistently sunny days were abandoned due to changes in the weather. The five sets of data described below, were selected from twenty seven experimental attempts. The results below are used in Chapter 5.

4.3.1 Winter – Cold, Variable Day (Forced Convection)

On the 25th of January 2006 forced convection (air mass flow ~ 0.005 kg s^{-1}) was run through the experiment described in Sections 4.2.1 to 4.2.7. A typical temperature profile is shown in Figure 4.18 where a typical output air temperature is plotted along with global horizontal solar irradiation.

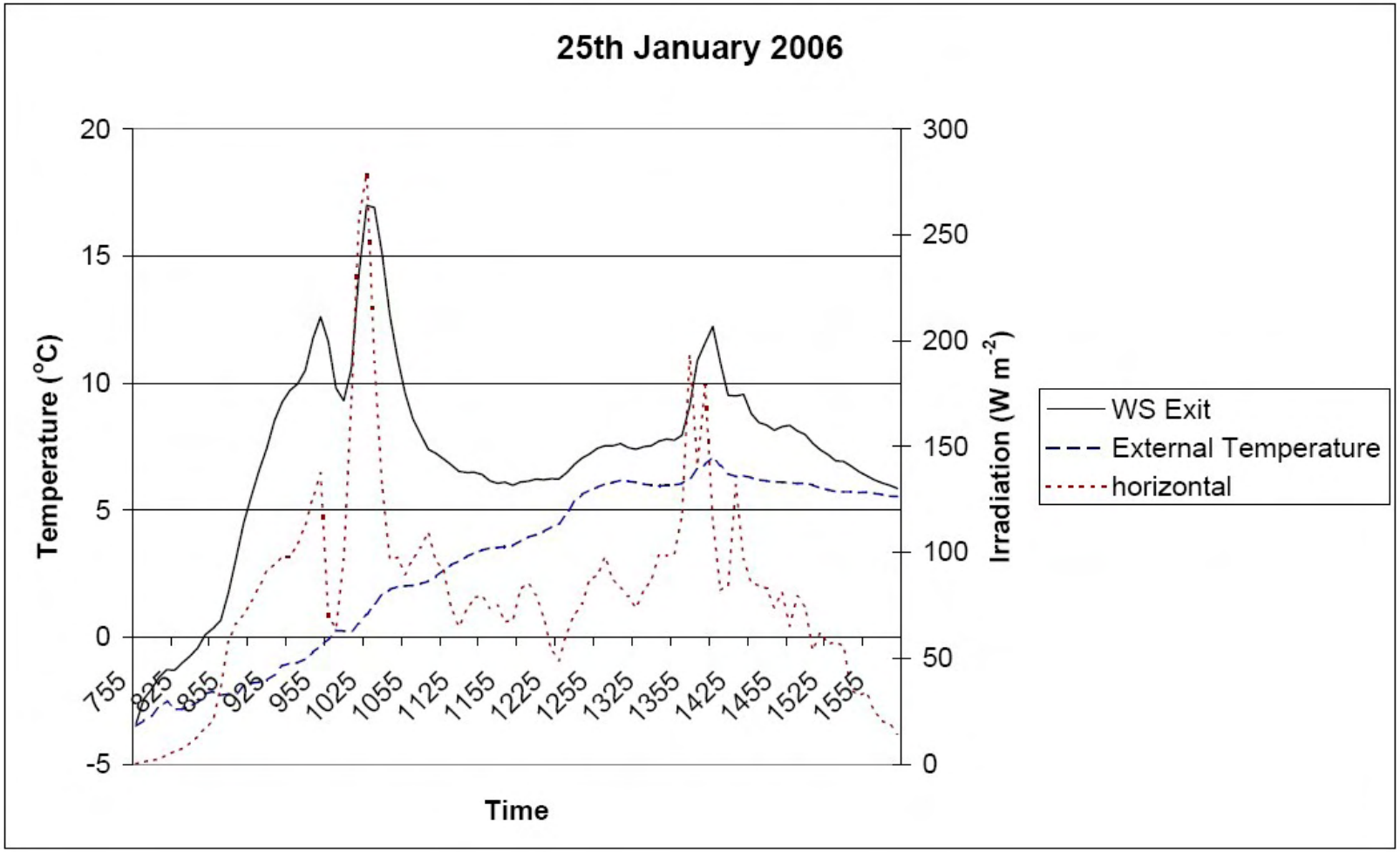

Figure 4.18. Temperature profile for 25th January 2006

During the night prior to this experiment there had been a heavy frost. The temperature profile shows that if the solar air heater was used to preheat ventilation air, it would bring in air above 0 ^{o}C by 09:00. It would have taken until 10:00 before external air would rise to that temperature. Although, it was not a particularly sunny day, the air within duct WD was heated by up to 18 ^{o}C above the external temperature at one point in the day, and was an average of 4 ^{o}C warmer than the external temperature throughout the day.

Between 08:00 and 17:00 on 25th January, the horizontal solar irradiation was measured to be 668 Wh m^{-2}. The energy output of the ducts over the same time period is shown in Table 4.4. The scaled energy output for ducts with a glazed area of 1 m^2 exposed to solar irradiation is also shown.

Table 4.4 Output of ducts from 08:00 to 17:00 on January 25th 2006

Duct	Ave air mass flow (kg s^{-1})	Energy Output (Wh)	Energy Output (Wh) per m^2
ND	0.0047	74	384
WD	0.0054	163	412
NS	0.0052	60	313
WS	0.0051	107	281

This indicates that between 42 and 62 % of the horizontal solar irradiation is being converted into useful energy for the building. If the efficiency is considered against vertical solar irradiation (801 Wh m^{-2}), the figures are between 35 and 51 %. It also indicates that for a relatively small area on a building, a contribution to the buildings heating requirements will be made.

4.3.2 Winter – Cold, Sunny Day (Forced Convection)

The 26th of January 2006 was a cold day with near constant clear skies. On this date forced convection (air mass flow ~ 0.005 kg s^{-1}) was run through the experiment described in Sections 4.2.1 to 4.2.7. A typical temperature profile is shown in Figure 4.19 where a typical output air temperature is plotted along with global horizontal solar irradiation.

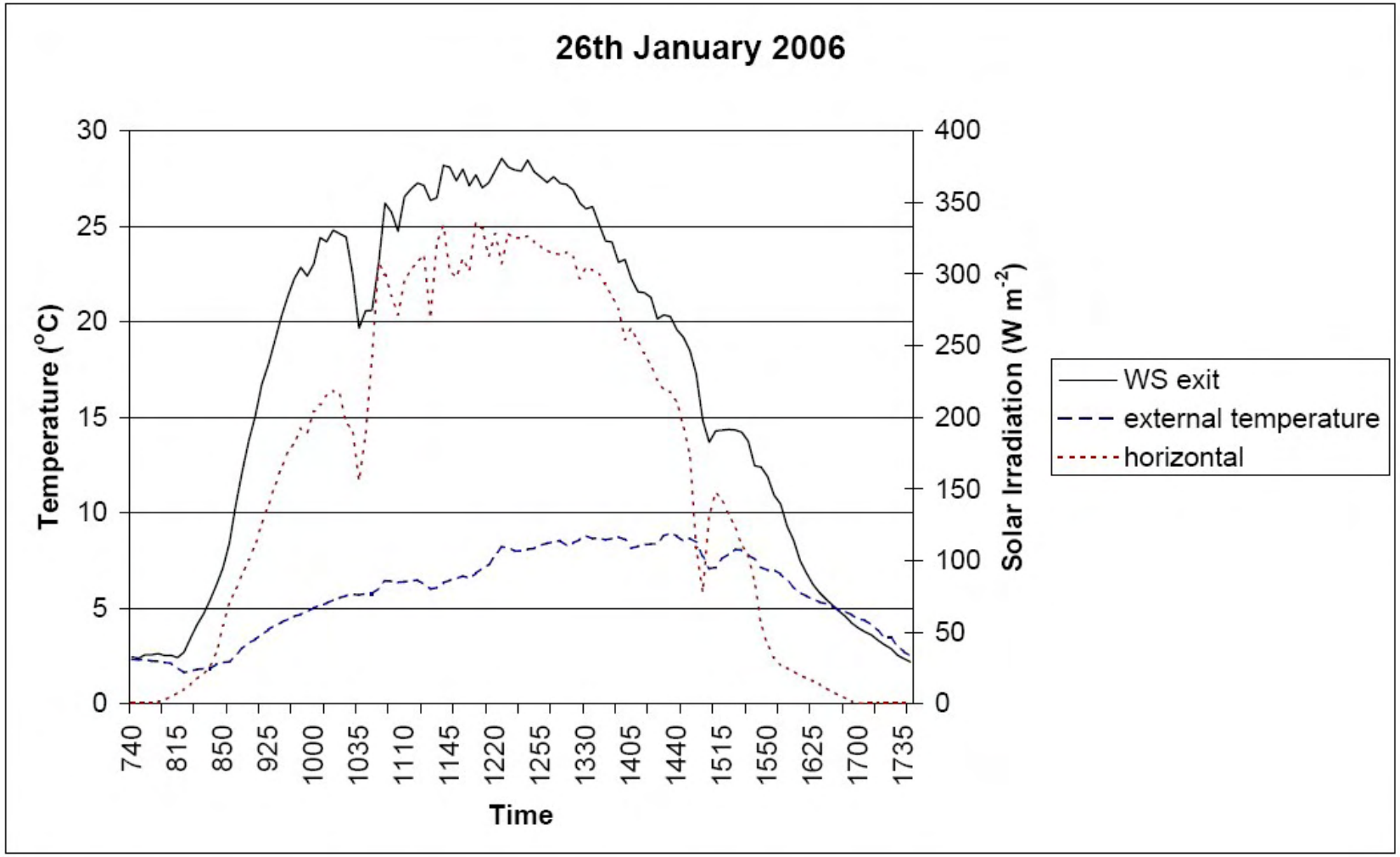

Figure 4.19. Temperature profile for 26th January 2006

Even though this is a sunny winter day, the horizontal solar irradiation never rises above 350 W m^{-2} and the external air temperature never rises above 10 ^{o}C. However, the panels increase the air temperature by between 10 and 25 ^{o}C.

Between 08:00 and 17:00 on 26th January, the horizontal solar irradiation was measured to be 1499 Wh m^{-2}. The energy output of the ducts over the same time period is shown in Table 4.5. The scaled energy output for ducts with a surface area of 1 m^2 exposed to solar irradiation is also shown.

Table 4.5 Output of ducts from 08:00 to 17:00 on January 26th 2006

Duct	Ave air mass flow (kg s^{-1})	Energy Output (Wh)	Energy Output (Wh) per m^2
ND	0.0047	316	1648
WD	0.0054	623	1577
NS	0.0051	283	1476
WS	0.0050	494	1292

This indicates that between 79 and 100 % of the horizontal solar irradiation is being converted into useful energy for the building. If the efficiency is considered against vertical solar irradiation (3692 Wh m^{-2}), the figures are between 35 and 39 %. This illustrates the effect of the solar angle. As the distance from the equator increases (i.e. at mid and high latitudes), the sun is at lower altitudes in the winter. This also allows easier transmission of the solar irradiation through vertical glazing. Figure E4 also shows that in winter, the measured vertical solar irradiation is significantly higher than the horizontal. For 26th January 2006 the vertical solar irradiation for the day is measured as 3692 Wh m^{-2} (approximately two and a half times greater than the horizontal solar irradiation). Judging the efficiency of the prototypes against horizontal solar irradiation is misleading; however, the solar irradiation data available for design purposes is generally measured from a horizontal surface. This issue was not so evident for 25th January 2006 since the cloudy weather resulted in a higher proportion of diffuse solar irradiation.

Figure 4.19 indicates that for a significant part of the day (09:30 to 14:30), air could be delivered into a building at 18^{o}C or higher. Between 09:00 to 09:30 and 14:30 to 16:30

the preheated air would still be warmer than the external temperature. A 1 m^2 area of the prototypes could result in a contribution to the heating energy of a building of between 1.3 and 1.6 kWh.

4.3.3 Summer – Sunny Day (Forced Convection)

On the 5th of May 2006 forced convection (air mass flow ~ 0.005 kg s^{-1}) was run through the experiment described in Sections 4.2.1 to 4.2.7. A typical temperature profile is shown in Figure 4.20 where a typical output air temperature is plotted along with global horizontal solar irradiation. This was the experimental run with the least cloud interruptions.

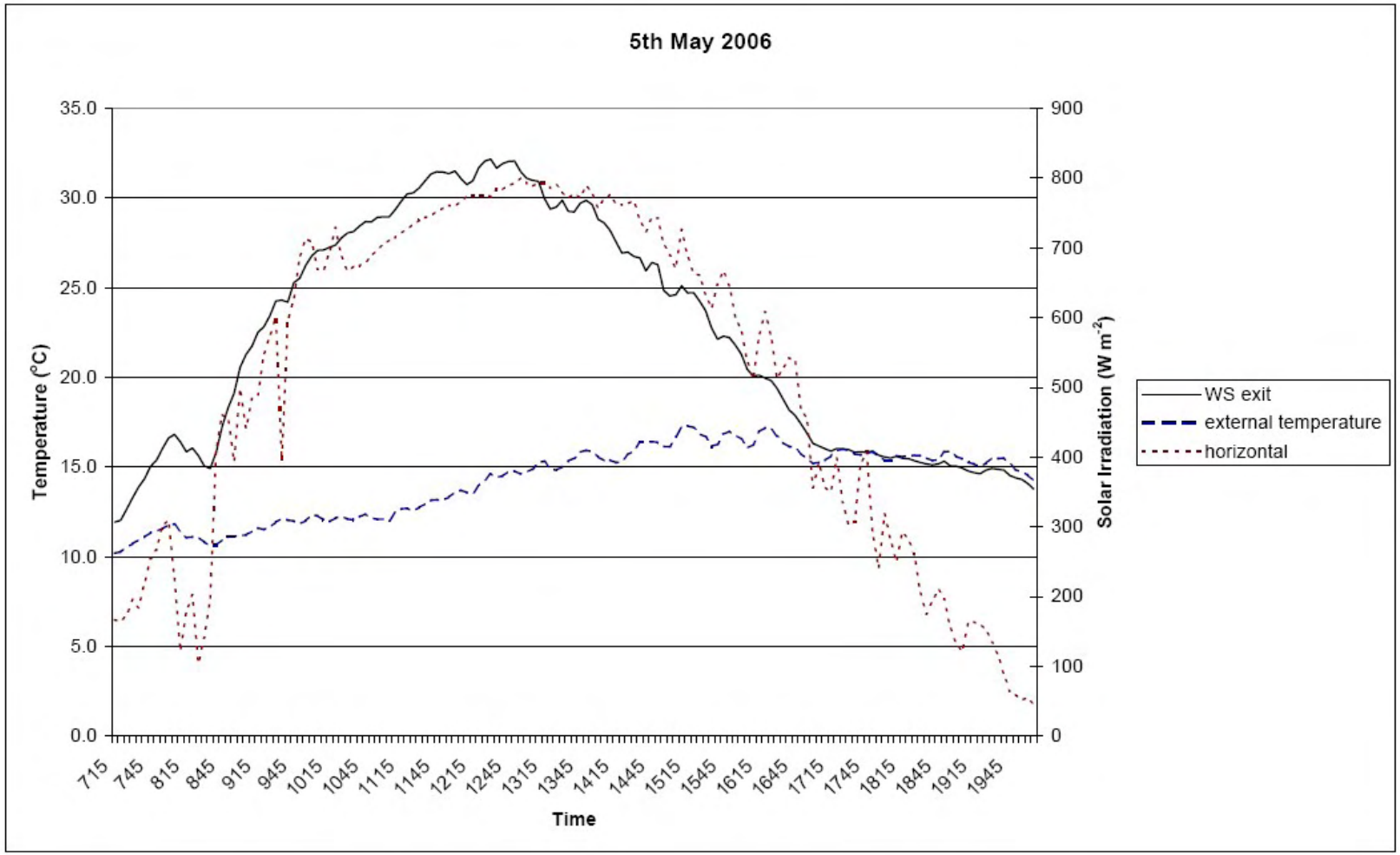

Figure 4.20. Temperature profile for 5th May 2006

Compared to the two winter days already analysed (Sections 4.3.1 and 4.3.2) there is significantly more solar energy available (800 W m^{-2} vs 279 W m^{-2} for 25th January 2006 and 336 W m^{-2} for 26th January 2006). However, the output temperatures have not increased. The peak output air temperature in Figure 4.20 is 26^{o}C. This is similar to the peak output air temperature observed in winter. The situation becomes clear when the vertical solar irradiation levels are compared in Figure 4.21. It can be seen that 26th January 2006 generally had higher vertical solar irradiation compared to 5th May 2006. This allowed the air temperature for 26th January 2006 to reach a higher temperature even though the external temperature was lower than on 5th May 2006.

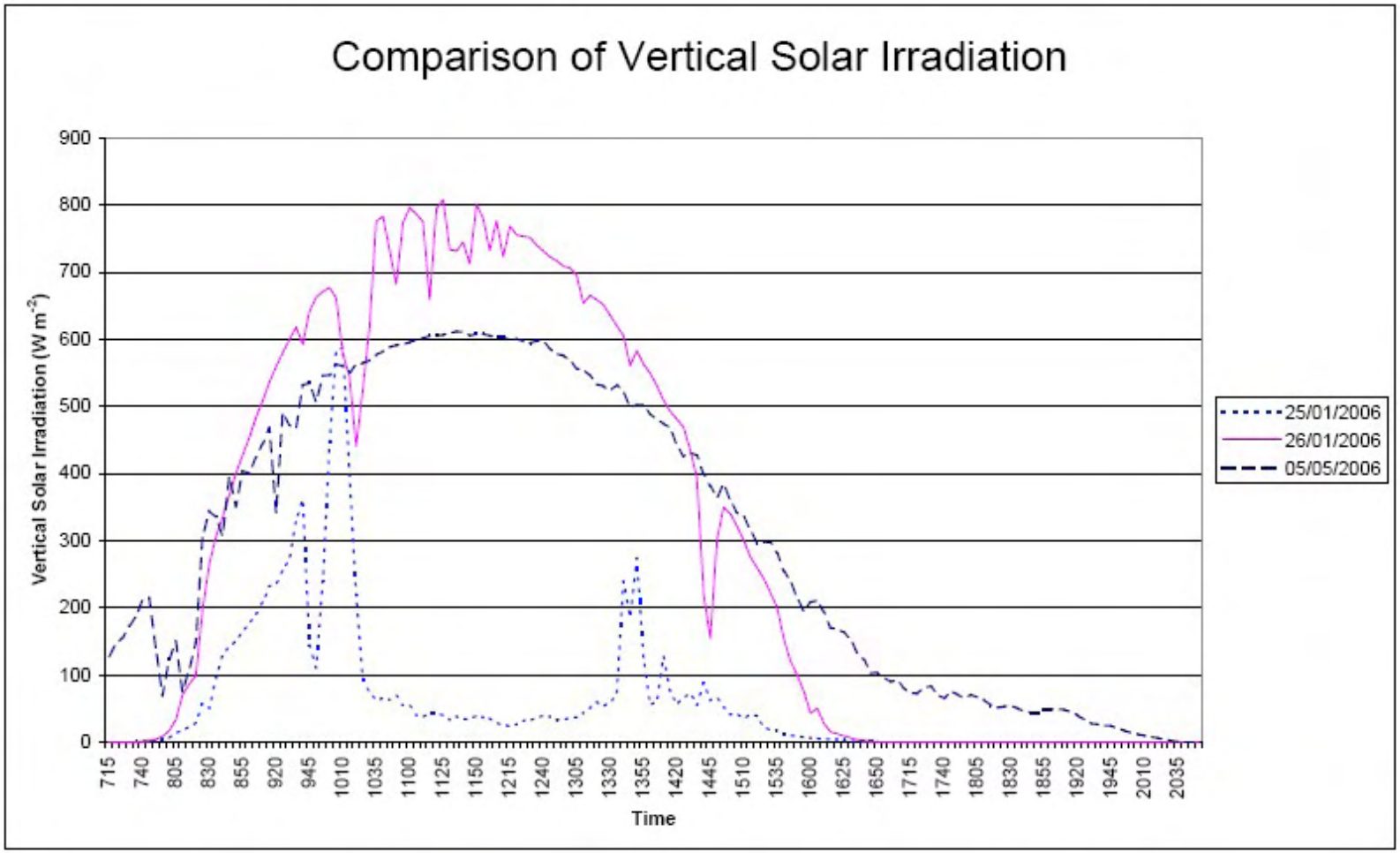

Figure 4.21. Comparison of Vertical Solar Irradiation for 25/1/06, 26/1/06 and 5/5/06

Between 08:00 and 21:00 on 5th May, the horizontal solar irradiation was measured to be 6442 Wh m^{-2}. The energy output of the ducts over the same time period is shown in Table 4.6. The scaled energy output for ducts with a surface area of 1 m^2 exposed to solar irradiation is also shown.

Table 4.6 Output of ducts from 08:00 to 21:00 on May 5th 2006

Duct	Ave air mass flow (kg s^{-1})	Energy Output (Wh)	Energy Output (Wh) per m^2
ND	0.0047	310	1615
WD	0.0054	586	1484
NS	0.0051	224	1167
WS	0.0050	501	1313

This indicates that only 17 to 24 % of the horizontal solar irradiation is being converted into useful energy for the building. However, the figures when compared against vertical solar irradiation are 28 to 38 %. These figures are very similar to those observed on 26th January 2006 (Table 4.5).

4.3.4 Summer – Sunny Day (Stagnant)

The system was analysed under stagnant conditions (i.e. full sun, without allowing the air to flow through the panels). This was to ensure that the system would be robust under such conditions. Concerns that could have arisen would have been glass cracking, sealant failing or the absorber temperature rising beyond the capability of the steel coating.

On the 11th of May 2006 the solar absorber temperature and air temperature were monitored without forced convection being applied. The pressure drop over the orifice plates was sufficient to prevent any air flow. The temperature profile is shown in Figure 4.22 where a typical air temperature is plotted along with global horizontal solar irradiation and a metal temperature profile.

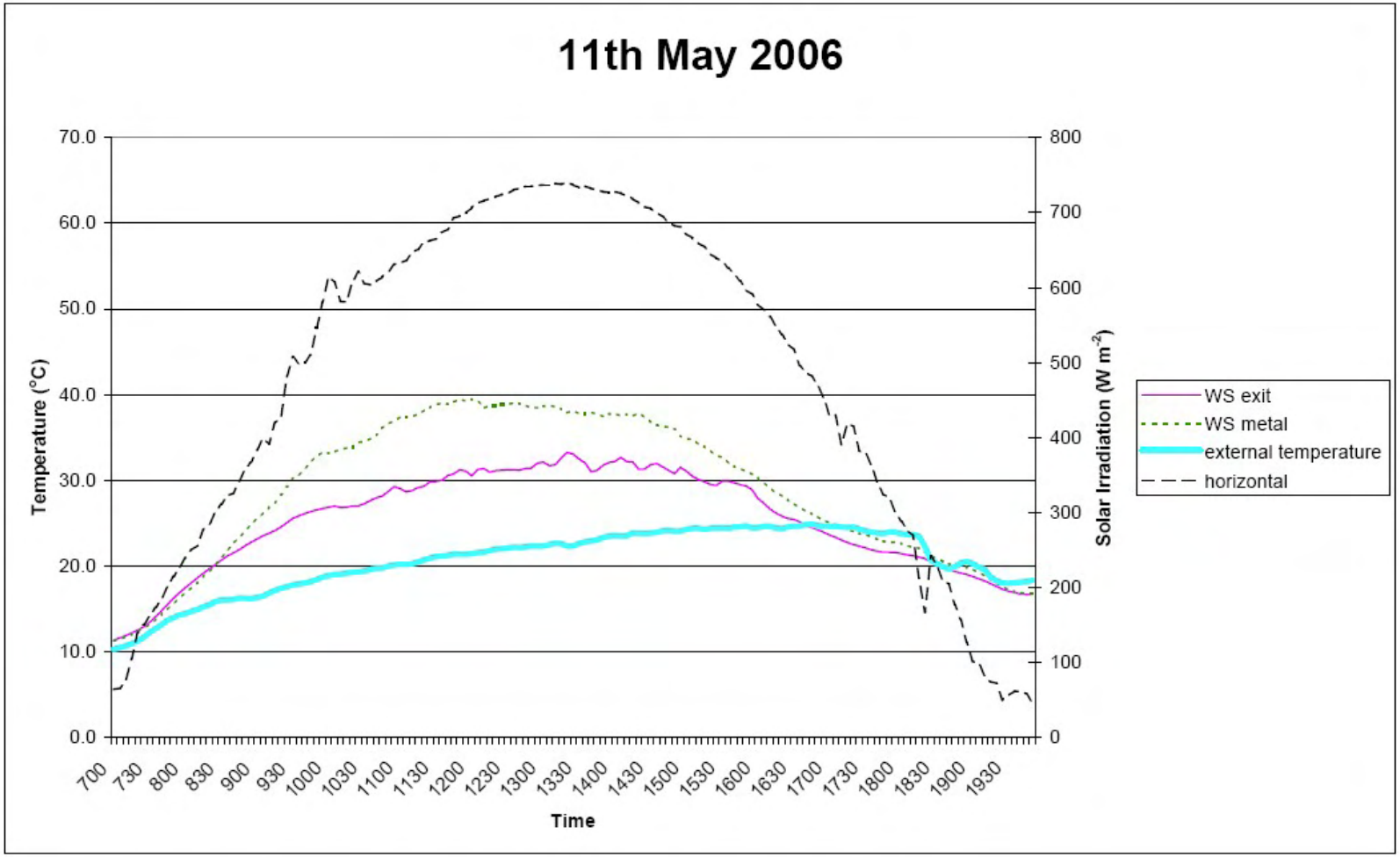

Figure 4.22. Temperature profile for 11th May 2006

In this instance, there is no output air flow or output energy to be considered. The Armacor® coated steel selected for this experiment is able to cope with continuous operating temperatures below 120 ^{o}C [17], and will not be affected by these stagnant conditions. The sealant (Elastosil SG 20) used to attach the glass to the duct is also able to cope with temperatures up to 150 ^{o}C [18]. However, some insulation materials (e.g. polystyrene and rubber) have melting temperatures between 67 and 77 ^{o}C [19], and could be adversely affected by the temperatures reached in stagnant conditions. There was no damage to the glass indicating that there were no issues with mismatch of expansion coefficients.

4.3.5 Summer – Sunny Day (Buoyant Convection)

Prior to the 3rd of July 2006 the experiment described in Sections 4.2.1 to 4.2.7 was altered to allow passive flow. The flexible pipework which attached the top of the ducts to the pipework containing the orifice plates was disconnected. Ideally the disconnection would have occurred at the top of the duct. However, health and safety concerns prevented the use of a forklift truck for this use. Instead the flexible pipe was disconnected at the top of the orifice plate pipework and secured to the scaffolding so that it would not flap.

On the 3rd of July 2006 the experiment was monitored in its passive condition. A typical temperature profile is shown in Figure 4.23 where a typical output air temperature is plotted along with global horizontal solar irradiation.

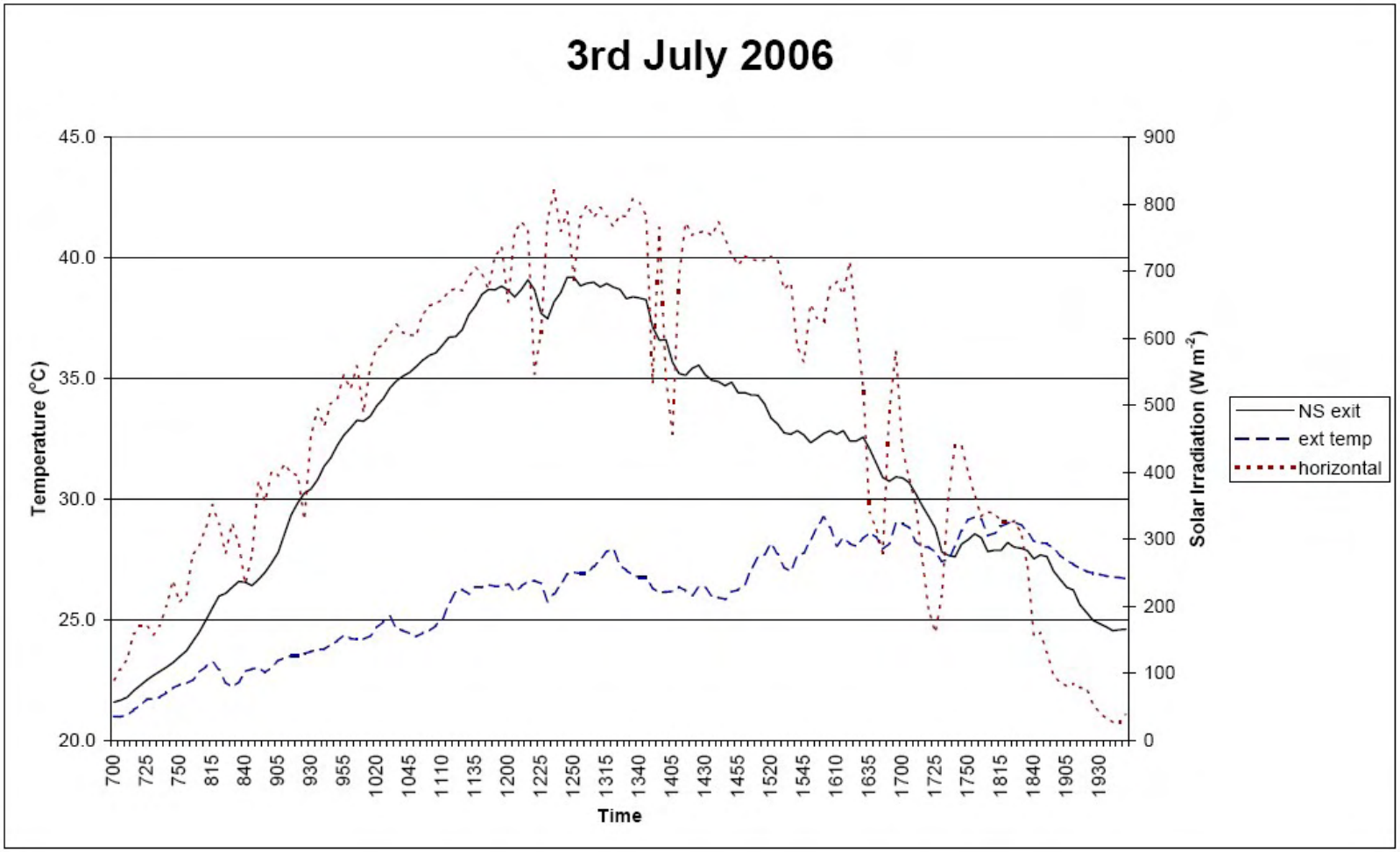

Figure 4.23. Temperature profile for 3rd July 2006

This temperature shows a higher output air temperature than was observed on 5th May 2006, indicating that the air mass flow was probably lower than on that date. However, because it was impossible to use the orifice plate system to measure the air mass flow for buoyant convection, an alternative analysis technique is required. This profile will be used in Chapter 5 to generate data and compare design models.

4.3.6 Ranking of Prototype Ducts – Forced Convection

The ranking of the prototype ducts can be considered for air exit temperature and for power output. The behaviour on a sunny winter's day (26/01/06) and a sunny summer's day (05/05/06) can be used to establish any difference in behaviour related to the different times of year. The air exit temperature can be considered for individual ducts. However, it is illogical to compare the power output of prototype ducts of different geometry since they have different areas exposed to the solar irradiation and take up different areas on a façade. The comparison of the prototypes for power output assumes:

- $10m^2$ area of façade
- each duct is separated from the next vertically by 0.1m
- each duct is separated from the next laterally by 0.02m

Where it is necessary to calculate the output of a 'fraction' of a duct to fit in the $10m^2$ area the fraction of the duct power output is apportioned evenly (e.g. for 25% of a duct, 25% of the ducts power output is included).

Table 4.7 shows the glazed area for each duct, the area each duct would take on a façade (including the overlaps) and the number of ducts which could be inserted into a $10m^2$ façade area.

Table 4.7 Glazed area, Façade area and number of ducts in a $10m^2$ area

Duct ID	Glazed area (m^2) of each duct	Façade area (m^2) of each duct	Number of ducts in $10m^2$ façade area
ND	0.191	0.216	46.2
WD	0.395	0.425	23.5
NS	0.191	0.216	46.2
WS	0.381	0.410	24.4

4.3.6.1 Air Exit Temperature (Individual Ducts)

The data for 26/01/06 is shown in Figure 4.24 and the data for 05/05/06 is shown in Figure 4.25. The two figures show the same ranking in air exit temperature (WD, WS, ND, NS), although the relationship between duct depth and air exit temperature is more pronounced in January, than it is in May.

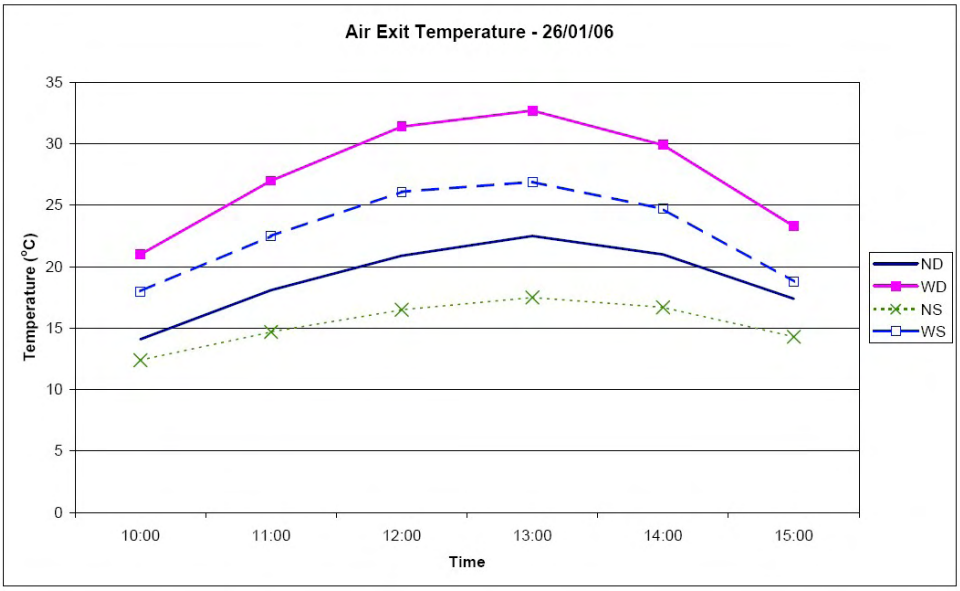

Figure 4.24. Air Exit Temperature (All ducts) 26/01/06

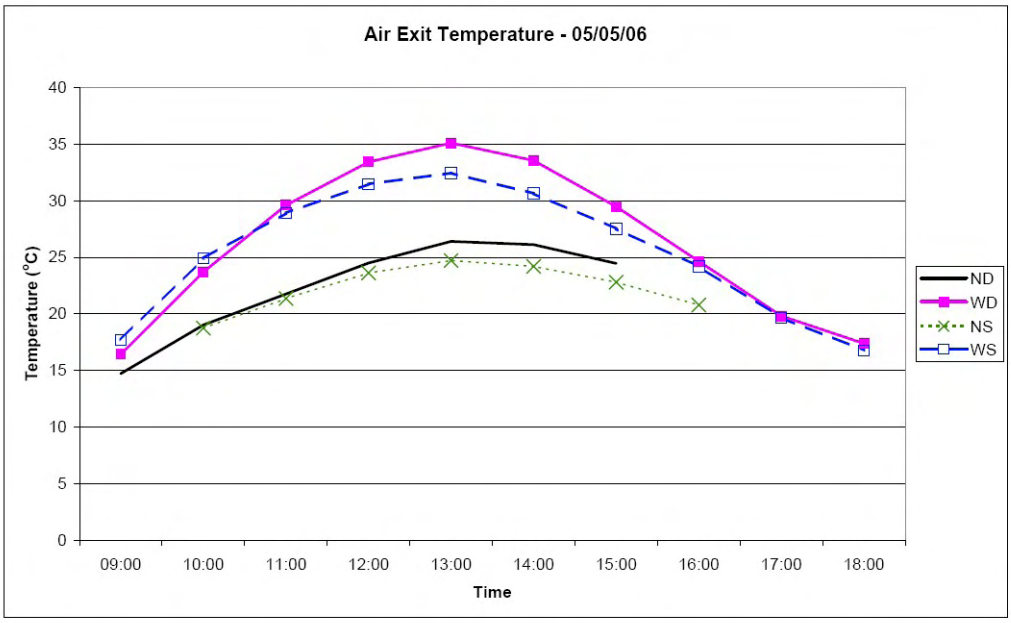

Figure 4.25. Air Exit Temperature (All Ducts) 05/05/06

4.3.6.2 Power Output (Façade Area of 10m^2)

The power output of the prototype ducts has been calculated from measured parameters (i.e. air mass flow, air entry temperature and air exit temperature).

Figure 4.26 shows the power output calculated from measured data on 26/01/06. The data for each prototype has been scaled as described above to a façade area of 10m^2. This indicates that the deeper ducts (ND and WD) have a higher power output than the shallower ducts (NS and WS). Figure 4.26 also indicates that all four ducts exceed 1.5kW for approximately five hours of the day.

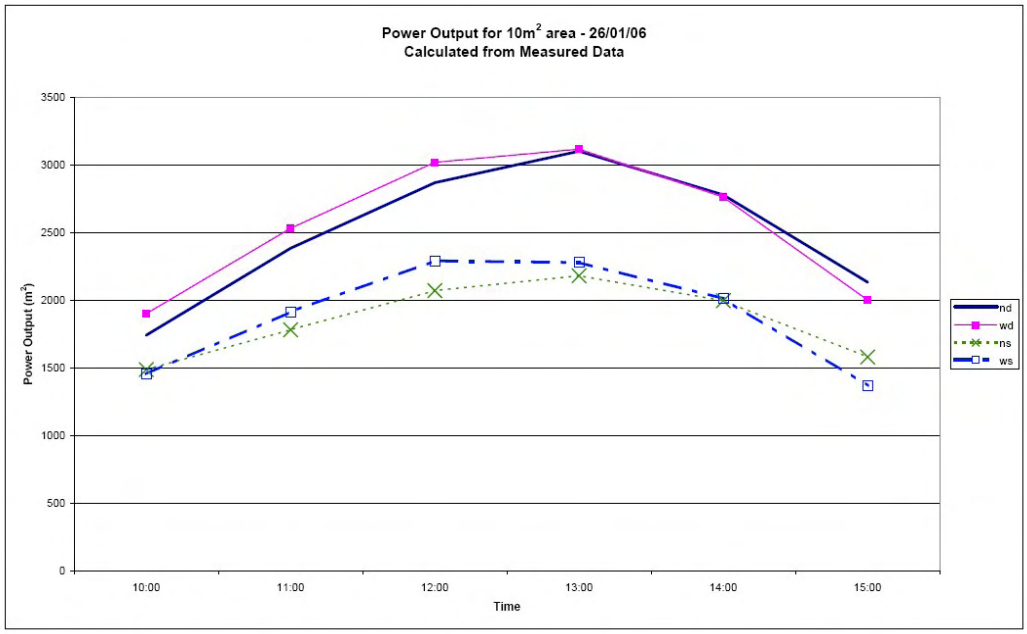

Figure 4.26. Power Output (calculated from measured data) 26/01/06

Figure 4.27 shows the power output calculated from measured data on 05/05/06. The data for each prototype has been scaled as described above to a façade area of 10m^2. This indicates a marginally higher power output for deeper duct than for shallow ducts; however, the trend is not as pronounced as it was on 26/01/06. The peak power of ducts ND and WD appear to be slightly offset from ducts NS and WS. This could be an indicator that deep ducts are more influenced by the ambient air temperature than by the solar irradiation, while shallow ducts have the opposite sensitivity. This could be due to the greater effect of shadows on deep ducts, than on shallow ducts. Figure 4.27 also indicates that all four ducts exceed 1kW for approximately five hours of the day. This

is lower than the observations from 26/01/06, indicating that the system can produce significant power output during sunny winter days.

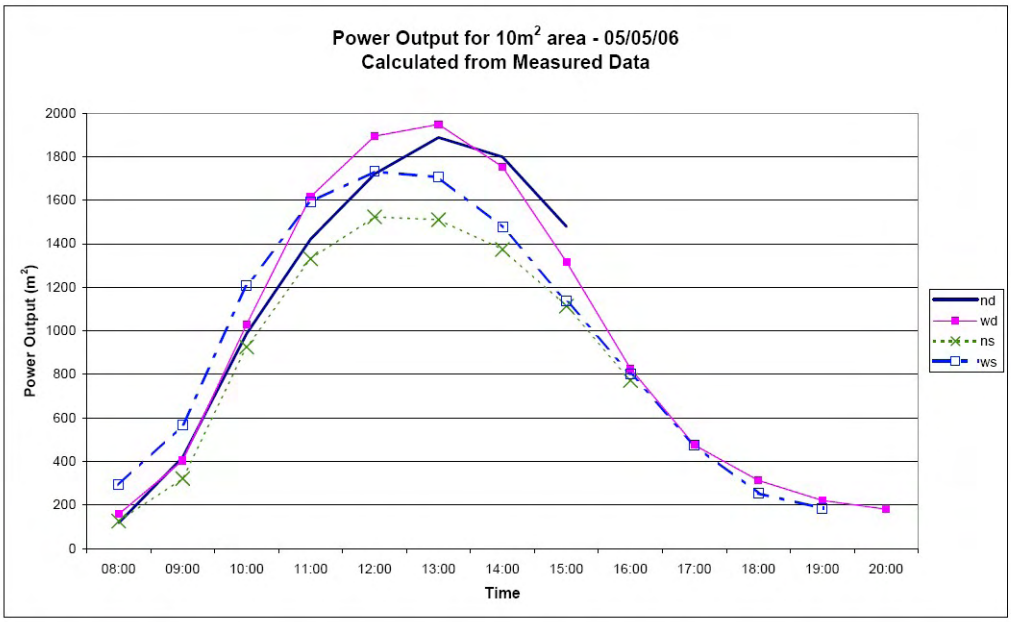

Figure 4.27. Power Output (calculated from measured data) 05/05/06

Figure 4.26 and Figure 4.27 can be used to indicate the ranking performance of the ducts at their peak. Both figures indicate the ranking (highest power output first) as: WD, ND, NS, WS.

4.4 Model Verification

The model described in Section 4.1 is going to be compared to the data for 5th May 2006. The propagated errors for measurements will be discussed in relation to the results. Further details of the error propagation analysis can be found in Appendix F, but are summarised in Table 4.8.

Table 4.8 Value ± Error of Model Components

	ND	WD	NS	WS
Input Power (W)	47 ± 5.8	96 ± 11.4	47 ± 6.1	93 ± 10.8
Useful Power Output (W)	24 ± 0.5	46 ± 0.9	18 ± 0.4	40 ± 0.8
Power Loss (W)	25 ± 4.4	45 ± 8.0	18 ± 4.2	47.5 ± 7.6

The input power has an error of approximately 12% associated with it, the useful power output has an error of approximately 2% associated with it, and the power loss has an error of approximately 15% associated with it. These errors represent how closely a detailed model can represent the system. It would be unrealistic to expect a design model using limited data to predict the behaviour of the system more closely than this.

4.4.1 Model Effectiveness

Model effectiveness is the proportion of the input power that can be accounted for as useful power output and lost power.

$$\text{Model effectiveness} = \frac{Input}{Output + Power\,loss} \qquad 25$$

If the mathematical model is 100% effective, then all the power will be accounted for.

These components and their accuracy for data obtained on 05/05/06 were detailed in Table 4.8. The model effectiveness and its accuracy were calculated for 05/05/06. This information is shown in Table 4.9.

Table 4.9 Calculations of model effectiveness – whole day.

Model Effectiveness			
ND	WD	NS	WS
94 ± 14.6	104 ± 15.6	129 ± 23.5	105 ± 15.6

The calculations for the NS duct were based on fewer measured results than the other ducts, which explains the larger variance from the aim of 100% model effectiveness. The inclusion of assumed values in the calculations was compensated for by allowing larger error bands around the values, which explains the larger error band for the model effectiveness of duct NS.

Model effectiveness against time has been plotted alongside horizontal solar irradiation for the 5th May 2006 in Figure 4.28 – 4.31.

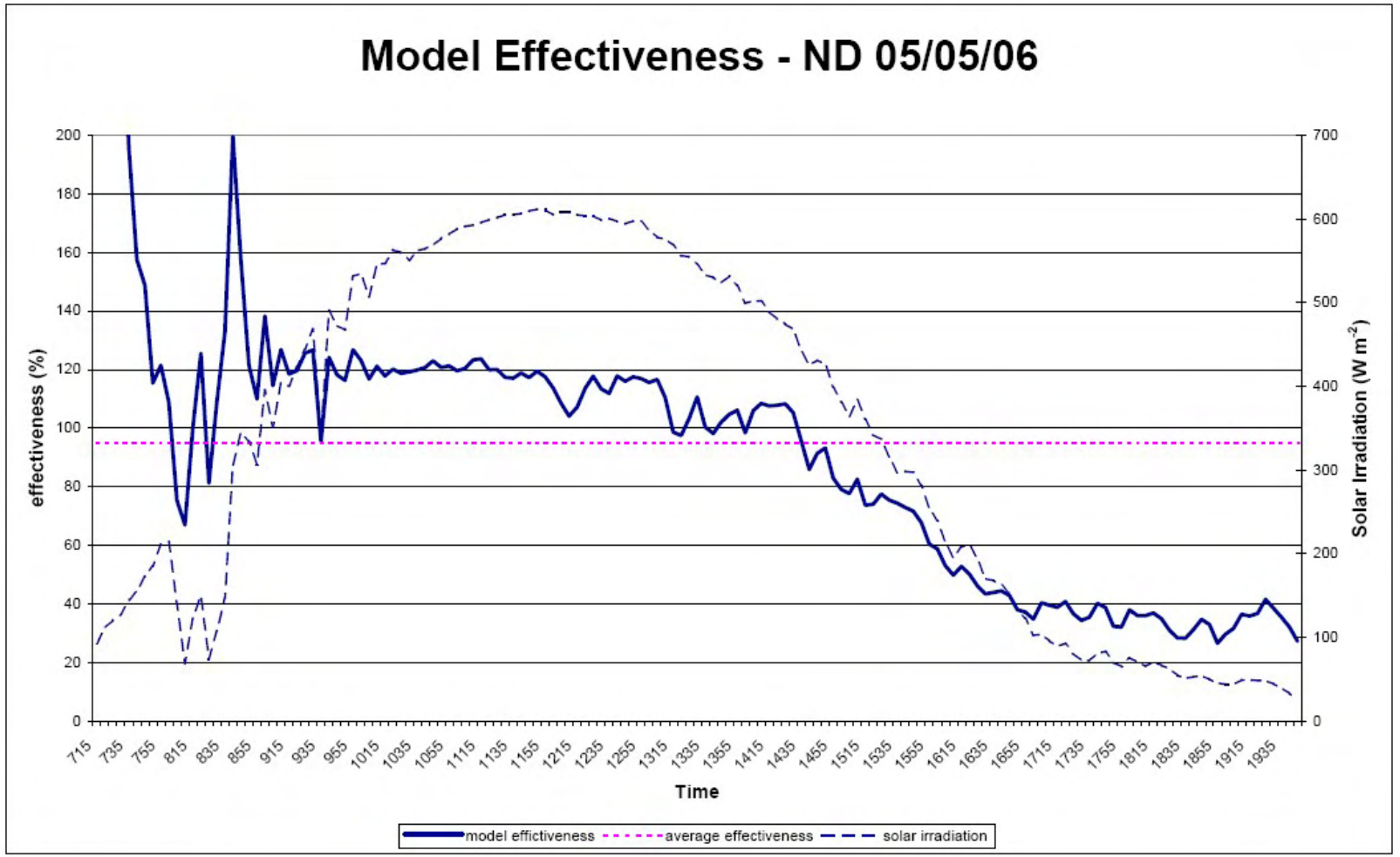

Figure 4.28. Model Effectiveness - ND 05/05/06

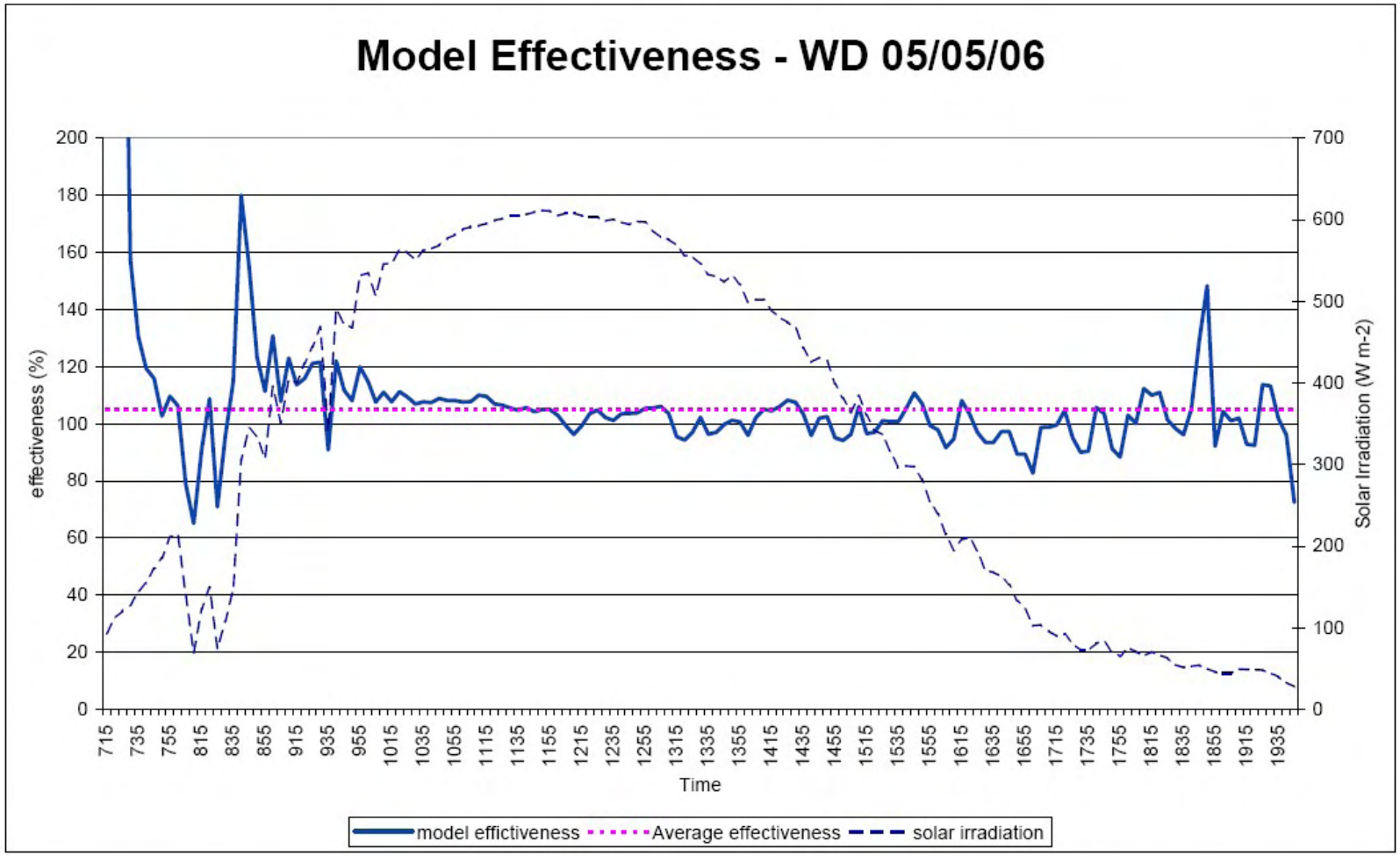

Figure 4.29. Model Effectiveness - WD 05/05/06

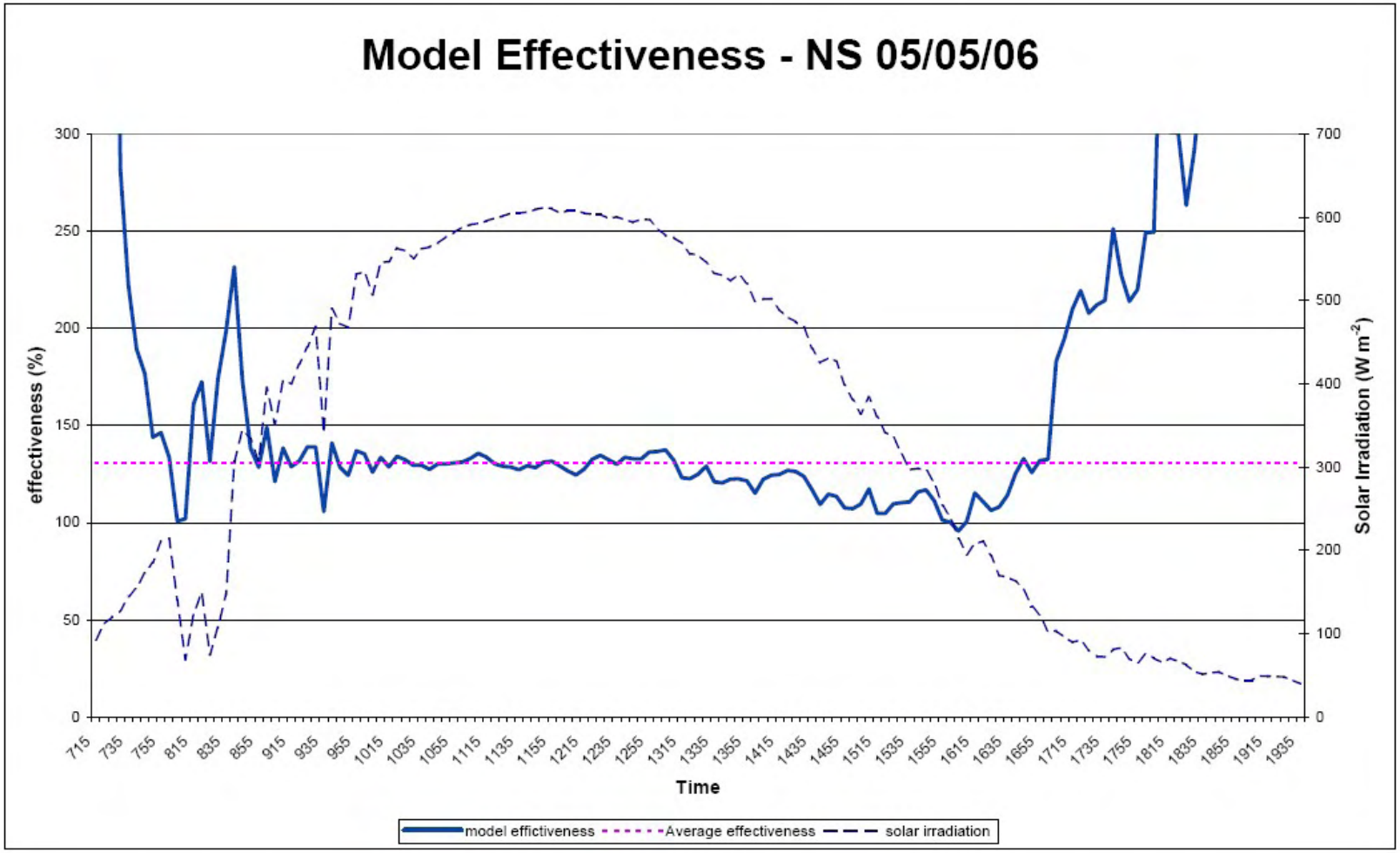

Figure 4.30. Model Effectiveness - NS 05/05/06

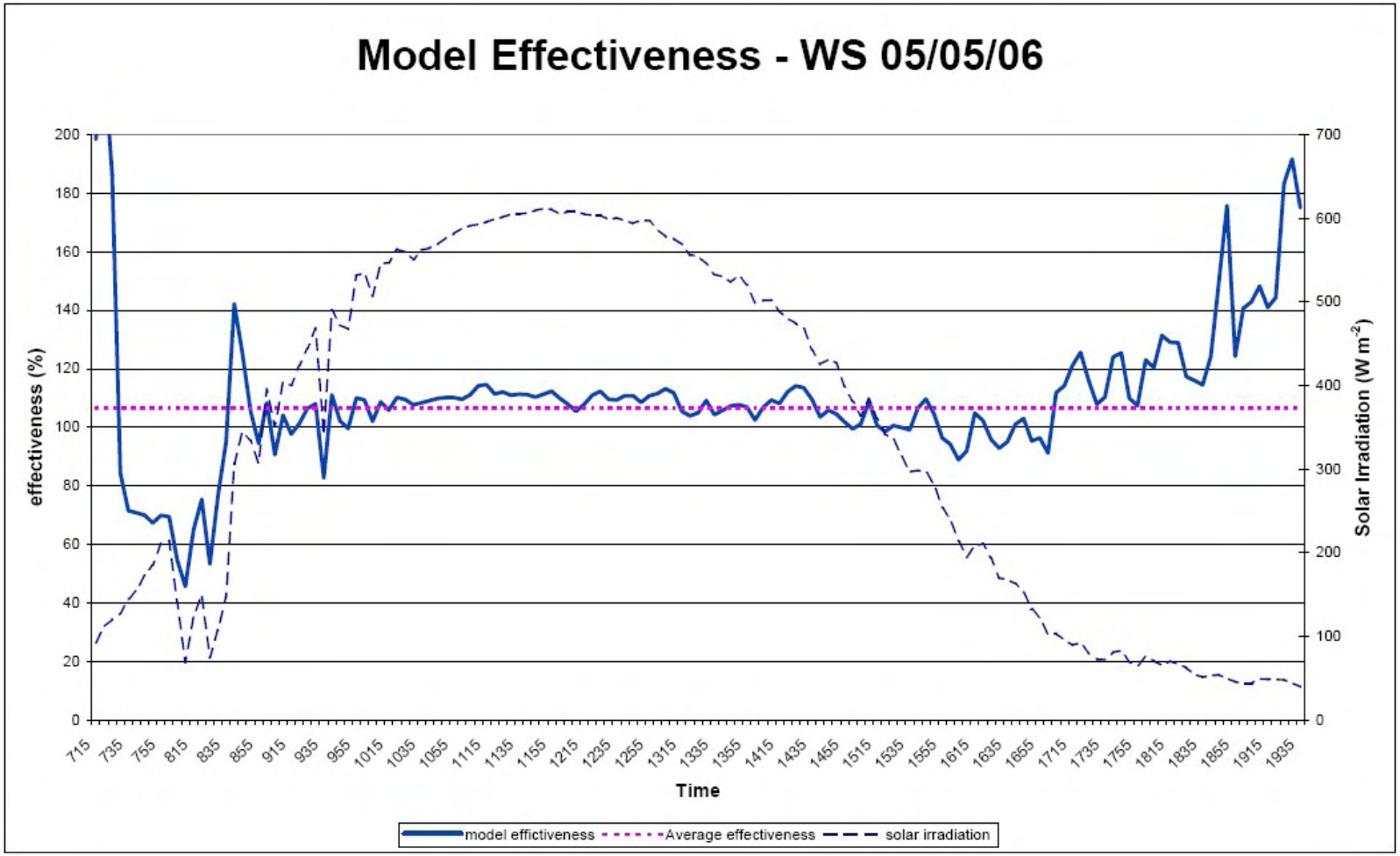

Figure 4.31. Model Effectiveness - WS 05/05/06

Ducts ND, WD and WS are reasonable over the whole day, with an approximate model effectiveness of 100%. However, the model underestimates the power output and loss by 25% for duct NS. This is because temperature measurements which were required to calculate the power loss for duct NS were not available.

Solar irradiation has also been plotted on the figures to illustrate the effect of changes, e.g. the sudden dips in solar irradiation between 07:45 and 08:45 as well as the other minor fluctuations. However, the model appears to be stable between 09:00 and 17:30 on this date.

There is very little difference in the temperatures at the beginning and end of the day. When the difference in input and output temperature is small in relation to the associated errors, the model effectiveness is poor. This in conjunction with the propagation of errors in the measurements through the calculations, explains why the model effectiveness averaged over an entire day does not equal 100%. The propagated errors indicate that the calculations are severely affected by the limited accuracy associated with the outer surface temperatures and the sky temperature. Table 4.10 shows the model effectiveness if only the stable part of the day is considered.

Table 4.10 Calculations of model effectiveness – stable part of each day.

Time	ND	WD	NS	WS
09:00 – 17:30	94 ± 11.7	103 ± 11.9	128 ± 17.6	105 ± 12.2

Although this makes little difference to the model effectiveness values, it lowers the errors associated with the calculations. The calculations for duct NS on 05/05/06 still has a high error. This is because it has more assumed temperatures than the other ducts. Figures 4.28 to 4.31 and Table 4.10 indicate that the model is effective in the stable part of the day.

4.4.2 Instantaneous Input versus Output

On 05/05/06 duct ND exhibits a model effectiveness less than 100% in the afternoon (Figure 4.28). At this time of day in the summer, the problem is unlikely to be related

to temperature differences which are small in relation to their errors. If the anomaly is accepted as real, it indicates that even though the solar irradiation reduces in the afternoon, heat is being found from another source. This suggests that the thermal mass of the system retains heat through the peak of the day, and releases it in the afternoon. This can be checked by examining a graph of the power in versus useful power out (Figure 4.32).

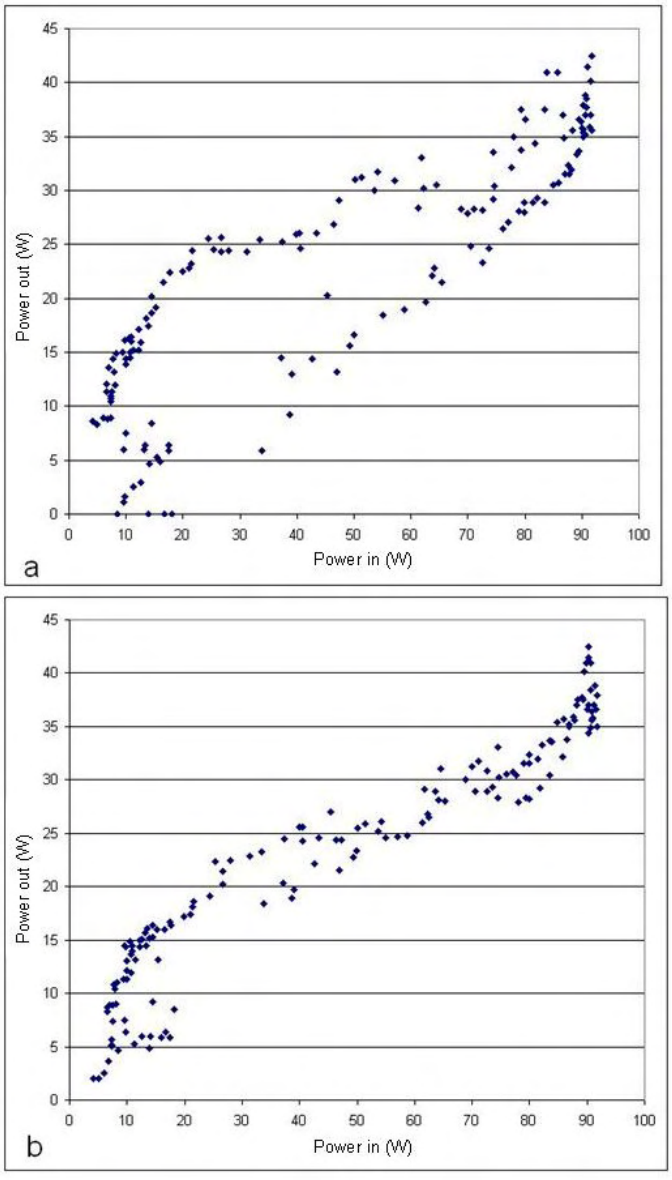

Figure 4.32. Power In vs Useful Power Output - ND 05/05/06

a - shows instantaneous comparison

b - shows data modified for a 40 minute thermal mass offset

Figure 4.32a shows a plot of instant power out versus power in, exhibiting a form of hysteresis, suggesting a time lag, which could be due to thermal mass. Figure 4.32b shows the plot corrected for a thermal mass time lag of 40 minutes.

The instantaneous input versus output graphs for the other three ducts are shown in Figure 4.33 – 4.35.

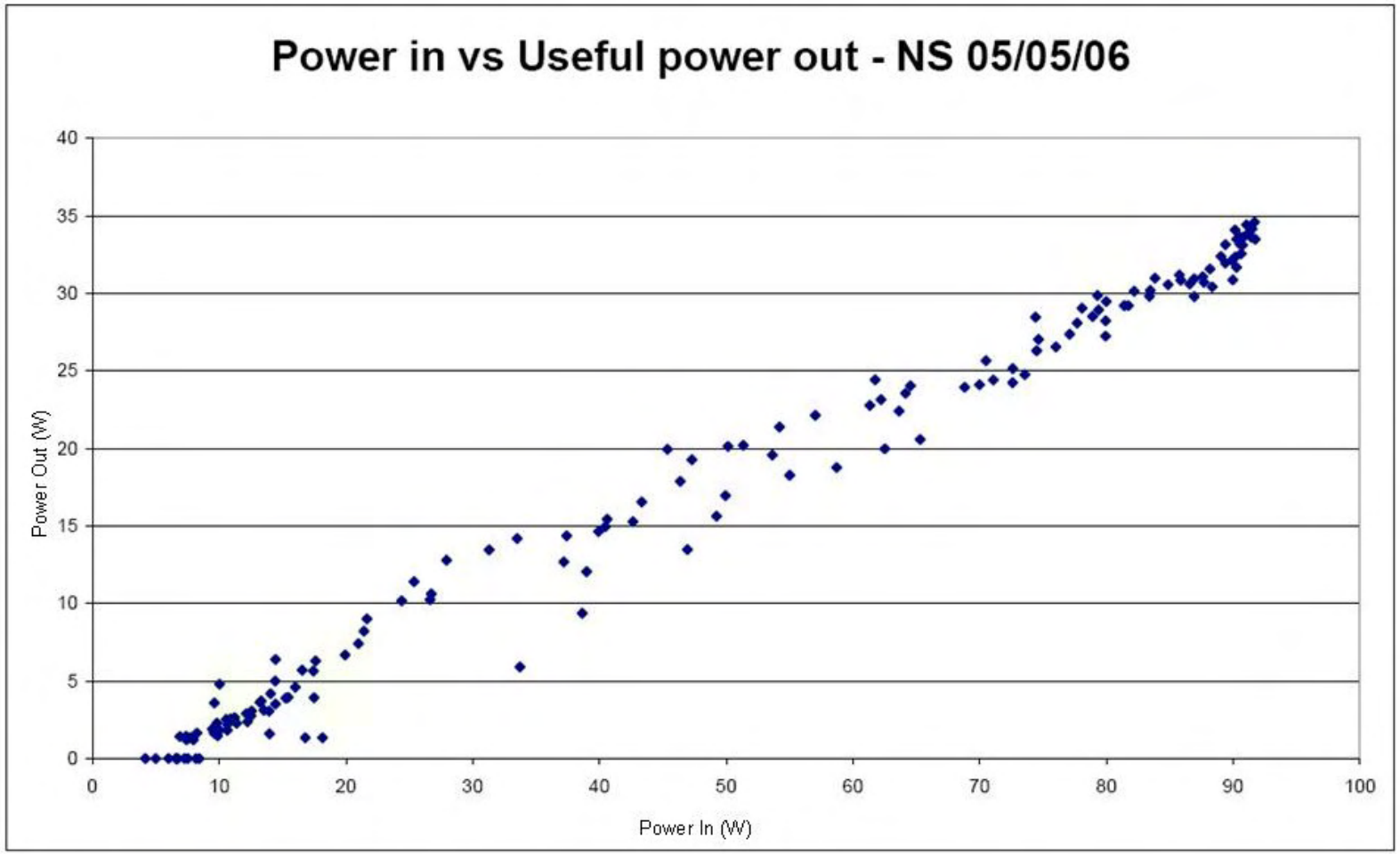

Figure 4.33. Power In vs Useful Power Output - NS 05/05/06

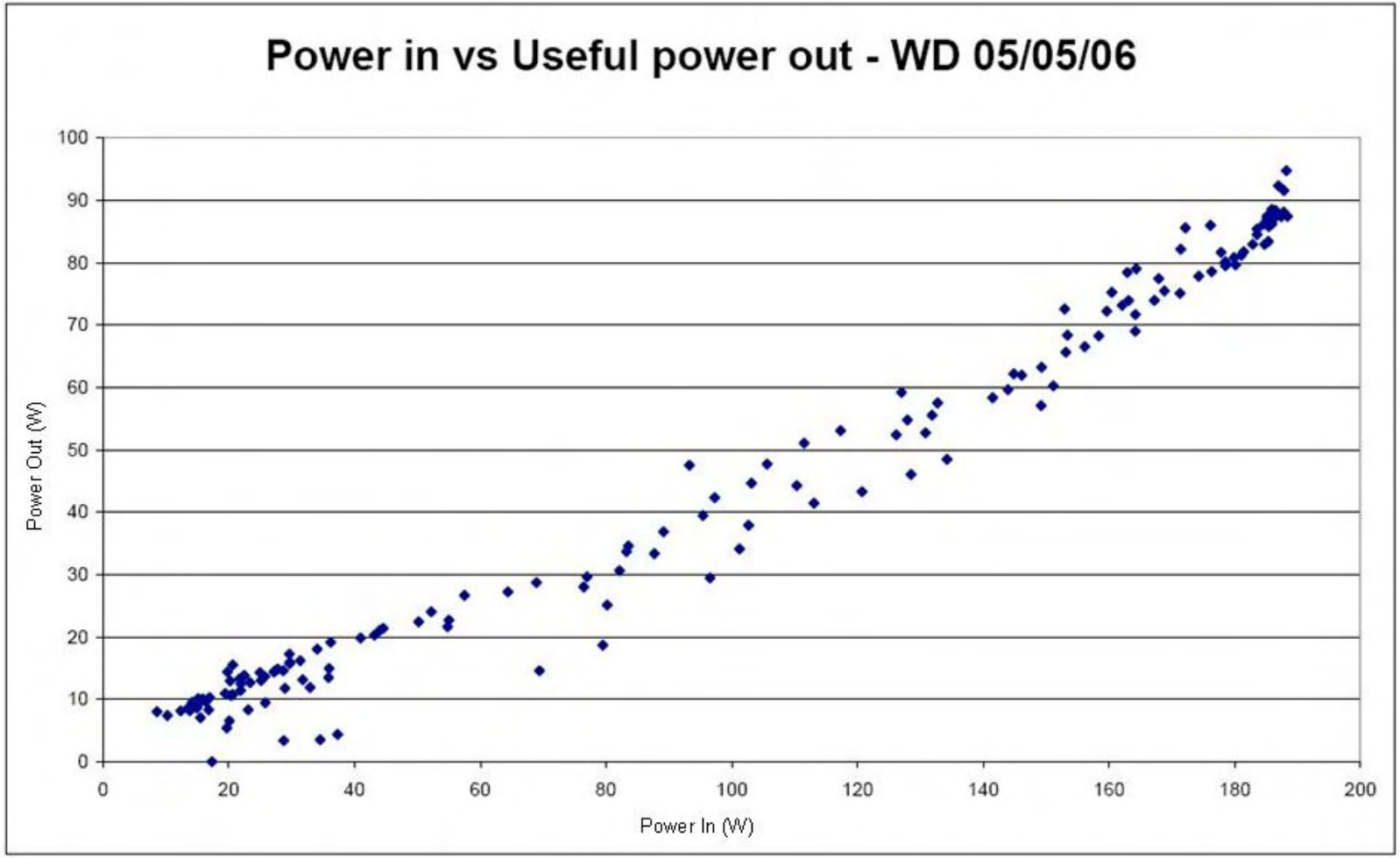

Figure 4.34. Power In vs Useful Power Output - WD 05/05/06

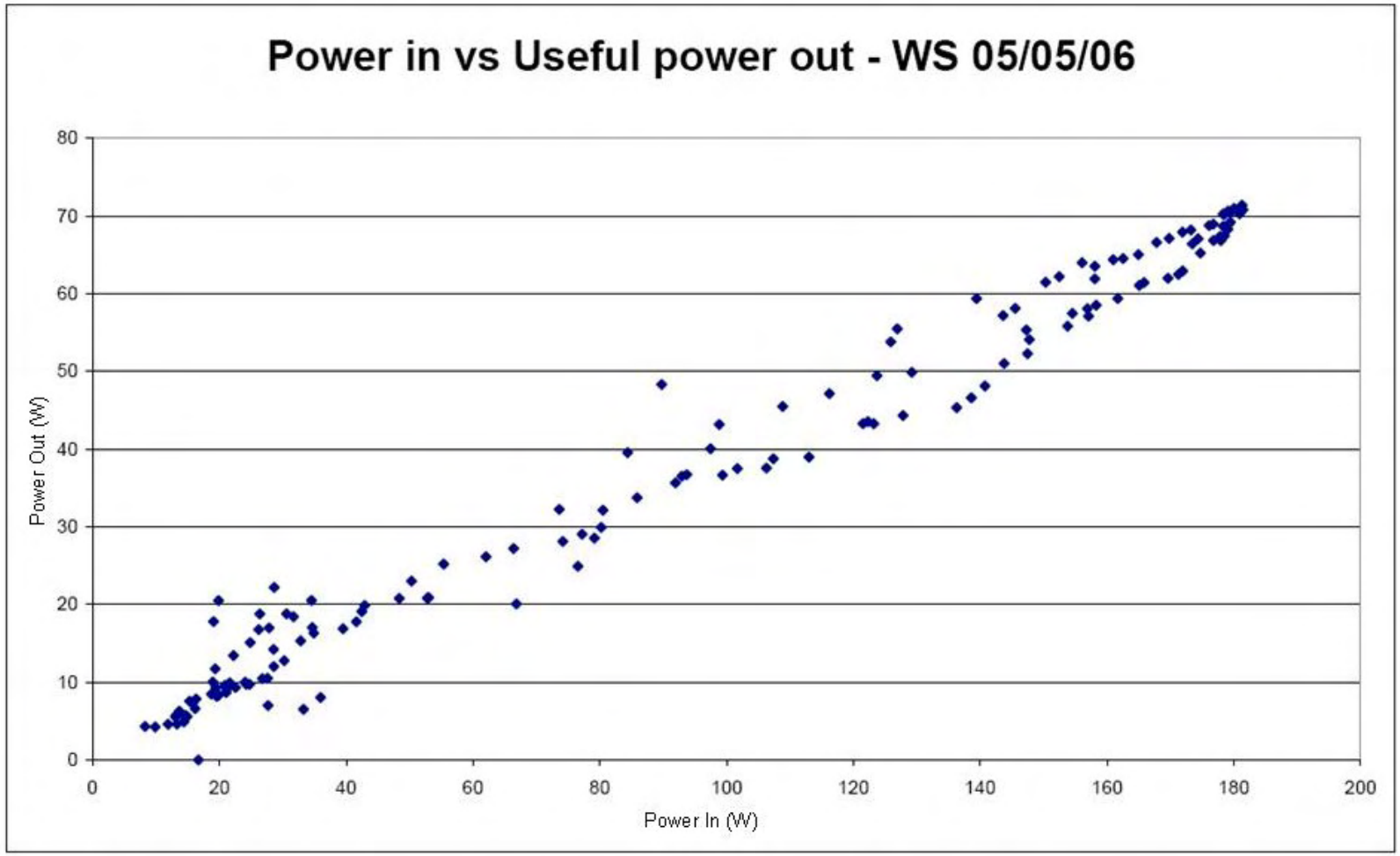

Figure 4.35. Power In vs Useful Power Output - WS 05/05/06

However, these graphs do not show any hysteresis curves which indicate a thermal lag. There is no reason why the thermal mass should be different between duct ND and the other ducts since their thermal mass is similar. So another explanation for the hysteresis curve in duct ND must be sought.

The experiment location is illustrated in Figure 4.36. Although the steel plant is relatively close to the experiment, the buildings at this end of the steel plant are not markedly tall. However, Graig Fawr Hill is 100m high, and has been noticed to block the early morning sunlight to the experiment. From Figure 4.37 it can be seen that the front of every duct is exposed to solar irradiation, as is the left side of duct WS and the right side of duct ND. The other surfaces are protected from solar irradiation by each other. As has already been noted, the early morning summer sun, which would impinge on the left side of duct WS, is blocked by a hill. However, there is nothing preventing the late evening summer sun from shining on the right side of duct ND. This also appears relevant to a change in model effectiveness after 14:45 on 05/05/06.

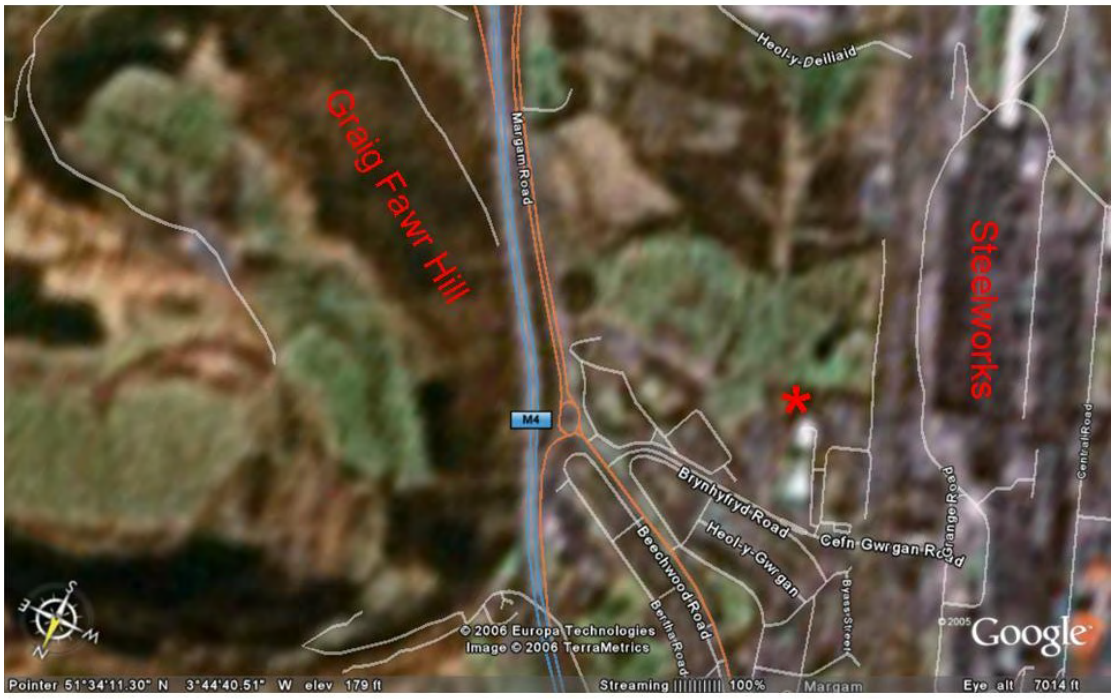

Figure 4.36. Experiment location marked by * [20]

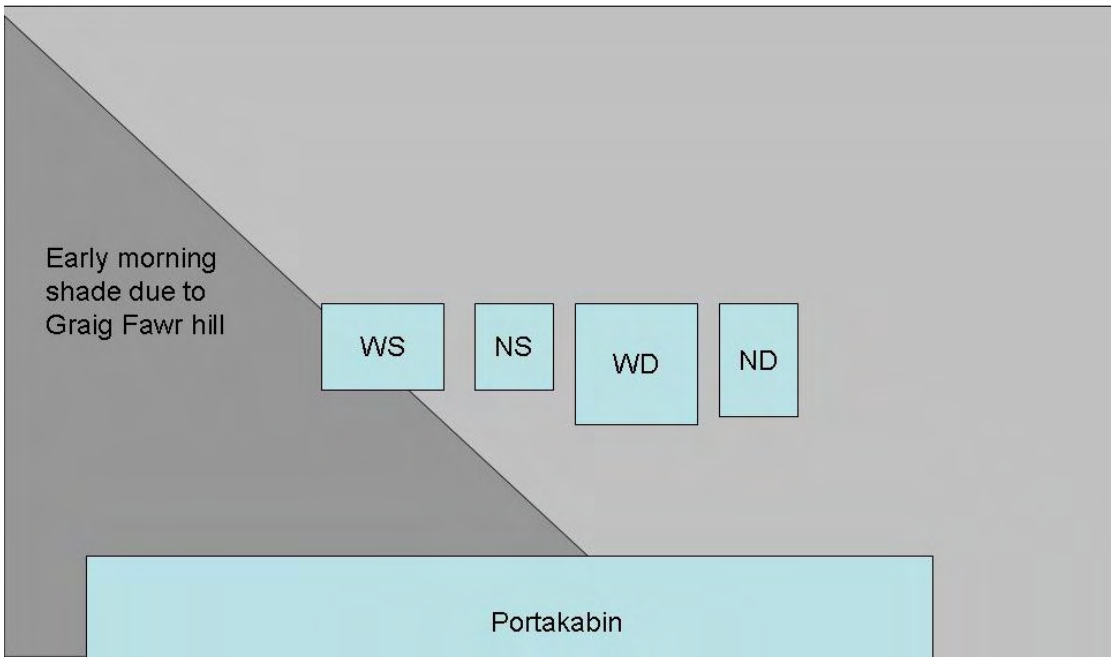

Figure 4.37. Experiment Layout

Looking at temperature data (Figure 4.38) it was found that the sunset side of the ND duct was significantly warmer than the shaded side in the afternoon. This led to the suspicion that the prototype was receiving extra solar irradiation through the side surface.

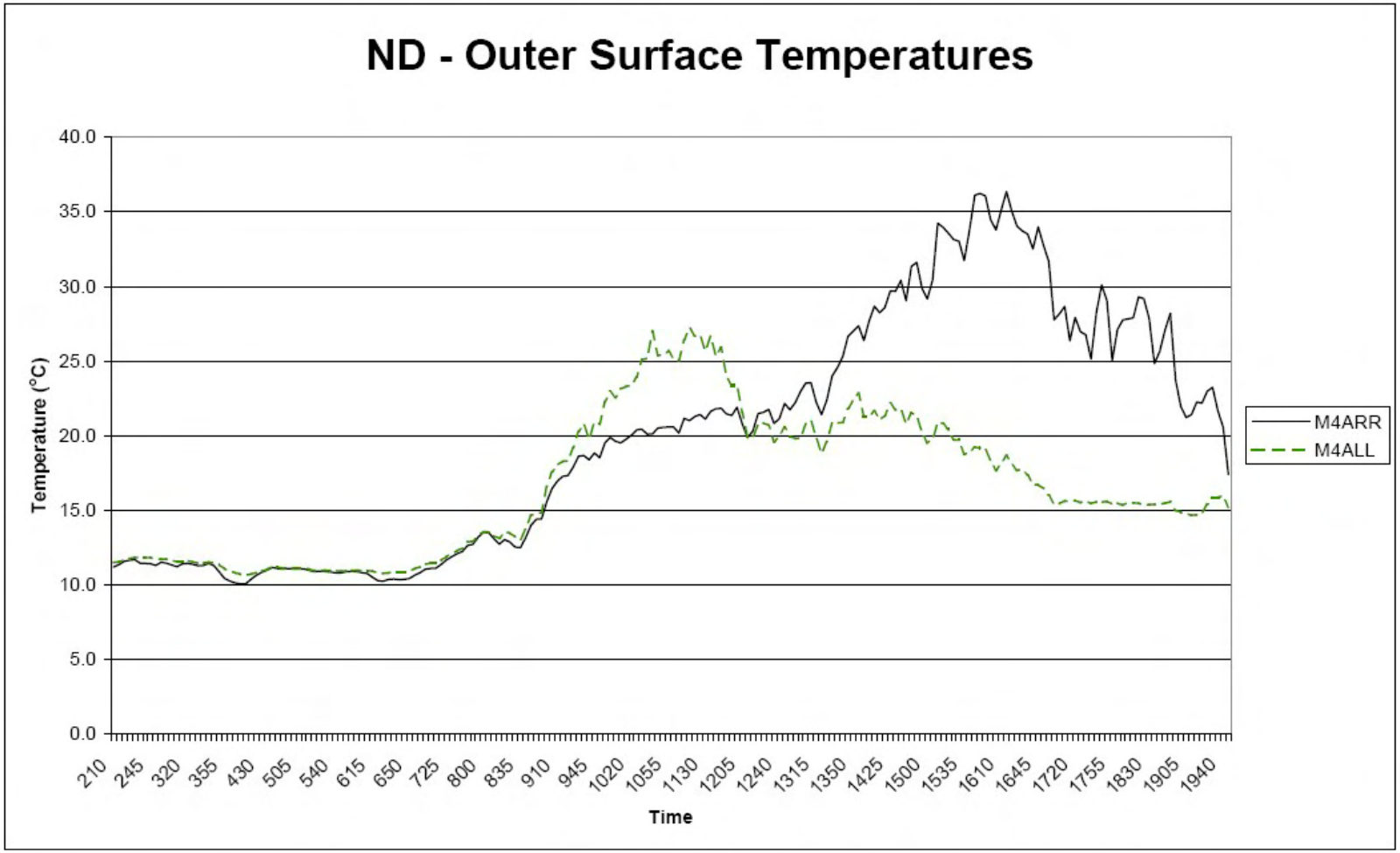

Figure 4.38. Outer Surface Temperatures - Duct ND, 05/05/06

This was confirmed by looking at the instantaneous input versus output graphs for morning and afternoon separately (Figure 4.39). A true thermal lag of 40 minutes would still show up in both graphs. However, these graphs look much more like Figure 4.33 – 4.35 which represent the other ducts.

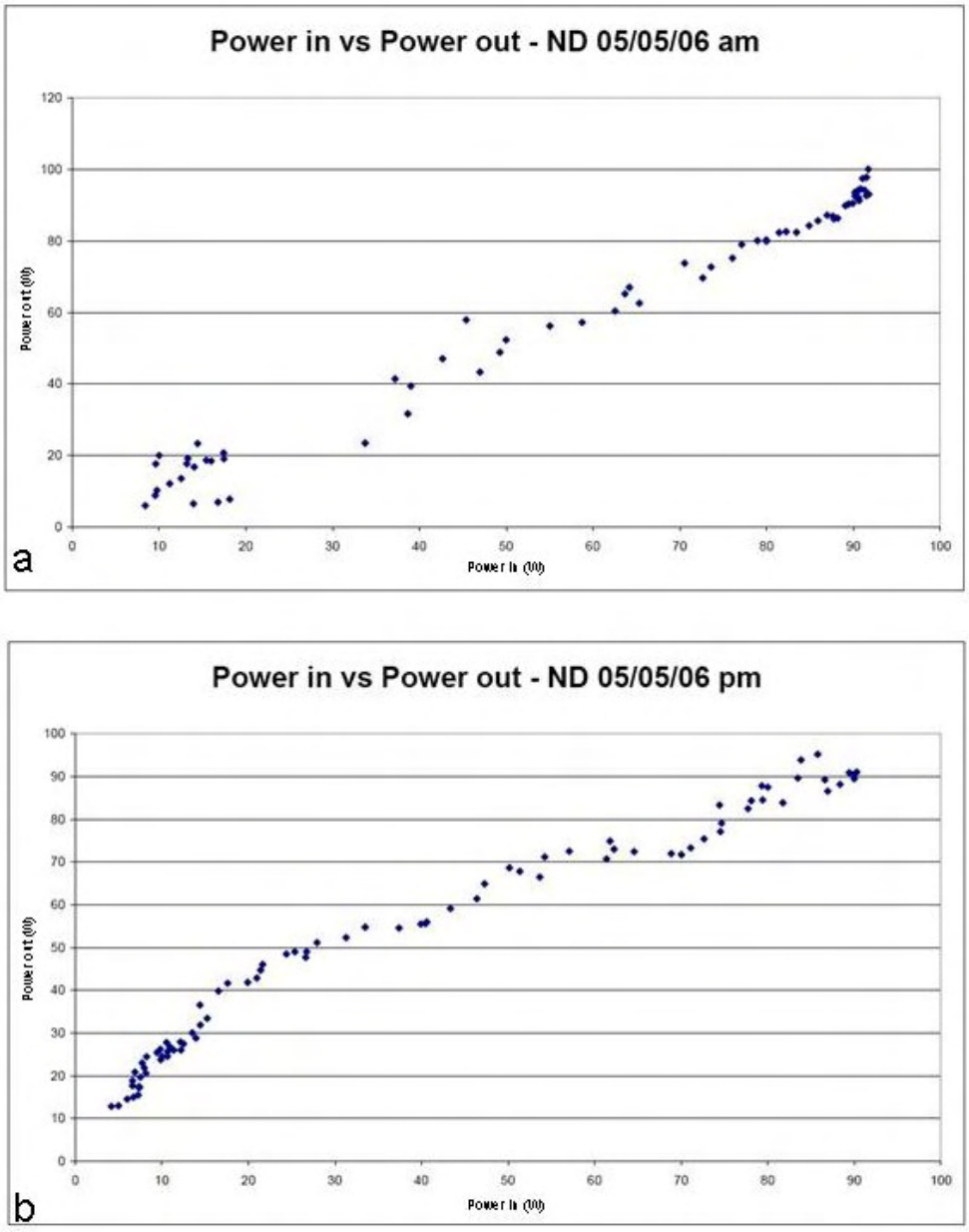

Figure 4.39. Power In vs Useful Power Output - ND 05/05/06

a - morning

b - afternoon

A similar issue in the mornings with duct WS was prevented by the shading from the hill. The data from NS, WS and WD show that the apparent thermal mass effect of ND could be attributed to solar gain through the side of the duct.

4.5 Conclusion

Empirical data has been obtained to indicate the performance of a solar air heater in UK climate conditions. It has shown that in winter conditions (26/01/06) one square meter of exposed duct could produce between 1300 and 1650 Wh on a sunny day. The efficiency of the system (compared against vertical global solar irradiation) is between 35 and 39%. In summer conditions (05/05/06) every square meter of exposed duct can produce between 1200 and 1600 Wh on a sunny day. The efficiency of the system (compared against vertical global solar irradiation) is between 28 and 38%. This shows that the winter low sun angle performance is as good as summer high solar performance.

Figure 4.40 indicates the length, width and depth of duct referred to in the following paragraph.

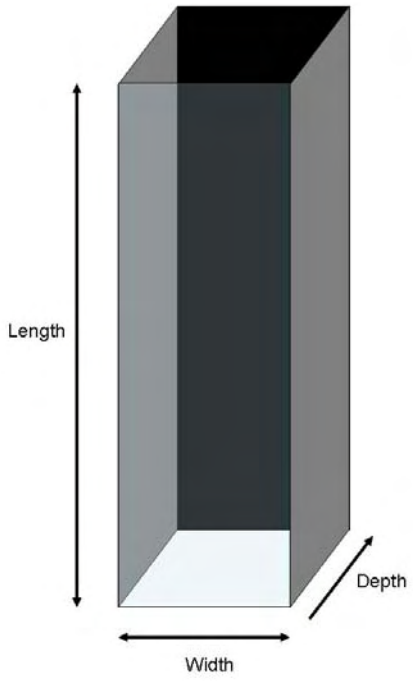

Figure 4.40. Schematic referencing length, width and depth of duct

A comparison of the power output of all four ducts normalised to a façade area of $10m^2$ indicates that deeper ducts generate more power, this effect is particularly pronounced on winter days. The analysis of the ducts over a normalised area also indicated that a significant amount of power could be generated by all four ducts.

The system has been proven to be robust under stagnant conditions, and has been shown to be capable of generating buoyant flow, even though this couldn't be measured. In addition thermal mass has been ruled out as a major effect on the system.

The model has been found to be effective within the bands of error already explained which have been attributed to the limitations of the equipment and the site. The model was written to aid the understanding of the system. It has been able to identify the input power, the useful output power and the proportions of power loss through the back, sides and glazing (approximately 22% of the loss through each side, 6% through the back and the remainder through the glazing). A major difference between the prototype and an actual structure is that, an actual structure will experience significantly less power losses through the sides and back, because these surfaces will not be exposed to outdoor weather conditions. In theory there should be no losses through the sides since they will be adjacent to ducts at the same temperature. This will allow the air to be heated to higher temperatures, which will slightly increase the power losses from the glazed surface, but still enable a higher useful power output.

The model developed in this chapter cannot be used as a predictive model because it needs information that would not be available at that stage (e.g. the actual temperature of the duct surfaces). Predictive models will be considered in Chapter 5, and the results compared with measurements made in this chapter. The model developed in this chapter will be useful for identifying concepts which should be incorporated in the design models in Chapter 5.

4.6 References

1. Li, D.H.W., J.C. Lan, and C.C.S. Lau, *A new approach for predicting vertical global solar irradiance*. Renewable Energy, 2002. **25**: p. 591-606.
2. Muneer, T., *Solar radiation & Daylight models*. 1997, Oxford: Architectural Press.p.1- 197; 0 7506 2495 7.

3. ASHRAE, *2005 ASHRAE Handbook: Fundamentals, SI Edition*, ed. R.a.A.C.E. American Society of Heating, Inc. 2005, Atlanta: ASHRAE; 1-931862-71-0.
4. British Standards Institution, *Thermal insulation for building equipment and industrial installations - Calculation Rules,* BS EN ISO 12241, 1998, British Standards Institution:
5. *HTB2 User Manual release 2.0a*. 1996: Welsh School of Architecture;
6. Kreith, F. and M.S. Bohn, *Principles of Heat Transfer*. 5 ed. 1993, New York: West Publishing Company.p.1- 720; 0 31401360 1.
7. Kipp & Zonen, *Pyranometer for Outdoor Installation CM5 - CM6*.
8. Vector Instruments. *A100R Contact Closure (Switching) Anemometer*. [cited 24th July 2006]; http://www.windspeed.co.uk/ws/index.php?option=displaypage&Itemid=67&op=page#downloads.
9. Vector Instruments, *Encoder Windvane: W200G*, Vector Instruments.
10. Vaisala Oy. *HMP45A & HMP45D Humidity and Temperature Probes - Operating Manual*. 1997 [cited 30th March 2006].
11. Tong, A., *Improving the accuracy of temperature measurements.* Sensor Review, 2001. **2001**(3): p. 193-198.
12. Papailiou, G. *Measurement of Glass Surface Temperature* 1995: Master of Science; School of Engineering at University of Wales, Cardiff.
13. Electro Optical Industries Inc. *Material Emissivity Properties*. [cited 5th April 2005]; http://www.electro-optical.com/bb_rad/emissivity/matlemisivty.htm.
14. Hirunlabh, J., et al., *Study of natural ventilation of houses by a metallic solar wall under tropical climate.* Renewable Energy, 1999. **18**: p. 109-119.
15. Ong, K.S., *A mathematical model of a solar chimney.* Renewable Energy, 2003. **28**: p. 1047-1060.
16. Ong, K.S., *Thermal performance of solar air heaters: Mathematical model and solution procedure.* Solar Energy, 1995. **55**(2): p. 93-109.
17. Corus Colors, *Colorcoat Armacor: A high-build organic coated steel for cost effective construction,* 2003, Corus Colors: Shotton
18. Sika, *Engineering Silicones: Elastosil*

Sika Facade Systems: All-round Expertise Guarantees Success, 2006, Sika:
19. Tennent, R.M., *Science Data Book*. 1992, Essex: Oliver & Boyd.p.1- 105; 0 05 002487 6.
20. *Experiment Location*. 2006 21st October 2006 [cited; www.earth.google.com.

5 Developing a Design Model

To develop the solar air heater as an operational system it is necessary that its behaviour under forced and buoyant convection can be predicted. The aim of this chapter is to evaluate existing design models for a solar duct and derive improved models for forced and buoyant convection based on the system parameters identified in Chapter 4. Initially models related to forced convection will be considered, models relating to buoyant convection will be considered subsequently.

The literature survey identified a number of models which had been written for solar air heaters under forced convection, for a solar chimney under buoyant convection or for the passive airflow behind a photovoltaic array. Although some of these models have been compared with computational fluid dynamic models, or laboratory condition experiments, they have not been compared to each other, or explicitly to an outdoor experiment. The design conditions are taken from measurements made on key dates with the experimental rig described in Chapter 4. The forced convection models are compared to the data from 26th January 2006 (sunny winter day) and 5th May 2006 (sunny summer day), while the buoyant convection models are compared to the data from 3rd July 2006 (sunny summer day).

5.1 Forced Convection Design Models

The literature survey found three models currently in existence to predict the behaviour of solar air heaters under forced convection. These were written by Ong (discussed in Section 2.4.2 and Appendix A), Yeh & Lin (Section 2.4.3 and Appendix A) and Ho & Loveday (Section 2.4.4 and Appendix A). These will be referred to here as the Ong_{fc}, Yeh_{fc} and Ho_{fc} models. In the first comparison the models were used without alterations, comparing those output parameters that were available from each model against the measured data; mean glazing temperature, mean absorbing surface temperature, mean duct air temperature, exit air temperature, power output. Where the models required meteorological data, data from the appropriate experiment date was used. Physical properties of the materials were estimated from common handbook data.

The procedure followed for each of the models is described in Appendix H. Table 5.1 shows a comparison of each model.

Table 5.1 Comparison of Models Ong_{fc}, Yeh_{fc} and Ho_{fc}

Parameter	Ong_{fc}	Yeh_{fc}	Ho_{fc}
Considers the air heater	In sections	In entirety	In entirety
Hydraulic diameter (D_h)	Parallel plates (B4)	Non circular duct (B1)	Non circular duct (B1)
Sky temperature (T_{sky})	Swinbank's correlation (C31)	Not Used	Not Used
Wind convection heat transfer (h_w)	McAdam's correlation (C20)	Adjusted McAdam's correlation (C23)	McAdam's correlation (C20)
Dynamic viscosity of air (μ)	Temperature dependent (H1)	Constant	Not Used
Kinematic viscosity of air (ν)	Not Used	Not Used	Constant
Specific heat capacity of air (c_p)	Temperature dependent (H2)	Constant	Constant
Thermal conductivity of air (k)	Temperature dependent (H3)	Constant	Constant
Nusselt number	Nusselt's correlation (C5)	Kay's correlation (C12)	Kay's correlation (C12)
Radiative heat transfer coefficient between parallel plates	Incorporating glass and solar absorber temperatures with glass and solar absorber emissivity (C28)	Incorporating fluid temperature with glass and solar absorber emissivity (C29)	Incorporating glass and solar absorber temperatures with glass and solar absorber emissivity (C28)
Radiative heat transfer coefficient between glass and sky	Incorporating glass, sky and ambient temperatures along with the emissivity of glass (C30)	Not Used	Incorporating glass and ambient temperatures along with the emissivity of glass (C33)

Table 5.1 Cont'd Comparison of Models Ong_{fc}, Yeh_{fc} and Ho_{fc}

Parameter	Ong_{fc}	Yeh_{fc}	Ho_{fc}
Overall top heat loss coefficient	Sum of wind and radiative heat transfer coefficients (H4)	Incorporating the solar absorber and ambient temperatures, the wind coefficient and the emissivity of the solar absorber surface (A19)	Unspecified – definition from BS EN ISO 12241 [1] used
Heat loss coefficient including sides	No	No	Yes
Overall bottom heat loss coefficient	Incorporating conductive and wind convective components (H5)	Ratio of thermal conductivity and thickness of insulation (H7)	Unspecified – definition from BS EN ISO 12241 [1] used
Considers heat gain from glass and absorbing surface separately	Yes	No	No
Considers direct and diffuse components of solar irradiation and angle of incidence	No	No	No
Considers heat transfer for sides	No	No	Yes

Table 5.1 Cont'd Comparison of Models Ong_{fc}, Yeh_{fc} and Ho_{fc}

Parameter	Ong_{fc}	Yeh_{fc}	Ho_{fc}
Solution procedure	Iterative solution of matrix equation.	Iterative solution of a series of equations.	Iterative solution of a series of equations.
	The meteorological data and physical properties of the materials used in the experiment (e.g. emissivity, absorptivity, etc) were applied to the model.		The meteorological data and physical properties of the materials used in the experiment (e.g. emissivity) were applied to the model. However, absorptivity of the solar absorber was not part or the original model.
Parameters Calculated Directly	The mean glass, mean absorber and mean duct air temperature are calculated directly from the model.	The mean absorber and mean duct air temperature are calculated directly from the model.	The mean outer glass, mean inner glass, mean absorber, mean outer, mean duct air and exit air temperature are calculated directly from the model.
Parameters Calculated Indirectly	The air exit temperature is calculated, assuming a linear temperature gradient. The power output is calculated from the air mass flow and the calculated air exit temperature.		The power output is calculated from the air mass flow and the calculated air exit temperature.

The ambient temperature, horizontal global solar irradiation, horizontal diffuse irradiation and air mass flow from a sunny winter's day (26/01/06) and a sunny summer's day (05/05/06) were averaged over one hour periods and used as inputs into the design models. Table 5.2 shows the input conditions averaged over the previous hour (i.e. the data for 09:00 is the average between 08:00 and 09:00).

Table 5.2 Input Conditions (Averaged over 1 hour periods)

Time period	Ambient Temp. (^{o}C)	Horizontal diffuse irradiation (W m^{-2})	Horizontal global irradiation (W m^{-2})	Air mass flow (kg s^{-1})			
				ND	WD	NS	WS
26/01/06							
09:00	2.6	14	29	0.0047	0.0054	0.0051	0.0050
10:00	6.1	46	152	0.0047	0.0054	0.0051	0.0050
11:00	7.2	62	227	0.0047	0.0054	0.0051	0.0051
12:00	7.8	71	302	0.0047	0.0054	0.0051	0.0051
13:00	8.3	59	323	0.0047	0.0054	0.0051	0.0050
14:00	8.3	58	297	0.0047	0.0054	0.0051	0.0050
15:00	7.6	50	202	0.0047	0.0054	0.0051	0.0050
16:00	6.2	33	94	0.0047	0.0054	0.0052	0.0050
17:00	4.4	12	12	0.0048	0.0054	0.0052	0.0050
05/05/06							
08:00	10.5	31	51	0.0044	0.0050	0.0047	0.0046
09:00	10.8	82	230	0.0044	0.0050	0.0047	0.0047
10:00	11.5	120	282	0.0044	0.0051	0.0048	0.0047
11:00	11.9	146	572	0.0045	0.0051	0.0048	0.0047
12:00	12.6	78	686	0.0045	0.0051	0.0048	0.0047
13:00	14.1	59	739	0.0045	0.0051	0.0048	0.0047
14:00	15.1	64	782	0.0044	0.0050	0.0048	0.0047
15:00	15.7	74	781	0.0044	0.0050	0.0047	0.0047
16:00	16.6	82	746	0.0044	0.0050	0.0048	0.0047
17:00	16.1	99	650	0.0044	0.0050	0.0048	0.0047
18:00	15.5	106	517	0.0044	0.0050	0.0048	0.0047
19:00	15.4	106	341	0.0044	0.0050	0.0048	0.0047
20:00	15.0	77	220	0.0044	0.0050	0.0048	0.0047

The incident radiation on the vertical surfaces has been calculated using equations E1 and E2 and are presented in Table 5.3.

Table 5.3 Vertical Solar Irradiation (Averaged over 1 hour periods)

Time period	Vertical Global Irradiation (W m^{-2})	Vertical direct irradiation (W m^{-2})	Vertical diffuse irradiation (W m^{-2})
26/01/06			
09:00	138	128	10
10:00	443	405	38
11:00	567	513	54
12:00	710	644	66
13:00	775	713	62
14:00	729	670	58
15:00	542	497	45
16:00	346	320	26
17:00	7	0	7
05/05/06			
08:00	94	37	57
09:00	178	89	88
10:00	414	283	130
11:00	541	434	107
12:00	594	491	103
13:00	615	505	110
14:00	579	463	115
15:00	503	387	115
16:00	361	246	115
17:00	202	97	105
18:00	87	0	87
19:00	61	0	61
20:00	39	0	39

The actual outputs from the experiment averaged over one hour periods for 26/01/06 and 05/05/06 are shown in Tables G1-G4 of Appendix G. Table G1 shows the mean glazed surface temperature (calculated from the average of the two thermocouples attached to the glass). Table G2 shows the mean absorbing surface temperature (calculated from the average of the two thermocouples attached to the back surface of the duct). Table G3 shows the measured mean air temperature (calculated from the average of the air entry and air exit thermocouples). Table G4 shows the measured air exit temperature. This data will be used to compare design models.

Table 5.4 shows the efficiency for the ducts, calculated from [2]:

$$\eta = \frac{Q_{use}}{Q_{in}} = \frac{Q_{use}}{EWL} \qquad 5.1$$

Where:

E is the solar irradiance (W m^{-2})

W is the duct width (m)

L is the duct length (m)

The values in Table 5.4 were calculated from the measured temperature rise and air mass flow in relation to the global vertical solar irradiation.

Table 5.4 Prototype Efficiency (Averaged over 1 hour periods)

Time period	Calculated Efficiency (%)			
	ND	WD	NS	WS
26/01/06				
09:00	**-37.6**	**-7.7**	**-20.5**	**-6.3**
10:00	35.9	37.7	31.6	29.1
11:00	42.8	43.3	32.1	32.3
12:00	43.4	43.5	31.4	32.7
13:00	46.7	44.6	32.9	32.9
14:00	48.0	45.2	34.7	33.1
15:00	60.5	52.7	44.0	35.9
16:00	**66.4**	44.9	40.7	32.8
17:00	**128.7**	**185.3**	**-122.0**	**-6.9**
05/05/06				
08:00	**3.2**	**8.4**	**4.0**	**15.9**
09:00	12.9	20.5	**5.1**	29.5
10:00	11.7	20.0	11.0	22.9
11:00	13.3	25.5	12.5	23.0
12:00	15.0	27.4	12.4	22.3
13:00	16.5	27.8	10.6	21.2
14:00	17.4	27.1	9.8	19.4
15:00	**17.3**	23.4	9.2	17.3
16:00	**22.7**	17.0	3.3	15.1
17:00	**37.3**	12.0	**-13.9**	10.2
18:00	**54.0**	14.0	**-40.2**	4.2
19:00	**63.0**	**9.3**	**-55.0**	**0.6**
20:00	**60.9**	**22.0**	**-60.9**	**-0.7**

Negative efficiencies are indicated at 09:00 of 26/01/06 for all ducts, at 17:00 of 26/01/06 for ducts NS and WS, after 16:00 of 05/05/06 for duct NS and at 20:00 of 05/05/06 for duct WS. For 17:00 of 26/01/06 the data for ducts ND and WD indicate efficiencies greater than 100%. In each of these cases, there is little difference between the entry and exit temperatures, and the accuracy of the thermocouple data

becomes significant. This has an impact on the calculations using these temperatures. Since this data has been identified as being unsatisfactory, it will not be considered for the comparison of design models. Other time periods which had small differences between the entry and exit temperatures which may affect the results were also identified. These were 08:00 on 05/05/06 for all ducts, 09:00 on 05/05/06 for duct NS and after 19:00 on 05/05/06 for ducts WD and WS. As a precaution, these time periods were also discounted from the comparison of design models. In Chapter 4, duct ND was found to be receiving solar irradiation through the side of the panel after 14:30 in the afternoon. For this reason, data for duct ND after 15:00 will not be considered for the comparison of design models.

For 26/01/06 data for all four ducts will be considered for the time period 10:00 – 15:00. For 05/05/06, data from the following time periods will be considered when evaluating the design models:

- ND 09:00 – 15:00
- WD 09:00 – 18:00
- NS 10:00 – 16:00
- WS 09:00 – 18:00.

The design models will be compared to real data and judged on the fit to the data by:

1. observing the closeness of fit in the figure
2. the mean bias
3. the Root Mean Square Error (RMSE)

The mean bias indicates the tendency of the model to under or overestimate a parameter. If the bias is consistent, then it can be subtracted to reach a closer estimate of the parameter. The RMSE refers to how large the discrepancy tends to be between the estimate and the real value. The ideal model would have a low mean bias and RMSE. The acceptable level of bias and RMSE depends on the parameter being measured.

5.1.1 Prediction of Mean Glazing Temperature

The following graphs show the correlation between the measured mean glazing temperature for ducts ND, WD and WS and the predictions given by the Ong_{fc} and Ho_{fc}

models. Duct NS could not be included for 26/01/06 due to a thermocouple failure. The error bars indicate the difficulty of obtaining the accurate temperature of glass under solar irradiation. In this instance a mean bias and RMSE of 3°C would be considered acceptable.

Figures 5.1 - 5.3 show the correlation for 26/01/06 and Figures 5.4 - 5.7 for 05/05/06.

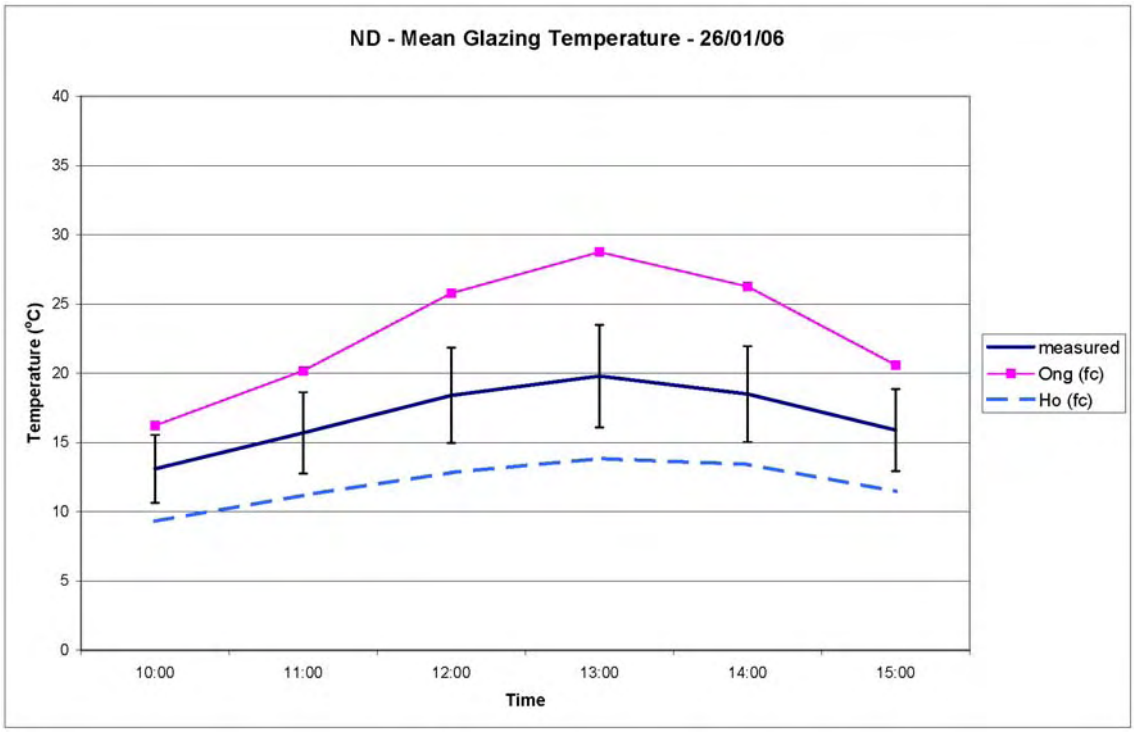

Figure 5.1. ND - Mean Glazing Temperature 26/01/06

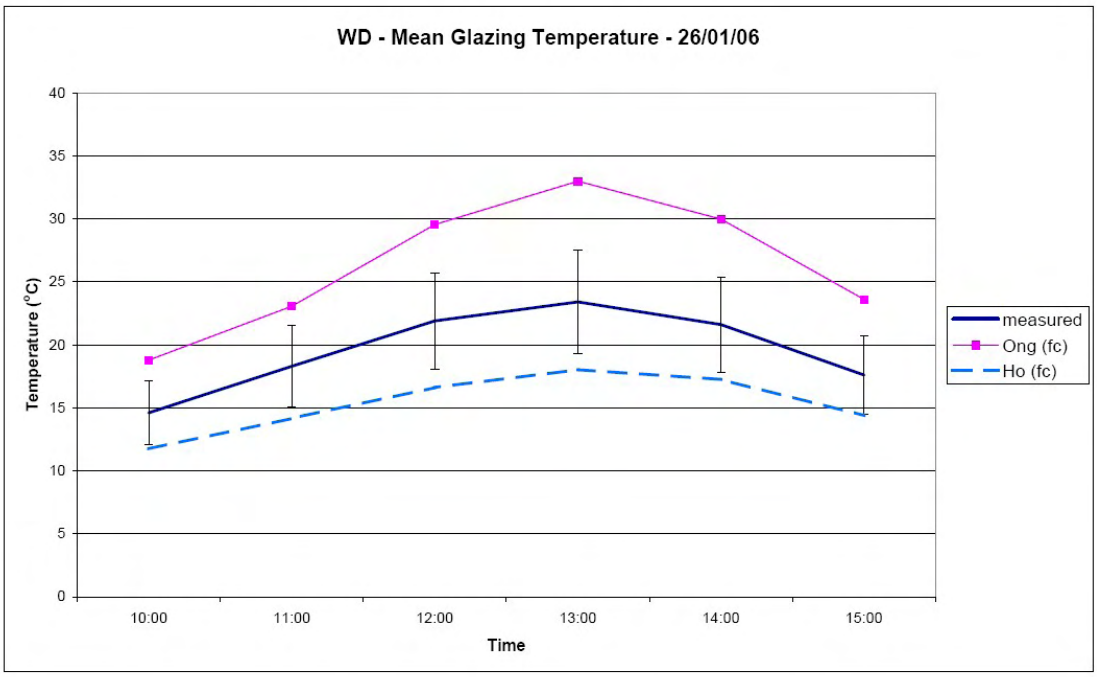

Figure 5.2. WD - Mean Glazing Temperature 26/01/06

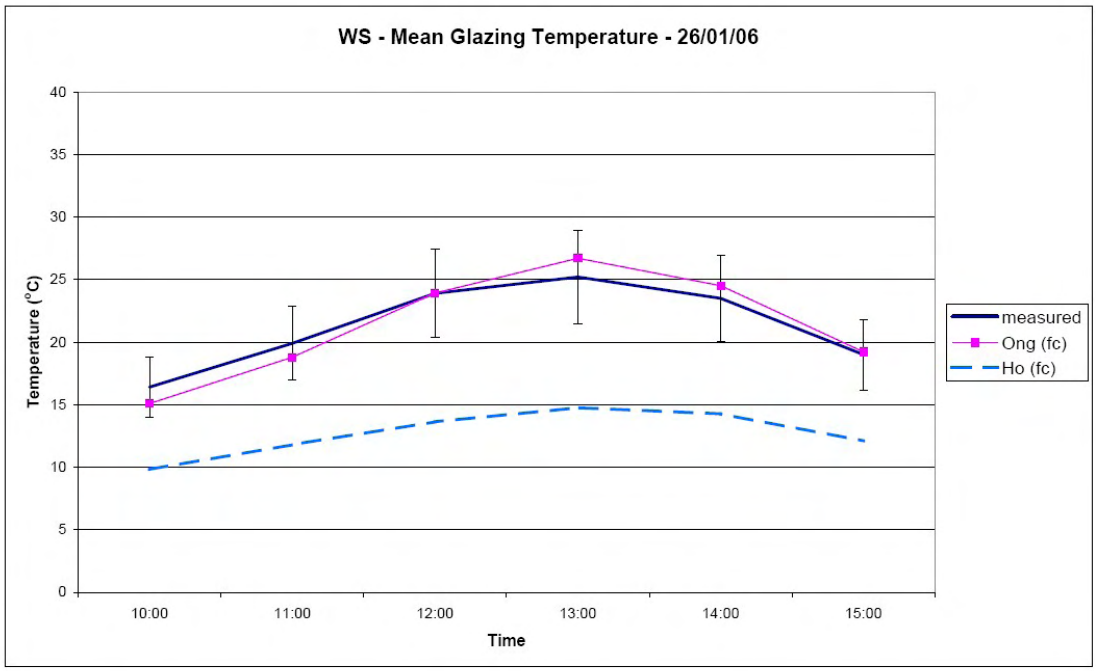

Figure 5.3. WS - Mean Glazing Temperature 26/01/06

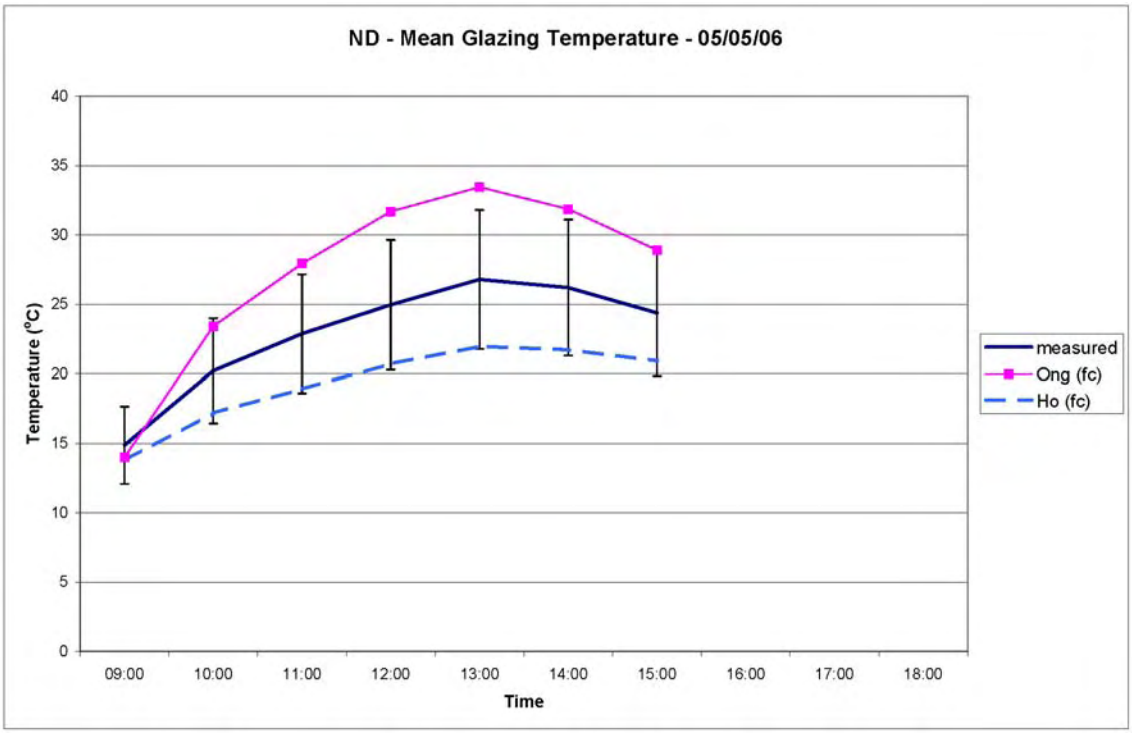

Figure 5.4. ND - Mean Glazing Temperature 05/05/06

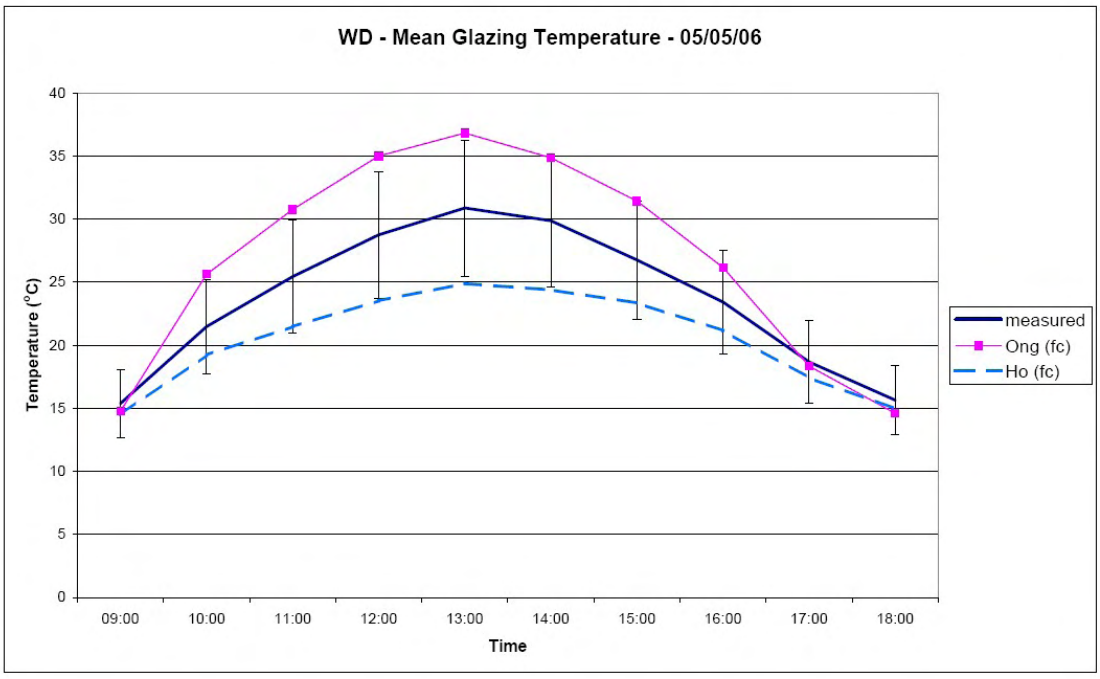

Figure 5.5. WD - Mean Glazing Temperature 05/05/06

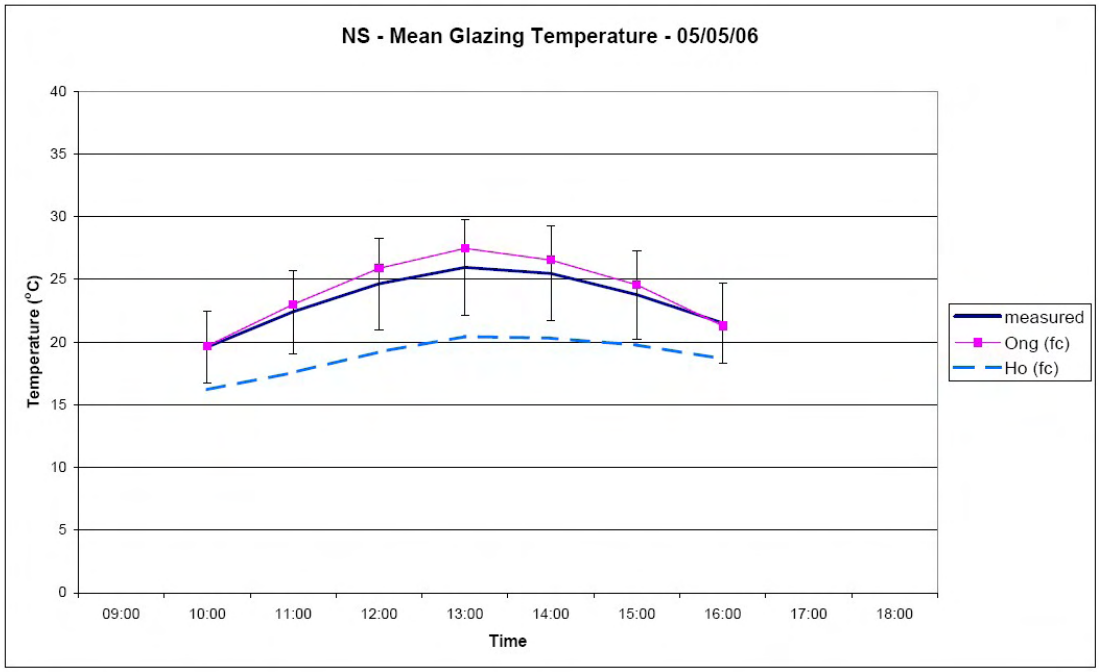

Figure 5.6. NS - Mean Glazing Temperature 05/05/06

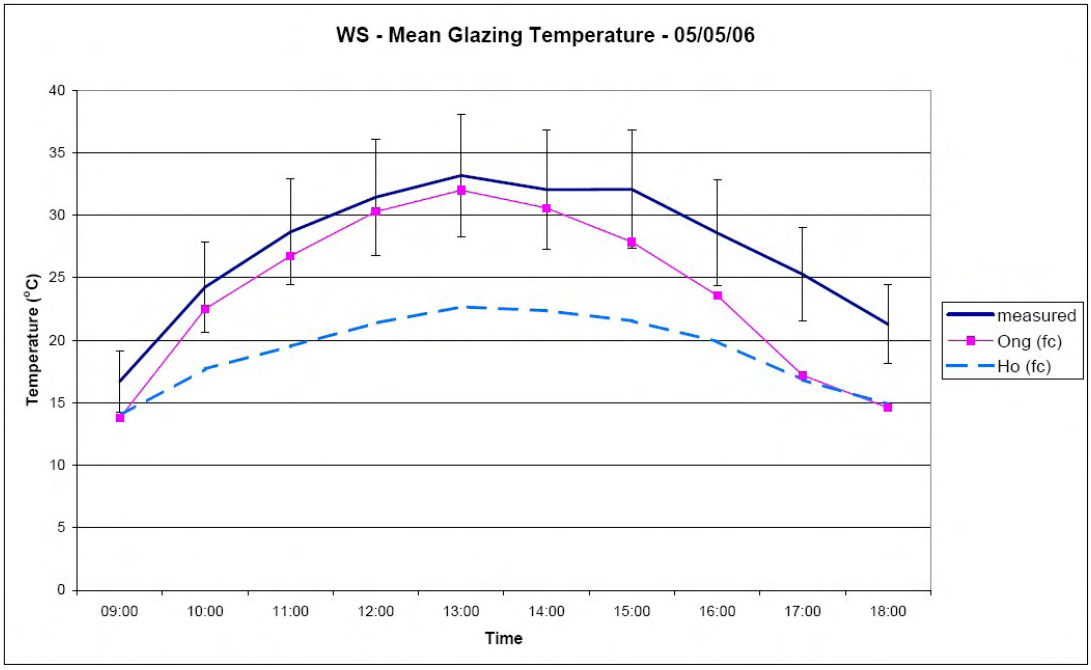

Figure 5.7. WS - Mean Glazing Temperature 05/05/06

Table 5.5 indicates the mean bias and RMSE for the two models for 26/01/06. Table 5.6 gives the same information for 05/05/06. In the tables 'All' refers to the mean bias and RMSE calculated for all four ducts.

Table 5.5 Bias and RMSE for Prediction of Mean Glazing Temperature 26/01/06

		Ong_{fc}	Ho_{fc}
Mean Bias (^oC)	ND	6.0	-4.9
	WD	6.8	-4.2
	NS	No data available for comparison	
	WS	0.1	-8.6
	All	4.3	-5.9
RMSE (^oC)	ND	6.4	4.9
	WD	7.0	4.3
	NS	No data available for comparison	
	WS	1.0	8.7
	All	5.5	6.3

Table 5.6 Bias and RMSE for Prediction of Mean Glazing Temperature 05/05/06

		Ong_{fc}	Ho_{fc}
Mean Bias (^oC)	ND	4.4	-3.6
	WD	3.2	-3.1
	NS	0.7	-4.5
	WS	-3.4	-8.3
	All	1.0	-5.0
RMSE (^oC)	ND	5.0	3.8
	WD	4.2	3.7
	NS	0.9	4.6
	WS	4.2	8.6
	All	3.6	5.6

The error bars in Figures 5.1 – 5.7 indicate that there is a significant measurement error inherent in the glazing temperature. In this instance a mean bias and RMSE of 3^oC would be considered acceptable.

From Table 5.5 it can be seen that both models show significant bias. The Ong_{fc} model tends to overestimate the glazing temperature, while the Ho_{fc} model tends to underestimate it. Over the three ducts considered, the Ong_{fc} model has a slightly lower RMSE.

From Table 5.6 it can be seen that the Ong_{fc} model is not consistently biased. However, the Ho_{fc} model strongly underestimates the glazing temperature for all of the ducts, and has a higher RMSE over all four ducts. Of the two models, Ong_{fc} is less biased and has a lower RMSE.

Figures 5.1 - 5.7 indicate that there is a reasonable correlation between the Ong_{fc} model and the measured values. In addition, the Ong_{fc} model has a mean bias and RMSE of less than $3^{o}C$ for specific ducts. However, it does not meet the requirement for all four ducts combined.

5.1.2 Prediction of Mean Absorbing Surface Temperature

The following graphs show the correlation between the measured mean absorbing surface temperature for ducts ND, WD, NS and WS and the predictions given by Ong_{fc}, Yeh_{fc} and Ho_{fc}. It should be noted that error bars have been included in the following graphs; however, the error is too small to show up on the graph. The errors in the measurement of the absorbing surface temperature are of the order of $0.1^{o}C$. In this instance a mean bias and RMSE of $2^{o}C$ would be considered acceptable.

Figures 5.8 - 5.11 show the correlation for 26/01/06 and Figures 5. 12 - 5. 15 for 05/05/06.

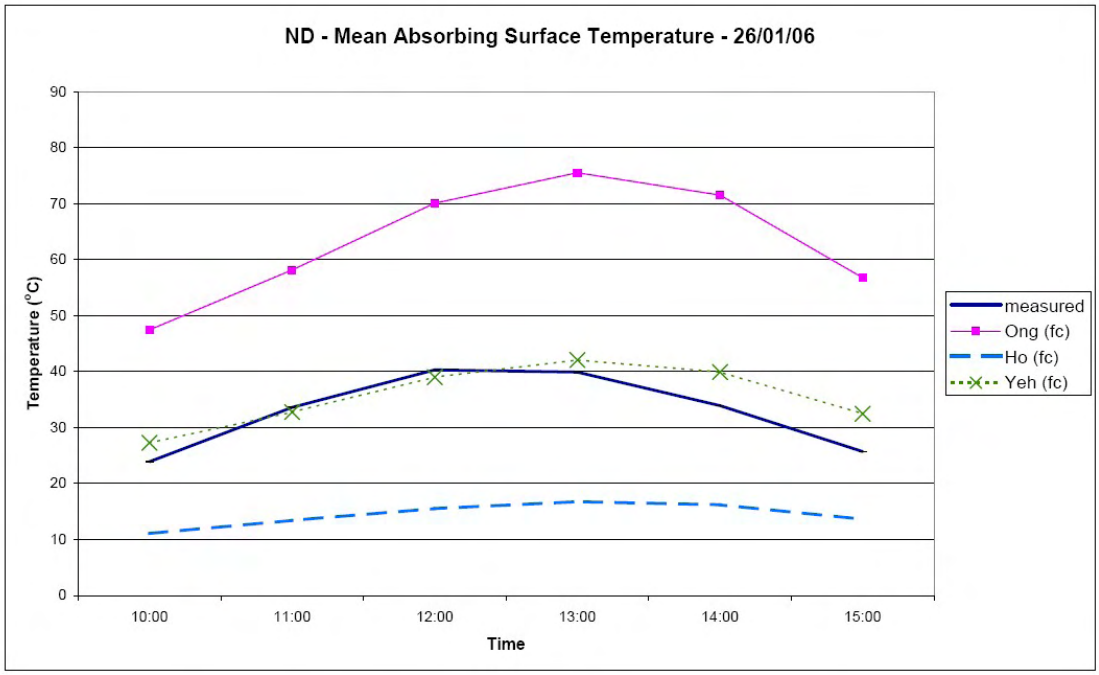

Figure 5.8. ND - Mean Absorbing Surface Temperature - 26/01/06

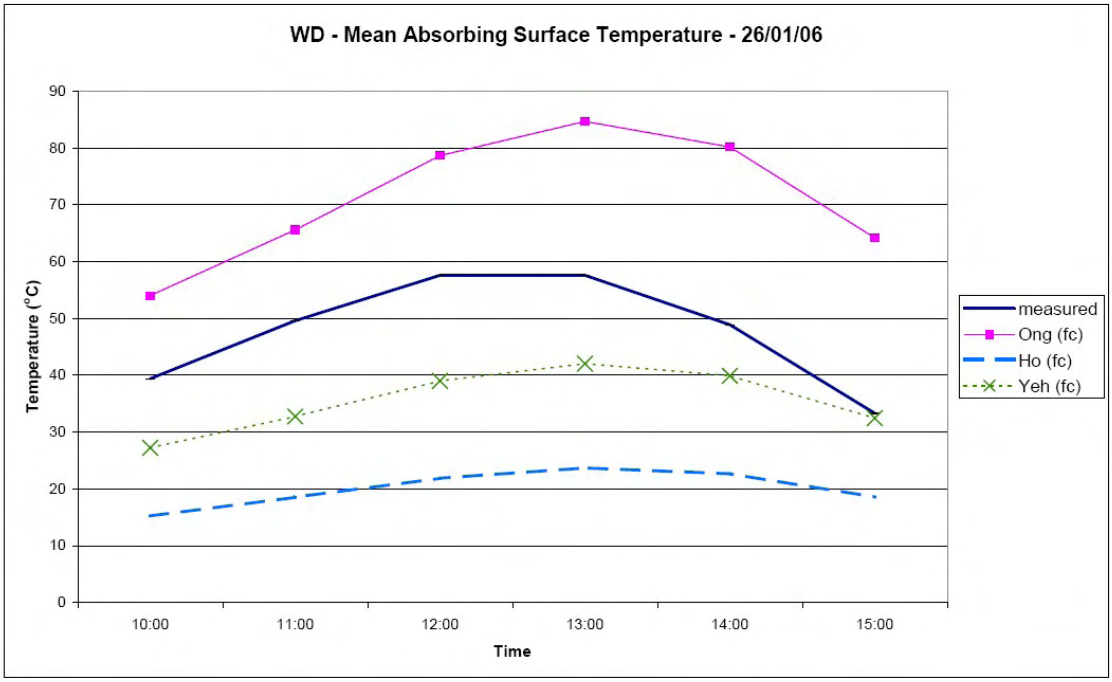

Figure 5.9. WD - Mean Absorbing Surface Temperature - 26/01/06

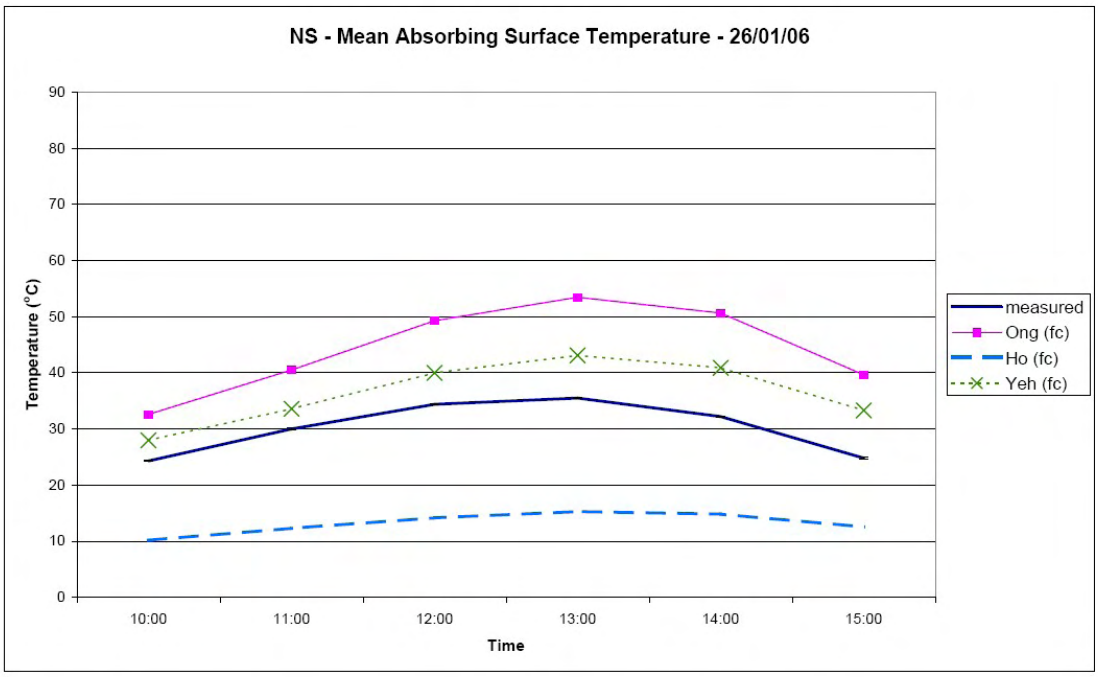

Figure 5.10. NS - Mean Absorbing Surface Temperature - 26/01/06

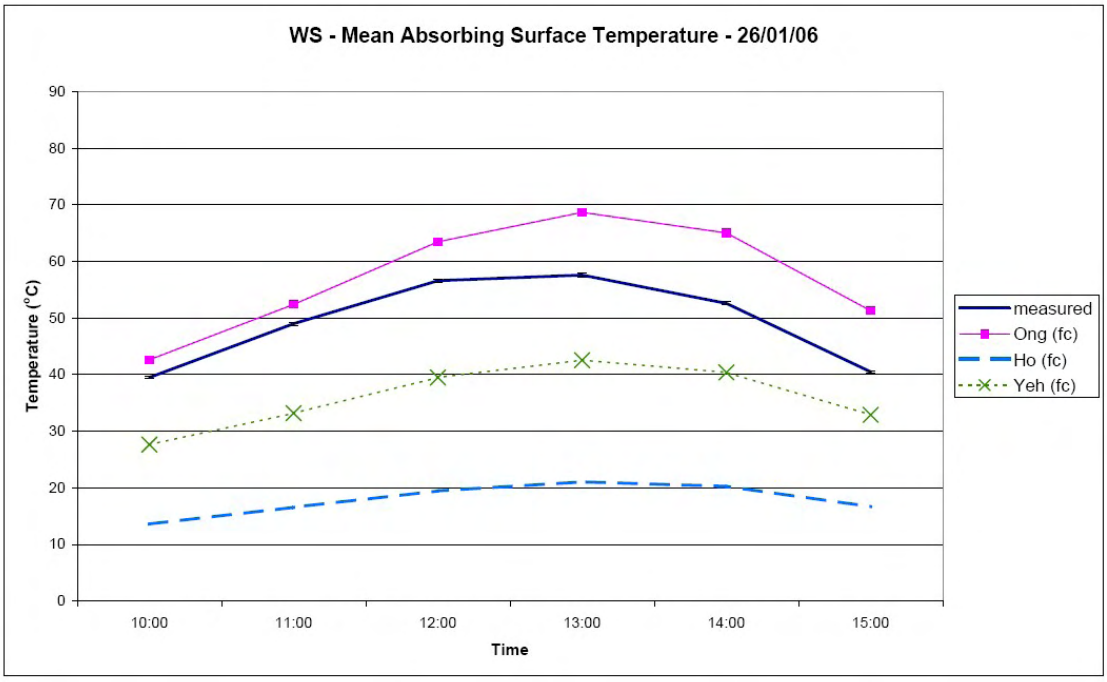

Figure 5.11. WS - Mean Absorbing Surface Temperature - 26/01/06

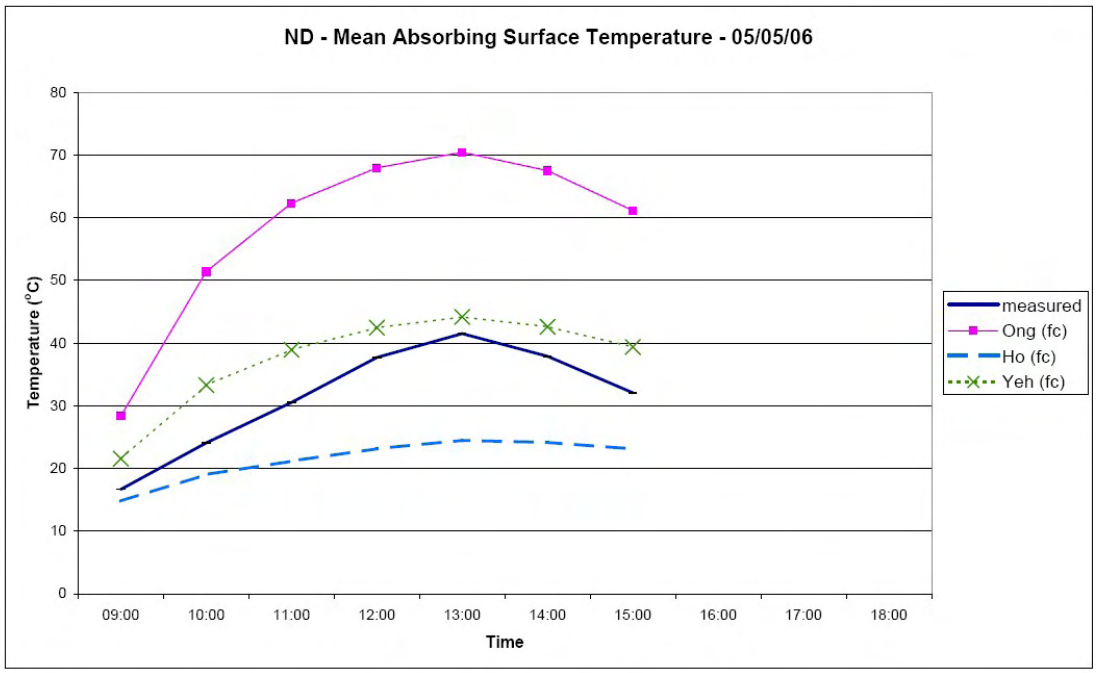

Figure 5.12. ND - Mean Absorbing Surface Temperature - 05/05/06

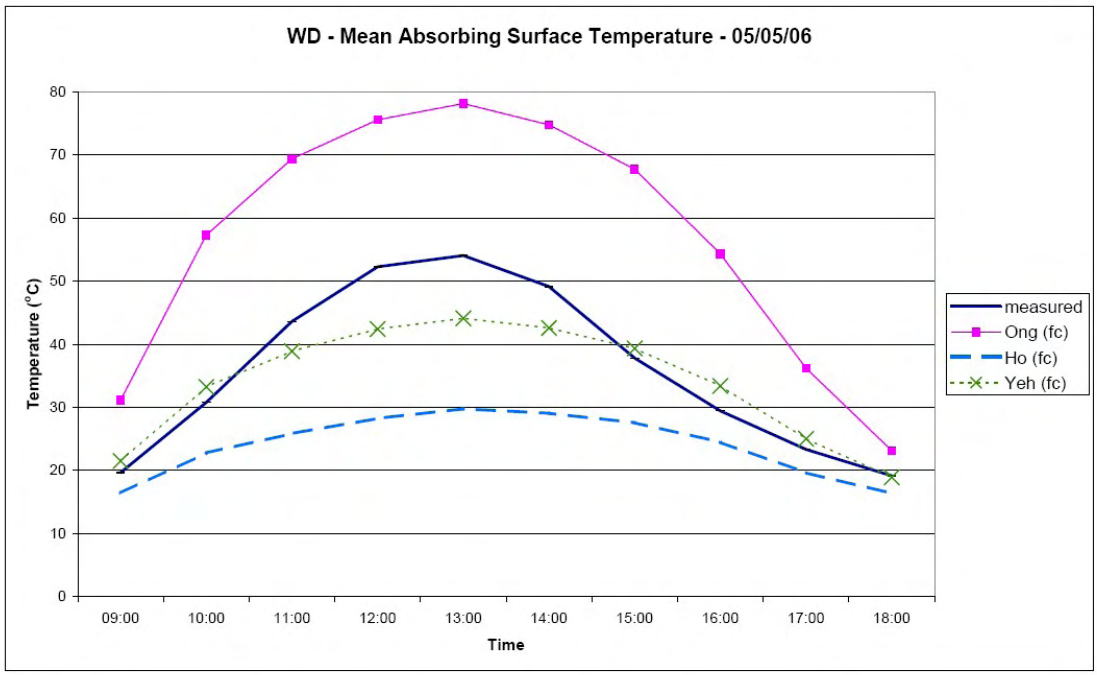

Figure 5.13. WD - Mean Absorbing Surface Temperature - 05/05/06

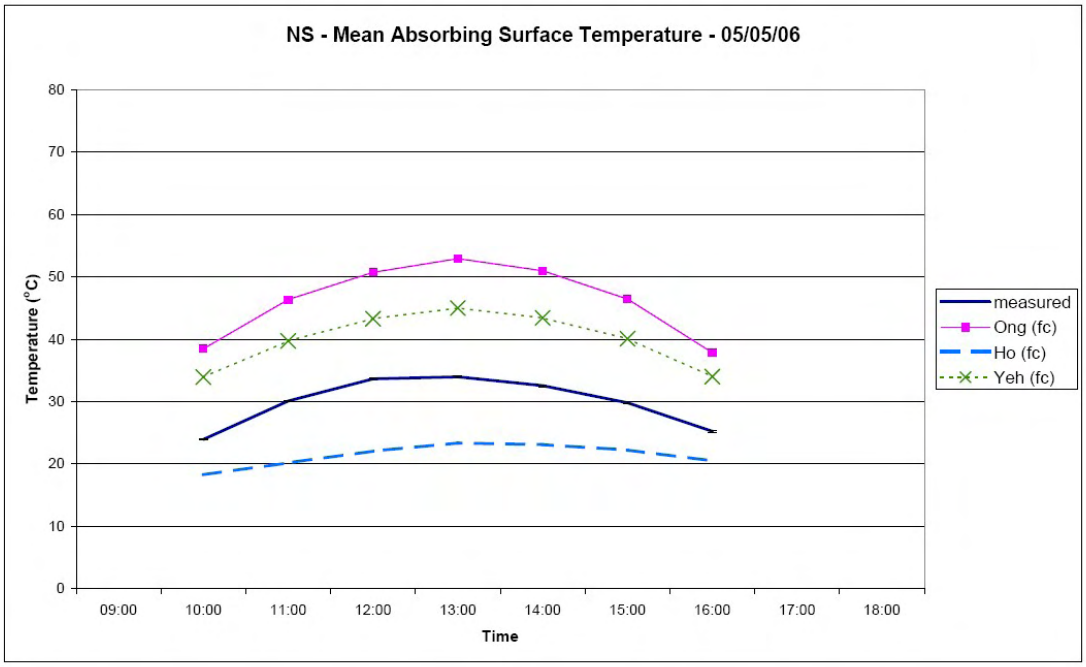

Figure 5.14. NS - Mean Absorbing Surface Temperature - 05/05/06

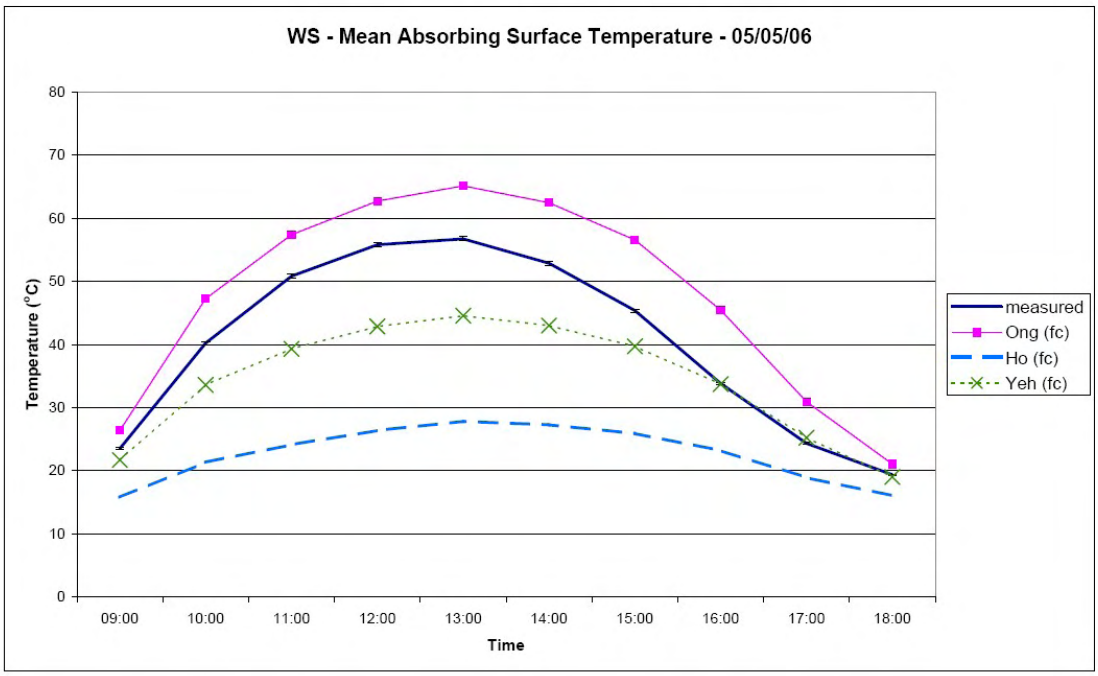

Figure 5.15. WS - Mean Absorbing Surface Temperature - 05/05/06

Table 5.7 indicates the mean bias and RMSE for the two models for 26/01/06. Table 5.8 gives the same information for 05/05/06.

Table 5.7 Bias and RMSE for Prediction of Absorbing Surface Temperature – 26/01/06

		Ong_{fc}	Yeh_{fc}	Ho_{fc}
Mean Bias (^oC)	ND	30.3	2.7	-18.5
	WD	23.5	-12.2	-27.6
	NS	14.2	6.3	-17.0
	WS	8.0	-13.3	-31.4
	All	19.0	-4.1	-23.6
RMSE (^oC)	ND	30.8	4.1	19.1
	WD	24.4	13.5	28.5
	NS	14.6	6.6	17.2
	WS	8.8	13.6	31.8
	All	21.4	10.4	24.9

Table 5.8 Bias and RMSE for Prediction of Absorbing Surface Temperature – 05/05/06

		Ong_{fc}	Yeh_{fc}	Ho_{fc}
Mean Bias (^oC)	ND	27.0	6.0	-10.1
	WD	20.8	-2.0	-11.9
	NS	16.4	10.0	-8.5
	WS	7.2	-6.0	-17.6
	All	17.2	0.9	-12.5
RMSE (^oC)	ND	27.7	6.4	11.3
	WD	22.3	5.4	14.5
	NS	16.5	10.1	8.8
	WS	7.9	7.9	20.1
	All	20.5	7.9	15.7

From Table 5.7 it can be seen that the Ong_{fc} model tends to overestimate the absorbing surface temperature, while the Ho_{fc} tends to underestimate it and the Yeh model is not consistently biased for each duct. Of the three models the Yeh_{fc} model has the lowest RMSE. The same trends are observed in Table 5.8.

Figures 5.8 - 5.15 indicate that none of the models have a particularly close correlation with the measured values. Tables 5.7 and 5.8 indicate that the Yeh_{fc} model is the most appropriate model to predict the absorbing surface temperature; however, it still has an RMSE of 7-10^{o}C, which is not satisfactory.

5.1.3 Prediction of Duct Mean Air Temperature

The following graphs show the correlation between the mean air temperature in the duct calculated from thermocouple readings for ducts ND, WD, NS and WS and the predictions given by Ong_{fc}, Yeh_{fc} and Ho_{fc}. It should be noted that error bars have been included in the following graphs; however, the error is too small to show up in the graph. The mean air temperature measurements are accurate to ± 0.03°C. In this instance a mean bias and RMSE of 2°C would be considered acceptable.

Figures 5.16 - 5.19 show the correlation for 26/01/06 and Figures 5. 20 - 5. 23 for 05/05/06.

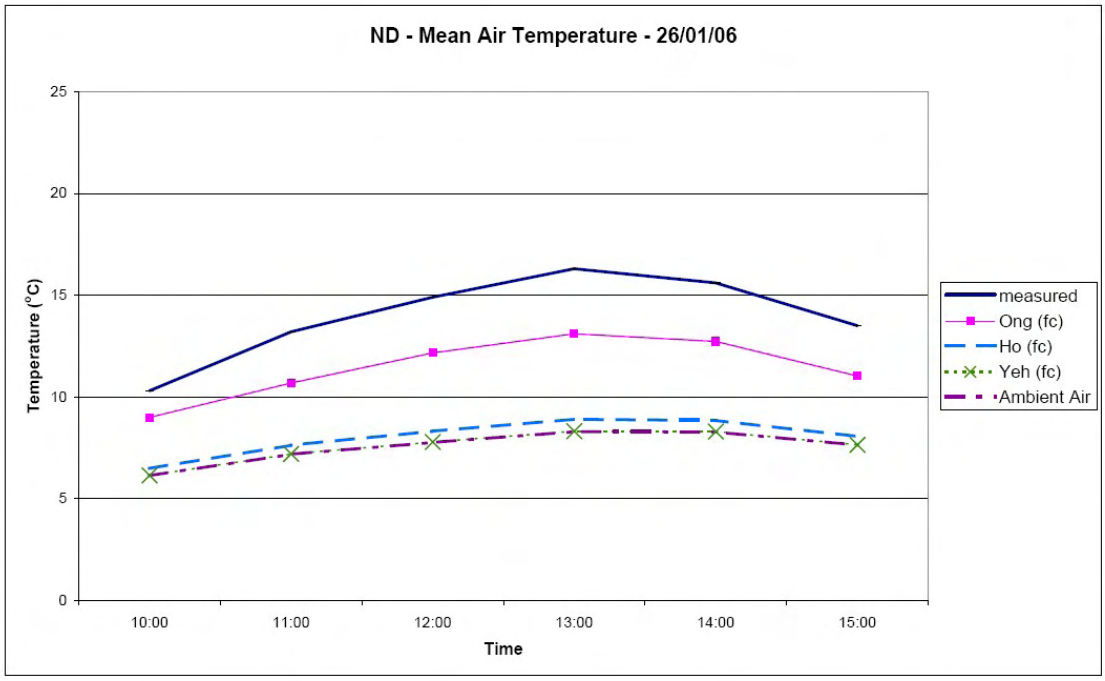

Figure 5.16. ND - Mean Air Temperature 26/01/06

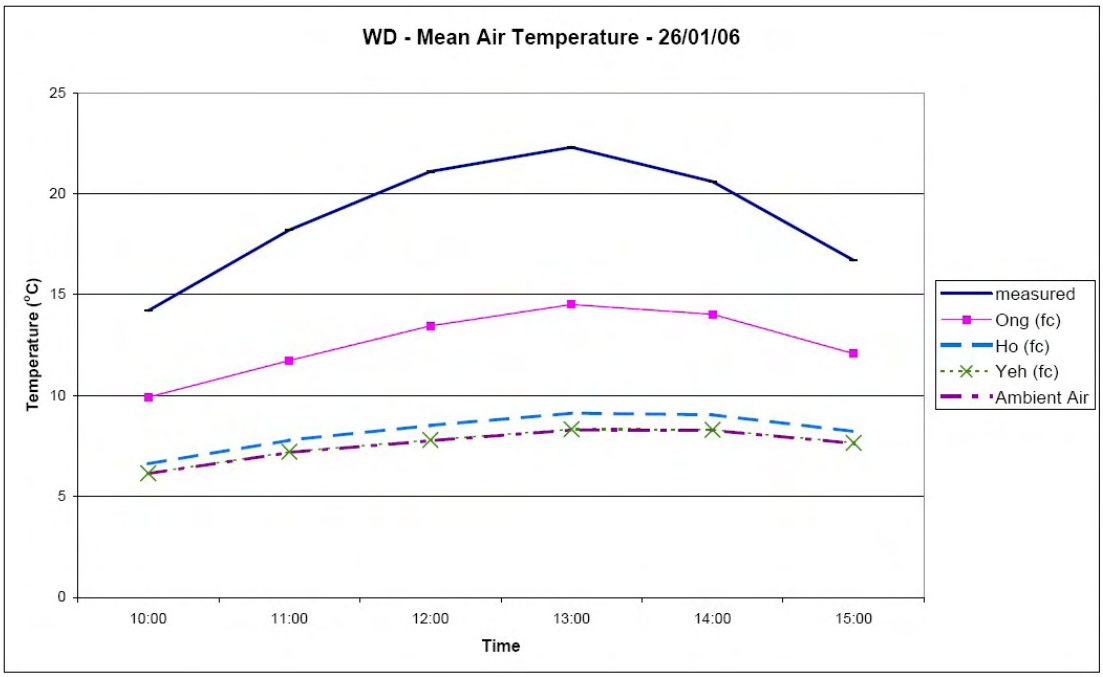

Figure 5.17. WD - Mean Air Temperature 26/01/06

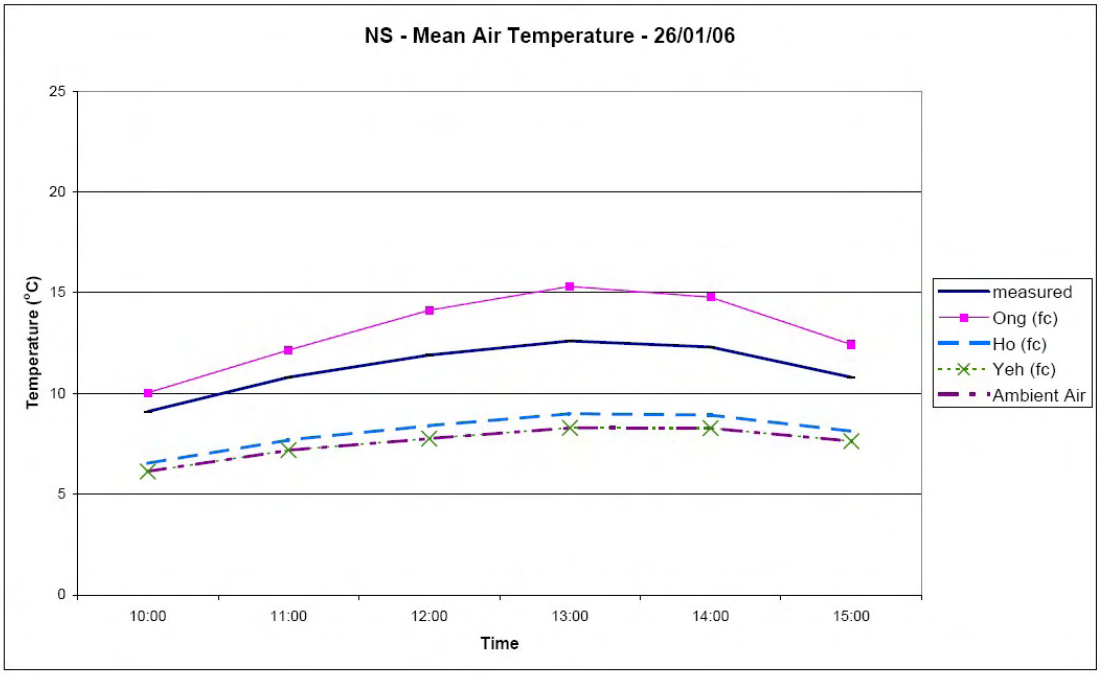

Figure 5.18. NS - Mean Air Temperature 26/01/06

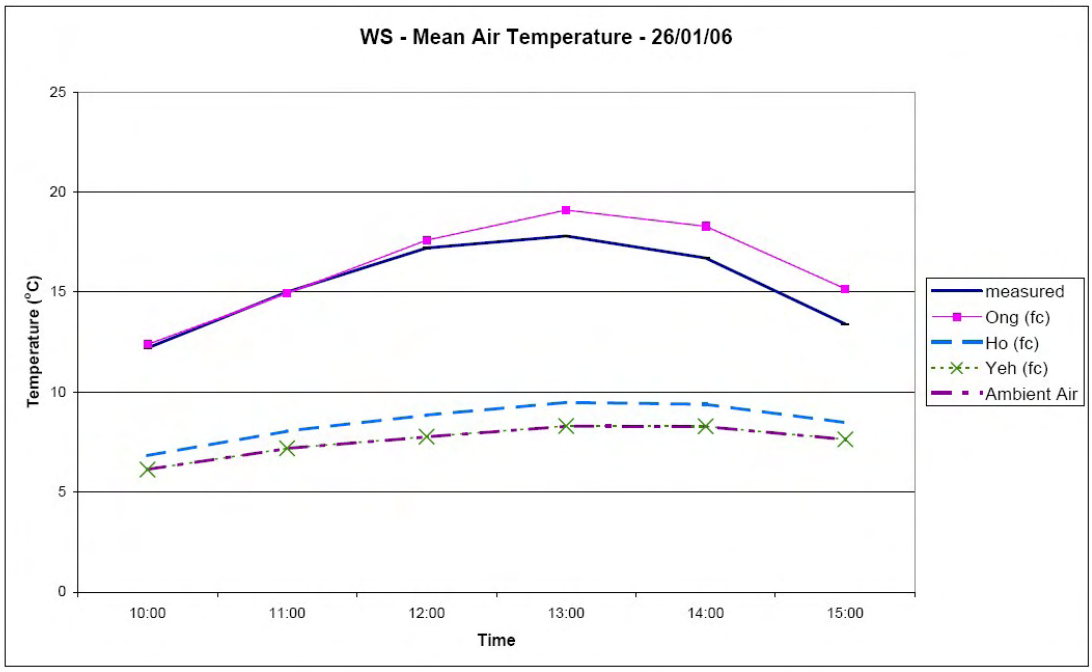

Figure 5.19. WS - Mean Air Temperature 26/01/06

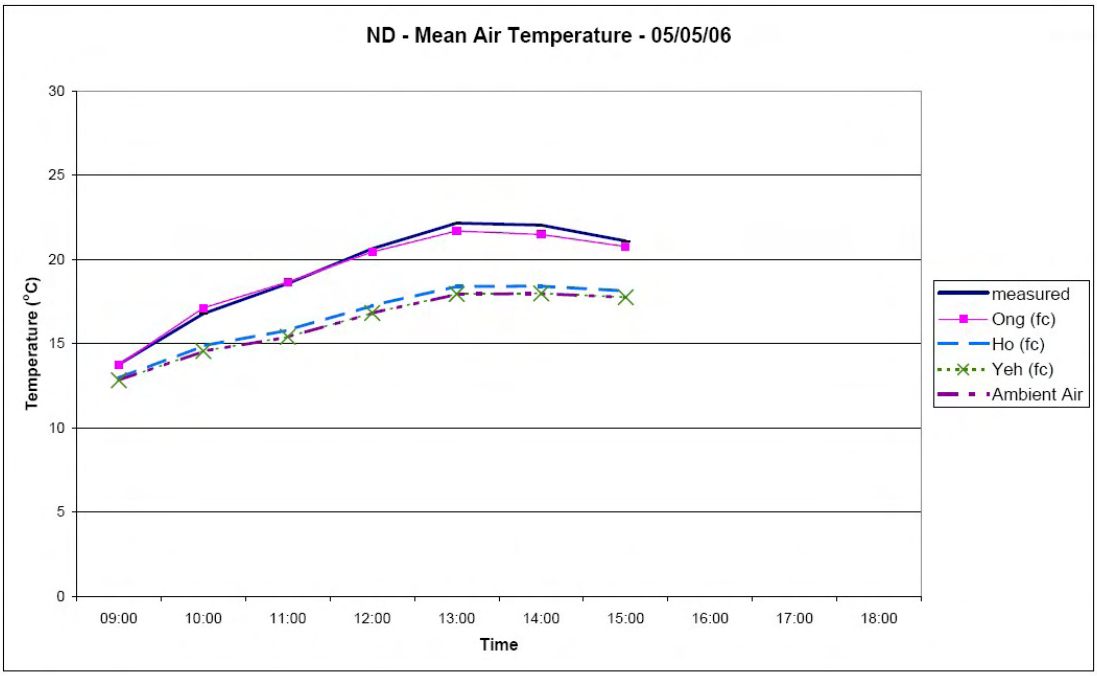

Figure 5.20. ND - Mean Air Temperature 05/05/06

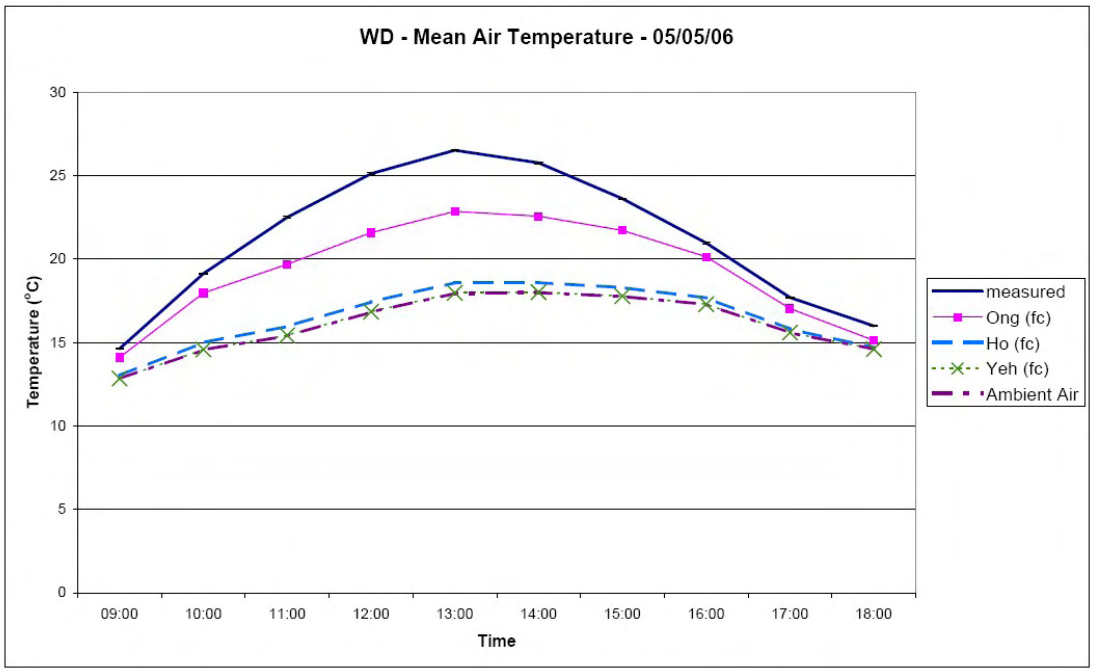

Figure 5.21. WD - Mean Air Temperature 05/05/06

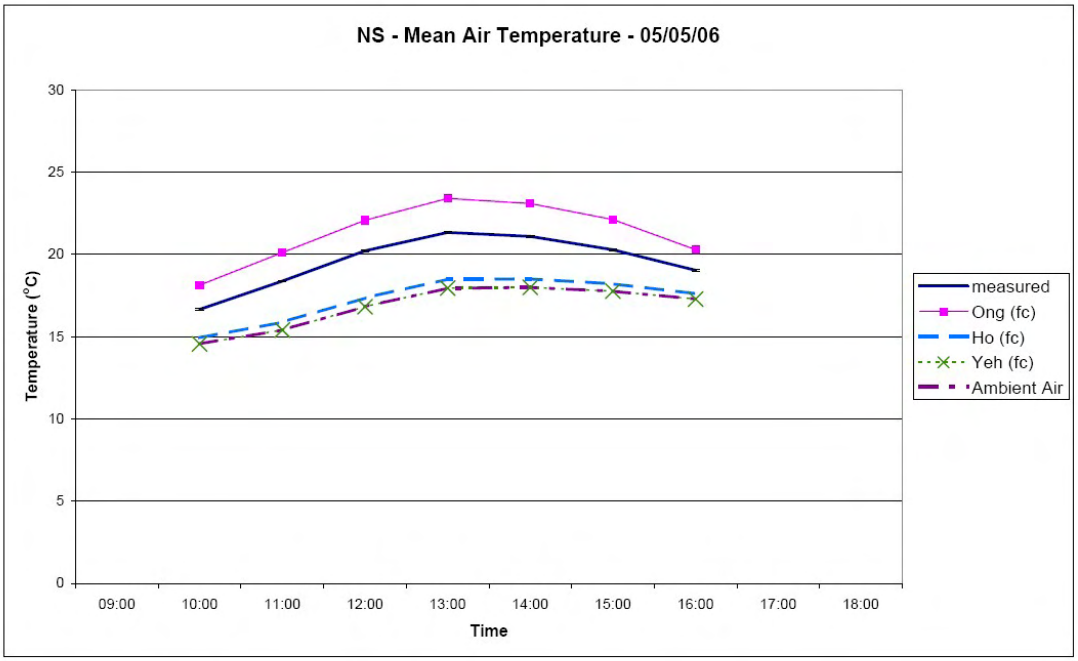

Figure 5.22. NS - Mean Air Temperature 05/05/06

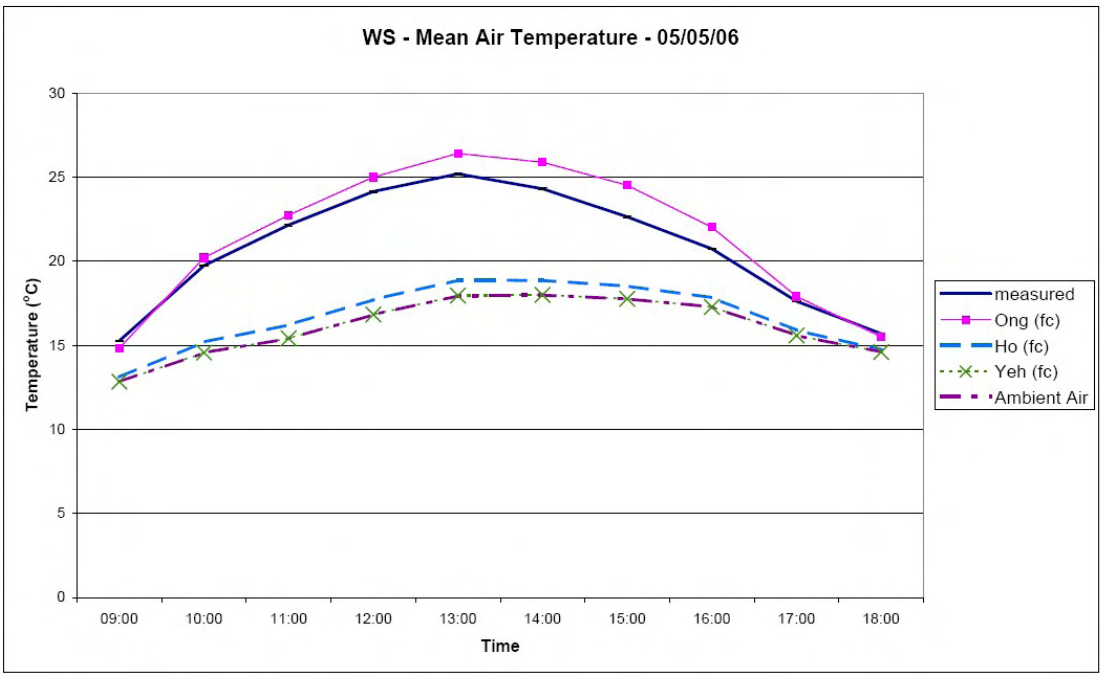

Figure 5.23. WS - Mean Air Temperature 05/05/06

Table 5.9 indicates the mean bias and RMSE for the two models for 26/01/06. Table 5.10 gives the same information for 05/05/06.

Table 5.9 Bias and RMSE for Prediction of Mean Air Temperature - 26/01/06

		Ong_{fc}	Yeh_{fc}	Ho_{fc}
Mean Bias (^{o}C)	ND	-2.5	-6.4	-5.9
	WD	-6.2	-11.3	-10.6
	NS	1.9	-3.7	-3.1
	WS	0.9	-7.8	-6.9
	All	-1.5	-7.3	-6.6
RMSE (^{o}C)	ND	2.6	6.5	6.0
	WD	6.4	11.5	10.8
	NS	2.0	3.7	3.2
	WS	1.1	8.0	7.0
	All	3.6	7.9	7.3

Table 5.10 Bias and RMSE for Prediction of Mean Air Temperature – 05/05/06

		Ong_{fc}	Yeh_{fc}	Ho_{fc}
Mean Bias (^oC)	ND	-0.2	-3.1	-2.7
	WD	-1.9	-5.1	-4.7
	NS	1.7	-2.7	-2.3
	WS	0.8	-4.7	-4.1
	All	0	-4.1	-3.6
RMSE (^oC)	ND	0.3	3.3	2.9
	WD	2.3	5.7	5.3
	NS	1.8	2.8	2.3
	WS	1.0	5.1	4.5
	All	1.7	4.9	4.3

From Table 5.9 it can be seen that the Ong_{fc} model doesn't have a definite bias, but that the Yeh_{fc} and Ho_{fc} models tend to underestimate the mean air temperature. The Ong_{fc} model has a lower RMSE than the other two models. A similar trend is observed in Table 5.10; however, all three models have a slightly lower RMSE for the summer day.

Figures 5.16 - 5.19 show that the Ho_{fc} and Yeh_{fc} generate similar results for all four ducts. Figures 5.20 - 5.23 show the same trend for 05/05/06. The mean air temperature predicted by the Yeh_{fc} model appears to be equivalent to the ambient air temperature. The mean air temperature predicted by the Ho_{fc} model appears to be much closer to the ambient temperature than the measured mean air temperature. For this reason, these models are not appropriate for predicting the exit air temperature. The Ong_{fc} model appears to be the closest predictor of the mean air temperature.

Although Tables 5.9 and 5.10 indicate that the Ong_{fc} model is the closest predictor of the mean air temperature, it still has a higher RMSE value than is acceptable for ducts ND and WD in January and WD for May.

5.1.4 Prediction of Exit Air Temperature

The following graphs show the correlation between the measured mean air temperature for ducts ND, WD, NS and WS and the predictions given by Ong_{fc}, Yeh_{fc} and Ho_{fc}. It should be noted that error bars have been included in the following graphs; however, the error is too small to show up in the graph. The errors in the measurement of the mean

air temperature are of the order of 0.03°C. In this instance a mean bias and RMSE of 2°C would be considered acceptable.

Figures 5.24 - 5.27 show the correlation for 26/01/06 and Figures 5.28 - 5.31 for 05/05/06.

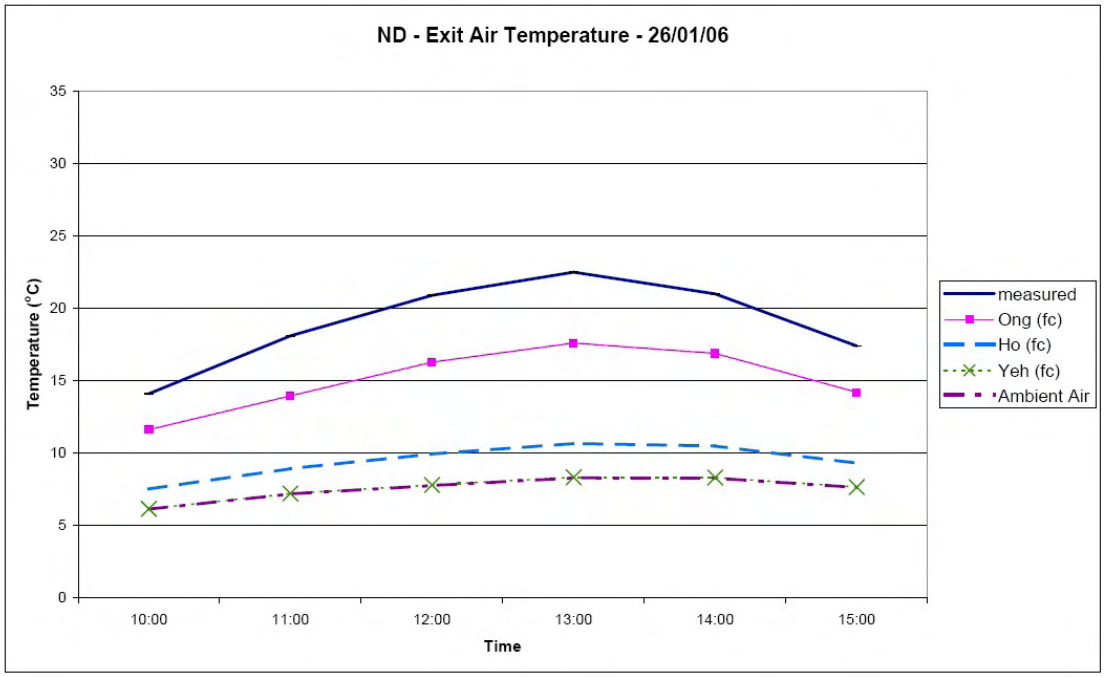

Figure 5.24. ND - Exit Air Temperature - 26/01/06

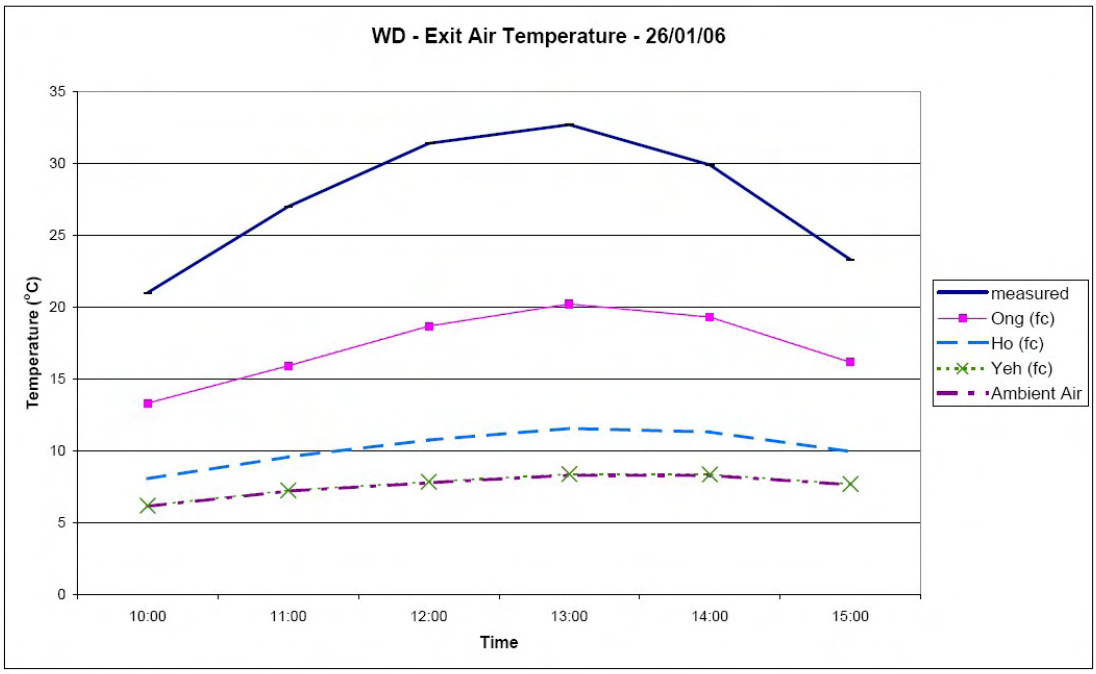

Figure 5.25. WD - Exit Air Temperature - 26/01/06

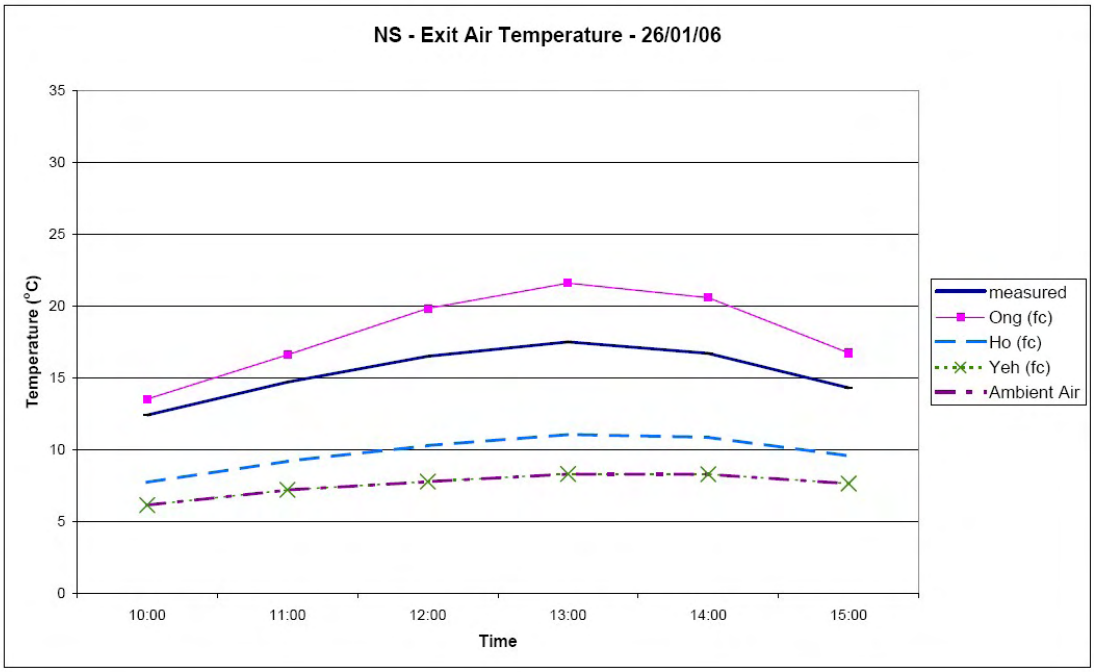

Figure 5.26. NS - Exit Air Temperature - 26/01/06

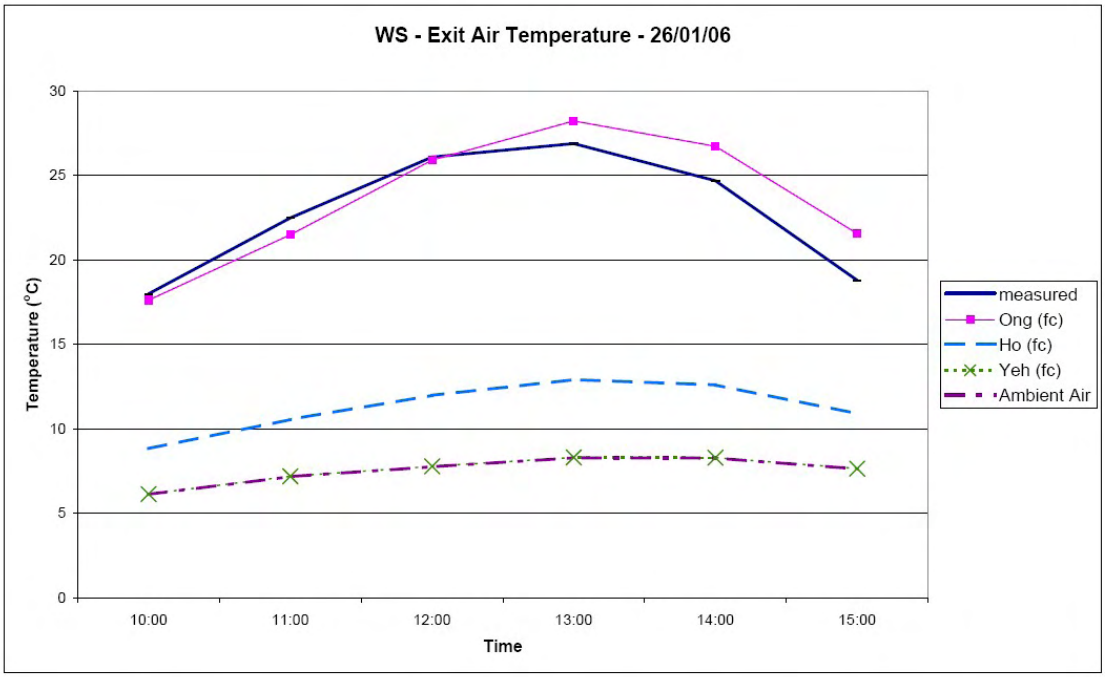

Figure 5.27. WS - Exit Air Temperature - 26/01/06

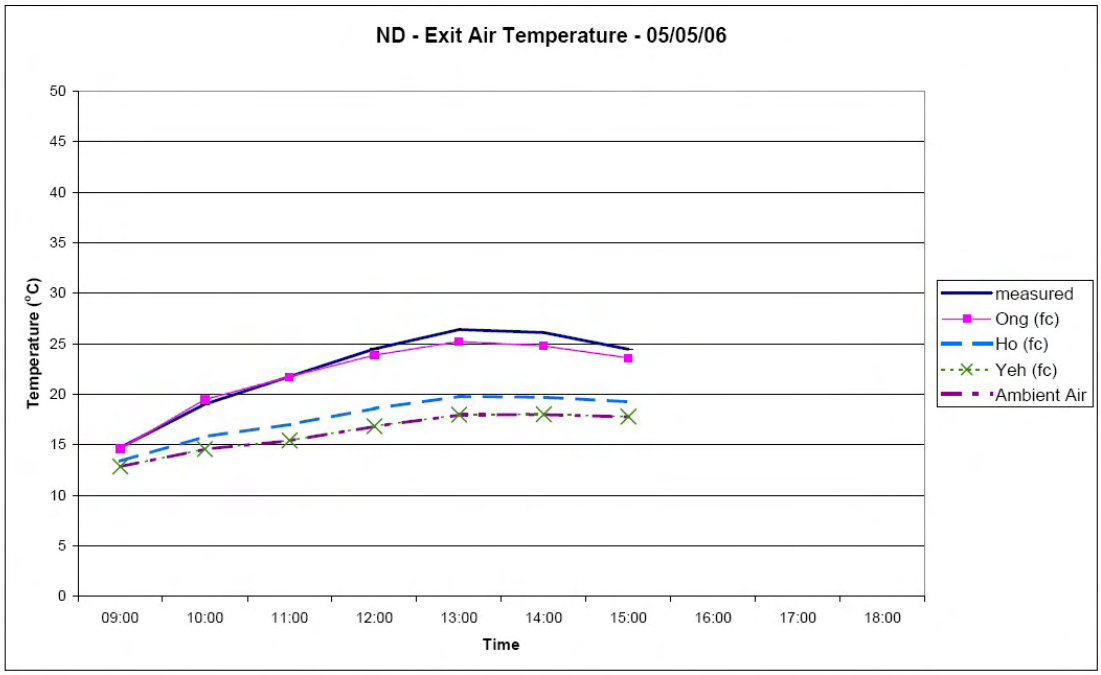

Figure 5.28. ND - Exit Air Temperature - 05/05/06

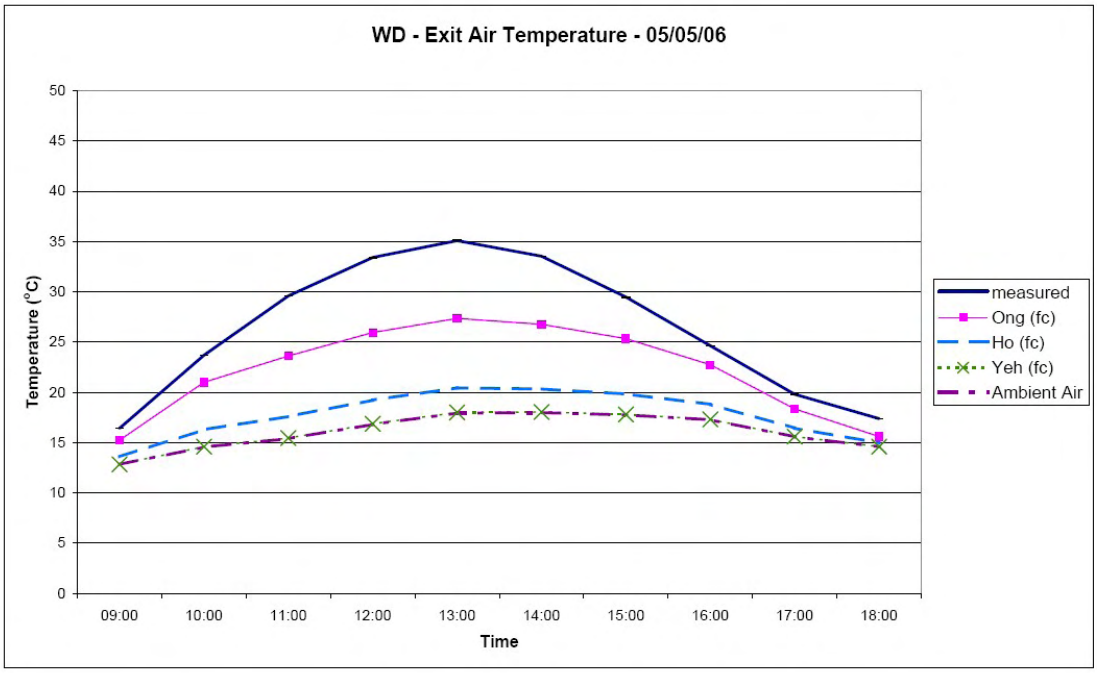

Figure 5.29. WD - Exit Air Temperature - 05/05/06

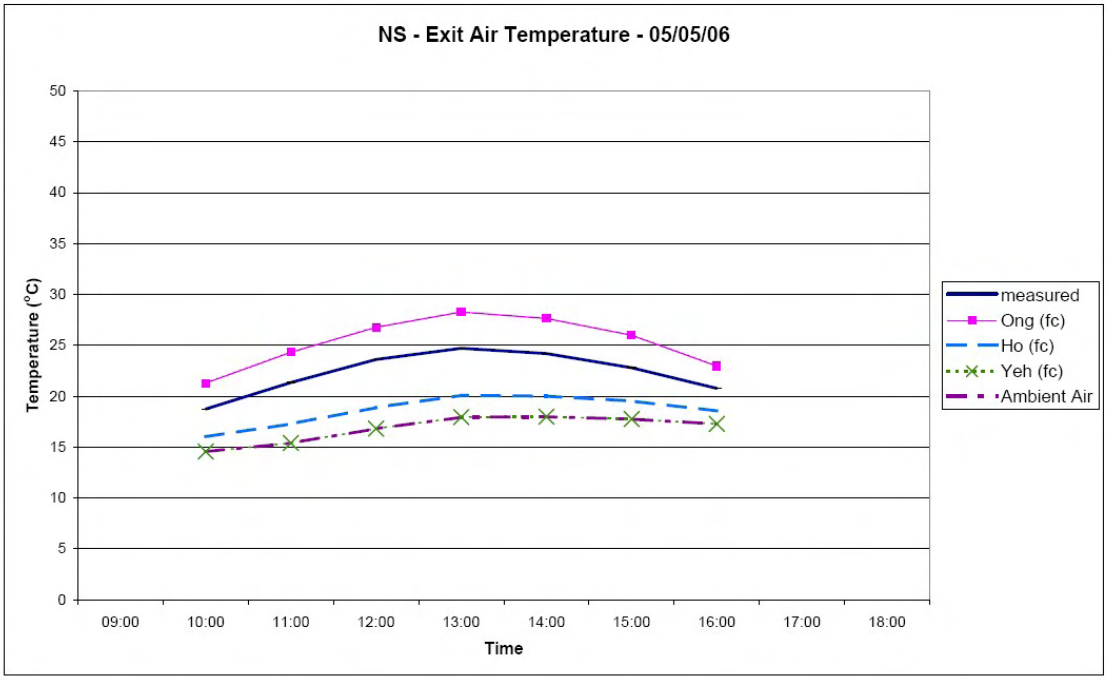

Figure 5.30. NS - Exit Air Temperature - 05/05/06

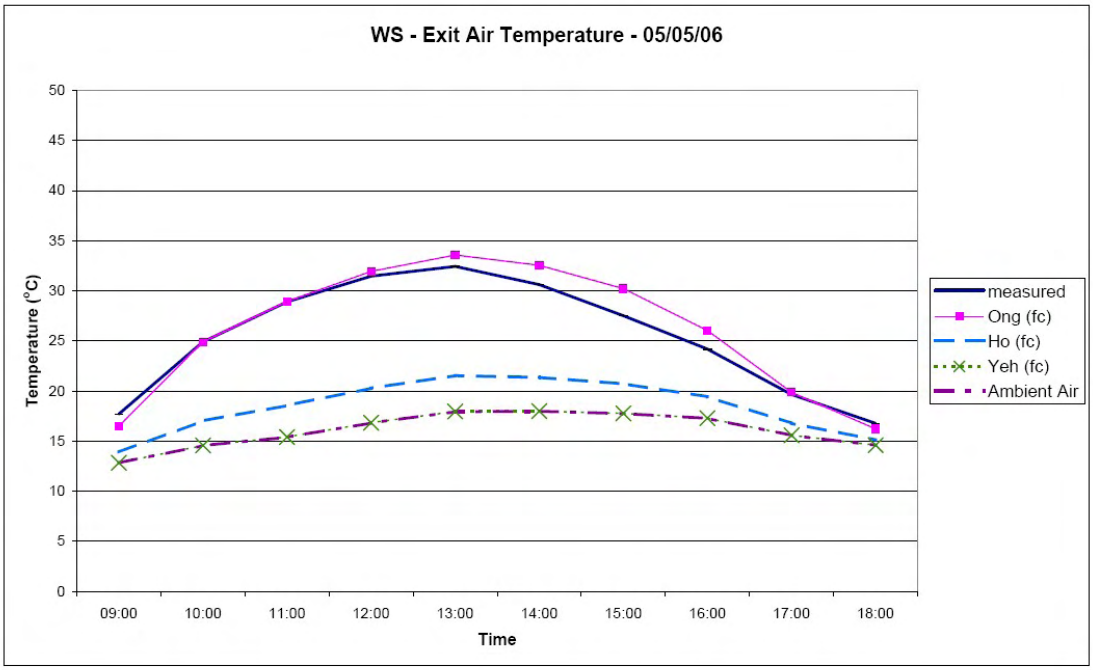

Figure 5.31. WS - Exit Air Temperature - 05/05/06

Table 5.11 indicates the mean bias and RMSE for the two models for 26/01/06. Table 5.12 gives the same information for 05/05/06.

Table 5.11 Bias and RMSE for Prediction of Exit Air Temperature - 26/01/06

		Ong_{fc}	Yeh_{fc}	Ho_{fc}
Mean Bias (^oC)	ND	-3.9	-11.4	-9.5
	WD	-10.3	-19.9	-17.4
	NS	2.8	-7.8	-5.6
	WS	0.8	-15.3	-11.5
	All	-2.7	-13.6	-11.0
RMSE (^oC)	ND	4.0	11.6	9.7
	WD	10.5	20.3	17.7
	NS	3.0	7.9	5.6
	WS	1.6	15.5	11.8
	All	5.9	14.6	12.0

Table 5.12 Bias and RMSE for Prediction of Exit Air Temperature – 05/05/06

		Ong_{fc}	Yeh_{fc}	Ho_{fc}
Mean Bias (^oC)	ND	-0.5	-6.2	-4.8
	WD	-4.1	-10.2	-8.6
	NS	3.0	-5.5	-3.7
	WS	0.7	-9.3	-6.9
	All	-0.5	-8.2	-6.3
RMSE (^oC)	ND	0.8	6.6	5.1
	WD	4.8	11.4	9.7
	NS	3.0	5.6	3.8
	WS	1.3	10.3	7.7
	All	3.2	9.7	7.7

From Table 5.11 it can be seen that the Ong_{fc} model has no consistent bias; however, the Yeh_{fc} and Ho_{fc} models tend to underestimate the exit air temperature. The Ong_{fc} model has a significantly lower RMSE compared to the other two models. A similar trend is observed in Table 5.12; however, all three models have a lower RMSE for the summer day.

Figures 5.24 - 5.27 show that Ho_{fc} and Yeh_{fc} generate similar results for all four ducts. Figures 5.28 - 5.31 show the same trend for 05/05/06. The exit air temperature predicted Yeh_{fc} appears to be equivalent to the ambient air temperature. The exit air temperature predicted by Ho_{fc} appears to be much closer to the ambient temperature than the measured exit air temperature. For this reason, these models are not appropriate for predicting the exit air temperature. The Ong_{fc} model appears to be the closest predictor of the air exit temperature.

Although Tables 5.11 and 5.12 indicate that the Ong_{fc} model is the closest predictor of the air exit temperature, it still has a higher RMSE value than is acceptable for ducts ND, WD and NS in January, and ducts WD and NS in May.

5.1.5 Prediction of Power Output

The following graphs show the correlation between the calculated power output for ducts ND, WD, NS and WS and the predictions given by Ong_{fc}, Yeh_{fc} and Ho_{fc}. The power output for a single duct is calculated using:

$$Q = \dot{m} c_p \Delta T \qquad \text{C40}$$

Where ΔT refers to the difference between the air inlet and air exit temperatures.

The error bars in the graphs represent the errors inherent in the measurements which are used to calculate the power output, these errors are in the order of 1.5 W. In this instance a mean bias and RMSE of 5W would be considered acceptable.

Figures 5.32 - 5.35 show the correlation for 26/01/06 and Figures 5.36 - 5.39 for 05/05/06.

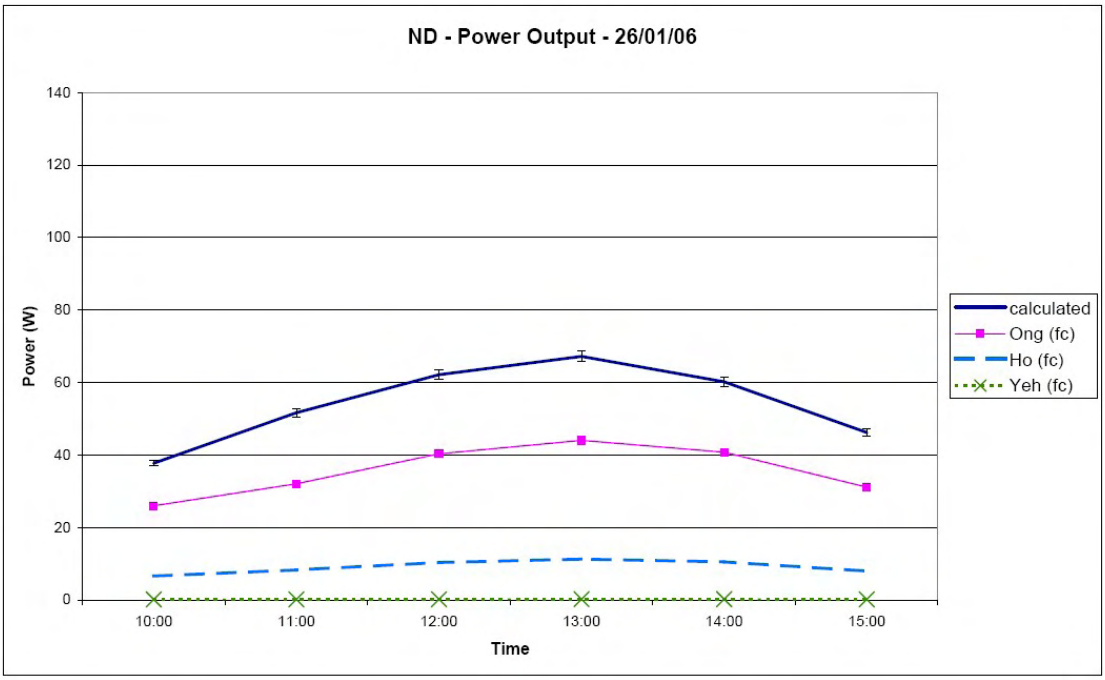

Figure 5.32. ND - Power Output - 26/01/06

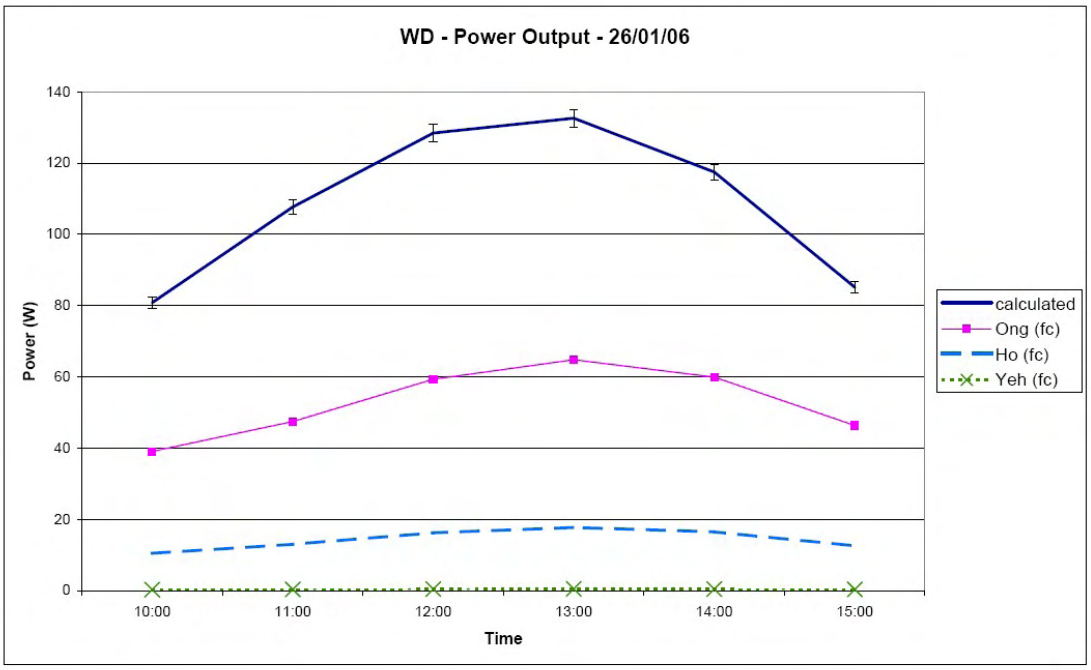

Figure 5.33. WD - Power Output - 26/01/06

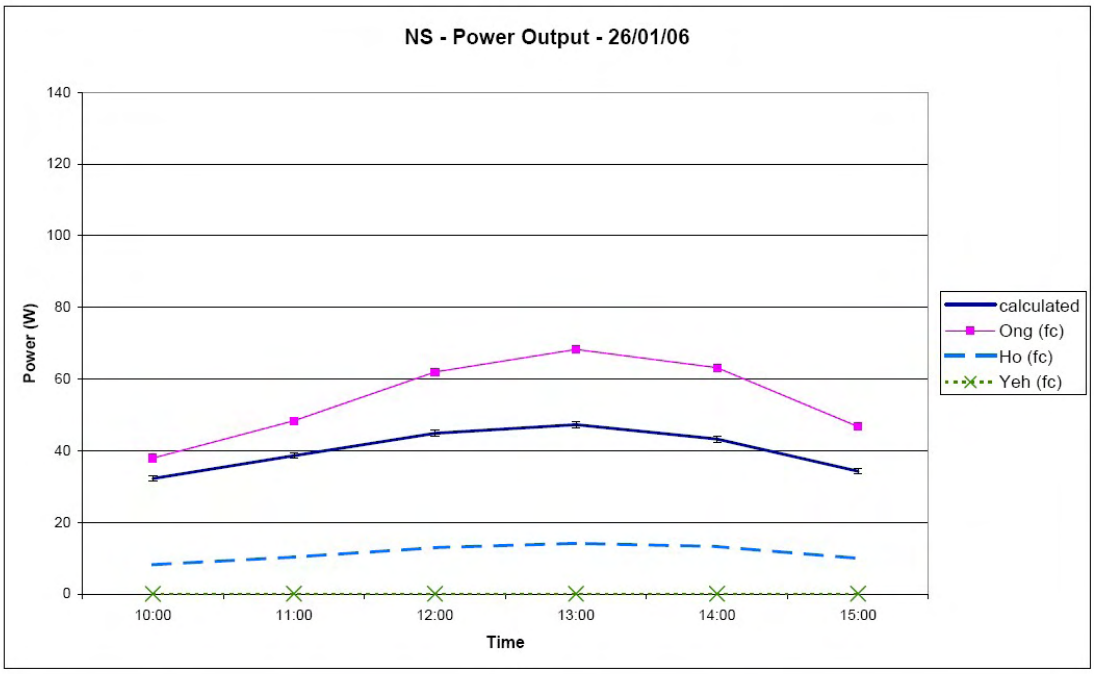

Figure 5.34. NS - Power Output - 26/01/06

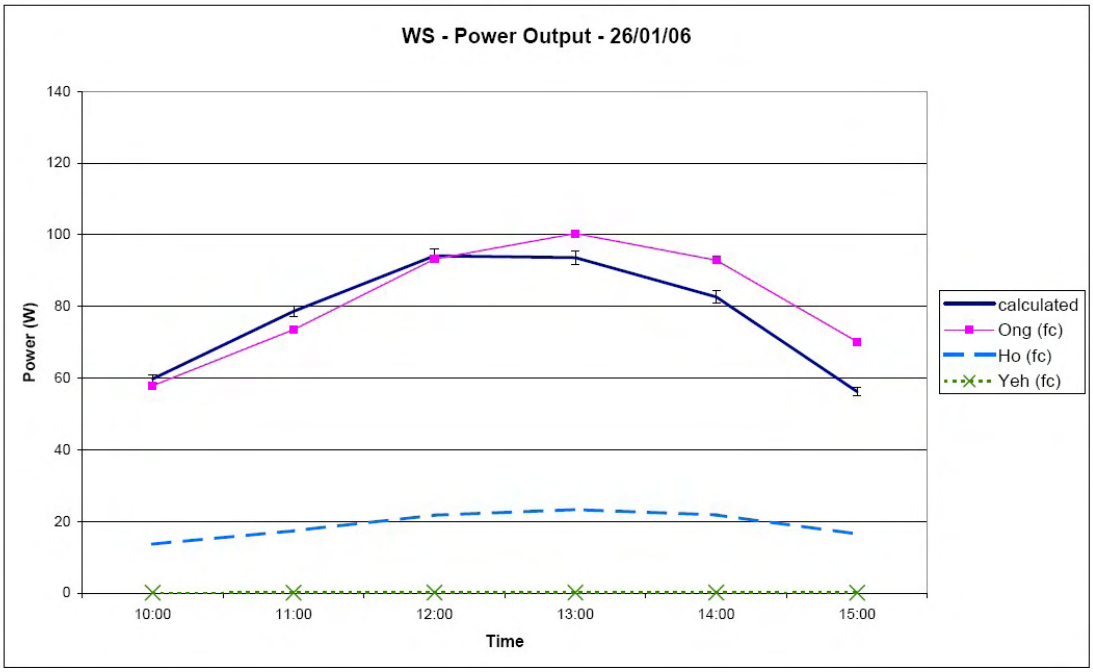

Figure 5.35. WS - Power Output - 26/01/06

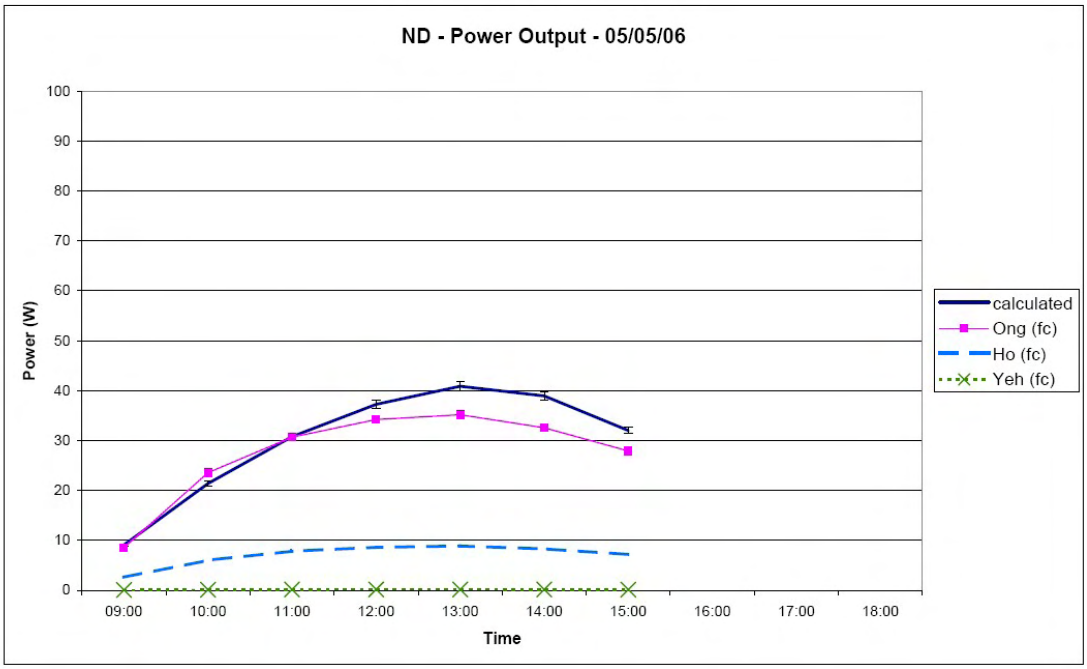

Figure 5.36. ND - Power Output - 05/05/06

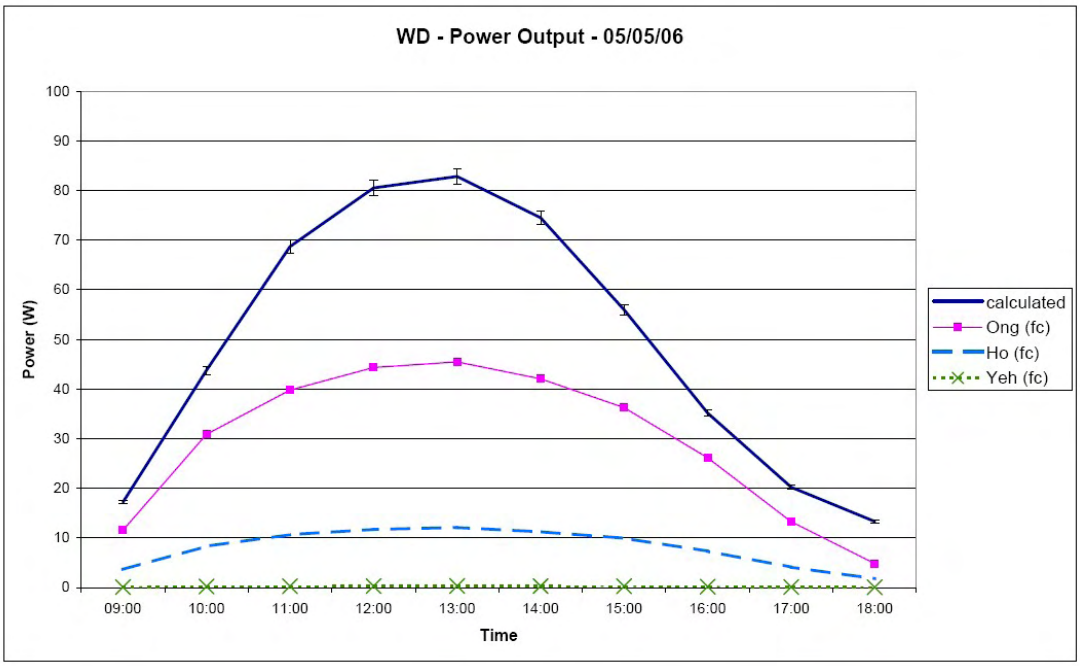

Figure 5.37. WD - Power Output - 05/05/06

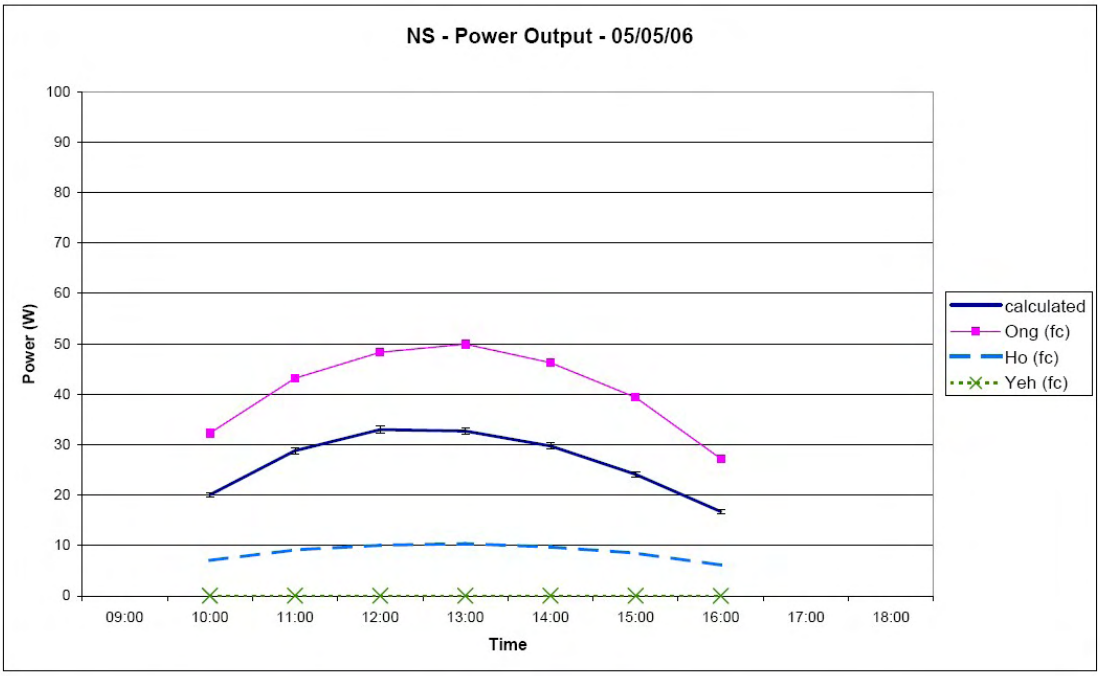

Figure 5.38. NS - Power Output - 05/05/06

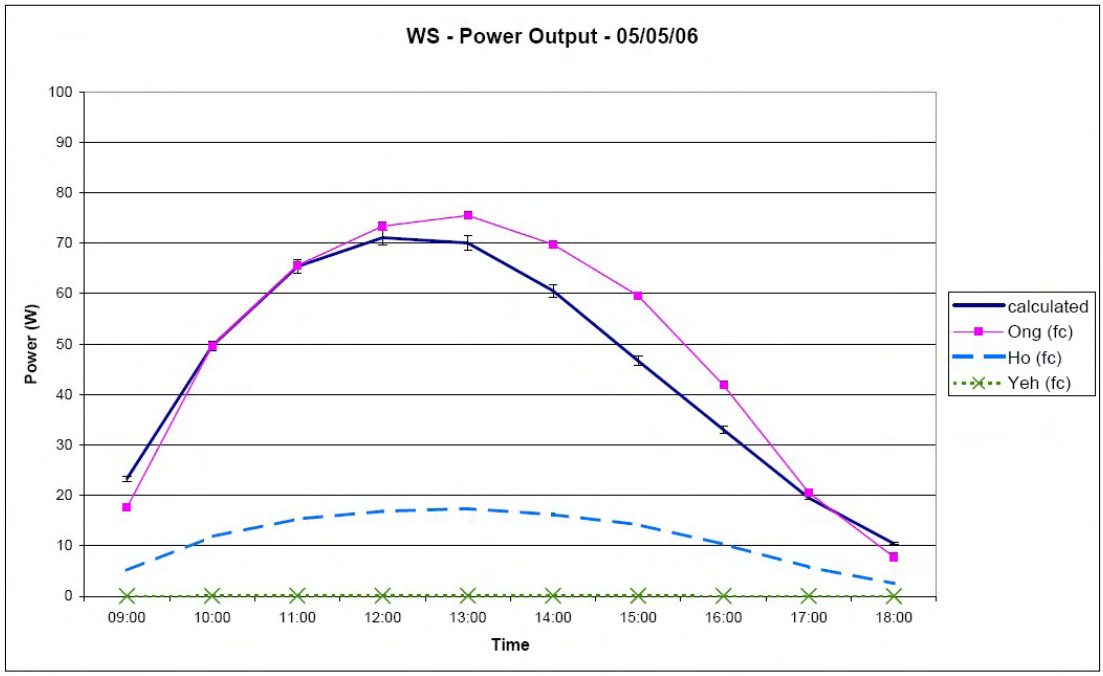

Figure 5.39. WS - Power Output - 05/05/06

Table 5.13 indicates the mean bias and RMSE for the two models for 26/01/06. Table 5.14 gives the same information for 05/05/06.

Table 5.13 Bias and RMSE for Prediction of Power Output - 26/01/06

		Ong_{fc}	Yeh_{fc}	Ho_{fc}
Mean Bias (W)	ND	-18.5	-54.0	-45.0
	WD	-55.9	-108.3	-94.3
	NS	14.3	-40.0	-28.6
	WS	3.8	-77.3	-58.4
	All	-14.1	-69.9	-56.6
RMSE (W)	ND	18.9	54.9	45.8
	WD	57.1	110.1	95.9
	NS	15.3	40.4	28.8
	WS	7.9	78.8	59.6
	All	31.3	75.8	62.6

Table 5.14 Bias and RMSE for Prediction of Power Output – 05/05/06

		Ong_{fc}	Yeh_{fc}	Ho_{fc}
Mean Bias (W)	ND	-2.5	-29.9	-23.0
	WD	-19.8	-49.0	-41.1
	NS	14.5	-26.4	-17.7
	WS	3.2	-44.9	-33.4
	All	-2.4	-39.2	-30.3
RMSE (W)	ND	3.9	31.7	24.5
	WD	23.2	55.3	46.7
	NS	14.7	27.0	18.3
	WS	6.4	49.6	37.1
	All	15.6	46.8	37.1

From Table 5.13 it can be seen that the Ong_{fc} model has no consistent bias, but that the Yeh_{fc} and Ho_{fc} models tend to underestimate the power output. The Ong_{fc} model has a much lower RMSE than the other two models. A similar trend for the bias is observed in Table 5.14; however all three models have a lower RMSE for the summer day.

Figures 5.32 - 5.39 show that the Yeh_{fc} model predicts a power output of zero, this is because it underestimates the air exit temperatures. Of the three models, the Ong_{fc} model is the most satisfactory; however, it still has a high RMSE.

5.1.6 Discussion

No one model shows a significant advantage over the others in predicting all five parameters being considered. However, some models are better at predicting certain parameters, e.g.:

- The glazing temperature is best predicted by the Ong_{fc} model
- The absorbing surface temperature is best predicted by the Yeh_{fc} model
- The mean air temperature is best predicted by the Ong_{fc} model
- The exit air temperature is best predicted by the Ong_{fc} model
- The power output is best predicted by the Ong_{fc} model

The Ong_{fc} model appears to be the best model since it is the best predictor for the majority of parameters. However, it would be beneficial if the models could be improved more generally.

5.1.6.1 Improvements to design models

Various parameters within the three models assessed in Section 5.1 and the model developed in Chapter 4 were compared to identify the best practice. Where possible the best practice was incorporated in each of the design models under consideration.

The alterations are described below:

1. The Ong_{fc} model uses hydraulic diameter for parallel plate ducts. The prototype ducts used in this project cannot be simply considered as parallel plates, therefore the hydraulic diameter as applied to rectangular ducts should be used instead.
2. Swinbank's correlation for the sky temperature (which is used in Ong_{fc}) can be replaced with the HTB2 algorithm, which is more sophisticated and takes account of the vertical orientation of the solar air heaters. This can also be introduced to Ho_{fcad}, allowing the calculation of the radiative heat transfer coefficient between the glass and the sky to be altered. This can now be calculated using the glass, sky and ambient temperatures.
3. Ong's use of formulae to calculate the temperature dependent air dynamic viscosity, air thermal conductivity and air specific heat capacity can be extended to the other models. Ong revised his formulae to calculate these parameters in his 2003 paper [3] – these revised formulae can be applied to all three models.
4. The definition of the Nusselt number used by Ong is suitable for use in the entry length of ducts where the ratio of length to hydraulic diameter (L/D_h) is less than 60. The prototype ducts were designed to replicate entry length conditions (see Table 5.15 for L/D_h) since heat transfer is expected to be greater in this area. Therefore the Nusselt number used by Ong is more appropriate, and should be applied to all three models.

Table 5.15 Ratio of L/D_h for Experimental Ducts

	ND	WD	NS	WS
L/Dh	22.7	16.6	41.5	35.3

5. None of the models currently consider the effects of angle of incidence or the behaviour of direct and diffuse components of solar irradiation. Similarly the second opportunity for absorption of solar irradiation due to reflection within the duct should be included. Due to the structure of the Yeh_{fc} model, it is not possible to include the effect of incident angle on the transmission and reflection of solar irradiation.

5.1.7 Modified Predictive Models for Forced Convection

The modified models are described in detail in Appendix H. The key parameters within the modified models are summarised in Table 5.16. The alterations are highlighted in bold text. The revised design models are referred to as: Ong_{fcad}, Yeh_{fcad} and Ho_{fcad} to differentiate them from their original formats.

Table 5.16 Comparison of Models Ong_{fcad}, Yeh_{fcad} and Ho_{fcad}

Parameter	Ong_{fcad}	Yeh_{fcad}	Ho_{fcad}
Considers the air heater	In sections	In entirety	In entirety
Hydraulic diameter (D_h)	**Non circular duct (B1)** substituted for Parallel plates (B4)	Non circular duct (B1)	Non circular duct (B1)
Sky temperature (T_{sky})	**HTB2 algorithm (4.13-4.17)** substituted for Swinbank's correlation (C31)	Not Used	**HTB2 algorithm (4.13-4.17) used**
Wind convection heat transfer (h_w)	McAdam's correlation (C20)	Adjusted McAdam's correlation (C23)	McAdam's correlation (C20)
Dynamic viscosity of air (μ)	Temperature dependent (H1)	**Temperature dependent (H1)** substituted for Constant	Not Used
Kinematic viscosity of air (ν)	Not Used	Not Used	Constant
Specific heat capacity of air (c_p)	Temperature dependent (H2)	**Temperature dependent (H2)** substituted for Constant	**Temperature dependent (H2)** substituted for Constant
Thermal conductivity of air (k)	Temperature dependent (H3)	**Temperature dependent (H3)** substituted for Constant**)**	**Temperature dependent (H3)** substituted for Constant
Nusselt number	Nusselt's correlation (C5)	**Nusselt's correlation (C5)** substituted for Kay's correlation (C12)	**Nusselt's correlation (C5)** substituted for Kay's correlation (C12)
Radiative heat transfer coefficient between parallel plates	Incorporating glass and solar absorber temperatures with glass and solar absorber emissivity (C28)	Incorporating fluid temperature with glass and solar absorber emissivity (C29)	Incorporating glass and solar absorber temperatures with glass and solar absorber emissivity (C28)
Radiative heat transfer coefficient between glass and sky	Incorporating glass, sky and ambient temperatures along with the emissivity of glass (C30)	Not Used	**Incorporating glass, sky and ambient temperatures along with the emissivity of glass (C30)** substituted for C33

Table 5.16 Cont'd Comparison of Models Ong_{fc}, Yeh_{fc} and Ho_{fc}

Parameter	Ong_{fc}	Yeh_{fc}	Ho_{fc}
Overall top heat loss coefficient	Sum of wind and radiative heat transfer coefficients (H4)	Incorporating the solar absorber and ambient temperatures, the wind coefficient and the emissivity of the solar absorber surface (A19)	Unspecified – definition from BS EN ISO 12241 [1] used
Heat loss coefficient including sides	No	No	Yes
Overall bottom heat loss coefficient	Incorporating conductive and wind convective components (H5)	Ratio of thermal conductivity and thickness of insulation (H7)	Unspecified – definition from BS EN ISO 12241 [1] used
Considers heat gain from glass and absorbing surface separately	Yes	No	No
Considers direct and diffuse components of solar irradiation, and angle of incidence.	**Yes**	No	**Yes**
Considers heat transfer for sides	No	No	Yes
Solution procedure	Iterative solution of matrix equation	Iterative solution of a series of equations defining the mean fluid and solar absorber surface temperatures	Iterative solution of a series of equations defining the mean fluid, exit fluid, outer glass surface, inner glass surface, solar absorber surface and rear surface temperatures

Table 5.16 Cont'd Comparison of Models Ong_{fc}, Yeh_{fc} and Ho_{fc}

Parameter	Ong_{fc}	Yeh_{fc}	Ho_{fc}
Solution procedure	Iterative solution of matrix equation.	Iterative solution of a series of equations.	Iterative solution of a series of equations.
	The meteorological data and physical properties of the materials used in the experiment (e.g. emissivity, absorptivity, etc) were applied to the model.		**Further reference to properties of the materials used in the experiment (e.g. absorptivity, etc) were applied to the model.**
Parameters Calculated Directly	The mean glass, mean absorber and mean duct air temperature are calculated directly from the model.	The mean absorber and mean duct air temperature are calculated directly from the model.	The mean outer glass, mean inner glass, mean absorber, mean outer, mean duct air and exit air temperature are calculated directly from the model.
Parameters Calculated Indirectly	The air exit temperature is calculated, assuming a linear temperature gradient. The power output is calculated from the air mass flow and the calculated air exit temperature.		The power output is calculated from the air mass flow and the calculated air exit temperature.

5.1.7.1 Prediction of Mean Glazing Temperature

The following graphs show the correlation between the measured mean glazing temperature for ducts ND, WD, NS and WS and the predictions given by Ong_{fcad} and Ho_{fcad}.

Figures 5.40 - 5.42 show the correlation for 26/01/06 and Figures 5.43 - 5.46 for 05/05/06.

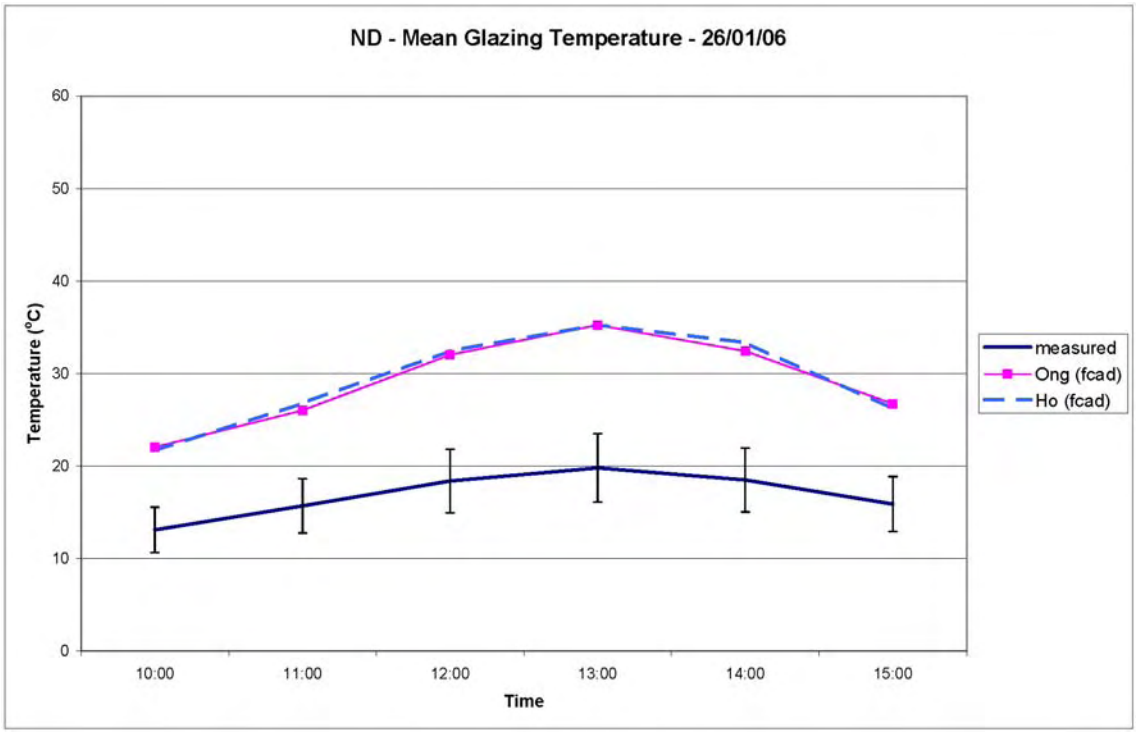

Figure 5.40. ND - Mean Glazing Temperature (Adapted Models) - 26/01/06

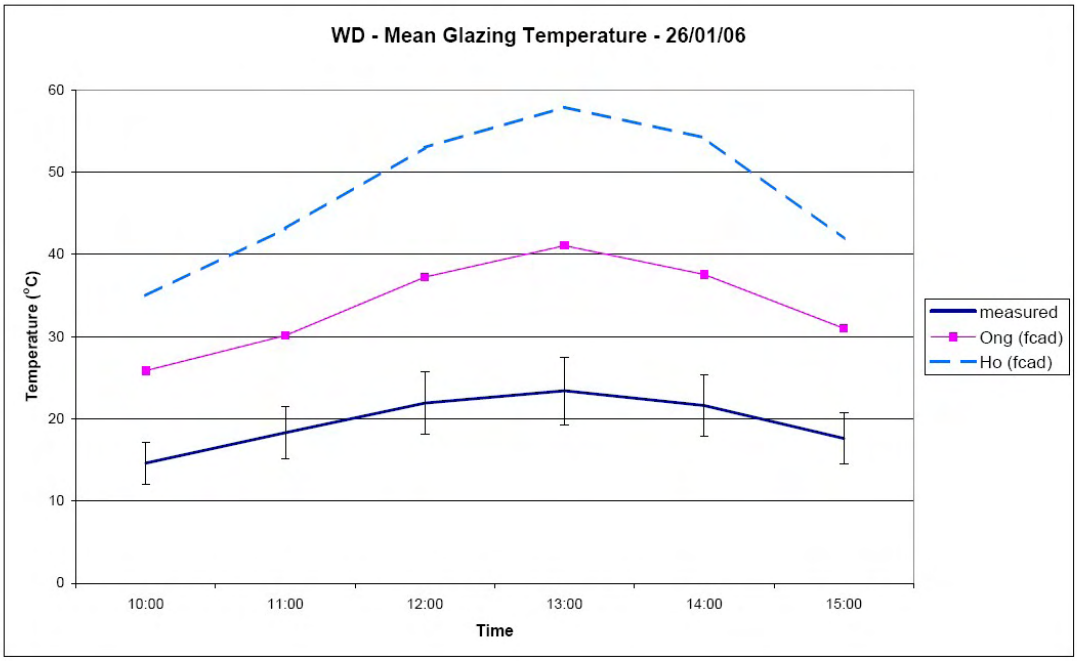

Figure 5.41. WD - Mean Glazing Temperature (Adapted Models) - 26/01/06

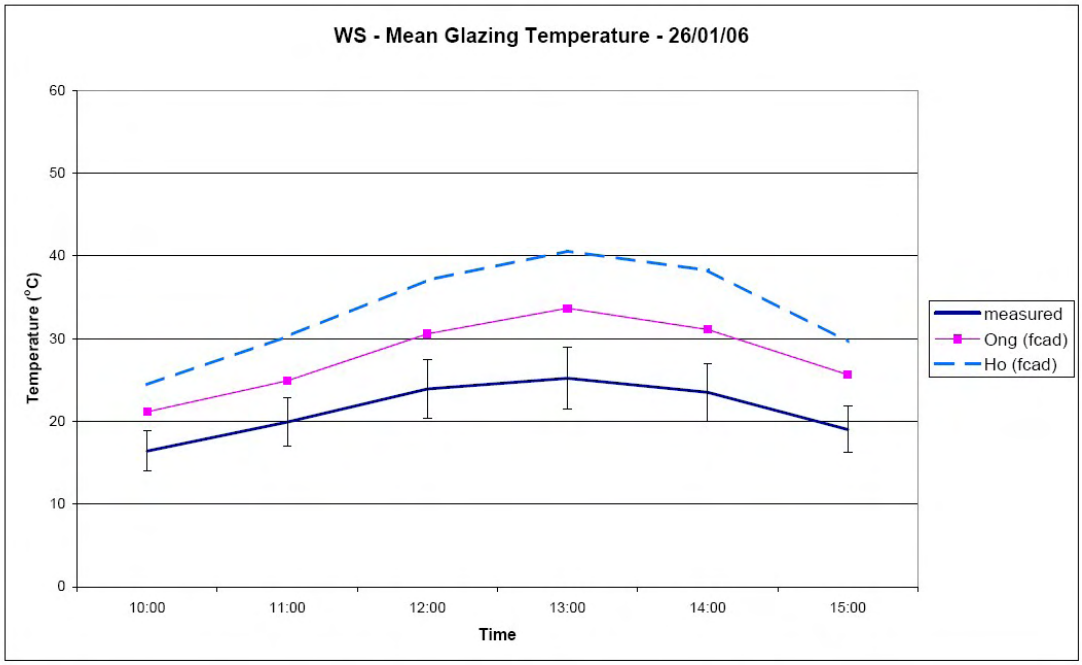

Figure 5.42. WS - Mean Glazing Temperature (Adapted Models) - 26/01/06

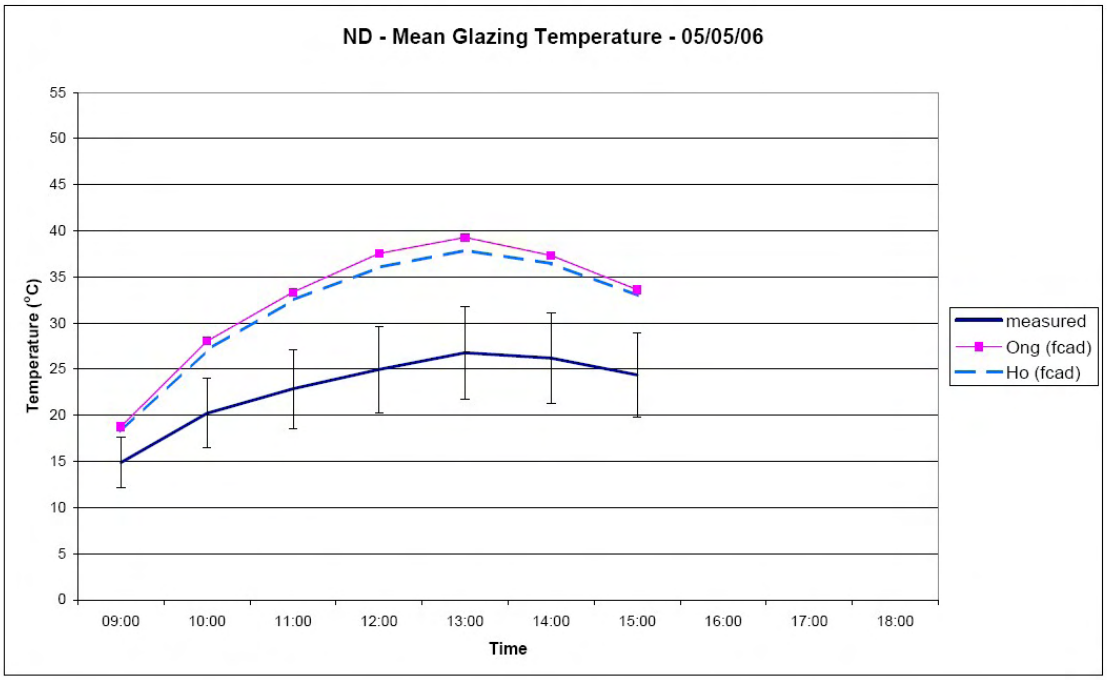

Figure 5.43. ND - Mean Glazing Temperature (Adapted Models) - 05/05/06

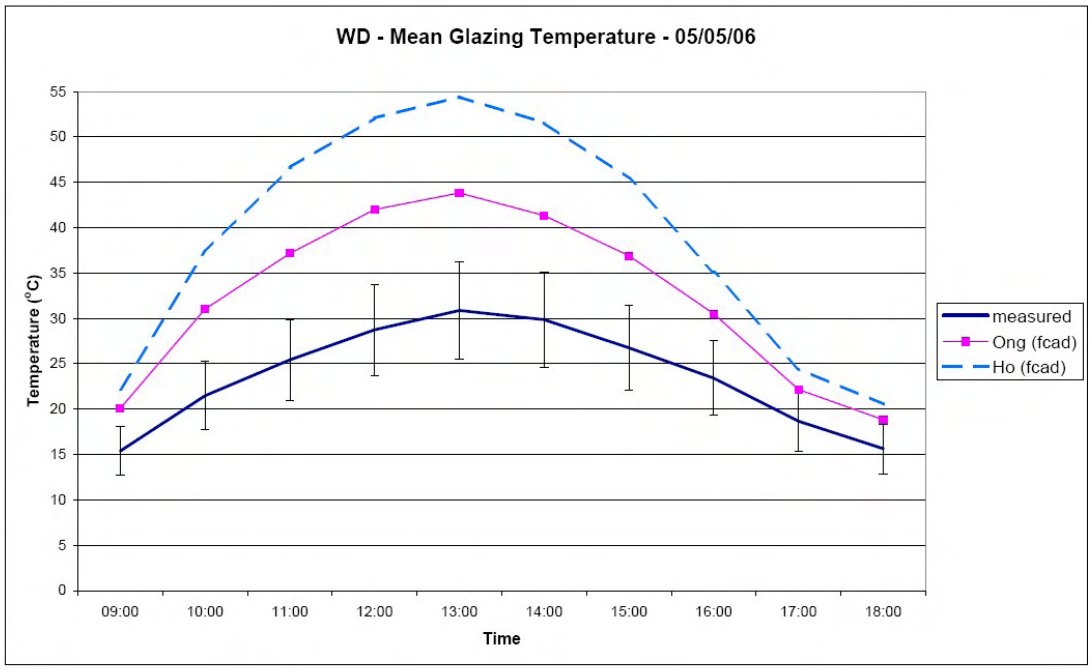

Figure 5.44. WD - Mean Glazing Temperature (Adapted Models) - 05/05/06

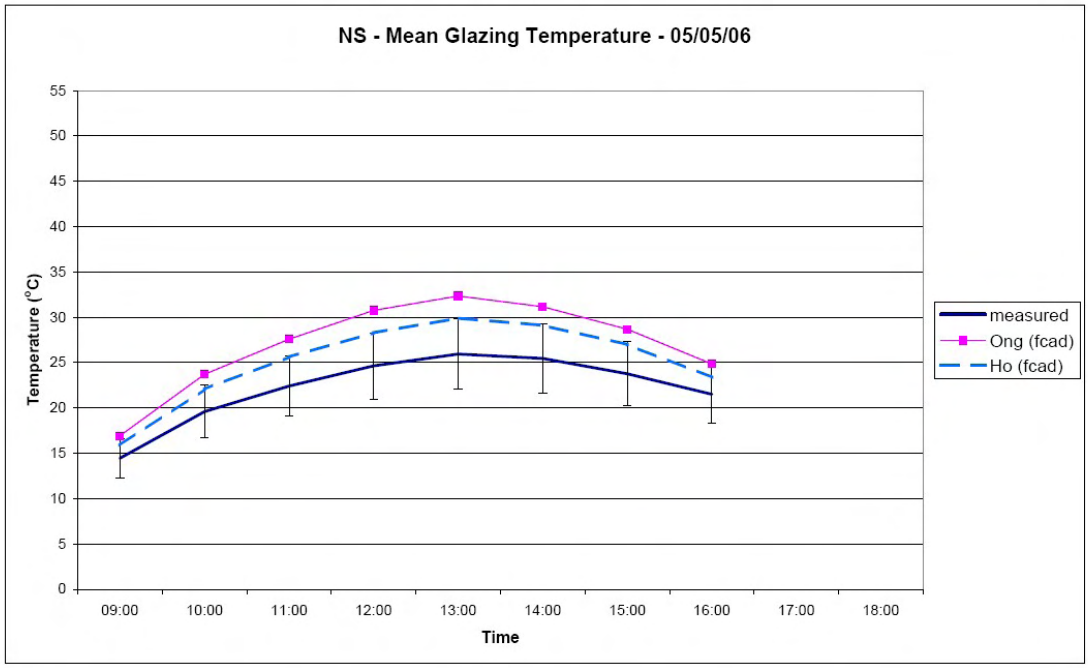

Figure 5.45. NS - Mean Glazing Temperature (Adapted Models) - 05/05/06

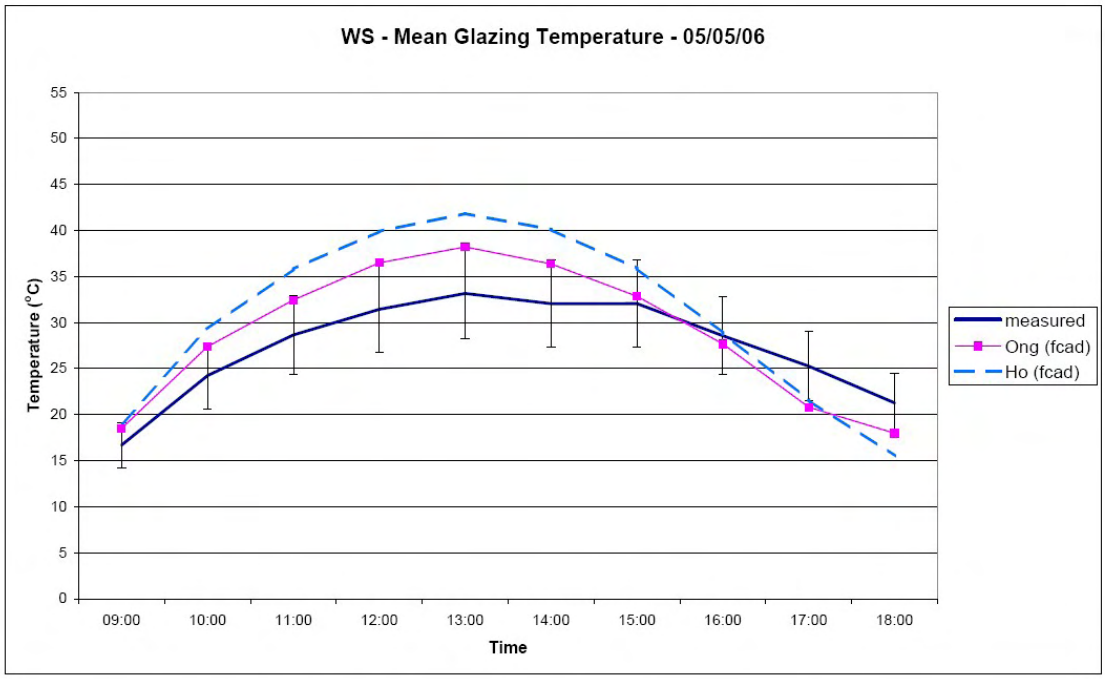

Figure 5.46. WS - Mean Glazing Temperature (Adapted Models) - 05/05/06

Table 5.17 indicates the mean bias and RMSE for the two models for 26/01/06. Table 5.18 gives the same information for 05/05/06.

Table 5.17 Bias and RMSE for Prediction of Mean Glazing Temperature 26/01/06

		Ong_{fcad}	Ho_{fcad}
Mean Bias (^oC)	ND	12.2	12.3
	WD	14.2	27.9
	NS	No data available for comparison	
	WS	6.5	12.0
	All	11.0	17.5
RMSE (^oC)	ND	12.4	12.7
	WD	14.4	28.4
	NS	No data available for comparison	
	WS	6.6	12.3
	All	10.1	16.7

Table 5.18 Bias and RMSE for Prediction of Mean Glazing Temperature 05/05/06

		Ong_{fcad}	Ho_{fcad}
Mean Bias (^oC)	ND	9.7	8.7
	WD	8.8	15.3
	NS	4.8	2.9
	WS	1.5	3.4
	All	6.0	7.8
RMSE (^oC)	ND	10.1	9.1
	WD	9.5	16.9
	NS	5.0	3.1
	WS	3.6	6.0
	All	7.8	11.1

From Table 5.17 it can be seen that both models tend to overestimate the glazing temperature. The Ong_{fcad} model has the lower bias and RMSE, and such could be regarded as the more accurate of the two models. Similar trends are observed in Table 5.18 for 05/05/06.

The prediction of the mean glazing temperature is poor in comparison to the original models illustrated in Figures 5.1 - 5.7. Both the mean bias and the RMSE of both models increased after alteration. The closest predictor of the four models is still the Ong_{fc} model; however, this does not meet the required accuracy (mean bias and RMSE $\leq 3^oC$).

5.1.7.2 Prediction of Mean Absorbing Surface Temperature

The following graphs show the correlation between the measured mean absorbing surface temperature for ducts ND, WD, NS and WS and the predictions given by Ong_{fcad}, Yeh_{fcad} and Ho_{fcad}.

Figures 5.47 - 5.50 show the correlation for 26/01/06 and Figures 5.51 - 5.54 for 05/05/06.

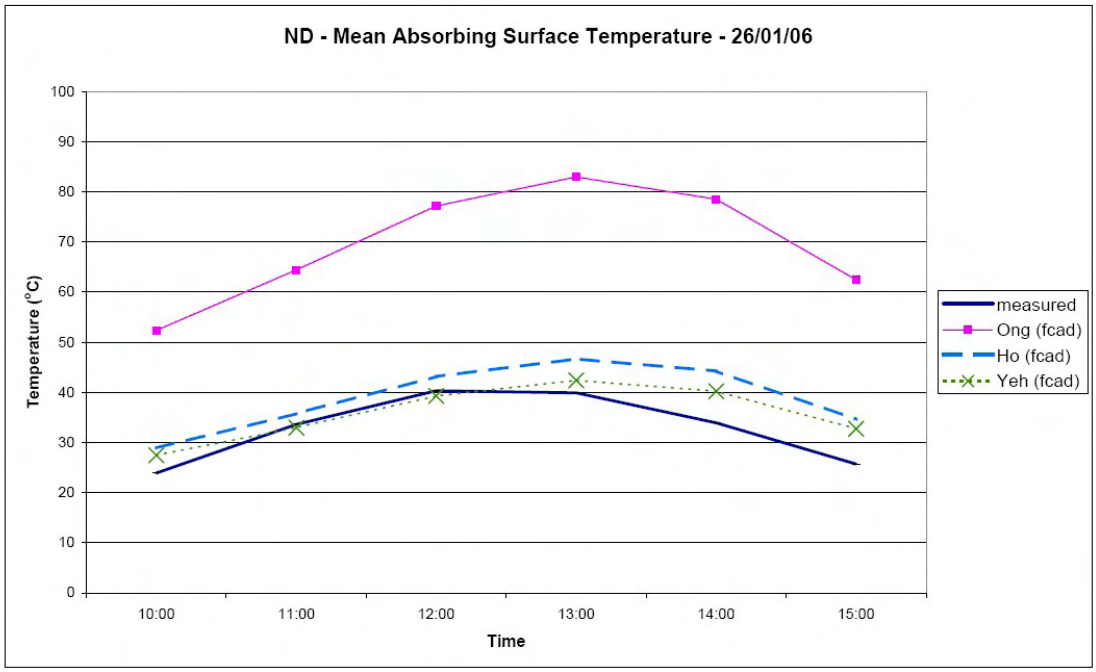

Figure 5.47. ND - Mean Absorbing Surface Temperature (Adapted Models) - 26/01/06

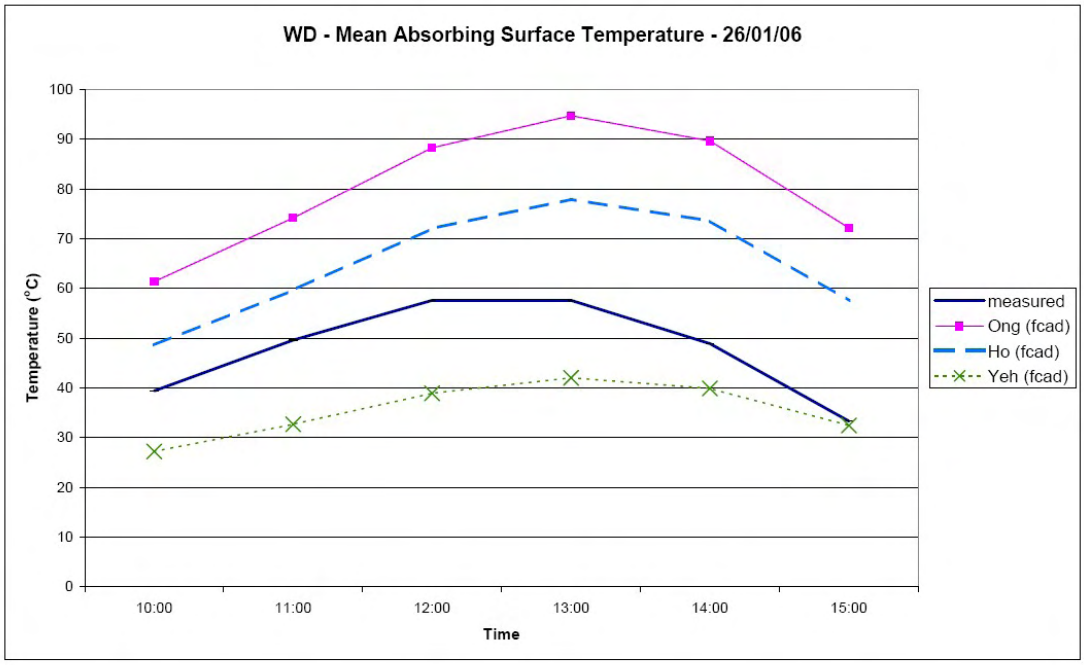

Figure 5.48. WD - Mean Absorbing Surface Temperature (Adapted Models) - 26/01/06

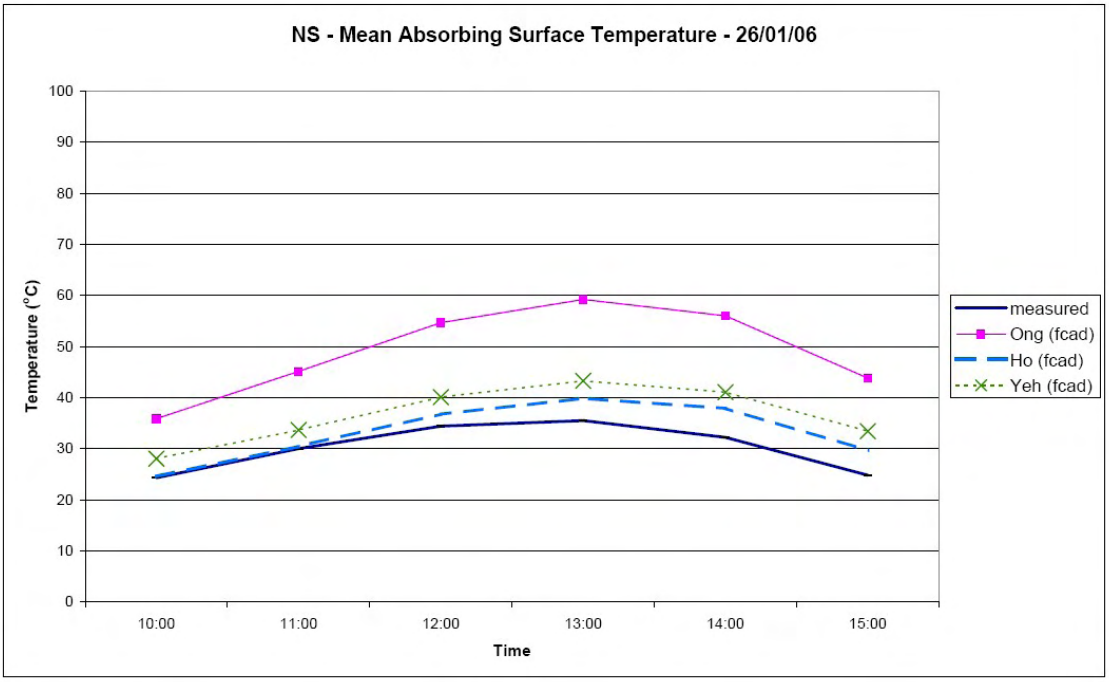

Figure 5.49. NS - Mean Absorbing Surface Temperature (Adapted Models) - 26/01/06

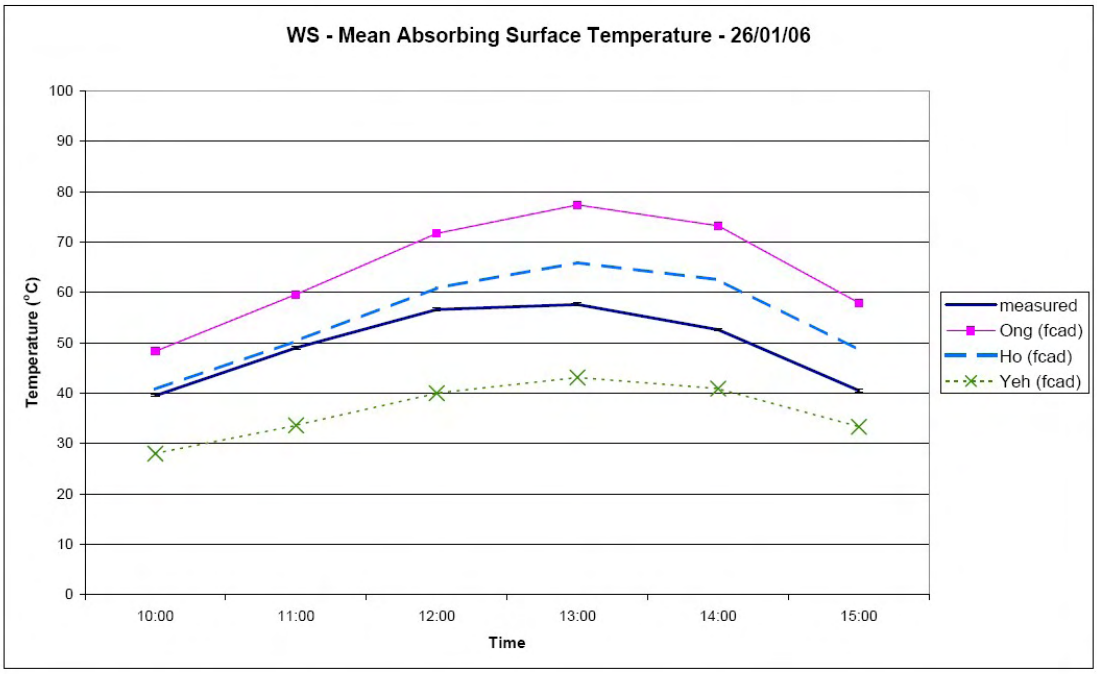

Figure 5.50. WS - Mean Absorbing Surface Temperature (Adapted Models) - 26/01/06

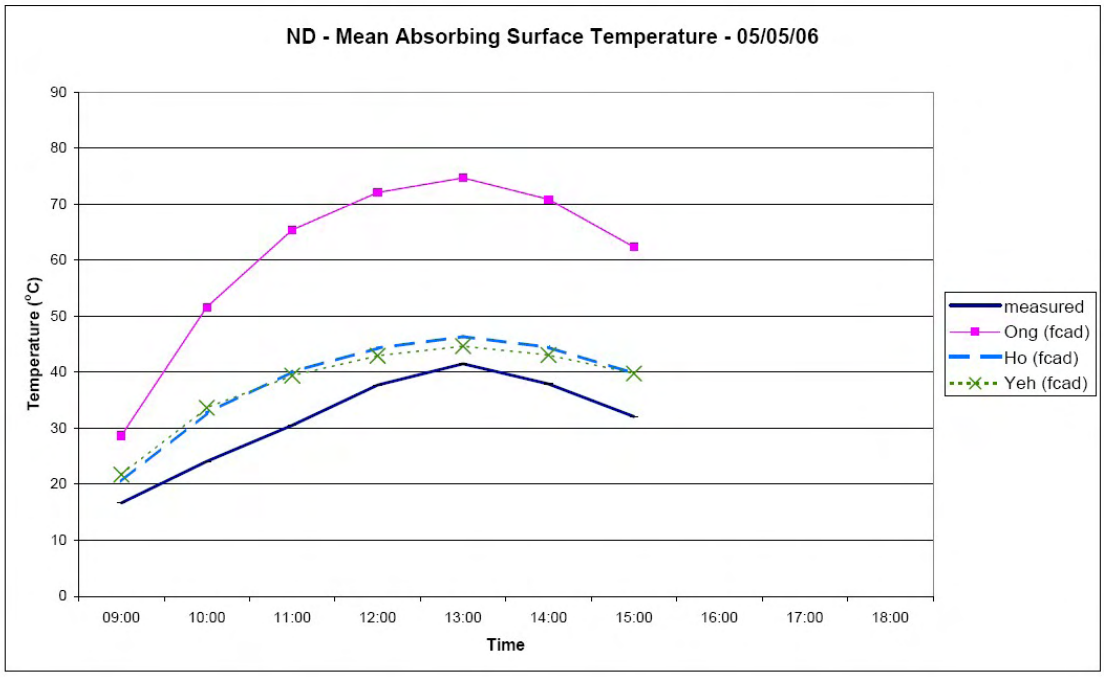

Figure 5.51. ND - Mean Absorbing Surface Temperature (Adapted Models) - 05/05/06

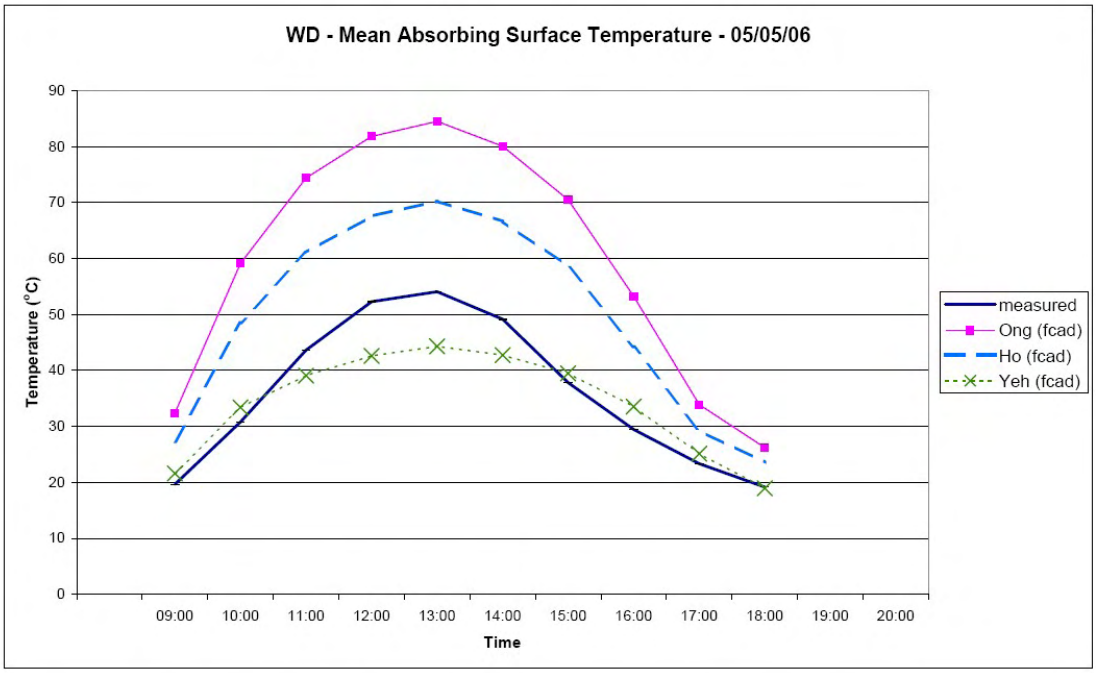

Figure 5.52. WD - Mean Absorbing Surface Temperature (Adapted Models) - 05/05/06

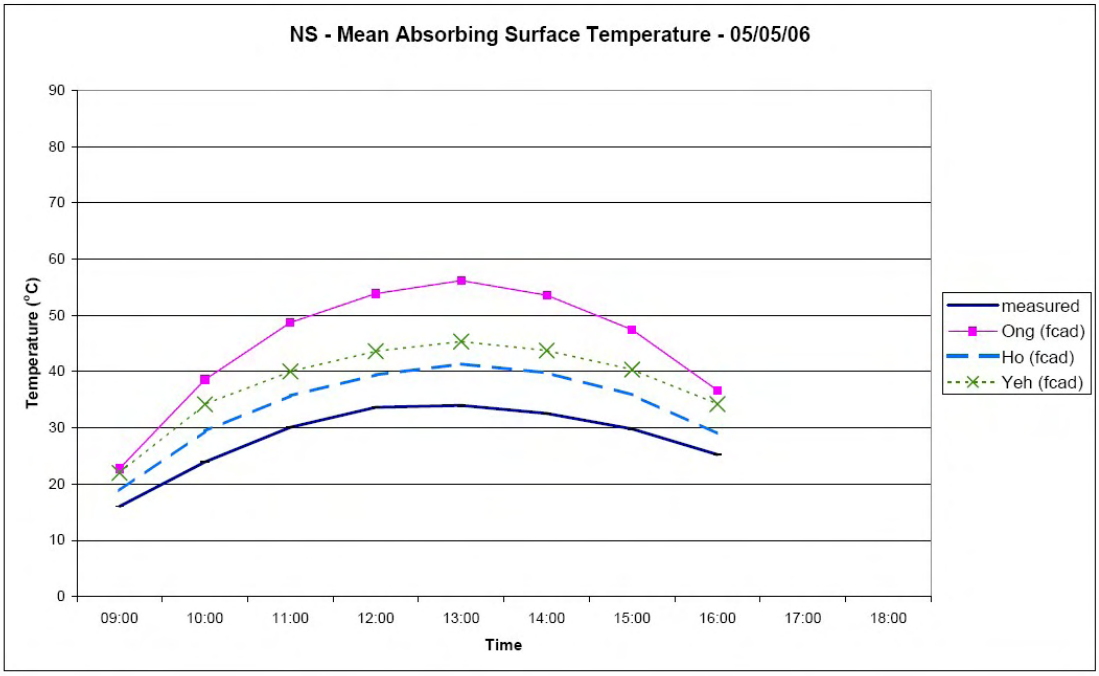

Figure 5.53. NS - Mean Absorbing Surface Temperature (Adapted Models) - 05/05/06

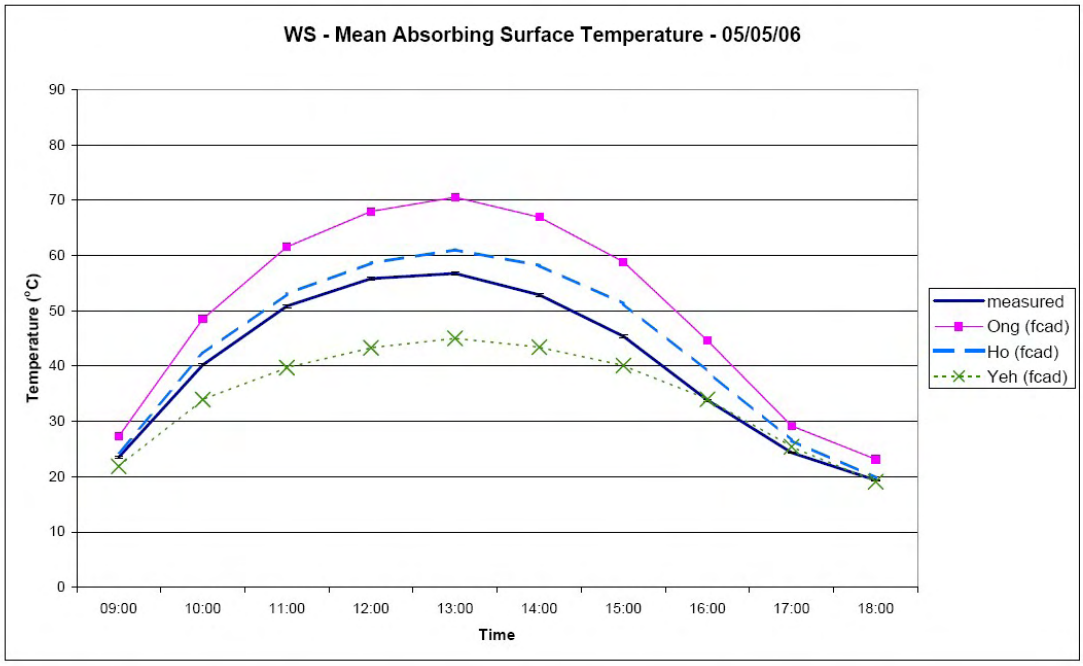

Figure 5.54. WS - Mean Absorbing Surface Temperature (Adapted Models) - 05/05/06

Table 5.19 indicates the mean bias and RMSE for the three models for 26/01/06. Table 5.20 gives the same information for 05/05/06.

Table 5.19 Bias and RMSE for Prediction of Absorbing Surface Temperature 26/01/06

		Ong_{fcad}	Yeh_{fcad}	Ho_{fcad}
Mean Bias (^{o}C)	ND	36.7	3.0	6.9
	WD	32.3	-12.2	17.2
	NS	18.9	6.4	3.0
	WS	15.4	-12.8	5.5
	All	25.8	-3.9	7.9
RMSE (^{o}C)	ND	37.2	4.3	6.7
	WD	33.1	13.6	18.3
	NS	19.4	6.7	3.7
	WS	16.1	13.2	6.5
	All	27.9	10.3	10.4

Table 5.20 Bias and RMSE for Prediction of Absorbing Surface Temperature – 05/05/06

		Ong_{fcad}	Yeh_{fcad}	Ho_{fcad}
Mean Bias (^oC)	ND	29.3	6.4	6.8
	WD	23.7	-1.9	13.8
	NS	16.6	9.8	5.5
	WS	9.6	-5.7	3.1
	All	19.1	1.4	7.4
RMSE (^oC)	ND	30.2	6.7	7.1
	WD	25.4	5.3	14.8
	NS	17.3	9.9	5.7
	WS	10.3	7.6	3.6
	All	22.7	7.9	9.6

From Table 5.19 it can be seen that the Ong_{fcad} and Ho_{fcad} models tend to overestimate the absorbing surface temperature, while the Yeh_{fcad} model is not consistently biased. The Yeh_{fcad} has the lowest overall bias and RMSE, and so can be considered the most accurate of the three models for this parameter. Similar trends are observed in Table 5.20 for 05/05/06.

The prediction of the mean absorbing temperature by the Ho_{fcad} model significantly improved in comparison to the original Ho_{fc} model illustrated in Figures 5.47 - 5.54. Both the mean bias and RMSE of the Ho_{fcad} model are lower than those for the Ho_{fc} model. Over the two dates, the Yeh_{fcad} model exhibits a slight improvement in mean bias and RMSE over the Yeh_{fc} model. The Ong_{fcad} model exhibits a slightly higher mean bias and RMSE than the Ong_{fc} model. Despite the improved correlation with the real data, the Ho_{fcad} model is not better than the Yeh_{fcad} model which is the closest predictor although it does not meet the required accuracy (mean bias and RMSE $\leq 2^oC$).

5.1.7.3 Prediction of Duct Mean Air Temperature

The following graphs show the correlation between the measured mean air temperature for ducts ND, WD, NS and WS and the predictions given by Ong_{fcad}, Yeh_{fcad} and Ho_{fcad}.

Figures 5.55 - 5.58 show the correlation for 26/01/06 and Figures 5.59 - 5.62 for 05/05/06.

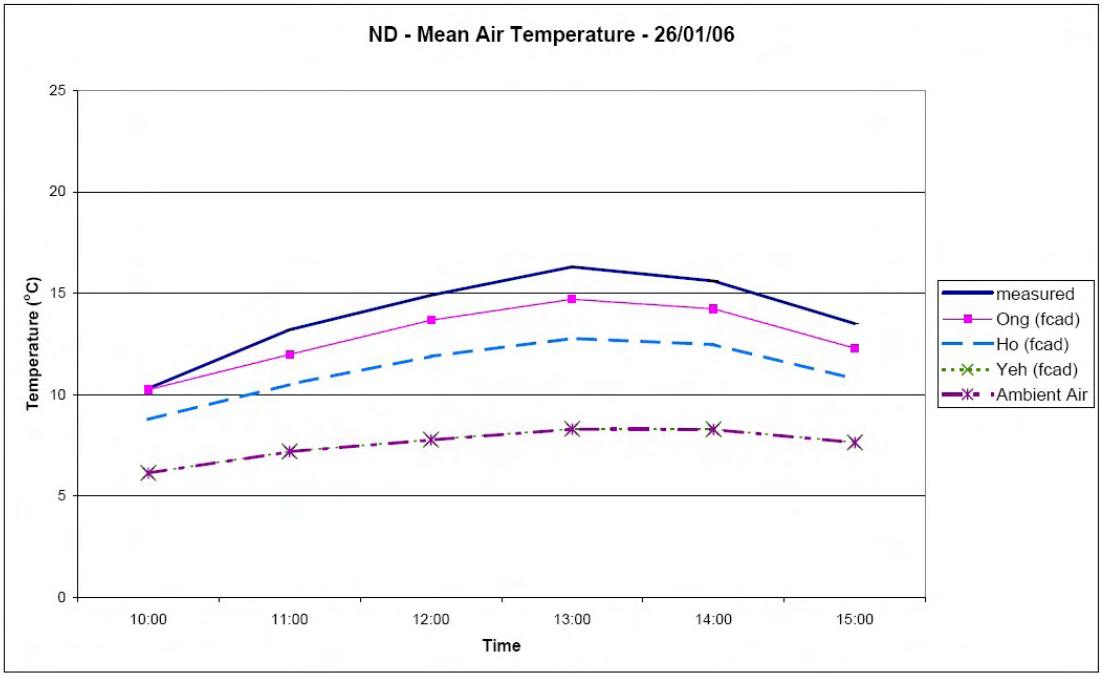

Figure 5.55. ND - Mean Air Temperature (Adapted Models) - 26/01/06

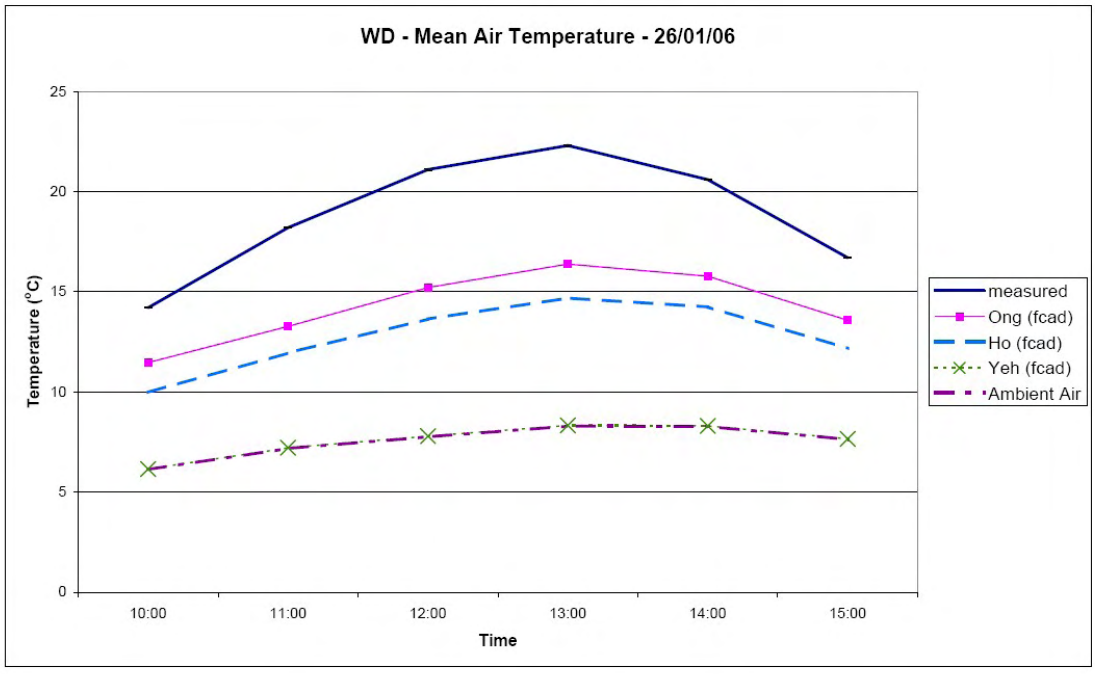

Figure 5.56. WD - Mean Air Temperature (Adapted Models) - 26/01/06

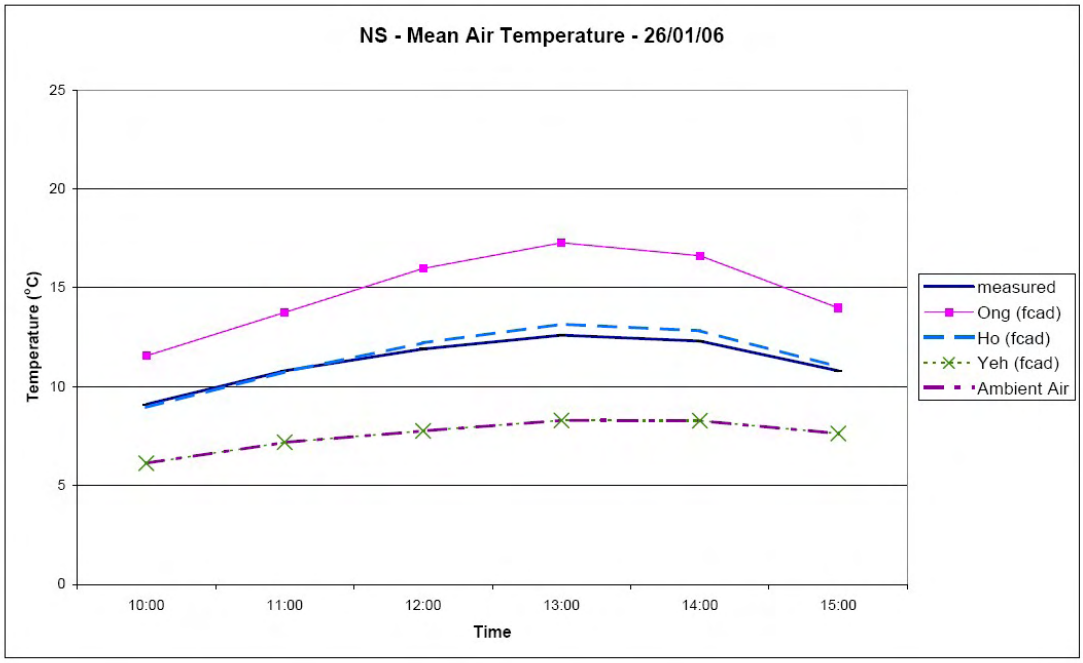

Figure 5.57. NS - Mean Air Temperature (Adapted Models) - 26/01/06

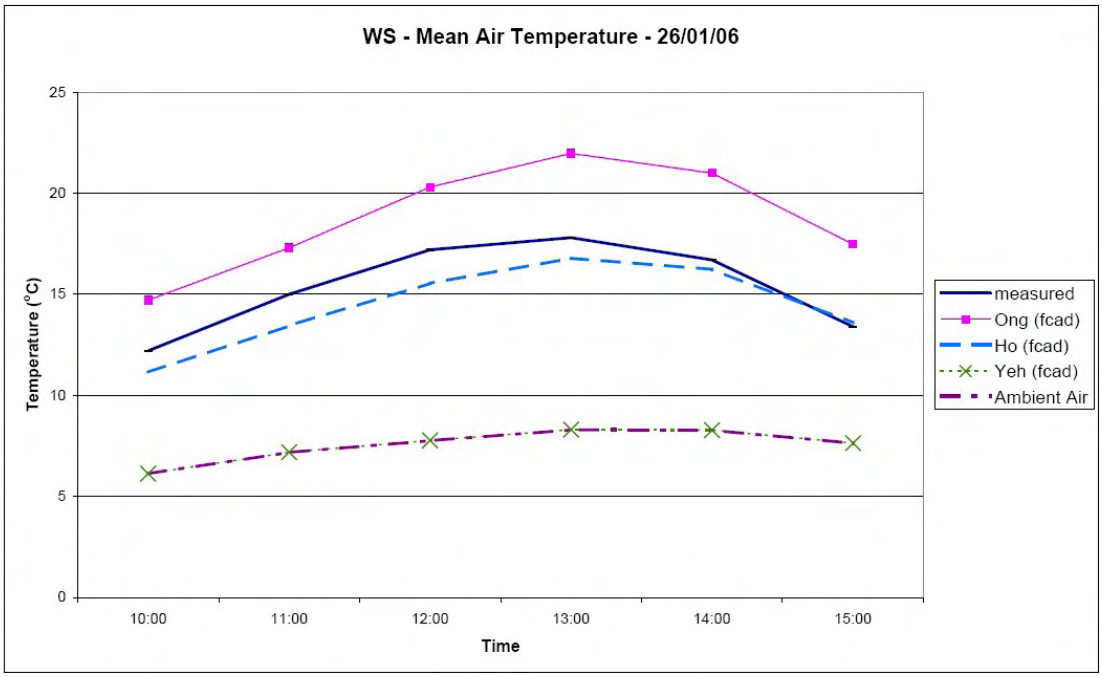

Figure 5.58. WS - Mean Air Temperature (Adapted Models) - 26/01/06

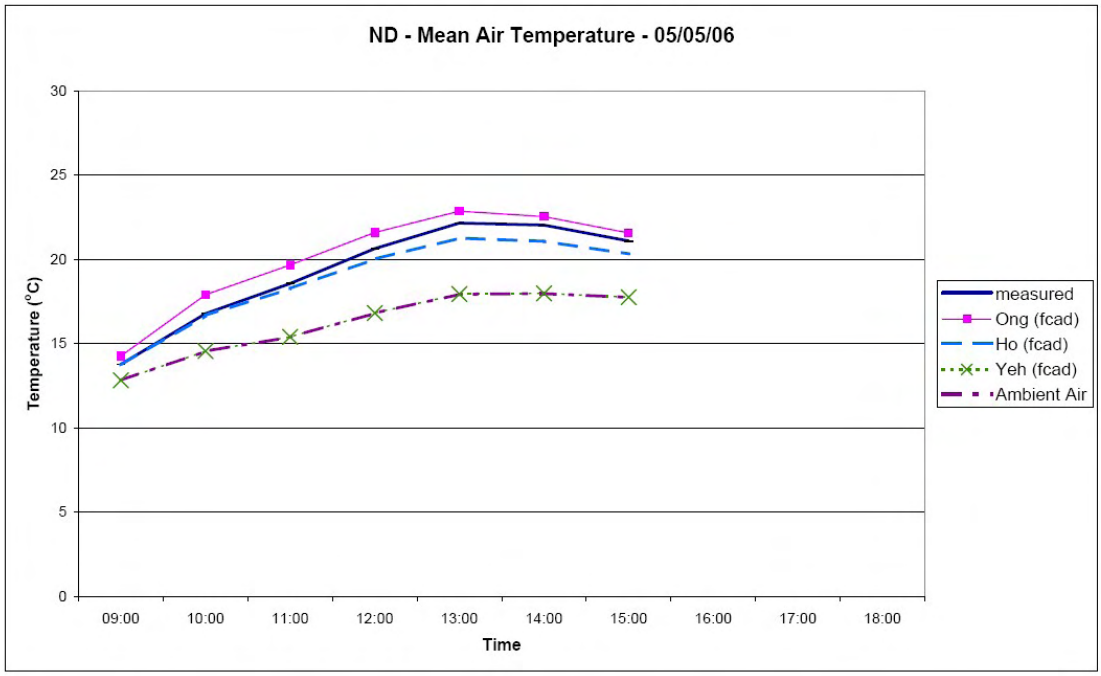

Figure 5.59. ND - Mean Air Temperature (Adapted Models) - 05/05/06

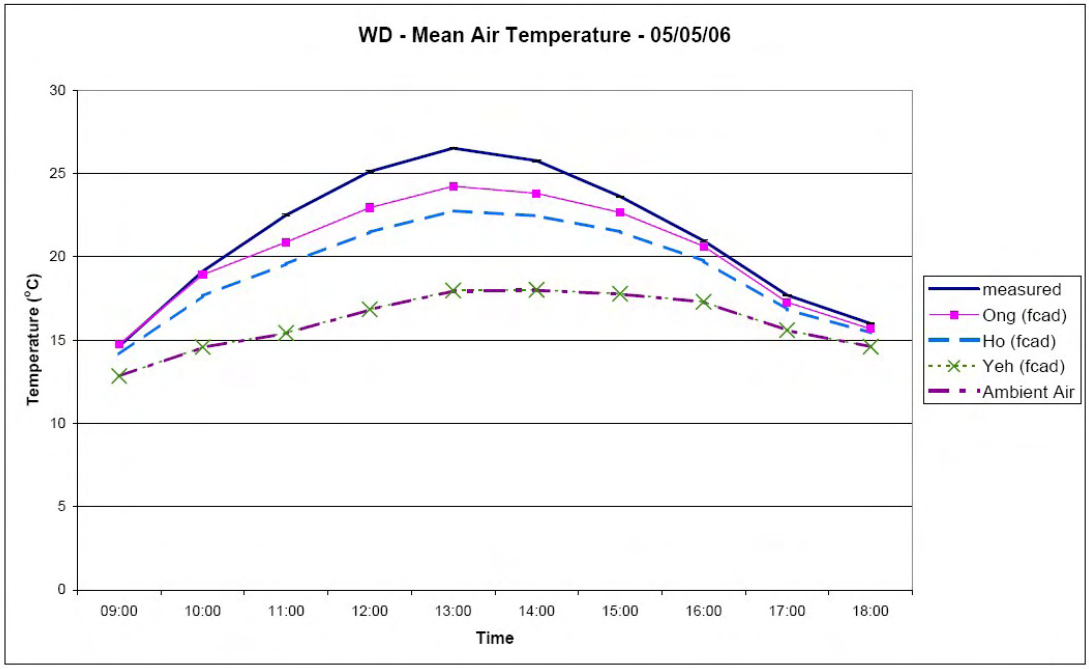

Figure 5.60. WD - Mean Air Temperature (Adapted Models) - 05/05/06

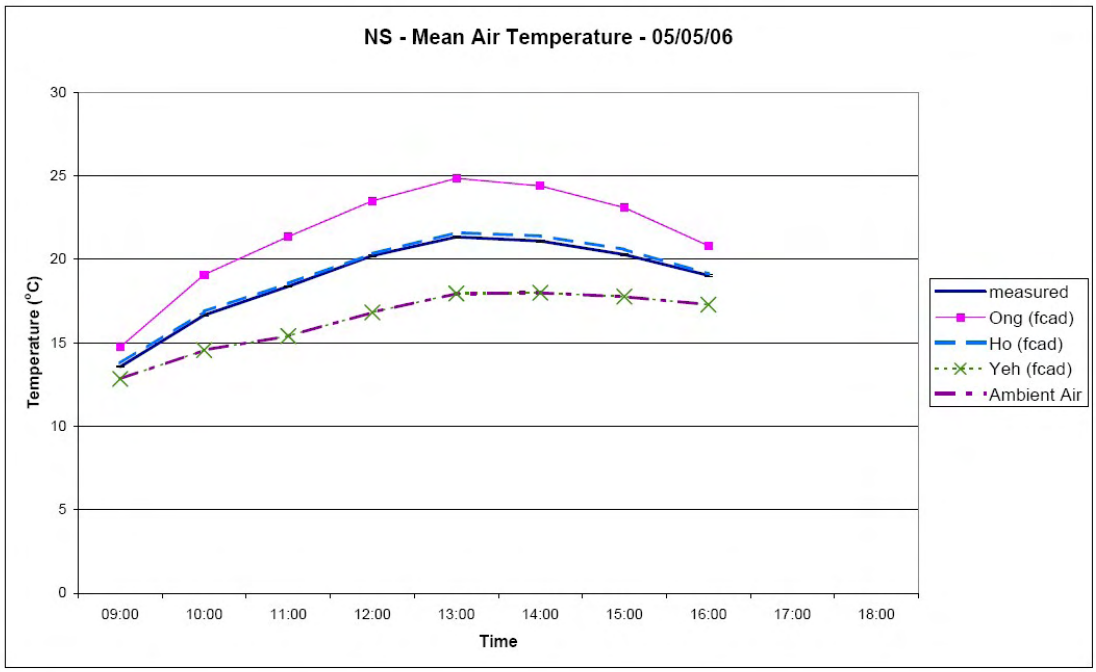

Figure 5.61. NS - Mean Air Temperature (Adapted Models) - 05/05/06

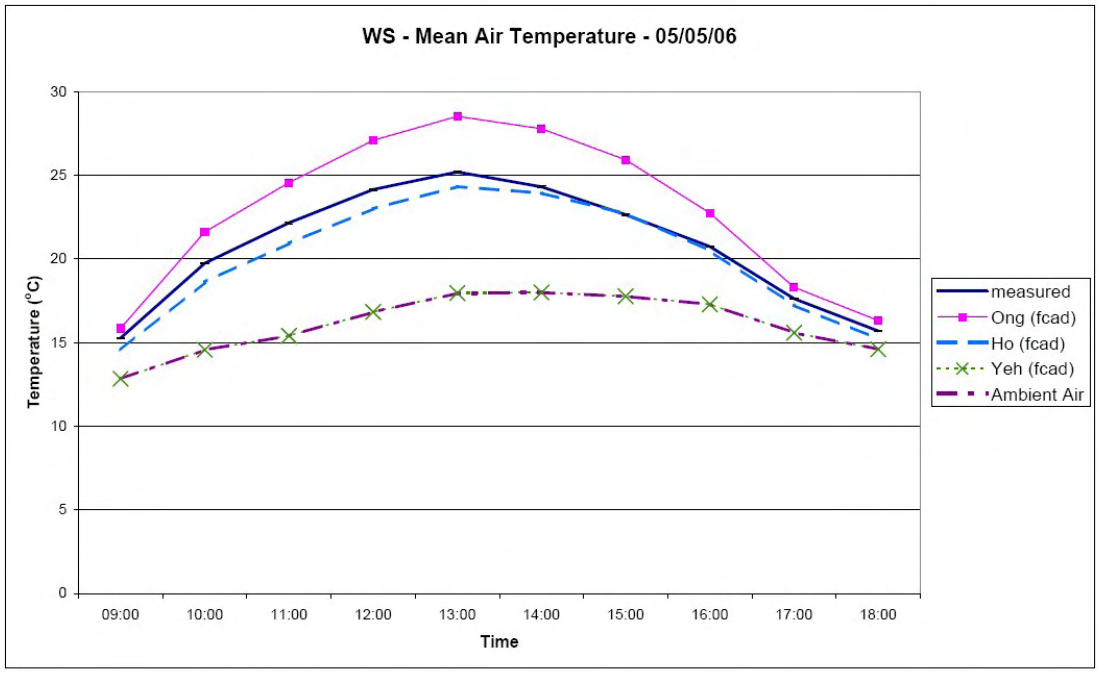

Figure 5.62. WS - Mean Air Temperature (Adapted Models) - 05/05/06

Table 5.21 indicates the mean bias and RMSE for the two models for 26/01/06. Table 5.22 gives the same information for 05/05/06.

Table 5.21 Bias and RMSE for Prediction of Mean Air Temperature - 26/01/06

		Ong_{fcad}	Yeh_{fcad}	Ho_{fcad}
Mean Bias (^oC)	ND	-1.1	-6.4	-2.8
	WD	-4.6	-11.3	-6.1
	NS	3.6	-3.7	0.2
	WS	3.4	-7.8	-0.9
	All	0.3	-7.3	-2.4
RMSE (^oC)	ND	1.2	6.5	2.8
	WD	4.7	11.5	6.2
	NS	3.7	3.7	0.4
	WS	3.5	8.0	1.1
	All	3.5	7.9	3.5

Table 5.22 Bias and RMSE for Prediction of Mean Air Temperature – 05/05/06

		Ong_{fcad}	Yeh_{fcad}	Ho_{fcad}
Mean Bias (^oC)	ND	0.8	-3.1	-0.5
	WD	-1.0	-5.1	-2.0
	NS	2.7	-2.5	0.2
	WS	2.1	-4.7	-0.7
	All	1.1	-4.0	-0.8
RMSE (^oC)	ND	0.8	3.3	0.6
	WD	1.3	5.8	2.4
	NS	2.8	2.6	0.2
	WS	2.4	5.1	0.8
	All	2.1	4.8	1.5

From Table 5.21 it can be seen that the Yeh_{fcad} model tends to underestimate the mean air temperature. The bias for the Ong_{fcad} and Ho_{fcad} models is less consistent. The Yeh_{fcad} model has a higher RMSE than the other two models. The same trends are observed in Table 5.22.

The prediction of the mean air temperature by the Ho_{fcad} model significantly improved in comparison to the original Ho_{fc} model illustrated in Figures 5.55 - 5.62. Both the mean bias and RMSE of the Ho_{fcad} model are lower than those for the Ho_{fc} model. The Yeh_{fcad} model does not exhibit a significant change in mean bias or RMSE from the Yeh_{fc} model. Over the two dates, the Ong_{fcad} model exhibits a slightly improved mean bias and RMSE in comparison to the Ong_{fc} model. The improved correlation with the real data, results in the Ho_{fcad} model having the lowest RMSE of the models, although

Ong_{fcad} has the lowest mean bias. There is little difference between the RMSE of the Ong_{fcad} and Ho_{fcad} models, so the Ong_{fcad} model has been selected as the closest model for the mean air temperature. However, the Ong_{fcad} model does not meet the required accuracy (mean bias and RMSE $\leq 2^{o}C$).

5.1.7.4 Prediction of Exit Air Temperature

The exit air temperature is proportional to the power output. The following graphs show the correlation between the measured exit air temperature for ducts ND, WD, NS and WS and the predictions given by Ong_{fcad}, Yeh_{fcad} and Ho_{fcad}.

Figures 5.63 - 5.66 show the correlation for 26/01/06 and Figures 5.67 - 5.70 for 05/05/06.

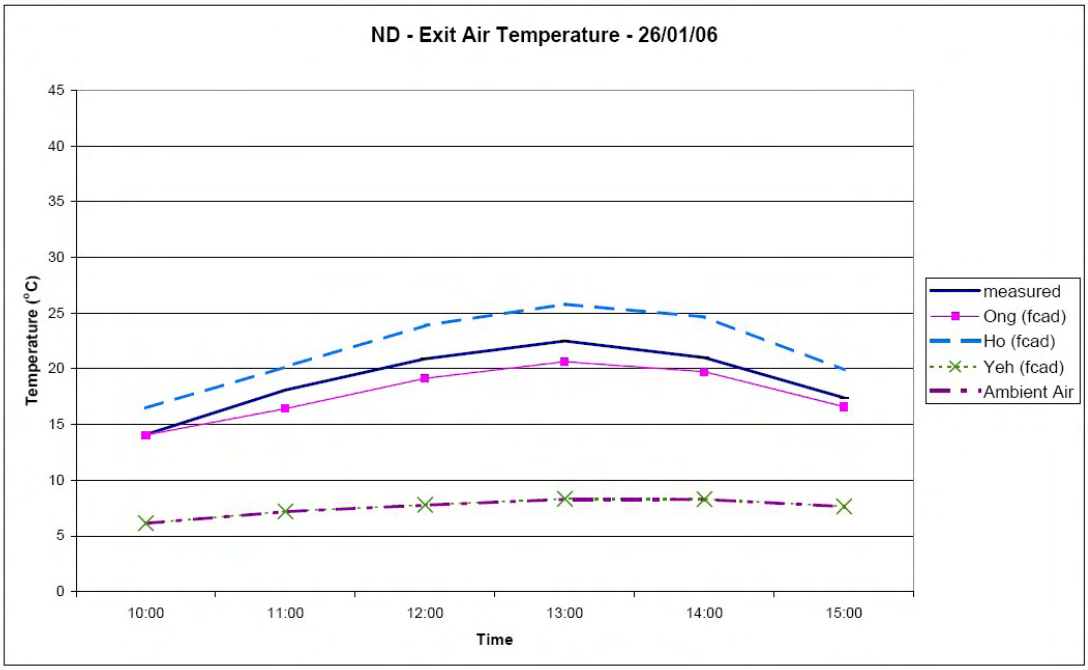

Figure 5.63. ND - Exit Air Temperature (Adapted Models) - 26/01/06

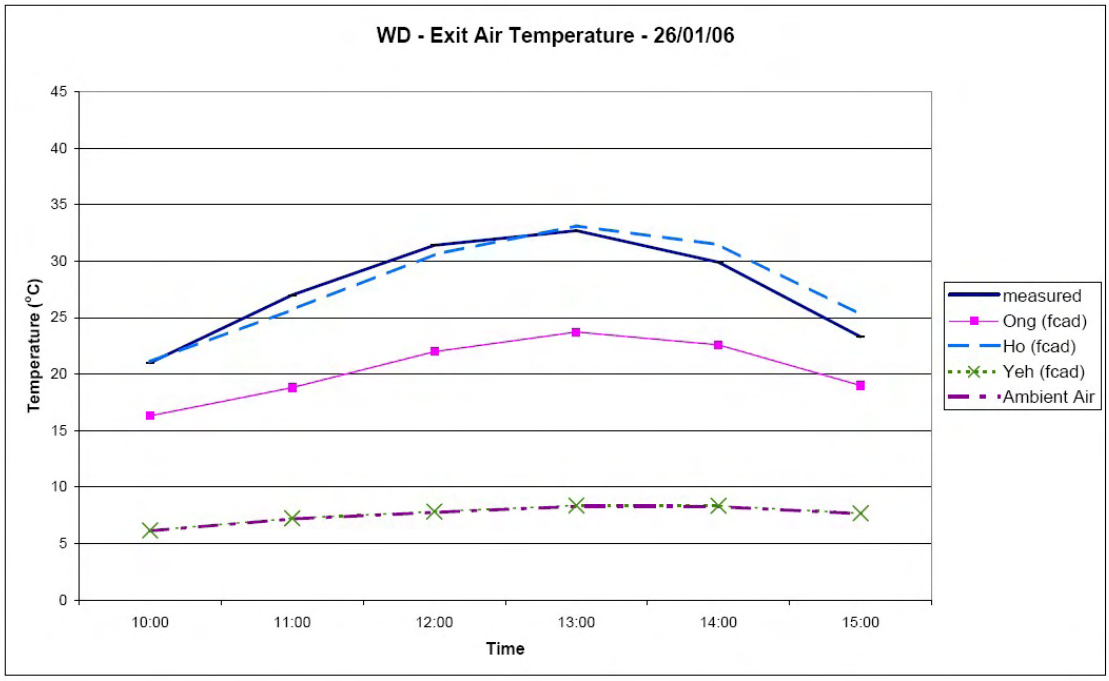

Figure 5.64. WD - Exit Air Temperature (Adapted Models) - 26/01/06

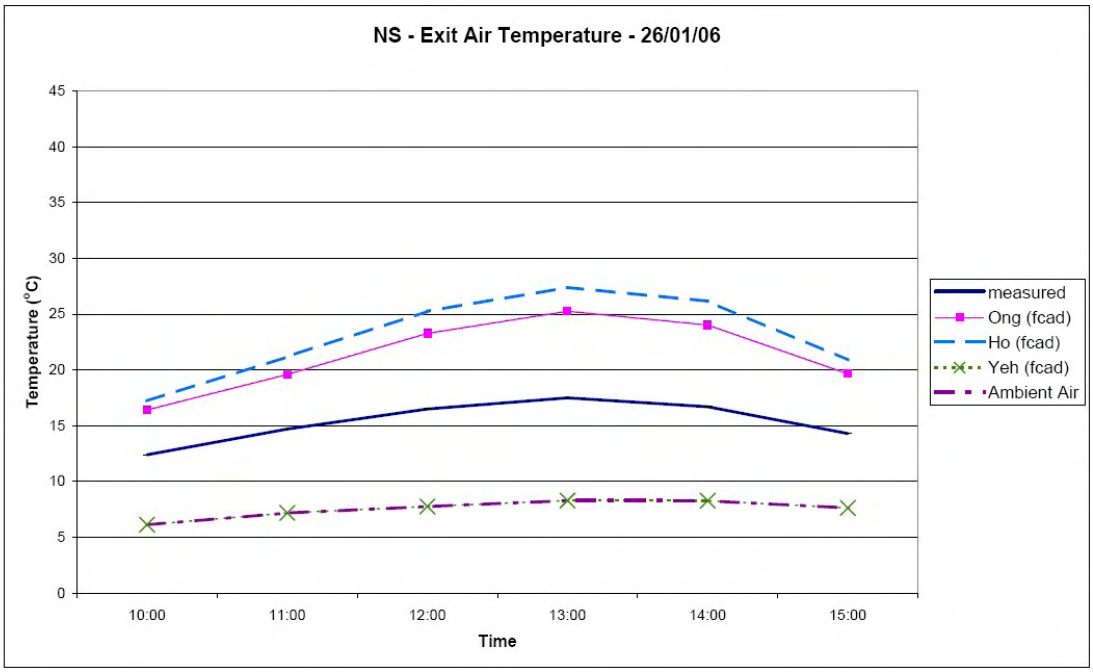

Figure 5.65. NS - Exit Air Temperature (Adapted Models) - 26/01/06

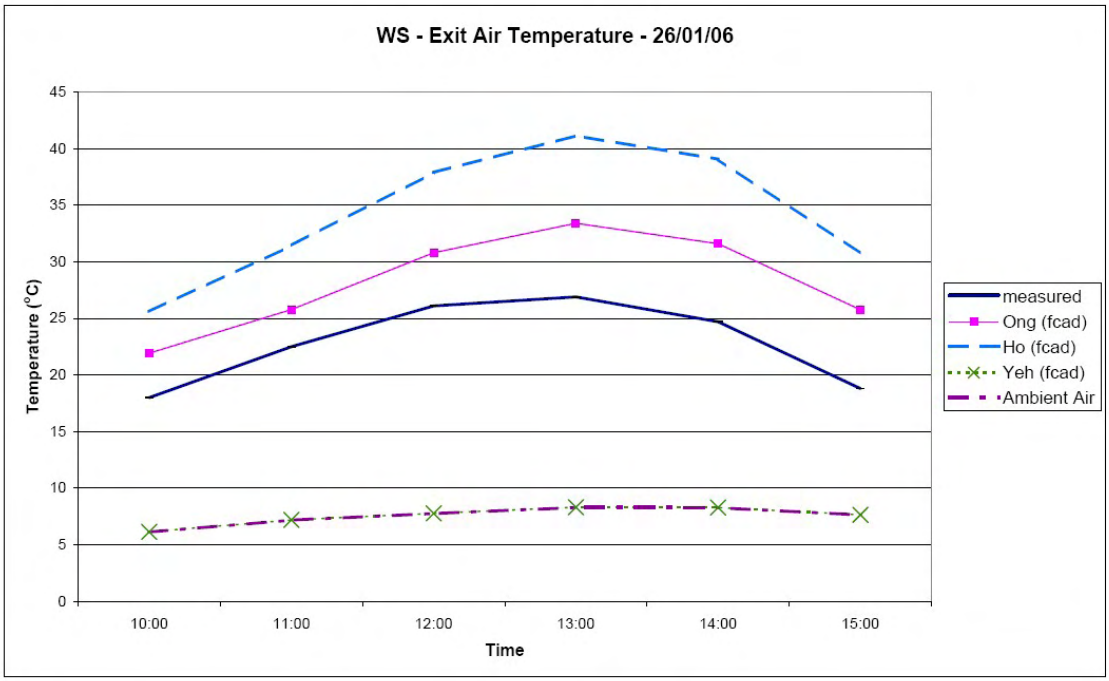

Figure 5.66. WS - Exit Air Temperature (Adapted Models) - 26/01/06

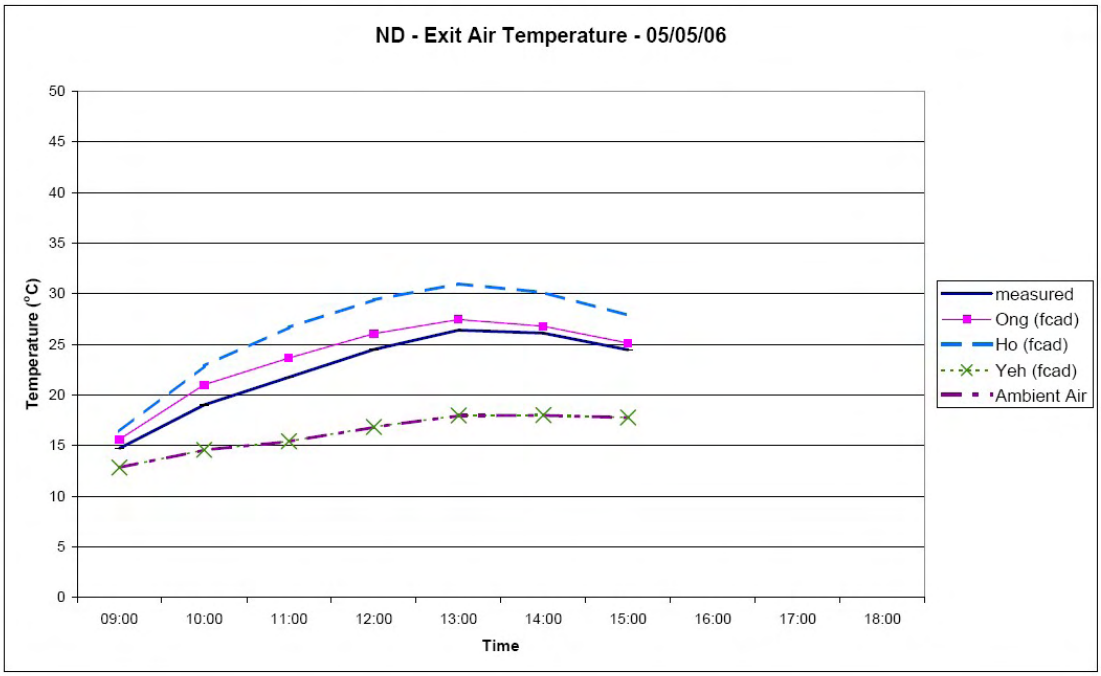

Figure 5.67. ND - Exit Air Temperature (Adapted Models) - 05/05/06

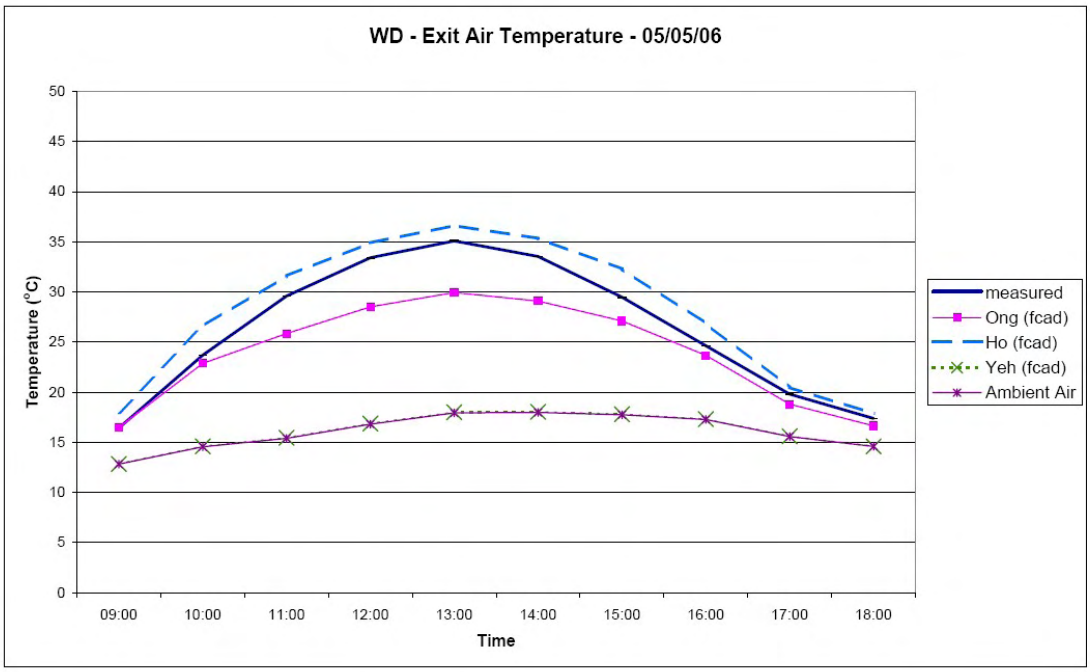

Figure 5.68. WD - Exit Air Temperature (Adapted Models) - 05/05/06

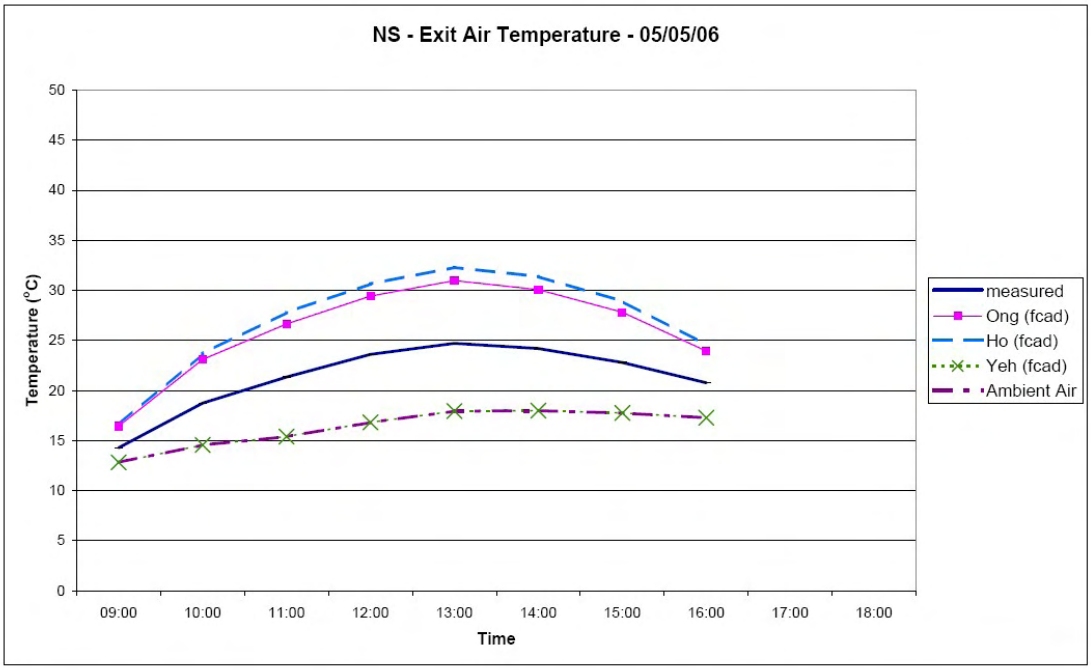

Figure 5.69. NS - Exit Air Temperature (Adapted Models) - 05/05/06

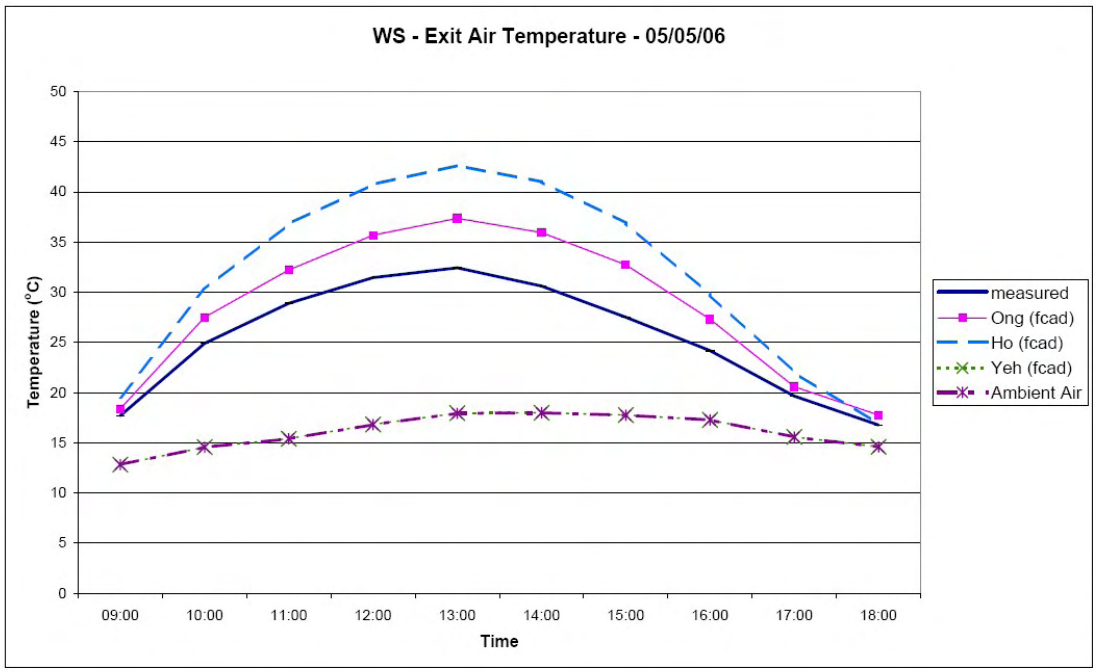

Figure 5.70. WS - Exit Air Temperature (Adapted Models) - 05/05/06

Table 5.23 indicates the mean bias and RMSE for the three models for 26/01/06. Table 5.24 gives the same information for 05/05/06.

Table 5.23 Bias and RMSE for Prediction of Exit Air Temperature - 26/01/06

		Ong_{fcad}	Yeh_{fcad}	Ho_{fcad}
Mean Bias (^oC)	ND	-1.2	-11.4	2.8
	WD	-7.2	-19.9	0.2
	NS	6.0	-7.8	7.6
	WS	5.4	-15.3	11.4
	All	0.8	-13.6	5.6
RMSE (^oC)	ND	1.4	11.6	2.9
	WD	7.4	20.3	1.2
	NS	6.2	7.9	7.9
	WS	5.6	15.5	11.7
	All	5.6	14.6	7.2

Table 5.24 Bias and RMSE for Prediction of Exit Air Temperature – 05/05/06

		Ong_{fcad}	Yeh_{fcad}	Ho_{fcad}
Mean Bias (^oC)	ND	1.2	-6.2	3.9
	WD	-2.4	-10.2	1.8
	NS	4.8	-5.0	5.7
	WS	3.2	-9.3	6.2
	All	1.5	-8.0	4.4
RMSE (^oC)	ND	1.4	6.6	4.0
	WD	3.1	11.5	1.9
	NS	4.9	5.3	5.9
	WS	3.6	10.3	7.2
	All	3.7	9.6	5.4

From Table 5.23 it can be seen that the Yeh_{fcad} model tends to underestimate the exit air temperature, the Ho_{fcad} model tends to overestimate it, and the Ong_{fcad} model has no consistent bias. Of the three models, Ho_{fcad} has the lowest RMSE. The same trends for bias are observed in Table 5.24; however, in this instance the Ong_{fcad} model has the lowest RMSE. Since the Ong_{fcad} model is the least biased, it would be the best choice of model for this parameter.

The prediction of the exit air temperature by the Ho_{fcad} model significantly improved in comparison to the original Ho_{fc} model illustrated in Figures 5.63 - 5.70. Both the mean bias and RMSE of the Ho_{fcad} model are lower than those for the Ho_{fc} model. The Yeh_{fcad} model does not exhibit a significant change in mean bias or RMSE from the Yeh_{fc} model. Over the two dates the Ong_{fcad} model exhibits a slightly reduced mean bias although the RMSE increases slightly in comparison to the Ong_{fc} model. The difference between the RMSE for the Ong_{fc} and Ong_{fcad} models is smaller than the difference in mean bias; therefore the Ong_{fcad} model is selected as the closest model to predict the exit air temperature. However the Ong_{fcad} model does not meet the required accuracy (mean bias and RMSE $\leq 2^oC$).

5.1.7.5 Prediction of Power Output

The following graphs show the correlation between the calculated power output for ducts ND, WD, NS and WS and the predictions given by Ong_{fcad}, Yeh_{fcad} and Ho_{fcad}.

Figures 5.71 - 5.74 show the correlation for 26/01/06 and Figures 5.75 - 5.78 for 05/05/06.

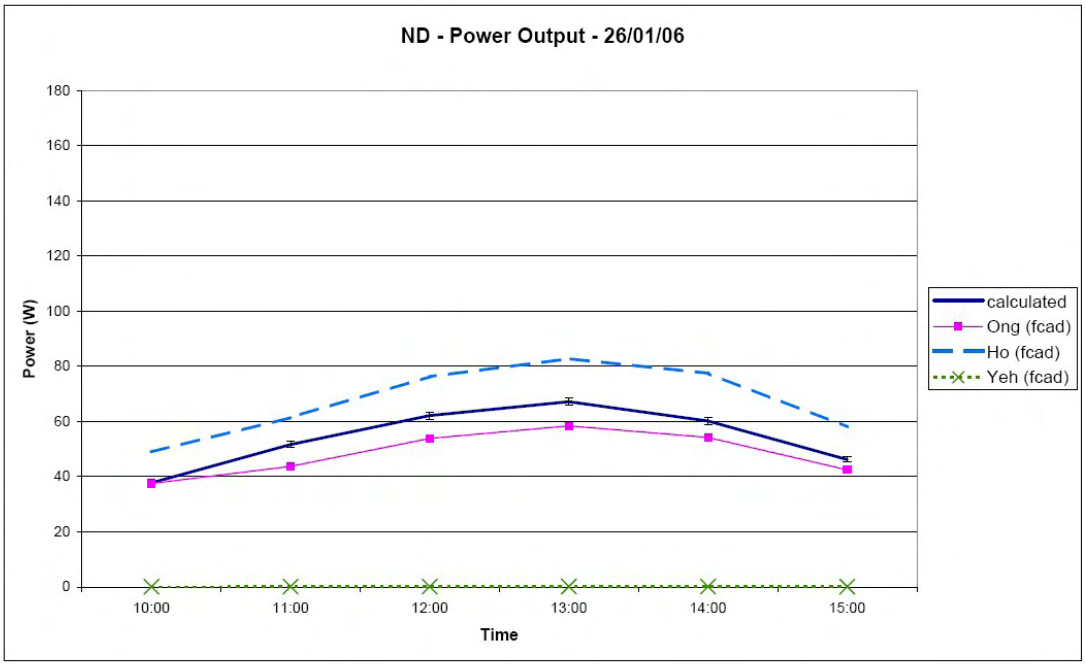

Figure 5.71. ND - Power Output (Adapted Models) - 26/01/06

Figure 5.72. WD - Power Output (Adapted Models) - 26/01/06

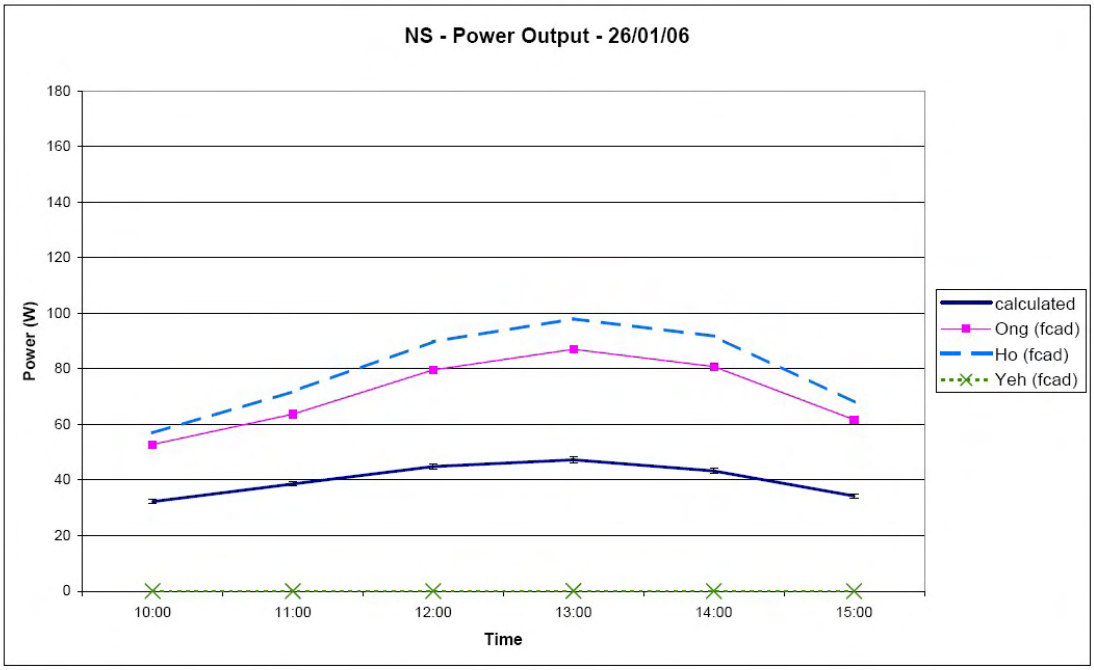

Figure 5.73. NS - Power Output (Adapted Models) - 26/01/06

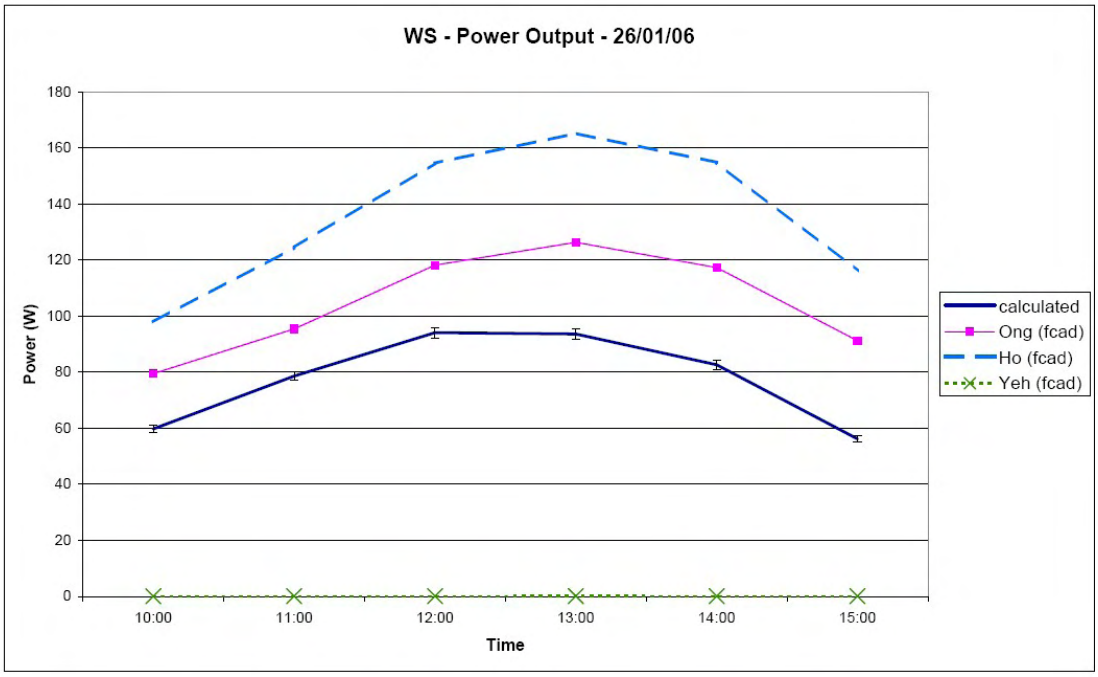

Figure 5.74. WS - Power Output (Adapted Models) - 26/01/06

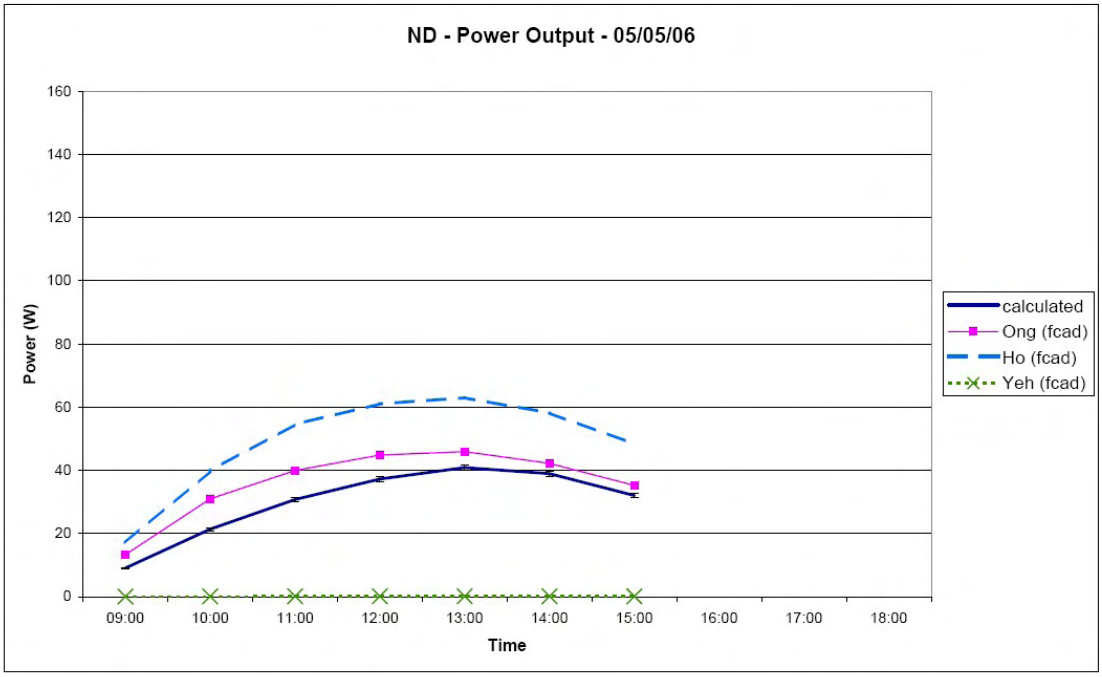

Figure 5.75. ND - Power Out (Adapted Models) - 05/05/06

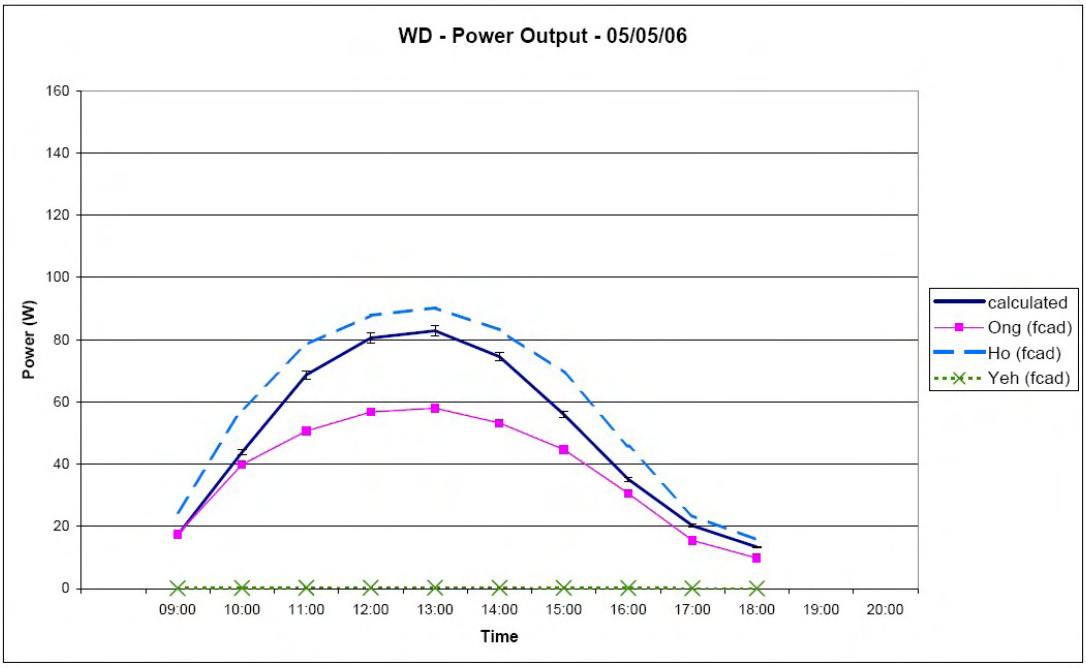

Figure 5.76. WD - Power Out (Adapted Models) - 05/05/06

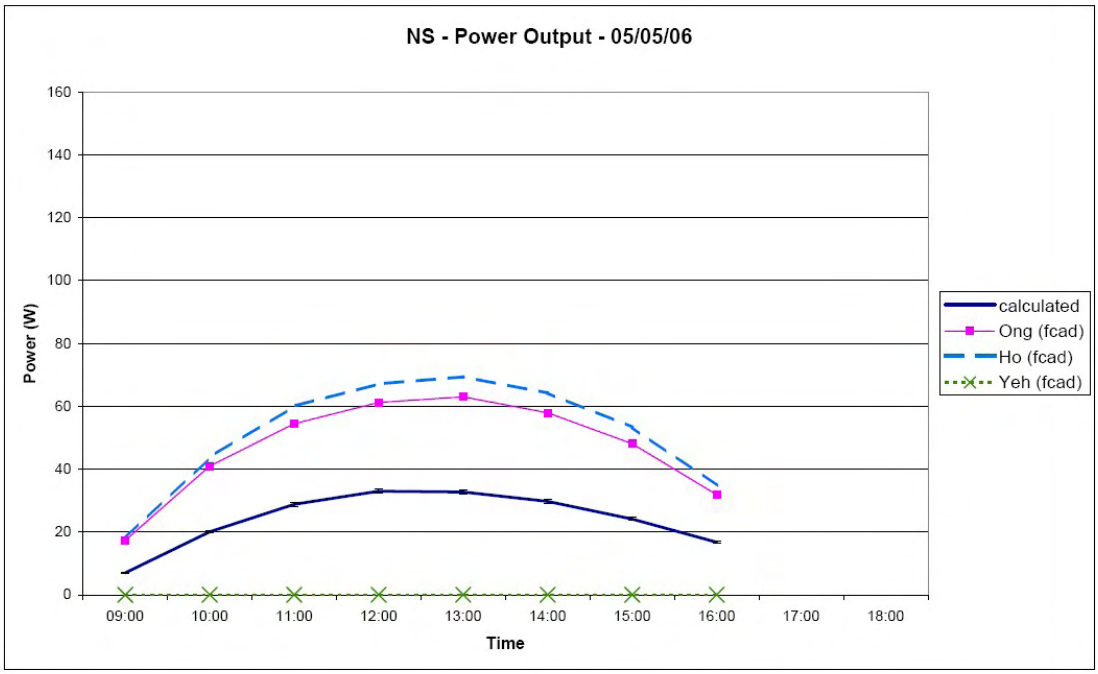

Figure 5.77. NS - Power Out (Adapted Models) - 05/05/06

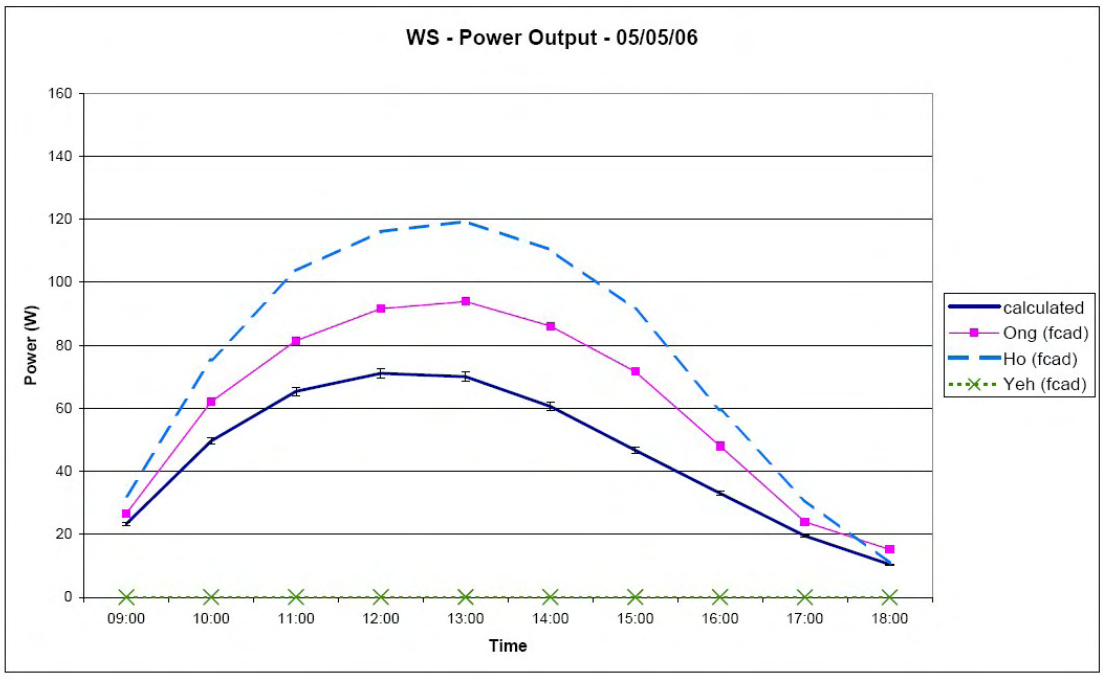

Figure 5.78. WS - Power Out (Adapted Models) - 05/05/06

Table 5.25 indicates the mean bias and RMSE for the three models for 26/01/06. Table 5.26 gives the same information for 05/05/06.

Table 5.25 Bias and RMSE for Prediction of Power Output - 26/01/06

		Ong_{fcad}	Yeh_{fcad}	Ho_{fcad}
Mean Bias (W)	ND	-5.9	-54.0	13.3
	WD	-38.8	-108.3	1.7
	NS	30.9	-40.0	39.
	WS	27.2	-77.3	58.0
	All	3.3	-69.9	28.1
RMSE (W)	ND	6.6	55.0	13.6
	WD	40.3	110.1	6.6
	NS	31.6	40.4	40.4
	WS	28.1	78.8	59.4
	All	29.4	75.8	36.7

Table 5.26 Bias and RMSE for Prediction of Power Output – 05/05/06

		Ong_{fc}	Yeh_{fc}	Ho_{fc}
Mean Bias (W)	ND	6.0	-29.9	18.8
	WD	-11.6	-49.0	8.4
	NS	22.8	-24.0	27.3
	WS	15.1	-44.9	30.0
	All	7.4	-38.3	21.0
RMSE (W)	ND	6.5	31.7	19.5
	WD	14.7	55.3	9.1
	NS	23.7	25.4	28.6
	WS	17.2	49.6	34.6
	All	17.6	46.0	26.1

From Table 5.25 it can be seen that the Yeh_{fcad} model tends to underestimate the power output, the Ho_{fcad} model tends to overestimate it, and the Ong_{fcad} model has no consistent bias. Of the three models, Ong_{fcad} has the lowest RMSE. The same trends for bias are observed in Table 5.26. Since the Ong_{fcad} model is the least biased and has the lowest RMSE, it would be the best choice of model for this parameter.

The prediction of the power output by the Ho_{fcad} model significantly improved in comparison to the original Ho_{fc} model illustrated in Figures 5.71 - 5.78. Both the mean bias and RMSE of the Ho_{fcad} model are lower than those for the Ho_{fc} model. The Yeh_{fcad} model does not exhibit a significant change in mean bias or RMSE from the Yeh_{fc} model. The Ong_{fcad} model exhibits a slightly reduced mean bias and RMSE for January, but suffers a slight deterioration in May. The Ong_{fcad} model has a slightly

smaller RMSE and so is considered the closest model for the power output, but does not meet the required level of accuracy. However, the Ong_{fcad} model does not meet the required accuracy (mean bias and RMSE ≤ 5W).

5.1.7.6 Discussion

The adaptations made a significant improvement in the predictions for the Ho_{fcad} model for some parameters (e.g. RMSE for mean air temperature in May reduced from 4.3 to 1.5^{o}C). There was also a slight improvement in the predictions of the Ong_{fcad} model for some parameters (e.g. mean bias for mean air temperature in January reduced from -1.5 to 0.3^{o}C). The Yeh_{fcad} model was not significantly improved.

There is still no one model which shows a significant advantage over the others in predicting all five parameters being considered. However, some models are better at predicting certain parameters, e.g.:

- The glazing temperature is best predicted by the Ong_{fc} model
- The absorbing surface temperature is best predicted by the Yeh_{fc} model
- The mean air temperature is best predicted by the Ho_{fcad} model
- The exit air temperature is best predicted by the Ong_{fc} model
- The power output is best predicted by the Ong_{fc} model

5.1.8 Averaged Predictive Models for Forced Convection

It has been noticed that the air temperature and power output are under predicted by some models and over predicted by others. This observation led to the conclusion that a combination of the models could prove advantageous.

Three combinations of models were considered:

1. the results from the Ong_{fc} model (obtained in sections 5.1.1 to 5.1.5) and the results from the Ong_{fcad} model (obtained in sections 5.1.7.1 to 5.1.7.5) were averaged. These results will be referred to as $Ong_{fc\&fcad}$
2. the results from the Ho_{fc} model (obtained in sections 5.1.1 to 5.1.5) and the results from the Ho_{fcad} models (obtained in sections 5.1.7.1 to 5.1.7.5) were averaged. These results will be referred to as $Ho_{fc\&fcad}$

3. the results from the Ong_{fcad} model (obtained in sections 5.1.7.1 to 5.1.7.5) and the results from the Ho_{fcad} model (obtained in sections 5.1.7.1 to 5.1.7.5) were averaged. These results will be referred to as $OngHo_{fcad}$

5.1.8.1 Prediction of Mean Glazing Temperature

The following graphs show the correlation between the measured mean glazing temperature for ducts ND, WD, NS and WS and the predictions given by $Ong_{fc\&fcad}$, $Ho_{fc\&fcad}$, and $OngHo_{fcad}$.

Figures 5.79 - 5.81 show the correlation for 26/01/06 and Figures 5.82 - 5.85 for 05/05/06.

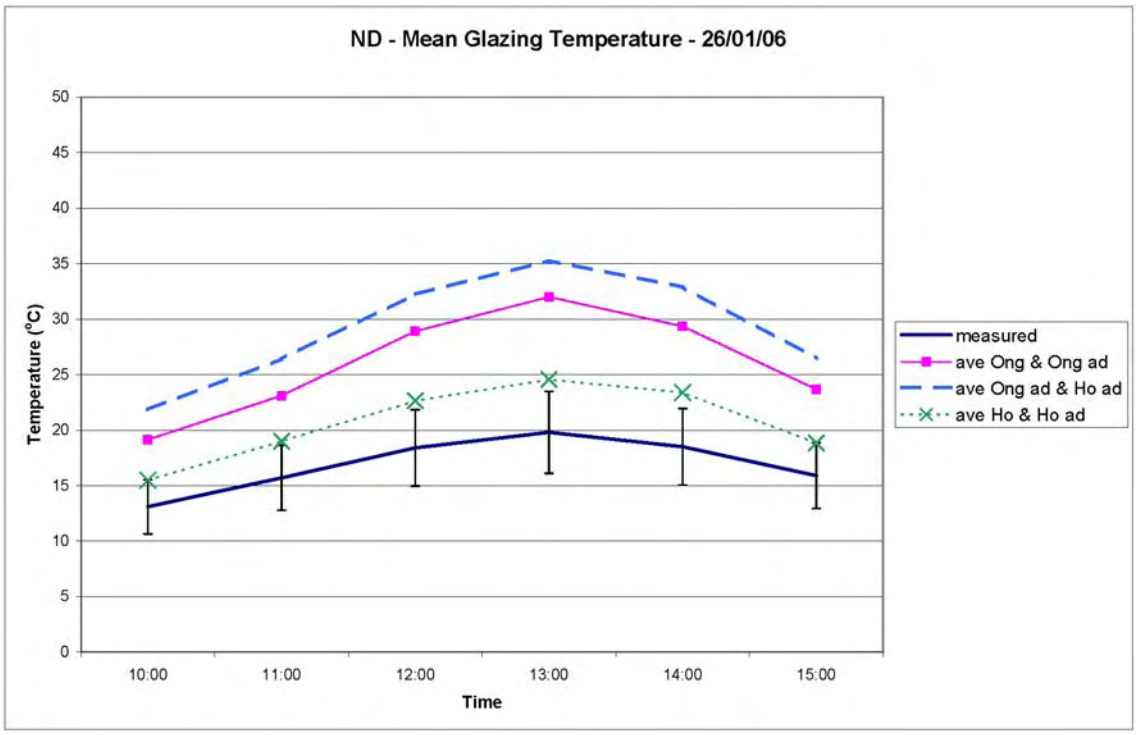

Figure 5.79. ND - Mean Glazing Temperature (Combined Models) - 26/01/06

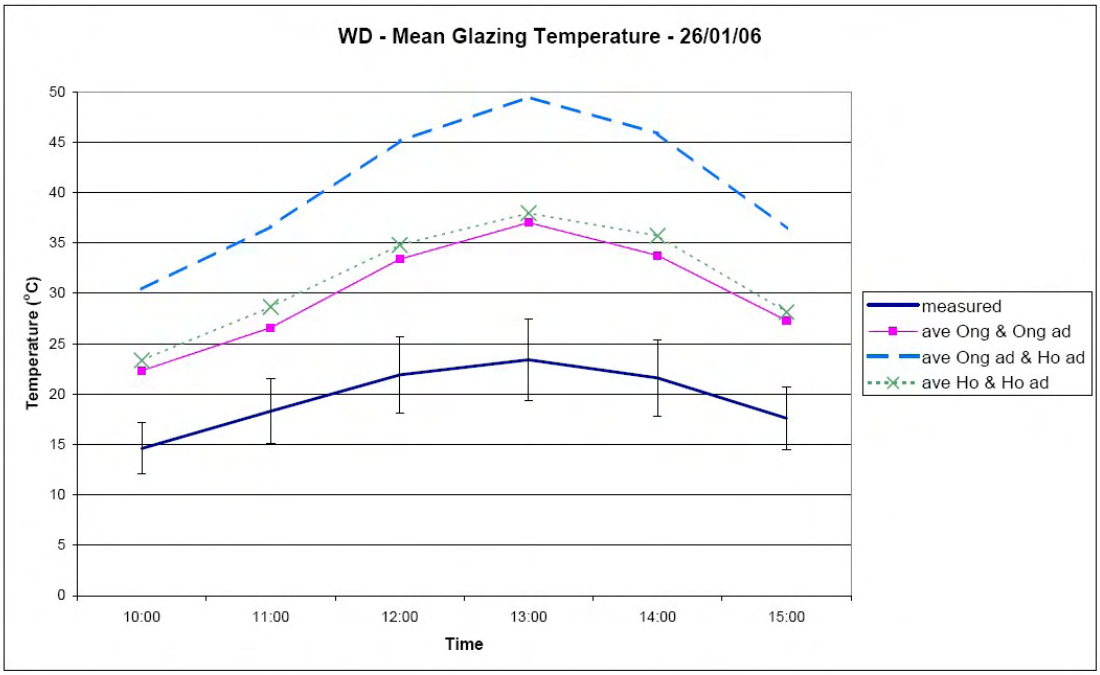

Figure 5.80. WD - Mean Glazing Temperature (Combined Models) - 26/01/06

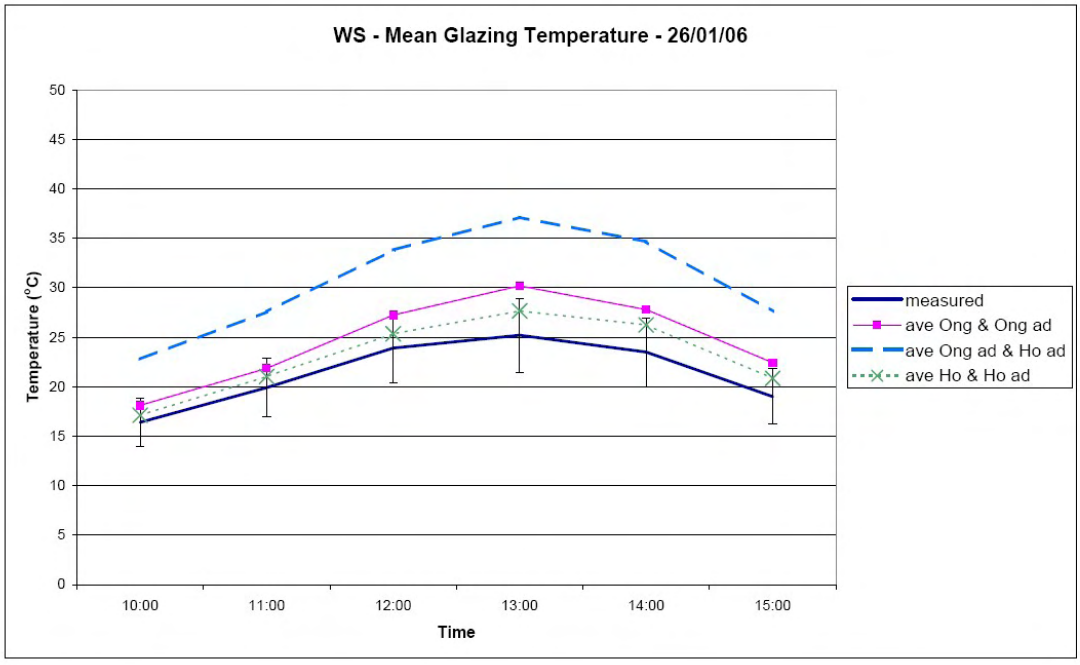

Figure 5.81. WS - Mean Glazing Temperature (Combined Models) - 26/01/06

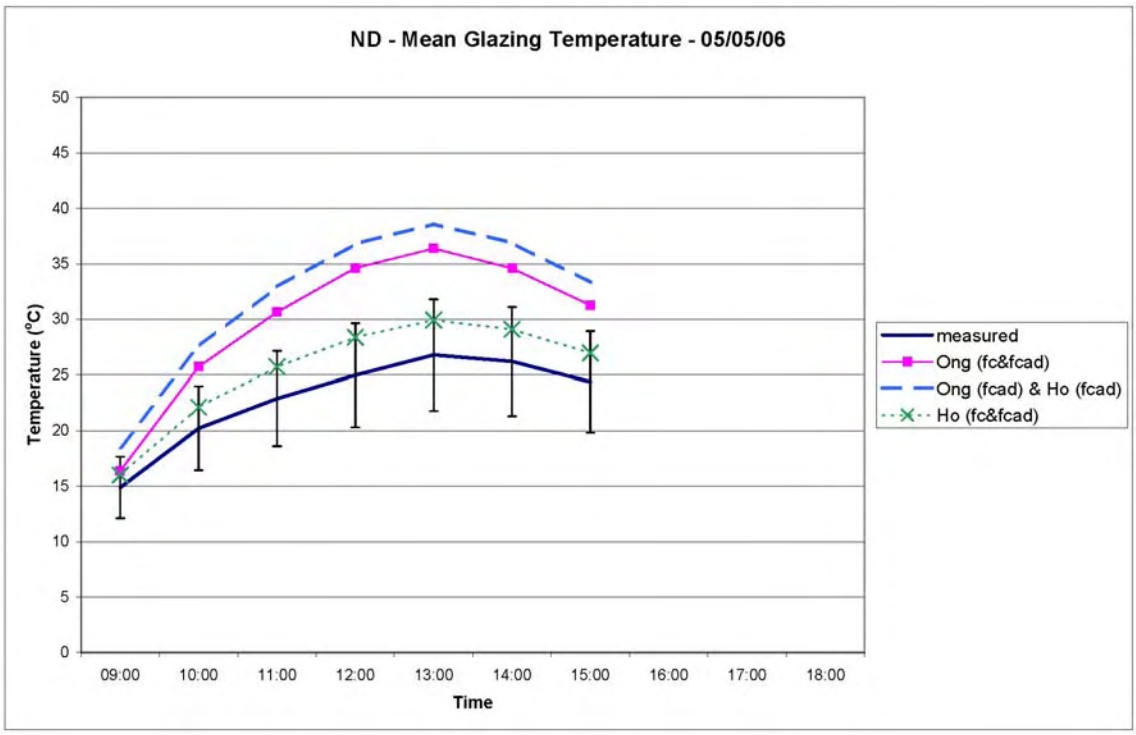

Figure 5.82. ND - Mean Glazing Temperature (Combined Models) - 05/05/06

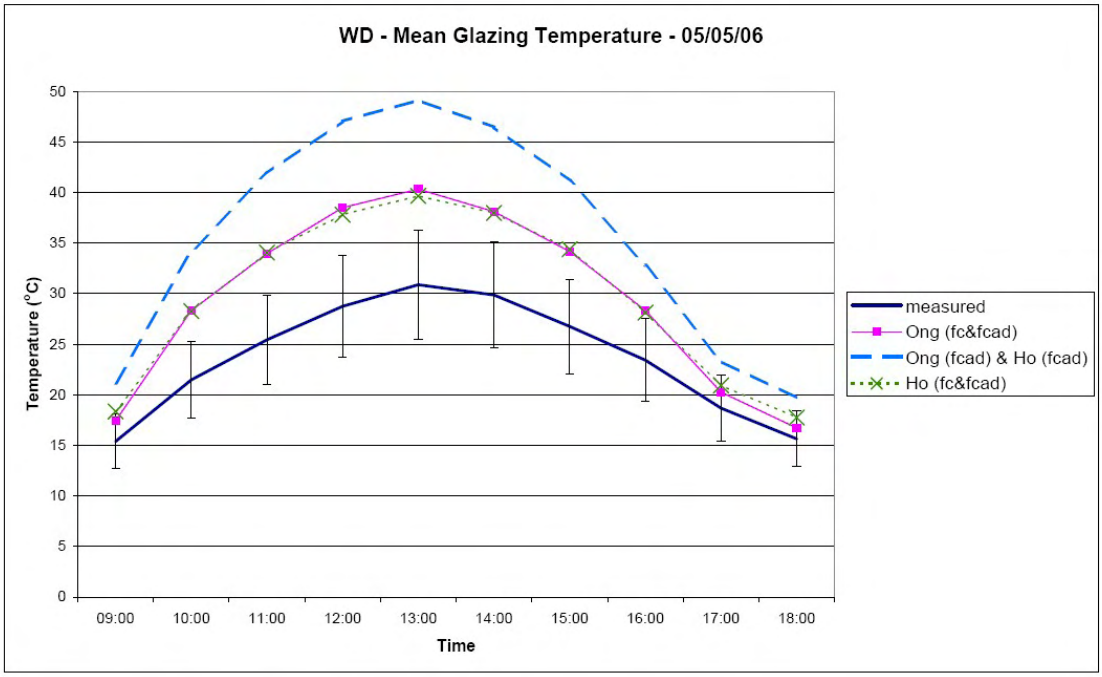

Figure 5.83. WD - Mean Glazing Temperature (Combined Models) - 05/05/06

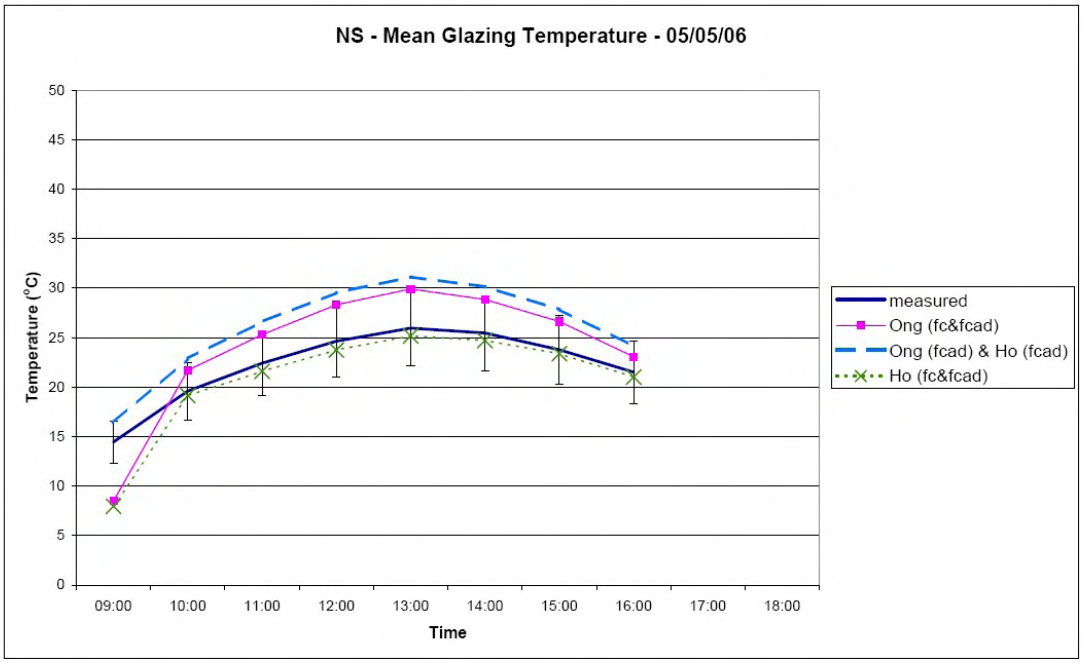

Figure 5.84. NS - Mean Glazing Temperature (Combined Models) - 05/05/06

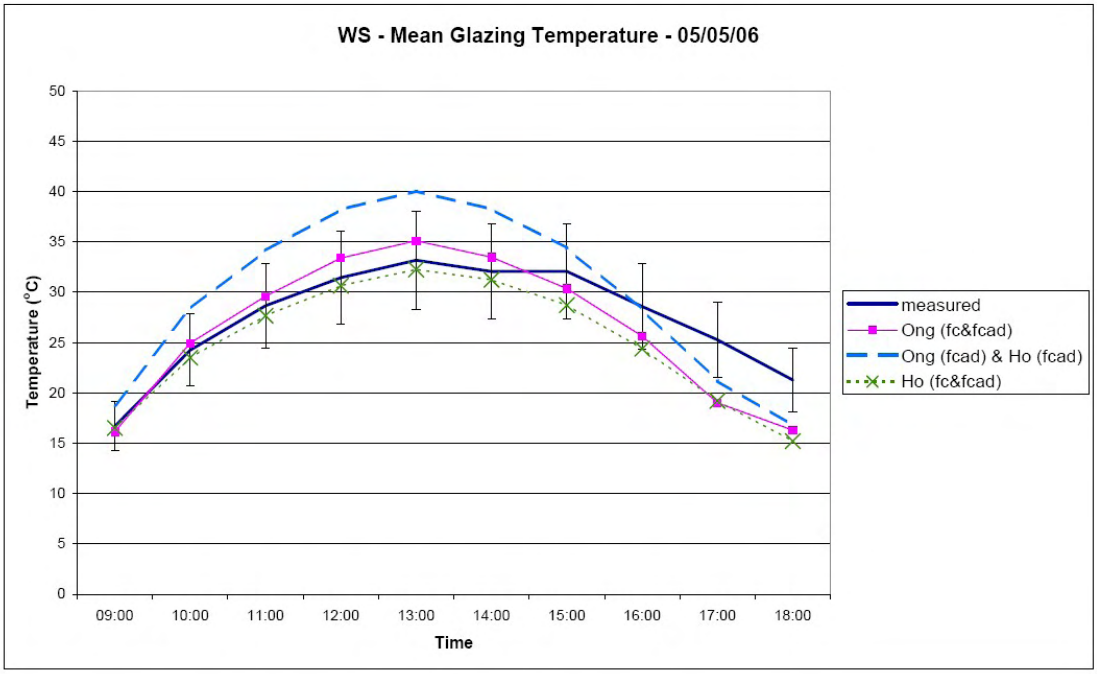

Figure 5.85. WS - Mean Glazing Temperature (Combined Models) - 05/05/06

Table 5.27 indicates the mean bias and RMSE for the three models for 26/01/06. Table 5.28 gives the same information for 05/05/06.

Table 5.27 Bias and RMSE for Prediction of Mean Glazing Temperature - 26/01/06

		$Ong_{fc\&fcad}$	$Ho_{fc\&fcad}$	$OngHo_{fcad}$
Mean Bias (^oC)	ND	9.1	3.8	12.3
	WD	10.5	11.9	21.1
	NS	No data available for comparison		
	WS	3.3	1.7	9.3
	All	7.6	5.8	14.2
RMSE (^oC)	ND	9.4	3.9	12.5
	WD	10.7	12.0	21.4
	NS	No data available for comparison		
	WS	3.5	1.9	9.5
	All	7.4	6.4	13.3

Table 5.28 Bias and RMSE for Prediction of Mean Glazing Temperature - 05/05/06

		$Ong_{fc\&fcad}$	$Ho_{fc\&fcad}$	$OngHo_{fcad}$
Mean Bias (^oC)	ND	8.0	2.8	10.1
	WD	6.0	6.1	12.1
	NS	1.8	-1.4	3.9
	WS	-1.0	-2.4	2.5
	All	3.3	1.9	7.9
RMSE (^oC)	ND	8.1	2.8	10.2
	WD	6.8	6.7	13.2
	NS	3.5	2.4	4.0
	WS	2.9	3.3	4.7
	All	5.6	4.2	9.3

From Table 5.27 it can be seen that all three models tend to overestimate the glazing temperature. The $Ho_{fc\&fcad}$ model has the lowest bias and RMSE. Table 5.28 shows that the $OngHo_{fcad}$ model overestimates the glazing temperature, but the bias for the other two models is less consistent. Again, the $Ho_{fc\&fcad}$ model has the lowest RMSE.

The $Ong_{fc\&fcad}$, $Ho_{fc\&fcad}$ and $OngHo_{fcad}$ models all make closer predictions of the mean glazing temperature than the Ong_{fcad} and Ho_{fcad}; however, Ong_{fc} is still the closest predictor of the mean glazing temperature.

5.1.8.2 Prediction of Mean Absorbing Surface Temperature

The following graphs show the correlation between the measured mean absorbing surface temperature for ducts ND, WD, NS and WS and the predictions given by $Ong_{fc\&fcad}$, $Ho_{fc\&fcad}$, and $OngHo_{fcad}$.

Figures 5.86 - 5.89 show the correlation for 26/01/06 and Figures 5.90 - 5.93 for 05/05/06.

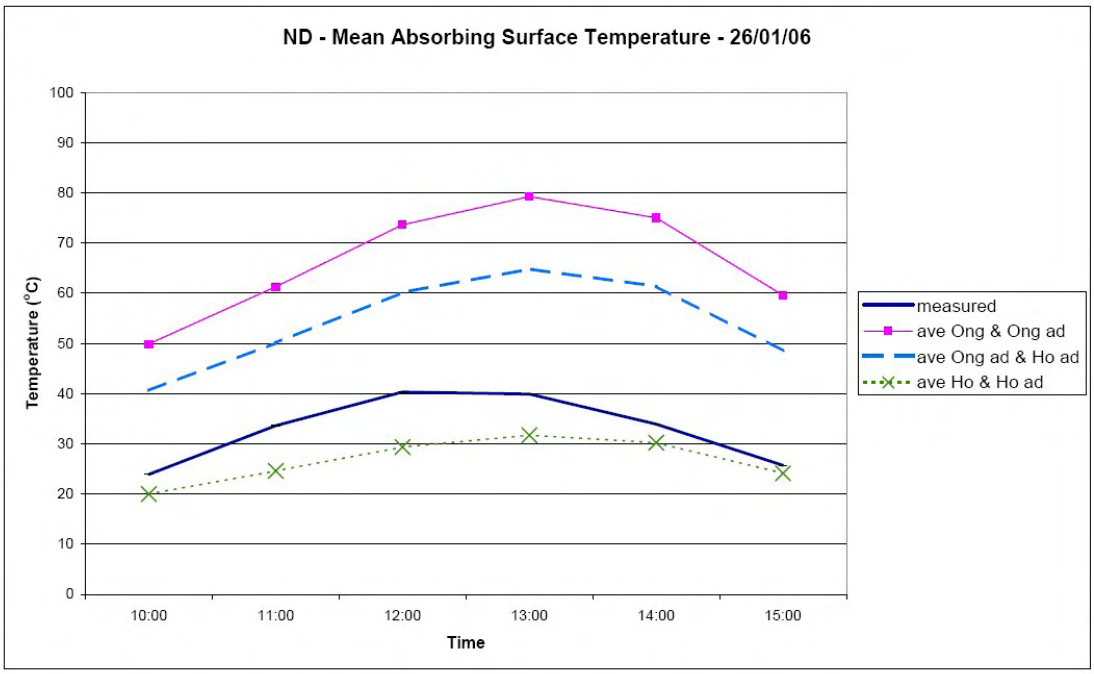

Figure 5.86. ND - Mean Absorbing Surface Temperature (Combined Models) - 26/01/06

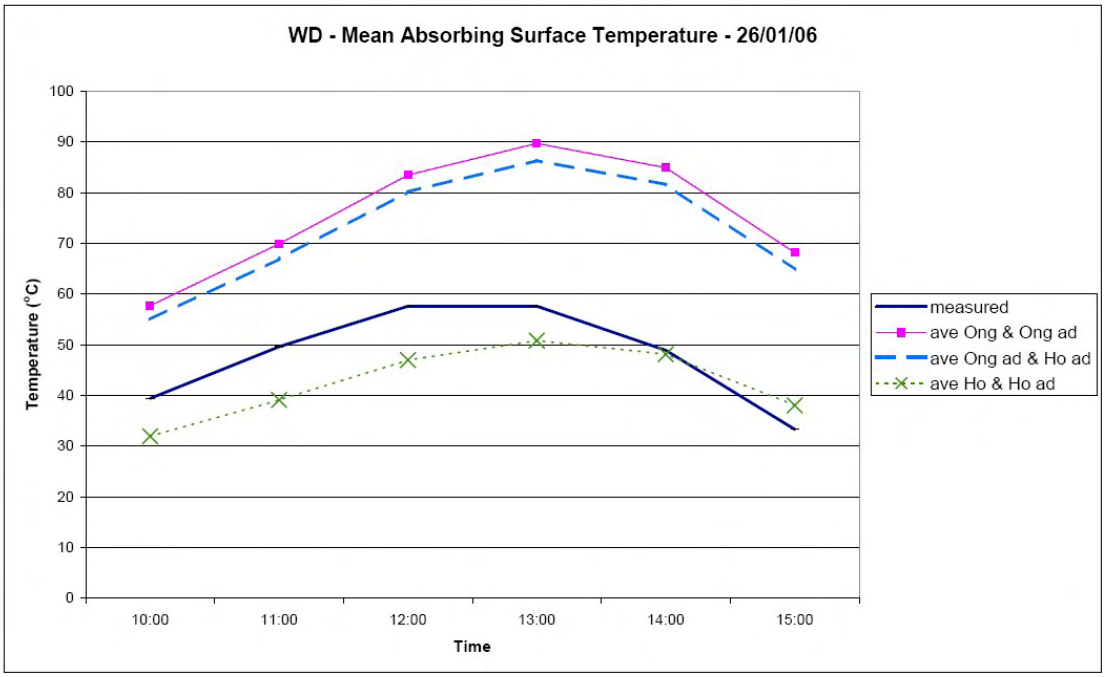

Figure 5.87. WD - Mean Absorbing Surface Temperature (Combined Models) - 26/01/06

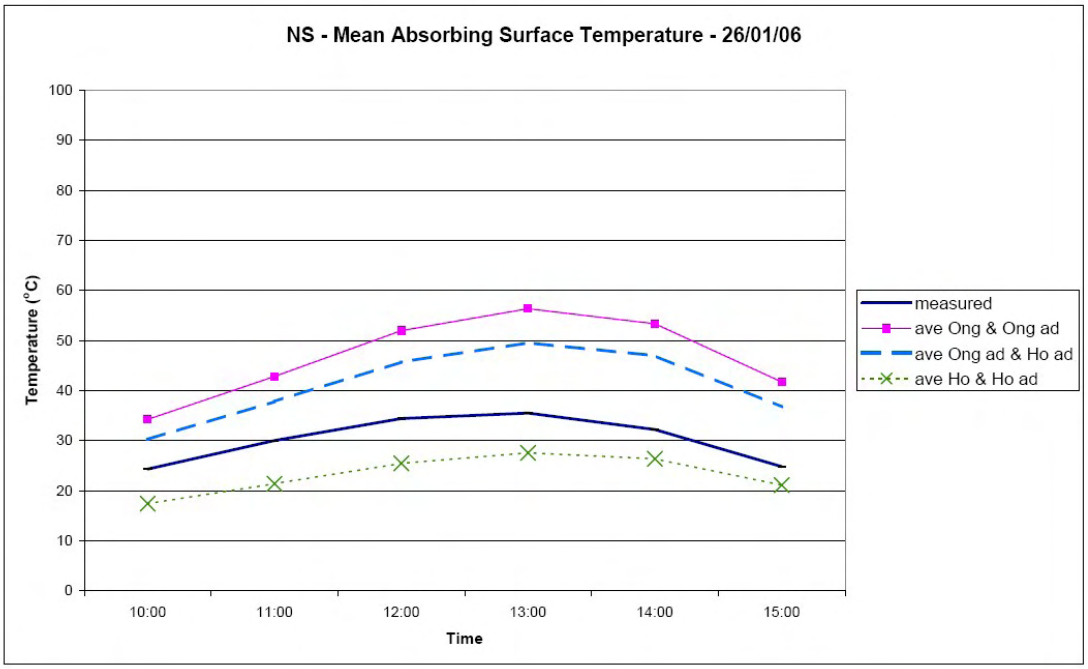

Figure 5.88. NS - Mean Absorbing Surface Temperature (Combined Models) - 26/01/06

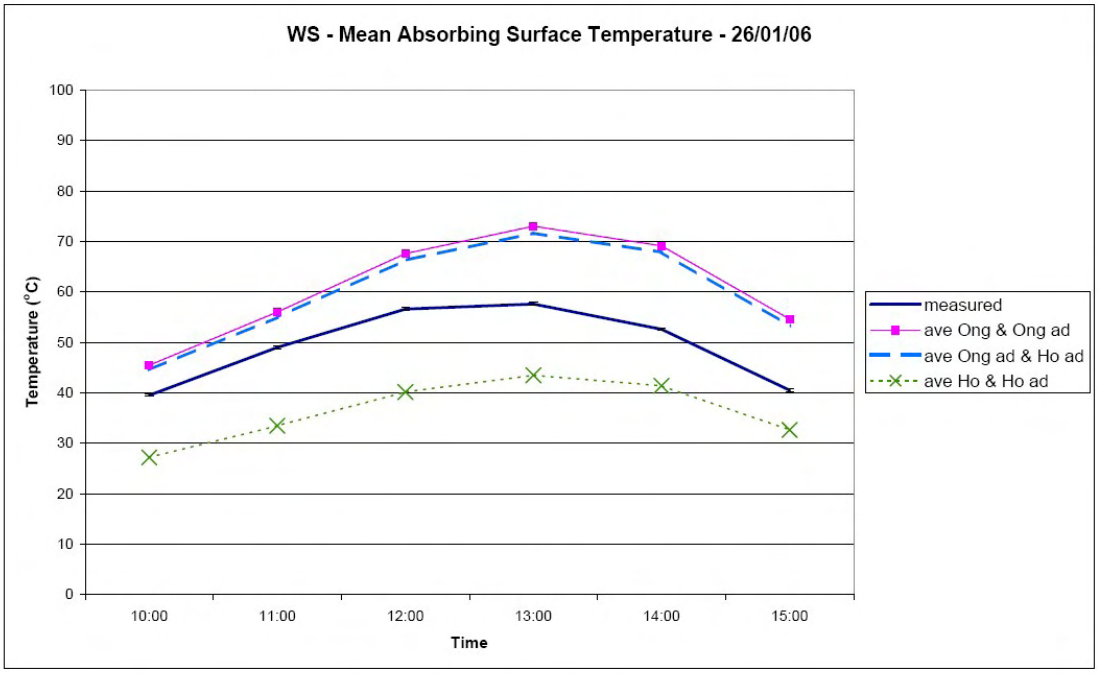

Figure 5.89. WS - Mean Absorbing Surface Temperature (Combined Models) - 26/01/06

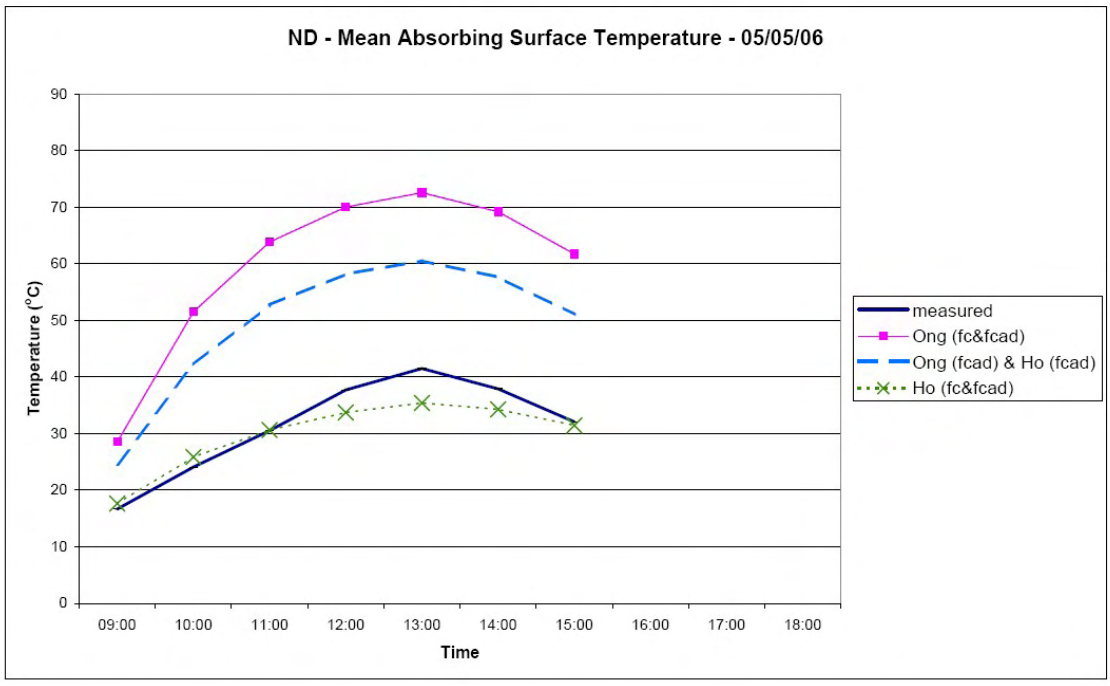

Figure 5.90. ND - Mean Absorbing Surface Temperature (Combined Models) - 05/05/06

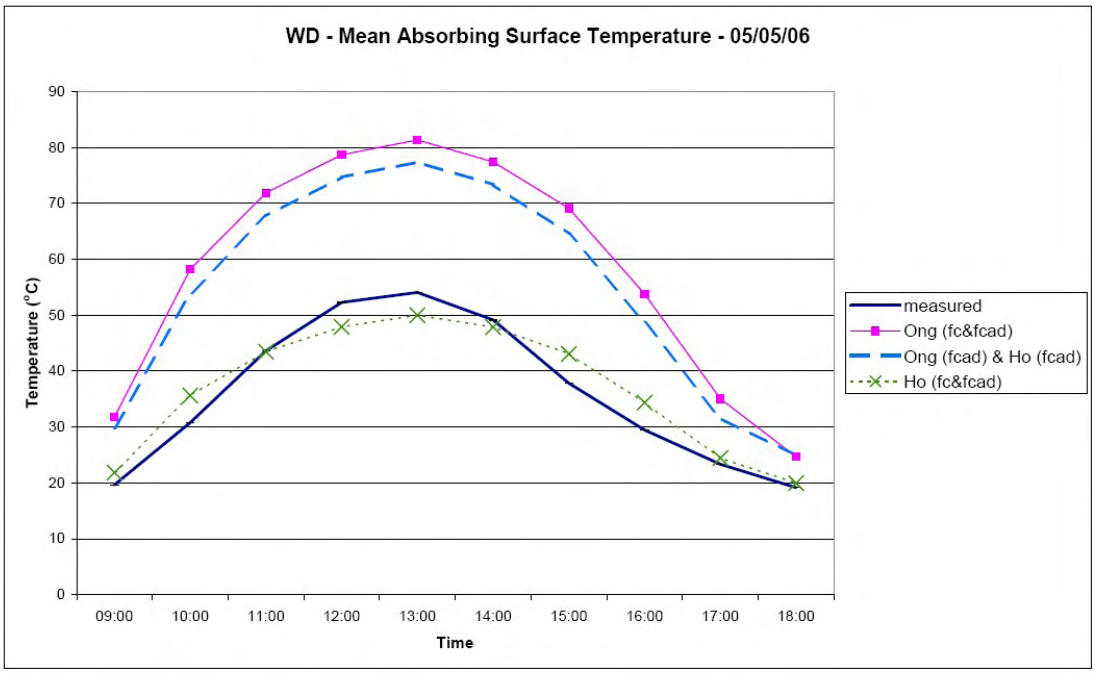

Figure 5.91. WD - Mean Absorbing Surface Temperature (Combined Models) - 05/05/06

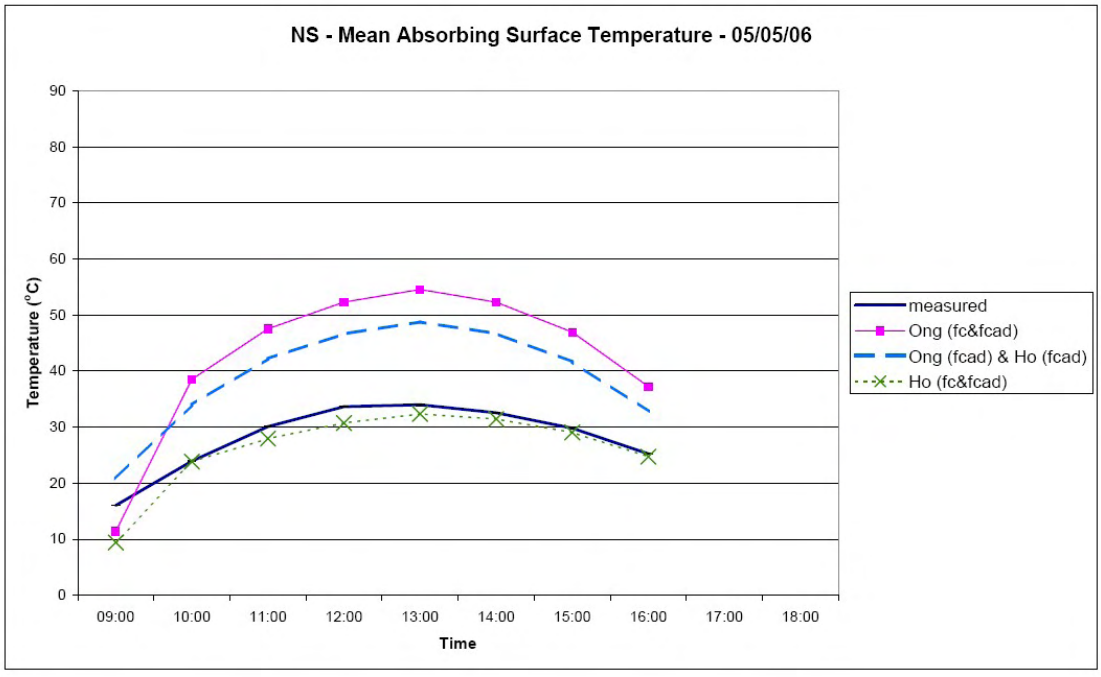

Figure 5.92. NS - Mean Absorbing Surface Temperature (Combined Models) - 05/05/06

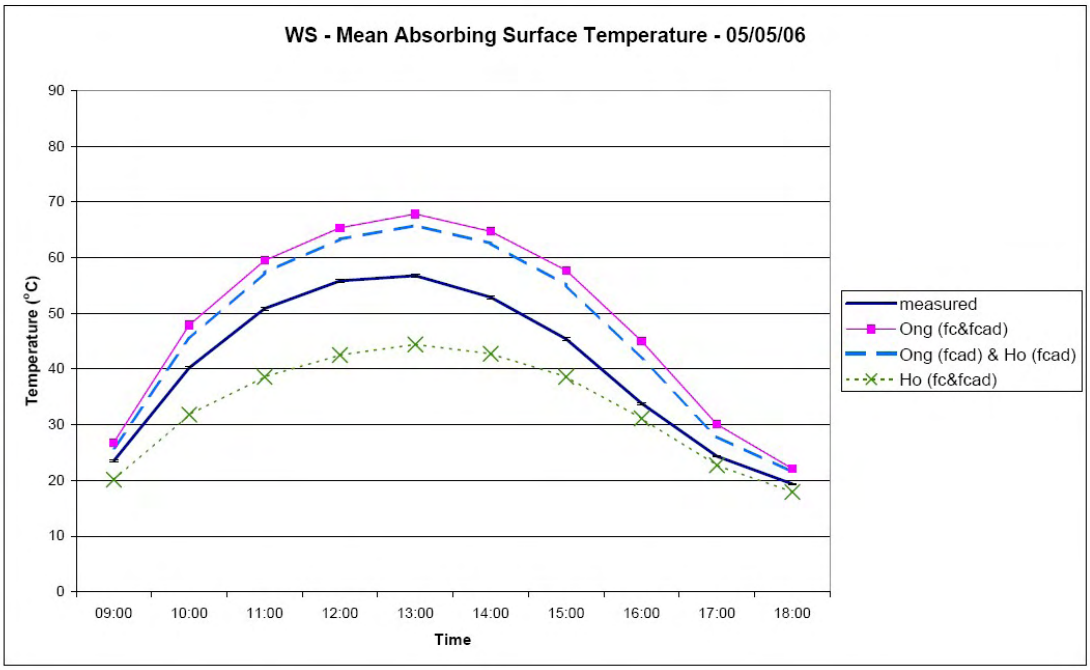

Figure 5.93. WS - Mean Absorbing Surface Temperature (Combined Models) - 05/05/06

Table 5.29 indicates the mean bias and RMSE for the three models for 26/01/06. Table 5.30 gives the same information for 05/05/06.

Table 5.29 Bias and RMSE for Prediction of Absorbing Surface Temperature - 26/01/06

		$Ong_{fc\&fcad}$	$Ho_{fc\&fcad}$	$OngHo_{fcad}$
Mean Bias (°C)	ND	33.6	-6.2	21.4
	WD	27.9	-5.3	24.7
	NS	16.5	-7.0	11.0
	WS	11.7	-12.9	10.5
	All	22.4	-7.8	16.9
RMSE (°C)	ND	34.0	7.1	21.8
	WD	28.8	7.7	25.6
	NS	17.0	7.2	11.4
	WS	12.4	13.3	11.2
	All	24.6	9.2	18.6

Table 5.30 Bias and RMSE for Prediction of Absorbing Surface Temperature – 05/05/06

		$Ong_{fc\&fcad}$	$Ho_{fc\&fcad}$	$OngHo_{fcad}$
Mean Bias (^oC)	ND	30.8	-2.1	19.7
	WD	22.3	0.9	18.7
	NS	14.4	-2.0	11.0
	WS	8.4	-7.3	6.3
	All	19.0	-2.8	14.3
RMSE (^oC)	ND	30.9	3.4	19.8
	WD	23.8	3.5	20.1
	NS	16.3	2.8	11.5
	WS	9.0	8.5	6.9
	All	21.4	5.6	15.9

From Table 5.29 it can be seen that $Ong_{fc\&fcad}$ and $OngHo_{fcad}$ tend to overestimate the absorbing surface temperature, while the $Ho_{fc\&fcad}$ model tends to underestimate it. The $Ho_{fc\&fcad}$ model has the lowest bias and RMSE. Table 5.30 shows a similar trend, although the bias of the $Ho_{fc\&fcad}$ model is less consistent.

The $Ong_{fc\&fcad}$ model had lower bias and RMSE than the Ong_{fcad} model, similarly the $Ho_{fc\&fcad}$ model had lower bias and RMSE than the Ho_{fcad} and Ho_{fc} models. The $OngHo_{fcad}$ model had lower bias and RMSE than the Ong_{fcad} model but not the Ho_{fcad} model. However, Yeh_{fc} remains the closest predictor of the mean absorbing surface temperature.

5.1.8.3 Prediction of Duct Mean Air Temperature

The following graphs show the correlation between the measured mean air temperature for ducts ND, WD, NS and WS and the predictions given by $Ong_{fc\&fcad}$, $Ho_{fc\&fcad}$, and $OngHo_{fcad}$.

Figures 5.94 - 5.97 show the correlation for 26/01/06 and Figures 5.98 - 5.101 for 05/05/06.

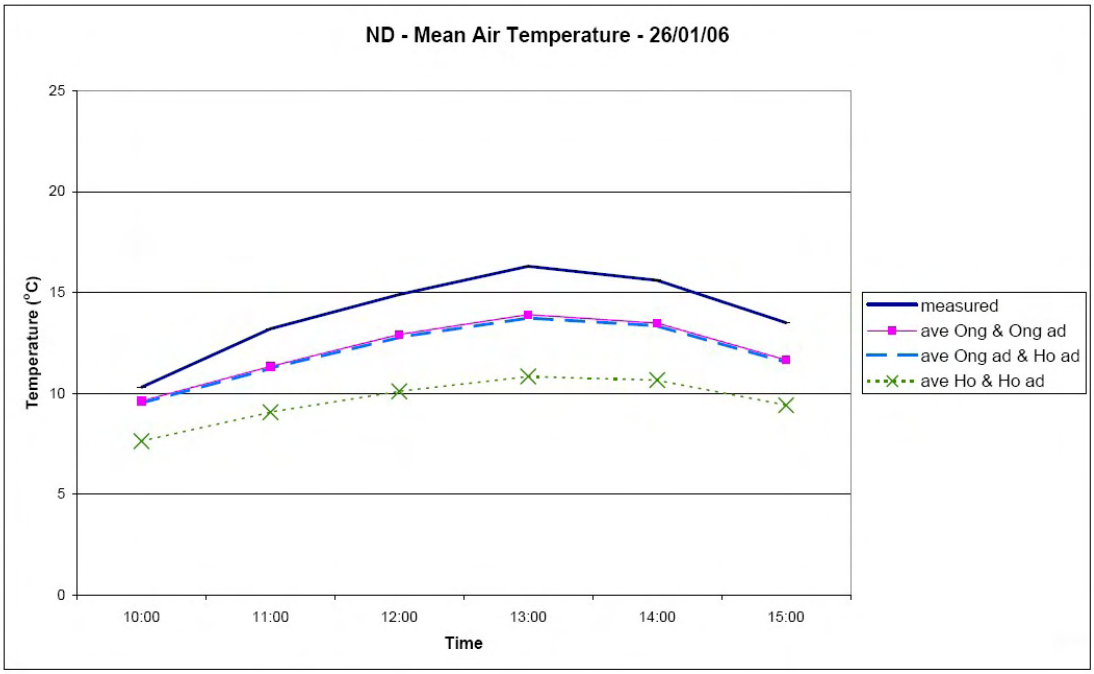

Figure 5.94. ND - Mean Air Temperature (Combined Models) - 26/01/06

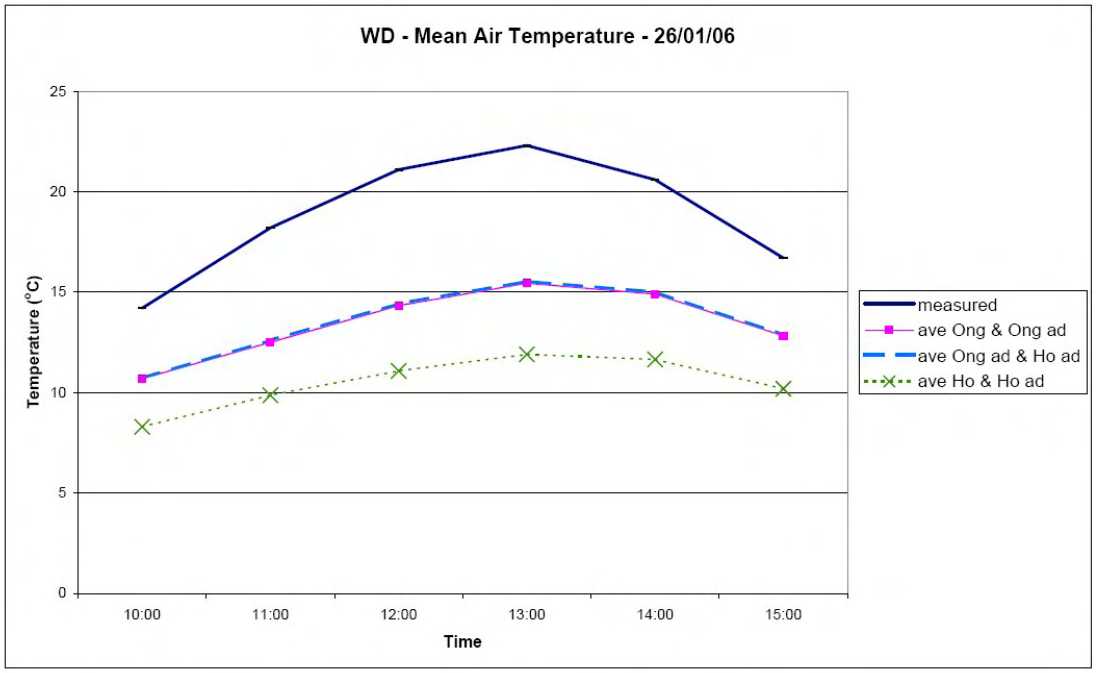

Figure 5.95. WD - Mean Air Temperature (Combined Models) - 26/01/06

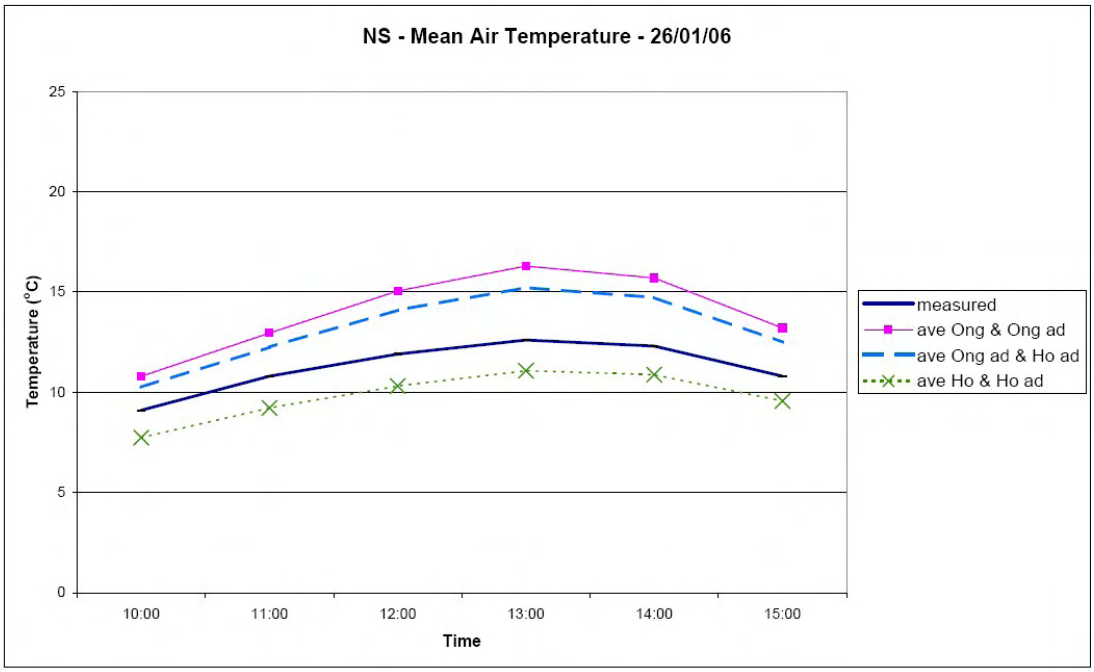

Figure 5.96. NS - Mean Air Temperature (Combined Models) - 26/01/06

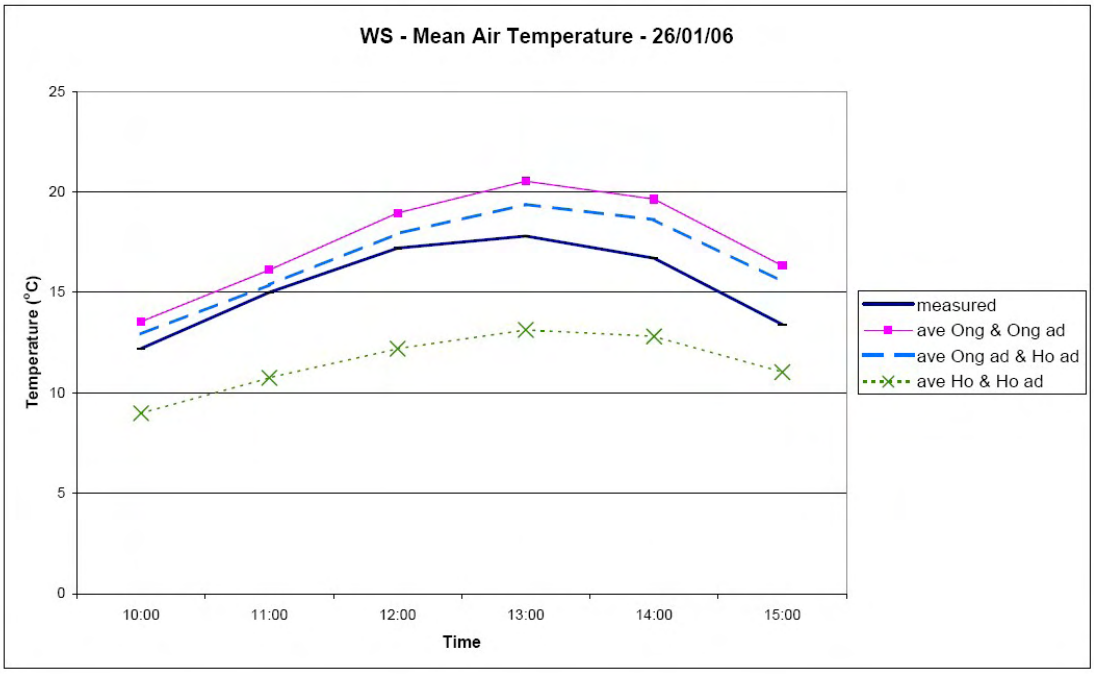

Figure 5.97. WS - Mean Air Temperature (Combined Models) - 26/01/06

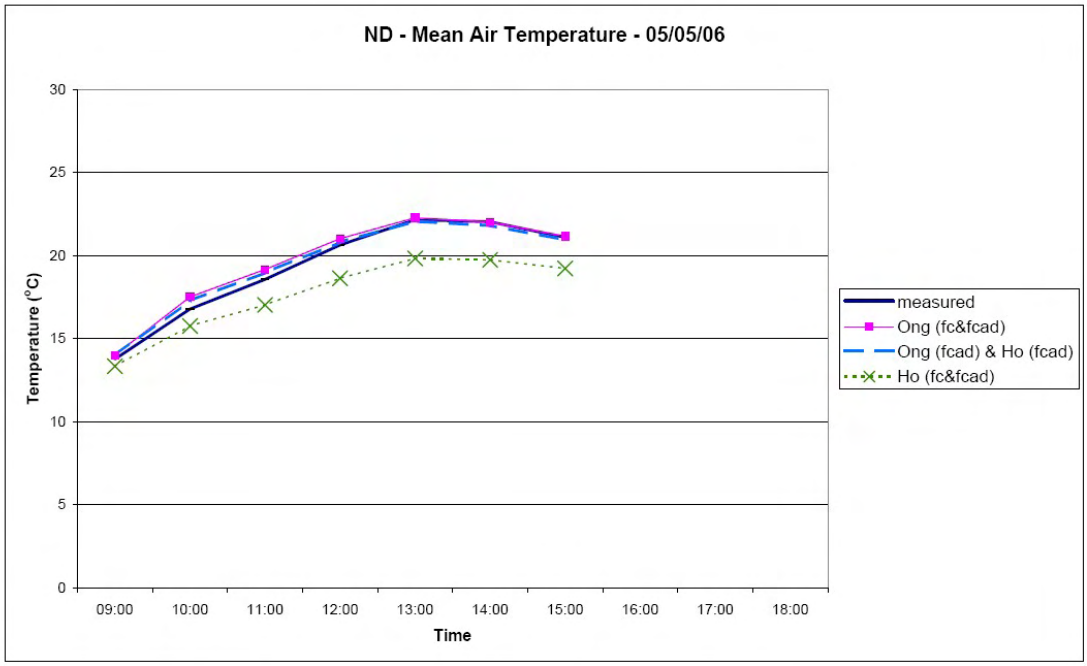

Figure 5.98. ND - Mean Air Temperature (Combined Models) - 05/05/06

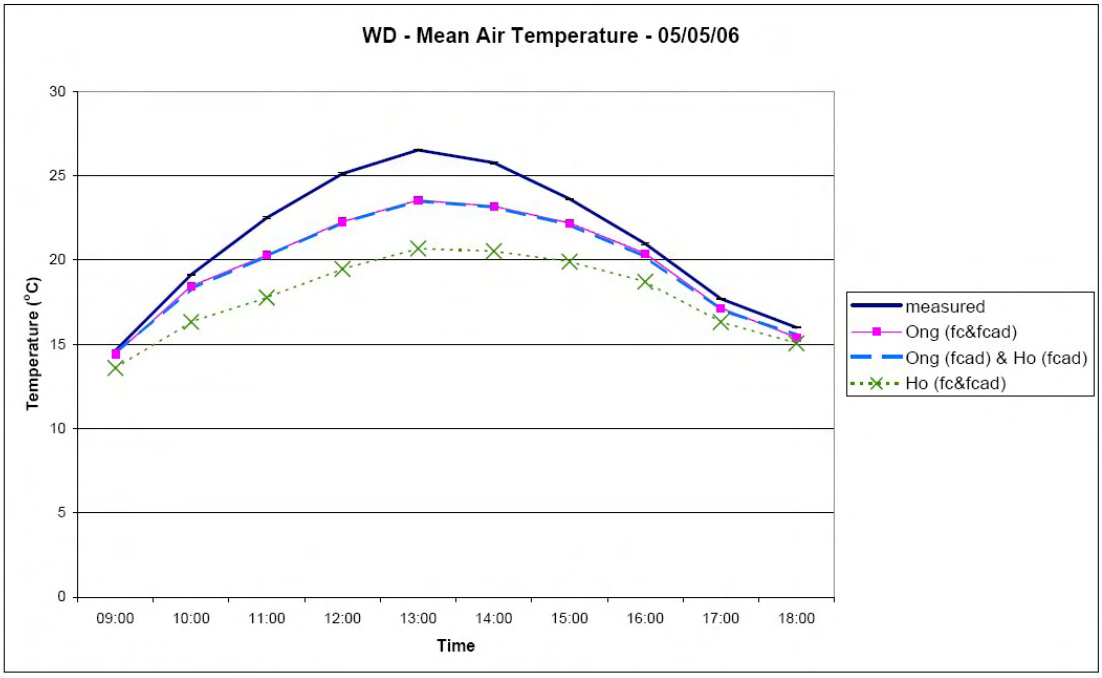

Figure 5.99. WD - Mean Air Temperature (Combined Models) - 05/05/06

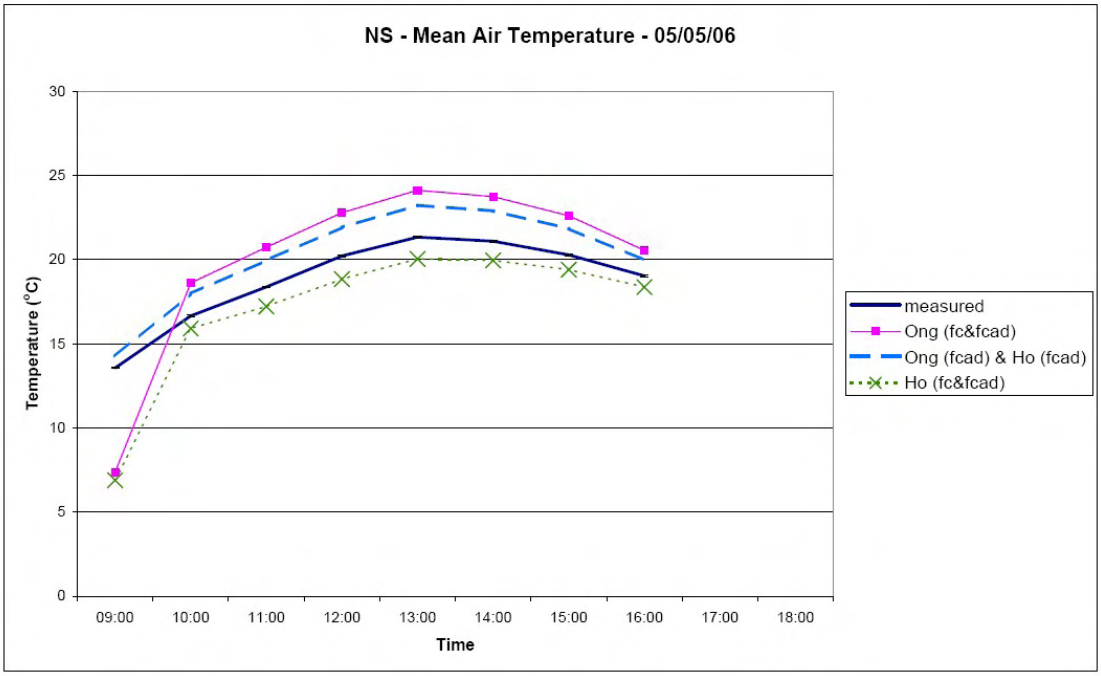

Figure 5.100. NS - Mean Air Temperature (Combined Models) - 05/05/06

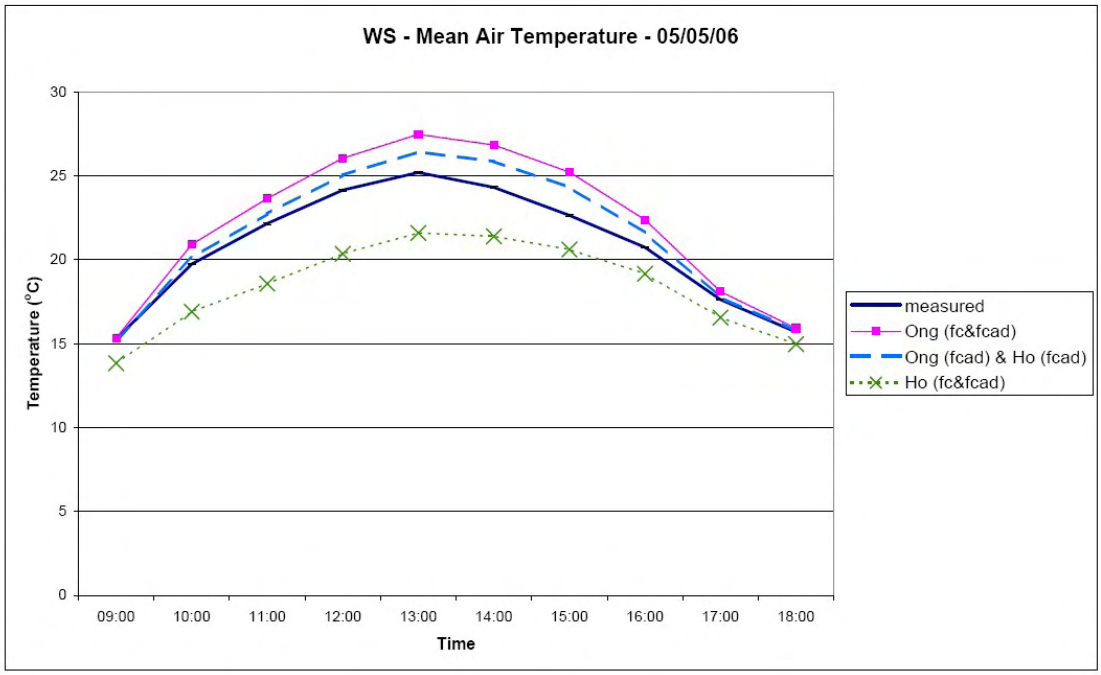

Figure 5.101. WS - Mean Air Temperature (Combined Models) - 05/05/06

Table 5.31 indicates the mean bias and RMSE for the three models for 26/01/06. Table 5.32 gives the same information for 05/05/06.

Table 5.31 Bias and RMSE for Prediction of Mean Air Temperature - 26/01/06

		$Ong_{fc\&fcad}$	$Ho_{fc\&fcad}$	$OngHo_{fcad}$
Mean Bias (^oC)	ND	-1.8	-4.4	-1.9
	WD	-5.4	-8.4	-5.3
	NS	2.7	-1.5	1.9
	WS	2.1	-3.9	1.2
	All	-0.6	-4.5	-1.0
RMSE (^oC)	ND	1.9	4.4	2.0
	WD	5.6	8.5	5.5
	NS	2.8	1.5	2.0
	WS	2.3	4.0	1.4
	All	3.5	5.3	3.2

Table 5.32 Bias and RMSE for Prediction of Mean Air Temperature – 05/05/06

		$Ong_{fc\&fcad}$	$Ho_{fc\&fcad}$	$OngHo_{fcad}$
Mean Bias (^oC)	ND	0.3	-1.8	0.1
	WD	-1.5	-3.4	-1.5
	NS	1.2	-1.7	1.4
	WS	1.4	-2.4	0.7
	All	0.3	-2.5	0.1
RMSE (^oC)	ND	0.4	1.9	0.3
	WD	1.8	3.8	1.8
	NS	3.1	2.6	1.5
	WS	1.7	2.6	0.9
	All	2.1	3.0	1.4

From Table 5.31 it can be seen that the $Ho_{fc\&fcad}$ model tends to underestimate the mean air temperature. $Ong_{fc\&fcad}$ and $OngHo_{fcad}$ do not have a consistent bias, and have a lower RMSE. Table 5.32 shows a similar trend. Statistically the performance of $Ong_{fc\&fcad}$ and $OngHo_{fcad}$ are similar when considered over the two dates.

The $Ong_{fc\&fcad}$ model had lower bias for January than the Ong_{fc} model and lower bias in May than the Ong_{fcad} model; however, the RMSE values did not reduce. The $Ho_{fc\&fcad}$ model had lower bias and RMSE for both months than Ho_{fc} and Ho_{fcad}. The $OngHo_{fcad}$ model had a lower bias than Ho_{fc} and Ho_{fcad} and a lower RMSE than Ong_{fc} and Ong_{fcad}. The $OngHo_{fcad}$ model has the lowest combination of bias and RMSE, and as such is considered the closest model. In particular, it should be noted that it meets the

requirement of having a bias and RMSE less than 2°C for each duct in May, although this is exceeded for duct WD in January.

5.1.8.4 Prediction of Exit Air Temperature

The exit air temperature is proportional to the power output. The following graphs show the correlation between the measured exit air temperature for ducts ND, WD, NS and WS and the predictions given by $Ong_{fc\&fcad}$, $Ho_{fc\&fcad}$, and $OngHo_{fcad}$.

Figures 5.102 - 5.105 show the correlation for 26/01/06 and Figures 5.106 - 5.109 for 05/05/06.

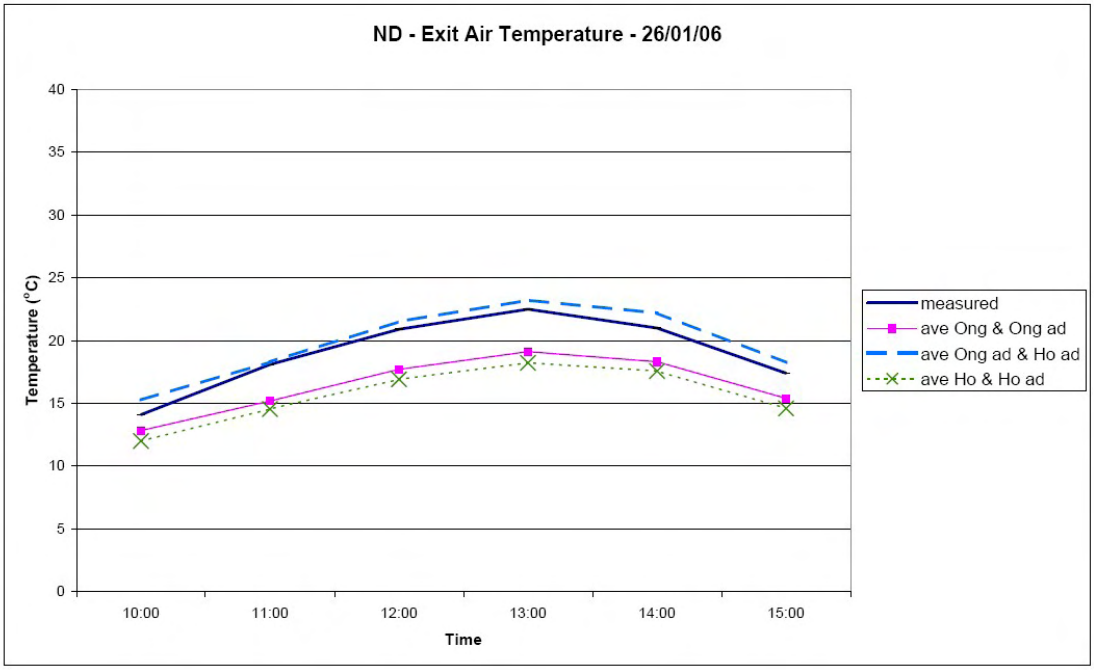

Figure 5.102. ND - Exit Air Temperature (Combined Models) - 26/01/06

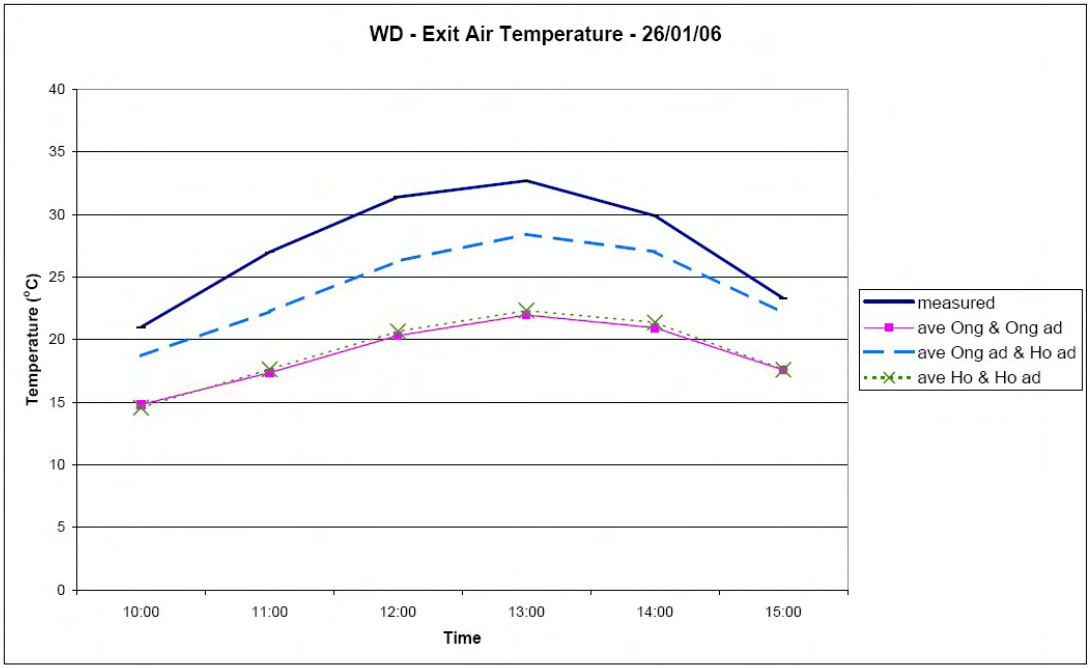

Figure 5.103. WD - Exit Air Temperature (Combined Models) - 26/01/06

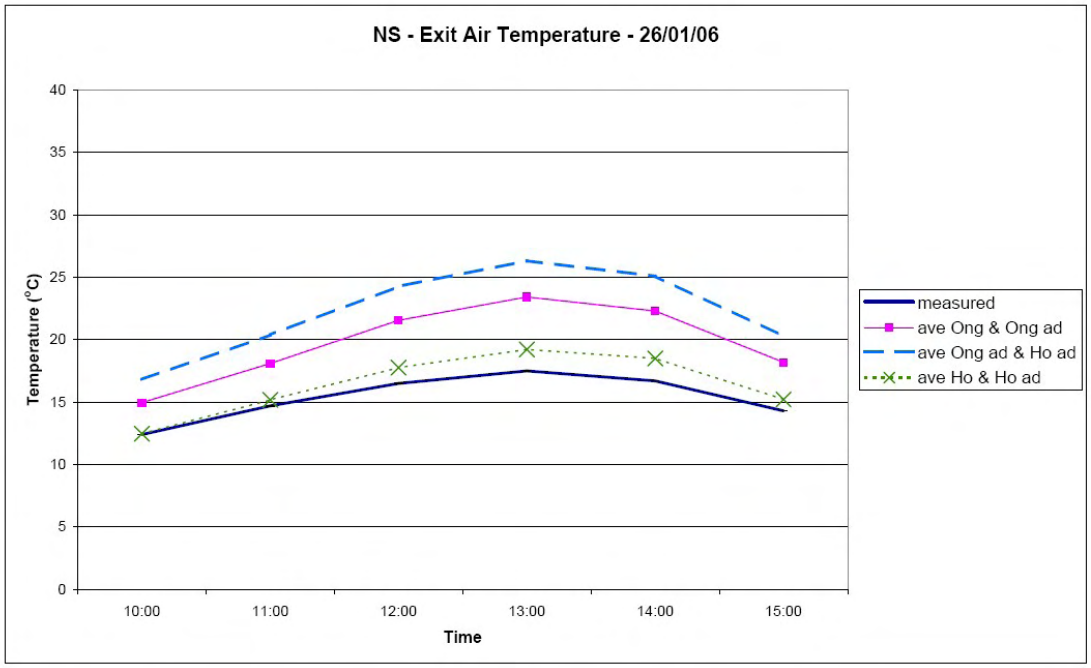

Figure 5.104. NS - Exit Air Temperature (Combined Models) - 26/01/06

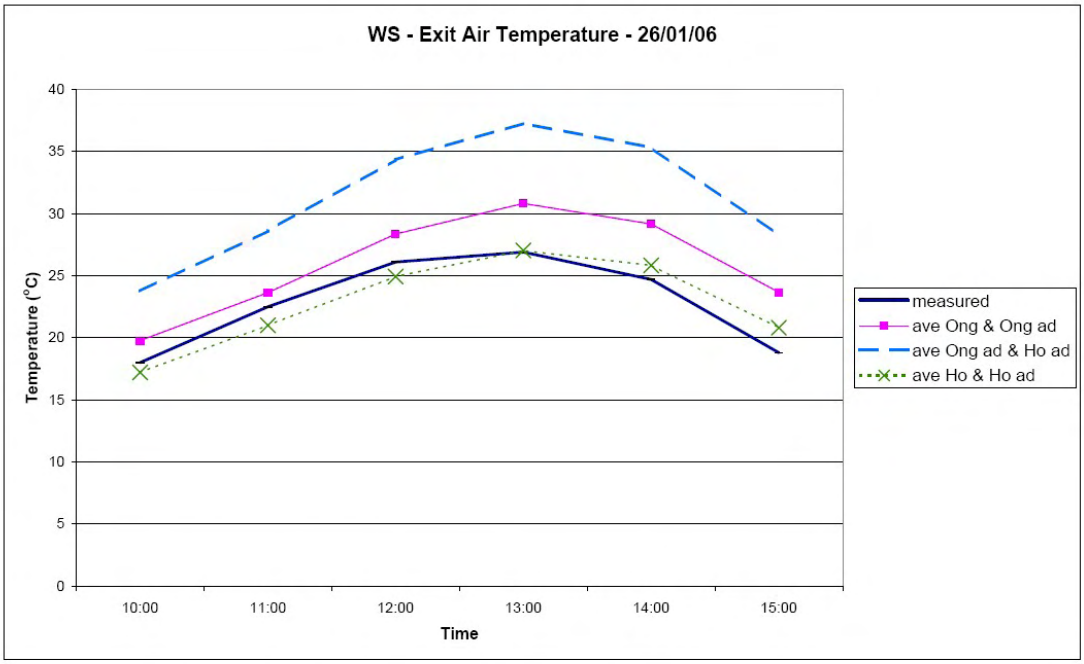

Figure 5.105. WS - Exit Air Temperature (Combined Models) - 26/01/06

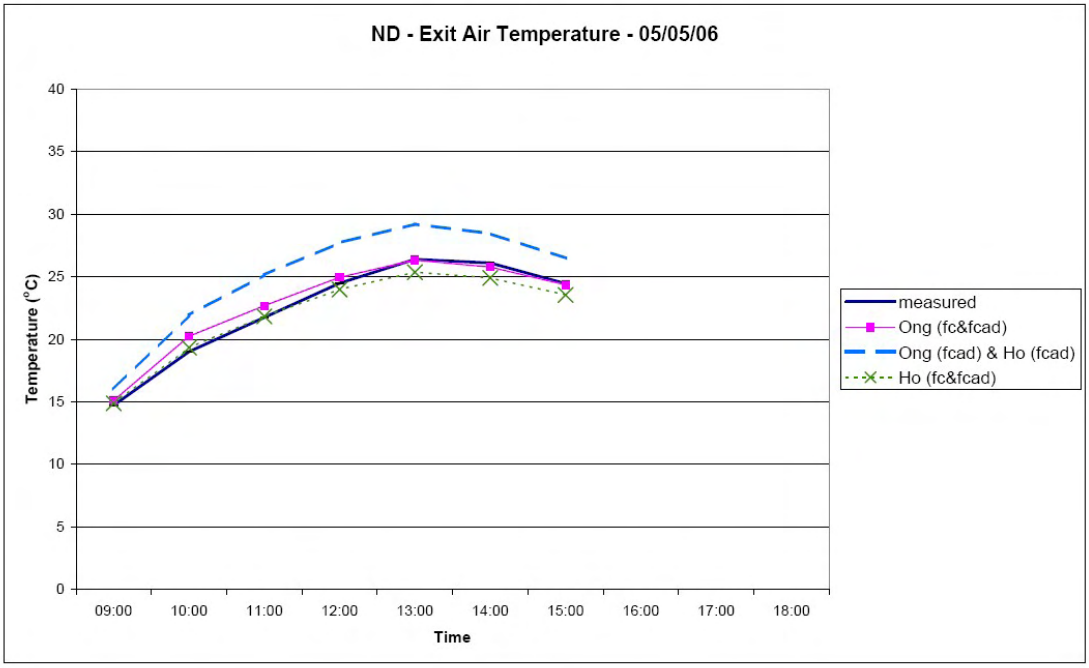

Figure 5.106. ND - Exit Air Temperature (Combined Models) - 05/05/06

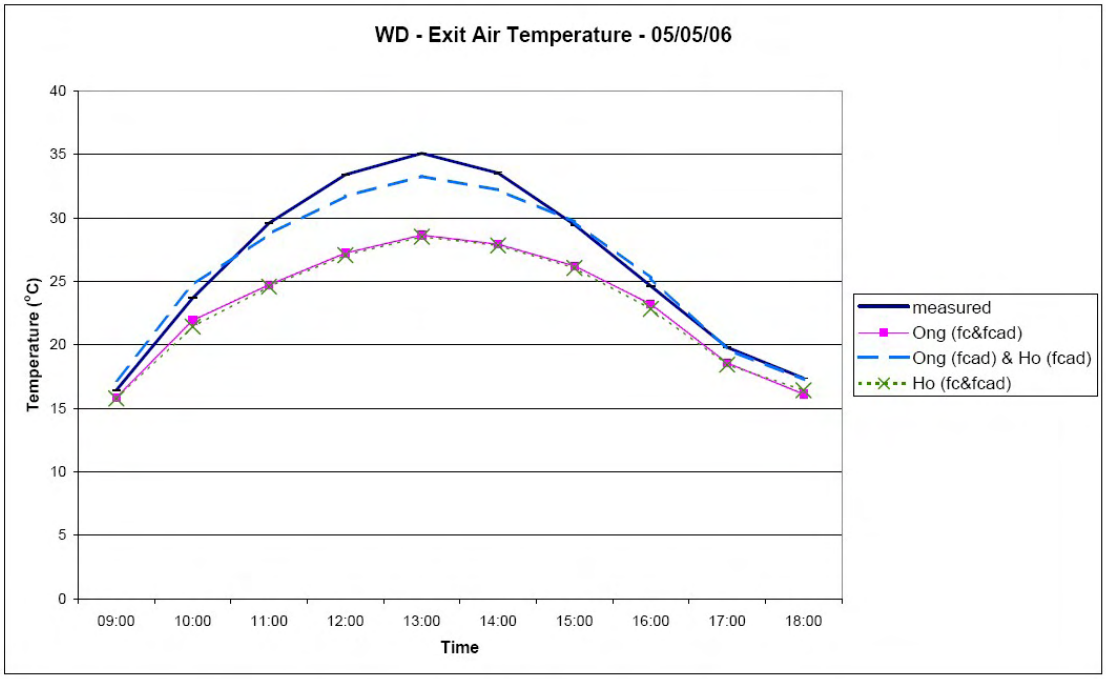

Figure 5.107. WD - Exit Air Temperature (Combined Models) - 05/05/06

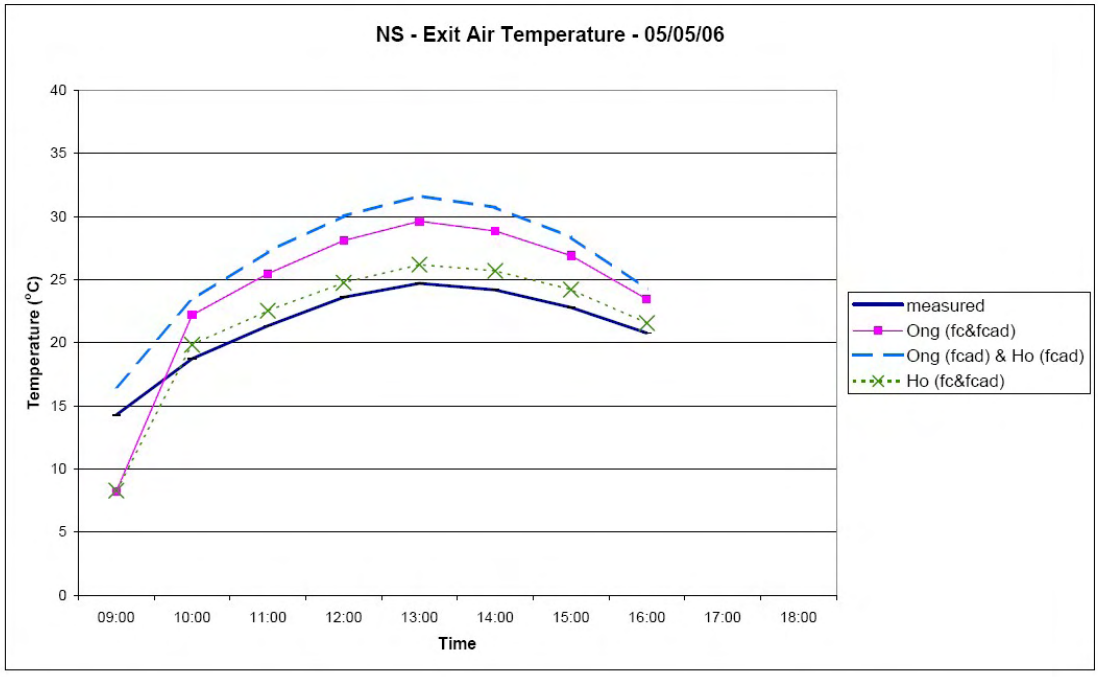

Figure 5.108. NS - Exit Air Temperature (Combined Models) - 05/05/06

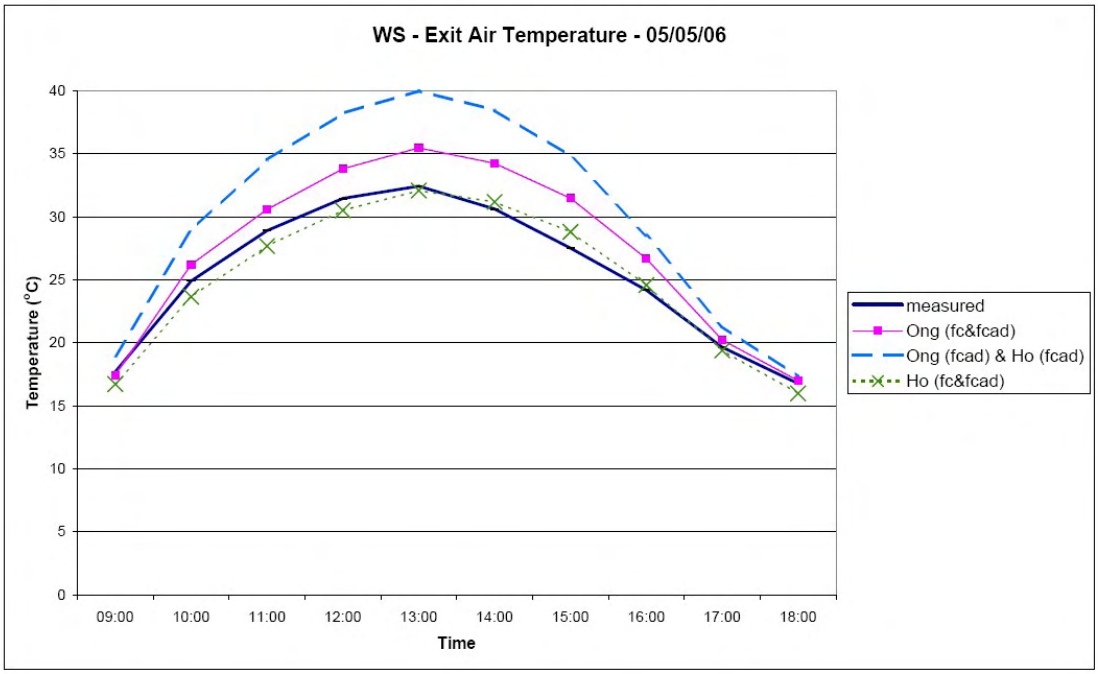

Figure 5.109. WS - Exit Air Temperature (Combined Models) - 05/05/06

Table 5.33 indicates the mean bias and RMSE for the three models for 26/01/06. Table 5.34 gives the same information for 05/05/06.

Table 5.33 Bias and RMSE for Prediction of Exit Air Temperature - 26/01/06

		Ave Ong & Ong_{ad}	Ave Ho & Ho_{ad}	Ave Ong_{ad} & Ho_{ad}
Mean Bias (^oC)	ND	-2.6	-3.4	0.8
	WD	-8.7	-8.5	-3.4
	NS	4.4	1.0	6.8
	WS	3.1	0	8.4
	All	-1.0	-2.7	3.2
RMSE (^oC)	ND	2.7	3.4	0.9
	WD	9.0	8.7	3.7
	NS	4.6	1.2	7.0
	WS	3.4	1.3	8.6
	All	5.5	4.8	5.9

Table 5.34 Bias and RMSE for Prediction of Exit Air Temperature – 05/05/06

		Ave Ong & Ong_{ad}	Ave Ho & Ho_{ad}	Ave Ong_{ad} & Ho_{ad}
Mean Bias (^oC)	ND	0.4	-0.5	2.8
	WD	-3.5	-3.4	-0.2
	NS	2.8	0.3	4.7
	WS	1.9	-0.4	3.9
	All	0.2	-1.2	2.7
RMSE (^oC)	ND	0.7	0.8	2.8
	WD	3.9	4.0	1.0
	NS	4.4	2.4	5.4
	WS	2.3	0.9	5.4
	All	3.4	2.7	4.3

From Table 5.33 it can be seen that none of the models have a consistent bias. Of the three models, $Ong_{fc\&fcad}$ has the least bias and $Ho_{fc\&fcad}$ has the lowest RMSE. Table 5.34 shows a similar trend.

The $Ong_{fc\&fcad}$ model had lower bias and RMSE for January than the Ong_{fc} model than the Ong_{fcad} model; however, the RMSE values did not reduce. The $Ho_{fc\&fcad}$ model had lower bias and RMSE for both months than Ho_{fc} and Ho_{fcad}. The $OngHo_{fcad}$ model had a lower bias than Ho_{fc} and Ho_{fcad}. The $Ong_{fc\&fcad}$ model has the lowest combination of bias and RMSE, and as such is considered the closest model.

5.1.8.5 Prediction of Power Output

The following graphs show the correlation between the calculated power output for ducts ND, WD, NS and WS and the predictions given by $Ong_{fc\&fcad}$, $Ho_{fc\&fcad}$, and $OngHo_{fcad}$.

Figures 5.110 - 5.113 show the correlation for 26/01/06 and Figures 5.114 - 5.117 for 05/05/06.

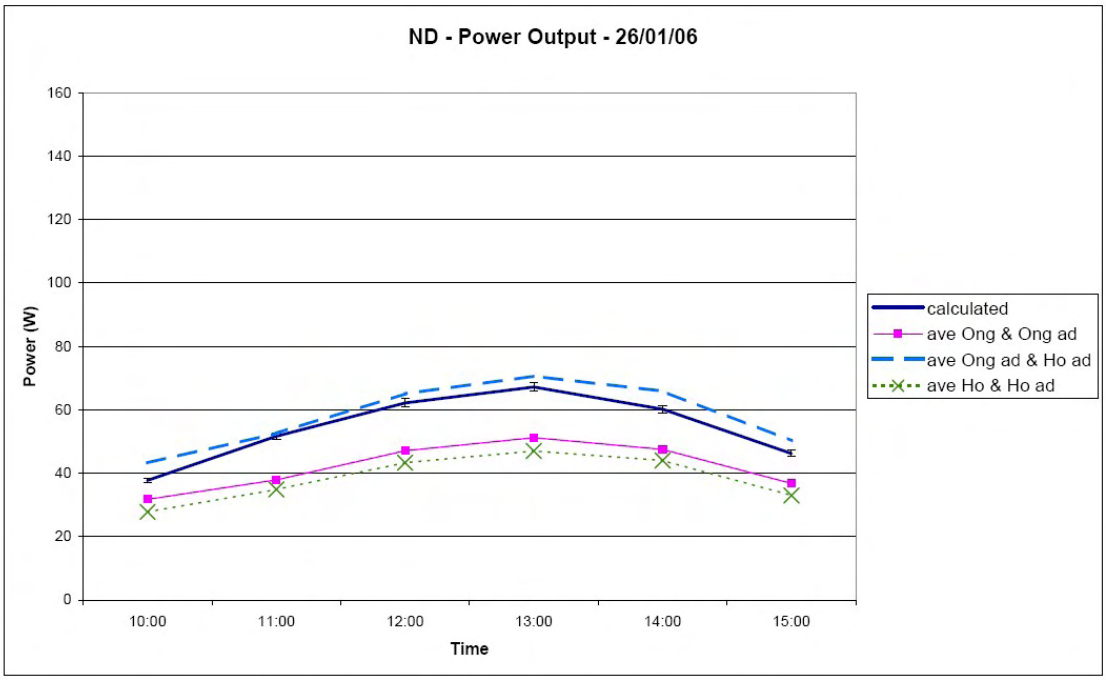

Figure 5.110. ND - Power Output (Combined Models) - 26/01/06

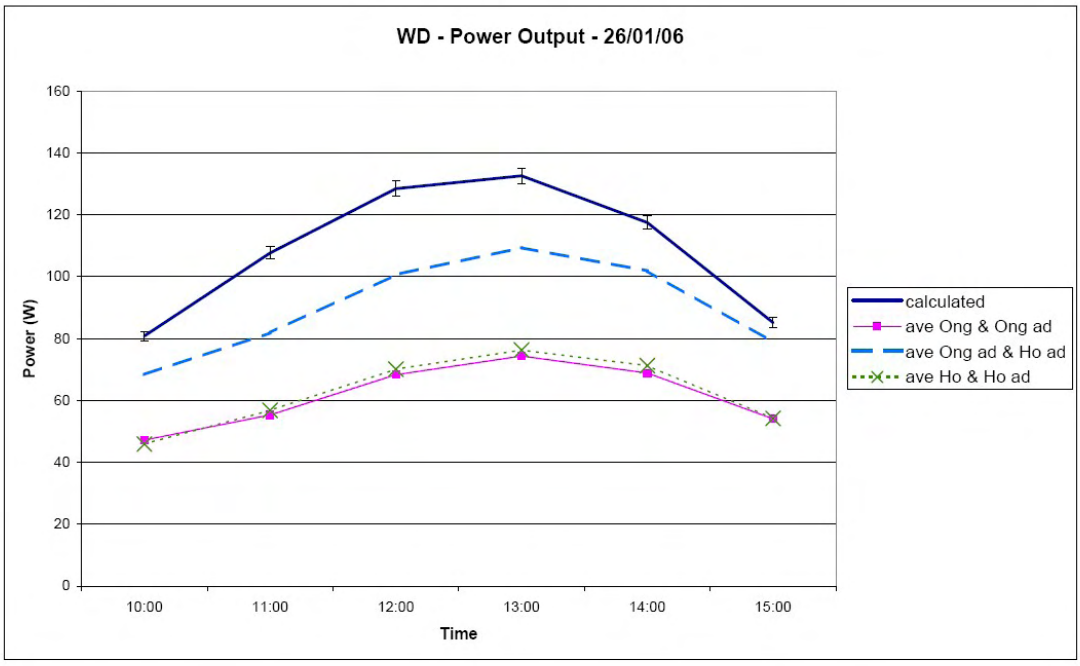

Figure 5.111. WD - Power Output (Combined Models) - 26/01/06

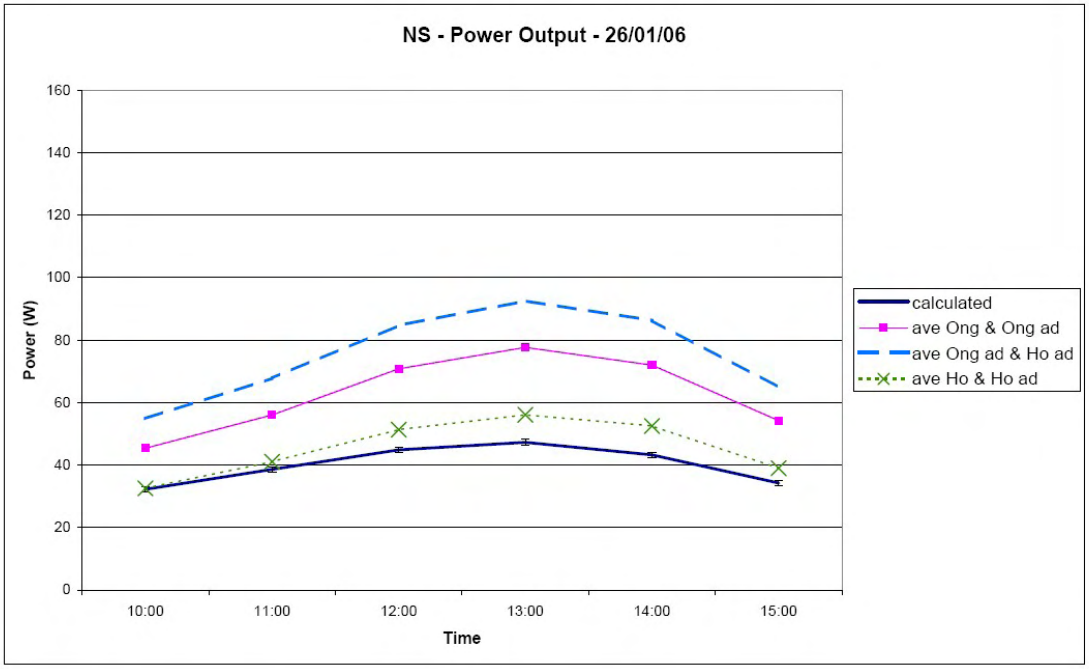

Figure 5.112. NS - Power Output (Combined Models) - 26/01/06

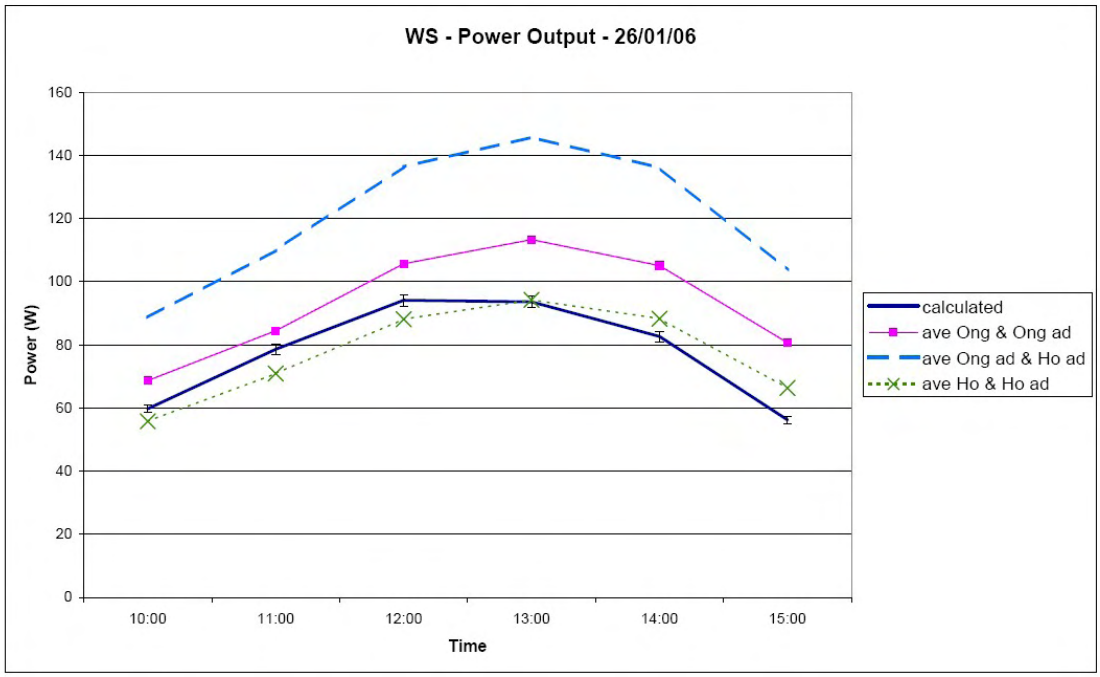

Figure 5.113. WS - Power Output (Combined Models) - 26/01/06

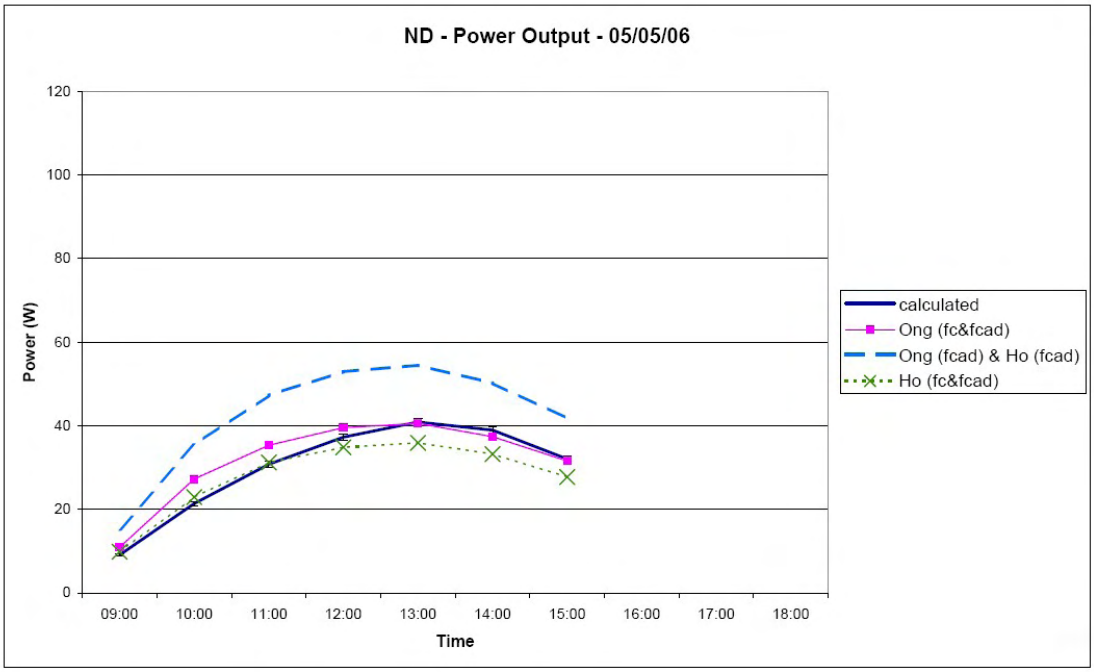

Figure 5.114. ND - Power Out (Combined Models) - 05/05/06

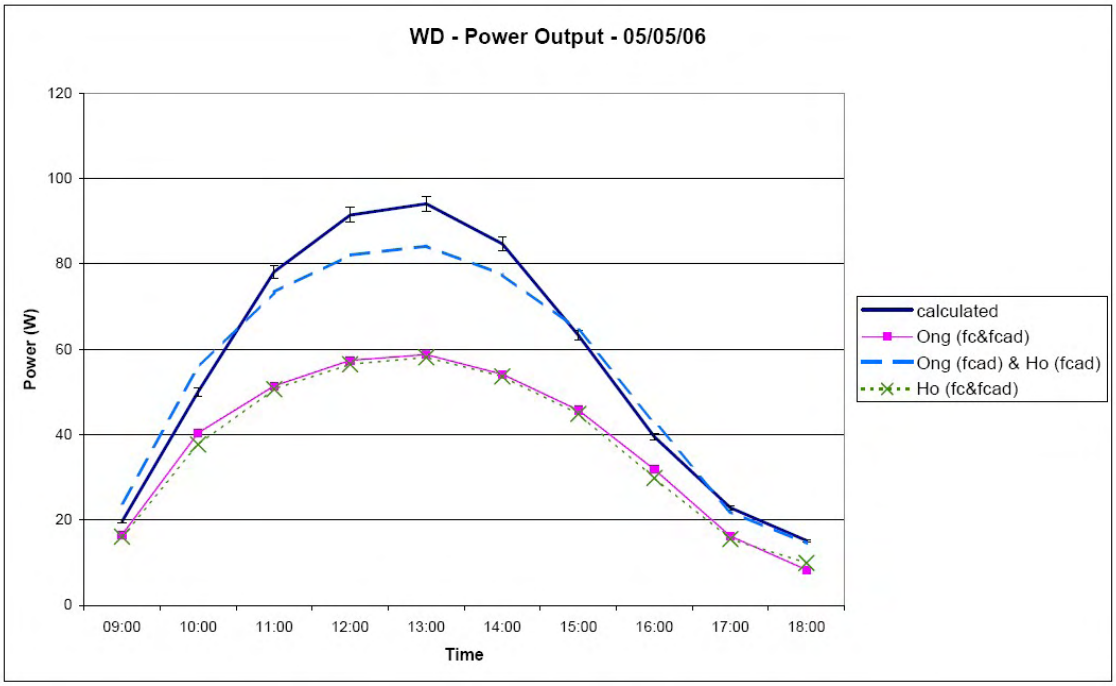

Figure 5.115. WD - Power Out (Combined Models) - 05/05/06

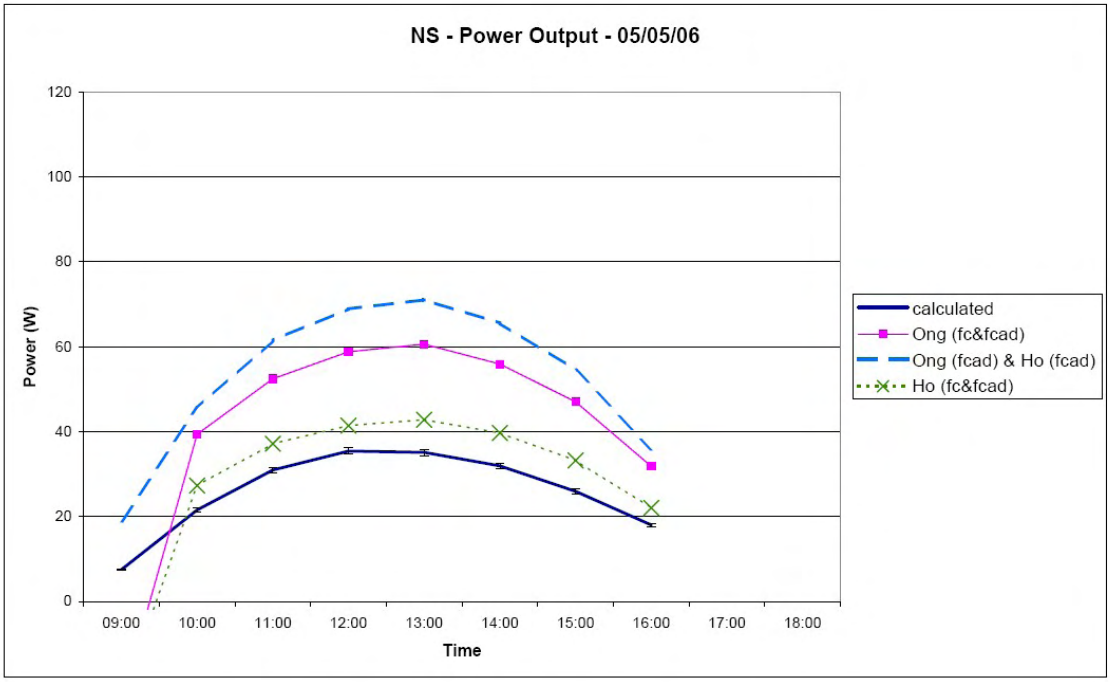

Figure 5.116. NS - Power Out (Combined Models) - 05/05/06

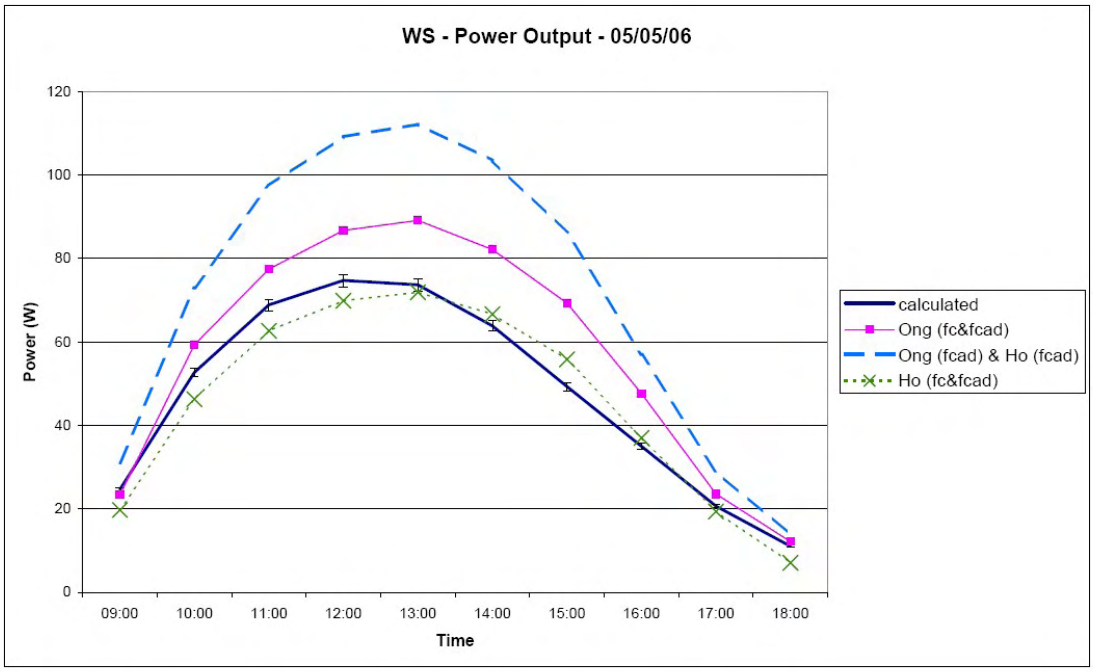

Figure 5.117. WS - Power Out (Combined Models) - 05/05/06

Table 5.35 indicates the mean bias and RMSE for the three models for 26/01/06. Table 5.36 gives the same information for 05/05/06.

Table 5.35 Bias and RMSE for Prediction of Power Output - 26/01/06

		$Ong_{fc\&fcad}$	$Ho_{fc\&fcad}$	$OngHo_{fcad}$
Mean Bias (W)	ND	-12.2	-16.0	3.8
	WD	-47.4	-46.3	-18.5
	NS	22.6	5.3	35.0
	WS	15.5	-0.2	42.6
	All	-5.4	-14.2	15.7
RMSE (W)	ND	12.6	16.2	4.1
	WD	48.7	47.4	20.1
	NS	23.4	6.2	36.0
	WS	17.0	6.4	43.7
	All	29.0	25.4	30.1

Table 5.36 Bias and RMSE for Prediction of Power Output – 05/05/06

		$Ong_{fc\&fcad}$	$Ho_{fc\&fcad}$	$OngHo_{fcad}$
Mean Bias (W)	ND	1.7	-2.6	13.4
	WD	-15.7	-16.4	-1.6
	NS	13.5	1.6	25.1
	WS	9.1	-1.7	22.5
	All	1.2	-5.8	14.8
RMSE (W)	ND	3.2	3.7	13.7
	WD	18.9	19.5	5.0
	NS	21.2	11.6	26.2
	WS	11.2	4.3	25.8
	All	16.4	12.9	20.5

From Table 5.35 it can be seen that none of the models have a consistent bias. Of the three models, $Ong_{fc\&fcad}$ has the least bias and $Ho_{fc\&fcad}$ has the lowest RMSE. Table 5.36 shows a similar trend.

The $Ong_{fc\&fcad}$ model had lower bias and RMSE for May than the Ong_{fcad} model than the Ong_{fcad} model; however, the RMSE values did not reduce. The $Ho_{fc\&fcad}$ model had lower bias and RMSE for both months than Ho_{fc} and Ho_{fcad}. The $OngHo_{fcad}$ model had a lower bias than Ho_{fc} and Ho_{fcad}. The $Ong_{fc\&fcad}$ model has the lowest combination of bias and RMSE, and as such is considered the closest model.

5.1.8.6 Discussion

Table 5.37 shows the combined bias and RMSE values for all the ducts for both dates.

Table 5.37 Bias and RMSE values for all ducts Averaged over 26/01/06 and 05/05/06

Model	Glazing Temperature (^oC)	Absorbing Surface Temperature (^oC)	Mean air Temperature (^oC)	Exit air Temperature (^oC)	Power out (W)
Bias					
Ong_{fc}	2.6	18.1	-0.8	-1.6	-8.2
Yeh_{fc}		-1.6	-5.7	-10.9	-54.6
Ho_{fc}	-5.5	-18.1	-5.1	-8.7	-43.5
Ong_{fcad}	8.5	22.5	0.7	1.1	5.4
Yeh_{fcad}		-1.3	-5.6	-10.8	-54.1
Ho_{fcad}	12.6	7.7	-1.6	5.0	24.5
$Ong_{fc\&fcad}$	5.4	20.7	-0.1	-0.4	-2.1
$Ho_{fc\&fcad}$	3.8	-5.3	-3.5	-2.0	-10.0
$OngHo_{fcad}$	11.1	15.6	-0.5	3.1	15.3
RMSE					
Ong_{fc}	4.6	20.9	2.6	4.6	23.5
Yeh_{fc}		9.2	6.4	12.1	61.3
Ho_{fc}	5.9	20.3	5.8	9.9	49.9
Ong_{fcad}	8.9	25.3	2.8	4.6	23.5
Yeh_{fcad}		9.1	6.4	12.1	60.9
Ho_{fcad}	13.9	10.0	2.5	6.3	31.4
$Ong_{fc\&fcad}$	6.5	23.0	2.8	4.4	22.7
$Ho_{fc\&fcad}$	5.3	7.4	4.1	3.7	19.2
$OngHo_{fcad}$	11.3	17.3	2.3	5.1	25.3

From Table 5.37 it can be seen that:

- Ong_{fc} has the lowest bias and RMSE for the glazing temperature
- Yeh_{fcad} has the best combination of low bias and low RMSE for the absorbing surface temperature
- $OngHo_{fcad}$ has the best combination of low bias and low RMSE for the mean air temperature
- $Ong_{fc\&fcad}$ has the best combination of low bias and low RMSE for the exit air temperature
- $Ong_{fc\&fcad}$ has the best combination of low bias and low RMSE for the power output

No one model adequately predicts all values for all parameters. Some models better predict certain parameters, other parameters are better represented by other models. The key parameters, exit temperature and power output are not well predicted for all ducts, but some models are capable of predicting for some geometries, e.g. $Ho_{fc\&fcad}$ gives a strong predictor for ducts NS and WS. $OngHo_{fcad}$ is a strong predictor for duct ND and in some cases WD. It is evident that all of the models have difficulty in predicting the behaviour of the WD duct. This may be due to shadows forming within the duct during the day. A comparison of the models for air exit temperature and power output has taken place with the data from the WD duct excluded. This comparison is shown in Table 5.38.

Table 5.38 Bias and RMSE values for ducts ND, NS and WS Averaged over 26/01/06 and 05/05/06

Model	Exit air Temperature (^oC)	Power out (W)
Bias		
Ong_{fc}	0.5	2.5
Yeh_{fc}	-9.3	-45.4
Ho_{fc}	-7.0	-34.4
Ong_{fcad}	3.2	16.0
Yeh_{fcad}	-9.2	-45.0
Ho_{fcad}	6.3	31.1
$Ong_{fc\&fcad}$	1.7	8.4
$Ho_{fc\&fcad}$	-0.5	-2.2
$OngHo_{fcad}$	4.8	23.7
RMSE		
Ong_{fc}	2.3	11.2
Yeh_{fc}	9.6	47.1
Ho_{fc}	7.3	35.7
Ong_{fcad}	3.8	19.0
Yeh_{fcad}	9.5	46.8
Ho_{fcad}	6.6	32.7
$Ong_{fc\&fcad}$	3.0	14.8
$Ho_{fc\&fcad}$	1.7	8.1
$OngHo_{fcad}$	5.0	24.9

The $Ho_{fc\&fcad}$ model has the best combination of mean bias and RMSE for both air exit temperature and the power output. For this reason it has been chosen as the model to predict the exit air temperature and power output. However, the model does not achieve

the target of mean bias and RMSE less than 2°C for ducts ND, NS and WS over both dates.

5.1.9 Prediction of Power Output under Forced Convection

The power output of individual ducts has been calculated from measured parameters in Section 4.3.6. The power output was normalised to a 10m^2 façade area, to allow comparison between the ducts. These results were presented for 26/01/06 (Figure 4.26) and 05/05/06 (Figure 4.27). This found that the ranking of power output was (highest to lowest) WD, ND, NS, WS. For comparison, the power output predicted by the $Ho_{fc\&fcad}$ model for a 10m^2 façade area has been calculated. The predicted power output ranking for 26/01/06 is NS, WS, ND, WD (Figure 5.118). For 05/05/06 the predicted power output ranking is similar (Figure 5.119), although it is no longer possible to discern a ranking between WS and ND.

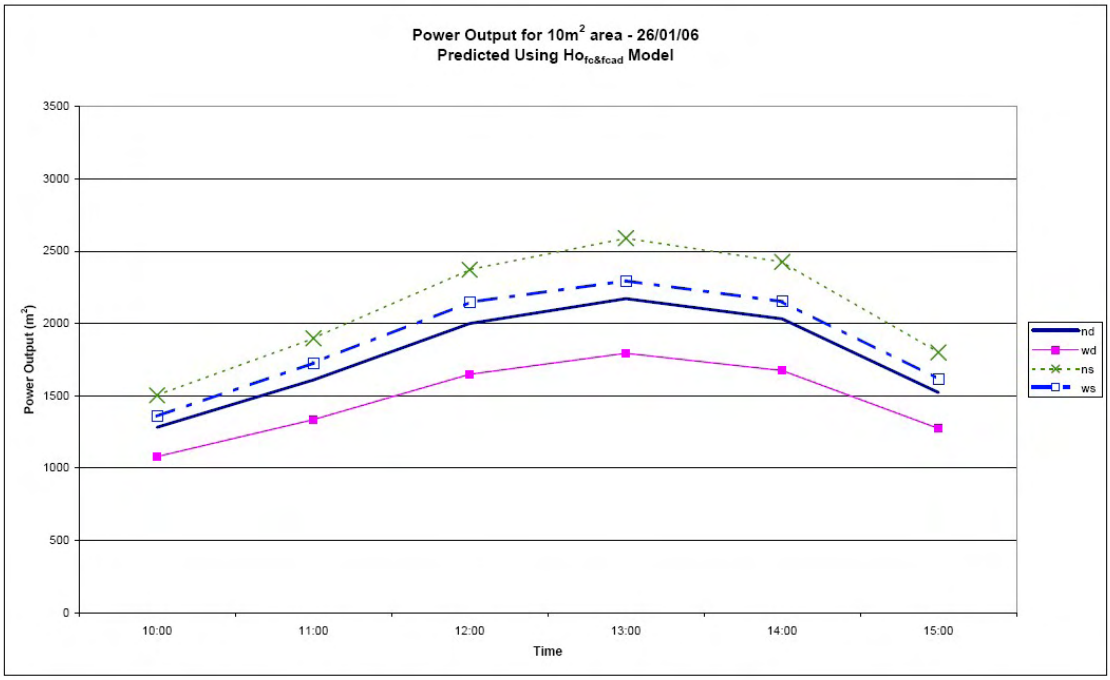

Figure 5.118. Power Output ($Ho_{fc\&fcad}$ Model) 26/01/06

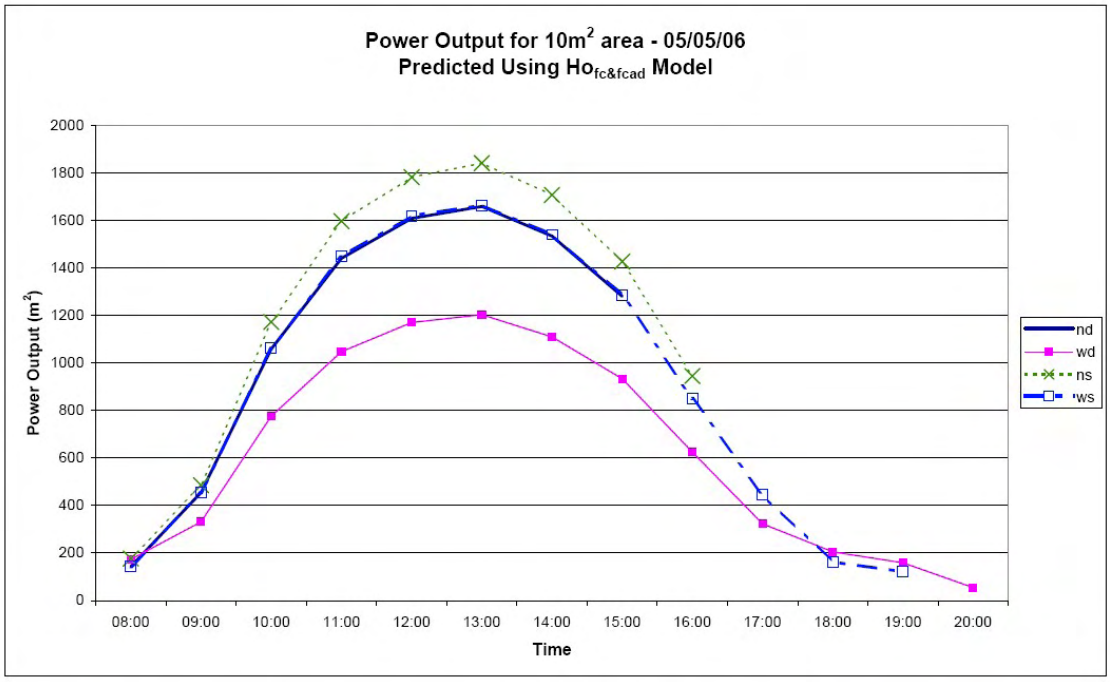

Figure 5.119. Power Output ($Ho_{fc\&fcad}$ Model) 05/05/06

The predicted power output ranking does not agree with that observed empirically in Section 4.3.6. The $Ho_{fc\&fcad}$ model is apparently insensitive to the benefits of increasing the duct depth. It also appears to be a little over sensitive to variations in the width, which show little impact in the empirical results. This analysis shows that although the $Ho_{fc\&fcad}$ model gave the closest correlation with air exit temperature and power output, it is not accurate enough.

The poor correlation between the design models and air exit temperature / power output of the deeper prototype ducts is likely to be caused by shadows within the duct. The areas cast into shadow during the day are larger for deep ducts than for shallow ones. Although the area of shadow could be calculated, a method to estimate the temperature of the shaded area has not been found.

5.2 Buoyant Convection Design Models

The literature survey found two models currently in existence to predict the behaviour of solar air heaters under buoyant convection.

- Ong [3] developed a model (discussed in Section 2.4.1 and Appendix A) which will be referred to as Ong_{bc}. In the first instance this model was used without

alterations. It was not necessary to re-arrange it to obtain the chosen parameters. Where meteorological data or physical properties of the materials were required, data from the experiment date was used.

- Brinkworth et al [4, 5] developed a model (discussed in Section 2.4.6 and Appendix A) which will be referred to as $Brinkworth_{bc}$. This model was developed to analyse the cooling of photovoltaic arrays, and has required adjustment for the current application. The original model assumed the front surface to be an opaque solar absorber. In this scenario, the rear surface of the duct would only receive the re-emitted heat from the solar absorber. The model was adapted for a transmitting front surface, which allowed the majority of the solar irradiation to reach the solar absorbing rear surface. This required the equations for the solar temperature and rear surface temperature to be re-arranged (shown in Appendix H).

The Yeh and Ho & Loveday models for forced convection used in Section 5.1 were adapted for buoyant convection by incorporating Brinkworth's calculation for air mass flow. The resulting models will be referred to as Yeh_{bc} and Ho_{bc}.

The heat transfer calculations in air movement are traditionally calculated using a Nusselt number. The Nusselt number is complicated by the type of fluid flow (laminar, transitional, turbulent) and the geometry of the duct (whether the flow in the entry length or not). These difficulties mean that a model requires different Nusselt number calculations depending on the situation. An alternative model for calculating the behaviour of the solar air heater was devised, based on a simple energy balance. This model also used Brinkworth's calculation for air mass flow. The resulting model will be referred to as $Stevenson_{bc}$.

Those output parameters that were available from each model were compared against the measured data; mean glazing temperature, mean absorbing surface temperature, mean duct air temperature, exit air temperature, power output. Where the models required meteorological data, data from the appropriate experiment date was used. Physical properties of the materials were estimated from common handbook data.

The procedure followed for each of the models is described in Appendix H. Table 5.39 shows a comparison of each model.

Table 5.39 Comparison of Models Ong_{bc}, Yeh_{bc}, Ho_{bc}, $Brinkworth_{bc}$ and $Stevenson_{bc}$

Parameter	Ong_{bc}	Yeh_{bc}	Ho_{bc}	$Brinkworth_{bc}$	$Stevenson_{bc}$
Considers the air heater	In entirety	In entirety	In entirety	In entirety	In entirety
Hydraulic diameter (D_h)	Unspecified – non circular duct (B1) used	Non circular duct (B1)	Non circular duct (B1)	Non circular duct (B1)	Non circular duct (B1)
Sky temperature (T_{sky})	Swinbank's correlation (C31)	Not Used	Not Used	Not Used	Not Used
Wind convection heat transfer (h_w)	McAdam's correlation (C20)	Adjusted McAdam's correlation (C23)	McAdam's correlation (C20)	McAdam's correlation (C20)	McAdam's correlation (C20)
Dynamic viscosity of air (μ)	Temperature dependent	Constant	Not Used	Constant	Constant
Kinematic viscosity of air (ν)	Not Used	Not Used	Constant	Constant	Not Used
Specific heat capacity of air (c_p)	Temperature dependent	Constant	Constant	Constant	Constant
Thermal conductivity of air (k)	Temperature dependent	Constant	Constant	Constant	Not Used
Density of air (ρ)	Temperature dependent	Not Used	Constant	Constant	Constant
Nusselt number	Incropera and Dewitt's correlations for natural convection (C16&C17)	**Incropera and Dewitt's correlations for natural convection (C16&C17)** substituted Kay's correlation (C12)	**Incropera and Dewitt's correlations for natural convection (C16&C17)** substituted Kay's correlation (C12)	Brinkworth (C18)	Not Used

Table 5.39 Cont'd Comparison of Models Ong_{bc}, Yeh_{bc}, Ho_{bc}, $Brinkworth_{bc}$ and $Stevenson_{bc}$

Parameter	Ong_{bc}	Yeh_{bc}	Ho_{bc}	$Brinkworth_{bc}$	$Stevenson_{bc}$
Radiative heat transfer coefficient between parallel plates	Incorporating glass and solar absorber temperatures with glass and solar absorber emissivity (C28)	Incorporating fluid temperature with glass and solar absorber emissivity (C29)	Incorporating glass and solar absorber temperatures with glass and solar absorber emissivity (C28)	Incorporating glass and solar absorber temperatures with glass and solar absorber emissivity (A58)	Not Used
Radiative heat transfer coefficient between glass and sky	Incorporating glass, sky and ambient temperatures along with the emissivity of glass (C30)	Not Used	Incorporating glass and ambient temperatures along with the emissivity of glass (C33)	Incorporating glass, fluid and sol-air temperatures (A59 & A60)	Not Used
Overall top heat loss coefficient	Sum of wind and radiative heat transfer coefficients (H4)	Incorporating the solar absorber and ambient temperatures, the wind coefficient and the emissivity of the solar absorber surface (A19)	Unspecified – definition from BS EN ISO 12241 [1] used	Sum of wind and radiative heat transfer coefficients (H4)	Definition from BS EN ISO 12241 [1] used without contribution from radiation
Heat loss coefficient including sides	No	No	Yes	No	Yes

Table 5.39 Cont'd Comparison of Models Ong_{bc}, Yeh_{bc}, Ho_{bc}, $Brinkworth_{bc}$ and $Stevenson_{bc}$

Parameter	Ong_{bc}	Yeh_{bc}	Ho_{bc}	$Brinkworth_{bc}$	$Stevenson_{bc}$
Overall bottom heat loss coefficient	Incorporating conductive and wind convective components (H5)	Ratio of thermal conductivity and thickness of insulation (H7)	Unspecified – definition from BS EN ISO 12241 [1] used	Ratio of thermal conductivity and thickness of insulation (H7)	Definition from BS EN ISO 12241 [1] used without contribution from radiation
Considers heat gain from glass and absorbing surface separately	Yes	No	No	No	No
Considers direct and diffuse components of solar irradiation and angle of incidence	No	No	No	No	No
Considers heat transfer for sides	No	No	Yes	Yes	No
Calculation for air mass flow includes effect of friction in duct	No	Yes	Yes	Yes	Yes

Table 5.39 Cont'd Comparison of Models Ong_{bc}, Yeh_{bc}, Ho_{bc}, $Brinkworth_{bc}$ and $Stevenson_{bc}$

Parameter	Ong_{bc}	Yeh_{bc}	Ho_{bc}	$Brinkworth_{bc}$	$Stevenson_{bc}$
Buoyant air mass flow	Incorporating duct geometry, air density and specific heat capacity, acceleration due to gravity, ambient and fluid temperature, assuming non-linear temperature gradient (H30 & H31)	Incorporating duct geometry, air density and specific heat capacity, acceleration due to gravity, ambient and fluid temperature, friction factor and solar irradiation (A57)	Incorporating duct geometry, air density and specific heat capacity, acceleration due to gravity, ambient and fluid temperature, friction factor and solar irradiation (A57)	Incorporating duct geometry, air density and specific heat capacity, acceleration due to gravity, ambient and fluid temperature, friction factor and solar irradiation (A57)	Incorporating duct geometry, air density and specific heat capacity, acceleration due to gravity, ambient and fluid temperature, friction factor and solar irradiation (A57)
Solution procedure	Iterative solution of matrix equation.	Iterative solution of a series of equations.	Iterative solution of a series of equations.	Iterative solution of a series of equations.	Iterative solution of a series of equations.
	The meteorological data and physical properties of the materials used in the experiment (e.g. emissivity, absorptivity, etc) were applied to the model.		The meteorological data and physical properties of the materials used in the experiment (e.g. emissivity) were applied to the model. However, absorptivity of the solar absorber was not part or the original model.	The meteorological data and physical properties of the materials used in the experiment (e.g. emissivity, absorptivity, etc) were applied to the model.	

Table 5.39 Cont'd Comparison of Models Ong_{bc}, Yeh_{bc}, Ho_{bc}, $Brinkworth_{bc}$ and $Stevenson_{bc}$

Parameter	Ong_{bc}	Yeh_{bc}	Ho_{bc}	$Brinkworth_{bc}$	$Stevenson_{bc}$
Parameters Calculated Directly	The mean glass, mean absorber, mean duct air, exit air temperature and air mass flow are calculated directly from the model.	The mean absorber, mean duct air, exit air temperature and air mass flow are calculated directly from the model.	The mean outer glass, mean inner glass, mean absorber, mean outer, mean duct air, exit air temperature and air mass flow are calculated directly from the model.	The mean glass, mean absorber, mean duct air, exit air temperature and air mass flow are calculated directly from the model.	The mean duct air, exit air temperature and air mass flow are calculated directly from the model.
Parameters Calculated Indirectly	The power output is calculated from the calculated air mass flow and air exit temperature.				

The ambient temperature, horizontal global solar irradiation and horizontal diffuse irradiation from a sunny summer's day (03/07/06) were averaged over one hour periods and used as inputs to the design models. The system has been analysed over the same time period as on the 05/05/06 (i.e. 09:00 – 18:00). The calculated incident radiation on the vertical surfaces has been calculated using equations E1 and E2 and is included in Table 5.40. Table 5.40 shows the conditions averaged over the previous hour (i.e. the data for 09:00 is the average between 08:00 and 09:00).

Table 5.40 Input Conditions (Averaged over 1 hour periods)

Time period	Ambient Temperature (^oC)	Horizontal diffuse irradiation (W m^{-2})	Horizontal global irradiation (W m^{-2})	Calculated Vertical direct irradiation (W m^{-2})	Calculated Vertical diffuse irradiation (W m^{-2})
09:00	23.4	211	320	33	138
10:00	25.5	196	453	116	143
11:00	28.3	207	593	203	163
12:00	30.3	212	684	261	174
13:00	32.0	261	739	260	204
14:00	32.9	253	743	248	201
15:00	33.3	221	719	218	182
16:00	31.6	209	667	141	171
17:00	30.5	249	528	31	116
18:00	29.6	167	328	0	94

The actual outputs from the experiment averaged over one hour periods for 03/07/06 are shown in Tables G5-G8 of Appendix G. Table G5 shows the mean glazed surface temperature (calculated from the average of the two thermocouples attached to the glass). Table G6 shows the mean absorbing surface temperature (calculated from the average of the two thermocouples attached to the back surface of the duct). Table G7 shows the measured mean air temperature (calculated from the average of the air entry and air exit thermocouples). Table G8 shows the exit air temperature. This data will be used to compare design models.

The WS duct was found to have a similar air exit temperature to the ambient temperature. Since this is poor performance (no power output) it is illustrated as a 'Non-Functional' duct in Figure 5.120. It has already been noted that the ambient

temperature sensor is somewhat affected by solar irradiation in the afternoons, and this explains why the air exit temperature from the WS duct is lower than the ambient temperature in the afternoons. The air exit temperatures of the other ducts exceed the ambient temperature and are considered 'Functional' ducts. These are shown for comparison.

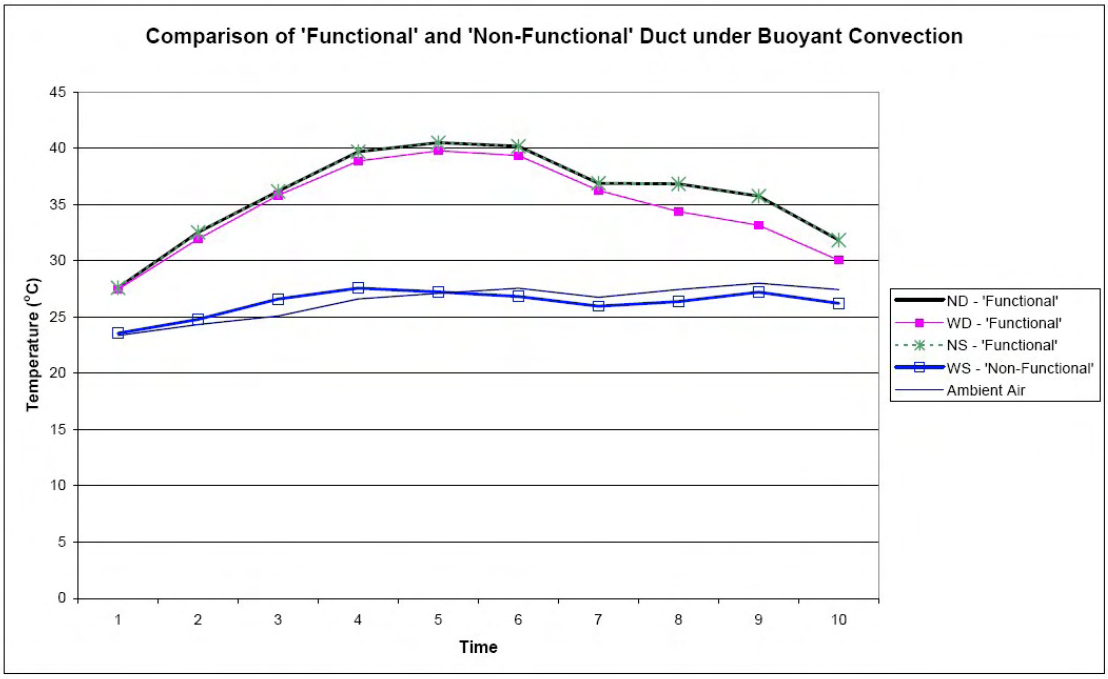

Figure 5.120. Comparison of 'Functional' vs 'Non-Functional' Duct under Buoyant Convection

The absorber temperature was measured at two points on all of the ducts. In the 'Functional' ducts, a higher temperature was observed at the higher position than the lower position. This indicated a temperature gradient throughout those ducts. In the 'Non-Functional' duct (WS), there was no significant difference observed between the temperatures at the two positions. This indicates that there is no temperature gradient through the duct. It is presumed that due to some unidentified disturbance in the flows (perhaps a recirculation current at the exit) there was no net flow through duct WS. For this reason the models will not be compared with duct WS.

Buoyant pressure is not capable of pushing air past the pressure drop caused by the orifice plates. For this reason the orifice plates were disconnected to allow the buoyant convection experiment to take place; however, this meant that air mass flow could not

be monitored during this experiment. Consequently the power output from the prototype ducts under buoyant convection could not be calculated. The purpose of this comparison is to evaluate the prediction of the surface and air temperatures. The model with the best match to the measured temperatures will be considered the most appropriate design model.

5.2.1 Prediction of Mean Glazing Temperature

The following graphs show the correlation between the measured mean glazing temperature for ducts ND, WD and NS and the predictions given by the Ong_{bc}, Ho_{bc} and $Brinkworth_{bc}$ models. The error bars illustrate the difficulty in measuring the glass temperature accurately under solar irradiation.

Figures 5.121 - 5.123 show the correlation for 03/07/06.

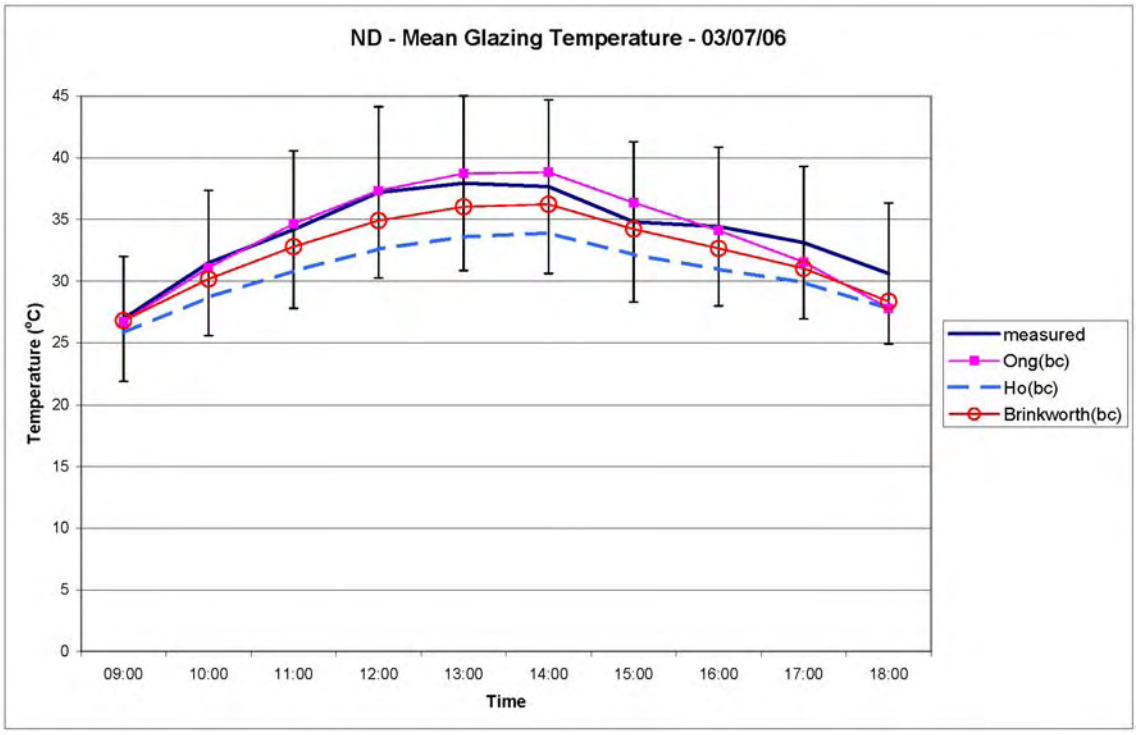

Figure 5.121. ND - Mean Glazing Temperature (Buoyant)

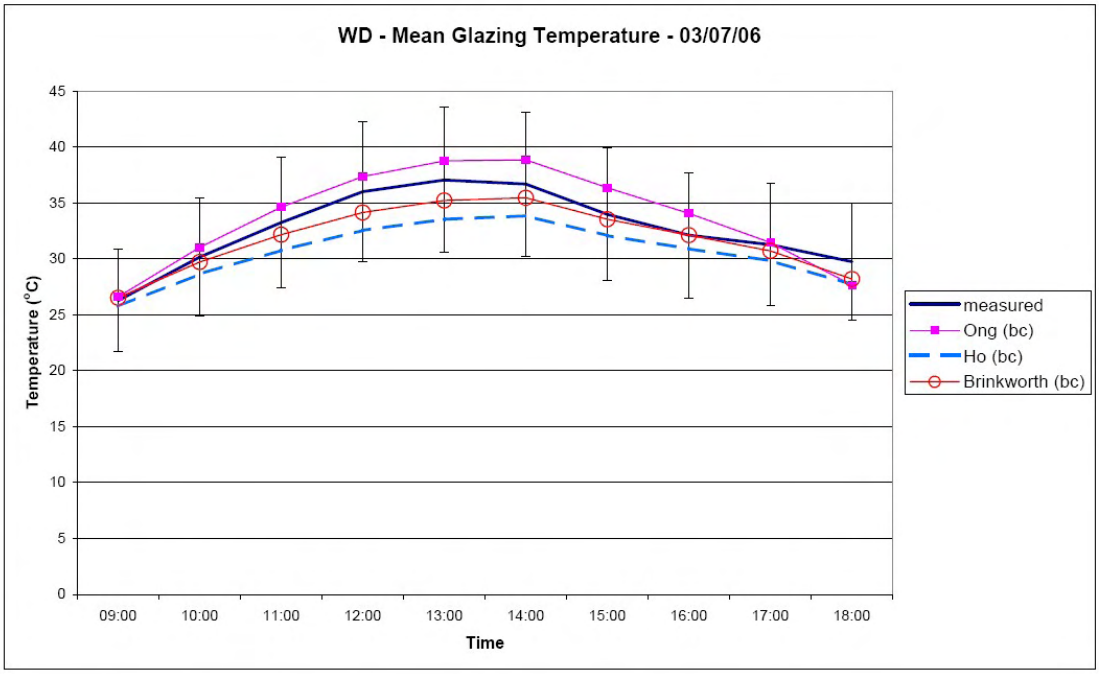

Figure 5.122. WD - Mean Glazing Temperature (Buoyant)

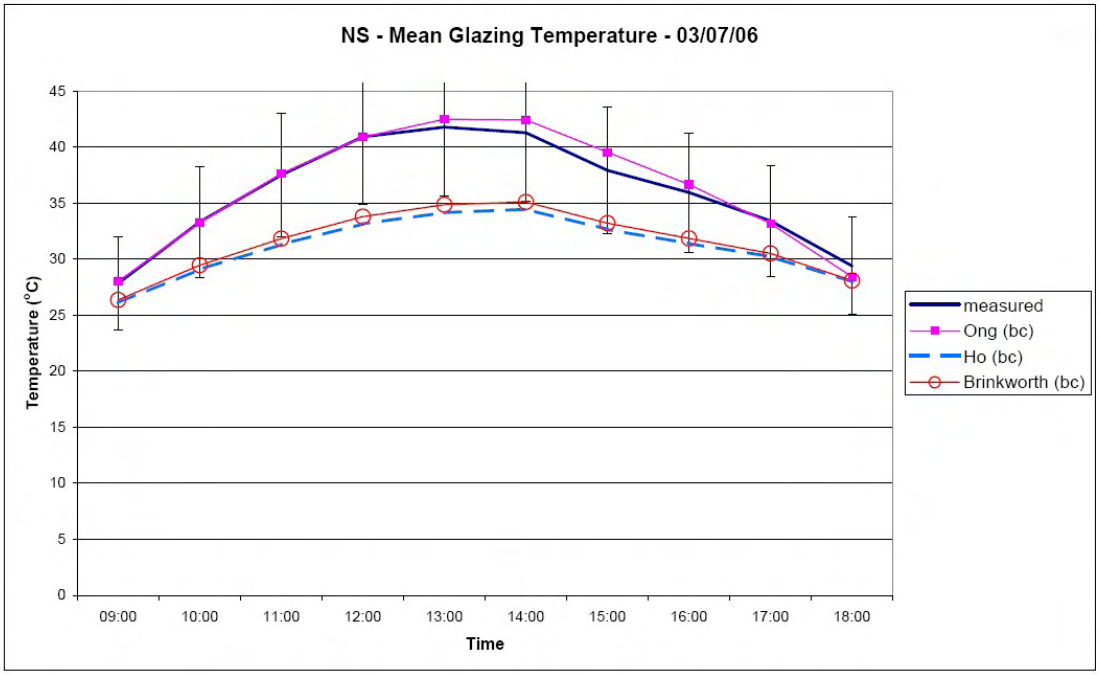

Figure 5.123. NS - Mean Glazing Temperature (Buoyant)

Table 5.41 indicates the mean bias and RMSE for the three models averaged over the time 09:00 to 18:00 for 03/07/06.

Table 5.41 Bias and RMSE for Design Model Prediction of Mean Glazing Temperature

		Ong_{bc}	Yeh_{bc}	Ho_{bc}	$Brinkworth_{bc}$	$Stevenson_{bc}$
Mean Bias (^oC)	ND	-0.1	N/A	-3.2	-1.5	N/A
	WD	1.0		-2.1	-0.9	
	NS	0.3		-4.9	-4.4	
	All	0.4		-3.4	-2.3	
RMSE (^oC)	ND	1.2		3.4	1.7	
	WD	1.6		2.3	1.1	
	NS	0.8		5.3	4.9	
	All	1.3		3.9	3.0	

From Table 5.41 it can be seen that the Ho_{bc} and $Brinkworth_{bc}$ models tend to underestimate the glazing temperature. There is no consistent bias associated with the Ong_{bc} model. Although all the models calculate values within the measurement error band, the Ong_{bc} model has the lowest bias and RMSE, and as such is considered the most accurate.

5.2.2 Prediction of Mean Absorbing Surface Temperature

The following graphs show the correlation between the measured mean absorber temperature for ducts ND, WD and NS and the predictions given by Ong_{bc}, Yeh_{bc}, Ho_{bc}, $Brinkworth_{bc}$. The $Stevenson_{bc}$ model does not predict the mean absorber surface temperature. Error bars have been included in the following graphs; however, the error is too small to show up on the graph.

Figures 5.124 - 5.126 show the correlation for 03/07/06.

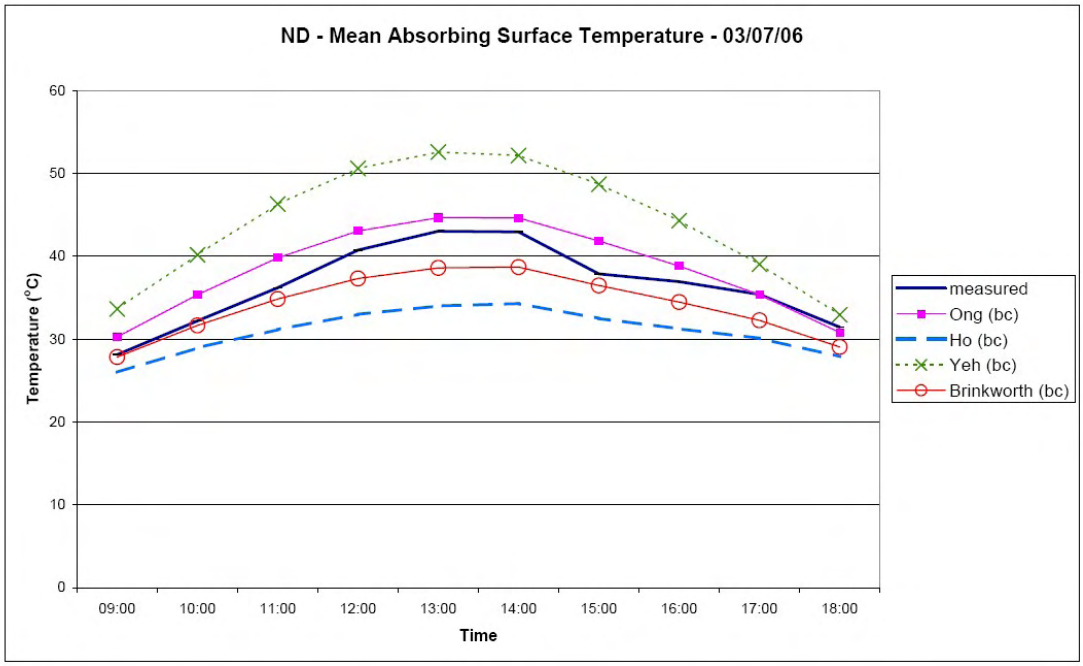

Figure 5.124. ND - Mean Absorber Temperature (Buoyant)

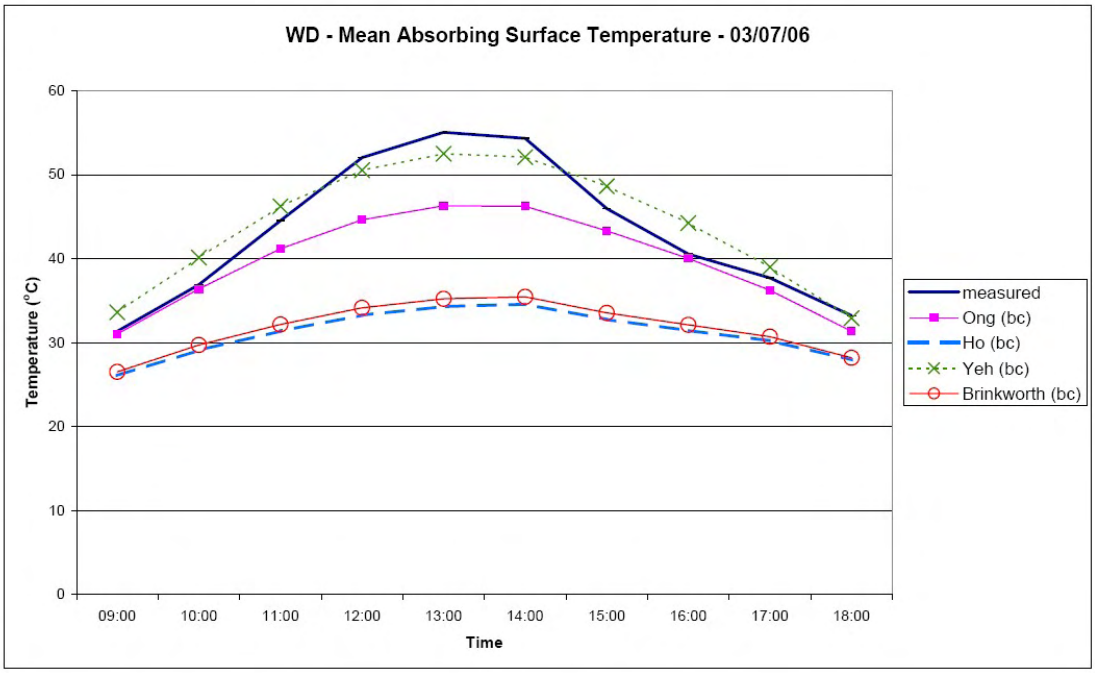

Figure 5.125. WD - Mean Absorber Temperature (Buoyant)

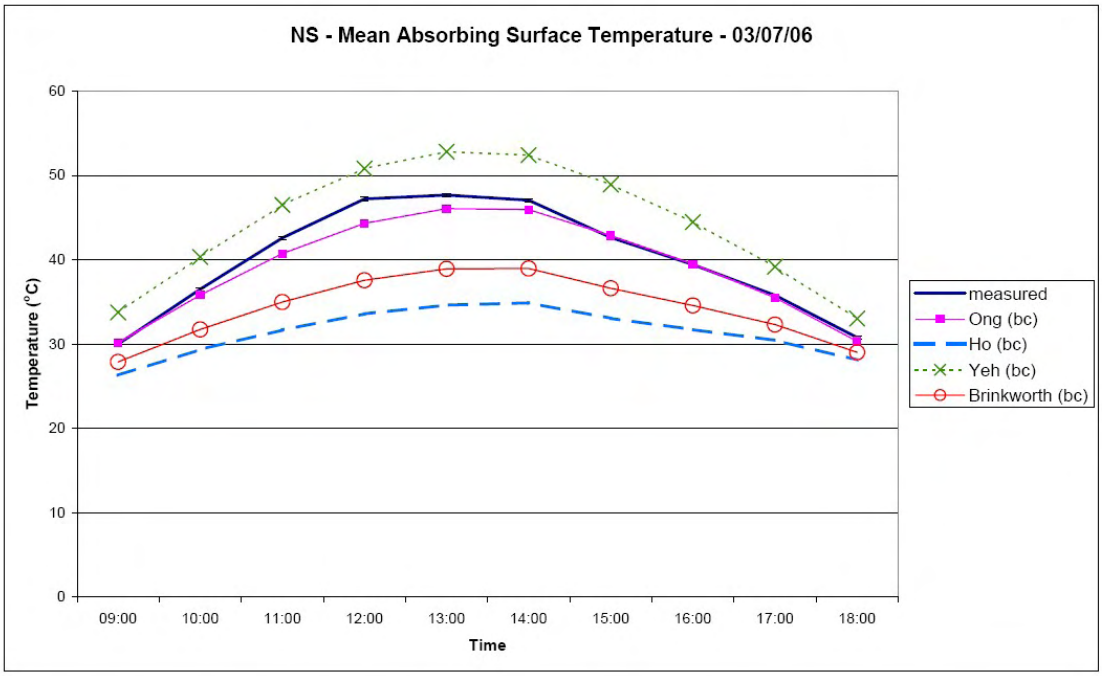

Figure 5.126. NS - Mean Absorber Temperature (Buoyant)

Table 5.42 indicates the mean bias and RMSE for the five models averaged over the time 09:00 to 18:00 for 03/07/06.

Table 5.42 Bias and RMSE for Design Model Prediction of Absorbing Surface Temperature

		Ong_{bc}	Yeh_{bc}	Ho_{bc}	$Brinkworth_{bc}$	$Stevenson_{bc}$
Mean Bias (^oC)	ND	2.0	7.6	-5.6	-2.4	N/A
	WD	-3.5	0.8	-12.1	-9.9	
	NS	-0.8	4.3	-8.6	-5.7	
	All	-0.8	4.2	-8.7	-6.0	
RMSE (^oC)	ND	2.4	8.1	6.0	2.7	
	WD	4.7	2.3	13.3	11.1	
	NS	1.3	4.4	9.4	6.3	
	All	3.1	5.5	10.0	7.6	

From Table 5.42 it can be seen that the Yeh_{bc} model tends to overestimate the mean temperature of the absorbing surface. Ho_{bc} and $Brinkworth_{bc}$ models tend to underestimate it. While there is no consistent bias associated with the Ong_{bc} model. The Ong_{bc} model has the lowest bias and RMSE, and as such is considered the most accurate.

5.2.3 Prediction of Duct Mean Air Temperature

The following graphs show the correlation between the measured mean air temperature for ducts ND, WD and NS and the predictions given by Ong_{bc}, Yeh_{bc}, Ho_{bc}, $Brinkworth_{bc}$ and $Stevenson_{bc}$.

Figures 5.127 - 5.129 show the correlation for 03/07/06.

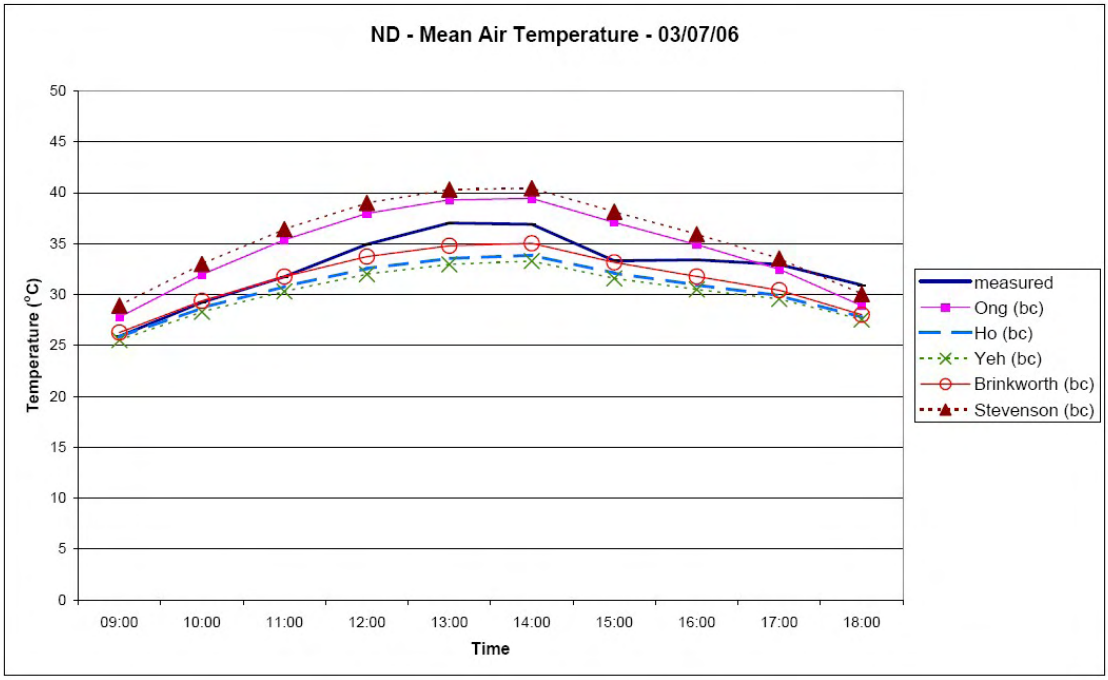

Figure 5.127. ND - Mean Air Temperature (Buoyant)

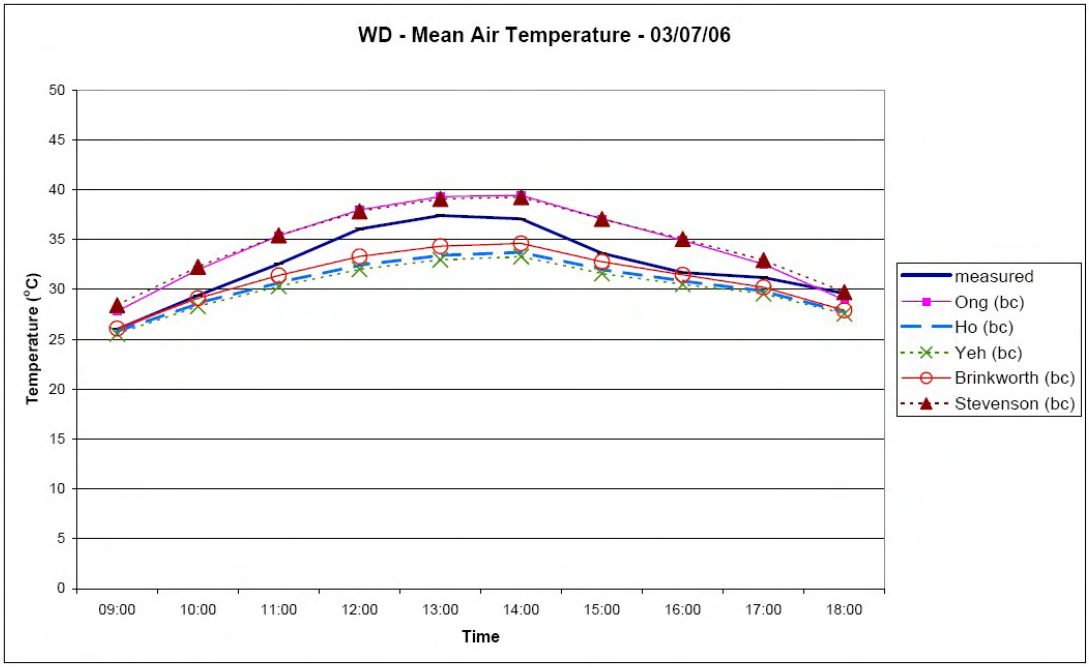

Figure 5.128. WD - Mean Air Temperature (Buoyant)

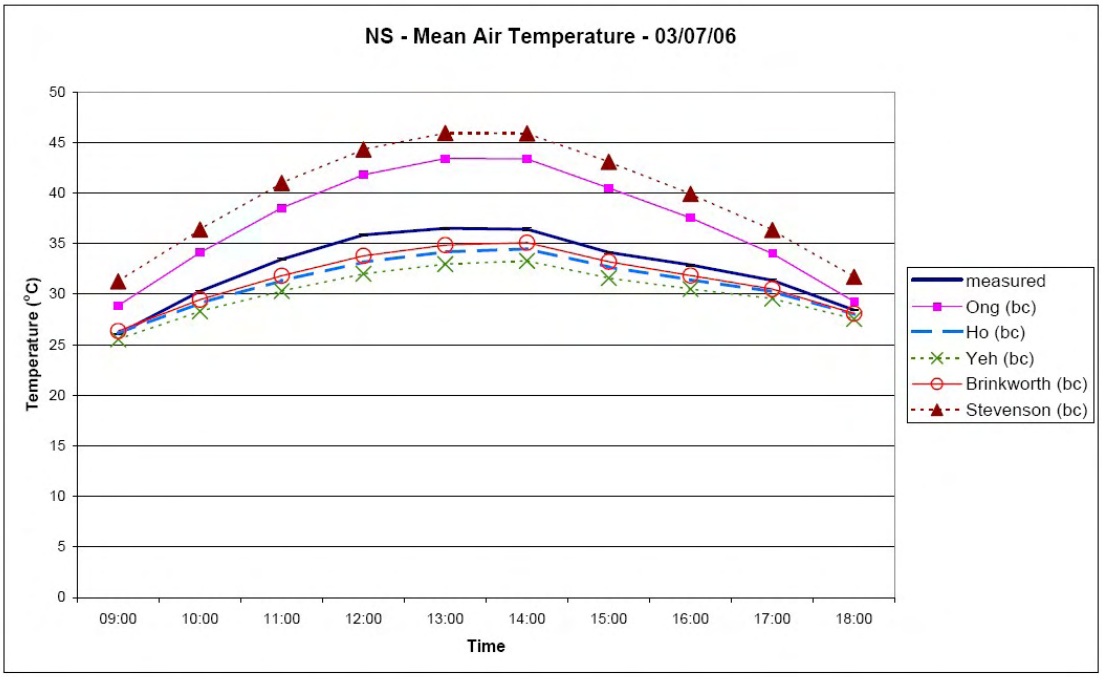

Figure 5.129. NS - Mean Air Temperature (Buoyant)

Table 5.43 indicates the mean bias and RMSE for the five models averaged over the time 09:00 to 18:00 for 03/07/06.

Table 5.43 Bias and RMSE for Design Model Prediction of Mean Air Temperature

		Ong_{bc}	Yeh_{bc}	Ho_{bc}	$Brinkworth_{bc}$	$Stevenson_{bc}$
Mean Bias (^oC)	ND	1.9	-2.5	-2.0	-1.2	2.9
	WD	2.1	-2.3	-2.0	-1.3	2.2
	NS	4.6	-2.4	-1.5	-1.0	7.0
	All	2.9	-2.4	-1.8	-1.2	4.1
RMSE (^oC)	ND	2.6	2.8	2.3	1.7	3.4
	WD	2.4	2.6	2.3	1.7	2.4
	NS	5.0	2.6	1.7	1.2	7.3
	All	3.5	2.7	2.1	1.5	4.9

From Table 5.43 it can be seen that the Ong_{bc} and $Stevenson_{bc}$ models tend to overestimate the mean air temperature; while the Yeh_{bc}, Ho_{bc} and $Brinkworth_{bc}$ models tend to underestimate. The $Brinkworth_{bc}$ model has the lowest bias and RMSE, and as such is considered the most accurate.

5.2.4 Prediction of Exit Air Temperature

The following graphs show the correlation between the measured exit air temperature for ducts ND, WD and NS and the predictions given by Ong_{bc}, Yeh_{bc}, Ho_{bc}, $Brinkworth_{bc}$ and $Stevenson_{bc}$.

Figures 5.130 - 5.132 show the correlation for 03/07/06.

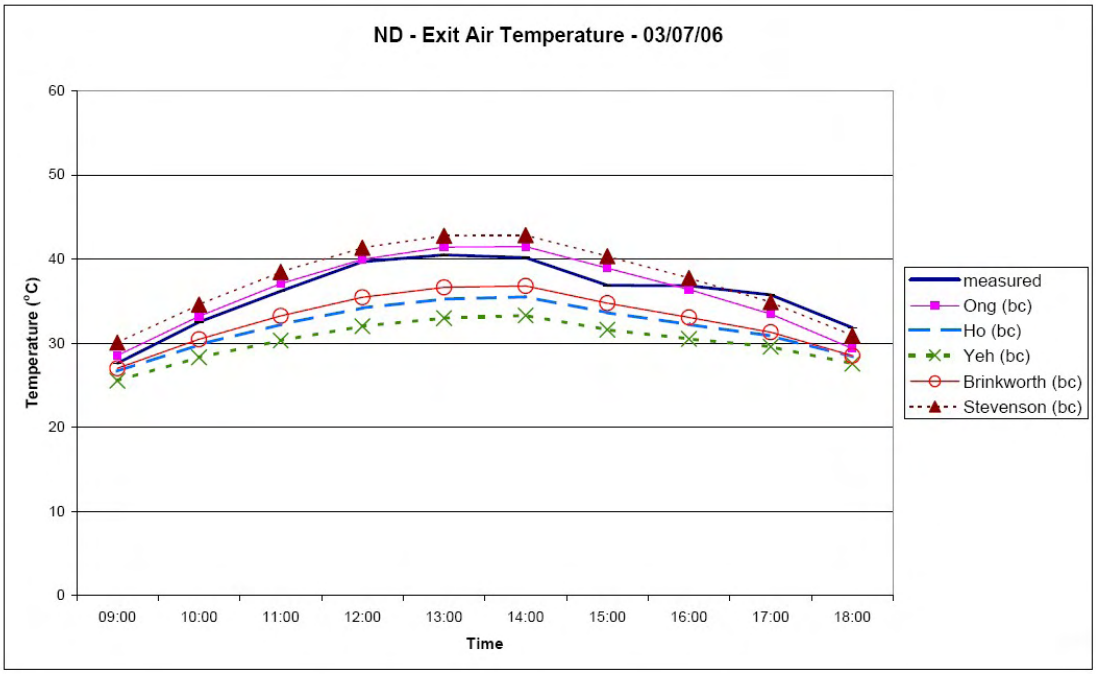

Figure 5.130. ND - Exit Air Temperature (Buoyant)

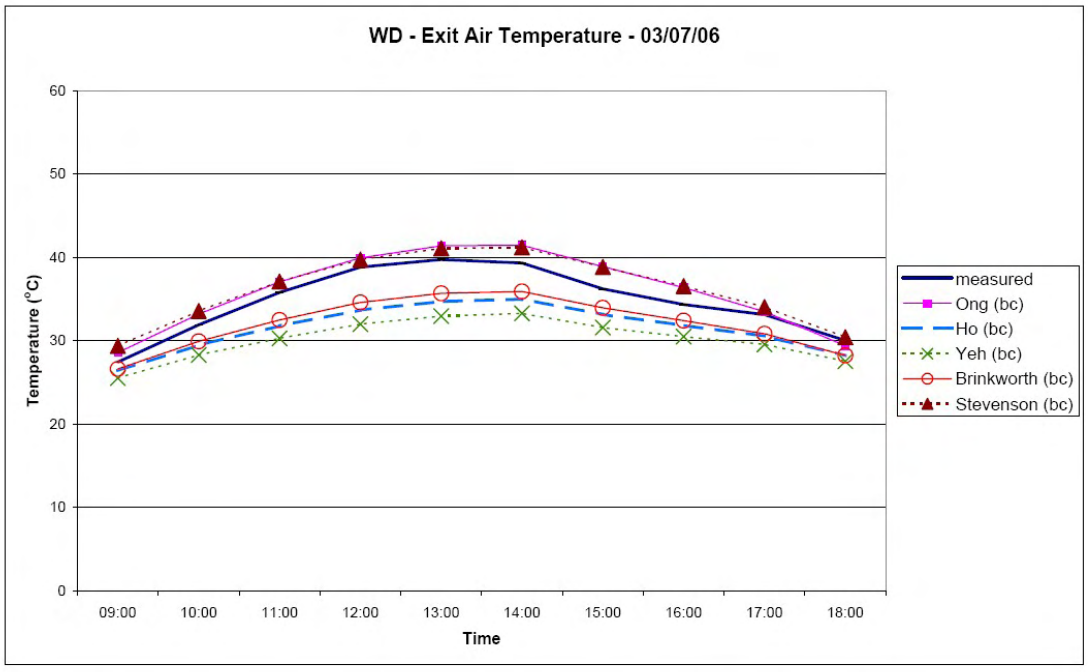

Figure 5.131. WD - Exit Air Temperature (Buoyant)

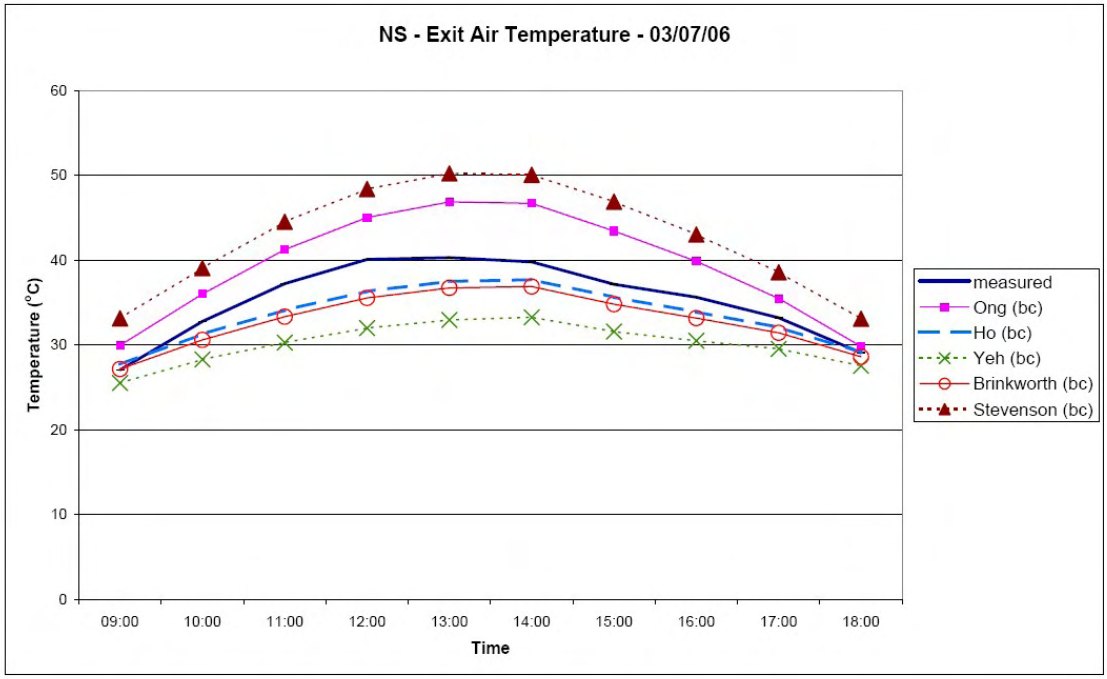

Figure 5.132. NS - Exit Air Temperature (Buoyant)

Table 5.44 indicates the mean bias and RMSE for the five models averaged over the time 09:00 to 18:00 for 03/07/06.

Table 5.44 Bias and RMSE for Design Model Prediction of Exit Air Temperature

		Ong_{bc}	Yeh_{bc}	Ho_{bc}	$Brinkworth_{bc}$	$Stevenson_{bc}$
Mean Bias (^oC)	ND	0.2	-5.6	-3.9	-3.1	1.6
	WD	1.3	-4.5	-3.2	-2.6	1.5
	NS	4.2	-5.1	-1.7	-2.4	7.5
	All	1.9	-5.1	-2.9	-2.7	3.5
RMSE (^oC)	ND	1.4	5.9	4.1	3.3	2.1
	WD	1.6	4.8	3.5	2.8	1.7
	NS	4.6	5.5	2.1	2.8	7.7
	All	2.9	5.4	3.3	3.0	4.7

From Table 5.44 it can be seen that the Ong_{bc} and $Stevenson_{bc}$ models tend to overestimate the exit air temperature; while the Yeh_{bc} , Ho_{bc} and $Brinkworth_{bc}$ models tend to underestimate. The Ong_{bc} model has the lowest bias and RMSE, and as such is considered the most accurate.

5.2.5 Discussion

Despite being simple in comparison with the other models, the $Stevenson_{bc}$ model is a reasonable predictor of mean air temperature. However, it is not the most accurate predictor for either parameter.

No one model shows a significant advantage over the others in predicting all five parameters being considered. Some models are better at predicting certain parameters, e.g.:

- The glazing temperature is best predicted by the Ong_{bc} model
- The absorbing surface temperature is best predicted by the Ong_{bc} model
- The mean air temperature is best predicted by the $Brinkworth_{bc}$ model
- The exit air temperature is best predicted by the Ong_{bc} model

However, it would be beneficial if the models could be improved more generally.

5.2.5.1 Improvements to Design Models

Various parameters within the five models assessed in Section 5.2 and the model developed in Chapter 4 were compared to identify the best practice. Where possible the best practice was incorporated in each of the design models under consideration.

The alterations are described below:

1. Although the Ong_{bc} model has proven to be an accurate predictor for the prototype ducts which are 1.9m long, the model does not take account of the friction effect which would be an issue for longer ducts. The air mass flow calculation developed by Brinkworth [4] does include the friction factor and should be introduced to the Ong_{bc} model.
2. Swinbank's correlation for the sky temperature (which is used in Ong_{bc}) can be replaced with the HTB2 algorithm, which is more sophisticated and takes account of the vertical orientation of the solar air heaters. This can also be introduced to Ho_{bcad}, allowing the calculation of the radiative heat transfer coefficient between the glass and the sky to be altered. This can now be calculated using the glass, sky and ambient temperatures.

3. Ong's [3] use of formulae to calculate the temperature dependent air dynamic viscosity, air thermal conductivity and air specific heat can be extended to the other models.
4. None of the models currently consider the effects of angle of incidence or the behaviour of direct and diffuse components of solar irradiation. Similarly the second opportunity for absorption of solar irradiation due to reflection within the duct should be included. Due to the structure of the Yeh_{bc} model, it is not possible to include the effect of incident angle on the transmission and reflection of solar irradiation.

5.2.6 Modified Predictive Models for Buoyant Convection

The procedure to apply the modified models is specified in Appendix H. The key parameters within the modified models are summarised in Table 5.45. The alterations are highlighted in bold text. The revised design models are referred to as Ong_{bcad}, Yeh_{bcad}, Ho_{bcad}, $Brinkworth_{bcad}$ and $Stevenson_{bcad}$ to differentiate them from their original formats.

Table 5.45 Comparison of Models Ong_{bcad}, Yeh_{bcad}, Ho_{bcad}, $Brinkworth_{bcad}$ and $Stevenson_{bcad}$

Parameter	Ong_{bcad}	Yeh_{bcad}	Ho_{bcad}	$Brinkworth_{bcad}$	$Stevenson_{bc}$
Considers the air heater	In entirety	In entirety	In entirety	In entirety	In entirety
Hydraulic diameter (D_h)	Unspecified – non circular duct (B1) used	Non circular duct (B1)	Non circular duct (B1)	Non circular duct (B1)	Non circular duct (B1)
Sky temperature (T_{sky})	**HTB2 algorithm (4.13-4.17)** substituted for Swinbank's correlation (C31)	Not Used	**HTB2 algorithm (4.13-4.17) used**	Not Used	Not Used
Wind convection heat transfer (h_w)	McAdam's correlation (C20)	Adjusted McAdam's correlation (C23)	McAdam's correlation (C20)	McAdam's correlation (C20)	McAdam's correlation (C20)
Dynamic viscosity of air (μ)	Temperature dependent (H18)	**Temperature dependent (H18)** substituted for Constan	Not Used	**Temperature dependent (H18)** substituted for Constan	**Temperature dependent (H18)** substituted for Constan
Kinematic viscosity of air (ν)	Not Used	Not Used	Constan**t**	Not Used	Not Used
Specific heat capacity of air (c_p)	Temperature dependent (H19)	**Temperature dependent (H19)** substituted for Constan	**Temperature dependent (H19)** substituted for Constan	**Temperature dependent (H19)** substituted for Constan	**Temperature dependent (H19)** substituted for Constan
Thermal conductivity of air (k)	Temperature dependent (H20)	**Temperature dependent (H20)** substituted for Constan	**Temperature dependent (H20)** substituted for Constan	**Temperature dependent (H20)** substituted for Constan	Not Used

Table 5.45 Cont'd Comparison of Models Ong_{bc}, Yeh_{bc}, Ho_{bc}, $Brinkworth_{bc}$ and $Stevenson_{bc}$

Parameter	Ong_{bcad}	Yeh_{bcad}	Ho_{bcad}	$Brinkworth_{bcad}$	$Stevenson_{bc}$
Density of air (ρ)	Temperature dependent (H28)	Not Used	**Temperature dependent (H28)** substituted for Constan	**Temperature dependent (H28)** substituted for Constan	**Temperature dependent (H28)** substituted for Constan
Nusselt number	Incropera and Dewitt's correlations for natural convection (C16 & C17)	Incropera and Dewitt's correlations for natural convection (C16 & C17)	Incropera and Dewitt's correlations for natural convection (C16 & C17)	Brinkworth (C18)	Not Used
Radiative heat transfer coefficient between parallel plates	Incorporating glass and solar absorber temperatures with glass and solar absorber emissivity (C28)	Incorporating fluid temperature with glass and solar absorber emissivity (C29)	Incorporating glass and solar absorber temperatures with glass and solar absorber emissivity (C28)	Incorporating glass and solar absorber temperatures with glass and solar absorber emissivity (A58)	Not Used
Radiative heat transfer coefficient between glass and sky	Incorporating glass, sky and ambient temperatures along with the emissivity of glass (C30)	Not Used	**Incorporating glass, sky and ambient temperatures along with the emissivity of glass (C30)** substituted C33	Incorporating glass, fluid and sol-air temperatures (A59 & A60)	Not Used

Table 5.45 Cont'd Comparison of Models Ong_{bc}, Yeh_{bc}, Ho_{bc}, $Brinkworth_{bc}$ and $Stevenson_{bc}$

Parameter	Ong_{bcad}	Yeh_{bcad}	Ho_{bcad}	$Brinkworth_{bcad}$	$Stevenson_{bc}$
Overall top heat loss coefficient	Sum of wind and radiative heat transfer coefficients (H4)	Incorporating the solar absorber and ambient temperatures, the wind coefficient and the emissivity of the solar absorber surface (A19)	Unspecified – definition from BS EN ISO 12241 [1] used	Sum of wind and radiative heat transfer coefficients (H4)	Definition from BS EN ISO 12241 [1] used without contribution from radiation
Heat loss coefficient including sides	No	No	Yes	No	Yes
Overall bottom heat loss coefficient	Incorporating conductive and wind convective components (H5)	Ratio of thermal conductivity and thickness of insulation (H7)	Unspecified – definition from BS EN ISO 12241 [1] used	Ratio of thermal conductivity and thickness of insulation (H7)	Definition from BS EN ISO 12241 [1] used without contribution from radiation
Considers heat gain from glass and absorbing surface separately	Yes	No	No	No	**Yes**
Considers direct and diffuse components of solar irradiation and angle of incidence	**Yes**	No	**Yes**	**Yes**	**Yes**
Considers heat transfer for sides	No	No	Yes	Yes	No

Table 5.45 Cont'd Comparison of Models Ong_{bc}, Yeh_{bc}, Ho_{bc}, $Brinkworth_{bc}$ and $Stevenson_{bc}$

Parameter	Ong_{bc}	Yeh_{bc}	Ho_{bc}	$Brinkworth_{bc}$	$Stevenson_{bc}$
Buoyant air mass flow	**Incorporating duct geometry, air density and specific heat capacity, acceleration due to gravity, ambient and fluid temperature, friction factor and solar irradiation (A57)** substituted for H30 & H31	Incorporating duct geometry, air density and specific heat capacity, acceleration due to gravity, ambient and fluid temperature, friction factor and solar irradiation (A57)	Incorporating duct geometry, air density and specific heat capacity, acceleration due to gravity, ambient and fluid temperature, friction factor and solar irradiation (A57)	Incorporating duct geometry, air density and specific heat capacity, acceleration due to gravity, ambient and fluid temperature, friction factor and solar irradiation (A57)	Incorporating duct geometry, air density and specific heat capacity, acceleration due to gravity, ambient and fluid temperature, friction factor and solar irradiation (A57)
Solution procedure	Iterative solution of matrix equation.	Iterative solution of a series of equations.	Iterative solution of a series of equations.	Iterative solution of a series of equations.	Iterative solution of a series of equations.
	The meteorological data and physical properties of the materials used in the experiment (e.g. emissivity, absorptivity, etc) were applied to the model.		**Further reference to properties of the materials used in the experiment (e.g. absorptivity, etc) were applied to the model.**	The meteorological data and physical properties of the materials used in the experiment (e.g. emissivity, absorptivity, etc) were applied to the model.	

Table 5.45 Cont'd Comparison of Models Ong_{bc}, Yeh_{bc}, Ho_{bc}, $Brinkworth_{bc}$ and $Stevenson_{bc}$

Parameter	Ong_{bc}	Yeh_{bc}	Ho_{bc}	$Brinkworth_{bc}$	$Stevenson_{bc}$
Parameters Calculated Directly	The mean glass, mean absorber, mean duct air, exit air temperature and air mass flow are calculated directly from the model.	The mean absorber, mean duct air, exit air temperature and air mass flow are calculated directly from the model.	The mean outer glass, mean inner glass, mean absorber, mean outer, mean duct air, exit air temperature and air mass flow are calculated directly from the model.	The mean glass, mean absorber, mean duct air, exit air temperature and air mass flow are calculated directly from the model.	The mean duct air, exit air temperature and air mass flow are calculated directly from the model.
Parameters Calculated Indirectly	The power output is calculated from the calculated air mass flow and air exit temperature.				

5.2.6.1 Prediction of Mean Glazing Temperature

The following graphs show the correlation between the measured mean glazing temperature for ducts ND, WD and NS and the predictions given by the $Ong_{bcad,}$ Ho_{bcad} and $Brinkworth_{bcad}$ models. The Yeh_{bcad} and $Stevenson_{bcad}$ models do not predict the glazing surface temperature.

Figures 5.133 - 5.135 show the correlation for 03/07/06.

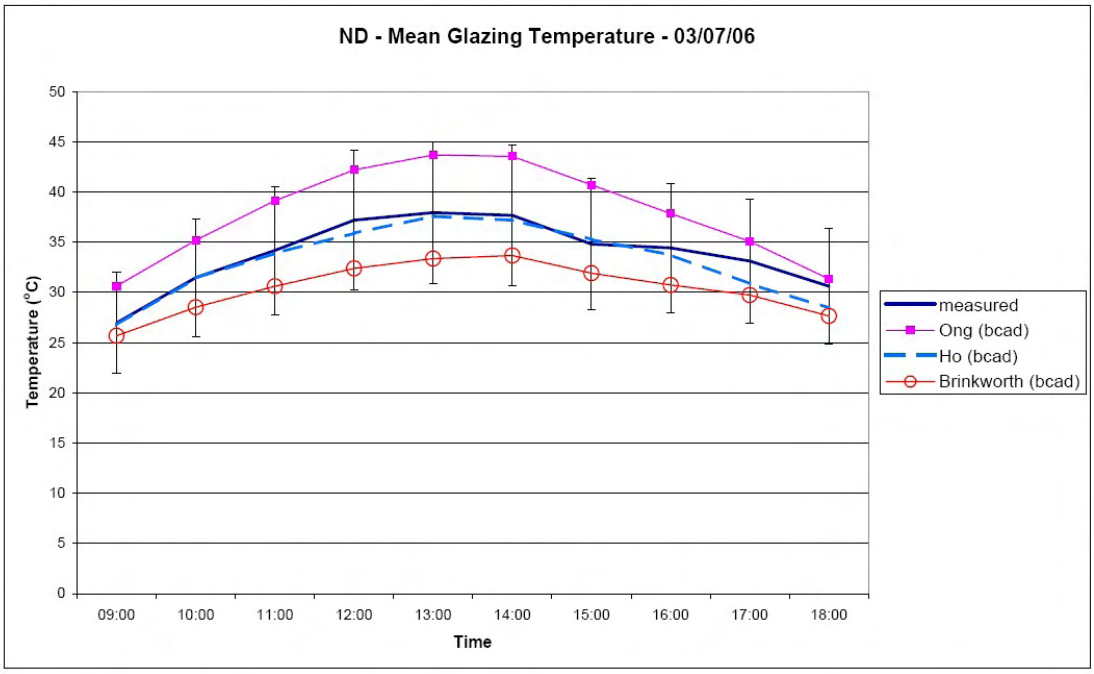

Figure 5.133. ND - Mean Glazing Temperature (Adapted buoyant models)

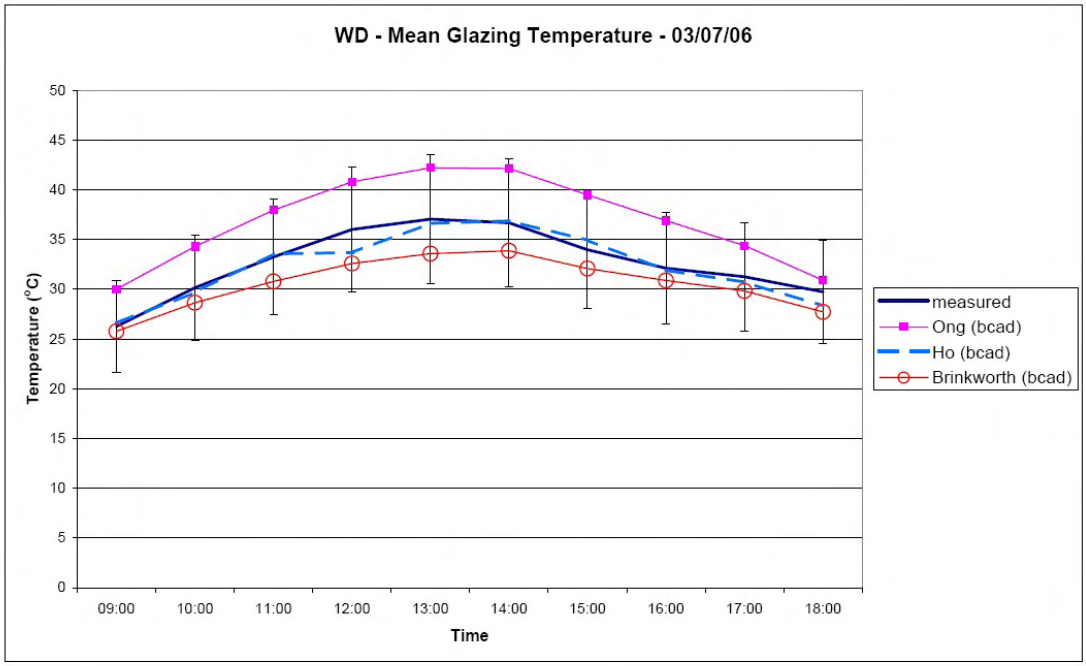

Figure 5.134. WD - Mean Glazing Temperature (Adapted buoyant models)

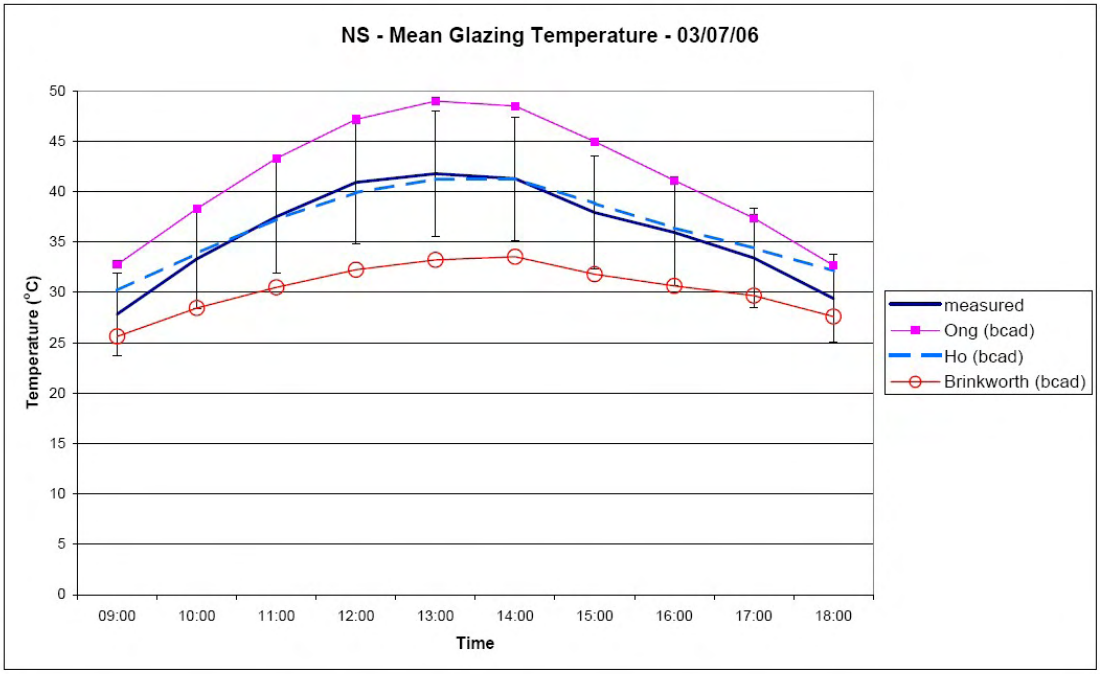

Figure 5.135. NS - Mean Glazing Temperature (Adapted buoyant models)

Table 5.46 indicates the mean bias and RMSE for the three models averaged over the time 09:00 to 18:00 for 03/07/06.

Table 5.46 Bias and RMSE for Design Model Prediction of Mean Glazing Temperature

		Ong_{bcad}	Yeh_{bcad}	Ho_{bcad}	$Brinkworth_{bcad}$	$Stevenson_{bcad}$
Mean Bias (^oC)	ND	4.1	N/A	-0.7	-3.4	N/A
	WD	4.3		-0.4	-2.1	
	NS	5.6		0.6	-5.6	
	All	4.6		-0.2	-3.7	
RMSE (^oC)	ND	4.4		1.1	3.5	
	WD	4.4		1.0	2.3	
	NS	5.7		1.3	6.1	
	All	4.9		1.1	4.3	

From Table 5.46 it can be seen that the $Brinkworth_{bcad}$ models tends to underestimate the mean glazing temperature, the Ong_{bcad} model tends to overestimate it and the Ho_{bcad} model does not show a consistent bias. The Ho_{bcad} model has the lowest bias and RMSE of the model assessed so far for mean glazing temperature, and as such is considered the most accurate.

5.2.6.2 Prediction of Mean Absorbing Surface Temperature

The following graphs show the correlation between the measured mean absorbing temperature for ducts ND, WD and NS and the predictions given by $Ong_{bcad,}$ Yeh_{bcad}, Ho_{bcad}, $Brinkworth_{bcad}$. The $Stevenson_{bcad}$ model does not predict the mean absorber surface temperature.

Figures 5.136 - 5.138 show the correlation for 03/07/06.

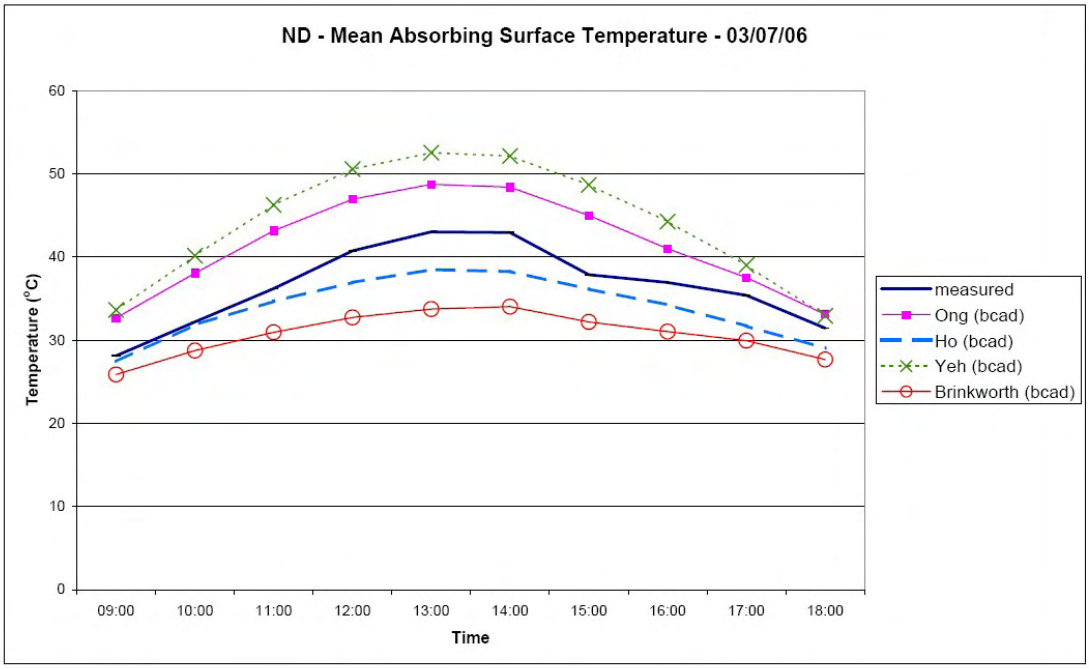

Figure 5.136. ND - Mean Absorber Temperature (Adapted buoyant models)

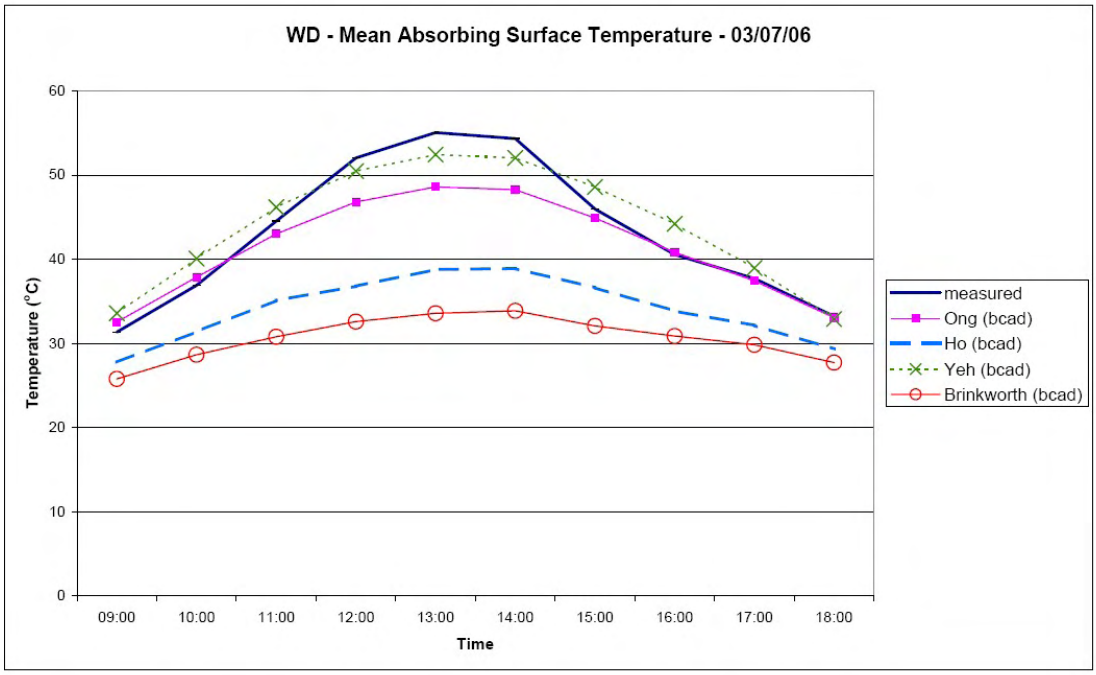

Figure 5.137. WD - Mean Absorber Temperature (Adapted buoyant models)

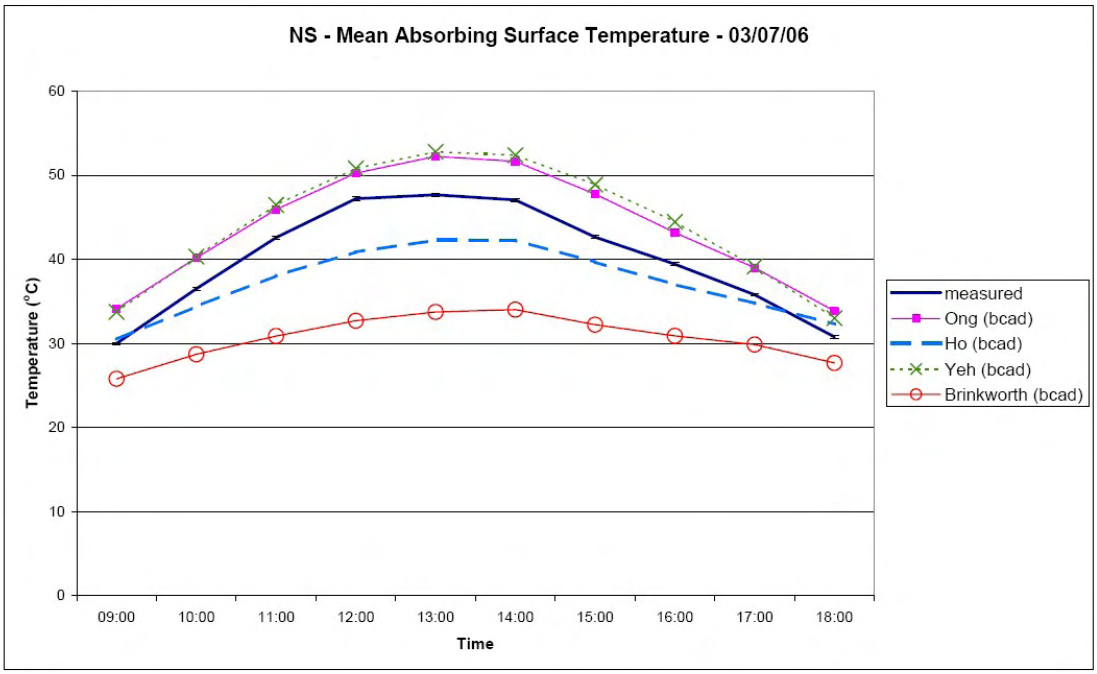

Figure 5.138. NS - Mean Absorber Temperature (Adapted buoyant models)

Table 5.47 indicates the mean bias and RMSE for the three models averaged over the time 09:00 to 18:00 for 03/07/06.

Table 5.47 Bias and RMSE for Design Model Prediction of Absorbing Surface Temperature

		Ong_{bcad}	Yeh_{bcad}	Ho_{bcad}	$Brinkworth_{bcad}$	$Stevenson_{bcad}$
Mean Bias (°C)	ND	5.0	7.5	-2.6	-5.8	N/A
	WD	-1.8	0.8	-9.1	-12.2	
	NS	3.8	4.2	-2.8	-9.3	
	All	2.3	4.2	-4.8	-9.1	
RMSE (°C)	ND	5.3	8.1	3.0	6.2	
	WD	3.3	2.3	10.2	13.5	
	NS	3.9	4.4	3.7	10.1	
	All	4.3	5.5	6.5	10.3	

From Table 5.47 it can be seen that the Yeh_{bcad} model tends to overestimate the mean temperature of the absorbing surface. Ho_{bcad} and $Brinkworth_{bcad}$ models tend to underestimate it. While there is no consistent bias associated with the Ong_{bcad} model. The Ong_{bcad} model has the lowest bias and RMSE of the models after excluding the

Ong_{bc} model. The Ong_{bcad} model is considered to be the best choice of predictor for the mean absorbing surface temperature.

5.2.6.3 Prediction of Duct Mean Air Temperature

The following graphs show the correlation between the measured mean air temperature for ducts ND, WD and NS and the predictions given by Ong_{bcad}, Yeh_{bcad}, Ho_{bcad}, $Brinkworth_{bcad}$ and $Stevenson_{bcad}$.

Figures 5.139 - 5.141 show the correlation for 03/07/06.

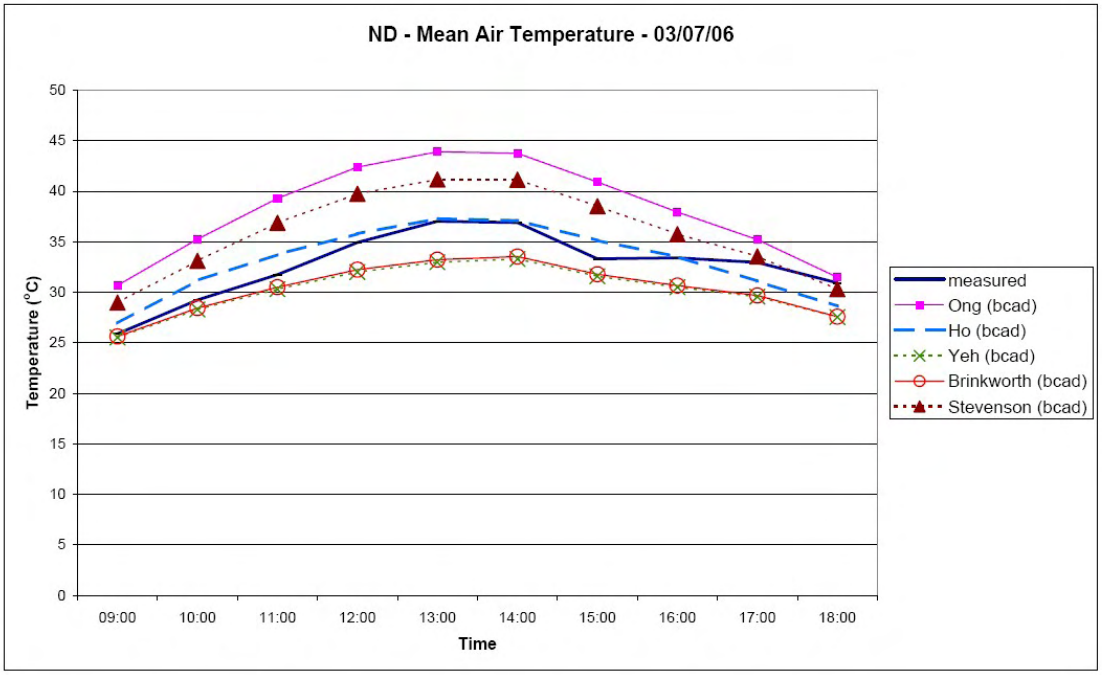

Figure 5.139. ND - Mean Air Temperature (Adapted buoyant models)

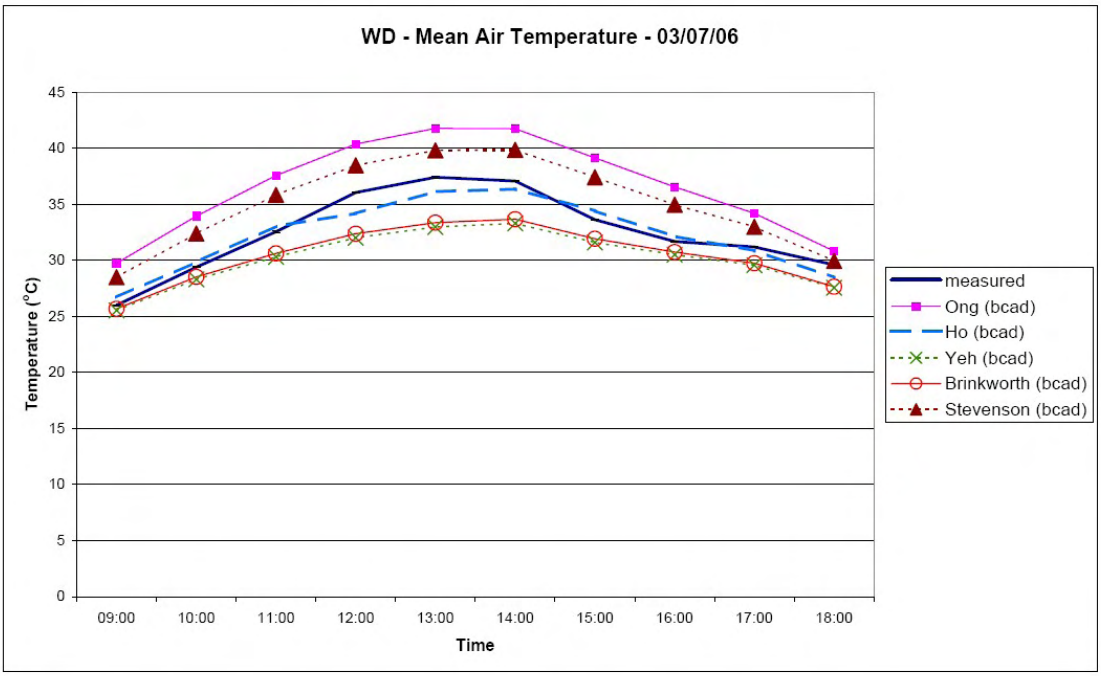

Figure 5.140. WD - Mean Air Temperature (Adapted buoyant models)

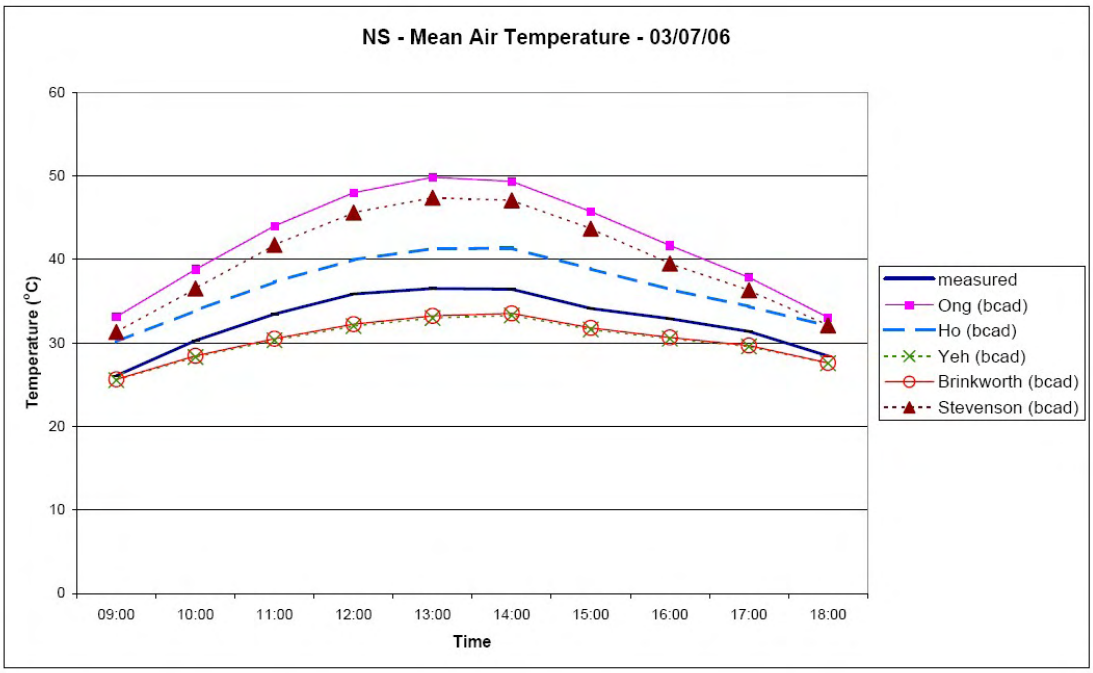

Figure 5.141. NS - Mean Air Temperature (Adapted buoyant models)

Table 5.48 indicates the mean bias and RMSE for the three models averaged over the time 09:00 to 18:00 for 03/07/06.

Table 5.48 Bias and RMSE for Design Model Prediction of Mean Air Temperature

		Ong_{bcad}	Yeh_{bcad}	Ho_{bcad}	$Brinkworth_{bcad}$	$Stevenson_{bcad}$
Mean Bias (^oC)	ND	5.4	-2.5	0.4	-2.3	3.3
	WD	4.1	-2.3	-0.2	-2.0	2.6
	NS	9.6	-2.4	4.0	-2.2	7.6
	All	6.4	-2.4	1.4	-2.2	4.5
RMSE (^oC)	ND	5.9	2.7	1.5	2.6	3.8
	WD	4.3	2.6	0.9	2.4	2.7
	NS	10.0	2.6	4.1	2.4	8.0
	All	7.1	2.7	2.5	2.5	5.3

From Table 5.48 it can be seen that the Ong_{bcad} and $Stevenson_{bcad}$ models tend to overestimate the mean air temperature; the Yeh_{bcad} and $Brinkworth_{bcad}$ models tend to underestimate it while the Ho_{bcad} model does not have a consistent bias. However, none of the models have a lower bias and RMSE than the Ong_{bc} model. The $Brinkworth_{bc}$ model has the lowest bias and RMSE of the models after excluding the Ong_{bc} model.

5.2.6.4 Prediction of Exit Air Temperature

The following graphs show the correlation between the measured exit air temperature for ducts ND, WD and NS and the predictions given by Ong_{bcad}, Yeh_{bcad}, Ho_{bcad}, $Brinkworth_{bcad}$ and $Stevenson_{bcad}$.

Figures 5.142 - 5.144 show the correlation for 03/07/06.

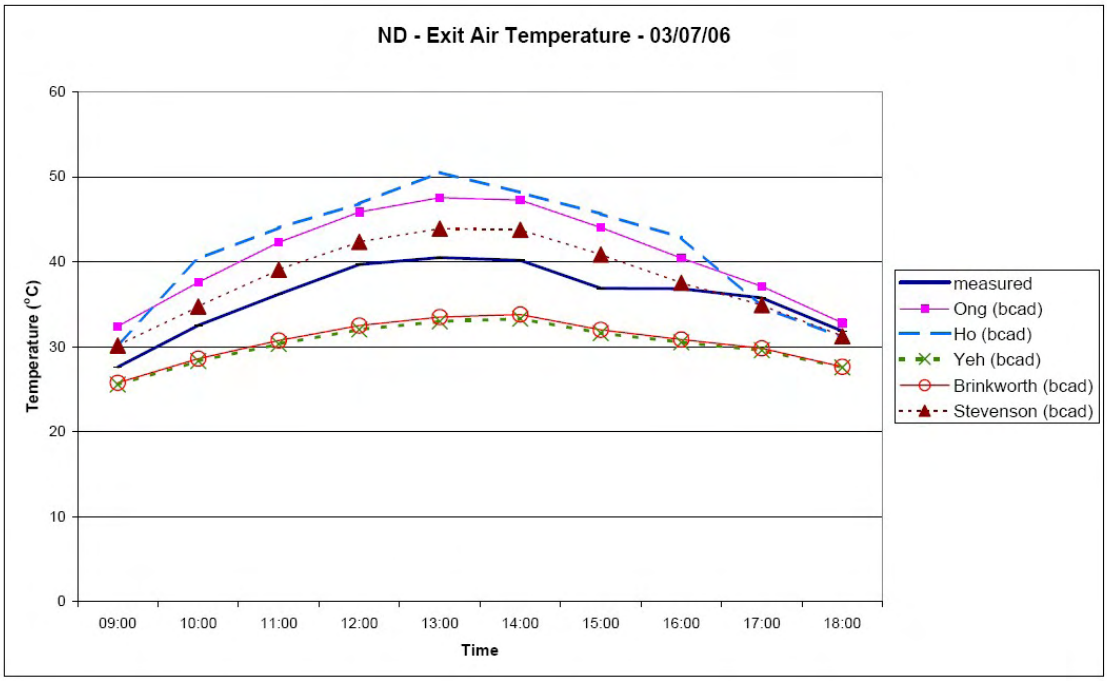

Figure 5.142. ND - Exit Air Temperature (Adapted buoyant models)

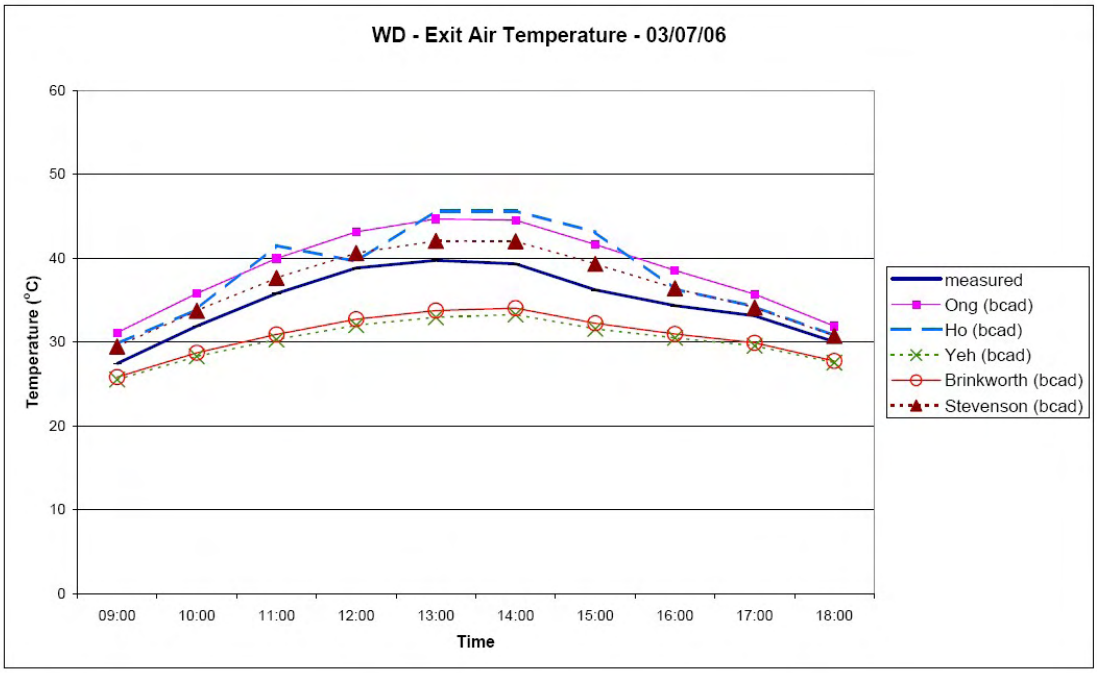

Figure 5.143. WD - Exit Air Temperature (Adapted buoyant models)

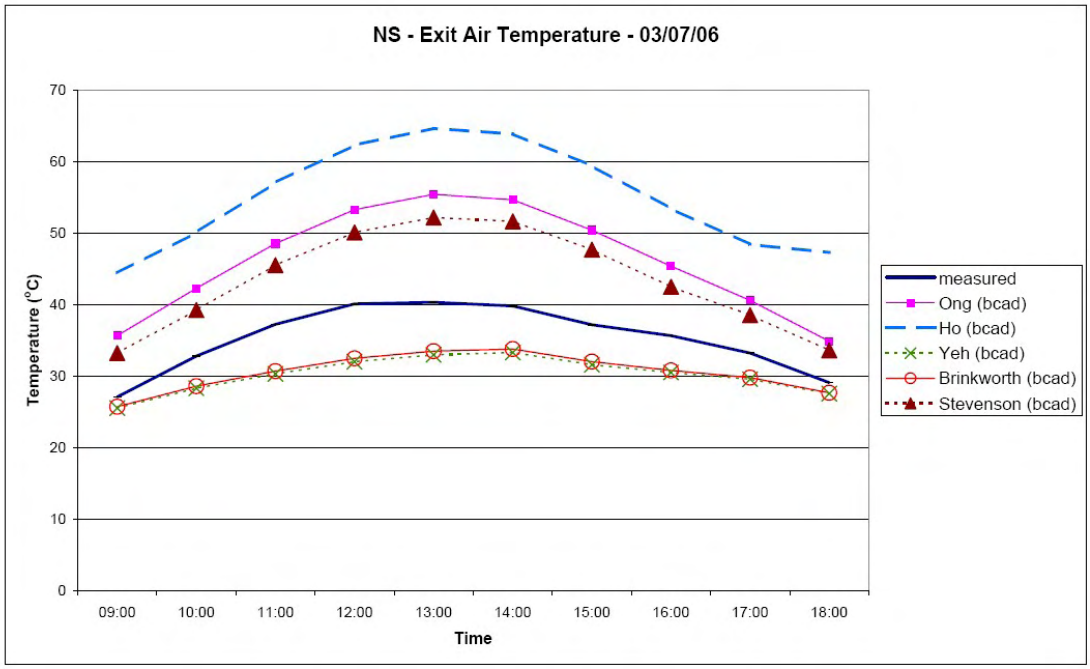

Figure 5.144. NS - Exit Air Temperature (Adapted buoyant models)

Table 5.49 indicates the mean bias and RMSE for the three models averaged over the time 09:00 to 18:00 for 03/07/06.

Table 5.49 Bias and RMSE for Design Model Prediction of Exit Air Temperature

		Ong_{bc}	Yeh_{bc}	Ho_{bc}	$Brinkworth_{bcad}$	$Stevenson_{bc}$
Mean Bias (^oC)	ND	5.0	-5.6	5.7	-5.3	-2.0
	WD	4.0	-4.5	3.4	-4.0	1.9
	NS	10.9	-5.1	19.9	-4.8	8.2
	All	6.6	-5.1	9.6	-4.7	4.1
RMSE (^oC)	ND	5.4	5.9	6.8	5.5	2.6
	WD	4.2	4.8	4.1	4.3	2.1
	NS	11.3	5.5	20.1	5.2	8.6
	All	7.6	5.4	12.5	5.0	5.3

From Table 5.49 it can be seen that the Ong_{bcad} and Ho_{bcad} models tend to overestimate the exit air temperature; while the Yeh_{bcad} and $Brinkworth_{bcad}$ models tend to underestimate it. The $Stevenson_{bcad}$ model is not consistently biased. The $Brinkworth_{bc}$ model has the lowest bias and RMSE of the models after excluding the Ong_{bc} model.

5.2.6.5 Discussion

Table 5.50 shows the combined bias and RMSE values for all the ducts.

Table 5.50 Bias and RMSE values for ducts ND, WD and NS - 03/07/06

Model	Glazing Temperature (^oC)	Absorbing Surface Temperature (^oC)	Mean air Temperature (^oC)	Exit air Temperature (^oC)
Bias				
Ong_{bc}	0.4	-0.8	2.9	1.9
Yeh_{bc}		4.2	-2.4	-5.1
Ho_{bc}	-3.4	-8.7	-1.8	-2.9
$Brink_{bc}$	-2.3	-6.0	-1.2	-2.7
$Steve_{bc}$			4.1	3.5
Ong_{bcad}	4.6	2.3	6.4	6.6
Yeh_{bcad}		4.2	-2.4	-5.1
Ho_{bcad}	-0.2	-4.8	1.4	9.6
$Brink_{bcad}$	-3.7	-9.1	-2.2	-4.7
$Steve_{bcad}$			4.5	4.1
RMSE				
Ong_{bc}	1.3	3.1	3.5	2.9
Yeh_{bc}		5.5	2.7	5.4
Ho_{bc}	3.9	10.0	2.1	3.3
$Brink_{bc}$	3.0	7.8	1.5	3.0
$Steve_{bc}$			4.9	4.7
Ong_{bcad}	4.9	4.3	7.1	7.6
Yeh_{bcad}		5.5	2.7	5.4
Ho_{bcad}	1.1	6.5	2.5	12.5
$Brink_{bcad}$	4.3	10.3	2.5	5.0
$Steve_{bcad}$			5.3	5.3

From Table 5.50 it can be seen that:

- Ho_{bcad} has the lowest bias and RMSE for the glazing temperature
- Ong_{bc} has the lowest bias and RMSE for the absorbing surface temperature; however, the Ong_{bc} model does not take account of the friction forces in the flow and is less likely to be appropriate for long ducts. After discounting the Ong_{bc} model, the Ong_{bcad} model has the lowest bias and RMSE.
- $Brinkworth_{bc}$ has the lowest bias and RMSE for the mean air temperature
- Ong_{bc} has the lowest bias and RMSE for the exit air temperature; however, the Ong_{bc} model does not take account of the friction forces in the flow and is less

likely to be appropriate for long ducts. After discounting the Ong_{bc} model, the $Brinkworth_{bc}$ model has the lowest bias and RMSE.

The Ho_{bcad} model has a mean bias and RMSE of less than 3^oC for its prediction of the mean glazing temperature of each of the ducts, which means it is an acceptable predictor for that parameter.

The absorbing surface temperature is not a critical parameter. For this reason, the Ong_{bcad} model is considered acceptable even though it exceeds 2^oC for the RMSE of all ducts, and for the bias of each duct except WD.

The mean air temperature is a critical parameter for the calculation of the air mass flow. The $Brinkworth_{bc}$ model has a mean bias and RMSE of less than 2^oC for its prediction of the mean air temperature of each of the ducts, which means it is an acceptable predictor for that parameter.

The mean bias and RMSE of the $Brinkworth_{bc}$ model exceeds the required accuracy of 2^oC for the exit air temperature. An improvement would be beneficial since the exit air temperature is a critical parameter. The mean bias for the $Brinkworth_{bc}$ model only ranges between -2.4 and 3.1^oC for the ducts being considered. If the model was only required for 1.9m long ducts, the bias could be reduced by adding 2.7^oC (the mean bias calculated for all of the ducts) to the exit air temperature predicted by the $Brinkworth_{bc}$ model. This would bring the overall mean bias to 0 and reduce the RMSE to 1.2^oC. However, the bias for ducts of different lengths cannot be anticipated from the data available, and this improvement cannot be implemented. The model will be used in its current form.

5.2.7 Prediction of Power Output

As in Section 5.1, the exit air temperature is considered to be a critical parameter since it is related to the power output. The mean air temperature is also a critical parameter, since it is required to calculate the air mass flow, which is a component of the power output calculation. The mean air temperature, the exit air temperature and the air mass flow are interrelated. The $Brinkworth_{bc}$ model has been shown to be the most accurate predictor of the mean air temperature and the exit air temperature. For this reason, it

seems logical to assume that this model will be the most accurate predictor of the air mass flow. The predicted air mass flow for ducts ND, WD and NS is illustrated in Figure 5.145.

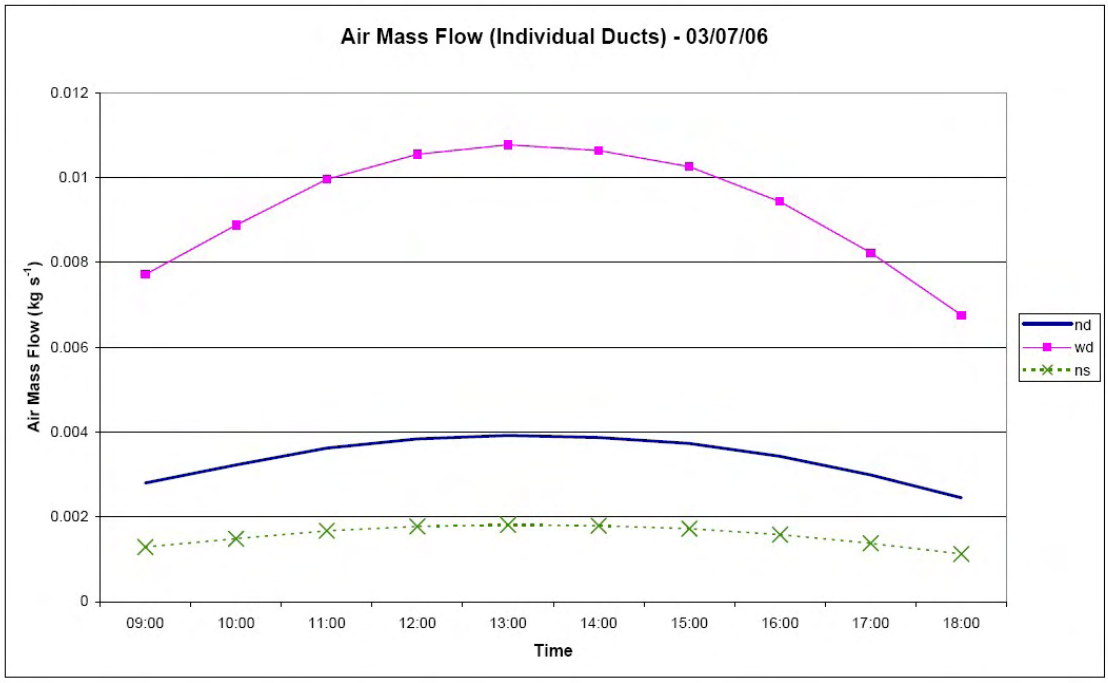

Figure 5.145. Air Mass Flow Predicted Using Brinkworth$_{bc}$ Model

The air mass flow for duct ND is slightly lower than the air mass flow used in the forced convection experiment on 05/05/06. The air exit temperatures obtained during the forced convection experiment were slightly lower than those measured during the buoyant convection experiment. This is to be expected with a slightly higher air mass flow. However, a quantitative comparison between the experiments is not possible since they were carried out on different days with different weather conditions.

The power output was calculated using the measured exit air temperature and air mass flow predicted using the Brinkworth$_{bc}$ model. These values were normalised for a 10m^2 façade area as previously in Section 5.1.9 and are shown in Figure 5.146. This calculation indicates a ranking for the ducts of ND, WD then NS.

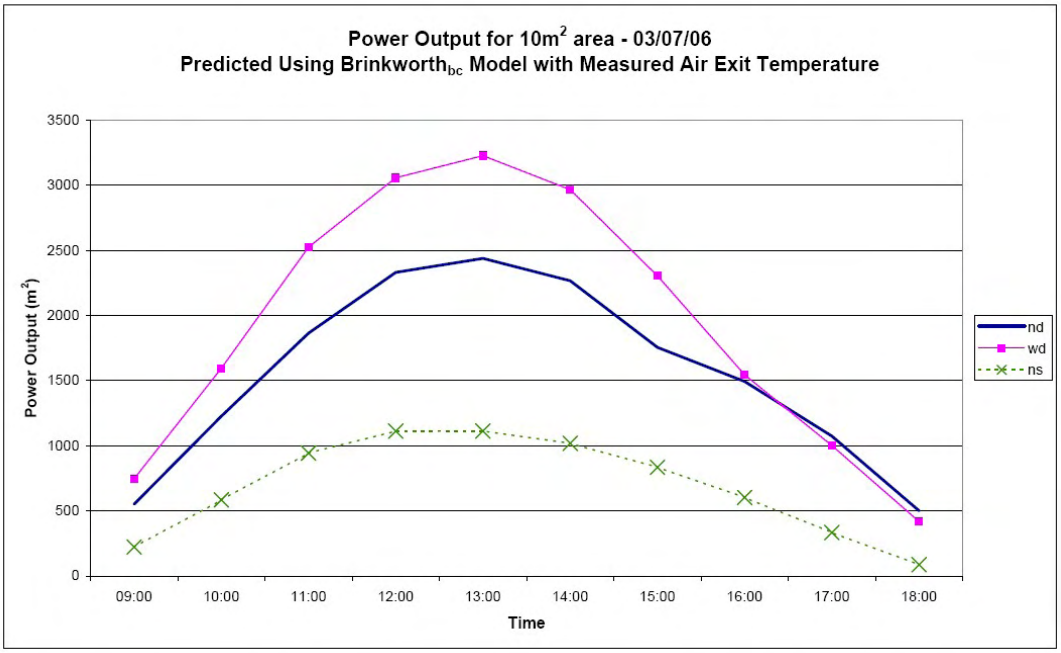

Figure 5.146. Power Output for 10m^2 Area - Air exit temperature measured, Air mass flow calculated using Brinkworth$_{bc}$ Model

The power output for each duct was also calculated using the Brinkworth$_{bc}$ model to predict the air mass flow and the air exit temperature. Again the power output was normalised for a 10m^2 façade area. The results are shown in Figure 5.147. This calculation also indicates a ranking of ND, WD and NS.

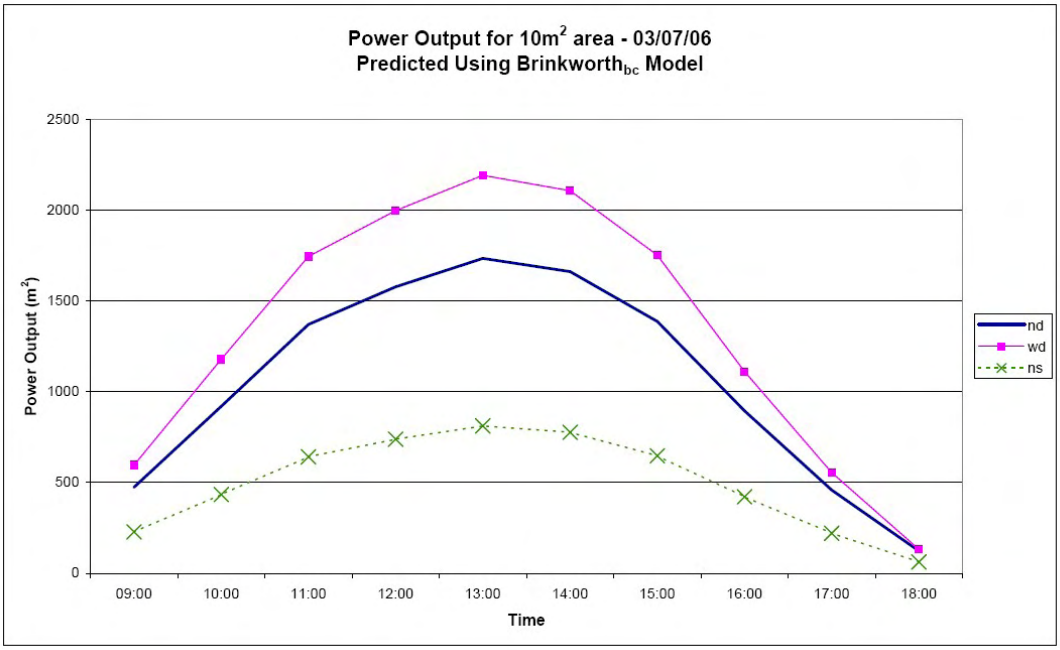

Figure 5.147. Power Out for 10m^2 area - predicted using Brinkworth$_{bc}$ Model

Although Figure 5.146 and Figure 5.147 indicate the same ranking for the ducts, the actual power outputs differ. Figure 5.146 predicts the peak outputs to range between 1000 and 3000W, while Figure 5.147 predicts the peak outputs to range between 750 and 2250 W. However, both figures indicate a power output greater than 1 kW for 6 hours of the day.

5.3 Conclusions

Three design models from the literature were considered for forced convection. Since none of the models were able to predict consistently the measured conditions as they stood, they were modified. The air exit temperature and power output were considered to be the most important in this application, so those parameters were given higher emphasis. The modified Ho model ($Ho_{fc\&fcad}$) was found to give the most accurate prediction of the air exit temperature and power output compared to results from the outdoor experiment. However, this was still limited, with an RMSE of 39 W in 100, and did not replicate the trends established through measurement. The model is believed to be limited in its prediction of deep ducts, due to internal shadows forming during the day. These shadows are more extensive in deep ducts than in shallow ducts. Although the area of the shadows could be predicted using geometry, a technique for estimating the temperature of the shaded area has not been found. The $Ho_{fc\&fcad}$ model will be used in Chapter 6 to optimise the geometry of the system for forced convection. However, conclusions drawn from using the model must be applied with care.

Two design models from the literature were found for buoyant convection (one of these was a variant on a design model considered for forced convection). The other two design models for forced convection were adapted to accommodate buoyant convection. In addition a simple model which did not incorporate the Nusselt number was developed for buoyant convection. Therefore, five models were considered for predicting buoyant convection. The Brinkworth model ($Brinkworth_{bc}$) was found to give the most accurate prediction of the air exit temperature from the outdoor experiment, with an RMSE of $9^{o}C$ in 100. Air mass flow could not be compared as it was not measured. The air mass flow predicted by the $Brinkworth_{bc}$ model was approximately 0.003 kg s^{-1} for duct ND, this was slightly lower than the air mass flow used in the forced convection experiment, which resulted in slightly lower air exit

temperatures. The Brinkworth_{bc} model will be used in Chapter 6 to optimise the geometry of the system for buoyant convection.

5.4 References

1. British Standards Institution, *Thermal insulation for building equipment and industrial installations - Calculation Rules*, BS EN ISO 12241, 1998.
2. Guan, C.N. *Dynamic Models of Solar Air Collector* 2006: Master of Science in Energy Systems; Department of Applied Sciences at Aachen University.
3. Ong, K.S., *A mathematical model of a solar chimney.* Renewable Energy, 2003. **28**: p. 1047-1060.
4. Brinkworth, B.J., R.H. Marshall, and Z. Ibarahim, *A Validated Model of Naturally Ventilated PV Cladding.* Solar Energy, 2000. **69**: p. 67-81.
5. Brinkworth, B.J. and M. Sandberg, *A validated procedure for determining the buoyancy-induced flow in ducts.* Building Services Engineering Research & Technology, 2005. **26**(1): p. 35-48.

6 Solar Duct Optimisation

There are two aims of this chapter. The first is to explore the sensitivity of the duct performance (i.e. air exit temperature, air mass flow, power output) to changes in the absorbing surface material.

The second is to establish the optimum geometry of the solar duct within expected manufacturing limitations for forced and buoyant convection cases. To optimise the system geometry, it must be understood which parameter the system is being optimised for: air exit temperature, air mass flow or power output. Hollands and Shewen [1] indicated that short solar ducts have higher levels of convective heat transfer coefficient and therefore have higher efficiencies; however, they may not generate the exit air temperature required from the system. For this reason, the optimum geometry will be calculated for each of the parameters defined.

6.1 Optimisation of the Absorbing Surface Material

Research has shown that architects would like a palette of colours and shades when designing with coated steel [2]. Colours are specifically related to a material's reflectivity in the visible spectrum, however, it can have an impact on its reflectivity over the wider spectrum. Coatings can be specifically designed to have a different solar reflectance than their colour would indicate (i.e. a reflective black coating has been designed for use in hot climates). Corus has not had reason to require a low reflectance, light coloured coating. Therefore, there is some concern over how much impact a light coloured coating would have on the efficiency of the system. Metallic silver Armacor® is a popular architectural product, but there is currently no reflectance data available for it. Reflectance data is available for standard black Armacor®. Both products were analysed and compared.

A frame was constructed to hold a metal sample (1 m x 1 m) with a pyranometer positioned at its centre point, 0.1m from the sample (Figure 6.1). At this position, 99 % of the signal received by the pyranometer should come from the metal sample [3]. The experiment was carried out between 12:00 and 14:00 on days with similar weather to

ensure that conditions were comparable. The time was chosen to ensure that the minimum area of the metal was obscured by shadow from Pyranometer 2.

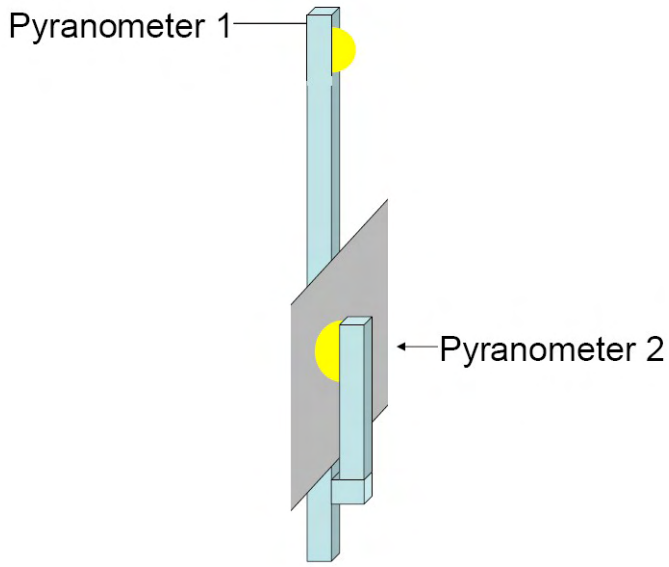

Figure 6.1. Experiment to calculate the reflectivity of black and silver painted steel

Over the testing period, the reflectivity of the black Armacor® was found to be 0.08 ± 0.02. The paint company was able to provide data on standard black paint which indicated it had a reflectance of 0.05 ± 0.01 (ASTM E903-96). These figures are comparable, and indicate the suitability of the technique to calculate the reflectivity of silver Armacor®, which was found to be 0.38.

The effect of changing the reflectivity of the solar absorbing material between 0.05 and 0.4 was explored for forced and buoyant convection, for the weather conditions which were measured on 05/05/06 (shown in Table 6.1). The $Ho_{fc\&fcad}$ model developed for forced convection, in Chapter 5 was used to calculate the daily average air exit temperature and total power output for a 0.005 kg s^{-1} flow of air through a duct 0.101 m wide, 0.1105 m deep and 1.9 m long. The $Brinkworth_{bc}$ model considered in Chapter 5 was used to calculate the air exit temperature, air mass flow and power output for buoyant flow through a duct of the same dimensions. Both of these models incorporate the reflectivity of the solar absorbing material indirectly by referring to the absorptivity. The results are shown in Table 6.2.

Table 6.1 Input Conditions for 05/05/06 (Averaged over 1 hour periods)

Time period	Ambient Temp. (^oC)	Horizontal diffuse irradiation (W m^{-2})	Horizontal global irradiation (W m^{-2})
08:00	10.5	31	51
09:00	10.8	82	230
10:00	11.5	120	282
11:00	11.9	146	572
12:00	12.6	78	686
13:00	14.1	59	739
14:00	15.1	64	782
15:00	15.7	74	781
16:00	16.6	82	746
17:00	16.1	99	650
18:00	15.5	106	517
19:00	15.4	106	341
20:00	15.0	77	220

Table 6.2 Effect of Solar Absorbing Reflectivity on Solar Duct Output

Reflectivity	Forced Convection @ 0.005 kg s^{-1}		Buoyant Convection		
	Average Air Exit Temperature (^oC)	Total Power Output (W)	Average Air Exit Temperature (^oC)	Average Air Mass Flow (kg s^{-1})	Total Power Output (W)
0.05	21.3	377	21.0	0.0043	382
0.1	21.0	359	20.7	0.0042	359
0.15	20.7	341	20.5	0.0041	338
0.2	20.4	321	20.3	0.0041	316
0.25	20.1	301	20.1	0.0040	295
0.3	19.9	286	19.8	0.0039	274
0.35	19.5	264	19.6	0.0038	252
0.4	19.3	246	19.4	0.0036	231

Table 6.2 shows that increasing the reflectivity of the solar absorbing material from 0.05 to 0.4 will cause a drop in average air exit temperature of 1.5 to 2.0^{o}C under the scenario considered. Although this may not seem a significant effect, it reduces the power output for the forced convection scenario by 35 %. For the buoyant scenario the reduction in air mass flow also has an effect, and the power output is reduced by 40 %.

To achieve the most benefit from a solar façade, the solar absorbing surface should have as low a reflectivity as possible. Future calculations will assume that black Armacor® with a reflectivity of 0.05 is used.

6.2 Optimisation of the Solar Duct Geometry

6.2.1 Experimental Method

Assuming a good design model is used, the optimisation technique would be able to accurately predict the optimum dimensions of a solar duct for any prescribed output (e.g. air exit temperature, power).

6.2.1.1 Optimised Outputs

The duct will be studied in two modes; forced and buoyant air flow. In each case the performance of the solar duct will be studied in two conditions:

- A single duct
- An array of 10 m^2 on a façade. This is to allow reasonable comparison between different geometries.

Ducts in an area would require a lateral and vertical separation. It has been assumed that each duct is separated from its neighbour by 0.02 m laterally. This allows contact area with the covering material. It also allows the ducts to be joined with a small flange to form a coherent façade. It has also been assumed that individual solar ducts will be separated from each other by a gap of 0.1 m vertically. This allows conduits to remove the heated air from the lower solar duct to the building as well as fresh air ingress to the higher solar duct.

Figure 6.2 shows how an array of ducts could be arranged on a façade.

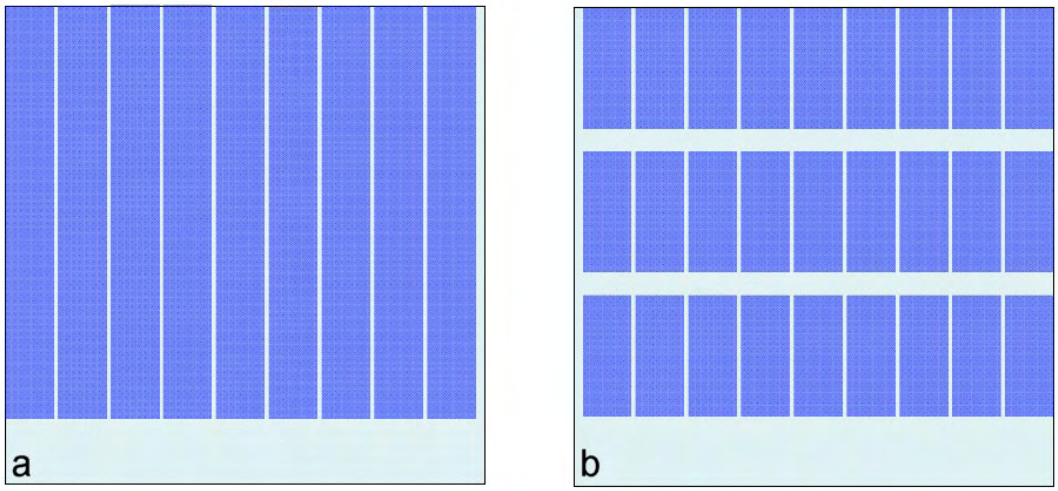

Figure 6.2. Array of ducts on part of a facade:
a long ducts
b short ducts

The spacing described above has been included in the calculation of a 10 m^2 façade area. Where it is necessary to calculate the output of a 'fraction' of a duct to fit in the 10 m^2 area the fraction is apportioned evenly (e.g. for 25 % of a duct, 25 % of the duct power output would be included). It should be noted that a façade area of 10 m^2 has less than 10 m^2 glazed surface exposed to the solar irradiation (due to the spacing of the ducts).

In a forced convection system, the air movement is generated by an outside source (e.g. fan), and solar irradiation is utilised to heat the air. The parameters of interest to optimising the duct are:

For a single duct:

- average exit air temperature over the day. The average temperature allows for variations in weather conditions over the day. Predictions based on average exit air temperature are of more use to a building designer, than those based on peak temperature. The exit air temperature will be calculated on an hourly basis between sunrise and sunset using the $Ho_{fc\&fcad}$ model for forced convection as developed in Section 5.1. The hourly results will be averaged.
- Net power output over the day. The power output and the required pumping power for a set air mass flowing through a single solar duct will be calculated on an hourly basis between sunrise and sunset. The net power output will be

found by subtracting the pumping power from the total power output. The hourly results will be averaged.

For an array of ducts within a façade area of 10 m^2:

- Air mass flow output over the day. The hourly air mass flow will be calculated. Since a forced flow of 0.01 kg s^{-1} $duct^{-1}$ is being considered, there will be no variation in the air mass flow during the day.
- net power output over the day. The power output and the required pumping power for a set air mass flowing through a single solar duct will be calculated on an hourly basis between sunrise and sunset. The net power output will be found by subtracting the pumping power from the total power output. The hourly results will be averaged. This result will be multiplied by an area factor to equate to a 10 m^2 area.

The plots of instantaneous power in vs useful power out in Section 4.4.2 indicated that the system had a very small time constant. This agrees with the work carried out by Ho and Loveday which indicated that similar system had a time constant of five minutes[4]. Therefore it is acceptable to make hourly calculations.

The total power output (Q) is related to the air mass flow ($\dot{m}$), the specific heat capacity c_p, and the difference between the air exit and air inlet temperatures:

$$Q = \dot{m} c_p \Delta T \qquad \text{C37}$$

The required pumping power for forced convection (P_{fan}) of a set air mass flow is related to the air volume flow ($\dot{Q}$), the pressure drop between the air exit and air inlet (Δp)and the fan efficiency (η):

$$P_{fan} = \frac{\dot{Q}\Delta p}{\eta} \qquad \text{B18}$$

Where the air mass flow selected for the experiment is 0.01 kg s^{-1} a 74% fan efficiency has been selected as this was previously used in the literature [5].

In a buoyant system, the solar irradiation is utilised to both heat and move the air. This would enable the device to either heat air or to supplement air ventilation. Therefore the parameters of interest are:

For a single duct:

- average exit air temperature over the day. This will be calculated on an hourly basis between sunrise and sunset using the Brinkworth$_{bc}$ model as indicated in Section 5.2. The hourly results will be averaged.
- average air mass flow over the day. This will be calculated on an hourly basis between sunrise and sunset using the Brinkworth$_{bc}$ model as indicated in Section 5.2.
- total power output over the day. The power output will be calculated on an hourly basis between sunrise and sunset using the exit air temperature and air mass flow as described above. The hourly results will be averaged.

For an array of ducts with a façade area of 10 m^2:

- total air output over the day will be calculated as above, then multiplied by a factor to equate to a 10 m^2 façade area.
- total power output over the day will be calculated as above, then multiplied by a factor to equate to a 10 m^2 façade area.

6.2.1.2 Factorial Method for Finding Optimum Geometry

The factorial analysis method has been fully described by Evans [6], and is an optimising technique which can cope with non-linear relationships. The method is widely used in engineering and industry.

A factorial analysis method considers the output (E) as a function of the input parameters and the inter-related input parameters. This is illustrated in Equation 1:

$$E = f(A, B, C, D, A^2, AB, AC, AD, B^2, BC, BD, C^2, CD, D^2) \qquad 6.1$$

In the above, there are four primary variables (A, B, C and D), so there is a 2^4 factorial design. A 2^4 factorial design explores the combined effects of four input parameters represented by letters (A, B, C, D). The minimum and maximum value for each parameter is represented as –1 and 1. The 2^4 factorial design is illustrated in Table 6.3.

Table 6.3 2^4 Factorial Design of Input Parameters for Linear Relationships

A	B	C	D
-1	-1	-1	-1
1	-1	-1	-1
-1	1	-1	-1
1	1	-1	-1
-1	-1	1	-1
1	-1	1	-1
-1	1	1	-1
1	1	1	-1
-1	-1	-1	1
1	-1	-1	1
-1	1	-1	1
1	1	-1	1
-1	-1	1	1
1	-1	1	1
-1	1	1	1
1	1	1	1

This allows for all combinations of the range of A, B, C and D. However, this does not accommodate non linear behaviour, since it assumes a linear relationship between the outputs of the maximum and minimum values. Therefore further conditions must be added to the experiment, these are shown in Table 6.4, where 0 represents the mid level for each parameter.

Table 6.4 Additions to 2^4 Factorial Design to Accommodate Non Linear Relationships

A	B	C	D
-1	0	0	0
1	0	0	0
0	-1	0	0
0	1	0	0
0	0	-1	0
0	0	1	0
0	0	0	-1
0	0	0	1
0	0	0	0

The factorial design indicates a range of values which can be used to generate a result from the initial model.

The logical result of the interacting factors is considered for second order variables of A, B, C, and D. This is illustrated in Table 6.5.

The four left hand columns in Table 6.5 are the primary parameters which can be varied. The 10 right hand columns of Table 6.5 are the secondary parameters which are the logical result of multiplying the primary parameters (e.g. if A = -1 and B = -1 then AB = 1).

This process produces 25 calculations of performance, each including the primary and secondary parameters. The influence of the primary parameters on performance is then assessed through multiple regression of performance as a function of all the parameters $f(A, B, C, D, A^2, AB, AC, AD, B^2, BC, BD, C^2, CD, D^2)$. The Excel function LINEST is used to carry out the multiple variable regression which draws a relationship between these first and second order variables and the equation results.

Table 6.5 First and Second Order Variables used to Calculate Non Linear Relationships

A	**B**	**C**	**D**	AB	AC	AD	BC	BD	CD	A^2	B^2	C^2	D^2
-1	**-1**	**-1**	**-1**	1	1	1	1	1	1	1	1	1	1
1	**-1**	**-1**	**-1**	-1	-1	-1	1	1	1	1	1	1	1
-1	**1**	**-1**	**-1**	-1	1	1	-1	-1	1	1	1	1	1
1	**1**	**-1**	**-1**	1	-1	-1	-1	-1	1	1	1	1	1
-1	**-1**	**1**	**-1**	1	-1	1	-1	1	-1	1	1	1	1
1	**-1**	**1**	**-1**	-1	1	-1	-1	1	-1	1	1	1	1
-1	**1**	**1**	**-1**	-1	-1	1	1	-1	-1	1	1	1	1
1	**1**	**1**	**-1**	1	1	-1	1	-1	-1	1	1	1	1
-1	**-1**	**-1**	**1**	1	1	-1	1	-1	-1	1	1	1	1
1	**-1**	**-1**	**1**	-1	-1	1	1	-1	-1	1	1	1	1
-1	**1**	**-1**	**1**	-1	1	-1	-1	1	-1	1	1	1	1
1	**1**	**-1**	**1**	1	-1	1	-1	1	-1	1	1	1	1
-1	**-1**	**1**	**1**	1	-1	-1	-1	-1	1	1	1	1	1
1	**-1**	**1**	**1**	-1	1	1	-1	-1	1	1	1	1	1
-1	**1**	**1**	**1**	-1	-1	-1	1	1	1	1	1	1	1
1	**1**	**1**	**1**	1	1	1	1	1	1	1	1	1	1
-1	**0**	**0**	**0**	0	0	0	0	0	0	1	0	0	0
1	**0**	**0**	**0**	0	0	0	0	0	0	1	0	0	0
0	**-1**	**0**	**0**	0	0	0	0	0	0	0	1	0	0
0	**1**	**0**	**0**	0	0	0	0	0	0	0	1	0	0
0	**0**	**-1**	**0**	0	0	0	0	0	0	0	0	1	0
0	**0**	**1**	**0**	0	0	0	0	0	0	0	0	1	0
0	**0**	**0**	**-1**	0	0	0	0	0	0	0	0	0	1
0	**0**	**0**	**1**	0	0	0	0	0	0	0	0	0	1
0	**0**	**0**	**0**	0	0	0	0	0	0	0	0	0	0

This analysis produces an equation to predict the output based on input parameters. The LINEST function generates a standard error for each term within the generated equation. If the ratio of the coefficient to the standard error is less than 1.94, the term is not statistically significant within the range assessed and it is excluded from the equation. The equation is solved to provide the optimal input parameters to achieve a goal, e.g. highest temperature.

The Excel Add-in SOLVER is used to determine the actual optimum parameters, by iterating through numerous solutions varying the input parameters from an initial starting point. SOLVER will only identify a local optima (i.e. if searching for a maximum, it will identify the first peak it finds after it starts searching rather than

continue searching through the entire range to identify the absolute maximum in that range). To ensure that the true optimum value was identified, SOLVER was applied from numerous starting points.

6.2.1.3 Geometry Components to be Optimised

Four geometry components will be considered and related to the parameters A, B, C and D which are shown in the Factorial analysis:

- Duct length A
- Duct width B
- Duct depth C
- Tilt Angle D

The geometry components are illustrated in Figure 6.3.

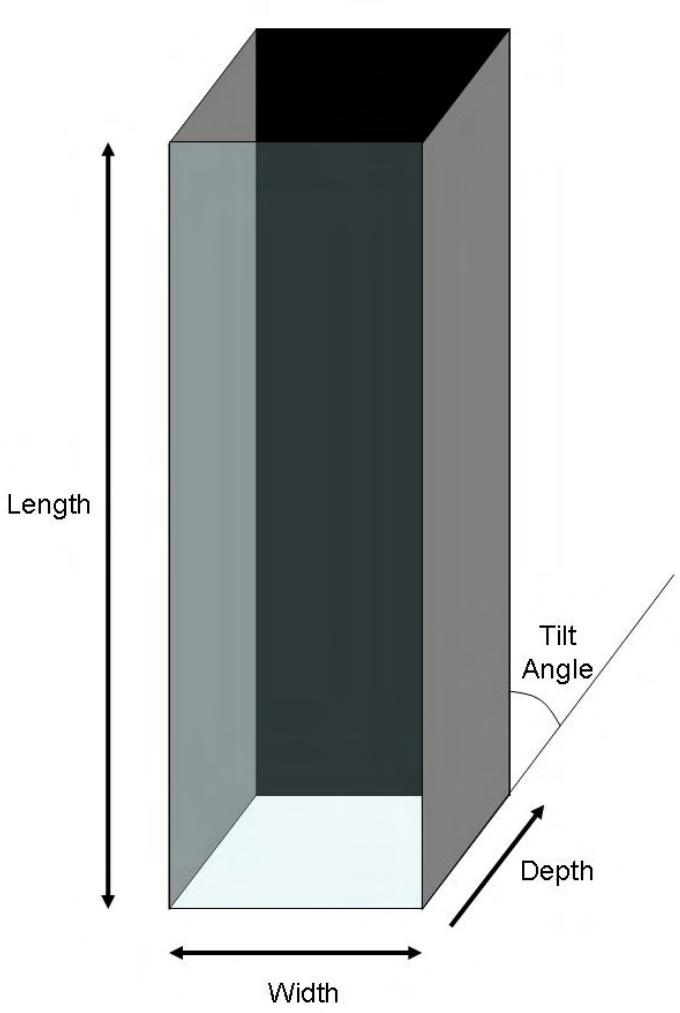

Figure 6.3. Schematic referencing length, width, depth and tilt angle of duct

Each of these geometry components have manufacturing / construction limitations which are described below:

- Length – items of less than 0.5 m would increase the assembly and manpower costs on a construction site, so this has been considered to be the minimum solar duct length. The maximum solar duct length is limited by the height of the building, or the interruption of the façade by windows. In the absence of a manufacturing limit, a maximum solar duct length of 12.5 m has been selected. This is analogous to the length of a solar duct fitted to a five storey building, allowing that the ground storey is not covered. The ground floor level has not been considered since it will be more prone to damage and more likely to suffer from shadows. The system is most likely to be used on retail / industrial buildings, which are unlikely to exceed a height of five storeys.
- Width and depth – although the manufacturing technique can accommodate a wide range of solar duct widths and depths there are limits to the initial width of the steel strip. Excessive solar duct width and depths will result in a very narrow panel available to apply to a building. The width range has been selected as 0.1 to 1.0 m. The depth range has been selected as 0.03 to 1.0 m. However, a solar duct which is 1.0 m deep by 1.0 m wide could not be manufactured due to limitations on initial strip width.
- Tilt Angle – a vertical façade will facilitate buoyant flow by giving a greater distance from the top to the bottom of the solar duct. Façades are typically vertical and there may be a desire to keep a tilt angle of 90^{o}. However, non vertical façades can be designed to take advantage of improved solar efficiency. North European locations tend to obtain optimum benefit from solar irradiation at a tilt angle of approximately 40^{o} to the horizontal. For these reasons, the tilt angle range has been selected as 40^{o} to 90^{o}. The OpTIC Centre at St Asaph is an example of a non-vertical façade and is shown in Figure 6.4. When seen from a side view (Figure 6.5) a storage area between the solar façade and the façade of the main building can be seen. This ‘over’ façade would also ensure that the main building façade would be shaded in sunny weather and could reduce the cooling burden of the building. However, it also reduces the possibility of using natural light in the building.

Figure 6.4. St Asaph OpTIC Centre - front view of PV facade

Figure 6.5. St Asaph OpTIC Centre - side view of PV facade

The range of values for each parameter to be included in the experiment are shown in Table 6.6.

Table 6.6 Range of Values for Solar Duct Geometry Parameters

	Lowest	Mid-point	Highest
Length (m)	0.5	6.5	12.5
Width (m)	0.1	0.55	1
Depth (m)	0.03	0.515	1
Tilt Angle (^{o})	40	65	90

The minimum and maximum values of each parameter are represented by -1 and 1. The minimum and maximum values are shown in Table 6.6. Table 6.5 shows the combinations of parameters which are used to explore the relationship between the four parameters and the output being assessed.

The systems will be considered for four key dates throughout the year:

- March 20th (Spring Equinox)
- June 21st (Summer Solstice)
- September 22nd (Autumn Equinox)
- December 21st (Winter Solstice)

6.2.1.4 Input Conditions

The best models identified in Chapter 5 for forced and buoyant convection both require meteorological data as inputs. Typical values of ambient temperature, horizontal direct solar irradiation, horizontal diffuse irradiation for the key dates were obtained from commercially available all-weather data [8] for Cardiff, UK. The data is averaged for 1 hour periods and shown in Tables 6.7 – 6.10. The times indicated in Tables 6.7 – 6.10 are solar times, and do not take account of daylight saving time.

Table 6.7 Ambient Temperature (hourly average) for key dates

Time	20th March (°C)	21st June (°C)	22nd September (°C)	21st December (°C)
03:00	5.8	15.7	13	-0.8
04:00	4.9	14.6	12.3	-1.1
05:00	6.0	14.7	13.3	-1.5
06:00	4.1	15.1	13.8	-1.5
07:00	7.3	15.5	13.9	-1.2
08:00	9.2	18.5	14.1	-0.5
09:00	11.9	16.9	14.9	0
10:00	12.3	19.0	16.3	0.2
11:00	12.1	19.5	18.2	1.7
12:00	13.4	19.4	18.6	4.5
13:00	12.5	19.3	18.3	5.1
14:00	14.0	20.1	17.6	6.1
15:00	12.8	19.6	17.5	6.1
16:00	12.8	18.2	18.8	6.0
17:00	13.6	16.6	18.4	5.2
18:00	11.5	16.9	16.6	5.7
19:00	12.3	16.1	16.1	6.4
20:00	10.7	16.1	15.9	7.3

Table 6.8 Horizontal Direct Solar Irradiation (hourly average) for key dates

Time	20th March (W m-2)	21st June (W m-2)	22nd September (W m-2)	21st December (W m-2)
03:00	0	0	0	0
04:00	0	24	0	0
05:00	0	61	0	0
06:00	14	116	7	0
07:00	156	303	45	0
08:00	306	569	122	2
09:00	417	512	132	42
10:00	400	860	405	72
11:00	275	784	338	145
12:00	293	960	429	233
13:00	245	872	440	129
14:00	152	751	270	19
15:00	95	336	277	5
16:00	58	436	69	0
17:00	27	281	31	0
18:00	0	153	0	0
19:00	0	35	0	0
20:00	0	0	0	0

Table 6.9 Horizontal Diffuse Solar Irradiation (hourly average) for key dates

Time	20th March (W m-2)	21st June (W m-2)	22nd September (W m-2)	21st December (W m-2)
03:00	0	0	0	0
04:00	0	11	0	0
05:00	0	44	0	0
06:00	6	103	5	0
07:00	74	194	29	0
08:00	98	203	85	0
09:00	177	327	89	33
10:00	232	107	231	72
11:00	202	297	219	105
12:00	207	119	250	49
13:00	173	124	224	75
14:00	130	102	174	14
15:00	76	250	135	0
16:00	43	174	68	0
17:00	16	149	14	0
18:00	0	93	0	0
19:00	0	31	0	0
20:00	0	0	0	0

Table 6.10 Cloud Cover (hourly average) for key dates

Time	20th March (%)	21st June (%)	22nd September* (%)	21st December* (%)
03:00	0	88	95	88
04:00	11	70	97	77
05:00	23	99	95	50
06:00	25	90	72	39
07:00	12	68	100#	43
08:00	15	18	97	41
09:00	31	59	100#	31
10:00	57	0	100#	31
11:00	80	25	100	84
12:00	83	0	97	38
13:00	87	0	100#	68
14:00	93	0	100#	28
15:00	100#	71	90	34
16:00	100#	21	100#	45
17:00	83	29	93	57
18:00	83	40	91	43
19:00	77	33	89	42
20:00	70	35	85	42

* cloud cover data is only available for the months of January to June. For this reason, it has been assumed that the cloud cover over the year is symmetrical about 30th June. The cloud cover data reported for 22nd September is actually for 10th April, while the cloud cover data for 21st December is actually for 10th January.
#Some data points exceeded 100%, these have been corrected to read 100%.
NB the corrections to the cloud cover, have only a slight effect on the calculation of the sky temperature, which in turn has only a slight effect on the output of the model.

The solar incident angles on the horizontal pyranometer and on the façade have been calculated using the Fortran codes supplied by Muneer in his book 'Solar Radiation & Daylight Models' [9]. 2006 dates have been used for these calculations. It has been assumed that the façade will be facing due south.

6.2.2 Forced Convection – Geometry Optimisation Results

The $Ho_{fc\&fcad}$ model was found to be the closest predicting model from those assessed in Chapter 5; however, it is not an ideal model. Optimisation results based on the use of the $Ho_{fc\&fcad}$ model will be considered in relation to the empirical results from Chapter

4. This will give an opportunity to identify optimisation results which should be treated with caution.

As an example, the factorial array and results produced for the average exit temperature for 21st June conditions are shown in Table 6.11.

Table 6.11 First and Second Order Variables with Average Exit Temperature Results.

A	**B**	**C**	**D**	AB	AC	AD	BC	BD	CD	A^2	B^2	C^2	D^2	Ave Exit Temp (^oC)
-1	**-1**	**-1**	**-1**	1	1	1	1	1	1	1	1	1	1	19.4
1	**-1**	**-1**	**-1**	-1	-1	-1	1	1	1	1	1	1	1	55.9
-1	**1**	**-1**	**-1**	-1	1	1	-1	-1	1	1	1	1	1	29.5
1	**1**	**-1**	**-1**	1	-1	-1	-1	-1	1	1	1	1	1	99.9
-1	**-1**	**1**	**-1**	1	-1	1	-1	1	-1	1	1	1	1	18.4
1	**-1**	**1**	**-1**	-1	1	-1	-1	1	-1	1	1	1	1	31.5
-1	**1**	**1**	**-1**	-1	-1	1	1	-1	-1	1	1	1	1	18.9
1	**1**	**1**	**-1**	1	1	-1	1	-1	-1	1	1	1	1	42.6
-1	**-1**	**-1**	**1**	1	1	-1	1	-1	-1	1	1	1	1	18.3
1	**-1**	**-1**	**1**	-1	-1	1	1	-1	-1	1	1	1	1	34.6
-1	**1**	**-1**	**1**	-1	1	-1	-1	1	-1	1	1	1	1	23.1
1	**1**	**-1**	**1**	1	-1	1	-1	1	-1	1	1	1	1	59.7
-1	**-1**	**1**	**1**	1	-1	-1	-1	-1	1	1	1	1	1	17.9
1	**-1**	**1**	**1**	-1	1	1	-1	-1	1	1	1	1	1	24.0
-1	**1**	**1**	**1**	-1	-1	-1	1	1	1	1	1	1	1	18.2
1	**1**	**1**	**1**	1	1	1	1	1	1	1	1	1	1	30.4
-1	**0**	**0**	**0**	0	0	0	0	0	0	1	0	0	0	19.3
1	**0**	**0**	**0**	0	0	0	0	0	0	1	0	0	0	47.0
0	**-1**	**0**	**0**	0	0	0	0	0	0	0	1	0	0	27.8
0	**1**	**0**	**0**	0	0	0	0	0	0	0	1	0	0	36.4
0	**0**	**-1**	**0**	0	0	0	0	0	0	0	0	1	0	71.2
0	**0**	**1**	**0**	0	0	0	0	0	0	0	0	1	0	30.6
0	**0**	**0**	**-1**	0	0	0	0	0	0	0	0	0	1	38.5
0	**0**	**0**	**1**	0	0	0	0	0	0	0	0	0	1	28.0
0	**0**	**0**	**0**	0	0	0	0	0	0	0	0	0	0	35.3

Tables showing this information for the other parameters investigated are shown in Appendix I.

From the data in Table 6.11, the LINEST function generated the following equation:

Average Exit Temperature = 37.9 + 13.5 A + 6.2 B – 10.0 C - 5.6 D + 4.4 AB – 6.6 AC - 4.5 AD – 4.1 BC + 12.6 C^2 r^2 value = 0.820 6.3

The r^2 value indicates how well the equation matches the results generated by the design model.

The optimum dimensions for maximum average exit temperature as calculated by SOLVER for the solar duct were calculated to be:
A 1 (i.e. maximum length within the range assessed)
B 1 (i.e. maximum width within the range assessed)
C –1 (i.e. minimum depth within the range assessed)
D –1 (i.e. minimum tilt angle within the range assessed).

This is a reasonable conclusion, since increasing the length and width would increase the area for collecting solar irradiation, using a tilt angle of 40^o would optimise the orientation of the panel to the sun, and minimising the depth would decrease the volume of air to be heated.

6.2.2.1 Daily Average Exit Temperature (Individual Duct)

Equations 2-5 describe the effect of the solar duct geometry on the average exit temperature throughout the day for each of the key dates. The average exit temperature is calculated from sunrise to sunset. The calculated optimum dimensions to produce the highest average exit temperature are listed in Table 6.12.

<u>20th March</u>

Average Exit Temperature = 31.1 + 13.1 A + 6.5 B - 9.5 C + 4.9 AB - 6.3 AC – 4.5 BC + 12.3 C^2 r^2 value = 0.819 6.2

<u>21st June</u>

Average Exit Temperature = 37.9 + 13.5 A + 6.2 B – 10.0 C - 5.6 D + 4.4 AB – 6.6 AC - 4.5 AD – 4.1 BC + 12.6 C^2 r^2 value = 0.820 6.3

22nd September

Average Exit Temperature = 37.6 + 13.8 A + 6.6 B – 10.1 C + 4.9 AB – 6.7 AC - 4.7 BC + 13.1 C^2 r^2 value = 0.814 6.4

21st December

Average Exit Temperature = 22.2 + 12.7 A + 6.3 B - 9.3 C + 4.7 AB – 6.2 AC – 4.3 BC + 11.5 C^2 r^2 value = 0.839 6.5

Table 6.12 Optimum Geometry for Average Exit Temperature (Individual Duct)

	Duct Length	Duct Width	Duct Depth	Duct Tilt Angle
20th March	Max	Max	Min	No Preference
21st June	Max	Max	Min	40°
22nd September	Max	Max	Min	No Preference
21st December	Max	Max	Min	No Preference

The sensitivity of the temperature to variations in duct length, width, depth and tilt angle was explored. Illustrative graphs are shown for 21st June.

Figure 6.6 shows the sensitivity of the average exit temperature to variations in duct length for duct widths of 0.1 and 1.0 m. This indicates that variations in duct length cause gradual changes in temperature. It also indicates that increasing the duct length results in higher air exit temperatures. Similar trends were observed for the March, September and December data. No empirical data was available to validate these predictions. Although the increase in air exit temperature with length appears linear within the range considered, it is expected that this trend would not be likely to continue indefinitely.

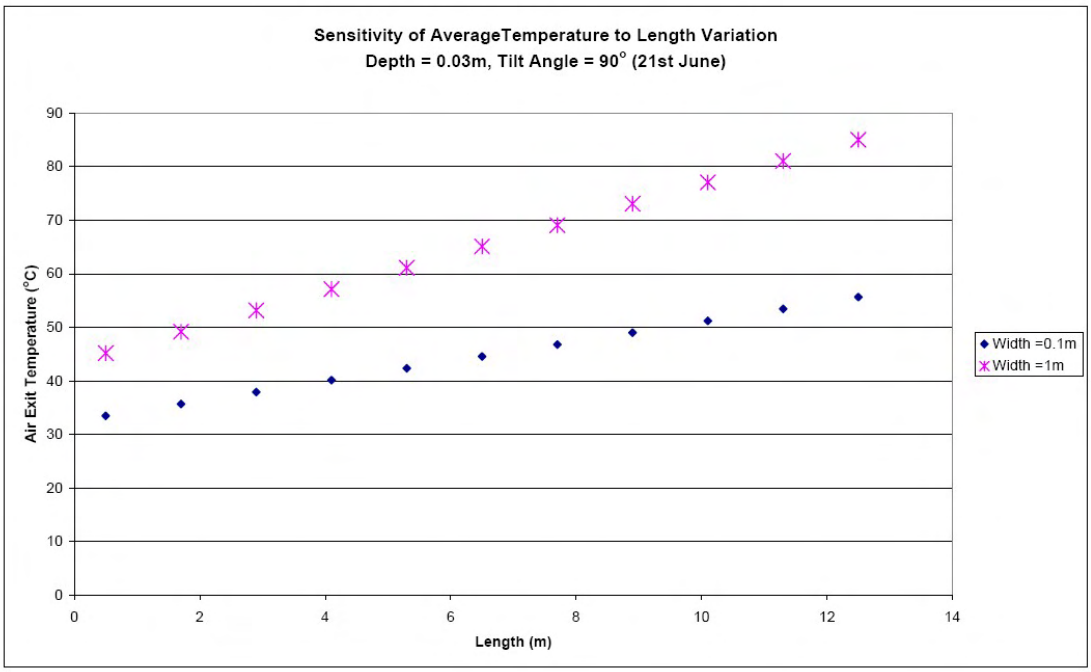

Figure 6.6. Sensitivity of Average Temperature to Length Variation

Figure 6.7 shows the sensitivity of the average exit temperature to variations in width for lengths of 0.5 and 12.5 m. This indicates that variations in duct width cause gradual changes in air exit temperature. It also indicates that increasing the duct width results in an increase in the air exit temperature. This trend has been confirmed by the field experiments in Chapter 4. Similar trends were observed for the March, September and December data.

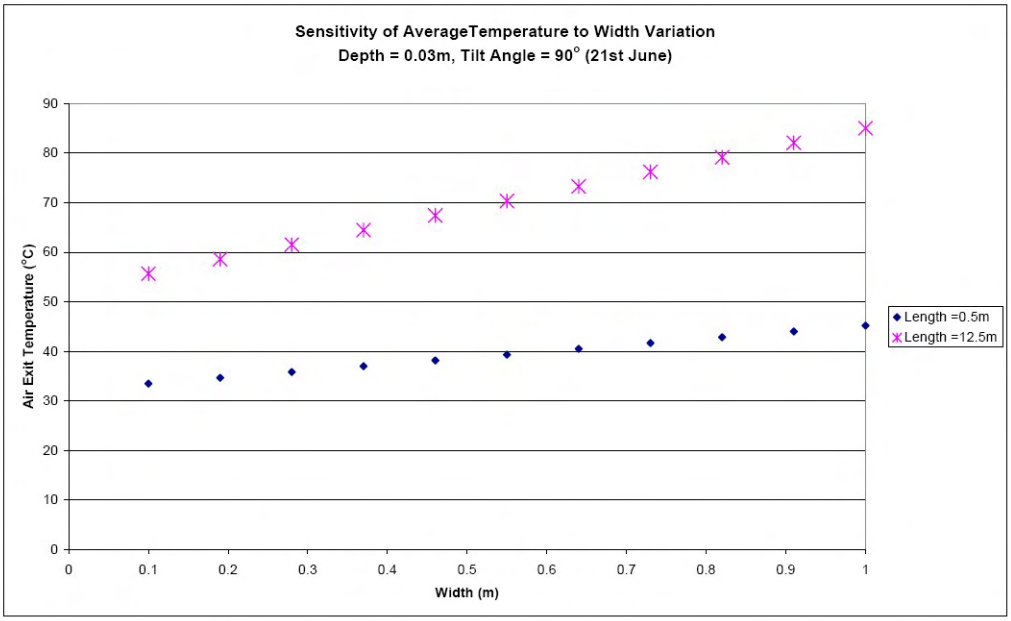

Figure 6.7. Sensitivity of Average Temperature to Width Variation

Figure 6.8 shows the sensitivity of the average exit temperature to variations in duct depth for duct lengths of 0.5 and 12.5 m. This indicates that variations in duct depth cause gradual changes in temperature. It also indicates that the smallest duct depth considered gives the highest air exit temperature, intermediate duct depths reduce the air exit temperature, and larger duct depths cause a recovery in air exit temperature. This trend is less pronounced for longer ducts. The empirical evidence from Chapter 4 suggests that increasing the depth from 0.03 to 0.1 m increases the air exit temperature; therefore, this prediction from the model should be treated with care. Similar trends were observed for the March, September and December data.

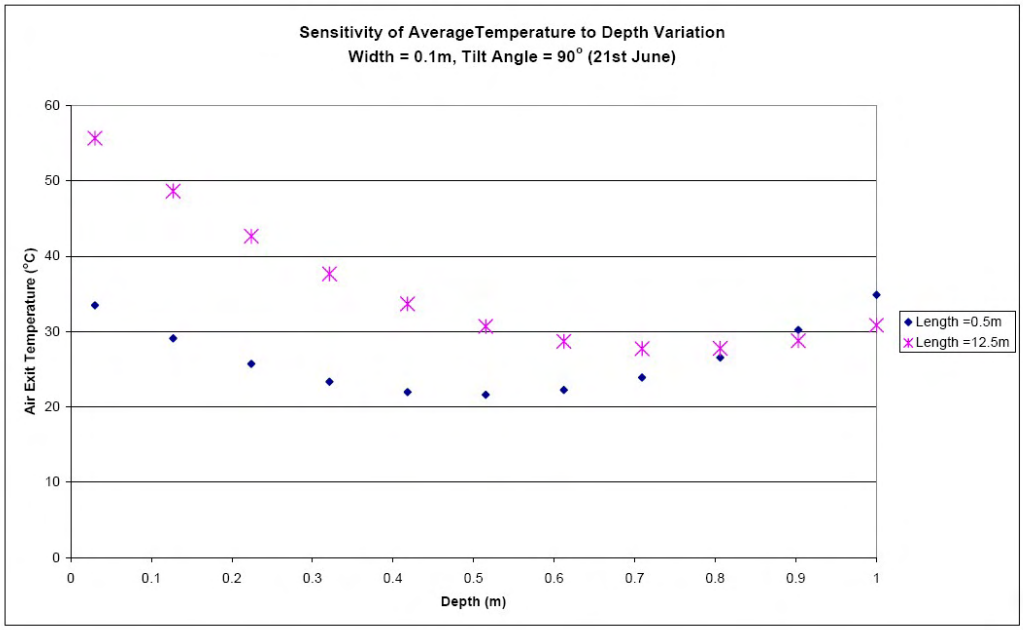

Figure 6.8. Sensitivity of Average Temperature to Depth Variation

Figure 6.9 shows the sensitivity of the average exit temperature to variations in tilt angle for lengths of 0.5 and 12.5 m. This indicates that variations in tilt angle cause gradual changes in temperature. It also indicates that the effect is more pronounced for longer ducts. The average air exit temperature is not sensitive to tilt angle in March, September or December. No empirical data was available to validate these predictions.

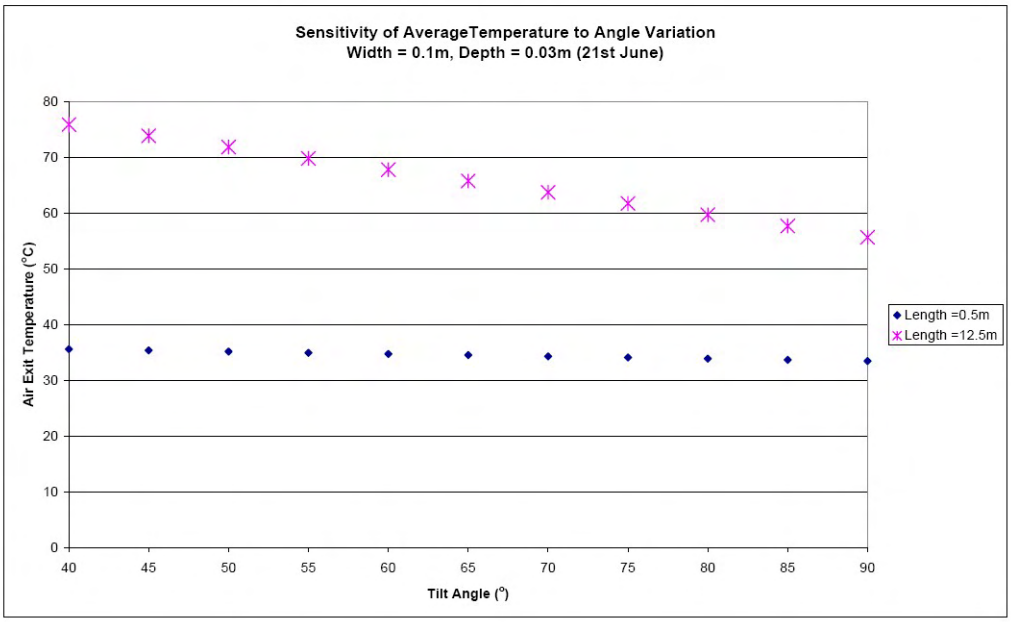

Figure 6.9. Sensitivity of Average Temperature to Tilt Angle Variation (with respect to horizontal)

6.2.2.2 Daily Net Power Output (Individual Duct)

Equations 6-9 describe the effect of the solar duct geometry on net power output for individual ducts on each of the key dates. The calculated optimum dimensions to produce the highest power output are shown in Table 6.13.

20th March

Net Power Output = 2586 + 1715 A + 853 B – 1243 C + 641 AB - 824 AC - 592 BC + 1606 C^2 r^2 value = 0.819 6.6

21st June

Net Power Output = 206 + 136 A + 62 B - 100 C – 56 D + 45 AB – 66 AC – 46 AD - 42 BC + 127 C^2 r^2 value = 0.820 6.7

22nd September

Net Power Output = 211 + 139 A + 66 B – 102 C + 49 AB - 67 AC - 47 BC + 132 C^2 r^2 value = 0.815 6.8

21st December

Net Power Output = 191 + 128 A + 64 B – 93 C + 48 AC - 43 BC + 116 C^2 r^2 value = 0.839 6.9

Table 6.13 Optimum Geometry for Net Power Output (Individual Duct)

	Duct Length	Duct Width	Duct Depth	Duct Tilt Angle
20th March	Max	Max	Min	No Preference
21st June	Max	Max	Min	40°
22nd September	Max	Max	Min	No Preference
21st December	Max	Max	Min	No Preference

The sensitivity of power output of a single duct to variations in length, width, depth and tilt angle was explored.

The sensitivity of the power output of a single duct to variations in length was found to be similar to that for the average exit temperature illustrated in Figure 6.6. This

sensitivity confirmed that increasing the length results in higher power outputs for a single duct.

The sensitivity of the power output of a single duct to variations in width was found to be similar to that for the average exit temperature illustrated in Figure 6.7. This sensitivity confirmed that increasing the width results in higher power outputs for a single duct.

The sensitivity of the power output of a single duct to variations in depth was found to be similar to that for the average exit temperature illustrated in Figure 6.8. This sensitivity indicated that intermediate depths may reduce the power output of an individual duct; however, the effect was less pronounced for longer ducts. As explained previously, this prediction of the model contradicts the empirical data and should be treated with care.

The power output of a single duct was only found to be sensitive to the tilt angle in June. The sensitivity was found to be similar to that for the average air exit temperature illustrated in Figure 6.9.

The total power output is proportional to the air exit temperature. The similarity in response to changes in geometry, indicate that the net power output is also proportional to the air exit temperature, and that the pumping power does not greatly affect the trends.

6.2.2.3 Daily Air Mass Output (10 m^2 Façade Area)

Equation 10 describes the effect of the solar duct geometry on air mass output for a 10 m^2 area.

$$\text{Net Power Output} = -0.04 - 0.4\,A - 0.3\,B + 0.4\,AB + 0.2\,A^2 \qquad r^2 \text{ value} = 0.923 \qquad 6.10$$

The optimum geometry implied by equation 10 is minimum length and minimum width. If the 10 m^2 area consists of short ducts (0.5 m), reducing the width increases the overall air mass flow. If the area consists of long ducts (12.5 m), varying the width has

virtually no effect on the overall air mass flow. This is a logical conclusion since varying the width of a short (0.5 m) duct between 1.0 and 0.1 m can increase the overall air mass flow of a 10 m^2 façade area from 0.2 kg s^{-1} to 2 kg s^{-1}. Similarly varying the width of a long (12.5 m) duct can only increases the overall air mass flow of a 10 m^2 façade area from 0.008 kg s^{-1} to 0.08 kg s^{-1}.

6.2.2.4 Daily Net Power Output (10 m^2 Façade Area)

Equations 6.11 - 6.14 describe the effect of the solar duct geometry on net power output for a 10 m^2 area on each of the key dates. (refer 6.2.1.1 for a description on how 10 m^2 was achieved). The calculated optimum dimensions to produce the highest power output for a 10 m^2 façade area are shown in Table 6.14.

20th March

$$\text{Net Power Output} = 6875 - 2569\,A - 5551\,B - 6112\,C - 1572\,D + 1480\,AC + 3613\,B^2 + 4582\,C^2 \qquad r^2 \text{ value} = 0.936 \qquad 6.11$$

21st June

$$\text{Net Power Output} = 541 - 218\,A - 486\,B - 530\,C - 380\,D + 194\,BD + 207\,CD + 322\,B^2 + 370\,C^2 \qquad r^2 \text{ value} = 0.922 \qquad 6.12$$

22nd September

$$\text{Net Power Output} = 569 - 193\,A - 458\,B - 513\,C - 145\,D + 127\,AC + 316\,B^2 + 367\,C^2 \qquad r^2 \text{ value} = 0.922 \qquad 6.13$$

21st December

$$\text{Net Power Output} = 499 - 196\,A - 412\,B - 463\,C + 104\,AC + 254\,BC + 342\,C^2 \qquad r^2 \text{ value} = 0.936 \qquad 6.14$$

Table 6.14 Optimum Geometry for Net Power Output (10 m^2)

	Duct Length	Duct Width	Duct Depth	Duct Tilt Angle
20th March	Min	Min	Min	40°
21st June	Min	Min	Min	40°
22nd September	Min	Min	Min	40°
21st December	Min	Min	Min	No Preference

The sensitivity of power output over a 10 m^2 façade area to variations in length, width, depth and tilt angle was explored.

The power output over a 10 m^2 façade area was found to reduce gradually as the length of the ducts was increased. This is the same trend which was observed for maximising the air mass flow over a façade area. It is the opposite trend to that experienced for the net power output of an individual duct. This indicates that the power output over a 10m^2 façade area is more influenced by increasing the air mass flow over the area, than by increasing the power output of the individual ducts within the array.

The power output over a 10 m^2 façade area was found to reduce gradually as the width was increased to 0.5 m, but increasing the width beyond this width had little effect (Figure 6.10). However, the empirical experiment in Chapter 4 showed that varying the duct width between 0.1 and 0.2 m did not have a significant effect on the power output of a normalised area, so this prediction from the model should be treated with care.

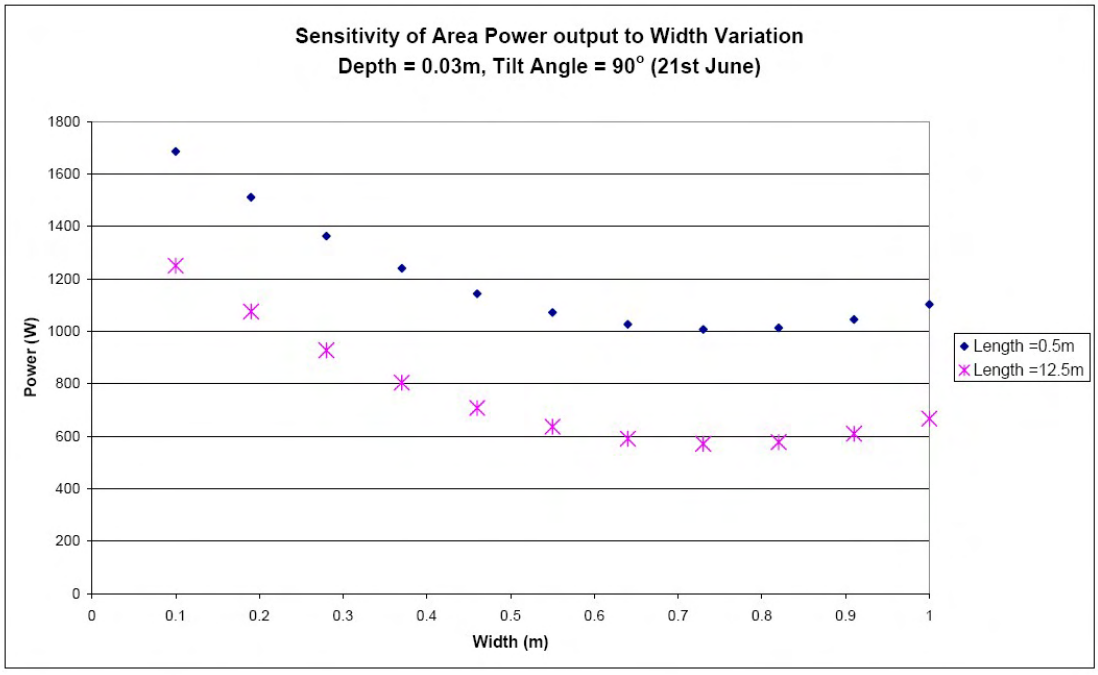

Figure 6.10. Sensitivity of Area Power Output to Width Variation

The power output over a 10 m^2 façade area was found to have a similar sensitivity to depth as was observed for air exit temperature and net power output. This sensitivity indicated that intermediate depths may reduce the power output. As previously explained this prediction of the model contradicts the empirical data and should be treated with care.

When considered over a 10 m^2 area, the influence of tilt angle became statistically significant for March and September where it had not been for a single duct. For June and December the influence of tilt angle had been statistically significant for the power output of a single duct, and remained so over an area. Figure 6.11 shows the sensitivity of the area power output to the tilt angle in March. This shows a very gradual decline in the power output for increasing tilt angle to vertical. The sensitivity in September is similar to that of March, and is not illustrated separately.

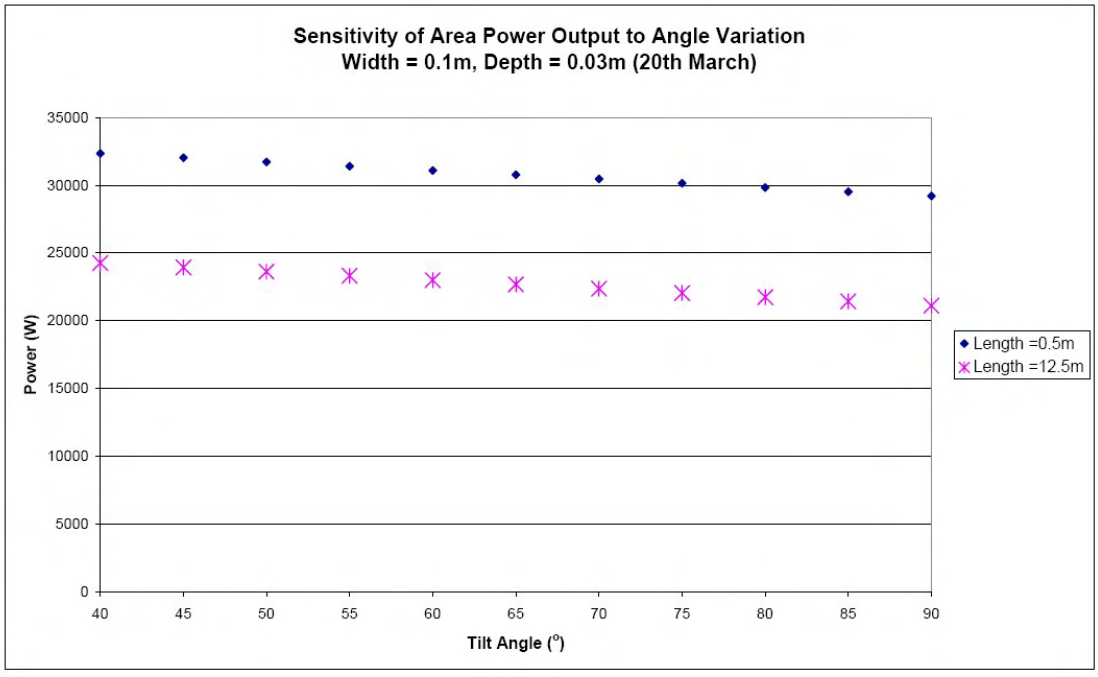

Figure 6.11. Sensitivity of Area Power Output to Angle Variation - March

Figure 6.12 shows a stronger sensitivity of the area power output to the tilt angle for June.

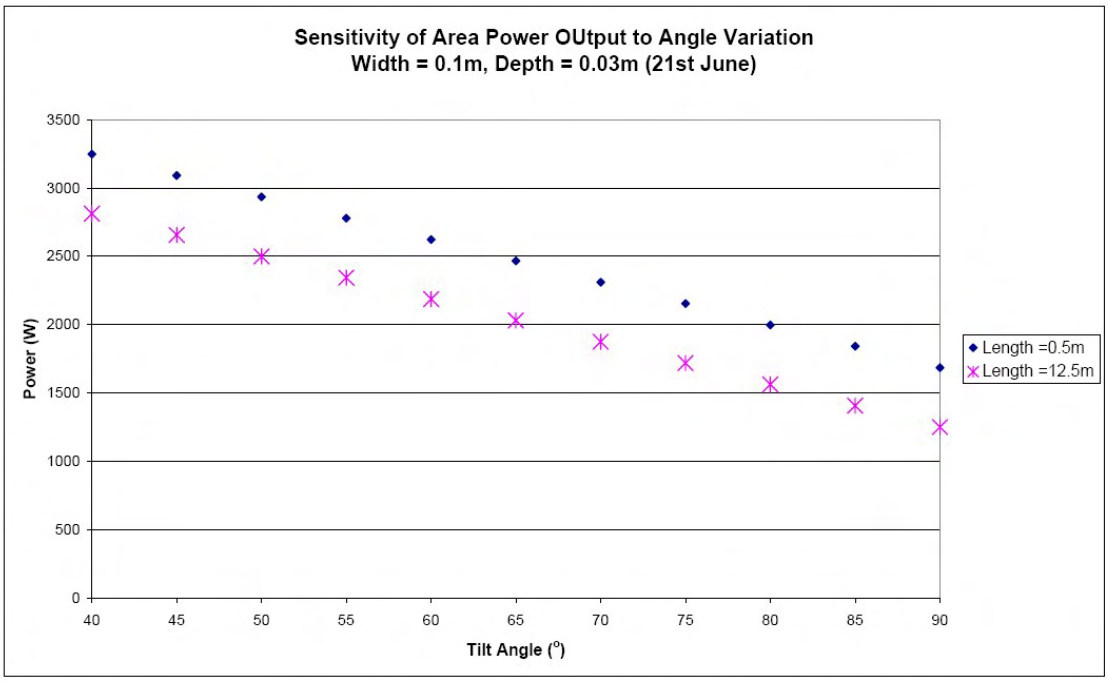

Figure 6.12. Sensitivity of Area Power Output to Angle Variation - June

The sensitivity of the power output to tilt angle is logical, given the known path of the sun in different seasons.

The geometry factors which are significant for optimising air mass flow over a 10 m^2 area façade, have reappeared as being significant for optimising power output over a 10 m^2 area façade. This indicates that optimising the power output over an area relies heavily on optimising the air mass flow for the area, and is less affected by optimising the air exit temperature. Since the optimum length and width have been determined by optimising the air mass flow, the impact of inaccuracies relating to the $Ho_{fc\&fcad}$ model have been reduced. However, any inaccuracies relating to the $Ho_{fc\&fcad}$ model will still be evident in the depth and tilt angle optimisation. The seasonal relationship between the tilt angle and the power output over an area has been established as being logical. However, the proposed optimal depth (0.03m) is contradicted by empirical data.

6.2.2.5 Summary of Results

Sections 6.2.2.1 to 6.2.2.4 indicate the optimum geometry for the average exit temperature of an individual duct, the net power output of a single duct, the air mass flow of a 10 m^2 façade area and the net power output of a 10 m^2 façade area. This

information is summarised in Table 6.15. General observations (e.g. 'min') have been converted to the corresponding dimension from the range evaluated.

Table 6.15 Optimised Solar Duct Geometry for Forced Ventilation

	Duct Length (m)	Duct Width (m)	Duct Depth (m)	Duct Tilt Angle (^{o})	
Average Exit Temperature (^{o}C)	12.5	1	0.03	June 40^o	M S D No Preference
Net Power Output (W)	12.5	1	0.03	June 40^o	M S D No Preference
Air Mass Flow over 10 m2 façade area (kg s^{-1})	0.5	0.1	No Preference	No Preference	
Net Power Output over 10 m^2 façade area (W)	0.5	0.1	0.03	M J S 40^o	December No Preference

Where necessary months have been abbreviated. M = March, J = June, S = September, D = December

It should be noted that the recommendation in Table 6.15 for minimum depth to facilitate the exit air temperature and power output has been contradicted by results from the empirical experiments in Chapter 4.

From Table 6.15 it can be seen that the optimum geometries for each parameter do not coincide:

- To maximise the air exit temperature: long, wide, shallow ducts are required. This duct geometry would provide an average air exit temperature of 74 ^{o}C in March, 80 ^{o}C in June, 82 ^{o}C in September and 64 ^{o}C in December. Air at such temperatures would have to be diluted with unheated air to reduce it to an acceptable temperature, but could be utilised for a direct ventilation system.
- To maximise the air mass flow over a façade area: short, narrow ducts are required.
- To maximise the power output over a façade area: short, narrow, shallow ducts are required. This duct geometry would provide an average air exit temperature of 13 ^{o}C in March, 19 ^{o}C in June, 18 ^{o}C in September and 4 ^{o}C in December. These temperatures would not be acceptable for a direct ventilation system but may be suitable for an indirect ventilation system.

The intended application of the system (i.e. to generate ventilation flow or to generate heat) should be decided at the design stage, in order to produce an optimal system.

6.2.3 Buoyant Convection – Geometry Optimisation Results

The same procedure is followed as for the forced convection results in Section 6.2.2.

6.2.3.1 Daily Average Exit Temperature (Individual Duct)

Equations 15-18 describe the effect of the solar duct geometry on the average exit temperature throughout the day for each of the key dates. The calculated optimum dimensions to produce the highest average exit temperature are shown in Table 6.16.

20^{th} March

$$\text{Average Exit Temperature} = 13.3 + 0.2A - 1.2\,B + 0.2\,C - 0.2\,D - 0.5\,BC + 0.8\,C^2 \qquad r^2 \text{ value} = 0.943 \qquad 6.15$$

21^{st} June

$$\text{Average Exit Temperature} = 19.4 + 0.2\,A - 1.1\,B + 0.3\,C - 0.7\,D - 0.5\,BC + 0.3\,BD + 0.7\,B^2 \qquad r^2 \text{ value} = 0.935 \qquad 6.16$$

22^{nd} September

$$\text{Average Exit Temperature} = 18.5 + 0.2\,A - 1.0\,B + 0.3\,C - 0.2\,D - 0.5\,BC + 0.7\,B^2 \qquad r^2 \text{ value} = 0.938 \qquad 6.17$$

21^{st} December

$$\text{Average Exit Temperature} = 5.5 + 0.3\,A - 1.4\,B + 0.2\,C + 0.2\,D - 0.7\,BC + 1.0\,B^2 \qquad r^2 \text{ value} = 0.954 \qquad 6.18$$

Table 6.16 Optimum Geometry for Air Exit Temperature (Individual Duct)

	Duct Length	Duct Width	Duct Depth	Duct Tilt Angle
20^{th} March	Max	Min	Max	40^o
21^{st} June	Max	Min	Max	40^o
22^{nd} September	Max	Min	Max	40^o
21^{st} December	Max	Min	Max	90^o

The sensitivity of the temperature to variations in length, width, depth and tilt angle was explored. Illustrative graphs are shown for 21st June.

Figure 6.13 shows the sensitivity of the average exit temperature to variations in length for widths of 0.1 and 1.0m. This indicates that variations in length cause gradual changes in temperature. It also confirms that increasing the length results in slightly higher air exit temperatures. Similar trends were observed for the March, September and December data. No empirical data was available to validate these predictions.

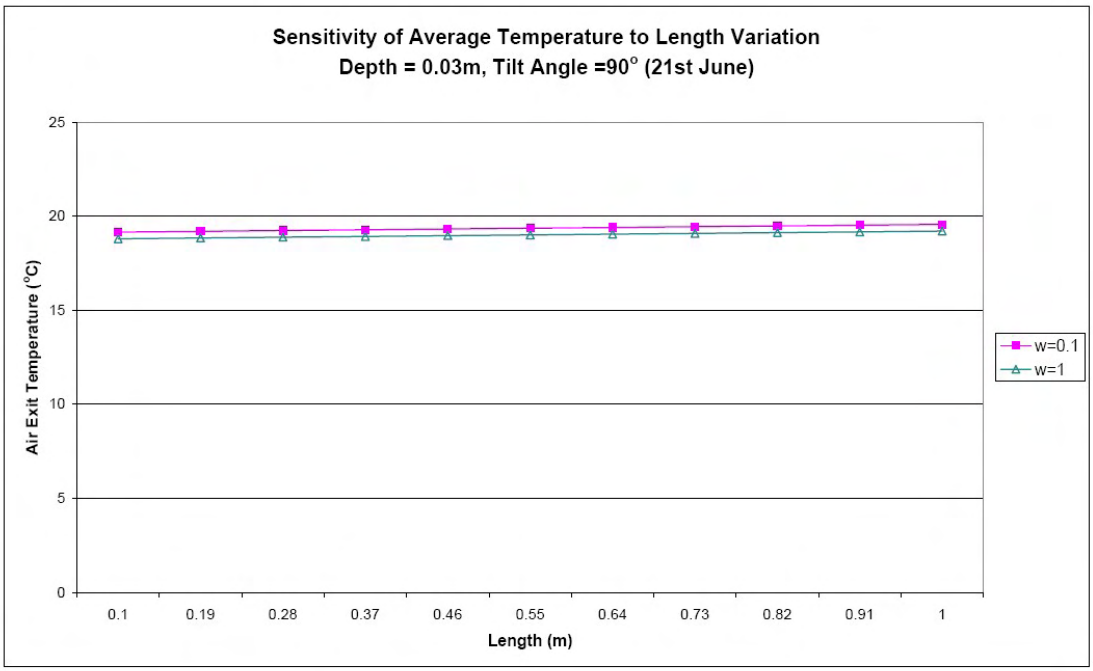

Figure 6.13. Sensitivity of Average Exit Temperature (Individual Duct) to Length Variation - Buoyant Flow

Figure 6.14 shows the sensitivity of the average exit temperature to variations in width for lengths of 0.5 and 12.5 m. This indicates that variations in width cause gradual changes in temperature. However, it indicates that intermediate widths cause a slight reduction in temperature as compared to the extremes of the range considered. The lowest widths give a slight advantage over the highest widths in the range considered. The effect of changing width is so slight, that it is difficult to verify; however, it has been noted in Section 5.2 that duct WD did have slightly lower temperatures than duct ND. Similar trends were observed for the March, September and December data.

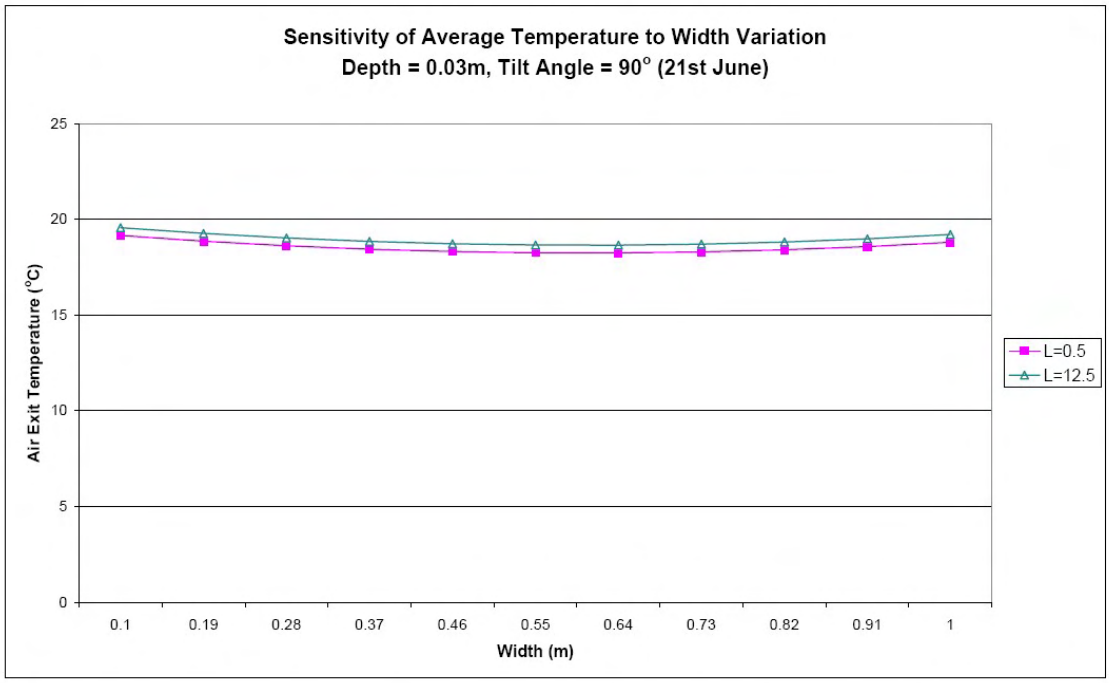

Figure 6.14. Sensitivity of Average Exit Temperature (Individual Duct) to Width Variation - Buoyant Flow

Figure 6.15 shows the sensitivity of the average exit temperature to variations in depth for lengths of 0.5 and 12.5 m. This indicates that variations in depth cause gradual changes in temperature. It also indicates that the larger depths give slightly higher air exit temperatures. Such a difference was not detected between ducts ND and NS. Similar trends were observed for the March, September and December data.

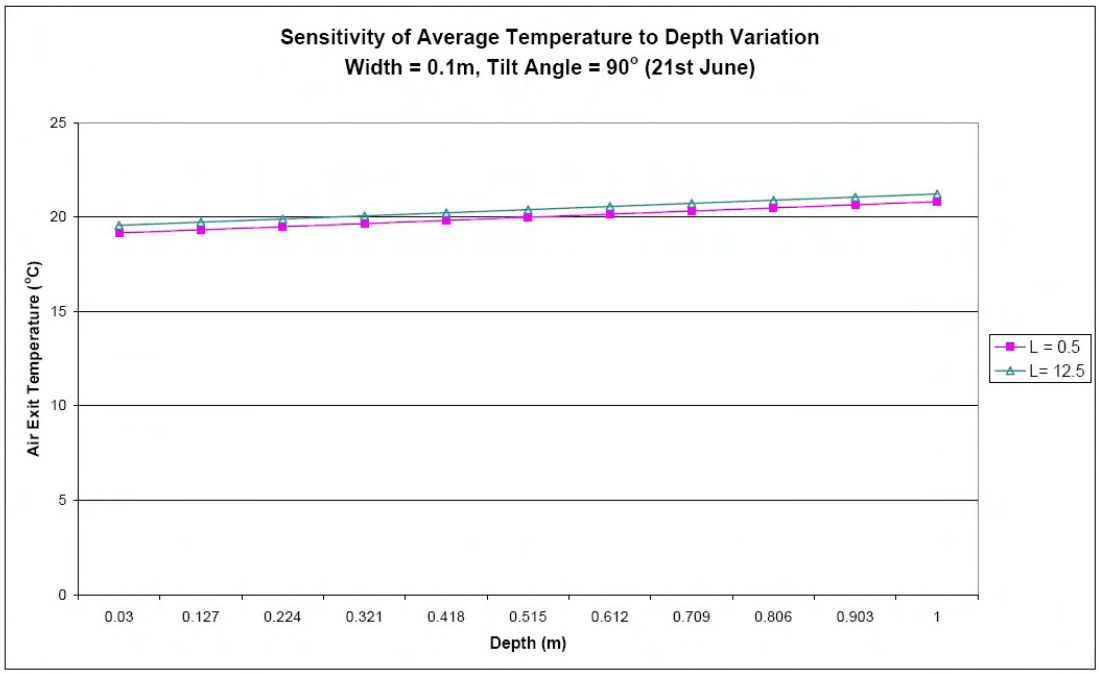

Figure 6.15. Sensitivity of Average Exit Temperature (Individual Duct) to Depth Variation - Buoyant Flow

Figure 6.16 shows the sensitivity of the average exit temperature to variations in tilt angle for lengths of 0.5 and 12.5 m. This indicates that variations in tilt angle cause gradual changes in temperature. It also indicates that higher temperatures are associated with lower tilt angles. Similar trends were observed for the March and September data; however the data for December exhibited a gradual trend which associated higher temperatures with higher tilt angles. No empirical data was available to validate these predictions.

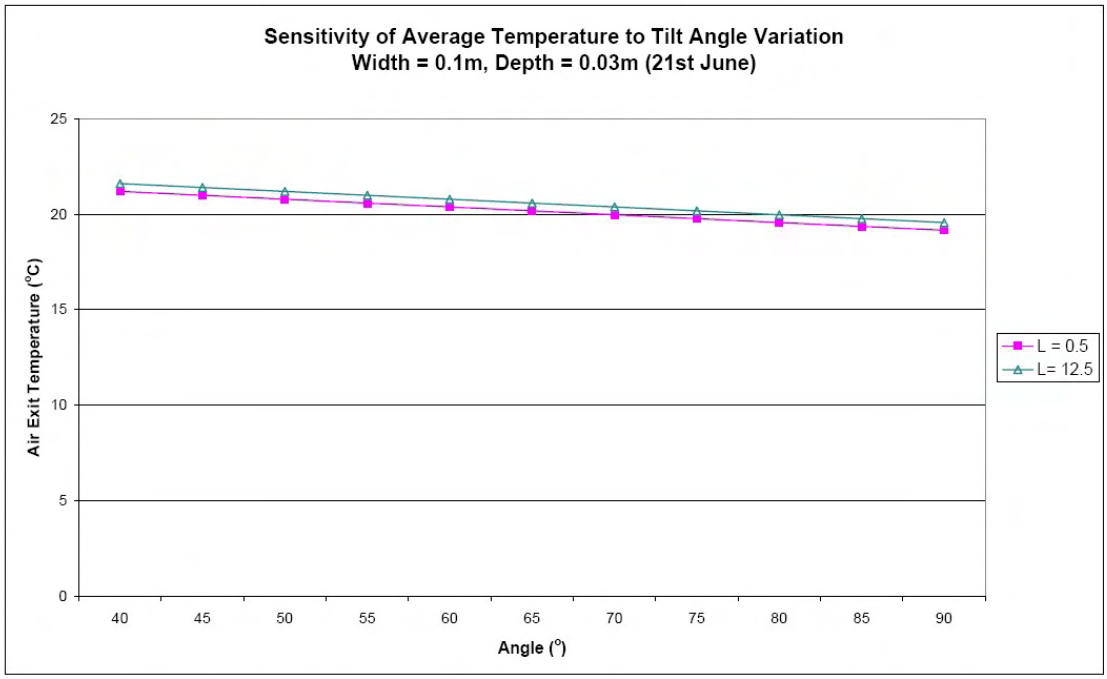

Figure 6.16. Sensitivity of Average Exit Temperature (Individual Duct) to Tilt Angle Variation - Buoyant Flow

6.2.3.2 Daily Average Air Mass Flow (Individual Duct)

Equations 19-22 describe the effect of the solar duct geometry on the average air mass flow throughout the day for each of the key dates. The calculated optimum dimensions to produce the highest average air mass flow are shown in Table 6.17.

<u>20th March</u>

Average Air Mass Flow = 0.37 + 0.31 A + 0.32 B + 0.30 C + 0.29 AB + 0.27 AC + 0.28 BC r^2 value = 0.890 6.19

<u>21st June</u>

Average Air Mass Flow = 0.37 + 0.31 A + 0.32 B + 0.29 C + 0.29 AB + 0.28 AC + 0.28 BC r^2 value = 0.878 6.20

<u>22nd September</u>

Average Air Mass Flow = 0.37 + 0.31 A + 0.32 B + 0.29 C + 0.28 AB + 0.27 AC + 0.27 BC r^2 value = 0.890 6.21

21st December

Average Air Mass Flow = 0.38 + 0.32 A + 0.33 B + 0.31 C + 0.30 AB + 0.29 AC + 0.29 BC r^2 value = 0.891 6.22

Table 6.17 Optimum Geometry for Air Mass Flow (Individual Duct)

	Duct Length	Duct Width	Duct Depth	Duct Tilt Angle
20th March	Max	Max	Max	No Preference
21st June	Max	Max	Max	No Preference
22nd September	Max	Max	Max	No Preference
21st December	Max	Max	Max	No Preference

The sensitivity of the temperature to variations in length, width and depth was explored. Illustrative graphs are shown for 21st June.

Figure 6.17 shows the sensitivity of the air mass flow to variations in length for widths of 0.1 and 1.0m. This indicates that variations in length cause gradual changes in air mass flow. This shows the complex relationship between the air mass flow and the duct geometry. A short narrow duct would have a significant air mass flow (although not as great as a long wide duct). Intermediate lengths and depths give a reduced air mass flow. The trends indicate that short wide ducts and long narrow ducts would have a negative air mass flow. It should be remembered that the sensitivities show predicted trends, not values predicted by the $Brinkworth_{bc}$ model. There is no empirical data to compare these predictions against. However, duct geometry combinations which are indicated to result in negative flows may be indicative of geometries which cause 'choking' where no buoyant flow occurs. Similar trends were observed for the March, September and December data.

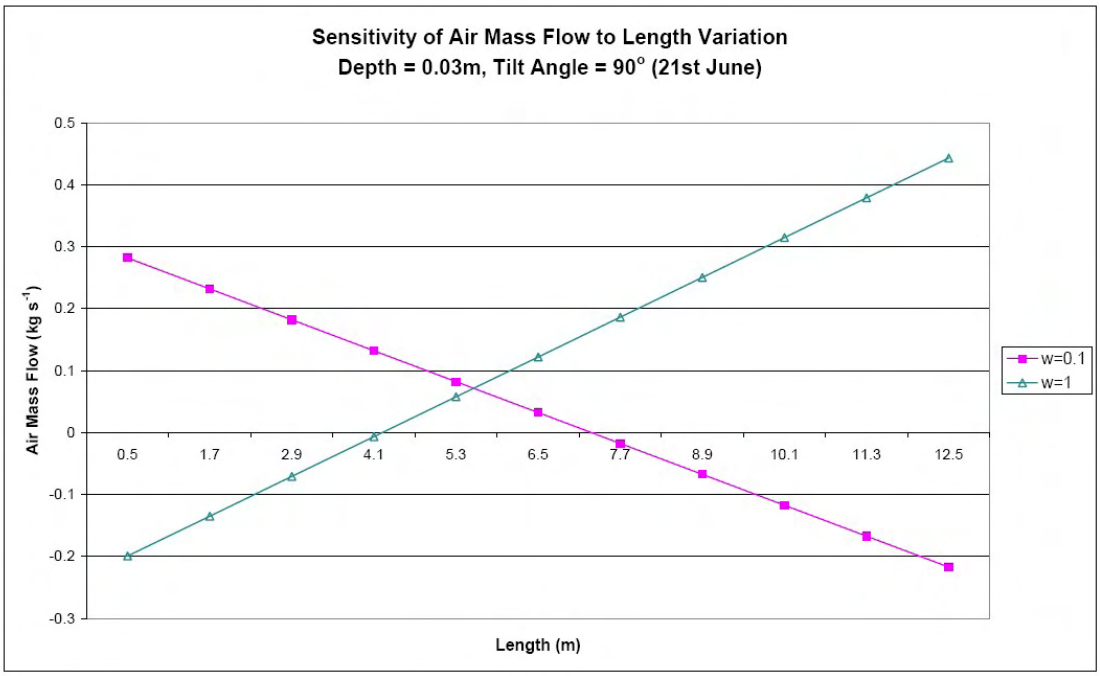

Figure 6.17. Sensitivity of Air Mass Flow (Individual Duct) to Length Variation - Buoyant Flow

Figure 6.18 shows the sensitivity of the average air mass flow to variations in width for lengths of 0.5 and 12.5 m. This indicates that variations in width cause gradual changes in air mass flow. The same complex relationship between the air mass flow, length and width is depicted as in Figure 6.17. Similar trends were observed for the March, September and December data. No empirical data was available to validate these predictions.

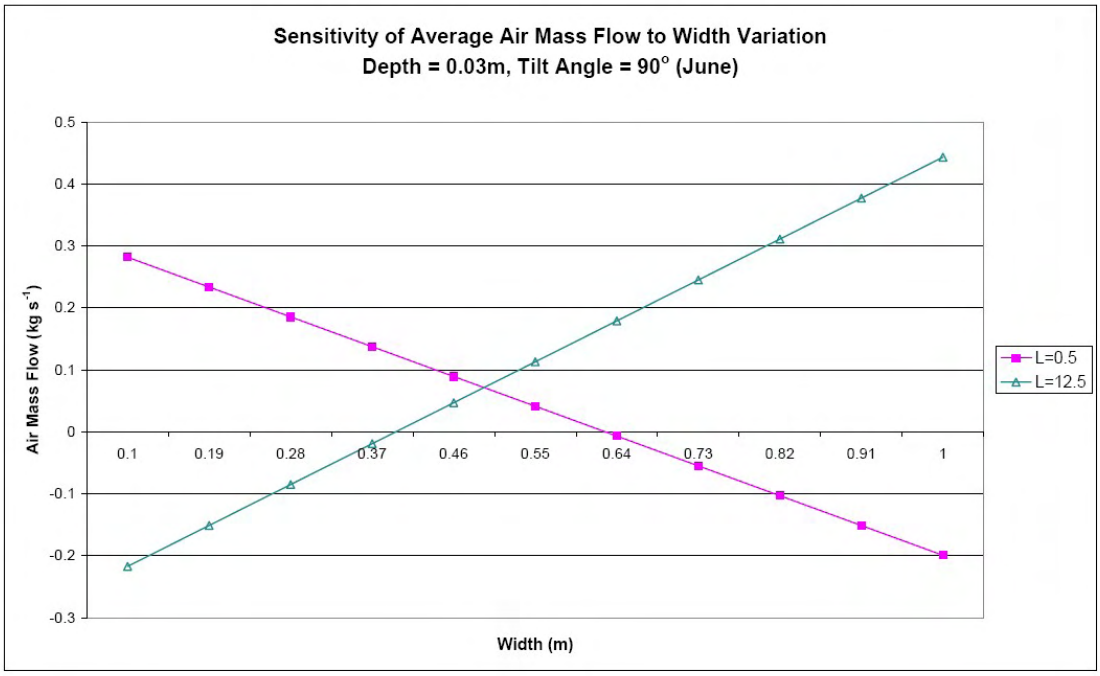

Figure 6.18. Sensitivity of Air Mass Flow (Individual Duct) to Width Variation - Buoyant Flow

Figure 6.19 shows the sensitivity of the air mass flow to variations in depth for lengths of 0.5 and 12.5 m. This indicates that variations in depth cause gradual changes in air mass flow. As in the previous two graphs, this shows a complex relationship between the air mass flow and the duct geometry. A short shallow duct would have a significant air mass flow (although not as great as a long deep duct). Intermediate lengths and depths give a reduced air mass flow. The trends indicate that short deep ducts and long shallow ducts would have a negative air mass flow. It should be remembered that the sensitivities show predicted trends, not values predicted by the Brinkworth_{bc} model. There is no empirical data to compare these predictions against. However, duct geometry combinations which are indicated to result in negative flows may be indicative of geometries which cause 'choking' where no buoyant flow occurs. Similar trends were observed for the March, September and December data. No empirical data was available to validate these predictions.

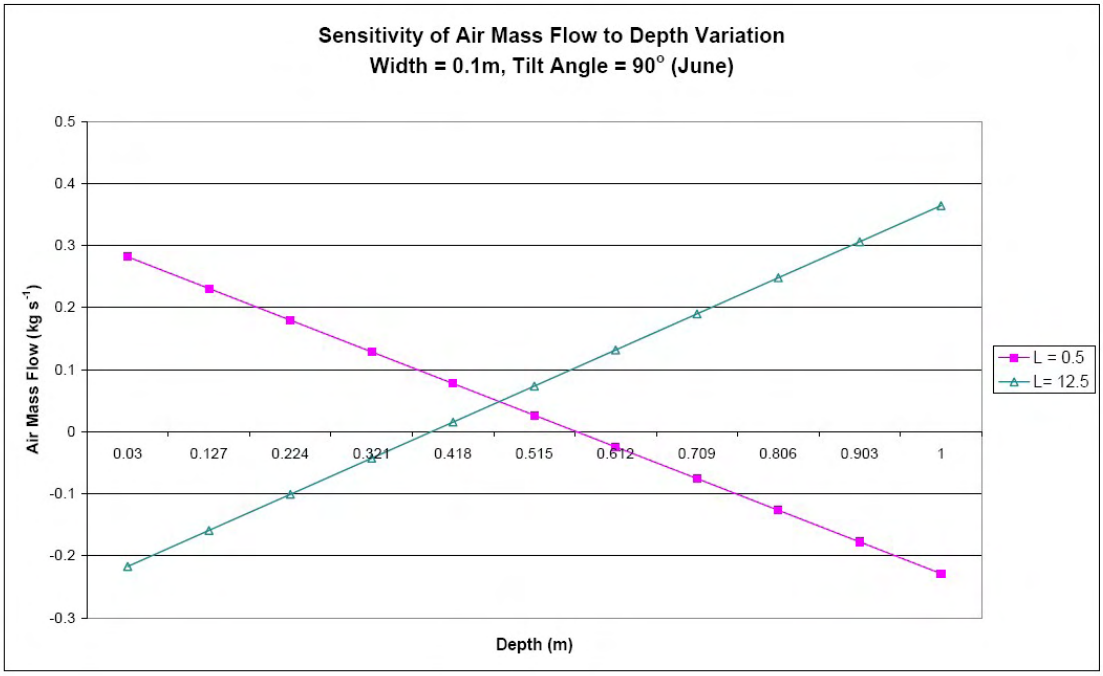

Figure 6.19. Sensitivity of Air Mass Flow (Individual Duct) to Depth Variation - Buoyant Flow

6.2.3.3 Daily Total Power Output (Individual Duct)

Equations 23-26 describe the effect of the solar duct geometry on total power output for an individual duct for each of the key dates. The calculated optimum dimensions to produce the highest power output are shown in Table 6.18.

<u>20th March</u>

Power Output = 829 – 510 A + 402 B + 455 C + 358 AB + 394 AC + 306 BC

r^2 value = 0.885 6.23

<u>21st June</u>

Power Output = 848 + 530 A + 421 B + 481 C + 376 AB + 418 AC + 329 BC

r^2 value = 0.785 6.24

<u>22nd September</u>

Power Output = 784 + 483 A + 388 B + 442 C +346 AB + 384 AC + 307 BC

r^2 value = 0.880 6.25

21st December

Power Output = 904 + 569 A + 436 B + 497 C + 389 AB + 433 AC + 323 BC

r^2 value = 0.900 6.26

Table 6.18 Optimum Geometry for Power Output (Individual Duct)

	Duct Length	Duct Width	Duct Depth	Duct Tilt Angle
20th March	Max	Max	Max	No Preference
21st June	Max	Max	Max	No Preference
22nd September	Max	Max	Max	No Preference
21st December	Max	Max	Max	No Preference

The sensitivity of the temperature to variations in length, width and depth was explored. Illustrative graphs are shown for 21st June.

The sensitivity of the power output of the duct is similar to that observed for the air mass flow. As an example, the sensitivity of power output to length is shown in Figure 6.20. Similar trends were observed for the March, September and December data. No empirical data was available to validate these predictions.

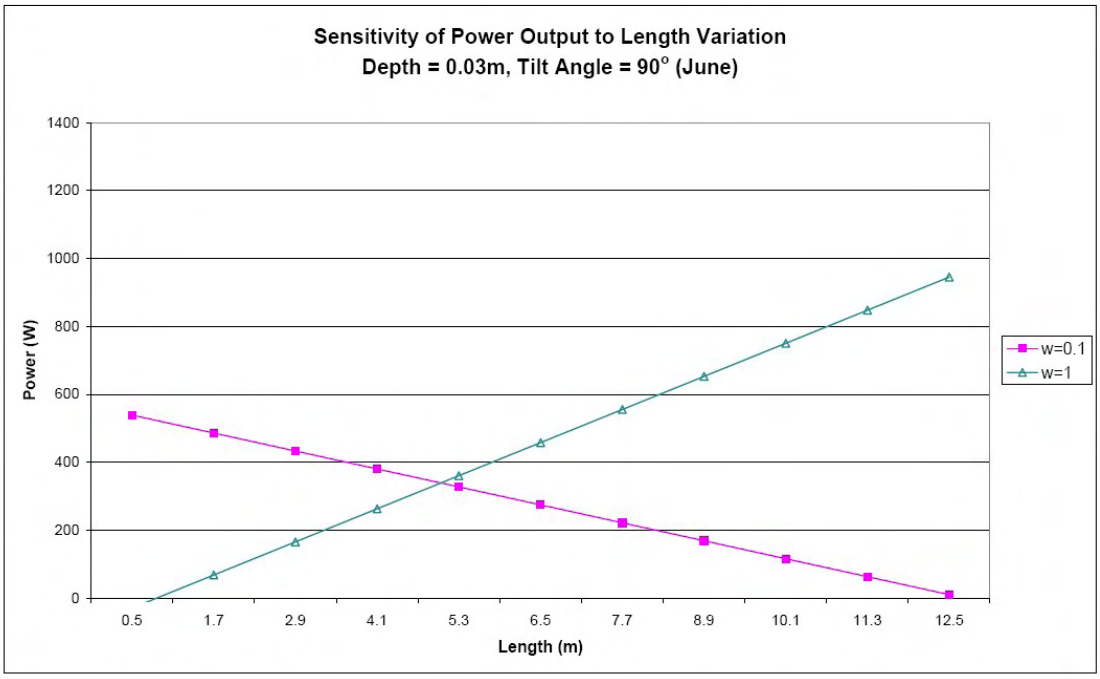

Figure 6.20. Sensitivity of Power (Individual Duct) to Length Variation - Buoyant Flow

6.2.3.4 Daily Average Air Mass Flow (10 m^2 Façade Area)

Equations 27-30 describe the effect of the solar duct geometry on the average air mass flow for a 10 m^2 area on each of the key dates. The calculated optimum dimensions to produce the highest air mass flow for a 10 m^2 area are shown in Table 6.19.

20^{th} March

$$\text{Average Air Mass Flow} = 0.99 + 0.32\,B + 0.59\,C + 0.27\,BC - 0.13\,B^2 - 0.14\,C^2 \qquad r^2 \text{ value} = 0.987 \qquad 6.27$$

21^{st} June

$$\text{Average Air Mass Flow} = 0.99 + 0.31\,B + 0.59\,C - 0.08\,D + 0.26\,BC - 0.07\,CD - 0.13\,B^2 - 0.14\,C^2 \qquad r^2 \text{ value} = 0.985 \qquad 6.28$$

22^{nd} September

$$\text{Average Air Mass Flow} = 0.98 + 0.31\,B + 0.59\,C + 0.26\,BC - 0.13\,B^2 - 0.14\,C^2 \qquad r^2 \text{ value} = 0.987 \qquad 6.29$$

21^{st} December

$$\text{Average Air Mass Flow} = 1.01 + 0.33\,B + 0.61\,C + 0.28\,BC - 0.14\,B^2 - 0.15\,C^2 \qquad r^2 \text{ value} = 0.989 \qquad 6.30$$

Table 6.19 Optimum Geometry for Air Mass Flow (10 m^2)

	Duct Length	Duct Width	Duct Depth	Duct Tilt Angle
20^{th} March	No Preference	Max	Max	No Preference
21^{st} June	No Preference	Max	Max	40^o
22^{nd} September	No Preference	Max	Max	No Preference
21^{st} December	No Preference	Max	Max	No Preference

Variations in width and depth cause gradual changes in the air mass flow over an area. Similar sensitivity trends were observed for all four dates. Similarly, variations in tilt angle caused gradual changes in the air mass flow over an area in June. No empirical data was available to validate these predictions.

6.2.3.5 Daily Total Power Output (10 m^2 Façade Area)

Equations 31-34 describe the effect of the solar duct geometry on total power output for a 10 m^2 area on each of the key dates. The calculated optimum dimensions to produce the highest power output for a 10 m^2 area are shown in Table 6.20.

20th March

Power Output = 2255 – 268 B + 1425 C – 225 D – 314 BC – 192 CD – 315 D^2

r^2 value = 0.976 6.31

21st June

Power Output = 2300 - 255 B + 1490 C – 670 D – 304 BC + 153 BD – 574 CD

r^2 value = 0.956 6.32

22nd September

Power Output = 2131 – 200 B + 1341 C – 217 D – 240 BC – 186 CD – 305 D^2

r^2 value = 0.971 6.33

21st December

Power Output = 2461 - 395 B + 1632 C + 178 D - 450 BC + 151 CD – 286 D^2

r^2 value = 0.986 6.34

Table 6.20 Optimum Geometry for Power Output (10 m^2)

	Duct Length	Duct Width	Duct Depth	Duct Tilt Angle
20th March	No Preference	Min	Max	49°
21st June	No Preference	Min	Max	40°
22nd September	No Preference	Min	Max	49°
21st December	No Preference	Min	Max	79°

The optimum geometry for power output over an area appears to be influenced by the optimum geometry for exit air temperature (minimum width) and the optimum geometry for air mass flow over an area (maximum depth).

Variations in width and depth cause gradual changes in the Power Output over an area. Similar sensitivity trends were observed for all four dates. No empirical data was available to validate these predictions.

When considered over a 10 m^2 area, the influence of tilt angle became statistically significant, where it had not been for a single duct. Variations in tilt angle caused gradual changes in the Power Output over an area; however, the optimum value varied between the seasons. An example of the sensitivity to tilt angle is shown for 20th March in Figure 6.21. No empirical data was available to validate these predictions.

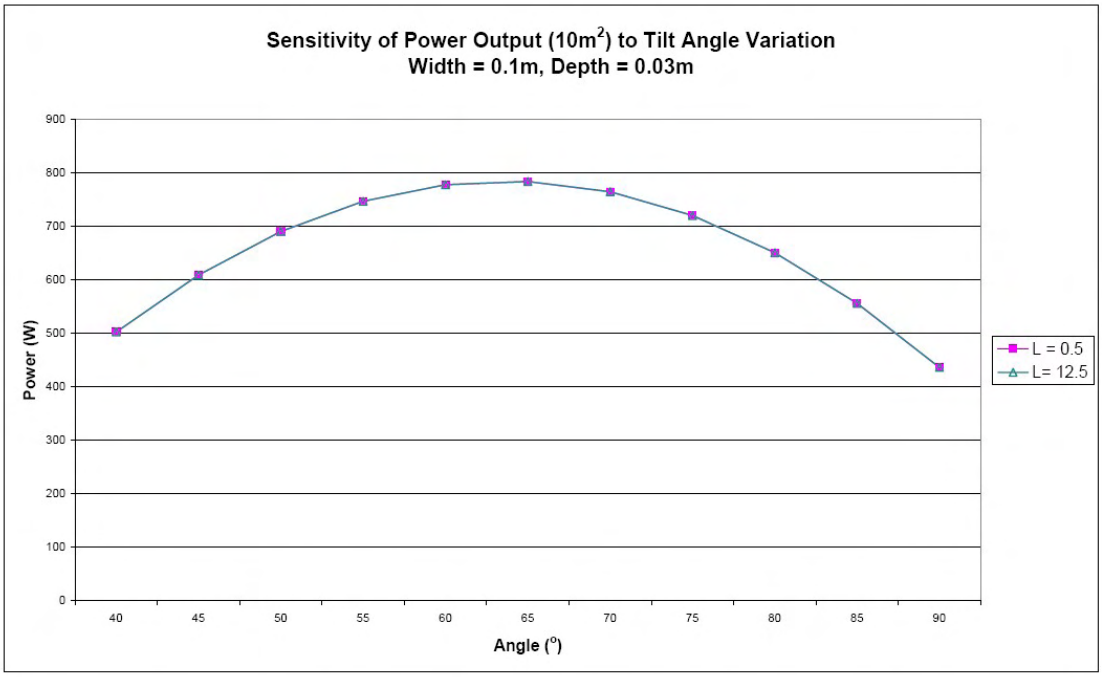

Figure 6.21. Sensitivity of Power Output (10m2) to Tilt Angle Variation - Buoyant Flow

6.2.3.6 Summary of Results

Sections 6.2.3.1 to 6.2.3.5 indicate the optimum geometry for the average exit temperature of an individual duct, the average air mass flow of a single duct, the power output of a single duct, the air mass flow of a 10 m^2 façade area and the power output of a 10 m^2 façade area. This is summarised in Table 6.21. General observations (e.g. 'min') have been converted to the corresponding dimension from the range evaluated.

Table 6.21 Optimised Solar Duct Geometry for Buoyant Ventilation

	Length (m)	Width (m)	Depth (m)	Tilt Angle (^{o})			
Average Exit Temperature (^{o}C)	12.5	0.1	1	M/J/S 40^o		D 90^o	
Air Mass Flow (kg s^{-1})	12.5	1	1	No Preference			
Power Output (W)	12.5	1	1	No Preference			
Air Mass Flow – 10 m^2 façade area (kg s^{-1})	No Preference	1	1	J 40^o		M/S/D No Preference	
Power Output – 10 m^2 façade area (W)	No Preference	0.1	1	M 49^o	J 40^o	S 49^o	D 79^o

Where M = March, J = June, S = September, D = December

From Table 6.21 it can be seen that there is a slight conflict between the geometry that would produce the highest air exit temperature and the geometry that would provide the highest power output over a 10 m^2 façade area. This conflict is confined to the tilt angle. The average exit temperature optimisation is polarised between 90^o in December and 40^o on the other dates considered. This conflict is less polarised for the power output over an area; where the optimum tilt angle required for December is 79^o, while the optimum for the other dates varies between 40 and 49^o. The sensitivity to the tilt angle has been shown to be gradual; therefore variations from the optimum will have a gradual impact. A reasonable compromise would be a 60^o tilt angle.

It should be noted that it would not be possible to meet the optimum width and depth dimensions for air mass flow due to the limitations of incoming strip width as described in Section 6.2.1.3. However, this should not present a difficulty as the width and depth dimensions for optimum exit temperature and power output are feasible.

If the optimum dimensions for the exit temperature were followed, the average exit temperature for December would be 9 ^{o}C. This would be too low a temperature to be used in a direct ventilation system in the winter.

The buoyant system may be able to generate air currents if incorporated into a direct ventilation system in the summer. Further work would be required to verify this as an application.

6.3 Conclusions

An attempt was made to address the aesthetic issues of façade colour by evaluating the effect of varying the reflectivity of the solar absorbing material. The reflectivity of a black solar absorbing material was measured and compared to that of a silver coloured solar absorbing material. The reflectivity was found to increase from 0.08 to 0.38. The design models identified in Chapter 5 for forced and buoyant convection were used to evaluate the impact of varying the reflectivity between 0.05 and 0.4. The power output was found to drop by 35 % for forced convection and by 40 % for buoyant convection.

A factorial experiment was carried out using the $Ho_{fc\&fcad}$ model to establish the optimum geometry for a variety of parameters under forced convection. Where possible the limitations of the $Ho_{fc\&fcad}$ model were mitigated by referring to the results of the empirical experiment in Chapter 4. It was found that the optimum geometry for the highest air exit temperature (maximum length and width) conflicted with that recommended for the highest power output over a 10 m^2 façade area (minimum length and width). The optimum geometry for power output over a 10 m^2 façade area was found to be heavily influenced by the optimum geometry for air mass flow, and so was relatively unaffected by the limitations of the $Ho_{fc\&fcad}$ model. The recommendation for minimum depth to facilitate highest exit temperature and power output over a 10 m^2 façade area is contradicted by the empirical results from Chapter 4. The optimum tilt angle agrees for both parameters, but varies depending on the season. The response to variations in geometry is gradual.

If the optimum duct for power output over an area were used, the temperatures generated would not be acceptable for a direct ventilation system but may be suitable for an indirect ventilation system. If the optimum dimensions for the exit temperature were followed the heated air would require dilution with unheated air to attain an acceptable temperature, but could then be utilised for a direct ventilation system.

A factorial experiment was also carried out using the $Brinkworth_{bc}$ model to establish the optimum geometry for a variety of parameters under buoyant convection. Where possible the limitations of the $Brinkworth_{bc}$ model were mitigated by referring to the results of the empirical experiment in Chapter 4. The optimum geometry for highest air

exit temperature is in reasonable accord with the optimum geometry for highest power output over a 10 m^2 façade area – both parameters require minimum width and maximum depth. The power output has no preference to length, allowing longer ducts to be used to accommodate higher air exit temperatures. The optimum tilt angle agrees for both parameters, but varies depending on the season. The response to variations in geometry is gradual.

The air temperatures in winter would be too low to be incorporated in a direct ventilation system in the winter.

The conflicts in optimum geometry for different parameters, seasons and between forced or buoyant convection requires a decision on the intended application of the system before construction (i.e. direct or indirect ventilation).

6.4 References

1. Hollands, K.G.T. and E.C. Shewen, *Optimization of flow passage geometry for air-heating, plate-type solar collectors.* Journal of Solar Energy Engineering, 1981. **103**: p. 323-330.
2. Munari-Probst, M., C. Roecker, and A. Scheuler. *Architectural Integration of Solar Thermal Collectors: Results of a European Survey*. in *ISES 2005 Solar World Congress*. 2005. Orlando, Florida, USA: International Solar Energy Society.
3. Kipp & Zonen, *Instruction Manual CM6B Pyranometer / CM7B Pyranometer*, 2003.
4. Ho, K.T.K. and D.L. Loveday, *New Approach for Analyzing Solar Collectors Subjected to Unequal Front/Rear Ambient Temperatures: The Equivalent Ambient Temperature Concept, Part 2: Validation and Implications for Design.* Transactions of American Society of Mechanical Engineers: Journal of Solar Energy Engineering, 2002. **124**: p. 268-275.
5. Hegazy, A.A. *Comparative Study of the Performances of Four Photovoltaic/Thermal Solar Air Collectors*. in *Energy Conversion and Management*. 2000.
6. Evans, M., *Optimisation of Manufacturing Processes: a Response Surface Approach*. 1st ed. 2003, Leeds: Maney Publishing.p.1- 320; 1902653866.
7. Cross, B., *The OpTIC Centre PV Design and Construction*, 2004, St Asaph.
8. Marsh, D.A. *UK - Cardiff Wales Weather Data*. [cited 24th February 2004]; http://www.squ1.com/site.html.
9. Muneer, T., *Solar radiation & Daylight models*. 1997, Oxford: Architectural Press.p.1- 197; 0 7506 2495 7.

7 Application of Solar Duct

The aim of this chapter is to predict the potential application of the system in Cardiff weather conditions during a typical year.

Optimum dimensions for forced and buoyant convection solar ducts were established in Section 6.2. The likely energy output of these solar ducts and related fuel cost savings over a typical year is discussed in this section. The domestic cost of fuel in 2006 was calculated to be 10.12 p per kWh for electricity and 2.492 p per kWh for gas.

Typical weather data for Cardiff has been analysed to obtain the average input conditions for each month of the year. These input conditions are shown in Section 7.1. The input conditions are fed into the $Ho_{fc\&fcad}$ model for forced and $Brinkworth_{bc}$ model for buoyant convection developed in Chapter 5. For each flow mode, the air exit temperature and (net) power output is calculated and displayed to show the variation over the year.

7.1 Input Conditions

Average input conditions for each month have been calculated and are shown in Tables 7.1-7.4. Commercially available weather data [1] for Cardiff, UK was used.

Table 7.1 Ambient Temperature (hourly average)

Time	J	F	M	A	M	J	J	A	S	O	N	D
03:00	7.1	7.6	8.8	7.7	12.4	13.5	14.7	14.5	13.7	11.3	7.0	6.9
04:00	7.0	7.5	8.5	7.6	12.4	13.6	14.3	14.5	13.3	11.2	6.9	6.8
05:00	7.0	7.3	8.4	7.3	12.3	14.0	14.7	14.5	13.5	11.0	6.8	6.6
06:00	7.0	7.0	8.5	7.8	13.3	14.9	15.4	15.5	13.7	11.1	6.9	6.5
07:00	6.8	7.2	9.0	8.7	14.3	15.0	16.4	16.4	14.6	11.3	6.7	6.5
08:00	6.8	7.6	9.6	9.5	15.2	15.8	17.1	17.5	15.4	12.0	7.4	6.7
09:00	7.1	8.5	10.2	10.4	15.6	16.1	17.7	18.1	16.0	12.4	8.0	7.2
10:00	7.7	9.4	10.6	10.6	16.4	16.5	18.2	18.7	16.8	13.3	8.9	74
11:00	7.8	10.3	11.2	11.2	16.8	17.4	18.9	19.4	17.1	13.8	9.3	8.0
12:00	8.2	10.9	11.8	11.2	17.8	17.4	19.0	20.0	17.5	14.2	9.9	8.5
13:00	8.3	11.3	12.0	11.3	18.5	17.9	19.1	20.3	17.9	14.1	10.2	8.7
14:00	8.6	11.8	12.0	11.5	19.0	18.4	19.3	20.7	18.0	14.2	10.1	8.8
15:00	8.2	11.7	11.7	11.2	19.1	18.3	19.3	20.2	18.2	13.9	9.9	8.5
16:00	8.2	11.5	11.5	10.9	18.8	17.4	18.8	20.5	18.0	13.5	9.4	8.4
17:00	7.8	10.5	10.8	10.7	18.4	17.1	18.3	19.7	17.0	13.0	8.7	7.9
18:00	7.8	10.0	10.5	10.0	17.9	16.7	17.8	19.0	16.5	12.3	8.6	8.0
19:00	7.5	9.5	10.3	9.4	16.9	16.1	17.1	18.0	15.9	12.2	8.3	8.0
20:00	7.5	9.3	9.9	9.1	16.2	15.3	16.6	16.9	15.6	11.9	8.1	7.7

Table 7.2 Horizontal Direct Solar Irradiation (hourly average)

Time	J	F	M	A	M	J	J	A	S	O	N	D
03:00												
04:00					12	16	12	1				
05:00				14	67	72	60	36	2			
06:00			6	68	164	146	135	122	40	1		
07:00		8	59	144	269	196	210	232	117	40	6	
08:00	12	62	131	256	389	307	305	348	198	121	53	11
09:00	50	143	206	335	460	388	360	418	289	169	108	50
10:00	101	212	273	389	527	461	452	500	346	250	165	89
11:00	124	248	305	464	596	514	503	517	370	262	190	107
12:00	135	264	313	446	584	568	497	542	397	251	197	104
13:00	139	253	271	372	625	597	522	512	383	221	176	88
14:00	100	195	208	351	536	511	449	441	313	185	110	47
15:00	45	120	157	258	433	415	371	348	240	110	48	16
16:00	4	44	83	177	296	295	297	276	136	38	3	
17:00		5	28	99	199	217	182	161	44	3		
18:00				26	89	109	87	54	2			
19:00				1	15	31	22	5				
20:00												

Table 7.3 Horizontal Diffuse Solar Irradiation (hourly average)

Time	J	F	M	A	M	J	J	A	S	O	N	D
03:00												
04:00					1	7	4					
05:00				6	41	50	44	15				
06:00			3	48	93	98	88	74	26			
07:00		3	40	91	144	143	145	113	69	27		
08:00	7	32	82	126	169	184	194	153	121	73	31	
09:00	37	69	121	174	199	210	219	197	159	97	64	35
10:00	64	106	153	203	222	241	258	214	196	113	85	59
11:00	77	122	174	190	211	256	289	210	205	132	93	66
12:00	77	132	175	182	208	244	283	199	192	132	85	63
13:00	72	115	149	176	203	207	246	209	173	119	70	50
14:00	50	92	123	147	160	207	200	158	138	86	45	27
15:00	15	54	90	140	151	177	174	135	102	47	14	1
16:00		13	53	95	125	142	144	112	62	13		
17:00			13	54	87	106	99	76	20			
18:00				6	41	60	51	24				
19:00						13	6					
20:00												

Table 7.4 Cloud Cover (hourly average)

Time	J	F	M	A	M	J	J*	A*	S*	O*	N*	D*
03:00	72	56	71	67	49	68	As for June	As for May	As for Apr	As for Mar	As for Feb	As for Jan
04:00	71	61	71	60	51	70						
05:00	73	58	67	61	58	73						
06:00	75	59	70	73	61	74						
07:00	78	58	72	75	60	80						
08:00	80	62	74	65	52	70						
09:00	77	60	74	65	52	67						
10:00	71	60	70	65	51	66						
11:00	75	61	71	56	45	61						
12:00	71	59	69	58	46	52						
13:00	65	54	73	67	35	41						
14:00	58	59	77	60	36	47						
15:00	52	54	75	66	39	50						
16:00	67	51	73	67	47	58						
17:00	79	60	65	57	41	52						
18:00	66	66	69	55	30	55						
19:00	65	48	71	61	48	41						
20:00	66	46	63	58	65	54						

* the cloud cover data for July to December appears to be corrupted. For this reason, it has been assumed that the cloud cover over the year is symmetrical about 30th June. The cloud cover data has a small impact on the calculated sky temperature which in turn has a small impact on the results of the $Ho_{fc\&fcad}$ model. For this reason the assumption is considered adequate.

7.2 Forced Convection

The $Ho_{fc\&fcad}$ model has been used to make the calculations relating to forced convection (bearing in mind the limitations already identified relating to the model). The hourly air exit temperature and net energy output for a 200 m^2 façade area have been calculated for an air mass flow of 0.01 kg s^{-1} per duct using the input conditions from Tables 7.1–7.4. An area of 200 m^2 has been used as it is more representative of the size of an industrial building façade. It has been assumed that the ducts will be arranged in an array as illustrated in (Figure 7.1b). It has also been assumed that there will be a gap of 0.02m laterally and 0.1m vertically between ducts. This is to allow for fresh air to be fed into the ducts and heated air to be fed into the building.

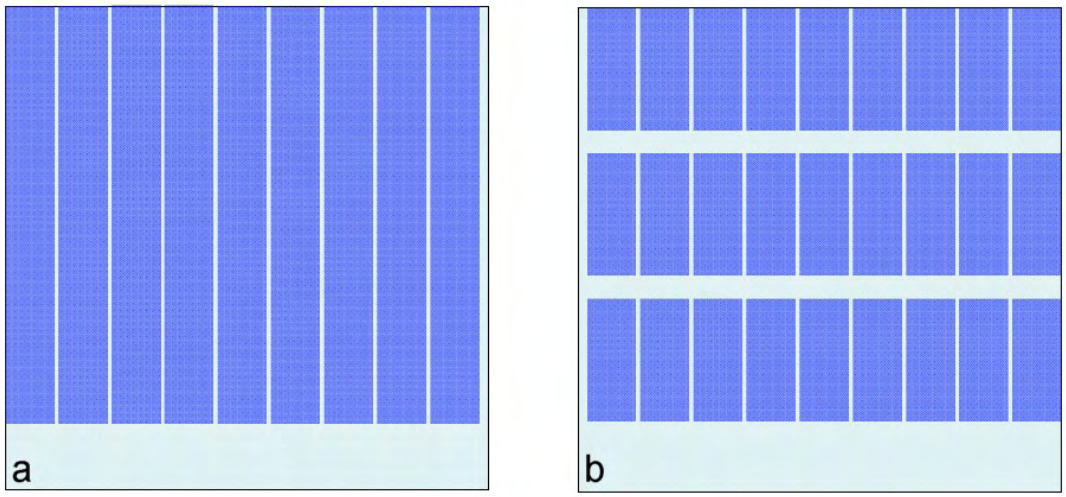

Figure 7.1. Array of ducts on part of a facade: a long ducts b short ducts

It is considered unlikely that a non-vertical façade would be built since it was not required for the winter conditions, when most heating would be required. Therefore the duct geometry considered, is the one optimised for power output over a 10 m^2 façade area in Chapter 6 (0.5 m long, 0.1 m wide and 0.03 m deep) on a vertical façade. The air exit temperature for representative months (i.e. January, April, July and October) is illustrated in (Figure 7.2). The air temperatures in January and April are too low for the air to be fed directly into the building (direct ventilation). However, it could be directed to a heating source before it is fed into the building (indirect ventilation). The air exit temperature in October is higher than the air exit temperature in April because of the higher ambient temperature.

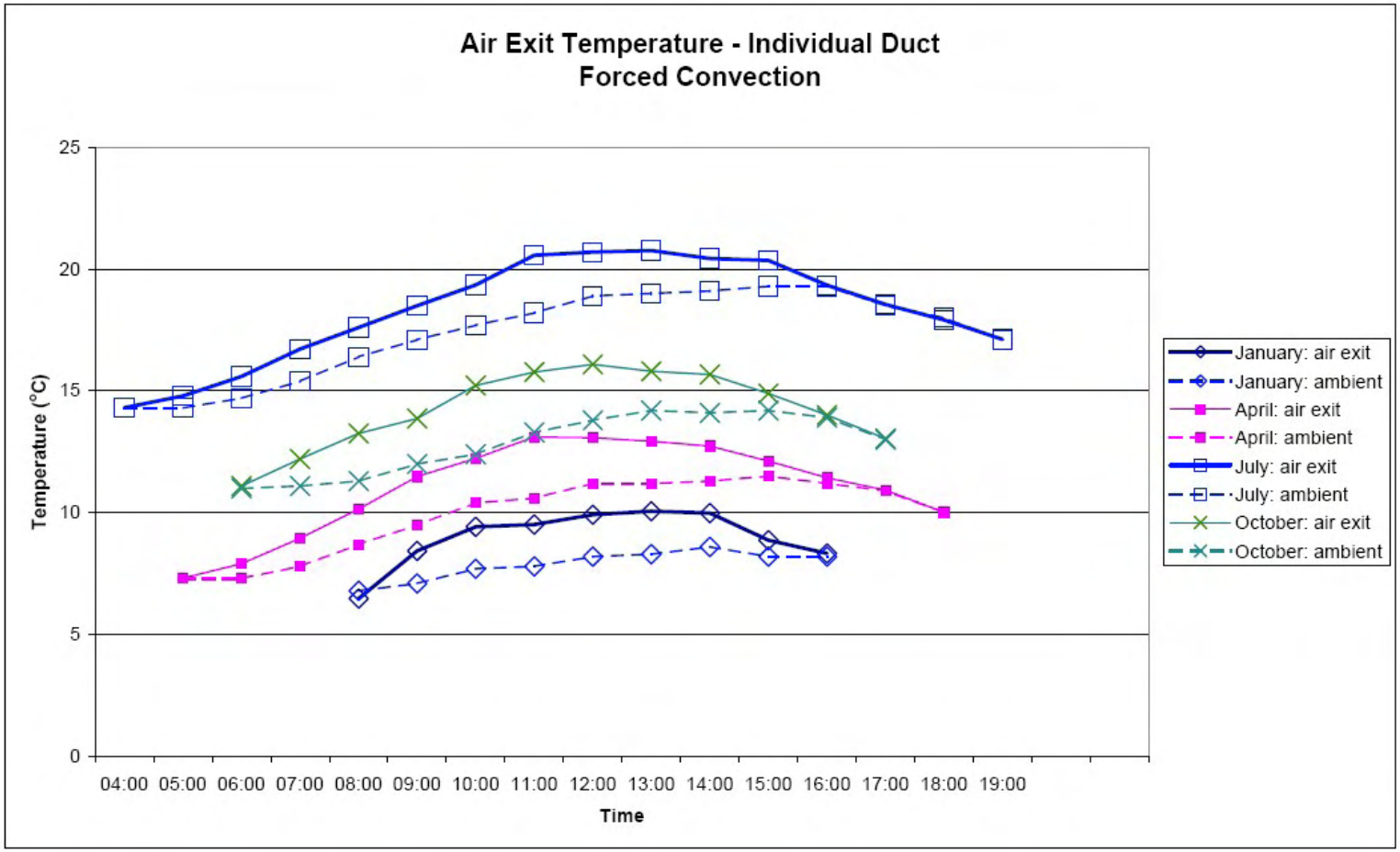

Figure 7.2. Forced Convection - Exit Air Temperature

The net energy output for a 200 m^2 façade area for representative months are illustrated in Figure 7.3. April, October and even December have higher peak energy output than July. However, the longer hours of sunshine available in summer months increase the summer energy output.

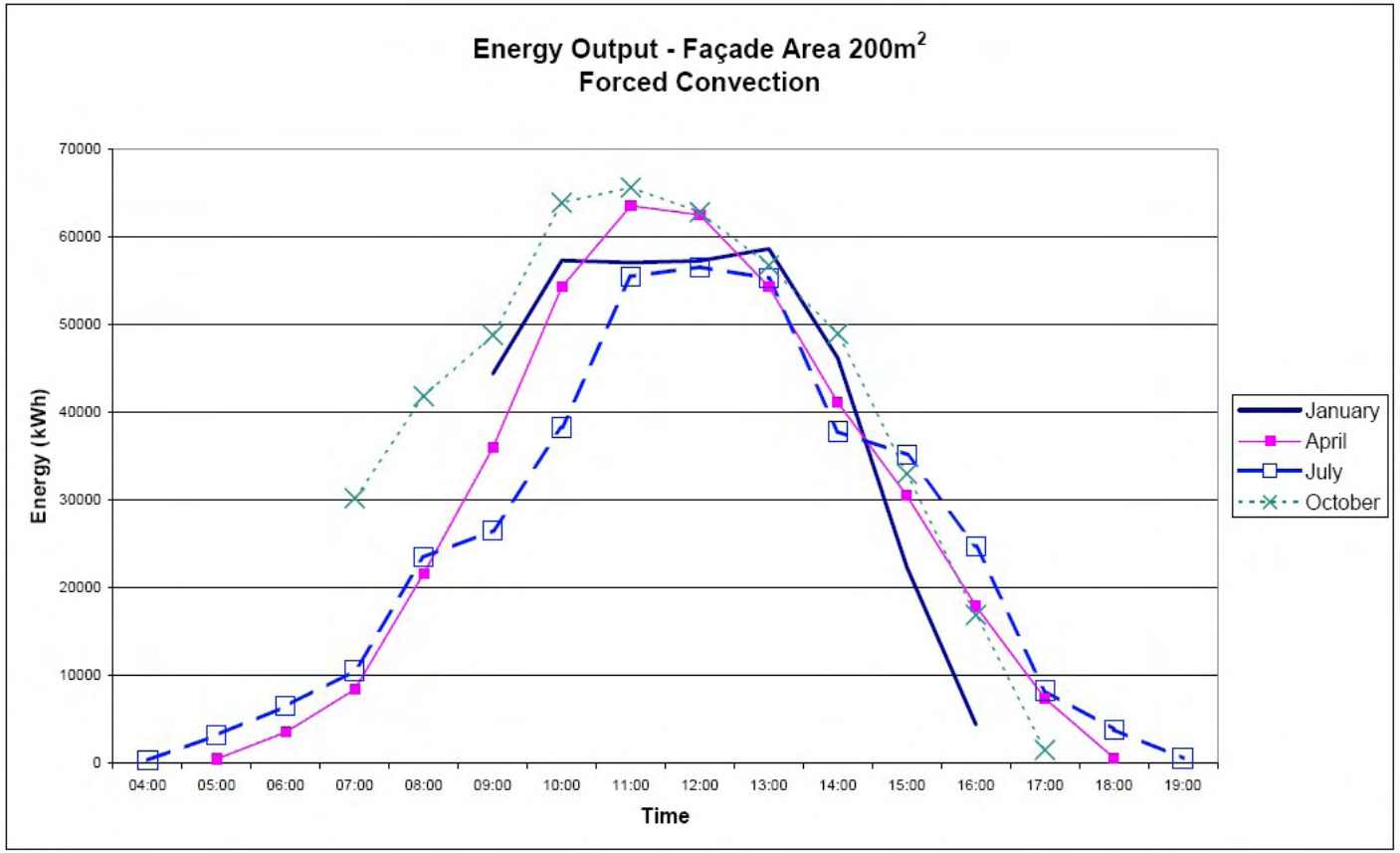

Figure 7.3. Forced Convection - Net Energy Output for 200 m^2 Facade Area (Seasonal)

A 200 m^2 façade could incorporate 3305 ducts of the specified dimensions. 33 kg s^{-1} of ventilation air would pass through the ducts at the specified flow.

The net energy output for a 200 m^2 area (based on the input data from Tables 7.1-7.4) is 150,595 kWh. Therefore, if the solar heating was displacing electricity, the cost saving would be £15,240 per year (£76 per m^2 per annum). If gas was displaced, the cost saving for the year would be £3,752 (£19 per m^2 per annum).

If the energy output is disregarded when the ambient temperature is above 18 ^oC, a 200 m^2 area would generate 116,468 kWh (net). The cost saving for displaced electricity would be £11,787 per year (£59 per m^2 per annum); while the cost saving for displaced gas would be £2,902 per year (£15 per m^2 per annum).

The evaluation of the design model in Chapter 5 indicated that the $Ho_{fc\&fcad}$ model was likely to underestimate the power output and was only accurate to 35%. Assuming the worst case scenario where the $Ho_{fc\&fcad}$ model over predicted the power output by 35%, the actual energy output would be 75,704 kW (net). The cost saving for electricity would be £7,661 (£38 per m^2 per annum), and the cost saving for gas would be £1,887 (£9 per m^2 per annum). The extra materials used to make a solar air façade would cost between £32 and £45 per m^2. If the solar heated air replaced electrically heated air, the cost of the materials could be repaid within 14 months. If gas heated air was replaced the repayment time would extend to 60 months.

The seasonal distribution of the net energy output is:

- Winter (Dec, Jan, Feb) 21.9 %
- Spring (Mar, Apr, May) 25.4 %
- Summer (Jun, Jul, Aug) 24.9 %
- Autumn (Sept, Oct, Nov) 27.8 %

This shows a reasonably even distribution of the energy output over the seasons, rather than a high output during summer and limited output during the other seasons. However, the ambient temperature rises above 18^oC more often in the summer months. If the output energy is discounted when the ambient temperature is greater than 18^oC, the seasonal distribution of the net energy output is:

- Winter (Dec, Jan, Feb) 28.3 %
- Spring (Mar, Apr, May) 28.0 %
- Summer (Jun, Jul, Aug) 10.7 %
- Autumn (Sept, Oct, Nov) 33.0 %

If an increased air exit temperature was required, it would be possible to interconnect the short ducts, allowing air to flow from one duct to another. As an example, if the air was passed through 23 of the specified ducts (Figure 7.4), the temperature on an average January day would peak at 43.7 ^{o}C which would be more than adequate for direct ventilation. On an average day in July, the temperature would peak at 52.9 ^{o}C which would have potential for heating water for use in the building. As was discussed in Chapter 6, connecting the ducts in such a way has a penalty. The air flow and power output would be significantly reduced – assuming that 23 ducts were connected the array could only produce 4.3 % of the power output possible if the ducts were allowed to operate individually.

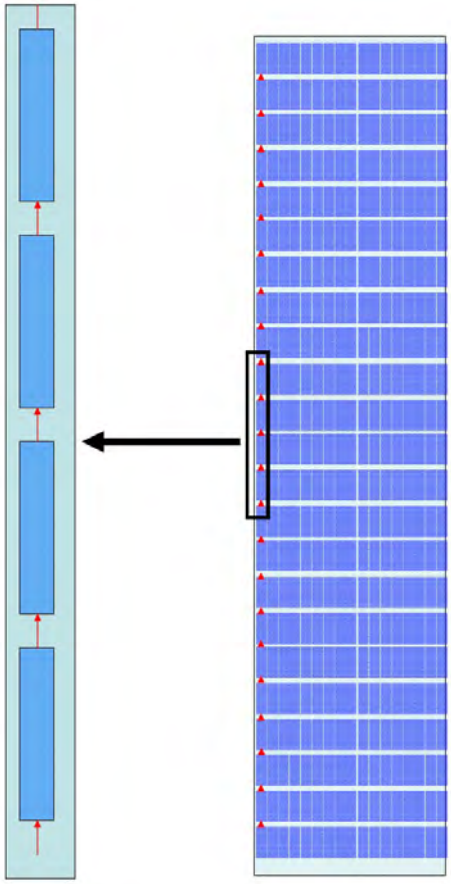

Figure 7.4. Air flow through array of 23 ducts

7.3 Buoyant Convection

The Brinkworth$_{bc}$ model has been used to make calculations relating to buoyant convection (bearing in mind the limitations already identified relating to the model). The hourly air exit temperature, air mass flow for a 200 m^2 façade area and energy output a 200 m^2 façade area have been calculated. The duct geometry optimised for power output over a 10 m^2 façade area in Chapter 6 (i.e. a solar duct of 12.5 m long, 0.1 m wide and 1 m deep at a tilt angle of 60^o) has been used with the input conditions from Tables 1-4. It has been assumed that the ducts will be arranged in an array, as illustrated in (Figure 7.1a). It has also been assumed that there will be a gap of 0.02m laterally between ducts.

The air exit temperature for representative months (i.e. January, April, July and October) is illustrated in (Figure 7.5).

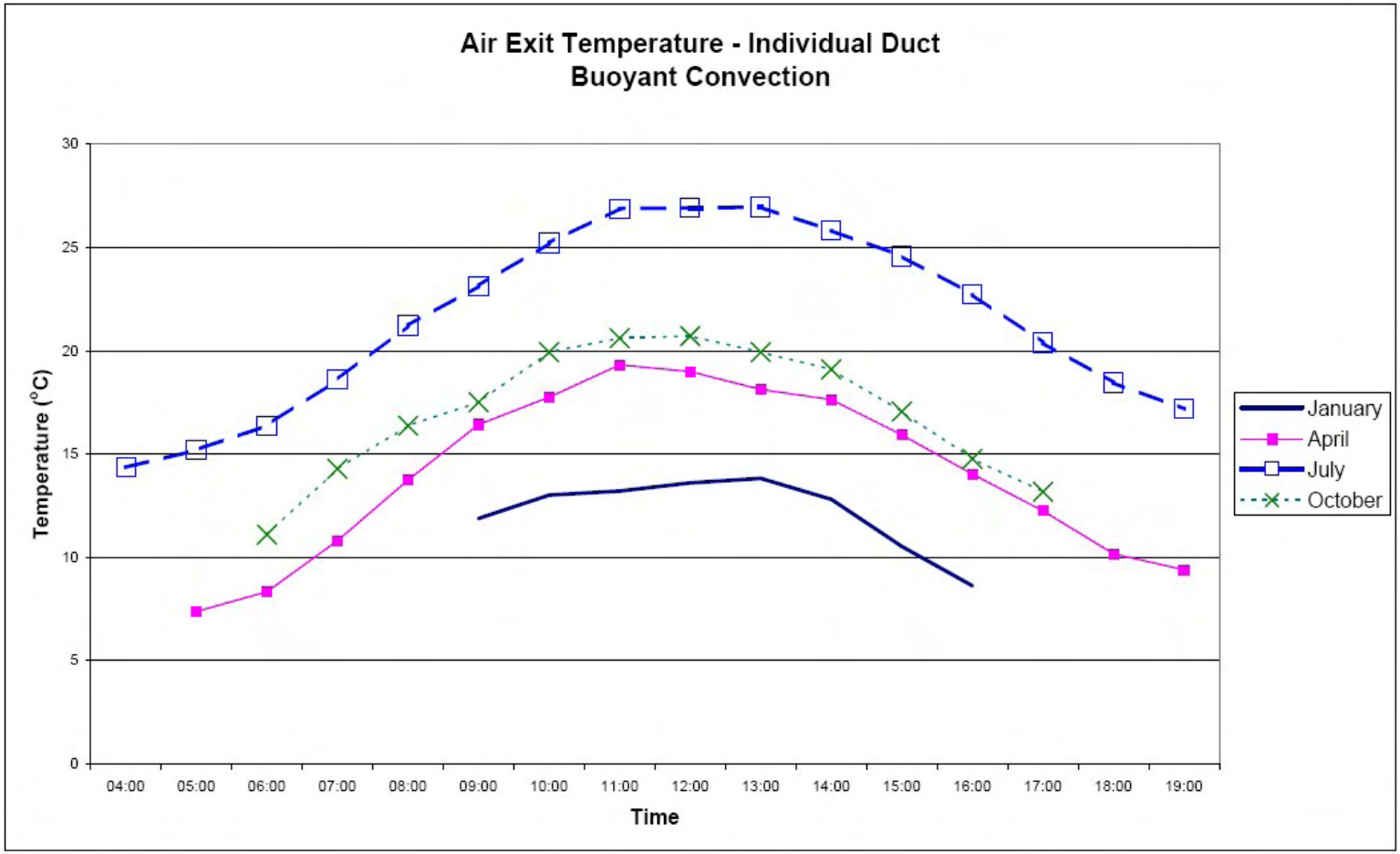

Figure 7.5. Buoyant Convection - Exit Air Temperature

The air temperature in January is too low to be used in a direct ventilation system, but could be useful in an indirect ventilation system.

The air mass flow for a 200 m^2 façade area is illustrated in Figure 7.6 for the same months. A 200 m^2 façade could incorporate 145 ducts of the specified dimensions. The average flow through the array of solar ducts would be 11.9 kg s^{-1}. This is equivalent to an average air mass flow of 0.08 kg s^{-1} through each duct. The air mass flow peaks at 17.5 kg s^{-1} in May. The air mass flow through a duct on the buoyant convection system is higher than for the forced convection system due to the different dimensions of the duct.

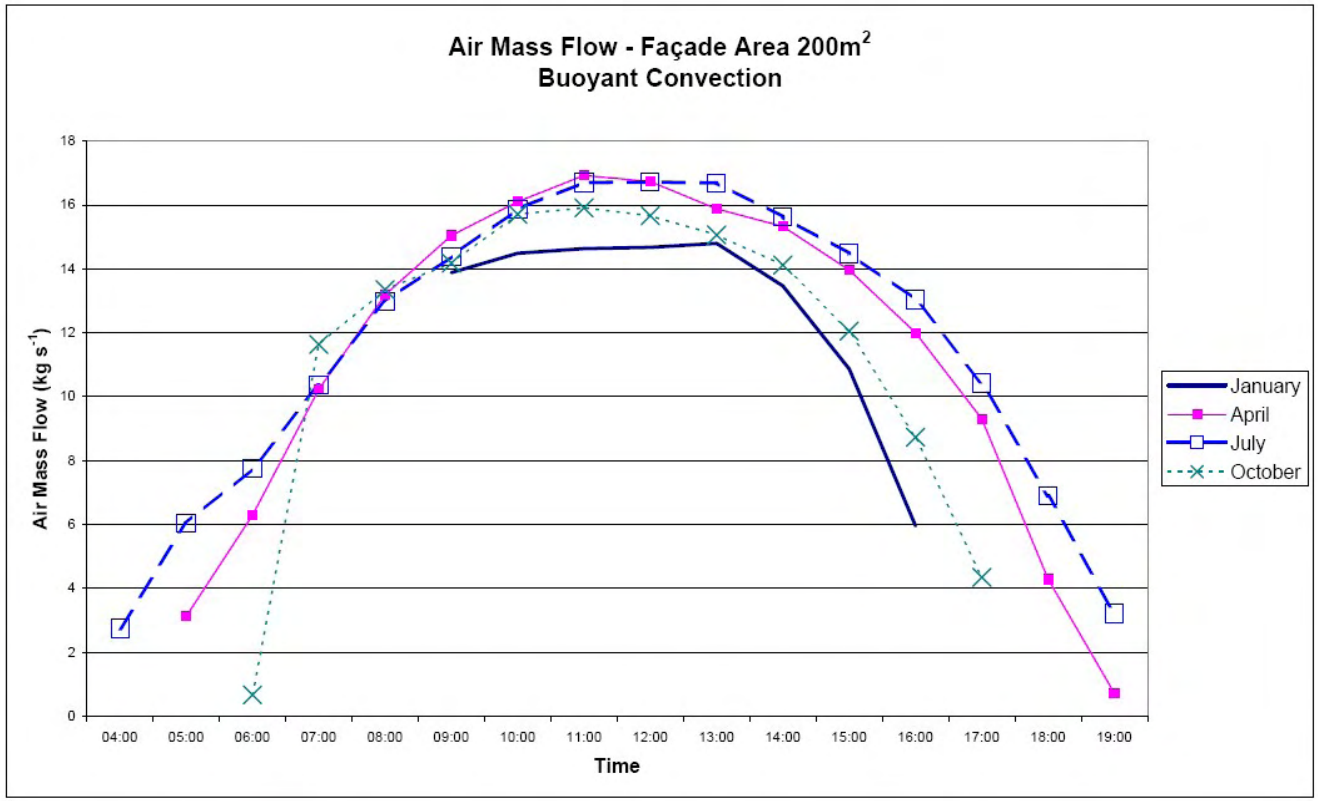

Figure 7.6. Buoyant Convection - Air Mass Flow (200 m^2)

Similarly, the net energy output for a 200 m^2 façade area is illustrated in Figure 7.7. In this instance, only April exceeds the peak energy output of July.

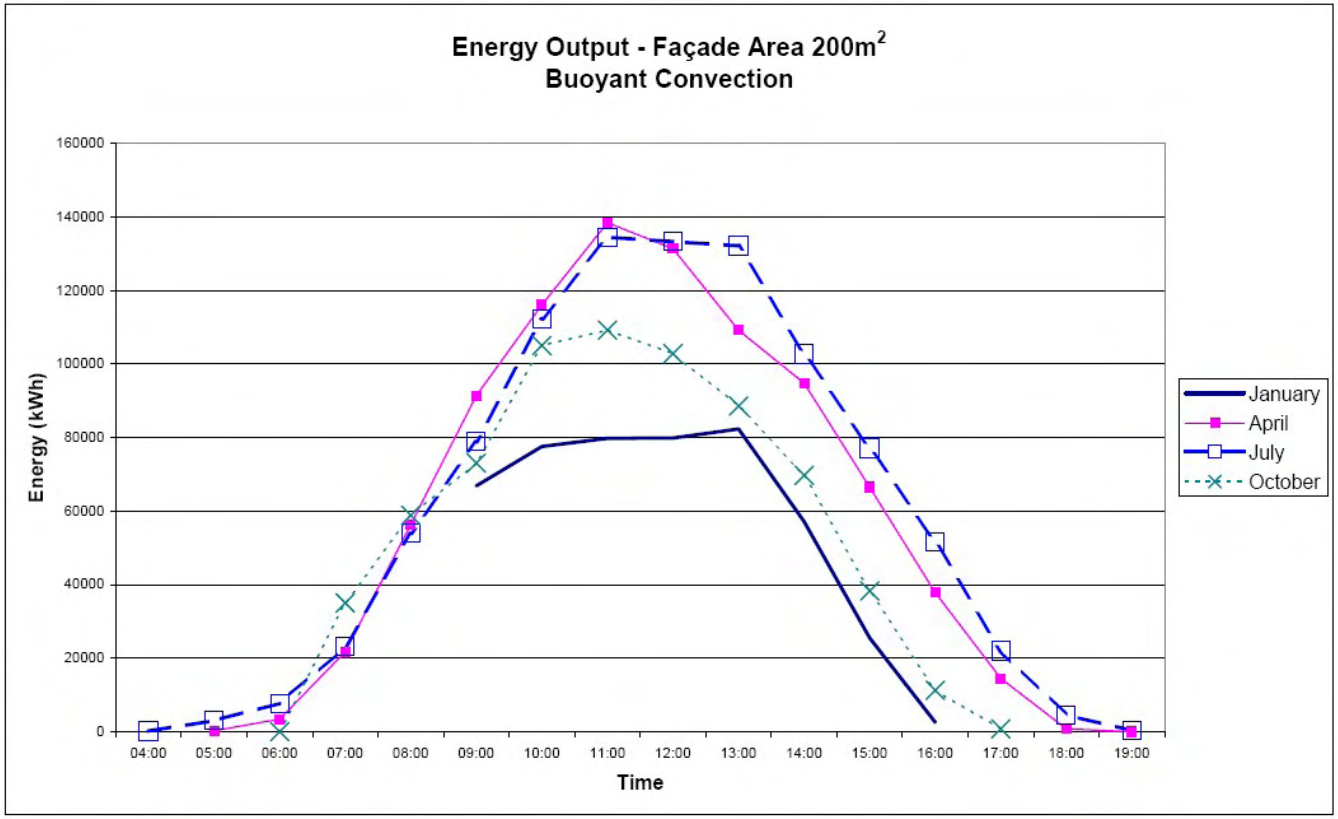

Figure 7.7. Buoyant Convection - Energy Output (200 m^2)

The total energy output for a 200 m^2 area (based on the input data from Tables 7.1-7.4) is 279,833 kWh. If the solar heating displaced electricity, the cost saving would be £28,319 per year (£142 per m^2 per annum). If gas was displaced, the cost saving for the year would be £6,973 per year (£35 per m^2 per annum). The extra materials used to make a solar air façade would cost between £35 and £42 per m^2. If the

solar heated air replaced electrically heated air, the cost of the materials could be repaid within 8 months. If gas heated air was replaced, the repayment time would extend to 34 months.

If the energy output is disregarded when the ambient temperature is above 18 ^{o}C, a 200 m^2 area would generate 202,996 kWh. The cost saving for displaced electricity would be £20,543 per year (£105 per m^2 per annum); while the cost saving for displaced gas would be £5,059 per year (£25 per m^2 per annum).

The comparison within Chapter 6 indicated that the $Brinkworth_{bc}$ model was more likely to underestimate the energy output than overestimate it. However, as in the previous section the figures allowing for a 35 % overestimate of the energy output have been calculated. In such an event, the total energy output would be 131,947 kW. The cost saving for displaced electricity would be £13,353 (£67 per m^2 per annum). The cost saving for displaced gas would be £3,288 (£16 per m2 per annum).

The seasonal distribution of the energy output is:

- Winter (Dec, Jan, Feb) 17.3 %
- Spring (Mar, Apr, May) 29.8 %
- Summer (Jun, Jul, Aug) 28.2 %
- Autumn (Sept, Oct, Nov) 24.7 %

The seasonal distribution of energy discounting times when the ambient temperature rises above 18^{o}C is:

- Winter (Dec, Jan, Feb) 23.9 %
- Spring (Mar, Apr, May) 34.2 %
- Summer (Jun, Jul, Aug) 10.8 %
- Autumn (Sept, Oct, Nov) 31.1 %

The heated air in the summer months could be used for low grade water heating (e.g. swimming pool water supplies) or it could be used to preheat water supplies for the building. Since this system uses long ducts and relies on buoyant air flow, there is less scope to feed air from one duct to another to raise the exit air temperature. However, the strength of this system lies in its high air mass flows without the penalty of using

electricity to drive fans. It may be possible to harness the air flow to create air currents through adjacent rooms using the Venturi effect.

7.4 Conclusions

The performance of both forced and buoyant convection systems were analysed. The optimum dimensions for power output for each flow mode was established in Chapter 6. For forced convection the optimum dimensions were 0.5m long, 0.1m wide and 0.03m deep on a vertical façade. 3305 ducts would be required to cover a 200m^2 façade area. For buoyant convection the optimum dimensions were 12.5m long, 0.1m wide and 1m deep at a tilt angle of 60^o. 145 ducts would be required to cover the façade area.

By comparing Figure 7.2 and Figure 7.5 it can be seen that slightly higher air exit temperatures are achieved through the buoyant convection system than through the forced convection system. However, the temperature must be considered with regard to the air flow through the ducts. An average flow of 0.08 kg s^{-1} is passed through each duct of the buoyant convection system (providing 11.9 kg s^{-1} in total). A constant flow of 0.01 kg s^{-1} is passed through each duct of the forced convection system (e.g. 33 kg s^{-1} in total). This illustrates that each duct of the buoyant convection system generates higher air temperatures and flows than each duct of the forced convection system. However, the buoyant convection system generates a smaller air mass flow over the entire façade area.

The systems have been assessed in terms of the calendar heating season, rather than periods centred on the solar equinoxes. This means that the spring average solar angle is different from the autumn average solar angle. In addition, real weather data has been used [1]. Therefore it is not surprising that the performance of each system varies slightly between spring and autumn. The vertical forced convection system experienced slightly higher energy output in autumn than in spring. However, the buoyant system has a tilt angle of 60^o and experiences a slightly higher energy output in spring than in autumn.

The buoyant convection system would potentially have a lower installation cost since fans would not be required for air movement. The buoyancy could be used as part of the control – there would not be enough solar irradiation to cause air movement unless there was enough solar irradiation to heat the air. However, building occupants may find the variation in air flow to be a disadvantage in comparison to the forced convection system.

A further disadvantage of the buoyant convection system would be the seasonal distribution of energy output. The buoyant convection system only produces 17.3 % of its power in the winter months (compared to 25.4 % for a forced convection system).

A further benefit of the forced convection system is the possibility of directing air flow through more than one duct to achieve higher air temperatures when required. This would enable the system to be used for direct ventilation in winter conditions. It would also enable the air temperature to be increased in the summer months, which may be advantageous for water heating.

Both forced and buoyant systems have the capacity to save a significant amount of heating energy over the course of a typical year. The choice between forced and buoyant convection systems should be based on the desired air exit temperature, air mass flow and energy output:

- If high air exit temperature is required, and variation in air flow is not a concern then the buoyant convection system should be used.
- If constant, high levels of air mass flow is required then the forced convection system should be used.

In practical terms, the buoyant system was not tested as a complete system (with an inlet, outlet and distribution system). The extra pressure losses associated with these devices may adversely affect the flows attainable. The forced system on the other hand, can be made more reliable for operation, but at the expense of higher fan powers.

7.5 References

1. Marsh, D.A. *UK - Cardiff Wales Weather Data*. [cited 24th February 2004]; http://www.squ1.com/site.html.

8 Conclusions

In this field, there is a lack of information on the performance of inexpensive, large scale, low efficiency, building integrated solar thermal air heating using cladding in the United Kingdom Climate. Therefore this investigation has investigated the potential of such an installation. This aim was to be met by achieving several objectives:

- Carrying out a literature survey on solar air heaters, particularly in relation to predicting and optimising their performance.
- Build full size laboratory prototypes to evaluate the flow characteristics of the system.
- Build full size prototype solar air heaters and test outdoors to evaluate the heat transfer characteristics of the system and provide real life data on solar potential in a UK climate.
- Develop a numerical design model for forced and buoyant air flow in solar air heaters.
- Using the design models in conjunction with a factorial analysis to optimise the air heater geometry for forced and buoyant convection.
- Using the design model to predict the annual output of an optimised system in Cardiff weather conditions.

These individual objectives have been met, and are discussed below.

8.1 Summary of Steps

8.1.1 Literature Survey

The literature survey identified areas to be addressed. These included:

- the development of aesthetic solar thermal collectors which architects could easily integrate with buildings.
- the selection of the most appropriate method of improving the efficiency of a solar air heating duct
- the selection of the most appropriate design model for forced and buoyant convection

Three aspects were considered under aesthetics. Although implementing an inexpensive system over a large area answered one aspect. Development of low reflectance, light coloured paint would be required to meet the variety of colours requested, and the preference for matt surfaces was not practical to incorporate in a glazed collector.

There was general agreement in the literature survey that the most cost effective method of improving the efficiency of a solar air system was by optimising the geometry. A conflict between improved heat transfer and reduced air pumping power was identified. This could be resolved by considering the optimum geometry for net power output (i.e. the total power output minus the pumping power).

A design model would be required to optimise the geometry of such a system. Five potential design models were found in the literature. Three of the models were intended for forced convection systems, while the other two were intended for buoyant convection systems. None of the models incorporated such aspects as the solar angle, and the different behaviour of direct and diffuse irradiation.

Therefore, the basic design of the solar air collector (i.e. black Armacor Colorcoat® covered with float glass to form a duct) was established. Further to this, a programme of work to optimise the geometry was devised. In addition, an experiment to explore the effect of changing the colour of the absorbing surface was included.

8.1.2 Laboratory Prototype Experiments – Flow Characteristics

The pressure drop along the length of a duct is predicted using the Darcy-Weisbach equation in conjunction with the friction factor. However, three different definitions of the friction factor were found in the literature. To establish the most appropriate calculation of the pressure drop, the predicted results had to be compared to measured results.

Prototype ducts based on profiled sheet with a glass cover were constructed so that they could be tested under varying forced flows. Four prototype geometries were considered. All four ducts were 2.4m long. The width varied between 0.1 and 0.15

m, while the depth varied between 0.034 and 0.063 m. The prototypes were tested under varying forced flows.

From the comparison of the predicted and measured values, the ASHRAE friction factor with an adjusted hydraulic diameter (increased by 9.75 %) was found to give the most accurate prediction of the pressure drop. This improved model was embedded in the calculations for the air pumping power and used in further calculations.

8.1.3 Outdoor Prototype Experiments – Heat Characteristics

An outdoor rig was constructed to allow analysis of the heat characteristics of the solar air heater, as well as establish empirical evidence of its performance. Four geometries of solar duct were assembled in a vertical array facing 7^{o} east of solar south. The ducts were 2.4m long, although only 1.9m of the length was exposed to solar irradiation. The width varied between 0.101 and 0.208m, while the depth varied between 0.04 and 0.11m. The prototypes were tested in real weather conditions in Port Talbot, South Wales, over a nine month period.

Empirical data found that in winter conditions the solar duct could produce 1300 - 1650 Wh m^{-2} day^{-1}. The efficiency of the solar ducts (compared against vertical global solar irradiation) was between 35 and 39 %. In summer conditions the prototypes produced 1150 - 1600 Wh m^{-2} day^{-1}. The efficiency of the solar ducts was between 28 and 38 %. This showed:

- there is a good potential power output
- winter low sun angle performance is as good as summer high solar performance.

In a test where air flow through the solar duct was prevented in summer sunny weather, stagnant conditions were created and the material temperatures rose significantly (the solar absorber temperature rose to $65^{o}C$). However, the temperature increase did not occur to an extent that could damage the components of the solar duct.

Comparison of the instantaneous input and output of the prototypes was used to establish that thermal mass was not an issue in this system and need not be considered further.

The results of this experiment were used to evaluate a descriptive model which demonstrated that the system had been fully understood. The model was found to be effective (± 5%) within the bands of error attributed to the limitations of the equipment and the site (± 15%), when it was operating as expected. This indicated that the thermal physics were understood. The model could not be used as a design model since it required information not available at the design stage; however, it indicated aspects which should or need not be incorporated in a design model.

8.1.4 Develop Simple Design Model

Three models from the literature (Ong_{fc}, Yeh_{fc} and Ho_{fc}) were compared against the prototype results to establish the most accurate model for forced convection. No one model was found to give an adequate prediction for all parameters concerned. The parameters of most concern were the air exit temperature and the power output since they were required for future calculations. However, the models did not give an accurate prediction (power output: Ong_{fc} ± 43%, Yeh_{fc} ± 112%, Ho_{fc} ± 91%). A comparison of the design models from the literature and the previously developed descriptive model was used to suggest aspects to include in the design models. These included:

- Using the hydraulic diameter for rectangular ducts in place of the hydraulic diameter for parallel plates,
- Using the HTB2 algorithm to predict the sky temperature,
- Using temperature dependent values for air dynamic viscosity, air thermal conductivity and air specific heat capacity,
- Using a Nusselt number which is appropriate for entry length conditions,
- Incorporating the different behaviour of direct and diffuse solar irradiation in the model, particularly in respect to their dependence on the angle of incidence.

The design models were adapted to include these aspects where possible. This alteration resulted in a closer prediction for the Ho model (power output: ± 57%). It was noted that the Ong and Ho adapted models tended to have the opposite bias to the original models. Therefore, averages of the original and adapted models were considered. The average of the original and adapted versions of the Ho model ($Ho_{fc\&fcad}$) was found to give the closest prediction of the power output (power output: ± 35%), with a tendency to underestimate the power output. The $Ho_{fc\&fcad}$ model is used to calculate the air exit temperature, which in turn is used to calculate the power output. The acceptable error for predicted power output (± 10%) was based on the likely tolerance of model users to inaccuracy of the model. However, this level of accuracy was not achieved over the range of geometries and seasons. In particular the model was found to be insensitive to variations in the duct depth and oversensitive to variations in the duct width when compared to the measured data.

If the closest design model can only predict the power output within 35%, it is not very useful, and needs further development. However, for the purposes of this investigation, the model identified as the closest predictor for power output ($Ho_{fc\&fcad}$) will be used for further calculations.

Two design models from the literature were found for buoyant convection. One of these was a variant on a model previously considered for forced convection. The remaining two design models for forced convection were also adapted to accommodate buoyant convection. In addition a simple model was developed to consider buoyant convection. Therefore, five models were considered for predicting buoyant convection. No one model was found to give an adequate prediction for all parameters concerned. The $Brinkworth_{bc}$ model was found to give the closest prediction of the mean air and exit air temperatures measured from the outdoor experiment (exit air temperature: ± 9%). The acceptable error for predicted exit air temperature (± 5%) was based on the likely tolerance of model users to inaccuracy of the model. However, this level of accuracy was not achieved over the range of geometries. Due to experimental restrictions, this model could not be tested against the air mass flow. However, the relationship between air mass flow and air

temperature is so interlinked that it was believed that a model which achieved a close estimate of the temperature would make a reasonable estimate of the air mass flow.

8.1.5 Solar Duct Optimisation

The effect of varying the façade colour was considered in terms of the reflectivity of the solar absorbing material. The reflectivity of a black solar absorbing material was measured and compared to that of a silver coloured solar absorbing material. The reflectivity was found to increase from 0.08 to 0.38. The design models identified in Chapter 5 for forced and buoyant convection were used to evaluate the impact of varying the reflectivity between 0.05 and 0.4 while using the meteorological data measured between 08:00 and 20:00 on the 05/05/06. The power output was found to drop by 35% for forced convection and by 40% for buoyant convection.

The duct dimensions were optimised using a factorial analysis based on the designs identified in Chapter 5. The factorial design enables variations in geometry to be assessed within identified limits. The dimension limits were chosen with regard to practical constraints.

Forced convection was modelled using the $Ho_{fc\&fcad}$ model, which can only predict the power output to an accuracy of 35%, and is known to be insensitive to changes in duct depth. Where possible these limitations of the $Ho_{fc\&fcad}$ model were mitigated by referring to the results of the empirical experiment in Chapter 4.

It was found that the optimum geometry for the highest air exit temperature was maximum length and width. Increasing depth between 0.04 and 0.11m has been found to be beneficial, but cannot be predicted beyond this level. The system is only sensitive to the tilt angle in June where a 40^o angle is preferred.

The optimum geometry for the net power output over a $10m^2$ façade area was minimum length and width. Increasing depth between 0.04 and 0.11m has been found to be beneficial, but cannot be predicted beyond this level. The system is only sensitive to the tilt angle in June where a 40^o angle is preferred. The optimum geometry for net power output over a $10m^2$ façade area was found to be heavily

influenced by the optimum geometry for air mass flow. A $10m^2$ façade area could include 165 short (0.5m), narrow (0.1m) ducts each passing 0.01 kg s^{-1}, supporting a total air mass flow of 1.65 kg s^{-1}. The same area could only include one long (9.9m), wide (1m) duct passing a total flow of 0.01 kg s^{-1}. The maximisation of air flow is far more significant to the net power output than the maximisation of air temperature. This reduces the effect of the $Ho_{fc\&fcad}$ model limitations on the calculation of the geometry for the optimum power output.

The optimum geometry for air exit temperature agrees partially with the optimum geometry for net power output. Both parameters are insensitive to tilt angle in the heating season, and can be kept vertical. The empirical data indicates that increasing the duct depth from 0.04 to 0.11m is beneficial to both air exit temperature and power output. However, the optimum geometry for air exit temperature also partially conflicts with the optimum geometry for net power output. So a compromise is required. This can be established by deciding the intended application of the system at the design stage (i.e. direct or indirect ventilation). Alternatively the ducts can be manufactured to meet the optimal dimensions for maximum net power output, but connected to allow air to pass through more than one duct when higher air temperatures are required.

Buoyant convection was modelled using the $Brinkworth_{bc}$ model. The accuracy of this model in predicting power output could not be calculated. However, it is known that it slightly underestimates the air exit temperature and as a result is likely to slightly underestimate the air mass flow and so the power output. Where possible, these limitations were mitigated by referring to the results of the empirical experiment in Chapter 4. The optimum geometry for highest air exit temperature is in reasonable accord with the optimum geometry for highest power output over a $10m^2$ façade area – both parameters require minimum width and maximum depth. The power output has no preference to length, allowing longer ducts to be used to accommodate higher air exit temperatures. The optimum tilt angle agrees for both parameters, but varies depending on the season. A compromise of 60^o has been assumed. The response to variations in geometry is gradual (i.e. small changes in input do not have large effects).

Although optimum dimensions have been identified, small variations from this would not be critical. Further work would be required to fully verify the optimisation recommendations for forced and buoyant convection. However, working on the general trends which have been found, there are clear differences in the optimal dimensions for different parameters, seasons and between forced and buoyant convection. This should be resolved by making a decision on the intended application of the system before design (i.e. direct or indirect ventilation).

8.1.6 Application of Solar duct

The duct geometries for both forced and buoyant convection systems optimised for power output were used in conjunction with average Cardiff weather conditions to calculate the air exit temperature, air mass flow and output power of a 200 m^2 south facing façade area. The energy output was disregarded when the ambient temperature was above 18 ^oC because heating was unlikely to be required at those times.

For forced convection, the annual output (worst case scenario) was calculated assuming an air mass flow of 0.01 kg s-1 per solar duct. The solar façade was specified to generate 33 kg s^{-1} of heated air, with a total (net of fan power) energy output of 75,704 kWh. The cost saving for displaced electricity would be £7,661 per year (£38 per m^2 per annum); while the cost saving for displaced gas would be £1,887 per year (£9 per m^2 per annum).

For buoyant convection, the annual output (worst case scenario) was calculated to be 131,947 kWh at an average air mass flow of 11.9 kg s^{-1} through the façade. The cost saving for displaced electricity would be £13,383 (£67 per m^2 per annum). The cost saving of displaced gas would be £3,288 (£16 per m^2 per annum).

24.9% (forced) and 28.2% (buoyant) of the energy produced by solar heating systems is produced in summer when space heating is not a strong requirement. However, the heated air may be useful in preheating water, adding to the savings identified above.

Both the forced and buoyant convection systems have the capacity to save a significant amount of heating energy over the course of a typical year. The extra

materials used to make a solar air façade would cost between £32 and £45 per m^2 (largely attributable to the cost of the glazing). Based on an application on a south facing façade, if the solar heated air replaced electrically heated air, the cost of the materials could be repaid within 14 months for the forced convection system or 8 months for the buoyant convection system. If gas heated air was replaced, the repayment time would extend to 60 months for the forced convection system or 34 months for the buoyant convection system.

8.2 Contribution to the Body of Knowledge

8.2.1 Design Model

Design models for forced and buoyant convection in a solar duct have been developed. These models have incorporated the air flow and air heating aspects of a solar duct.

The pressure drop across the length of a solar duct has been analysed, and found to correlate well with standard engineering equations with a slight modification to the hydraulic diameter. This part of the model is critical to the calculation of pumping power for forced convection and the air mass flow for buoyant convection.

The descriptive model developed in Chapter 4 was able to identify that thermal mass was not an issue which needed to be addressed within a design model. Design models identified from the literature (three for forced convection and two for buoyant convection) were assessed against empirical data. The Ho model for forced convection was developed to obtain a closer correlation with the data from the outdoor prototype. The Brinkworth model for buoyant convection was found to have the closest correlation with the data from the outdoor prototype. Neither model was found to be as accurate as had been hoped. In particular the forced convection model was identified as being insensitive to changes in depth, slightly oversensitive to changes in width and only capable of predicting the power output to an accuracy of 35%. This model would need further development to be useful. This development should concentrate on the effect of internal shading within the duct related to the solar

incident angle. A more detailed model may be able to inform the design of the duct profile.

8.2.2 Solar Duct Optimisation

Utilising a more reflective coating on the absorber surface to achieve a more aesthetic appearance was found to reduce the predicted power output by 35% for forced convection and by 40% for buoyant convection. This indicates that the development of different coloured low reflectivity coatings may be needed.

The optimal geometry of solar duct for forced and buoyant convection was investigated. Although the results could only be regarded as indicative, clear differences in the optimal dimensions for different parameters, seasons and between forced and buoyant convection were identified. In summary, the optimum geometry for each output is listed below:

- Forced convection
  - highest air exit temperature – 12.5 m long, 1 m wide, 0.03 m deep
  - highest air mass flow over façade area – 0.5 m long, 0.1 m wide
  - highest net power output over façade area – 0.5 m long, 0.1 m wide, 0.03 m deep
- Buoyant convection
  - highest air exit temperature - 12.5 m long, 0.1 m wide, 1 m deep, vertical
  - highest air mass flow over façade area – 12.5 m long, 1 m wide, 1 m deep
  - highest net power output over façade area - 0.1 m wide, 1 m deep, tilt angle 60^{o}.

Where the optimum parameter is not stated (e.g. tilt angle for highest air exit temperature under forced convection), the parameter is not critical for that output.

This established that a hybrid system would not be feasible. The intended application of the system (i.e. direct or indirect ventilation) should be established before the design stage.

8.2.3 Effect of Solar Duct Geometry on Power Output (Normalised Area)

The effect of varying duct width and depth were evaluated in the field tests. Varying width was found to have little effect on the power output over a normalised area. However, increasing the duct depth was found to increase the power output.

8.2.4 Winter Use

The field tests indicated that there could be a higher power output from a solar duct on a sunny winter day than on a sunny summer day. Prediction of the behaviour of the optimised forced and buoyant solar ducts indicates that they will produce approximately 17-22% of their useful energy during typical winter weather conditions. Both these findings contradict the layman's view that solar energy in UK winter climate conditions is not useful.

8.2.5 Develop Design for Useful Product

The geometry optimised for power output over a façade area was analysed for both forced and buoyant convection, in a UK climate, based on a 200m^2 façade. Both systems have been found to have significant potential heat saving in a UK climate. A 200m^2 vertical façade consisting of 3305 ducts (0.5m long, 0.1m wide and 0.03m deep) is capable of delivering 75,704 kWh under forced convection. A 200m^2 façade at a tilt angle of 60^o and accommodating 145 ducts (12.5m long, 0.1m wide and 1m deep) is capable of delivering 131,947 kWh under buoyant convection. Although a higher overall energy output is indicated for the buoyant convection solar duct, the forced convection solar duct is more controllable. Both designs may be useful in future buildings.

8.2.6 Cost Savings

The cost savings for the optimised systems were calculated assuming the cost of electricity to be 10.12p kWh and the cost of gas to be 2.492p kWh. The predicted annual cost savings per square meter (allowing for the limitations of the design model) are:

- £38 for a forced convection system displacing electricity (potential payback for material costs ~ 14 months)
- £ 9 for a forced convection system displacing gas (potential payback for material costs ~ 60 months)
- £67 for a buoyant convection system displacing electricity (potential payback for material costs ~ 8 months)
- £16 for a buoyant convection system displacing gas (potential payback for material costs ~ 34 months).

8.2.7 Learning Points

1. An attempt was made to develop a sheath to protect the thermocouple from the effects of direct solar irradiation. The sheath consisted of copper tubing painted with a heat reflecting aluminium paint. The tube was attached to the main solar duct via a 1.5 cm thermal break of plastic tubing. However, the sheath was not capable of protecting the thermocouple from solar irradiation.
2. Prototypes should be protected from solar irradiation on all surfaces apart from the one that is expected to receive solar irradiation in real life.
3. Care should be taken in selecting sites for field testing of solar prototypes. Issues which should be assessed are:
   - shadows from distant obstructions (e.g. hills, large buildings)
   - reflections from distant bodies of water
   - ability to establish orientation when sited under electricity transmission wires / pylons.
   - the difficulties of keeping thermocouples intact when sited in an area occupied by feral cats.
4. Constant vigilance is required to identify when thermocouples have broken or are degenerating.
5. Items to be used in outdoor experiments should not be manufactured from mild steel.

8.3 Future Work

The design models developed by Ong, Yeh, Ho and Brinkworth should be re-evaluated in terms of their sensitivity to depth. The lack of sensitivity to depth is

likely to be caused by shadows within the duct. The areas cast into shadow during the day are larger for deep ducts than for shallow ones. Although the area of shadow could be calculated, a method to estimate the temperature of the shaded area has not been found at this time.

Appendix A – Models Describing Solar Air Heating Systems

The interest in solar air heating systems has led to the development of several mathematical models to describe them. Labelling has been changed from the original papers to allow consistency throughout the report.

The majority of models considered the duct as two parallel plates, with one surface experiencing uniform heat flux, while the other surface is adiabatic. This closely matches the theoretical situation for which Nusselt numbers have been developed. However, radiative transfer from the absorbing surface causes the temperature of the insulated surface to increase (no longer adiabatic). This is considered to be a minor discrepancy.

A1 Ong [1]

Ong indicated the heat transfers occurring between two parallel plates and derived a thermal network from this (Figure A.1).

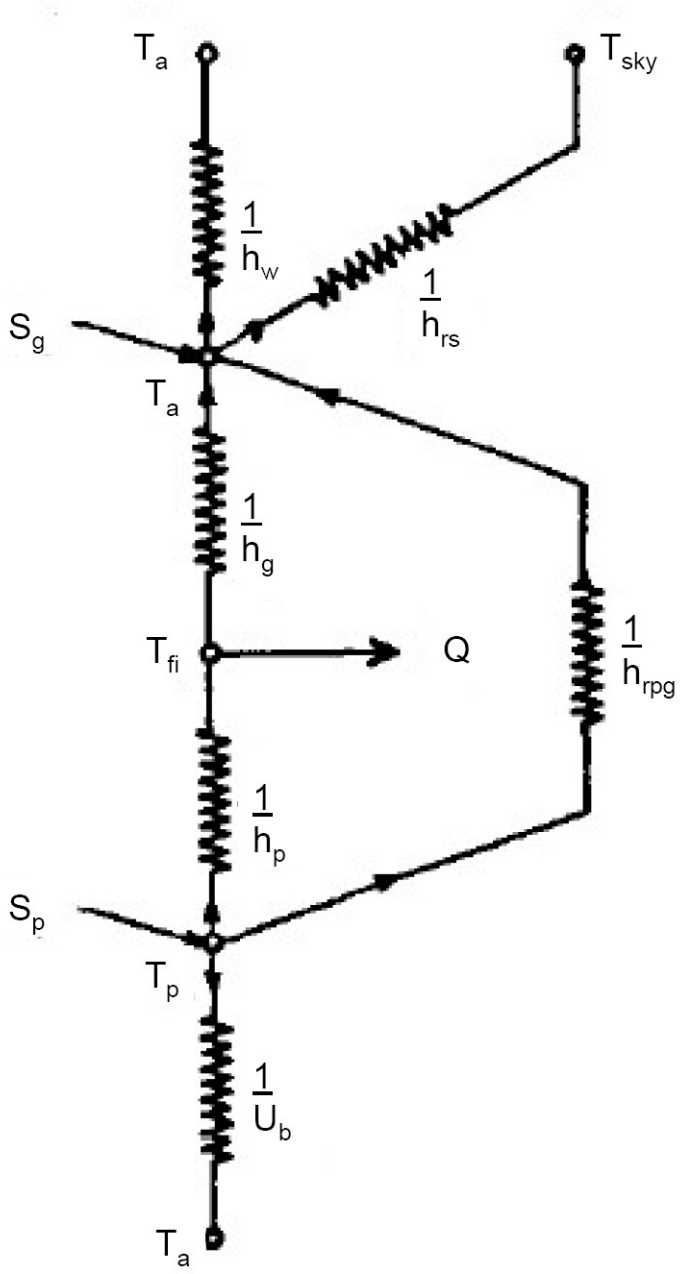

Figure A.1. Representation of the thermal network for a solar air collector [1]

The heat balance equations at the points T_g, T_f and T_p are described below [1]:

T_g: $$S_g + h_{rpg}\left(T_p - T_g\right) + h_g\left(\overline{T}_f - T_g\right) = U_t\left(T_g - T_{amb}\right) \qquad \text{A1}$$

Where:

S_g solar radiation absorbed by the glass (W m^{-2})

h_{rpg} heat transfer coefficient between the absorbing plate and the glass

h_g heat transfer coefficient between the air and the glass

U_t heat loss coefficient from the top surface

T_p temperature of the absorbing plate

T_g temperature of the glass

T_{amb} ambient temperature

$\overline{T}_f$ mean air temperature

T_f: $$h_p\left(T_p - \overline{T}_f\right) = h_g\left(\overline{T}_f - T_g\right) + q \qquad \text{A2}$$

Where:

h_p heat transfer coefficient between the air and the absorbing plate

q heat transferred to air stream (W m^{-2})

T_p: $$S_p = h_p\left(T_p - \overline{T}_f\right) + h_{rpg}\left(T_p - T_g\right) + U_b\left(T_p - T_{amb}\right) \qquad \text{A3}$$

Where:

S_p solar radiation absorbed by the absorbing surface (W m^{-2})

U_b heat loss coefficient from the bottom surface

Considering the useful heat loss to the air as [1]:

$$q = \Gamma\left(\overline{T}_f - T_{f,i}\right) \qquad \text{A4}$$

Where:

T_{fi} air inlet temperature

$$\Gamma = \frac{2\dot{m}c_p}{WL} \qquad \text{A5}$$

and re-arranging the equations so that all terms relating to T_g, T_{f1} and T_p are grouped.

The equations become [1]:

T_g: $$\left(h_g + h_{rpg} + U_t\right)T_g - h_g T_f - h_{rpg} T_p = S_g + U_t T_{amb} \quad \text{A6}$$

T_{f1}: $$h_g T_g - \left(h_g + h_p + \Gamma\right)T_f + h_p T_p = -\Gamma T_f \quad \text{A7}$$

T_p: $$-h_{rpg} T_g - h_p T_f + \left(h_p + h_{rpg} + U_b\right)T_p = S_p + U_b T_{amb} \quad \text{A8}$$

which can be represented as matrices [1]:

$$\begin{bmatrix} h_g + h_{rpg} + U_t & -h_g & -h^*_{rpg} \\ h_g & -\left(h_g + h_p + \Gamma\right) & h_p \\ -h_{rpg} & -h_p & h_p + h_{rpg} + U_b \end{bmatrix} \begin{bmatrix} T_g \\ T_f \\ T_p \end{bmatrix} = \begin{bmatrix} U_t T_{amb} + S_g \\ -\Gamma T_{f,i} \\ S_p + U_b T_{amb} \end{bmatrix} \quad \text{A9}$$

* although Ong's 1995 paper [1] shows this as a positive cell, he corrects it in his 2003 paper [2].

If these are considered in the form [1]:

$$[A][T] = [B] \quad \text{A10}$$

The mean temperature can be determined by matrix inversion:

$$[T] = [A]^{-1}[B] \quad \text{A11}$$

Assumptions such as the linearity of the fluid temperature gradient are only valid for short ducts. A long collector can be analysed as a series of ducts less than 1 m long. Initial guesses are made for the wall and mean fluid temperatures. The ambient air temperature is used for the input fluid temperature, and the heat transfer coefficients are evaluated and inserted into the matrix. Calculating the mean temperature by matrix inversion provides a closer estimate of the temperatures. The heat transfer coefficients are recalculated for these new estimates, and the procedure is repeated until the consecutive mean temperatures differ by less than 0.01 ^oC.

The definitions of the terms $\overline{T}_f$ h_g, h_p, h_{rpg}, U_t, U_b, S_g and S_p are below:

$$\overline{T}_f = \frac{\left(T_{fi} + T_{fo}\right)}{2} \quad \text{A12}$$

The convective heat transfer coefficient for each surface is assumed to be equal (i.e. $h_g = h_p$). They are given by:

$$h_g = h_p = \frac{kNu}{D_h} \quad \text{C2}$$

Where

D_h hydraulic diameter (m) = 2b (b = duct depth) B4

Nu Nusselt number which is defined depending on flow conditions:

$$Nu = 0.036\,\mathrm{Re}^{0.8}\,\mathrm{Pr}^{1/3}\left(\frac{D_h}{L}\right)^{0.055}$$ for forced convection C5

$$Nu = 0.68 + \frac{0.67Ra^{1/4}}{\left[1+\left(\frac{0.492}{\mathrm{Pr}}\right)^{9/16}\right]^{4/9}}$$ for laminar buoyant convection C16

Or

$$Nu = \left\{0.825 + \frac{0.387Ra^{1/6}}{\left[1+\left(\frac{0.492}{\mathrm{Pr}}\right)^{9/16}\right]^{8/27}}\right\}^2$$ for turbulent buoyant convection C17

Where the Reynolds number (Re), Rayleigh number (Ra) and Prandtl number (Pr) are described in Appendix B.

The radiative heat transfer coefficient between the plates (h_{rpg}) is given by:

$$h_{rpg} = \frac{\sigma\left(T_p^2 + T_g^2\right)\left(T_p + T_g\right)}{\frac{1}{\varepsilon_p} + \frac{1}{\varepsilon_g} - 1}$$ C28

Where:

σ Stefan Boltzmann Constant (5.67 E-8 W m^{-2} K^{-4})

ε_p emissivity of solar absorbing plate

ε_g emissivity of glass

The heat loss from the top surface is given by:

$$U_t = h_w + h_{rs}$$ A13

Where:

h_w wind convection heat transfer coefficient $h_w = 5.7 + 3.8v$ C20

h_{rs} coefficient of heat transfer between the glass and the sky

$$h_{rs} = \frac{\sigma\varepsilon_g\left(T_g + T_s\right)\left(T_g^2 + T_s^2\right)\left(T_g - T_s\right)}{\left(T_g - T_{amb}\right)}$$ C30

Where the sky temperature (T_s) is defined by $T_s = 0.0552 T_{amb}^{1.5}$ C31

The heat loss from the bottom surface is given by:

$$U_b = \frac{1}{i = \sum_{1}^{n} \frac{d_{bi}}{k_{bi}} + \frac{1}{h_w}} \quad \text{A14}$$

Where:

i number of layers the heat travels through

d_{bi} thickness of each layer on the bottom surface (m)

k_{bi} thermal conductivity of each layer on the bottom surface (W m^{-1} K^{-1})

Solar radiation absorbed by the glass surface is given by:

$$S_g = \alpha_g E \quad \text{A15}$$

Where:

α_g absorptivity of glass

E solar irradiation (W m^{-2})

Solar radiation absorbed by the absorbing plate is given by:

$$S_p = \tau_g \alpha_p E \quad \text{A16}$$

Where:

τ_g transmissivity of glass

α_p absorptivity of absorbing surface

Ong did not include any validation of his matrix inversion model against experimental data when he wrote the paper. However, he did use experimental data which had been reported by Hirunlabh et al [3] to validate his model for a solar chimney in a later paper [2].

Ong utilised a similar procedure to calculate the behaviour of a solar air heater under buoyant convection [2]. In this instance he assumed that the mean air temperature could be calculated from:

$$\overline{T}_f = \gamma T_{fo} + (1 - \gamma) T_{fi} \quad \text{A17}$$

where $\gamma = 0.75$.

A2 Yeh & Lin [4]

Yeh used the Hottel-Whillier-Bliss (efficiency) equation as the basis of his calculations:

$$\eta = F_R\left(\alpha_p \tau_g - U_L\left(T'_{fi} - T'_{amb}\right)/E'\right) \qquad \text{C36}$$

Where:

η efficiency

$$F_R = \frac{\dot{m}' c_p}{A_{sur} U_L}\left\{1 - \exp\left[-\frac{U_L F' A_{sur}}{\dot{m}' c_p'}\right]\right\} \qquad \text{C37}$$

U_L loss coefficient from the top surface

E’ solar irradiation (kJ m^{-2} h^{-1})

$\dot{m}'$ air mass flow (kg h^{-1})

c_p’ specific heat capacity (kJ kg^{-1} K^{-1})

$$F' = \left(1 + \frac{U_L}{h_g} + \left[\frac{1}{h_g} + \frac{1}{h_{rpg}}\right]^{-1}\right)^{-1} \qquad \text{C38}$$

When considering heat loss from the bottom of the collector (U_b), he assumes the only losses are through conduction [4]:

$$U_b = \frac{k'}{d} \qquad \text{A18}$$

Where:

k’ thermal conductivity (kJ h^{-1} m^{-1} K^{-1})

For heat loss from the top of the collector he uses Klein’s [5] empirical equation [4]:

$$U_t = \left\{\frac{\frac{\overline{T}'_p}{520}}{\left[\frac{T'_p - T'_{amb}}{1 + \left(1 + 0.089h_w - 0.1166h_w\varepsilon_p\right)\left(1 + 0.07866\right)}\right]^{0.43\left(1 - \frac{100}{T'_p}\right)}} + \frac{1}{h_w}\right\}^{-1} + \frac{\sigma'\left(\overline{T}'_p + T'_{amb}\right)\left(\overline{T}'^2_p + \overline{T}'^2_{amb}\right)}{\frac{1}{\varepsilon_p + 0.00591h_w} + \frac{2 + \left(1 + 0.089h_w - 0.1166h_w\varepsilon_p\right)\left(1 + 0.07866\right) - 1 + 0.133\varepsilon_p}{\varepsilon_g - 1}} \qquad \text{A19}$$

Where:

h_w wind convection heat transfer coefficient $h_w = 4.9 + 3.27v$ C23

The radiative heat transfer coefficient between two plates (h_{rpg}) is given by:

$$h_{rpg} \approx \frac{4\sigma' T'^3_f}{\frac{1}{\varepsilon_p} + \frac{1}{\varepsilon_g} - 1} \qquad \text{C29}$$

The collector geometry (L, W, b), system properties (τ, α, c_p, ρ, μ', k'_{air}, k'_{ins}, d_{ins}, ε_g, ε_p, ε_b) and operating conditions (E', T'_{amb}, v', $\dot{m}'$, T'_{fi}) with assumed mean fluid and mean plate temperatures are used to make the calculations leading up to the initial efficiency calculation. These values can be input to:

$$\bar{T}'_f = T'_{fi} + \frac{\eta E'}{U_L F_R}\left(1 - \frac{F_R}{F'}\right) \qquad \text{A20}$$

and

$$\bar{T}'_p = T'_{f,i} + \frac{\eta E'}{U_L F_R}\left(1 - F_R\right) \qquad \text{A21}$$

to obtain values for the mean fluid and mean plate temperatures. The procedure is repeated until the variance between iterations is excluded from the temperatures, and the final efficiency can be calculated. This analysis technique has been validated against a physical experiment, where it was found to give a better correlation for lower air mass flow rates. The technique was analysed for mass flow rates of 0.0107, 0.0161 and 0.0214 kg s^{-1}.

Care should be taken when utilising Yeh & Lin's model that the correct units are used.

A3 Ho and Loveday [6]

Like Ong [1], Ho and Loveday carried out an energy balance at the top surface, at the fluid and at the bottom surface. These energy balances differed from Ong's since Ho and Loveday have assumed that the top surface does not absorb any solar irradiation. Ho and Loveday's equations also include the factor K to compensate for the area difference caused by the profile of the absorber surface. Instead of arranging the energy balance equations to be solved by the matrix inversion technique; Ho and Loveday

rearrange them to be solved explicitly. The equation for the fluid temperature is solved by integrating it with the boundary conditions $T_f = T_{fi}$ when y = 0 (i.e. at the inlet) and $T_f = T_{fo}$ when y = L (i.e. at the outlet). This gives:

$$T_{fo} = \left(\frac{P_6}{P_5} + T_{fi} \right) \exp(P_7) - \frac{P_6}{P_5} \qquad \text{A22}$$

where

$$P_7 = \frac{P_5 WL}{\dot{m} c_p} \qquad \text{A23}$$

$$P_6 = \frac{U_{t\&e}}{U_{t\&e} + h_g Kh_{rpg}} \left(P_4 h_g - \frac{Kh_p}{P_1} \right) T_{amb\,f} - \frac{U_b P_2}{P_1} T_{amb\,r} - \frac{P_2}{P_1} E(\tau\alpha)_e \qquad \text{A24}$$

Where:

$U_{t\&e}$ heat loss coefficient from the front and edges of the collector

$T_{amb\,f}$ ambient temperature at front of collector

$T_{amb\,r}$ ambient temperature at rear of collector

$(\tau\alpha)_e$ effective transmittance-absorptance product

$$P_5 = h_g \left(\frac{P_3}{U_t' + h_g + Kh_{rpg}} - 1 \right) - Kh_p \left(\frac{P_2}{P_1} + 1 \right) \qquad \text{A25}$$

$$P_4 = 1 - \frac{Kh_{rpg}}{P_1 (U_{t\&e} + h_g + Kh_{rpg})} \qquad \text{A26}$$

$$P_3 = h_g - \frac{Kh_{rpg} P_2}{P_1} \qquad \text{A27}$$

$$P_2 = \frac{h_g}{U_{t\&e} + h_g + Kh_{rpg}} + \frac{h_p}{h_{rpg}} \qquad \text{A28}$$

$$P_1 = \frac{Kh_{rpg}}{U_{tYe} + h_g Kh_{rpg}} - \frac{h_p}{h_{rpg}} - 1 - \frac{U_b}{Kh_{rpg}} \qquad \text{A29}$$

$$U_{t\&e} = U_t + \frac{2U_e A_e}{LW} \qquad \text{A30}$$

Where:

U_e heat loss coefficient from the edges of the collector

The mean fluid temperature can then be derived as:

$$\bar{T}_f = \frac{\dot{m}c_p}{2P_5WL}\left(\frac{P_6}{P_5}+T_{fi}\right)\left[\exp\left(\frac{P_5WL}{\dot{m}c_p}\right)-1\right]+\frac{1}{2}\left(T_i-\frac{P_6}{P_5}\right) \qquad \text{A31}$$

with other surface temperatures being derived as:

$$T_g = \frac{U_bT_a}{P_1\left(U_{t\&e}+h_g+Kh_{rpg}\right)}+\left\{\frac{h_g}{U_{t\&e}+h_g+Kh_{rpg}}-Kh_{rpg}\frac{\left[\dfrac{h_g}{U_{t\&e}+h_g+Kh_{rpg}}+\dfrac{h_p}{h_{rpg}}\right]}{P_1\left(U_{t\&e}+h_g+Kh_{rpg}\right)}\right\}T_f$$

$$+\left\{\frac{U_{t\&e}}{U_{t\&e}+h_g+Kh_{rpg}}-\frac{Kh_{rpg}U_{t\&e}}{P_1\left(U_{t\&e}+h_g+Kh_{rpg}\right)^2}\right\}T_a-\frac{1}{P_1\left(U_{t\&e}+h_g+Kh_{rpg}\right)}E(\tau\alpha)_e \qquad \text{A32}$$

and

$$T_p = -\frac{U_b}{Kh_{rpg}P_1}T_a-\frac{U_{t\&e}}{\left(U_{t\&e}+h_g+Kh_{rpg}\right)P_1}T_a-\frac{1}{P_1}\left[\frac{h_2}{U_{t\&e}+h_g+Kh_{rpg}}+\frac{h_p}{h_{rpg}}\right]T_f$$

$$-\frac{1}{Kh_{rpg}P_1}E(\tau\alpha)_e \qquad \text{A33}$$

It is assumed that the convection heat coefficient for the inner cover surface is the same as that for the absorber surface:

i.e. $h_g = h_p = \dfrac{kNu}{D_h}$ C2

where

$Nu = 0.0158\,\mathrm{Re}^{0.8}$ C12

The radiation heat transfer coefficient between the inner cover surface and the absorber surface is given by h_{rgp}:

$$h_{rgp} = \frac{\sigma\left(\left(T_g+273.15\right)^2+\left(T_p+273.15\right)^2\right)\left(T_g+T_p+546.3\right)}{\dfrac{1}{\varepsilon_g}+\dfrac{1}{\varepsilon_p}-1} \qquad \text{C28}$$

The natural convection in the partitions of the polycarbonate is accounted for by:

$$Nu = \left\{ 0.0605 Ra^{1/3}, \left\{ 1 + \left[\frac{0.104 Ra^{0.294}}{1 + \left(\frac{6310}{Ra} \right)^{1.36}} \right]^3 \right\}^{1/3}, 0.242 \left(\frac{Ra}{AR} \right) 0.272 \right\}_{\max} \qquad \text{A34}$$

Where:

AR Aspect Ratio

Ra Rayleigh number (B12)

This model was validated through experimental testing. An advantage of this model over Ong's is that it can handle different ambient temperatures from the front and rear of the collector. N.B. Ho and Loveday's calculations require the temperatures to be expressed in degrees Centigrade.

A4 Guan [7]

The model used by Delahaye et al [8], is described by Guan in his thesis.

Absorbed solar power is described by:

$$S_p = E \tau_g \alpha_p WL \qquad \text{A35}$$

The power transmitted from the heated absorber plate to the flowing air inside the duct is described by:

$$Q_{pf} = h\left(T_p - \overline{T}_f\right) WL \qquad \text{A36}$$

The power radiated from the heated absorber plate to the cover is described by:

$$Q_{pg} = h_{rpg}\left(T_p - T_g\right) WL \qquad \text{A37}$$

The power lost from the heated absorber plate through its insulation to the environment is described by:

$$Q_{pamb} = U_{ins}\left(T_p - T_{amb}\right) WL \qquad \text{A38}$$

The energy balance of the absorber plate can be shown as:

$$Q_p = S_p - Q_{pf} - Q_{pg} - Q_{pamb} \qquad \text{A39}$$

The power absorbed by the absorbing plate can also be shown as:

$$Q_p = c_p m_p \frac{dT_p}{dt} \qquad \text{A40}$$

The last two equations can be considered equivalent:

$$c_p m_p \frac{dT_p}{dt} = S_p - Q_{pf} - Q_{pg} - Q_{p\,amb} \qquad \text{A41}$$

This can be manipulated to form:

$$k_p \frac{dT_p}{dt} = E\tau_g\alpha_p - h\left(T_p - \overline{T}_f\right) - h_{r,pg}\left(T_p - T_g\right) - h_{ins}\left(T_p - T_{amb}\right) \qquad \text{A42}$$

Where

$$k_p = c_p \rho_p d_p \qquad \text{A43}$$

The following assumptions are made

- The front and back of the absorbing plate are the same temperature.
- The front and back of the glass cover are the same temperature.
- The heated layer of insulation in contact with the absorber is the same temperature as the absorber.
- The heated layer of insulation is 1/50 of the total insulation thickness.
- The other surface of the insulation is at ambient temperature
- The rest of the insulation acts as a conductor that transfers heat.

$$Q_{use} = \dot{m}c_p\left(T_{fo} - T_{fi}\right) \qquad \text{A44}$$

$$Q_{loss} = U_{total}WL\left(T_p - T_{amb}\right) \qquad \text{A45}$$

Collector efficiency can be calculated from:

$$\eta = \frac{Q_{use}}{Q_{in}} = \frac{Q_{use}}{EWL} \qquad \text{A46}$$

The hydraulic diameter is calculated from equation B2 unless the width is much greater than the breadth, in which case equation B4 is suitable.

The Reynolds number is calculated from equation B5.

The Prandtl number is calculated from equation B6.

For radiative heat transfer between a body and the ambient environment, Guan uses equation C32.

For convective heat transfer between a body and the ambient environment Guan uses:

$$h_{g\,amb} = \max\left\{5, \frac{8.6v^{0.6}}{\sqrt[3]{B}^{0.4}}\right\} \qquad \text{A47}$$

which is considered to be more representative than McAdams equation C18 at large wind speeds. For radiative heat transfer between the absorber and cover plates, Guan uses equation C25.

For heat transfer between the absorbing plate and the air flow, Guan uses equation C2. Since an automated model is being developed, the duct can be divided into segments and can also represent Nusselt numbers where there is a mix of laminar and turbulent flow (i.e. transitional flow).

The energy equilibrium equations for the collector are:

$$k_g \frac{dT_g}{dt} = h_{rpg}\left(T_p - T_g\right) - h\left(T_g - T_f\right) - \left(h_{rg\,amb} + h_{g-a}\right)\left(T_g - T_a\right) \qquad \text{A48}$$

$$k_g = c_p \rho_g d_g \qquad \text{A49}$$

$$k_p \frac{dT_p}{dt} = E\tau_g\alpha_p - h\left(T_p - T_f\right) - h_{rpg}\left(T_p - T_g\right) - h_{ins}\left(T_p - T_{amb}\right) \qquad \text{A50}$$

$$k_p = c_p \rho_p d_p \qquad \text{A51}$$

thus encompassing the thermal mass of the system. However, the complexity of this model requires it to be operated within a computer package (e.g. Matlab).

A5 Brinkworth et al [9-14]

The work of Brinkworth et al culminated in a joint paper with Sandberg [15] which described his model for buoyantly induced flow in ducts.

The driving forces for air movement are considered to be [15]:

Buoyancy

$$\Delta p_{bu} = \frac{gqsL^2 \sin\phi}{T_{amb} V b c_p} \qquad \text{A52}$$

Where:

g force of acceleration due to gravity (9.8 m s^{-2})

s stratification parameter - assumed to be 0.5

ϕ tilt angle (^{o})

V air velocity (m s^{-1})

Wind

$$\Delta p_w = \left(Cp_{in} - Cp_{out}\right)\frac{\rho v^2}{2} \qquad \text{A53}$$

Where:

Cp pressure coefficient

ρ density of air (kg m^{-3})

While Resistances are considered to be:

Wall friction

$$\Delta p_{fr} = \rho f \frac{L}{D_h}\frac{V^2}{2} \qquad \text{B15}$$

where f is the Darcy-Weisbach friction factor for a smooth walled duct. For most cases of interest to Brinkworth and Sandberg, the flow is turbulent and the following equation is used as long as $L/D_h \geq 20$:

$$f = 0.316\,\mathrm{Re}^{-1/4} \qquad \text{A54}$$

where the Reynolds number is calculated using:

$$\mathrm{Re} = \frac{VD_h}{\nu} \qquad \text{A55}$$

Where:

ν kinematic viscosity (m^2 s^{-1})

Hydraulic Resistance

Other pressure drops can be expressed as [15]:

$$\Delta p_h = \frac{\left(1 + I_{in} + I_{ri} + I_{out}\right)\rho V^2}{2} \qquad \text{A56}$$

Where 1 represents the pressure drop required to accelerate the air from rest to the mean velocity V, and the coefficients I_{in} and I_{out} represent any pressure drops occurring at entry and exit from the duct. If the duct inlet is sharp edged and flush with the wall the value of I_{in} is generally taken to be 0.5, however, this value may be larger for a protruding inlet. I_{ri} represents pressure loss due to obstructions such as structural members crossing the duct.

The basic model has been validated for vertical smooth-walled ducts without obstructions or wind effects for L/D_h between 5 to 30. The correlation still holds (but not as tightly) for L/D_h up to 50 [15]:

$$V^3 = \frac{gqL^2}{T'_{amb}\, b\rho c_p \left[1.5 + \frac{fL}{D_h}\right]} \qquad \text{A57}$$

which is not explicitly solvable (since Re depends on f) but is evaluated by successive approximation. Ignoring the wall friction this equation indicates that $V^{1/3}$ will increase with heat input for a fixed geometry.

Brinkworth et al [10, 11] had previously reported their findings on the heat transfer part of the model. They considered the mean Nusselt number (Nu) in terms of the dimensionless length (L^+):

$$N\bar{u} = 5.35 + \frac{0.07}{L^+} \qquad \text{C18}$$

where

$$L^+ = \left(\frac{48\,\mathrm{Pr}}{Gr}\right)^{0.5} \qquad \text{C19}$$

Where:

Gr Grashof number (B8).

They use the following definition of radiative heat loss from the absorbing plate to the glass cover [10]:

$$q_{rpg} = 4\sigma\left(\frac{\bar{T}_p + \bar{T}_g}{2} + 273.15\right)^3 \left(\frac{\varepsilon_p}{2 - \varepsilon_p}\right)\left(\bar{T}_p - \bar{T}_g\right) \qquad \text{A58}$$

They rewrite the heat transfer between the outer surface and the fluid as [10]:

$$h_{gf}\left(T'_g - T'_f\right) = \frac{h_g U_t}{h_g + U_t}\left[T'_{sol} - T'_f\right] = h_{f\,amb}\left[T'_{sol} - T'_f\right] \qquad \text{A59}$$

where

$$T'_{sol} = \frac{\left(\alpha - \eta\left(T_g\right)\right)E - q_{rpg}}{U_t} + T_{amb} \qquad \text{A60}$$

Where η is the efficiency of PV cladding material, for non PV surfaces (e.g. glass), η=0.

The heat transfer between the inner surface and the fluid is written as [10]:

$$h_p\left(T'_p - T'_f\right) = \frac{h_p U_b}{h_p + U_b}\left[T'_b - T'_f\right] = h_p\left[T'_b - T'_f\right] \qquad \text{A61}$$

where

$$T'_b = \frac{q_{rpg}}{U_b} + T_b \qquad \text{A62}$$

The exit temperature is given by [10]:

$$T'_{fo} = T'_{fi} + \left(1 - e^{-\lambda}\right)\left(\frac{h_g A_g\left(T'_{sol} - T'_{fi}\right) + h_p A_p\left(T'_b - T'_{fi}\right)}{h_g A_g + h_p A_p}\right) \qquad \text{A63}$$

where

$$\lambda = \frac{h_g A_g + h_p A_p}{\dot{m} c_p} \qquad \text{A64}$$

A6 References

1. Ong, K.S., *Thermal performance of solar air heaters: Mathematical model and solution procedure.* Solar Energy, 1995. **55**(2): p. 93-109.
2. Ong, K.S., *A mathematical model of a solar chimney.* Renewable Energy, 2003. **28**: p. 1047-1060.
3. Hirunlabh, J., et al., *Study of natural ventilation of houses by a metallic solar wall under tropical climate.* Renewable Energy, 1999. **18**: p. 109-119.
4. Yeh, H.-M. and T.-T. Lin, *Efficiency Improvement of Flat-Plate Solar Air Heaters.* Energy, 1996. **21**(6): p. 435-443.
5. Klein, S.A., *Calculation of flat-plate collector loss coefficients.* Solar Energy, 1979. **17**(1): p. 79-80.
6. Ho, K.T.K. and D.L. Loveday, *Covered profiled steel cladding as an air heating solar collector: laboratory testing, modelling and validation.* Energy and Buildings, 1997. **26**: p. 293-301.
7. Guan, C.N. *Dynamic Models of Solar Air Collector* 2006: Master of Science in Energy Systems; Department of Applied Sciences at Aachen University.
8. Delahaye, A., et al. *Solar Air Collector - Development and Optimization of Existing Elements for Facades*. in *ISES 2005 Solar World Congress*. 2005. Orlando, Florida, USA: International Solar Energy Society.
9. Brinkworth, B.J., et al., *Thermal regulation of photovoltaic cladding.* Solar Energy, 1997. **61**(3): p. 169-178.

10. Brinkworth, B.J., R.H. Marshall, and Z. Ibarahim, *A Validated Model of Naturally Ventilated PV Cladding.* Solar Energy, 2000. **69**: p. 67-81.
11. Brinkworth, B.J., *A procedure for the routine calculation of laminar free and mixed convection in inclined ducts.* International Journal of Heat and Fluid Flow, 2000. **21**: p. 456-462.
12. Brinkworth, B.J., *Estimation of flow and heat transfer for the design of PV cooling ducts.* Solar Energy, 2000. **69**(5): p. 413-420.
13. Brinkworth, B.J., R.H. Marshall, and Z. Ibarahim, *A Validated Model of Naturally Ventilated PV Cladding*, in *Solar Energy*. 2000. p. 68.
14. Brinkworth, B.J., *Coupling of Convective and Radiative Heat Transfer in PV Cooling Ducts.* Transactions of American Society of Mechanical Engineers: Journal of Solar Energy Engineering, 2002. **124**: p. 250-255.
15. Brinkworth, B.J. and M. Sandberg, *A validated procedure for determining the buoyancy-induced flow in ducts.* Building Services Engineering Research & Technology, 2005. **26**(1): p. 35-48.

Appendix B – Fluid Dynamics

Several of the terms, equations and concepts used in fluid dynamics are explained in this appendix. The concepts include the types of flow which a fluid experiences. The terms include hydraulic diameter (D_h), equivalent diameter (D_e), Reynolds number (Re), Prandtl number (Pr), Grashof number (Gr), Rayleigh number (Ra), entrance length (L_e), pressure drop (Δp), friction factor (f) and fan pumping power (P_{fan}). The relationship between air mass flow and air velocity is also described.

B1 Air Flow Types

Laminar flow is regarded as the smooth and orderly flow of a liquid. This does not entail much mixing and is not beneficial for heat transfer.

Transitional flow describes the situation when orderly laminar flow begins to break up and where eddies begin to develop.

Turbulent flow is a disorderly flow of liquid with apparently random motion superimposed upon the actual flow direction. This flow entails fully developed eddies which causes mixing and entrainment and enhances heat transfer.

B2 Diameter

Many fluid dynamic formulae require a diameter to be input. For round pipes, this would simply be the diameter of the pipe. For non-circular ducts, the hydraulic diameter is used:

$$D_h = \frac{4A_c}{P_w} \qquad [1] \qquad \text{B1}$$

Where:

A_c cross sectional area (m^2)

P_w wetted perimeter (m)

For rectangular ducts, this becomes:

$$D_h = \frac{4Wb}{2(W+b)} \qquad \text{B2}$$

An equivalent diameter has been developed especially for rectangular ducts:

$$D_e = \frac{1.3(Wb)^{0.625}}{(W+b)^{0.25}} \qquad [1] \qquad \text{B3}$$

For the special case of two parallel plates, which is frequently used in fluid dynamics, the hydraulic diameter is:

$$D_h = 2b \qquad [2] \qquad \text{B4}$$

B3 Reynolds number

The Reynolds number (Re) was developed by Reynolds in 1883 to deduce the character of a flow. He found that the behaviour of a fluid can be defined as the ratio of inertia to viscous forces. When Re is very small, viscous forces dominate. Conversely when Re is very large inertia forces dominate. Re is formed from four variables: the dynamic viscosity (μ) and the density (ρ) are physical properties of air which do not usually change value significantly. However, the velocity (V) and the hydraulic diameter (D_h) of a flow may change with location within the flow [3].

Since the transition between laminar and turbulent air flow is a gradual process which passes through a state called ‘transitional’, it is difficult to place an absolute value of the Reynolds number as being laminar, transitional or turbulent, but the following guidelines are considered valid for flow within ducts [1]:

- Where Re<2300 the air flow is considered to be laminar.
- Where 2300<Re<10,000 the air flow is considered to be transitional - predictions within this range are considered to be unreliable
- Where Re>10000 the flow is considered to be fully turbulent.

Although other literature sources use slightly different boundary guidelines, they are of the same order of magnitude.

The Reynolds number is given by [1]:

$$\mathrm{Re} = \frac{VL}{\nu} = \frac{\rho VL}{\mu} = \frac{\rho VD_h}{\mu} = \frac{\dot{m}D_h}{A_c\mu} \qquad \text{B5}$$

B4 Prandtl Number

The Prandtl number is a combination of a fluid's specific heat capacity, viscosity and conductivity. These properties do not change significantly for the conditions considered in this project and therefore the Prandtl number remains relatively constant. It is given by [1, 4]:

$$\mathrm{Pr} = \frac{c_p\mu}{k} \qquad \text{B6}$$

or

$$\mathrm{Pr} = \frac{\nu}{\alpha} \qquad \text{B7}$$

and approximates to 0.7 for air.

The Prandtl number is required for the calculation of the Rayleigh number.

B5 Grashof Number

The Grashof number is required for the analysis of gases undergoing natural convection. In particular it is required for the calculation of the Rayleigh number [1].

$$Gr = \frac{L^3\beta g\Delta T}{\nu^2} \qquad \text{B8}$$

$$Gr = \frac{g\rho^2\beta\Delta TL^3}{\mu^2} \qquad \text{B9}$$

Brinkworth et al [5] used an alternative definition of the Grashof number:

$$Gr = \frac{g\beta qD_h^5}{L\nu^2 k} \qquad \text{B10}$$

B6 Relationship between Air Mass Flow, Air Velocity and Specific Mass Rate

The mass flow rate $\dot{m}$ through a duct is constant from beginning to end unless there is a leak. However, differences in the cross sectional area of a duct can cause localised changes in air velocity (V).

The relationship between air mass flow and air velocity is [1]:

$$V = \frac{\dot{m}}{\rho A_c} \qquad \text{B11}$$

In some instances the air mass flow rate is referred to in terms of the collector plate area (with the units kg s^{-1} m^{-2}). Within this document such a mass flow rate is referred to as the specific mass rate $\dot{M}$ to distinguish it from the mass flow rate defined above.

B7 Rayleigh Number

When the temperature is non-uniform and buoyancy forces become significant then it is the Rayleigh number which becomes relevant as the indicator of the character of the flow. The Rayleigh number is given by [1]:

$$Ra = Gr\,\mathrm{Pr} \qquad \text{B12}$$

B8 Entrance Length [1, 6]

Hydrodynamic

When air enters a duct, the air at the duct surfaces behaves differently to the air in the centre of the duct. This is because the friction forces slow the air in contact with the surfaces. This effect builds up, until more central fluid layers are in turn slowed down. The edge of the affected air is called the boundary layer. The friction effect forces the fluid to flow in a laminar fashion. However, if the Reynolds number exceeds 10,000 the boundary layers will become turbulent before they meet – establishing fully developed turbulent flow. The length it takes for the flow throughout the duct to become uniform is known as the entrance length.

The hydrodynamic entrance length can be defined in terms of the Reynolds number:

$$L_e = 0.06 \,\mathrm{Re}\, D_h \qquad \text{B13}$$

However, the flow after a length equivalent to six diameters is reasonably close to the final flow, particularly for higher Reynolds numbers [1].

Kakac et al [6] defined the boundary layer region as being the region where the velocity component parallel to the surface is less than 99% of its free-stream value.

Thermal

A difference in temperature between the air and the duct walls can cause a similar effect. The thermal effects diffuse gradually from the surface causing a heat affected region near the duct wall, while the inner flow is unchanged. The length it takes for the thermal effect to spread throughout the entire flow is known as the thermal entrance length.

The hydrodynamic and thermal entrance length can develop simultaneously or separately (e.g. if a change in temperature of the duct wall occurs after the fluid has completed its hydrodynamic entrance length, the thermal entry length would be separate).

B9 Pressure Drop

The pressure drop caused by fluid friction in fully developed flows is given by the Darcy-Weisbach equation [2]:

$$\Delta p = \frac{\dot{M}^2}{\rho}\left(\frac{L}{b}\right)^3 f \qquad \text{B14}$$

Which can also be represented as [1, 7]:

$$\Delta p = \rho f \frac{L}{D_h}\frac{V^2}{2} \qquad \text{B15}$$

B10 Friction factor

As mentioned previously, fluid is affected by friction effects when it is brought into contact with a surface. These are generally calculated in terms of the friction factor. Hollands and Shewen [2] used a generic definition of the friction factor:

$f = f_0 + \gamma \frac{b}{L} n$ where f_o, γ and n are defined for the situation; while b and L are defined by the geometry.

For forced convection, n=1. Hollands and Shewen [2] have derived values for f_o and γ from work carried out by Kays [8], the values are appropriate for air passing between parallel plates. These values are shown in Table B.1.

Table B.1 Values for f_o and γ for friction factor

Flow type	Re range	f_o	γ
Laminar	Re<2550	$24/\mathrm{Re}$	0.9
Transitional	$2550<\mathrm{Re}\leq 10^4$	0.0094	$2.92\ \mathrm{Re}^{-0.15}$
Early Turbulent	$10^4<\mathrm{Re}\leq 10^5$	$0.059\ \mathrm{Re}^{-0.2}$	0.73

Other definitions of the friction factor include [9]:

$$f' = 0.11\left(\frac{R}{D_h} + \frac{68}{\mathrm{Re}}\right)^{0.25} \qquad \text{B16}$$

If f' ≥ 0.018: f=f'
If f' < 0.018: f= 0.85*f' + 0.0028.

And Churchill's friction factor [1]:

$$f = 8\left[\left(\frac{8}{\mathrm{Re}}\right)^{1/2} + \frac{1}{(A+B)^{1.5}}\right]^{1/12} \qquad \text{B17}$$

where:

$$A = \left[2.457 \ln\left(\frac{1}{\left(\frac{7}{\mathrm{Re}}\right)^{0.9} + \frac{0.27R}{D_h}}\right)\right]^{16} \qquad \text{B17a}$$

$$B = \left(\frac{37530}{\mathrm{Re}}\right)^{16} \qquad \text{B17b}$$

B11 Fan Pumping Power

The fan pumping power required to create air movement is given by [10]:

$$P_{fan} = \frac{\dot{Q}\Delta p}{\eta} \qquad \text{B18}$$

B12 References

1. ASHRAE, *2005 ASHRAE Handbook: Fundamentals, SI Edition*, ed. R.a.A.C.E. American Society of Heating, Inc. 2005, Atlanta: ASHRAE; 1-931862-71-0.
2. Hollands, K.G.T. and E.C. Shewen, *Optimization of flow passage geometry for air-heating, plate-type solar collectors.* Journal of Solar Energy Engineering, 1981. **103**: p. 323-330.
3. Williams, E.W. *The Effects of Wind & Stack on Ventilation and Air Movement Patterns in Naturally Ventilated Commercial Buildings With Atria* 1994: MSc; Welsh School of Architecture at University of Wales Cardiff.
4. Incropera, F.P. and D.P. DeWitt, *Fundamentals of Heat and Mass Transfer*. 4th ed. 1996: John Wiley & Sons.p.1- 886; 0 471 30460 3.
5. Brinkworth, B.J., *A procedure for the routine calculation of laminar free and mixed convection in inclined ducts.* International Journal of Heat and Fluid Flow, 2000. **21**: p. 456-462.
6. Kakac, S., R.K. Shah, and W. Aung, *Handbook of Single-Phase Convective Heat Transfer*. 1987, New York: John Wiley & Sons; 0-471-81702-3.
7. Matrawy, K.K., *Theoretical analysis for an air heater with a box-type absorber*. Solar Energy, 1998. **63**(3): p. 191-198.
8. Kays, W.M. and H.C. Perkins, *Forced convection, internal flow in ducts*, in *Handbook of Heat Transfer*. 1973, McGraw & Hill: New York. 7-1 to 7-193.
9. ASHRAE, *1989 ASHRAE Handbook: Fundamentals, SI Edition*, ed. R.a.A.C.E. American Society of Heating, Inc. 1989, Atlanta: ASHRAE; 0-910110-57-3.
10. *Fan power consumption*. [cited 21st January 2007]; http://www.engineeringtoolbox.com/fans-efficiency-power-consumption-d_197.html.

.

Appendix C - Thermodynamics

Several of the terms, equations and concepts used in thermodynamics are explained in this appendix. The concepts include the three modes of heat transfer (conduction, convection and radiation) and how they contribute to the overall heat transfer. The Nusselt number is an important requirement for calculating convection, and is influenced by many parameters. Therefore, there are several equations which can be used to calculate the Nusselt number in different circumstances. The equations for the Nusselt number included in this appendix show the different approaches that have been taken by different researchers. Unless otherwise stated, the Nusselt number selected by a researcher for their model has been used in the modified models.

Researchers have similarly developed different methods of calculating wind convection, radiative heat transfer and solar air heater efficiency. These are described below, along with mean temperature and power output.

C1 Modes of Heat Transfer

There are three modes of heat transfer: conduction, radiation and convection. The behaviour of the three mechanisms in a given situation can be represented as a thermal circuit (Figure C.1).

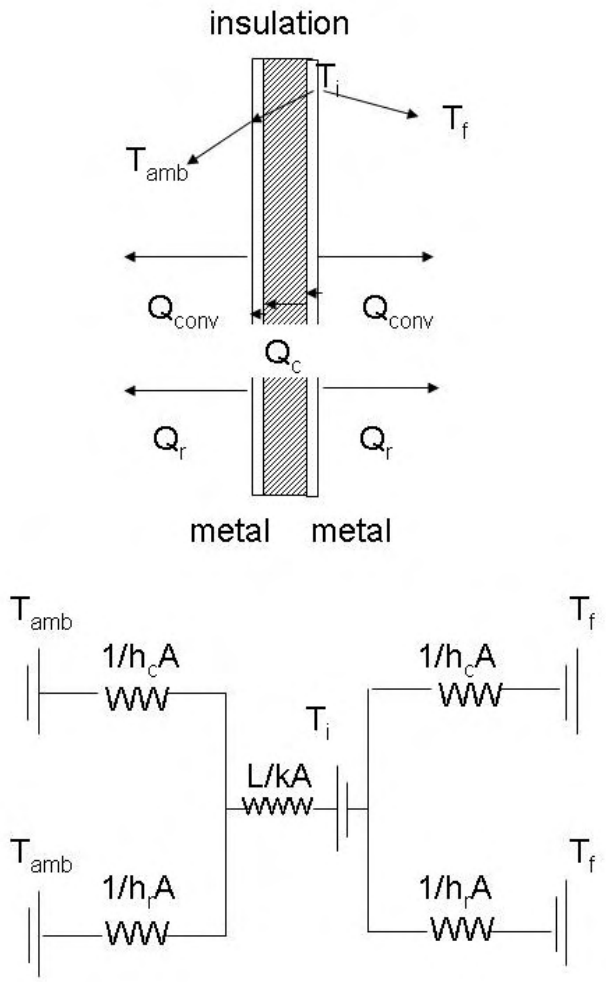

Figure C.1. Thermal circuit illustrating heat loss through conduction, convection and radiation

The resistances in this thermal circuit can be treated in the same way as electrical resistances in an electrical circuit would be.

C1.1 Conduction

The heat loss due to conduction depends on the thermal conductivity (k), area (A) of the material and the distance it has to travel through the material (d). The heat flow rate (q) due to conduction can be described by the following equation [1]:

$$q = \frac{k}{d}(T_1 - T_2) \qquad \text{C1}$$

C1.2 Convection

The heat loss due to convection depends on the area of the material (A) and the convective heat transfer coefficient (h_c). The convective heat transfer coefficient is related to the Nusselt number (Nu) and the thermal conductivity (k).

If the Nusselt number is being related to heat transfer within a duct it is related to the hydraulic diameter (D_h) and represented as [2]:

$$h_c = \frac{kNu}{D_h} \qquad \text{C2}$$

However, if it is being related to heat transfer between two parallel plates it is related to the duct length (L) and represented as [2]:

$$h_c = \frac{kNu}{L} \qquad \text{C3}$$

Nusselt Number

The Nusselt number is different depending on the situation. Significant amounts of work have gone into identifying suitable Nusselt calculations for boundary cases [3]. A reasonable knowledge of fluid dynamics and heat transfer is required to ensure that the correct Nusselt number is used.

Hollands and Shewen [4] used a generic definition of the Nusselt number:

$$Nu = Nu_0 + \beta \frac{b}{L} n \qquad \text{C4}$$

where Nu_0, β and n are defined for the flow type; while b and L are defined by the geometry.

Entrance Region (defined as L/D<60)

Nusselt's [5] equation (from Ong's [6] literature review) is related to the Reynolds number (Re) and the Prandtl number (Pr):

$$Nu = 0.036\,\mathrm{Re}^{0.8}\,\mathrm{Pr}^{1/3}\left(\frac{D_h}{L}\right)^{0.055} \qquad \text{C5}$$

Tan & Charters [7] equation (from Ong's [6] literature review) for 9,500<Re<22,000, includes the entrance region, but is suitable as long as $L/D_h > 3.57$.

$$Nu = Nu_0\left(1+\frac{SD_h}{L}\right) \qquad \text{C6}$$

where $S = 14.3\log\frac{L}{D_h} - 7.9$ for $3.57 < L/D_h \le 60$

$S = 17.53$ for $L/D_h > 60$

and $S = 0$ for $L/D_h = 3.57$

Ho and Loveday [8] used :

$$Nu = Nu_{fd}\left[1+\left(\frac{D_h}{L}\right)^{0.7}\right] \text{ (where } Nu_{fd} \text{ is defined by C16)} \qquad \text{C7}$$

Laminar flow

Ong [6] and Yeh [9] both quote Heaton as the source of an equation for the Nusselt number for parallel plates with one side insulated (adiabatic) and the other subjected to constant heat flux. However, Ong [6] quotes:

$$Nu = Nu_\infty + \frac{a\left[\mathrm{Re}\,\mathrm{Pr}\left(\frac{D_h}{L}\right)\right]^m}{1+b\left[\mathrm{Re}\,\mathrm{Pr}\left(\frac{D_h}{L}\right)\right]^n} \qquad \text{C8}$$

where a=0.00190, b=0.00563, m=1.71, n=1.17, and Nu_∞ =5.4 for Pr=0.7

While Yeh [9] quotes:

$$Nu = 4.4 + \frac{0.00398\left[0.7\,\mathrm{Re}\left(\frac{D_h}{L}\right)\right]^{1.66}}{1+0.0114\left[0.7\,\mathrm{Re}\left(\frac{D_h}{L}\right)\right]^{1.12}} \qquad \text{C9}$$

A more general equation for laminar flow within a pipe is used for the descriptive model in Chapter 4 [2]:

$$Nu_{lam} = 1.86\left(\frac{\mathrm{Re}\,\mathrm{Pr}}{L/D_h}\right)^{1/3}\left(\frac{\mu}{\mu_{sur}}\right)^{0.14} \qquad \text{C10}$$

Where μ is the dynamic viscosity (N s m^{-2})

Transitional flow

From Ong's [6] literature review: Hausen developed an empirical correlation for the Nusselt number:

$$Nu = 0.116\left(\mathrm{Re}^{2/3} - 125\right)\mathrm{Pr}^{1/3}\left[1 + \left(D_h/L\right)^{2/3}\right]\left(\frac{\mu}{\mu_{sur}}\right)^{0.14} \qquad \text{C11}$$

Turbulent flow

Yeh [10] followed the work of Kays [11] to derive this Nu number for fully developed turbulent flow with one side heated and the other side insulated:

$$Nu = 0.0158\,\mathrm{Re}^{0.8} \qquad \text{(which relates to C7)} \qquad \text{C12}$$

From Ong's [6] literature review: Tan and Charters equation for 9500<Re<22,000,

$$Nu_{\infty} = 0.018\,\mathrm{Re}^{0.8}\,\mathrm{Pr}^{0.4} \qquad \text{C13}$$

A more general equation for turbulent flow within a pipe is used for the descriptive model in Chapter 4 [2]:

$$Nu_{turb} = \frac{\left(f_s/2\right)\left(\mathrm{Re} - 1000\right)\mathrm{Pr}}{1 + 12.7\left(f_s/2\right)^{1/2}\left(\mathrm{Pr}^{2/3} - 1\right)}\left[1 + \left(\frac{D_h}{L}\right)^{2/3}\right]\left(\frac{T}{T_{sur}}\right)^{0.45} \qquad \text{C14}$$

where

$$f_s = \frac{1}{\left(1.58\ln\mathrm{Re} - 3.28\right)^2} \qquad \text{C15}$$

Natural Convection

In his 2003 paper, Ong [12] used Incropera and DeWitt's [13] equation's for natural convection between a wall and glass:

Laminar flow

$$Nu = 0.68 + \frac{0.67 Ra^{1/4}}{\left[1 + \left(\frac{0.492}{\mathrm{Pr}}\right)^{9/16}\right]^{4/9}} \qquad \text{C16}$$

Where:

Ra Rayleigh number

Turbulent flow

$$Nu = \left\{0.825 + \frac{0.387 Ra^{1/6}}{\left[1 + \left(\frac{0.492}{\mathrm{Pr}}\right)^{9/16}\right]^{8/27}}\right\}^2 \qquad \text{C17}$$

Brinkworth [14, 15] uses the following equation for natural convection:

$$N\overline{u} = 5.35 + \frac{0.07}{L^+} \qquad \text{C18}$$

where L^+ is a dimensionless length defined by:

$$L^+ = \left(\frac{48\,\mathrm{Pr}}{Gr}\right)^{0.5} \qquad \text{C19}$$

Wind convection

Ong [6] compared the methods of determining the convection heat transfer coefficient due to wind developed by McAdams (C20) [16], Watnuff (C21) [17] and Sparrow (C22) [18]:

$$h_w = 5.7 + 3.8v \qquad \text{C20}$$

$$h_w = 2.8 + 3.3v \qquad \text{C21}$$

$$Nu_w = 0.0158\,\mathrm{Re}^{0.8} \qquad \text{C22}$$

and selected the McAdams version. Of the three equations, the McAdams is the most widely used.

Yeh [10] adapted the McAdams equation for his model:

$$h_w = 4.9 + 3.27v' \qquad \text{C23}$$

The British Standard BS EN ISO 12241 considers the convection heat transfer coefficient to be dependent on whether the wind is laminar or turbulent. The air flow is considered to be laminar if [1]:

$$vH \le 8m^2 s^{-1} \qquad \text{C24}$$

and turbulent otherwise.

The convection coefficient for laminar air flow is [1]:

$$h_c = 3.96\sqrt{\frac{v}{H}} \qquad \text{C25}$$

and for turbulent airflow:

$$h_c = 5.76\left(\frac{v}{H}\right)^{0.5} \qquad \text{C26}$$

C1.3 Radiation

The heat loss due to convection depends on the area of the material (A) and the radiative heat transfer coefficient (h_r).

Radiative heat transfer coefficient between parallel plates

Hollands and Shewen [4] used the following equation:

$$h_r = \frac{\sigma\left(T_1^2 + T_2^2\right)\left(T_1 + T_2\right)}{\frac{1-\varepsilon_1}{\varepsilon_1} + \frac{1-\varepsilon_2}{\varepsilon_2} + 1} \qquad \text{C27}$$

Where:

σ Stefan Boltzmann Constant (5.67E-8 W m^{-2} K^{-4})

ε emisivity of surface

Ong [6] used:

$$h_r = \frac{\sigma\left(T_1^2 + T_2^2\right)\left(T_1 + T_2\right)}{\frac{1}{\varepsilon_1} + \frac{1}{\varepsilon_2} - 1} \qquad \text{C28}$$

Yeh [10] used:

$$h_r \approx \frac{4\sigma T_f^3}{\frac{1}{\varepsilon_1}+\frac{1}{\varepsilon_2}-1} \qquad \text{C29}$$

Radiative heat transfer coefficient between a body and the sky / ambient environment

Ong [6] used the following equation:

$$h_{rs} = \frac{\sigma\varepsilon_1(T_1+T_s)(T_1^2+T_s^2)(T_1-T_s)}{(T_1-T_{amb})} \qquad \text{C30}$$

Where the sky temperature (T_s) is given by Swinbank [19] as:

$$T'_s = 0.0552T'^{1.5}_{amb} \qquad \text{C31}$$

Ho and Loveday [8] used Duffie and Beckman's [20] equation:

$$h_{rs} = \sigma\varepsilon_c\left[(T_1+273)^2+(T_{amb}+273)^2\right](T_1+T_{amb}+546) \qquad \text{C32}$$

or written in terms of temperatures already in Kelvin:

$$h_{rs} = \sigma\varepsilon_c\left[T'^2_1+T'^2_{amb}\right](T'_1+T'_{amb}) \qquad \text{C33}$$

C2 Mean Temperature

The fluid temperature can be assumed to vary linearly over short distances, and can be determined from:

$$\overline{T}_f = \gamma T_{fo} + (1-\gamma)T_{fi} \qquad \text{C34}$$

where $\gamma = 0.5$. If a non-linear temperature gradient is experienced γ can be varied accordingly.

C3 Solar Air Heater Efficiency

The basic equation for efficiency is:

$$\eta = \frac{Q}{EA} \qquad \text{C35}$$

This can be represented as the Hottel-Whillier-Bliss equation:

$$\eta = F_R\left((\tau\alpha)_e - U_L\left(T_i - T_a\right)/I\right) \quad \text{C36}$$

where

$$F_R = \frac{\dot{m}c_p}{A_c U_L}\left\{1 - \exp\left[-\frac{U_L F' A_c}{\dot{m}c_p}\right]\right\} \quad \text{C37}$$

and

$$F' = \left(1 + \frac{U_L}{h_1} + \left[\frac{1}{h_1} + \frac{1}{h_r}\right]^{-1}\right)^{-1} \quad \text{C38}$$

Ong [6] used the following equation:

$$\eta = \dot{m}c_p \frac{T_{fo} - T_{amb}}{EWL} \quad \text{C39}$$

C4 Power Output

Power output for an individual duct can be calculated from:

$$Q = \dot{m}c_p \Delta T \quad \text{C40}$$

C5 References

1. British Standards Institution, *Thermal insulation for building equipment and industrial installations - Calculation Rules,* BS EN ISO 12241, 1998, British Standards Institution.
2. ASHRAE, *2005 ASHRAE Handbook: Fundamentals, SI Edition*, ed. R.a.A.C.E. American Society of Heating, Inc. 2005, Atlanta: ASHRAE; 1-931862-71-0.
3. Kakac, S., R.K. Shah, and W. Aung, *Handbook of Single-Phase Convective Heat Transfer*. 1987, New York: John Wiley & Sons; 0-471-81702-3.
4. Hollands, K.G.T. and E.C. Shewen, *Optimization of flow passage geometry for air-heating, plate-type solar collectors.* Journal of Solar Energy Engineering, 1981. **103**: p. 323-330.
5. Nusselt, W., *Der warmeaustatsch zwischen wand und wasser im rohr.* Forsch. Geb. Ingenieurwes, 1931. **2**: p. 309.
6. Ong, K.S., *Thermal performance of solar air heaters: Mathematical model and solution procedure.* Solar Energy, 1995. **55**(2): p. 93-109.
7. Tan, H.M. and W.W.S. Charters, *An experimental investigation of forced-convective heat transfer for fully-developed turbulent flow in a rectangular duct with a symmetric heating.* Solar Energy, 1970. **13**: p. 121-125.

8. Ho, K.T.K. and D.L. Loveday, *Covered profiled steel cladding as an air heating solar collector: laboratory testing, modelling and validation.* Energy and Buildings, 1997. **26**: p. 293-301.
9. Yeh, H.-M., C.-D. Ho, and J.-Z. Hou, *The improvement of collector efficiency in solar air heaters by simultaneously air flow over and under the absorbing plate.* Energy, 1999. **24**: p. 857-871.
10. Yeh, H.-M. and T.-T. Lin, *Efficiency Improvement of Flat-Plate Solar Air Heaters.* Energy, 1996. **21**(6): p. 435-443.
11. Kays, W.M. and H.C. Perkins, *Forced convection, internal flow in ducts*, in *Handbook of Heat Transfer*. 1973, McGraw & Hill: New York. 7-1 to 7-193.
12. Ong, K.S., *A mathematical model of a solar chimney.* Renewable Energy, 2003. **28**: p. 1047-1060.
13. Incropera, F.P. and D.P. DeWitt, *Fundamentals of Heat and Mass Transfer*. 4th ed. 1996: John Wiley & Sons.p.1- 886; 0 471 30460 3.
14. Brinkworth, B.J., R.H. Marshall, and Z. Ibarahim, *A Validated Model of Naturally Ventilated PV Cladding.* Solar Energy, 2000. **69**: p. 67-81.
15. Brinkworth, B.J., *A procedure for the routine calculation of laminar free and mixed convection in inclined ducts.* International Journal of Heat and Fluid Flow, 2000. **21**: p. 456-462.
16. McAdams, W.H., *Heat Transmission*. 3rd ed. 1954, New York: McGraw & Hill.
17. Watmuff, J.H., W.W.S. Charters, and D. Proctor, *Solar and wind induced external coefficients for solar collectors.* COMPLES, 1977(2): p. 56.
18. Sparrow, E.M., J.W. Ramsey, and E.A. Mass, *Effect of finite width on heat transfer and fluid flow about an inclined rectangular plate.* Transactions of American Society of Mechanical Engineers: Journal Heat Transfer, 1979. **101**(2).
19. Swinbank, W.C., *Long-wave radiation from clear skies.* Q. J. R. Meteorol. Soc, 1963. **89**: p. 339.
20. Duffie, J.A. and W.A. Beckman, *Solar Engineering of Thermal Process*. 1991, New York: Wiley.

Appendix D – Air Mass Flow

D1 Measurement of Air Flow

There are several methods of measuring air flow.

- Laser Doppler anemometers are considered to be accurate but are expensive, and therefore not an option for this project.
- Hot wire anemometers are cheaper, but are not particularly accurate.
- The tracer gas technique requires a gas to be introduced at the bottom of a channel with a known volume flow rate. The volume concentration is measured at the exit. This is also considered to be an accurate technique. However, the technique may not have been robust enough for outdoor use, and it required equipment which was not available.
- A relatively inexpensive technique with a reasonable degree of accuracy is to measure the pressure drop across and orifice plate. This technique was used, and is described below.

D1.1 Orifice Plate Design

The orifice plates and pressure tappings were designed and constructed in accordance with BS EN ISO 5167-1:2003 and BS EN ISO 5167-2:2003 [1, 2]. An orifice plate schematic is shown in (Figure D.1)

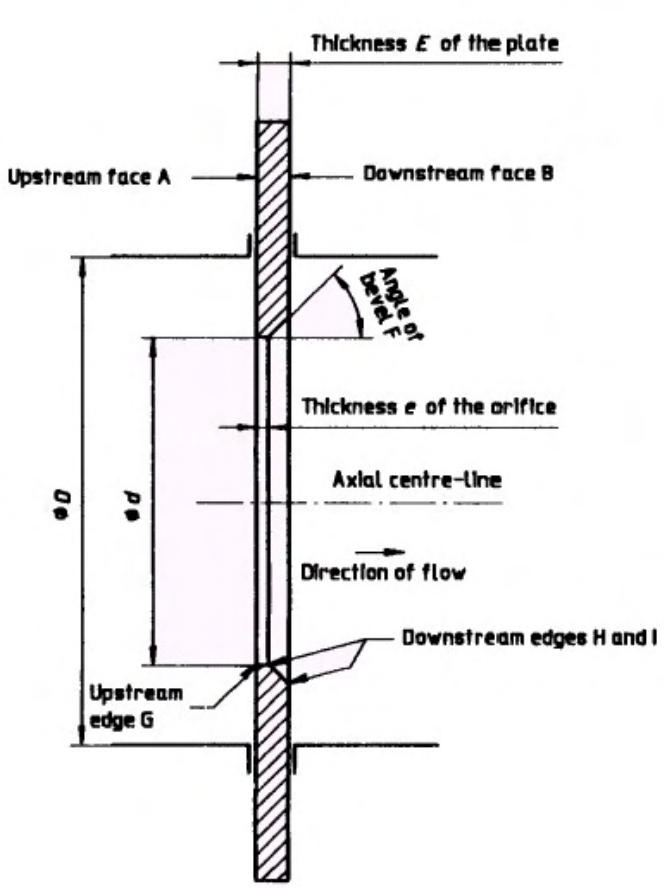

Figure D.1. Cross Section Schematic of an Orifice Plate [1]

General conditions for orifice plate design are dependent on the type of pressure tappings used and are described in [2]. The conditions for an orifice plate with corner pressure tappings are summarised below:

- The orifice diameter (d) must be greater than 12.5 mm
- The tube diameter (D) must be greater than 50 mm but less than 1,000 mm
- The ratio (β) of orifice diameter to tube diameter (d/D) must be between 0.1 and 0.75
- The upstream Reynolds number (Re) must be greater than 5,000, unless β is greater than 0.56, in which case the Re must be greater than 16,000.

The Reynolds number is calculated using equation B5 (Appendix B).

The selected pipe has a diameter of 54.7 mm. The Re for the specified air mass flow (0.01 kg s^{-1}) through 54.7 mm diameter pipework is 12,803. This means that the

required air mass flow through this pipe work is acceptable as long as β is kept below 0.56.

The relationship between air mass flow and the differential pressure across the orifice plates (Δp) is [1]:

$$\frac{C\varepsilon\beta^2}{\sqrt{1-\beta^4}} = \frac{4\dot{m}}{\pi D^2\sqrt{2\Delta p\rho}} \qquad \text{D1}$$

Where:

C coefficient of discharge

ε expansion factor

$\dot{m}$ air mass flow (kg s^{-1})

D internal diameter of upstream pipe

Δp differential pressure across the orifice plate (Pa)

ρ air density (kg m^{-3})

The following assumption can be made:

$$\frac{C\varepsilon}{\sqrt{1-\beta^4}} \approx 0.6 \qquad \text{D2}$$

Allowing equation D1 to be rearranged as:

$$\Delta p = \left(\frac{4\dot{m}}{0.6\pi\beta^2 D^2\sqrt{2\rho}}\right)^2 \qquad \text{D3}$$

which can be used to calculate the approximate differential pressure across the orifice plate for a range of orifice diameters. Based on the available pressure gauges, a suitable range for the differential pressure had been set (between 500 and 2000 Pa). From the calculated differential pressures values, an orifice diameter of 22 mm (β = 0.402) was found to meet this criteria (Δp ~ 800 Pa).

Setting a value for β allows the length of the upstream and downstream pipe work to be calculated. Since flexible pipe is being used within the experiment, an allowance for up to two 90^o bends in perpendicular planes can be made by requiring an upstream length of 44D (2.4 m). A downstream diameter of 6D (0.3 m) has also been calculated.

The air mass flow is controlled to the correct level by measuring the differential pressure across the orifice plates (Δp). The precise value for Δp is dependent on the value of the expansion factor (ε), which is in turn dependent on Δp. Having calculated an approximate value of Δp, it is now possible to calculate a value for the upstream expansion factor (ε_1). The following equation is valid as long as $p_2/p_1 \geq 0.75$ [1].

$$\varepsilon_1 = 1 - \left(0.41 + 0.35\beta^4\right)\frac{\Delta p}{\kappa p_1} \qquad \text{D4}$$

Where:

κ isentropic exponent

p_1 upstream pressure (Pa)

Assuming the upstream pressure (p_1) is 100,000 Pa (atmospheric pressure), and taking the approximate value of the differential pressure (800 Pa). The expansion factor can be calculated as 0.9977. In turn, this value for the expansion factor can be fed into equation D1, allowing a more accurate differential pressure to be calculated. However, the coefficient of discharge must be calculated before equation D1 can be used. The Reader-Harris / Gallagher equation is [1]:

$$C = 0.5961 + 0.0261\beta^2 - 0.216\beta^8 + 0.000521\left(\frac{10^6\beta}{\mathrm{Re}}\right)^{0.7} + \left(0.0188 + 0.063A\right)\beta^{3.5}\left(\frac{10^6}{\mathrm{Re}}\right)^{0.3}$$

$$+ \left(0.043 + 0.08e^{-10L_1} - 0.123e^{-7L_1}\right)\left(1 - 0.11A\right)\frac{\beta^4}{1-\beta^4} - 0.031\left(M'_2 - 0.8M'^{1.1}_2\right)\beta^{1.3}$$

$$+ 0.011\left(0.75 - \beta\right)\left(2.8 - \frac{D}{25.4}\right) \qquad \text{D5}$$

where:

$$A = \left(\frac{19000\beta}{\mathrm{Re}_D}\right)^{0.8} \qquad \text{D5a}$$

$$M'2 = \frac{2L'_2}{1-\beta} \qquad \text{D5b}$$

For an orifice plate with corner tappings $L_1 = L'_2 = 0$

The revised differential pressure is fed into equation D4 to recalculate the upstream expansion factor. This process is reiterated until the value for the differential pressure converges. In this instance, a differential pressure of 738 Pa is expected.

D1.2 Orifice Plate Checks

The roughness of the upstream pipework for a distance of 10D is specified. The maximum pipe internal roughness (R) allowable is $R/D < 15$ [1] for a system with a Reynolds number ~ 1E4 and a β ~ 0.4. The roughness of plastic is specified as < 0.01 mm [1]. This meets the requirements specified.

The flatness of the upstream face of the plate is considered acceptable when $Gap < {0.005(D-d)}/{2}$ where Gap is the maximum gap between the plate and a straight edge of length D laid across any diameter of the plate [1]. Therefore, the maximum acceptable gap across a diameter is 0.16 mm. A dial test indicator has been used to check the variation in height along the surface of the orifice plates. The gaps across four representative diameters are: 0.08 mm, 0.08 mm, 0.03 mm and 0.05 mm.

The upstream face of the orifice plate shall have a roughness criterion $R < 10^{-4}d$ within a circle of diameter not less than D which is concentric with the orifice. For the orifice diameter being considered, this would require R to be less than 0.022 mm. The upstream orifice faces have a turned finish. The average surface roughness for a turned finish generally lies between 0.0004 and 0.0063 mm [3].

The diameter of orifice d shall be taken as the mean of the measurements of at least four diameters at approximately equal angles to each other. No diameter shall differ by more than 0.05 % from the value of the mean diameter. The measurements taken and the calculations derived from them are shown in Table D.1.

Table D.1 Orifice diameter measurements and calculations

Orifice plate	#1	#2	#3	#4
Measurement 1 (mm)	21.97	21.96	21.96	21.97
Measurement 2 (mm)	21.96	21.98	21.97	21.96
Measurement 3 (mm)	21.98	21.96	21.96	21.96
Measurement 4 (mm)	21.97	21.98	21.96	21.97
Mean (mm)	21.97	21.97	21.96	21.96
Allowable deviation from mean (mm)	0.01	0.01	0.01	0.01
Acceptable?	Yes	Yes	Yes	Yes

D2 Calculation of uncertainty in the mass flow rate

The uncertainty in the mass flow rate is calculated using equation D6 [1]:

$$\frac{\delta \dot{m}}{\dot{m}} = \sqrt{\left(\frac{\delta C}{C}\right)^2 + \left(\frac{\delta \varepsilon}{\varepsilon}\right)^2 + \left(\frac{2\beta^4}{1-\beta^4}\right)^2 \left(\frac{\delta D}{D}\right)^2 + \left(\frac{2}{1-\beta^4}\right)^2 \left(\frac{\delta d}{d}\right)^2 + \frac{1}{4}\left(\frac{\delta \Delta p}{\Delta p}\right)^2 + \frac{1}{4}\left(\frac{\delta p_1}{p_1}\right)^2}$$

D6

D2.1 Uncertainty of discharge coefficient *C*

When β, *D*, *Re* and *R*/*D* are assumed to be known without error, the relative uncertainty of the value of *C* is equal to [2]:

– (0.7 – β) % for $0.1 \le \beta < 0.2$

– 0.5 % for $0.2 \le \beta \le 0.6$

– (1.667β – 0.5) % for $0.6 < \beta \le 0.75$

Since $D < 71.12$ mm, the following relative uncertainty should be added arithmetically to the above values [2]:

$$+0.9(0.75-\beta)\left(2.8-\frac{D}{25.4}\right)\% \qquad \text{D6a}$$

If β >0.5 and Re <10 000, an added uncertainty of 0.5 % should be added arithmetically to the above values [2].

In this instance, the uncertainty of the discharge coefficient is 1.377 %.

D2.2 Uncertainty of expansibility [expansion] factor ε

When β, $\Delta p/p_1$ and κ are assumed to be known without error, the relative uncertainty of the value of ε is equal to [2]:

$$3.5\frac{\Delta p}{\kappa p_1}\% \qquad \text{D7}$$

A typical value of the uncertainty due to the expansibility factor (for an air mass flow of 0.01 kg s^{-1}) is 0.019 %.

D2.3 Uncertainty of pipe and orifice diameter

Assuming that the specifications within the British Standard have been met, the maximum value for $\delta D/D$ will not exceed 0.4 % whereas the maximum value for $\delta d/d$ will not exceed 0.1 % [1].

D2.4 Uncertainty of pressure readings

The values of $\delta\Delta p/\Delta p$ and $\delta p_1/ p_1$ depend on the method of measuring these quantities. For the equipment used during this project a typical value of $\delta\Delta p/\Delta p$ at 0.01 kg s^{-1} is 1.14 % and $\delta p_1/ p_1$ has been calculated to be 0.01 %.

When these individual uncertainties are fitted into equation D6, the overall uncertainty for calculating the air mass flow is 1.5 %.

D3 Calculation of Air Mass Flow

The air mass flow is calculated from the following equation [2]:

$$\dot{m} = \frac{C}{\left(1-\beta^4\right)^{0.5}} \varepsilon \frac{\pi}{4} d^2 \left(2\Delta p \rho\right)^{0.5} \qquad \text{D8}$$

where:

- C is calculated using the Reader-Harris/Gallagher equation (D5).
- The air density was calculated allowing for variations in air temperature and humidity.
- The measured pressure difference across the pressure tappings were presented as voltages. These were translated into pressure readings using the equations derived from the calibration graph in (Figure D.2).
- the expansion factor is calculated from equation D9 [2]:

$$\varepsilon = 1 - \left(0.351 + 0.256\beta^4 + 0.93\beta^8\right)\left[1 - \left(\frac{p_2}{p_1}\right)^{1/k}\right] \qquad \text{D9}$$

- where the upstream pressure (p1) was taken as the atmospheric pressure reading from the weather station at the Welsh School of Architecture in Cardiff.

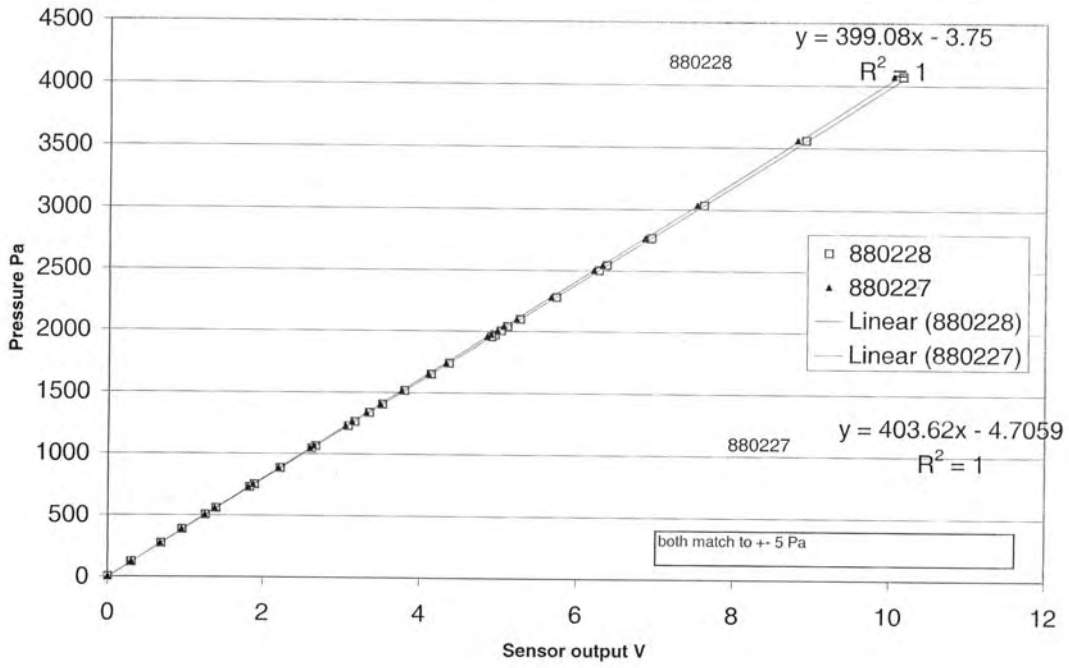

Figure D.2. calibration graph for orifice pressure gauge

D4 References

1. British Standards Institution, *Measurement of fluid flow by means of pressure differential devices inserted into circular cross-section conduits running full - Part 1: General principles and requirements,* BS EN ISO 5167-1, 2003, British Standards Institution.
2. British Standards Institution, *Measurement of fluid flow by means of pressure differential devices inserted into circular cross-section conduits running full - Part 2: Orifice Plates,* BS EN ISO 5167-2, 2003.
3. *Machinery's Handbook 24. 1992, New York: Industrial Pressings Inc. p.1-2543*; 0-8311-2424-5.

Appendix E – Solar Angle Calculations

E1 Solar Position

It is generally convenient to assume that the earth is stationary and flat at a given site and that the sun moves over it. The sun's position can be described by its azimuth and altitude relative to a point on the earth (Figure E.1) [1]. The calculations to obtain the azimuth and altitude can be complex. In this project, such calculations have been made using the Fortran codes supplied by Muneer in his book 'Solar Radiation & Daylight Models' [2].

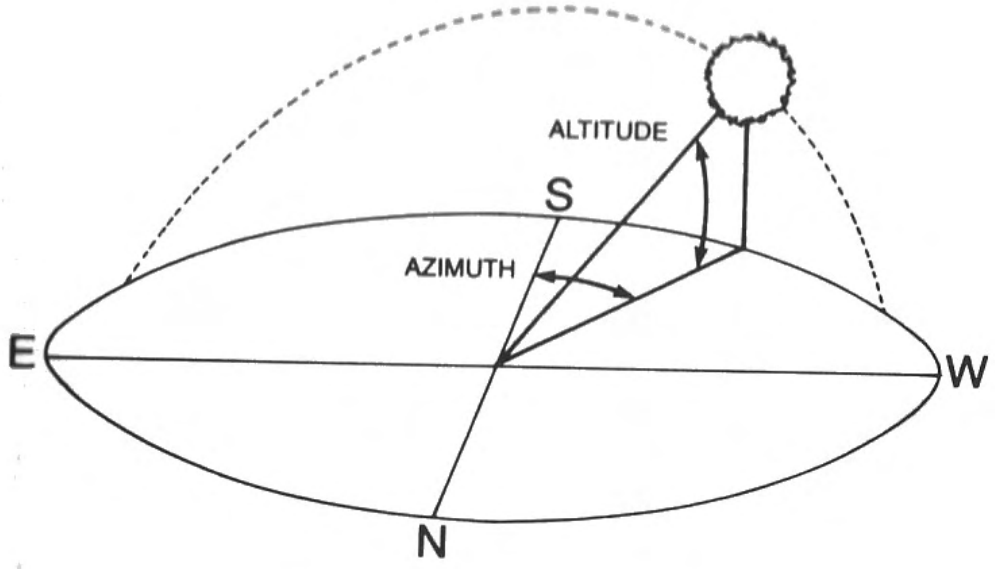

Figure E.1. Illustration of Solar Altitude and Azimuth [1]

E2 Solar Irradiation – Seasonal Changes

The earth's axis of rotation is tilted approximately 23.5^{o} away from a line perpendicular to its orbit. This causes the earth to experience changing seasons (Figure E.2).

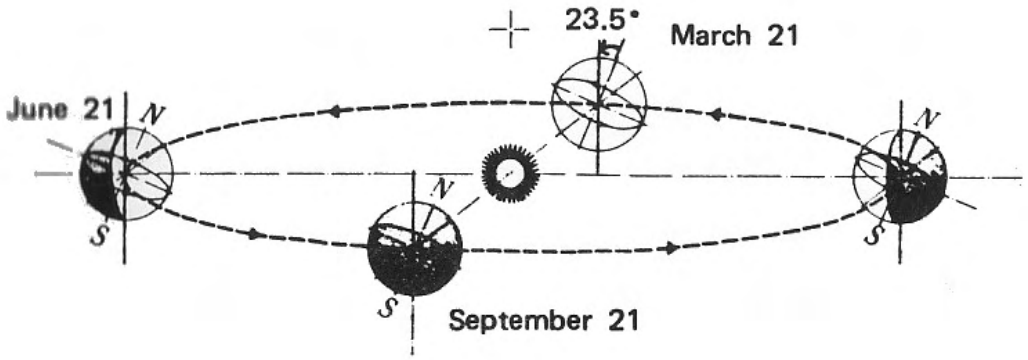

Figure E.2. Path of the Earth around the Sun [1]

The different seasons affect the times at which solar irradiance is experienced and also its distribution over horizontal and vertical surfaces. This is illustrated in Figures E.3 and E.4.

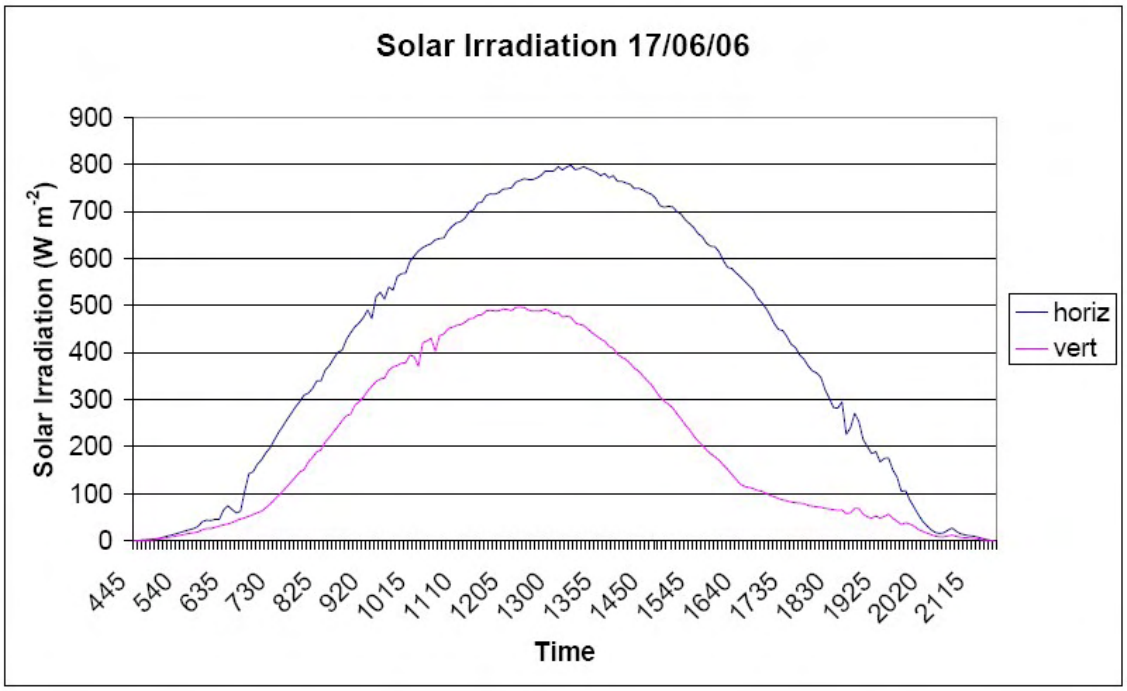

Figure E.3. Distribution of solar irradiance - summer

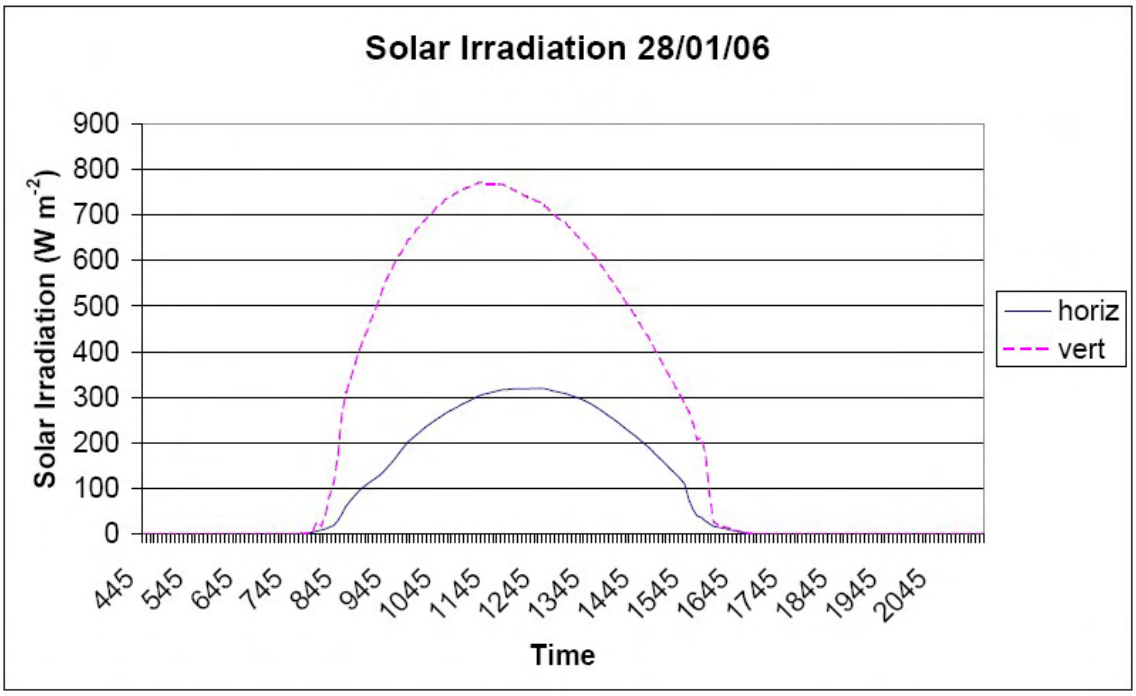

Figure E.4. Distribution of solar irradiance - winter

Figure E.3 shows that horizontal surfaces are more highly irradiated than vertical surfaces in summer. Whereas, Figure E.4 shows that vertical surfaces are more highly irradiated than horizontal surfaces in winter

E3 Solar Irradiation – Calculations for non horizontal surfaces

Typically solar irradiation data is available for horizontal surfaces. The global irradiance on a surface (E_g) can be written as [3]:

$$E_g = E_{dir} + E_{diff} + R \qquad \text{E1}$$

where:

E_{dir} = direct beam irradiance on a surface (W m^{-2})

E_{diff} = sky-diffuse irradiance on a surface (W m^{-2})

R = reflected irradiance on a surface (W m^{-2})

Mathematically the direct beam irradiance can be expressed as [3]:

$$E_{dir} = \frac{E_{hdir}}{\sin \alpha} \cos \theta \qquad \text{E2}$$

where

E_{hdir} = hourly direct beam irradiance on a horizontal surface (W m^{-2})

α = solar altitude (^{o})

θ = angle of incidence (^{o})

The combined sky-diffuse and reflected irradiance can be calculated using:

$$E_{diff} + R_h = AlE_{hg} + jE_{hdiff} \qquad \text{E3}$$

Where j is the ratio of diffuse irradiation visible to the surface in relation to a horizontal surface (i.e. for a vertical surface, j=0.5)

E4 References

1. Crowley, J.S. and L.Z. Zimmerman, *Practical Passive Solar Design*. 1984, New York: McGraw & Hill. 251.
2. Muneer, T., *Solar radiation & Daylight models*. 1997, Oxford: Architectural Press. 197.
3. Li, D.H.W., J.C. Lan, and C.C.S. Lau, *A new approach for predicting vertical global solar irradiance.* Renewable Energy, 2002. **25**: p. 591-606.
4. ASHRAE, *2005 ASHRAE Handbook: Fundamentals, SI Edition*, ed. R.a.A.C.E. American Society of Heating, Inc. 2005, Atlanta: ASHRAE.

Appendix F – Error Propagation

The error propagation for the model described in Section 4.1 is detailed in this appendix.

F1 Error Propagation Equations

Equations for error propagation in relation to addition, subtraction, multiplication, division, powers, exponentials and logarithms can be found [1].

Addition and Subtraction

C=xA + yB or C=xA – yB

$$\sigma_C = \sqrt{x^2\sigma_A^2 + y^2\sigma_B^2} \qquad \text{F1}$$

Multiplication and Division

C=xA*yB or C=xA/yB

$$\frac{\sigma_C}{C} = \sqrt{\frac{\sigma_A^2}{A^2} + \frac{\sigma_B^2}{B^2}} \qquad \text{F2}$$

Power

$C=aA^{\pm N}$

$$\frac{\sigma_C}{C} = N\frac{\sigma_A}{A} \qquad \text{F3}$$

Exponentials

$C=a\ e^{\pm bA}$

$$\frac{\sigma_C}{C} = b\sigma_A \qquad \text{F4}$$

Logarithms

$C=a\ \ln(\pm bA)$

$$\sigma_C = a\frac{\sigma_A}{A} \qquad \text{F5}$$

F2 Errors Identified for Base Parameters

The errors associated with the parameters are listed below with actual, typical or average values from 05/05/06.

Table F1 Properties of float glass

Symbol	Description	Error (±)	Reason for error	Average/Typical Value
$\alpha_{glass}(\theta)$	Absorptivity related to solar incident angle	0.05	Specified by table author [2]	0.14
$\alpha_{glass\ diff}$	Absorptivity (diffuse)	0.05		0.17
$R_{glass}(\theta)$	Reflectivity related to solar incident angle	0.05		0.22
$R_{glass\ diff}$	Reflectivity (diffuse)	0.05		0.14
d_g	Glass thickness	0.0002 m	Specification [3]	0.006 m
ε_g	Glass emissivity	0.02	Calculation accuracy [4]	0.91

Table F2 Properties of air:

Symbol	Description	Error (±)	Reason for error	Average/ Typical Value
k_{air}	Thermal conductivity of air	0.0014 W m^{-1} K^{-1}	Resolution of data table - values available for 20°C variations in temperature[5]	0.025 W m^{-1} K^{-1}
ρ_{air}	Air density	0.07 kg m^{-3}		1.29 kg m^{-3}
μ	Dynamic Viscosity	9.24E-7 kg m^{-1} s^{-1}		1.76E-5 kg m^{-1} s^{-1}
c_p	Specific heat capacity	0.8 J kg^{-1} K^{-1}		1005 J kg^{-1} K^{-1}
$\dot{m}_{ND}$	Air mass flow ND	1.5+05 %	Resolution of calculation method including corrosion of orifice plate [6]	0.0048 kg s^{-1}
$\dot{m}_{WD}$	Air mass flow WD	1.5+0.5 %		0.0054 kg s^{-1}
$\dot{m}_{NS}$	Air mass flow NS	1.5+0.1 %		0.0051 kg s^{-1}
$\dot{m}_{WS}$	Air mass flow WS	1.5+0.7 %		0.0050 kg s^{-1}

Table F3 Parameters of Prototype Ducts

Symbol	Description	Error (±)	Reason for error	Value
$b_{d\ ND}$	Duct depth ND	0.001 m	Ruler resolution	0.110 m
$b_{d\ WD}$	Duct depth WD	0.001 m		0.110 m
$b_{d\ NS}$	Duct depth NS	0.001 m		0.041 m
$b_{d\ WS}$	Duct depth WS	0.001 m		0.041 m
$b_{s\ ND}$	Prototype depth ND	0.001 m	Ruler resolution	0.260 m
$b_{s\ WD}$	Prototype depth WD	0.001 m		0.275 m
$b_{s\ NS}$	Prototype depth NS	0.001 m		0.190 m
$b_{s\ WS}$	Prototype depth WS	0.001 m		0.200 m
$w_{d\ ND}$	Duct width ND	0.001 m	Ruler resolution	0.101 m
$w_{d\ WD}$	Duct width WD	0.001 m		0.208 m
$w_{d\ NS}$	Duct width NS	0.001 m		0.101 m
$w_{d\ WS}$	Duct width WS	0.001 m		0.201 m
$w_{g\ ND}$	Glass width ND	0.001 m	Ruler resolution	0.140 m
$w_{g\ WD}$	Glass width WD	0.001 m		0.240 m
$w_{g\ NS}$	Glass width NS	0.001 m		0.140 m
$w_{g\ WS}$	Glass width WS	0.001 m		0.240 m
$w_{s\ ND}$	Prototype width ND	0.001 m	Ruler resolution	0.188 m
$w_{s\ WD}$	Prototype width WD	0.001 m		0.285 m
$w_{s\ NS}$	Prototype width NS	0.001 m		0.177 m
$w_{s\ WS}$	Prototype width WS	0.001 m		0.277 m
L_g	Exposed glass length	0.002 m	Tape Measure resolution	1.900 m
L_s	Duct length	0.002 m		2.400 m
H	Height of system	0.002 m		3.400 m
$d_{Ins\ ND\ side}$	Thickness of insulation (side) ND	0.01 m	Allowing for discontinuities and overlaps in the insulation.	0.04 m
$d_{Ins\ WD\ side}$	Thickness of insulation (side) WD	0.01 m		0.04 m
$d_{Ins\ NS\ side}$	Thickness of insulation (side) NS	0.01 m		0.04 m
$d_{Ins\ WS\ side}$	Thickness of insulation (side) WS	0.01 m		0.04 m
$d_{Ins\ ND\ back}$	Thickness of insulation (back) ND	0.01 m	Allowing for discontinuities and overlaps in the insulation.	0.15 m
$d_{Ins\ WD\ back}$	Thickness of insulation (back) WD	0.01 m		0.16 m
$d_{Ins\ NS\ back}$	Thickness of insulation (back) NS	0.01 m		0.15 m
$d_{Ins\ WS\ back}$	Thickness of insulation (back) WS	0.01 m		0.16 m
d_s	Thickness of steel substrate	10 %	specification	0.00046m
d_{zn}	Thickness of zinc coating	10 %	specification	0.00004m
d_{pt}	Thickness of paint (top surface)	10 %	specification	0.00005m
d_{pb}	Thickness of paint (backing surface)	10 %	specification	0.00001m

Table F3 Cont'd Parameters of Prototype Ducts

Symbol	Description	Error (±)	Reason for error	Value
R_p	Reflectivity of duct coating	0.01	Variance in results provided by paint company [7]	0.05
$\varepsilon_{black\ paint}$	Emissivity of coating on duct	0.02	Assumed same accuracy of calculation as for glass	0.91

Table F4 Meteorological measurements

Symbol	Description	Error (±)	Reason for error	Average/Typical Value	
				26/01/06	05/05/06
C	Cloud cover	0.1	Human perception	0.2	0.2
E_{hg}	Solar irradiation horizontal global	1 %	Non-linearity for horizontal detector [8]	148 W m^{-2}	524 W m^{-2}
E_{vg}	Solar irradiation vertical global	2 %	Non-linearity for vertical detector [8]	340 W m^{-2}	333 W m^{-2}
E_{hdiff}	Solar irradiation horizontal diffuse	1 %	Non-linearity for horizontal detector [8]	38 W m^{-2}	89 W m^{-2}
T_{amb}	Ambient air temperature	1 ^oC	0.03^oC from calibration with thermocouples. 1^oC due to solar interference from observation.	6.6 ^oC	15.6 ^oC
v	Wind velocity	0.1 m s^{-1}	Calibration of anemometer [9]	0.9 m s^{-1}	1.1 m s^{-1}
θ	Incident Solar angle	0.26 ^{o}	Allowing for 10 minutes of time error in noon calculation.	45.8 ^{o}	73.5 ^{o}

Table F5 Thermocouple Measurements

Symbol	Description	Error (±)	Reason for error	Average Value	
				26/01/06	05/05/06
A1ND	Air entry ND	0.01 °C	From thermocouple calibration	8.1 °C	17.11 °C
A1WD	Air entry WD	0.02 °C		8.4 °C	19.36 °C
A1NS	Air entry NS	0.02 °C		6.2 °C	14.83 °C
A1WS	Air entry WS	0.02 °C		6.9 °C	16.40 °C
A5ND	Air exit ND	0.02 °C	From thermocouple calibration	14.0 °C	20.71 °C
A5WD	Air exit WD	0.03 °C		18.2 °C	24.11 °C
A5NS	Air exit NS	0.03 °C		11.3 °C	19.05 °C
A5WS	Air exit WS	0.02 °C		15.0 °C	23.41 °C
G2ND	Lower glass temperature ND	2.62 °C	From thermocouple calibration + information on glass measurement [10]	11.9 °C	20.59 °C
G2WD	Lower glass temperature WD	2.82 °C		12.6 °C	20.99 °C
G2NS	Lower glass temperature NS	2.61 °C		11.7 °C	20.20 °C
G2WS	Lower glass temperature WS	2.63 °C		14.2 °C	22.71 °C
G4ND	Upper glass temperature ND	2.62 °C	From thermocouple calibration + information on glass measurement [10]	12.9 °C	20.42 °C
G4WD	Upper glass temperature WD	2.85 °C		14.5 °C	22.44 °C
G4NS	Upper glass temperature NS	2.63 °C		N/A	18.95 °C
G4WS	Upper glass temperature WS	2.63°C		14.8 °C	23.78 °C
M2ND	Lower metal temperature ND	0.03 °C	From thermocouple calibration	19.7 °C	26.56 °C
M2WD	Lower metal temperature WD	0.03 °C		26.2 °C	31.11 °C
M2NS	Lower metal temperature NS	0.17 °C		19.3 °C	22.19 °C
M2WS	Lower metal temperature WS	0.03 °C		29.4 °C	33.93 °C
M4ND	Lower metal temperature ND	0.03 °C	From thermocouple calibration	21.2 °C	27.66 °C
M4WD	Lower metal temperature WD	0.03 °C		26.8 °C	33.09 °C
M4NS	Lower metal temperature NS	0.11 °C		18.6 °C	25.51 °C
M4WS	Lower metal temperature WS	0.31 °C		31.0 °C	37.40 °C

Table F5 Cont'd Thermocouple Measurements*

Symbol	Description**	Error (±)	Reason for error	Average Value
M4NDRR	Outer right hand surface temperature ND	0.02 °C	From thermocouple calibration	23.56 °C
M4WDRR	Outer right hand surface temperature WD	0.03 °C	From thermocouple calibration	19.28 °C
M4NSRR	Outer right hand surface temperature NS	0.79 °C	From thermocouple calibration of M4WDRR + average variation from M4WDRR during 60 hour period check	19.28 °C
M4WSRR	Outer right hand surface temperature WS	0.63 °C		19.28 °C
M4NDLL	Outer left hand surface temperature ND	0.04 °C	From thermocouple calibration	18.76 °C
M4WDLL	Outer left hand surface temperature WD	0.33 °C	From thermocouple calibration of M4NDLL + average variation from M4NDLL during 45 min period check	18.76 °C
M4NSLL	Outer left hand surface temperature NS	2.9 °C		18.76 °C
M4WSLL	Outer left hand surface temperature WS	0.03 °C	From thermocouple calibration	18.76 °C
M4NDR	Duct right hand surface temperature ND	0.03 °C	From thermocouple calibration	27.00 °C
M4WDR	Duct right hand surface temperature WD	0.03 °C		31.65 °C
M4NSR	Duct right hand surface temperature NS	0.65 °C		23.71 °C
M4WSR	Duct right hand surface temperature WS	0.04 °C		31.49 °C
M4NDL	Duct left hand surface temperature ND	0.03 °C	From thermocouple calibration	25.20 °C
M4WDL	Duct left hand surface temperature WD	0.02 °C		29.09 °C
M4NSL	Duct left hand surface temperature NS	0.38 °C		29.35 °C
M4WSL	Duct left hand surface temperature WS	0.03 °C		32.21 °C

* these thermocouple readings were not available from the experiment on 26/01/06
** left and right side identified from rear of experiment

Table F5 Cont'd Thermocouple Measurements*

Symbol	Description**	Error (±)	Reason for error	Average Value
M4ND Back	Back surface temperature ND	0.03 °C	From thermocouple calibration	16.69 °C
M4WD Back	Back surface temperature WD	0.74 °C	From thermocouple calibration of M4NDBack + average variation from M4NDBack during 60 hour period check	16.69 °C
M4NS Back	Back surface temperature NS	1.05 °C		16.69 °C
M4WS Back	Back surface temperature WS	1.11 °C		16.69 °C

* these thermocouple readings were not available from the experiment on 26/01/06
**left and right side identified from rear of experiment

F3 Error Propagation Calculations

F3.1 Primary Parameters

F3.1.1 Input Power

The errors associated specifically with components that are required to calculate the input power are listed below. Then the overall errors associated with the input power calculation are specified.

Vertical Diffuse Solar Irradiation

The vertical diffuse solar irradiation (E_{diff}) is calculated using Equation 1 from Section 5.1.1. The error in the albedo was found earlier in Appendix F. The error in E_{hg} and E_{hdiff} are found in Table F4. Equations F1 and F2 are used to calculate the error of the calculation as: 34 ± 4 W m^{-2} for 26/01/06 and 98 ± 14 W m^{-2} for 05/05/06.

Vertical Direct Solar Irradiation

The vertical direct solar irradiation (E_{vd}) is calculated by subtracting the vertical diffuse solar irradiation (E_{vdiff}) from the measured diffuse solar irradiation (E_{hg}). The error in E_{vdiff} is found in the previous section. The error in E_{hg} is found in Table F4. Equation

F1 is used to calculate the error of the calculation as: 306 ± 8 W m^{-2} for 26/01/06 and 236 ± 15 W m^{-2} for 05/05/06.

Direct Solar Gain

The direct solar gain (Q_{dir}) is calculated using equation 2 from Section 5.1.1. The error in E_{vd} was calculated earlier in Appendix F. The errors in A_g are shown in Table F14 and for SHGC in Table F22. Equation F2 is used to calculate the error of the calculation, and the results are shown for each duct in Table F6.

Table F6 Value ± Error of Direct Solar Gain (Q_{dir})

Date	Q_{dir} (W)	ND	WD	NS	WS
26/01/06	Error	3	7	3	7
	Value	47	96	47	93
05/05/06*	Error	33	16	13	12
	Value	33	67	33	65

* The errors are high because the Direct Solar Gain is related to the SHGC calculation. The SHGC calculation has large errors because it is related to the difference between the glass surface and sky temperatures. This temperature difference is small in relation to the propagated error in the sky temperature and the mean glass surface temperature. The error is particularly high for duct ND because the temperature difference between the glass temperature and the sky temperature is very low (0.2 ^{o}C). These errors do not apply to the data for 26/01/06 since these use textbook values of the SHGC.

Diffuse Solar Gain

The diffuse solar gain (Q_{diff}) is calculated using equation 3 from Section 4.1.1. The errors in A_g are shown in Table F14, SHGC in F22 and E_{vdiff} in F6. Equation F2 is used to calculate the error of the calculation, and the results are shown for each duct in Table F7.

Table F7 Value ± Error of Diffuse Solar Gain (Q_{diff})

Date	Q_{diff} (W)	ND	WD	NS	WS
26/01/06	Error	1	1	1	1
	Value	5	10	5	9
05/05/06*	Error	12	7	5	5
	Value	15	30	15	29

* The errors are high because the Direct Solar Gain is related to the SHGC calculation. The SHGC calculation has large errors because it is related to the difference between the glass surface and sky temperatures. This temperature difference is small in relation to the propagated error in the sky temperature and the mean glass surface temperature. The error is particularly high for duct ND because the temperature difference between the glass temperature and the sky temperature is very low (0.2 ^{o}C). These errors do not apply to the data for 26/01/06 since these use textbook values of the SHGC.

Input Power

The input power (Q_{in}) is calculated using equation 4 from Section 4.1.1. The errors in Q_{dir} and Q_{diff} were calculated previously in Appendix F. Equation F1 is used to calculate the error of the calculation, and the results are shown for each duct in Table F8.

Table F8 Value ± Error of Input Power (Q_{in})

Date	Q_{in} (W)	ND	WD	NS	WS
26/01/06	Error	3	7	3	7
	Value	51	106	51	102
05/05/06*	Error	35	18	14	14
	Value	47	97	47	94

*The errors are high because the Input Power is related to the Diffuse and Direct Solar Gains. Both the Diffuse and Direct Solar Gains are related to the SHGC calculation. The SHGC calculation has large errors because it is related to the difference between the glass surface and sky temperatures. This temperature difference is small in relation to the propagated error in the sky temperature and the mean glass surface temperature. The error is particularly high for duct ND because the temperature difference between the glass temperature and the sky temperature is very low (0.2 ^{o}C).

F3.1.2 Useful Power Output

The Useful Power Output (Q_{out}) is calculated using equation 5 from Section 4.1.2. The error in the air mass flow ($\dot{m}$) is found in Table F2, the specific heat capacity in Table F2, the air exit temperatures in Table F5. The error in the ambient temperature was calculated previously in Appendix F. Equations F1 and F2 are used to calculate the error of the calculation, and the results are shown for each duct in Table F9.

Table F9 Value ± Error of Useful Power Output (Q_{out})

Date	Q_{out} (W)	ND	WD	NS	WS
26/01/06	Error	0.7	1.2	0.5	0.9
	Value	35	63	24	43
05/05/06	Error	0.5	0.9	0.4	0.8
	Value	24	46	18	40

Power Losses

The errors associated specifically with components that are required to calculate the power losses are listed below. Then the overall errors associated with the power loss calculation are specified.

Losses due to Reflection

The losses due to reflection (Q_R) are calculated using equations 8, 11 and 13 from Section 5.1.3.1. The error in reflectivity of the duct surface (R_p) is found in Table F3, the diffuse reflectivity of the glass in Table F1, the Direct Solar Gain in Table F6, the Diffuse Solar Gain in Table F7 and the diffuse Solar Heat Gain Coefficient in Table F22. Equations F1 and F2 are used to calculate the error of the calculation, and the results are shown for each duct in Table F10.

Table F10 Value ± Error of Power Loss due to Reflection (Q_R)

Date	Q_R (W)	ND	WD	NS	WS
26/01/06	Error	0.4	0.8	0.4	0.8
	Value	1.9	3.9	1.9	3.8
05/05/06*	Error	1.8	1.0	0.8	0.8
	Value	1.9	3.8	1.9	3.7

*The errors are high because the power loss due to reflection is related to the SHGC calculation. The SHGC calculation has large errors because it is related to the difference between the glass surface and sky temperatures. This temperature difference is small in relation to the propagated error in the sky temperature and the mean glass surface temperature. The error is particularly high for duct ND because the temperature difference between the glass temperature and the sky temperature is very low (0.2 ^{o}C).

Power Losses from Surface

The loss from the surface (Q_{sur}) is calculated using Equation 23 in Section 4.1.3.2. The error in the external heat transfer coefficients due to convection are given in Section F3.2, while the coefficients due to radiation are found in Table F18. The error in the thermal resistance due to conductivity is found in Table F23. The error in the area of the prototype elements is given in Table F14 and the error in the surface temperatures in Table F5. The errors associated with the ambient, sky and average glass surface temperatures are calculated later in Appendix F. Equations F1 and F2 are used to calculate the error of the calculation, and the results are shown for each duct in Table F11.

Table F11 Value ± Error of Surface Power Loss (Q_{Sur}) 05/05/06

Surface	Q_{Sur} (W)	ND	WD	NS	WS
Front	Error	173 [b]	65 [b]	50 [b]	39 [b]
	Value	12	26	10	32
Back	Error	0.4	0.9	0.3	1.1
	Value	1.3	2.7	0.9	3.2
Right [a]	Error	0.7	1.0	0.4	0.2
	Value	6.6	9.6	3.4	7.0
Left [a]	Error	0.5	0.8	0.5	0.8
	Value	5.5	8.1	4.1	7.4

[a] side identified from rear of experiment

[b] The error is particularly high for the identified surfaces because the surface power loss is related to the difference between the surface temperature and the sky temperature. This temperature difference is small in relation to the propagated error in the sky temperature and the mean glass surface temperature.

Power Losses

The total power loss (Q_{loss}) is calculated using Equation 19 in Section 4.1.3. The error in the reflection losses are found in Table F10. The error in the surface power losses are found in Table F11. Equation F1 is used to calculate the error of the calculation, and the results are shown for each duct in Table F12.

Table F12 Value ± Error of Power Loss (Q_{loss})

Date	Q_{loss} (W)	ND	WD	NS	WS
26/01/06	Error	17	26	22	560
	Value	29	52	24	53
05/05/06	Error	174	65	50	40
	Value	27	50	20	54

The errors are high because the total power loss is related to the power losses from the front surface due to reflection and radiation. The losses due to reflection are related to the SHGC which is in turn related to the difference between the sky and the average glass surface temperature – these both have large propagated errors. The losses due to radiation are related to SHGC as well as directly related to the difference between the surface and sky temperatures.

F3.1.3 Model Effectiveness

The model effectiveness is calculated using Equation 25 in Section 4.4.1. The errors in the input power, useful power output and power losses were calculated previously in Appendix F. Equations F1 and F2 are used to calculate the error of the calculation, and the results are shown for each duct in Table F13.

Table F13 Value ± Error of Model Effectiveness

Date	Model Effectiveness	ND	WD	NS	WS
26/01/06	Error	27	24	57	688
	Value	98	104	124	118
05/05/06	Error	318	70	172	45
	Value	92	101	126	101

The errors are high because the model effectiveness is related to the input power and the power losses. Both of these components have large errors which are related to the surface to sky temperature difference being small in comparison with the propagated errors in these parameters.

F3.2 Secondary Parameters

Albedo

The experiment described in Section 4.2.6.1 to determine the albedo requires one horizontal pyranometer reading to be divided by another. The resolution of a horizontal pyranometer is 1% (Table F4). Equation F2 is used to calculate the propagated error of the average albedo as 0.083 ± 0.001. However, during the five days that the albedo was monitored, it was found to vary from 0.055 to 0.159 (Figure 1). This indicates that the propagated error from the instrument resolution is not the overriding factor. The peak albedo values appear to occur either early in the morning or late in the evening. This could be due to reflections off of specific objects at those solar angles. However, the overall variation in the results masks the calculated propagated error from the resolution of the pyranometers. The albedo can be stated with 95% confidence as 0.08 ± 0.026.

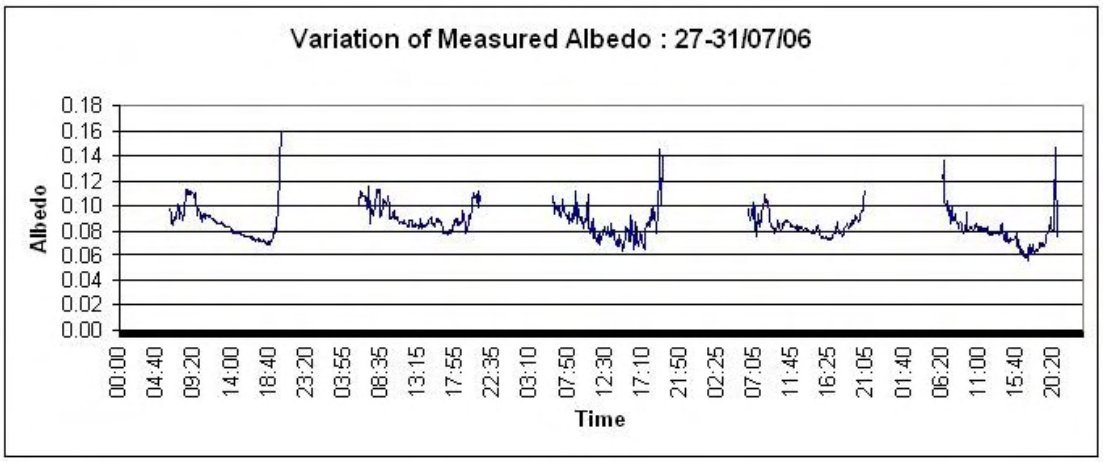

Figure 1. Variation of Measured Albedo: 27-31/07/06

Area

Several calculations require the area of an element of the prototypes. Each element which is composed of a length (glass or duct) and a width or depth will have approximately the same resolution errors propagated through the calculations. The errors in the duct measurements (width, depth and length) are found in Table F3. Equation F2 is used to calculate the error in the area, and the results are shown for each duct in Table F14.

Table F14 Value ± Error of Area of Prototype Elements

	m^2	ND	WD	NS	WS
	Error	0.002	0.002	0.002	0.002
$A_{g\ solar}$	Value	0.192	0.395	0.192	0.382
$A_{f\ ext}$	Value	0.336	0.576	0.336	0.576
$A_{b\ ext}$	Value	0.425	0.684	0.425	0.665
$A_{s\ ext}$	Value	0.672	0.708	0.504	0.528

The cross sectional area of the ducts is composed of a width and depth, and the relevant errors are found in Table F3. Equation F2 is used to calculate the error in the area, and the results are shown for each duct in Table F15.

Table F15 Value ± Error of Cross Sectional Area

A_c (m^2)	ND	WD	NS	WS
Error	0.0001	0.0002	0.0001	0.0002
Value	0.0111	0.0229	0.0041	0.0082

Heat Transfer Coefficients

The internal convection and radiation heat transfer coefficients were not calculated for the experiment on 26/01/06. This is because the appropriate thermocouples were not present at this time. Therefore, textbook values of the Solar Heat Gain Coefficient were used, rather than a calculation that used the heat transfer coefficients.

Heat Transfer Coefficient – Internal Convection (h_{ci})

Equation C2 is used to calculate the internal convection heat transfer coefficient. The errors in the conductivity of air are shown in Table F2, Nusselt number in Table F20 and the length in Table F3. Equation F2 is used to calculate the error in the calculation, and the results are shown for each duct in Table F16.

Table F16 Value ± Error of Internal Convection Heat Transfer Coefficient

Date	h_{ci}	ND	WD	NS	WS
05/05/06	Error	0.01	0.01	0.02	0.01
	Value	0.10	0.08	0.16	0.08

Heat Transfer Coefficient – Internal Radiation (h_{ri})

Equation C27 is used to calculate the internal radiation heat transfer coefficient. The errors in the average glass temperature and average duct temperature are shown in Table F25, and the glass emissivity in Table F1. Equations F2 and F3 are used to calculate the error in the calculation, and the results are shown for each duct in Table F17.

Table F17 Value ± Error of Internal Radiation Heat Transfer Coefficient

Date	h_{ri}	ND	WD	NS	WS
05/05/06	Error	2.35	1.67	2.94	1.48
	Value	5.39	5.56	5.31	5.67

Heat Transfer Coefficient – External Convection (h_{co})

Equations C25 and C26 can be used to calculate the external convection heat transfer coefficient. The error in the wind speed measurement is given in Table F4 and the height of the system in Table F3. Equations F2 and F3 are used to calculate the error in the calculation as 2.0 ± 0.1 for 26/01/06 and 2.2 ± 0.1 for 05/05/06.

Heat Transfer Coefficient – External Radiation (h_{ro})

Equation 10 in Section 4.1.1.2 is used to calculate the external radiation heat transfer coefficient. The errors in the glass emissivity are shown in Table F1. The errors in the average surface temperatures are shown in Table F25, the errors in the ambient temperature and the sky temperature are discussed in the same section. Equations F2 and F3 are used to calculate the error in the calculation, and the results are shown for each duct in Table F18.

Table F18 Value ± Error of External Radiation Heat Transfer Coefficient

Date	h_{ro}		ND	WD	NS	WS
26/01/06	Front	Error	9[c]	6[c]	13[cd]	5[c]
		Value	5	5	5	5
	Back	Error	6[ce]	6[ce]	6[ce]	6[ce]
		Value	7	7	7	7
	Left[a]	Error	2[ce]	2[ce]	2[ce]	436[ce]
		Value	7	7	7	7
	Right[a]	Error	5[ce]	2[ce]	2[ce]	2[ce]
		Value	7	7	7	7
		Value	5.1	5.1	5	5
05/05/06	Front	Error	113[b]	19[b]	40[b]	9[b]
		Value	5	5	5	5
	Back	Error	0.2	5[c]	7[c]	7[c]
		Value	5.0	5	5	5
	Left[a]	Error	0.1	0.8[c]	7[c]	4[bc]
		Value	5.1	5.1	5	5
	Right[a]	Error	7[b]	0.1	2[c]	1[c]
		Value	5	5.1	5	5

[a] side identified from rear of experiment

[b] The error is high for the identified surfaces because the difference between the surface temperature and the sky temperature is small in relation to the propagated error in the sky temperature calculation. The error is particularly high for duct ND since the difference between the surface temperature and the sky temperature is only 0.2^{o}C.

[c] The error is high for the identified surfaces because the difference between the surface temperature and the external temperature is very low in comparison with the error in the surface temperature measurement (these are assumed temperatures).

[d] The error is particularly high for this surface since one thermocouple had broken, and an average temperature could not be calculated.

[e] The error is particularly high for these surfaces since measured values were not available. The basis of the assumed values is described in the section on temperatures.

Hydraulic Diameter

Equation B2 is used to calculate the hydraulic diameter (D_h). The errors in the duct measurements (width and depth) are found in Table F3. Equations F1 and F2 are used to calculate the error in the calculation, and the results are shown for each duct in Table F19.

Table F19 Value ± Error of Hydraulic Diameter

D_h (m^2)	ND	WD	NS	WS
Error	0.002	0.002	0.002	0.002
Value	0.105	0.144	0.058	0.068

Nusselt Number

The Nusselt number (Nu) was not calculated for the experiment on 26/01/06. This is because necessary temperature data was not available.

Laminar

Equation C10 is used to calculate the Nusselt Number for laminar flow through a pipe. The error in the Reynold number is shown in Table F21, the hydraulic diameter in Table F19, the length of the duct in Table F3, and dynamic viscosity of air in Table F2. The error in the Prandtl number is shown in the next section. Equations F2 and F3 are used to calculate the propagation error. The results are shown for each duct in Table F20.

Turbulent

Equations C14 and C15 are used to calculate the Nusselt Number for turbulent flow through a pipe. The error in the Reynold number is shown in Table F21, the mean air temperature in F24 and mean duct temperature in Table F25, the hydraulic diameter in Table F19, the length of the duct in Table F3. The error in the Prandtl number is shown in the next section. Equations F2 and F3 are used to calculate the propagated error. The results are shown for each duct in Table F20.

Table F20 Value ± Error of Nusselt Number

Date	Nu		ND	WD	NS	WS
05/05/06	laminar	Error	0.3	0.3	0.9	0.6
		Value	9.3	6.3	15.1	8.0
	turbulent	Error	1.1	0.9	1.8	0.9
		Value	9.4	8.1	15.0	7.7

Prandtl Number

Equation B6 is used to calculate the Prandtl Number (Pr). The errors in the specific heat capacity, thermal conductivity and dynamic viscosity of air are found in Table F2. Equation F2 is used to calculate the error in the calculation as 0.7 ± 0.05.

Reynolds Number

Equation B5 is used to calculate the Reynolds number (Re). The errors in air mass flow and dynamic viscosity are found in Table F2, the errors in hydraulic diameter in Table F19, the errors in the cross sectional area in Table F15. Equation F2 is used to calculate the error in the calculation, and the results are shown for each duct in Table F21. The Reynolds number could not calculated for the experiment on 26/01/06 due to lack of data.

Table F21 Value ± Error of Reynolds Number

Date	Re	ND	WD	NS	WS
05/05/06	Error	155	111	281	157
	Value	2576	1927	4130	2354

Solar Heat Gain Coefficient

The procedure for calculating the solar heat gain coefficient (SHGC) is given in Appendix G. The angle dependent version ($SHGC_{\theta}$) requires the use of angle dependent transmission and absorption figures. While the diffuse version ($SHGC_{diff}$) requires the use of diffuse transmission and absorption figures.

The error propagation is derived from the internal heat transfer coefficients for radiation and convection and the external heat transfer coefficients for radiation and convection (Tables F16 and F17), the thermal resistance due to conductivity (Table F23) and the solar absorption from Table F1. The errors in the transmission are discussed in the next section. The propagated error in the angle dependent and diffuse SHGC are shown in Table F22.

Table F22 Value ± Error of SHGC

Date	SHGC		ND	WD	NS	WS
05/05/06	$SHGC_{\theta}$	Error	0.5	0.1	0.2	0.1
		Ave Value	0.5	0.5	0.5	0.5
	$SHGC_{diff}$	Error	0.6	0.1	0.2	0.1
		Value	0.8	0.8	0.8	0.8

The errors are high because the SHGC calculation is related to the difference between the surface and sky temperatures. This temperature difference is small in relation to the propagated error in the sky temperature and the mean glass surface temperature.

The earlier experiment (25th January 2006) took place before the required thermocouples had been put in place to allow the SHGC to be calculated. For these results, the SHGC figures listed in ASHRAE[2] were used. To check the validity of using the published SHGC figures, they were compared with the calculated results above. This comparison is shown in (Figure 2). The textbook values are only marginally lower than the calculated values, and their use appears to be acceptable. The errors associated with the textbook SHGC values are ± 0.05[2].

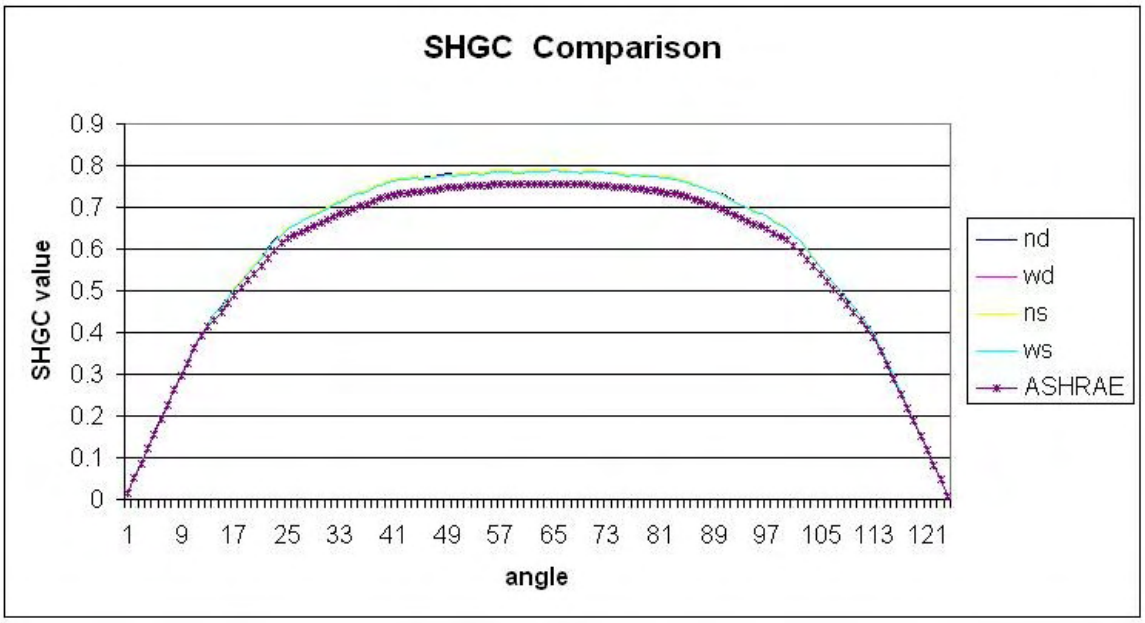

Figure 2. Comparison of SHGC

Solar Transmission

For a glazing component transmissivity (τ), absorptivity (α) and reflectivity (R) are related: $\tau+\alpha+R=1$. The solar components for 6mm thick float glass [2] exceed 1, indicating a misprint in the tables. Since the tables indicate a higher transmissivity for 6mm thick float glass than for 3mm thick float glass, this seems to be the misprint. For this reason, the transmissivity was calculated from $1-(\alpha+R)$. The errors in the absorption and reflectivity components are shown in Table F1. Equation F1 is used to calculate the error for the average transmissivity as 0.49 ± 0.07.

Thermal Resistance due to Conductivity

Equation 11 in Section 4.1.1.2.1 shows the calculation for thermal resistance due to conductivity. The error in the thickness of the glass is shown in Table F1, of the steel, zinc, paint and insulation in Table F23.

Table F23 Value ± Error of Thermal Resistance due to Conductivity

R	m K W^{-1}	ND	WD	NS	WS
Glass / front	Error	0.0002			
	Value	0.006			
Back	Error	1	1	1	1
	Value	4	4	4	4
Left*	Error	0.3	0.3	0.3	0.3
	Value	1.0	1.0	1.0	1.0
Right*	Error	0.3	0.3	0.3	0.3
	Value	1.0	1.0	1.0	1.0

*side identified from rear of experiment

Temperatures

Ambient Temperature

As stated in Section 4.2.7.3 the ambient air temperature is calculated from the average of the readings from thermocouple A1NS and A1WS (errors given in Table F5).

Equation F1 is used to calculate the error in the calculation as 6.56 ± 0.01 ^{o}C for 26/01/06 and 15.61 ± 0.01 ^{o}C for 05/05/06.

Average Air Temperature in Duct

The average air temperature for each duct is calculated from the average of the readings of the entry and the exit thermocouple (errors given in Table F5). Equation F1 is used to calculate the error in the calculation, and the results are shown for each duct in Table F24. The average air temperature was not calculated for the experiment on 26/01/06. This is because textbook values of the Solar Heat Gain Coefficient were used, rather than a calculation that used the average air temperature.

Table F24 Value ± Error of Average Air Temperature

Date	T_{ave} (^{o}C)	ND	WD	NS	WS
05/05/06	Error	0.01	0.02	0.02	0.01
	Value	18.16	19.86	17.33	19.51

Average Surface Temperature

The average duct temperature is calculated from the average of the readings of the two glass surface temperatures and the four metal surface temperatures (errors given in Table F5). The average glass temperature is calculated from the average of the readings of the two glass surface temperatures (Table F5). The average back temperature is calculated from the average of the readings of the two back surface temperatures (Table F5). Equation F1 is used to calculate the error in the calculations, and the results are shown for each duct in Table F25. The average duct temperature was not calculated for the experiment on 26/01/06. This is because textbook values of the Solar Heat Gain Coefficient were used, rather than a calculation that used the average duct temperature.

Table F25 Value ± Error of Average Surface Temperatures

Date	Temperature		ND	WD	NS	WS
26/01/06	T_{glass} (^oC)	Error	2	2	3*	2
		Value	12	14	12	15
05/05/06	T_{duct} (^oC)	Error	0.5	0.5	0.5	0.5
		Value	25.0	28.5	23.0	30.5
	T_{glass} (^oC)	Error	2	2	2	2
		Value	21	22	20	23

*due to thermocouple failure, there was only one temperature measurement available for the glass temperature on duct NS, therefore the value is not an average value.

.

Sky Temperatures

The methodology used to calculate the sky temperature is shown in Section 4.1.1.2.1. The error in T_{amb} is shown above. Equations F1, F2 and F3 are used to calculate the error in the calculation as 9 ± 3^oC for 26/01/06 and 20 ± 3^oC for 05/05/06.

F4 References

1. Lindberg, V. *Uncertainties and Error Propagation: Part 1 of a Manual on Uncertainties, Graphing and the Vernier Caliper*. 2000 [cited 24th March 2007]; Available from: http://www.rit.edu/~uphysics/uncertainties/Uncertaintiespart2.html#addsub.
2. ASHRAE, *2005 ASHRAE Handbook: Fundamentals, SI Edition*, ed. R.a.A.C.E. American Society of Heating, Inc. 2005, Atlanta: ASHRAE; 1-931862-71-0.
3. British Standards Institution, *British Standard; BS EN 572-2:2004 Glass in building - Basic soda lime silicate glass products - Part 2: Float Glass*, 1998.
4. British Standards Institution, *British Standard; BS EN12898:2004 Glass in building - Determination of the emissivity*, 2001.
5. The Engineering Toolbox. *Air Properties - temperature, density, specific heat, thermal conductivity, expansion coefficient, kinematic viscosity and Prandtl number for temperatures between -150^oC and 400^oC*. [cited 16th October 2006]; Available from: http://www.engineeringtoolbox.com/air-properties-d_156.html.
6. British Standards Institution, *Measurement of fluid flow by means of pressure differential devices inserted into circular cross-section conduits running full - Part 1: General principles and requirements*, BS EN ISO 5167-1, 2003.
7. Maxted, J., *Personal Communication: E-mail regarding heat absorption of Colorcoat Armacor*, to E.V. Stevenson, 2006: Liverpool.
8. Kipp & Zonen, *Pyranometer for Outdoor Installation CM5 - CM6*.
9. Vector Instruments. *A100R Contact Closure (Switching) Anemometer*. [cited 24th July 2006]; Available from: http://www.windspeed.co.uk/ws/index.php?option=displaypage&Itemid=67&op=page#downloads.
10. Papailiou, G. *Measurement of Glass Surface Temperature* 1995: Masters of Science; School of Engineering at University of Wales, Cardiff.

Appendix G - Data for Design Model Development

Table G1 Measured mean glazed surface temperature (Averaged over 1 hour periods)

Time period	Average Glazed Surface Temperature (^{o}C)			
	ND	WD	NS	WS
26/01/06				
09:00	2.5	2.7	Not available due to thermocouple failure	2.9
10:00	13.1	14.6		16.4
11:00	15.7	18.3		19.9
12:00	18.4	21.9		23.9
13:00	19.8	23.4		25.2
14:00	18.5	21.6		23.5
15:00	15.9	17.6		19.0
16:00	11.4	11.5		12.2
17:00	4.5	4.5		4.3
05/05/06				
08:00	12.7	13.0	12.6	13.8
09:00	14.9	15.4	14.5	16.7
10:00	20.2	21.5	19.6	24.2
11:00	22.9	25.4	22.4	28.7
12:00	25.0	28.7	24.6	31.4
13:00	26.8	30.9	26.0	33.2
14:00	26.2	29.9	25.5	32.0
15:00	24.4	26.8	23.8	28.8
16:00	22.9	23.5	21.5	24.6
17:00	19.5	18.7	17.7	19.2
18:00	16.7	15.6	15.0	15.8
19:00	16.1	14.9	14.7	15.0
20:00	15.0	14.3	14.0	14.3

Table G2 Measured mean absorbing surface temperature (Averaged over 1 hour periods)

Time period	Average Absorbing Surface Temperature (^{o}C)			
	ND	WD	NS	WS
26/01/06				
09:00	4.1	7.5	5.1	7.4
10:00	23.9	39.4	24.3	39.5
11:00	33.6	49.6	30.0	49.0
12:00	40.3	57.6	34.4	56.6
13:00	39.9	57.6	35.5	57.6
14:00	33.9	48.9	32.2	52.6
15:00	25.7	33.3	24.8	40.5
16:00	16.7	18.8	14.7	23.1
17:00	6.8	7.4	5.4	6.9
05/05/06				
08:00	13.5	15.1	13.3	17.1
09:00	16.7	19.7	16.0	23.5
10:00	24.1	30.8	23.9	40.2
11:00	30.5	43.6	30.1	50.9
12:00	37.7	52.3	33.7	55.8
13:00	41.5	54.1	34.0	56.8
14:00	37.9	49.2	32.6	52.9
15:00	32.1	37.8	29.8	45.4
16:00	28.6	29.4	25.2	33.8
17:00	25.3	23.3	19.8	24.3
18:00	21.3	19.2	16.3	19.4
19:00	20.2	18.2	15.8	18.1
20:00	17.9	17.4	15.2	16.8

Table G3 Measured mean air temperature (Averaged over 1 hour periods)

Time period	Average Air Temperature (^{o}C)			
	ND	WD	NS	WS
26/01/06				
09:00	2.7	3.6	2.9	3.5
10:00	10.3	14.2	9.1	12.2
11:00	13.2	18.2	10.8	15.0
12:00	14.9	21.1	11.9	17.2
13:00	16.3	22.3	12.6	17.8
14:00	15.6	20.6	12.3	16.7
15:00	13.5	16.7	10.8	13.4
16:00	10.2	10.8	7.9	9.3
17:00	5.3	5.7	4.4	4.9
05/05/06				
08:00	12.3	12.7	12.3	13.3
09:00	13.8	14.6	13.6	15.3
10:00	16.8	19.1	16.6	19.7
11:00	18.6	22.5	18.4	22.2
12:00	20.7	25.1	20.2	24.1
13:00	22.2	26.5	21.3	25.2
14:00	22.0	25.8	21.1	24.3
15:00	21.1	23.6	20.3	22.6
16:00	20.3	21.0	19.0	20.7
17:00	18.2	17.7	16.5	17.6
18:00	16.5	16.0	14.9	15.7
19:00	16.1	15.6	14.7	15.4
20:00	15.3	15.1	14.4	14.8

Table G4 Measured Exit air temperature (Averaged over 1 hour periods)

Time period	Exit Air Temperature (^{o}C)			
	ND	WD	NS	WS
26/01/06				
09:00	3.1	4.7	3.4	4.3
10:00	14.1	21.0	12.4	18.0
11:00	18.1	27.0	14.7	22.5
12:00	20.9	31.4	16.5	26.1
13:00	22.5	32.7	17.5	26.9
14:00	21.0	29.9	16.7	24.7
15:00	17.4	23.3	14.3	18.8
16:00	12.6	14.2	9.9	12.3
17:00	5.7	6.6	4.7	5.3
05/05/06				
08:00	12.6	13.4	12.6	14.5
09:00	14.7	16.4	14.3	17.7
10:00	19.0	23.7	18.7	24.9
11:00	21.8	29.6	21.3	28.9
12:00	24.5	33.4	23.6	31.5
13:00	26.4	35.1	24.7	32.4
14:00	26.1	33.5	24.2	30.6
15:00	24.5	29.5	22.8	27.5
16:00	23.4	24.6	20.8	24.2
17:00	20.9	19.8	17.4	19.7
18:00	18.4	17.4	15.2	16.8
19:00	17.7	16.6	14.9	16.2
20:00	16.3	16.0	14.4	15.3

Table G5 Measured mean glazed surface temperature (Averaged over 1 hour periods) – 03/07/06

Time period	Average Glazed Surface Temperature (^{o}C)			
	ND	WD	NS	WS
09:00	27.3	27.5	27.9	Thermocouple damaged
10:00	32.5	32.3	33.8	
11:00	35.7	36.1	38.0	
12:00	38.8	39.4	41.5	
13:00	39.4	40.6	42.0	
14:00	39.0	40.2	41.3	
15:00	35.8	36.9	37.9	
16:00	35.2	34.8	35.9	
17:00	33.5	32.9	35.3	
18:00	30.2	29.8	29.2	

Table G6 Measured mean absorbing surface temperature (Averaged over 1 hour periods) – 03/07/06

Time period	Average Absorbing Surface Temperature (^{o}C)			
	ND	WD	NS	WS
09:00	27.5	32.2	29.8	35.7
10:00	31.4	38.2	36.6	44.9
11:00	34.7	46.1	42.4	54.4
12:00	38.7	54.0	47.0	59.9
13:00	39.9	57.2	47.3	60.4
14:00	39.4	56.5	46.6	59.1
15:00	35.6	47.9	42.4	52.2
16:00	35.6	41.8	39.5	45.8
17:00	34.0	38.7	35.6	41.4
18:00	30.0	33.7	30.4	34.4

Table G7 Measured mean air temperature (Averaged over 1 hour periods) – 03/07/06

Time period	Average Air Temperature (^{o}C)			
	ND	WD	NS	WS
09:00	26.6	26.5	26.3	24.5
10:00	30.4	30.1	30.5	26.5
11:00	33.2	33.0	33.8	28.4
12:00	35.8	35.4	36.1	29.8
13:00	36.7	36.4	36.6	30.1
14:00	36.7	36.3	36.5	30.1
15:00	34.2	33.9	34.4	28.8
16:00	33.7	32.4	33.1	28.4
17:00	32.6	31.3	31.4	28.4
18:00	29.7	28.8	28.3	26.9

Table G8 Measured Exit air temperature (Averaged over 1 hour periods) – 0 03/07/06

Time period	Exit Air Temperature (^{o}C)			
	ND	WD	NS	WS
09:00	27.6	27.5	27.1	23.6
10:00	32.5	31.9	32.8	24.8
11:00	36.2	35.8	37.2	26.6
12:00	39.7	38.9	40.1	27.6
13:00	40.5	39.8	40.3	27.2
14:00	40.2	39.3	39.8	26.8
15:00	36.9	36.2	37.2	26.0
16:00	36.8	34.4	35.7	26.4
17:00	35.7	33.1	33.2	27.2
18:00	31.8	30.0	29.1	26.2

Appendix H - Procedure for Design Models

Forced Convection – Basic Model

H1 Ong Model for Forced Convection (Ong_{fc}) [1]

The procedure for the Ong_{fc} model is:

1. Obtain the following data:
   - Duct – air mass flow ($\dot{m}$ - kg s^{-1}), duct width (W - m), duct depth (b - m), duct length (L - m), emissivity of glass (ε_g) and absorber surface (ε_p), the thickness of insulating layers on the back of the duct (d_b - m), the thermal conductivity of insulating layers on the back of the duct (k_{ins} - W m^{-1} K^{-1}), the absorptivity of glass (α_g) and the absorbing surface (α_p), the transmissivity of glass (τ_g)
   - Meteorological – ambient temperature (T'_{amb} - K), the fluid inlet temperature ($T'_{f,i}$ - K) if different from ambient temperature, the incident solar radiation intensity (E_{vg} - W m^{-2}), wind velocity (v - m s^{-1})
   - Constants – Stefan Boltzmann constant (σ - W m^{-2} K^{-4})
2. calculate the hydraulic diameter (D_h – m) for parallel plate ducts (B4) and cross sectional area (A_c - m^2)
3. divide the collector into short (0.5 – 1.0m) sections for which the temperature gradient can be assumed to be linear

For the first section:

4. guess the initial mean temperature of the air ($\overline{T}'_f$), glass ($\overline{T}'_g$) and solar absorber ($\overline{T}'_p$). A reasonable first assumption is that they are equal to T'_{amb}+ 1K.
5. calculate the sky temperature (T'_s - K) using Swinbank's equation [1]:

$$T'_s = 0.0552 T'^{1.5}_{amb} \qquad \text{C31}$$

6. calculate the wind convection heat transfer coefficient (h_w) using McAdam's correlation [1]:

$$h_w = 5.7 + 3.8v \qquad \text{C20}$$

7. calculate the dynamic viscosity (μ – kg m^{-1} s^{-1}) using [1]:

$$\mu = \left[1.983 + 0.00184(\overline{T}_f - 27)\right]10^{-5} \qquad \text{H1}$$

8. calculate the Reynolds number (Re) using [2]:

$$\text{Re} = \frac{\dot{m}D_h}{A_c\mu} \qquad \text{B5}$$

9. calculate the specific heat capacity (c_p – J kg^{-1}K^{-1}) of the air using [1]:

$$c_p = \left[1.0057 + 0.000066(\overline{T}_f - 27)\right]10^3 \qquad \text{H2}$$

The factor of 1000 was missing from the equation as printed in this paper, but was present in Ong's 2003 paper [3]

10. calculate the thermal conductivity (k – W m^{-1} K^{-1}) of the air using [1]:

$$k = 0.02624 + 0.0000758(\overline{T}_f - 27) \qquad \text{H3}$$

11. calculate the Prandtl number (Pr) using [2]:

$$\text{Pr} = \frac{c_p\mu}{k} \qquad \text{B6}$$

12. calculate the Nusselt number (Nu) using Nusselt's correlation [1]:

$$Nu = 0.036\,\text{Re}^{0.8}\,\text{Pr}^{1/3}\left(\frac{D_h}{L}\right)^{0.055} \qquad \text{C5}$$

13. calculate the convective heat transfer coefficient for the glass surface (h_g) and the absorber surface (h_p)using [2]:

$$h_g = h_p = \frac{kNu}{D_h} \qquad \text{C2}$$

14. calculate the radiative heat transfer coefficient between glass and absorbing surface (h_{rpg}) using [1]:

$$h_{rpg} = \frac{\sigma\left(\overline{T}'^2_g + \overline{T}'^2_p\right)\left(\overline{T}'_g + \overline{T}'_p\right)}{\frac{1}{\varepsilon_g} + \frac{1}{\varepsilon_p} - 1} \qquad \text{C28}$$

15. calculate the radiative heat transfer coefficient between the glass and the sky (h_{rs}) using [1]:

$$h_{rs} = \frac{\sigma\varepsilon_g\left(\overline{T}'_g + T'_s\right)\left(\overline{T}'^2_g + T'^2_s\right)\left(\overline{T}'_g - T'_s\right)}{\left(\overline{T}'_g - T'_{amb}\right)} \qquad \text{C30}$$

16. calculate the overall top heat loss coefficient (U_t – W m^{-2} K^{-1}) using [1]:

$$U_t = h_w + h_{rs} \qquad \text{H4}$$

17. calculate the overall bottom heat loss coefficient (U_b – W m^{-2} K^{-1}) using [1]:

$$U_b = \frac{1}{i = \sum_1^n \frac{d_{bi}}{k_{bi}} + \frac{1}{h_w}} \qquad \text{H5}$$

18. calculate the solar radiation heat flux absorbed by the glass surface (S_1 – W m^{-2}) using [1]:

$$S_g = \alpha_g E \qquad \text{A15}$$

19. calculate the solar radiation heat flux absorbed by the absorbing surface (S_2 – W m^{-2}) using [1]:

$$S_p = \tau_g \alpha_p E \qquad \text{A16}$$

20. calculate Γ using [1]:

$$\Gamma = \frac{2\dot{m}c_p}{WL} \qquad \text{H6}$$

21. The temperatures can be found by solving the matrix equation [1]:

$$[T] = [A]^{-1}[B] \qquad \text{A11}$$

where:

$$[T] = \begin{bmatrix} \overline{T}'_g \\ \overline{T}'_f \\ \overline{T}'_p \end{bmatrix} \quad [A] = \begin{bmatrix} h_g + h_{rpg} + U_t & -h_g & -h_{rpg} \\ h_g & -(h_g + h_p + \Gamma) & h_p \\ -h_{rpg} & -h_p & h_p + h_{rpg} + U_b \end{bmatrix}$$

and $[B] = \begin{bmatrix} U_t T'_{amb} + S_g \\ -\Gamma T'_{f,i} \\ S_p + U_b T'_{amb} \end{bmatrix}$

22. Solving for the temperatures is an iterative procedure. The calculated temperatures should be used as the next guess for the initial temperatures (used in step 4), and the process repeated until the difference between the initial and the calculated temperatures is less than 0.01°C.
23. The difference between the air inlet temperature ($T'_{f,i}$) and the mean air temperature ($\overline{T}'_f$) calculated in step 21 should be used to determine the air outlet temperature from the duct section ($T'_{f,o}$).

For the next section:

24. $T'_{f,o}$ is used as the air inlet temperature for the next section.
25. Steps 5 to 22 are carried out for the next section.

When calculating the mean temperature for the glass, absorber surface or air it should be remembered that the mean for the whole duct is required – not just from the final duct section.

H2 Yeh Model for Forced Convection (Yeh_{fc}) [4]

The procedure for the Yeh_{fc} model is:

1. Obtain the following data (please note the required units):
   - Duct – $\dot{m}'$ (kg h^{-1}), W (m), b (m), L (m), ε_g, ε_p, α_p, τ_g
   - Meteorological –T'_{amb}, $T'_{f,i}$, E'_{vg} (kJ h^{-1} m^{-2} h^{-1}), v (m s^{-1})
   - Constants – σ' (kJ h^{-1} m^{-2} K^{-4}), μ' (kg m^{-1} h^{-1}), k (kJh^{-1} m^{-1} K^{-1}), c_p (kJ kg^{-1} K^{-1})
2. calculate A_c and D_h (B1)
3. calculate h_w using McAdam's correlation which Yeh adjusted to [4]:

$$h_w = 4.9 + 3.27v \qquad \text{C23}$$

4. Guess $\overline{T}'_f$ and $\overline{T}'_p$. A reasonable first assumption is that they are equal to T'_{amb}+ 1K.
5. calculate h_{rpg} using [4]:

$$h_{rpg} \approx \frac{4\sigma \overline{T}'^3_f}{\frac{1}{\varepsilon_p} + \frac{1}{\varepsilon_g} - 1} \qquad \text{C29}$$

6. calculate Re using [2]:

$$\text{Re} = \frac{\dot{m} D_h}{A_c \mu} \qquad \text{B5}$$

7. calculate Nu using [4]:

$$Nu = 0.0158\,\text{Re}^{0.8} \qquad \text{C12}$$

8. calculate h_p using [4]:

$$h_p = \frac{kNu}{D_h} \qquad \text{C2}$$

9. calculate U_t using [4]:

$$U_t = \left\{ \frac{\frac{\overline{T}'_p}{520}}{\left[\frac{\overline{T}'_p - T'_{amb}}{1+\left(1+0.089h'_w-0.1166h'_w\varepsilon_p\right)\left(1+0.07866\right)} \right]^{0.43\left(1-\frac{100}{\overline{T}'_p}\right)}} + \frac{1}{h'_w} \right\}^{-1} +$$

$$\frac{\sigma'\left(\overline{T}'_p + T'_{amb}\right)\left(\overline{T}'^2_p + T'^2_{amb}\right)}{\frac{1}{\varepsilon_p + 0.00591h'_w} + \frac{2+\left(1+0.089h'_w-0.1166h'_w\varepsilon_p\right)\left(1+0.07866\right)-1+0.133\varepsilon_p}{\varepsilon_g - 1}}$$

A19

10. calculate U_b using [4]:

$$U_b = \frac{k_{ins}}{d_{ins}}$$ H7

11. calculate the overall heat loss coefficient for both surfaces (U_L) using [4]:

$$U_L = U_t + U_b$$ H8

12. calculate the efficiency factor of the solar air heater (F') using [4]:

$$F' = \left(1 + \frac{U_L}{h_p} + \left[\frac{1}{h_p} + \frac{1}{h_{rpg}} \right]^{-1} \right)^{-1}$$ C38

13. calculate the heat removal factor for the solar air heater (F_R) using [4]:

$$F_R = \frac{\dot{m}'c_p}{A_{sur}U_L}\left\{1 - \exp\left[-\frac{U_L F' A_{sur}}{\dot{m}'c_p} \right]\right\}$$ C37

14. calculate the collector efficiency (η) using [4]:

$$\eta = F_R\left(\alpha_p\tau_g - U_L\left(T'_{fi} - T'_{amb}\right)/E'\right)$$ C36

15. calculate $\overline{T}'_f$ using [4]:

$$\overline{T}'_f = T'_{fi} + \frac{\eta E'}{U_L F_R}\left(1 - \frac{F_R}{F'}\right)$$ A20

16. calculate $\overline{T}'_p$ using [4]:

$$\overline{T}'_p = T'_{f,i} + \frac{\eta E'}{U_L F_R}\left(1 - F_R\right)$$ A21

17. Solving for the temperatures is an iterative procedure. The calculated temperatures replace the initial temperatures used in step 4, and the process

repeated until the difference between the initial and the calculated temperatures is less than 0.01°C.

H3 Ho Model for Forced Convection (Ho_{fc}) [5]

The procedure for the Ho_{fc} model is:

1. Obtain the following data:

- Duct – $\dot{m}$ (kg s^{-1}), W (m), b (m), L (m), ε_g, ε_p, the thickness of the glass (d_g - m), the thickness of the insulating layers on the back (d_b - m) and edge (d_e - m) of the duct, the thermal conductivity of the glass (k_g – W m^{-1} K^{-1}) and of the insulating layers on the back of the duct (k_{ins} - W m^{-1} K^{-1}), α_p and τ_g
- Meteorological –T_{amb} (°C), $T_{f,i}$ (°C) if different from ambient temperature, the rear ambient temperature (T_{ambr} - °C) if different from the front ambient temperature, E_{vg} (W m^{-2}), v (m s^{-1})
- Constants –σ (W m^{-2} K^{-4}), k (W m^{-1} K^{-1}), μ (kg m^{-1} s^{-1}) and c_p (J $kg^{-1}K^{-1}$)

2. Guess the initial temperatures of the glass outer surface ($\overline{T}_{o1}$ - °C), the glass inner surface ($\overline{T}_g$ - °C), the solar absorber surface ($\overline{T}_p$ - °C) and the rear surface temperature ($\overline{T}_{o4}$ - °C)

3. calculate h_{rpg} using [5]:

$$h_{rpg} = \frac{\sigma\left(\overline{T}'^{2}_{g} + \overline{T}'^{2}_{p}\right)\left(\overline{T}'_{g} + \overline{T}'_{p}\right)}{\frac{1}{\varepsilon_g} + \frac{1}{\varepsilon_p} - 1} \qquad \text{C28}$$

4. calculate h_{rs} using [5]:

$$h_{rs} = \sigma\varepsilon_g\left[T'^{2}_{o1} + T'^{2}_{amb}\right]\left(T'_{o1} + T'_{amb}\right) \qquad \text{C33}$$

5. calculate h_w using McAdam's correlation [5]:

$$h_w = 5.7 + 3.8v \qquad \text{C20}$$

6. calculate the overall top heat loss coefficient (U_t) using [6]:

$$U_t = 1/\left(\frac{1}{h_{rs}} + \frac{d_g}{k_g} + \frac{1}{h_w}\right) \qquad \text{H9}$$

7. calculate the overall edge heat loss coefficient (U_e) using [6]:

$$U_e = 1/\left(\frac{1}{h_{rs}} + \frac{d_e}{k_e} + \frac{1}{h_w}\right) \qquad \text{H10}$$

8. calculate the overall top heat loss coefficient including the edges($U_{t\&e}$) using [5]:

$$U_{t\&e} = U_t + \frac{2U_e A_e}{LW} \qquad \text{H11}$$

9. calculate the overall bottom heat loss coefficient (U_b) using [6]:

$$U_b = 1/\left(\frac{1}{h_{rs}} + \frac{d_b}{k_b} + \frac{1}{h_w}\right) \qquad \text{H12}$$

10. calculate Re using [2] :

$$\mathrm{Re} = \frac{\dot{m} D_h}{A_c \mu} \qquad \text{B5}$$

11. calculate Nu using [5] :

$$Nu = 0.0158\,\mathrm{Re}^{0.8} \qquad \text{C12}$$

12. calculate h_g and h_p using [5]:

$$h_g = h_p = \frac{kNu}{D_h} \qquad \text{C2}$$

13. calculate K using [5]:

$$K = \frac{A_{collector}}{A_{absorber}} \qquad \text{H13}$$

14. calculate P1 using [5]:

$$P_1 = \frac{Kh_{rpg}}{U_{t\&e} + h_g + Kh_{rpg}} - \frac{h_p}{h_{rpg}} - 1 - \frac{U_b}{Kh_{rpg}} \qquad \text{A29}$$

15. calculate P2 using [5]:

$$P_2 = \frac{h_g}{U_{t\&e} + h_g + Kh_{rpg}} + \frac{h_p}{h_{rpg}} \qquad \text{A28}$$

16. calculate P3 using [5]:

$$P_3 = h_g - \frac{Kh_{rpg} P_2}{P_1} \qquad \text{A27}$$

17. calculate P4 using [5]:

$$P_4 = 1 - \frac{Kh_{rpg}}{P_1\left(U_{t\&e} + h_g + Kh_{rpg}\right)} \qquad \text{A26}$$

18. calculate P5 using [5]:

$$P_5 = h_g\left(\frac{P_3}{U_t'+h_g+Kh_{rpg}}-1\right)-Kh_p\left(\frac{P_2}{P_1}+1\right) \qquad \text{A25}$$

19. Calculate the effective transmittance-absorptance product $(\tau\alpha)_e$ of the collector using [5]:

$$(\tau\alpha)_e = \tau_g\alpha_p \qquad \text{H14}$$

20. calculate P6 using [5]:

$$P_6 = \frac{U_{t\&e}}{U_{t\&e}+h_g+Kh_{rgp}}\left(P_4h_g-\frac{Kh_p}{P_1}\right)T_{amb\,f}-\frac{U_bP_2}{P_1}T_{amb\,r}-\frac{P_2}{P_1}E(\tau\alpha)_e$$

A24

21. calculate P7 using [5]:

$$P_7 = \frac{P_5WL}{\dot{m}c_p} \qquad \text{A23}$$

22. Calculate the air exit temperature (T_{fo}) using [5]:

$$T_{fo} = \left(\frac{P_6}{P_5}+T_{fi}\right)\exp(P_7)-\frac{P_6}{P_5} \qquad \text{H15}$$

23. Calculate the mean air temperature ($\overline{T}_f$) using [5]:

$$\overline{T}_f = \frac{\dot{m}c_p}{2P_5WL}\left(\frac{P_6}{P_5}+T_{fi}\right)\left[\exp\left(\frac{P_5WL}{\dot{m}c_p}\right)-1\right]+\frac{1}{2}\left(T_{fi}-\frac{P_6}{P_5}\right) \qquad \text{A31}$$

24. Calculate the glass inner temperature ($\overline{T}_g$) using [5]:

$$\overline{T}_g = \frac{U_bT_a}{P_1\left(U_{t\&e}+h_g+Kh_{rpg}\right)}+\left\{\frac{h_g}{U_{t\&e}+h_g+Kh_{rpg}}-Kh_{rpg}\frac{\left[\frac{h_g}{U_{t\&e}+h_g+Kh_{rpg}}+\frac{h_p}{h_{rpg}}\right]}{P_1\left(U_{t\&e}+h_g+Kh_{rpg}\right)}\right\}\overline{T}_f$$

$$+\left\{\frac{U_{t\&e}}{U_{t\&e}+h_g+Kh_{rpg}}-\frac{Kh_{rpg}U_{t\&e}}{P_1\left(U_{t\&e}+h_g+Kh_{rpg}\right)^2}\right\}T_a-\frac{1}{P_1\left(U_{t\&e}+h_g+Kh_{rpg}\right)}E(\tau\alpha)_e$$

A32

25. Calculate the solar absorber temperature using [5]:

$$\overline{T}_p = -\frac{U_b}{Kh_{rpg}P_1}T_a - \frac{U_{t\&e}}{\left(U_{t\&e}+h_g+Kh_{rpg}\right)P_1}T_a - \frac{1}{P_1}\left[\frac{h_2}{U_{t\&e}+h_g+Kh_{rpg}}+\frac{h_p}{h_{rpg}}\right]\overline{T}_f - \frac{1}{Kh_{rpg}P_1}E(\tau\alpha)_e \qquad \text{A33}$$

26. Calculate the glass outer temperature (T_{o1}) using [5]:

$$\overline{T}_{o1} = \frac{\frac{k_g}{d_g}\overline{T}_g + \left(h_w + h_{rgs}\right)T_{amb}}{h_w + h_{rgs} + \frac{k_g}{d_g}} \qquad \text{H16}$$

27. Calculate the rear surface temperature (T_{o4}) using [5]:

$$\overline{T}_{o4} = \frac{\frac{k_b}{d_b}\overline{T}_p + \left(h_w + h_{rps}\right)T_{amb}}{h_w + h_{rps} + \frac{k_b}{d_b}} \qquad \text{H17}$$

28. Solving for the temperatures is an iterative procedure. The calculated temperatures replace the initial temperatures used in step 2, and the process is repeated until the difference between the initial and the calculated temperatures is less than 0.01^{o}C.

Forced Convection – Modified Model

H4 Ong Model for Forced Convection (Ong_{fcad}) [1]

The procedure for the Ong_{fc} model is:

1. Obtain the following data:

- Duct – $\dot{m}$ (kg s^{-1}), W (m), b (m), L (m), ε_g, ε_p, d_b (m), k_{ins} (W m^{-1} K^{-1}), α_g α_p, reflectivity of glass (R_g), reflectivity of absorbing surface (R_p), the angle dependent and diffuse solar heat gain coefficient ($SHGC_\theta$ and $SHGC_{diff}$) of the glass
- Meteorological –T'$_{amb}$ (K), T'$_{f,i}$ (K) if different from ambient temperature, E_{vdir} (W m^{-2}), E_{vdiff} (W m^{-2}), v (m s^{-1})

- Constants –σ - W m^{-2} K^{-4}

2. calculate hydraulic diameter (D_h – m) for parallel plate ducts (B4) and cross sectional area (A_c – m^2)
3. divide the collector into short (0.5 – 1.0m) sections for which the temperature gradient can be assumed to be linear

For the first section:

4. guess the initial mean temperature of the air ($\overline{T}'_f$), glass ($\overline{T}'_g$) and solar absorber ($\overline{T}'_p$). A reasonable first assumption is that they are equal to T'_{amb}+ 1K.
5. calculate the hydraulic diameter (D_h – m) for a non circular duct (B1) and cross sectional area (A_c - m^2)
6. calculate the sky temperature using the HTB2 algorithm described in Section 4.1.12.1 equations 4.13-4.17. The cloud cover for the dates considered has been set to 0.1.
7. calculate h_w using McAdam's correlation [1]:

$$h_w = 5.7 + 3.8v \qquad \text{C20}$$

8. calculate μ using [3]:

$$\mu = \left[1.846 + 0.00472(\overline{T}'_f - 300)\right]10^{-5} \qquad \text{H18}$$

9. calculate Re using [2]:

$$\text{Re} = \frac{\dot{m}D_h}{A_c\mu} \qquad \text{B5}$$

10. calculate c_p using [3]:

$$c_p = \left[1.007 + 0.00004(\overline{T}'_f - 300)\right]10^3 \qquad \text{H19}$$

11. calculate k using [3]:

$$k = 0.0263 + 0.000074(\overline{T}'_f - 300) \qquad \text{H20}$$

12. calculate the Prandtl number using [2]:

$$\text{Pr} = \frac{c_p\mu}{k} \qquad \text{B6}$$

13. calculate h_g and h_p using [2]:

$$h_g = h_p = \frac{kNu}{D_h} \qquad \text{C2}$$

14. calculate Nu using Nusselt's correlation [1]:

$$Nu = 0.036\,\mathrm{Re}^{0.8}\,\mathrm{Pr}^{1/3}\left(\frac{D_h}{L}\right)^{0.055} \qquad \text{C5}$$

15. calculate h_{rpg} using [1]:

$$h_{rpg} = \frac{\sigma\left(\overline{T}'^{2}_{g} + \overline{T}'^{2}_{p}\right)\left(\overline{T}'_{g} + \overline{T}'_{p}\right)}{\frac{1}{\varepsilon_g} + \frac{1}{\varepsilon_p} - 1} \qquad \text{C28}$$

16. calculate h_{rs} using [1]:

$$h_{rs} = \frac{\sigma\varepsilon_g\left(\overline{T}'_{g} + T'_{s}\right)\left(\overline{T}'^{2}_{g} + T'^{2}_{s}\right)\left(\overline{T}'_{g} - T'_{s}\right)}{\left(\overline{T}'_{g} - T'_{amb}\right)} \qquad \text{C30}$$

17. calculate U_t using [1]:

$$U_t = h_w + h_{rs} \qquad \text{H4}$$

18. calculate U_b using [1]:

$$U_b = \frac{1}{i = \sum_{1}^{n} \frac{d_{bi}}{k_{bi}} + \frac{1}{h_w}} \qquad \text{H5}$$

19. the solar radiation heat flux absorbed by the glass surface (S_1) is related to the individual components of solar irradiation, i.e. direct (E_{vdir}), diffuse (E_{vdiff}) and arising from the internal reflections of irradiation (R1). These components are related to the angle dependent and diffuse absorptivities of glass ($\alpha_{g\theta}$ and α_{gdiff}):

$$S_1 = \alpha_{g\theta} E_{vdir} + \alpha_{gdiff}\left(E_{vdiff} + R1\right) \qquad \text{H21}$$

The component of solar irradiation which passes through the glass is related to the angle dependent Solar Heat Gain Coefficient ($SHGC_\theta$). This component is reflected against the absorbing surface back to the glass. The reflected component (R1) is defined using:

$$R1 = E_{vdir} SHGC_\theta R_p \qquad \text{H22}$$

20. the solar radiation heat flux absorbed by the absorbing surface (S_2) is related to the individual components of solar irradiation, i.e. direct (E_{vdir}), diffuse (E_{vdiff}) which passes through the glass (related to the angle dependent and diffuse solar heat gain coefficients of glass - $SHGC_\theta$ and $SHGC_{diff}$) and reflected irradiation which is bounced back to the absorbing surface (R2):

$$S_2 = \left[E_{vdir} SHGC_\theta + \left(E_{vdiff} + R2\right) SHGC_{diff}\right]\alpha_p \qquad \text{H23}$$

The solar irradiation which passes through the glass will experience a partial reflection from the absorbing surface, followed by a partial reflection from the rear side of the glass, returning to the absorbing surface. This reflected component (R2) is defined using:

$$R2 = R1R_g \qquad \text{H24}$$

21. calculate Γ using:

$$\Gamma = \frac{2\dot{m}c_p}{WL} \text{ [1]} \qquad \text{H6}$$

22. The temperatures can be found by solving the matrix equation:

$$[T] = [A]^{-1}[B] \text{ [1]} \qquad \text{A11}$$

where:

$$[T] = \begin{bmatrix} \overline{T}'_g \\ \overline{T}'_f \\ \overline{T}'_p \end{bmatrix} \quad [A] = \begin{bmatrix} h_g + h_{rpg} + U_t & -h_g & -h_{rpg} \\ h_g & -\left(h_g + h_p + \Gamma\right) & h_p \\ -h_{rpg} & -h_p & h_p + h_{rpg} + U_b \end{bmatrix}$$

and $[B] = \begin{bmatrix} U_t T'_{amb} + S_g \\ -\Gamma T'_{f,i} \\ S_p + U_b T'_{amb} \end{bmatrix}$

23. Solving for the temperatures is an iterative procedure. The calculated temperatures should be used as the next guess for the initial temperatures (used in step 4), and the process repeated until the difference between the initial and the calculated temperatures is less than 0.01^oC.
24. The difference between the air inlet temperature ($T'_{f,i}$) and the mean air temperature ($\overline{T}'_f$) calculated in step 22 should be used to determine the air outlet temperature from the duct section ($T'_{f,o}$).

For the next section:

25. $T'_{f,o}$ is used as the air inlet temperature for the next section.
26. Steps 5 to 19 should be carried out for the next section.

When calculating the mean temperature for the glass or absorber surface, it should be remembered that the mean for the whole duct is required – not just from the final duct section.

H5 Yeh Model for Forced Convection (Yeh_{fcad}) [4]

The procedure for the Yeh_{fc} model is:

1. Obtain the following data (please note the required units):
   - Duct – $\dot{m}'$ (kg h^{-1}), W (m), b (m), L (m), ε_g, ε_p, α_p, $SHGC_\theta$, $SHGC_{diff}$
   - Meteorological –T'_{amb} (K), $T'_{f,i}$ (K) if different from ambient temperature, E'_{vg} (kJ h^{-1} m^{-2} h^{-1}), v (m s^{-1})
   - Constants –σ' (kJ h^{-1} m^{-2} K^{-4})
2. calculate A_c and D_h (B1)
3. calculate h_w using McAdam's correlation which Yeh adjusted to [4]:

   $$h_w = 4.9 + 3.27v \qquad \text{C23}$$

4. Guess $\overline{T}'_f$ and $\overline{T}'_p$. A reasonable first assumption is that they are equal to T'_{amb}+ 1K.
5. calculate h_{rpg} using [4]:

   $$h_{rpg} \approx \frac{4\sigma \overline{T}'^3_f}{\frac{1}{\varepsilon_g} + \frac{1}{\varepsilon_p} - 1} \qquad \text{C29}$$

6. calculate μ using [3]:

   $$\mu = \left[1.846 + 0.00472(\overline{T}'_f - 300)\right]10^{-5} \qquad \text{H18}$$

   Then multiply by 3600 to adapt the units to kg m^{-1} h^{-1}:
7. calculate Re using [2]:

   $$\text{Re} = \frac{\dot{m} D_h}{A_c \mu} \qquad \text{B5}$$

8. calculate c_p using [3]:

   $$c_p = \left[1.007 + 0.00004(\overline{T}'_f - 300)\right]10^3 \qquad \text{H19}$$

   Then divide by 1000 to adapt the units to kJ kg^{-1} K^{-1}
9. calculate k using [3]:

   $$k = 0.0263 + 0.000074(\overline{T}'_f - 300) \qquad \text{H20}$$

   Then multiply by 3600 and divide by 1000 to adapt the units to kJ h^{-1} m^{-1} K^{-1}

10. calculate the Prandtl number using [2]:

$$\mathrm{Pr} = \frac{c_p \mu}{k} \qquad \text{B6}$$

11. calculate Nu using Nusselt's correlation [1]:

$$Nu = 0.036\,\mathrm{Re}^{0.8}\,\mathrm{Pr}^{1/3}\left(\frac{D_h}{L}\right)^{0.055} \qquad \text{C5}$$

12. calculate h_p using [4]:

$$h_p = \frac{kNu}{D_h} \qquad \text{C2}$$

13. calculate U_t using [4]:

$$U_t = \left\{ \frac{\frac{\overline{T}'_p}{520}}{\left[\frac{\overline{T}'_p - T'_{amb}}{1+\left(1+0.089h'_w - 0.1166h'_w\varepsilon_p\right)\left(1+0.07866\right)}\right]^{0.43\left(1-\frac{100}{\overline{T}'_p}\right)}} + \frac{1}{h'_w} \right\}^{-1} + \frac{\sigma'\left(\overline{T}'_p + T'_{amb}\right)\left(\overline{T}'^2_p + T'^2_{amb}\right)}{\frac{1}{\varepsilon_p + 0.00591h'_w} + \frac{2+\left(1+0.089h'_w - 0.1166h'_w\varepsilon_p\right)\left(1+0.07866\right)-1+0.133\varepsilon_p}{\varepsilon_g - 1}}$$

A19

14. calculate U_b using [4]:

$$U_b = \frac{k_{ins}}{d_{ins}} \qquad \text{H7}$$

15. calculate U_L using [4]:

$$U_L = U_t + U_b \qquad \text{H8}$$

16. calculate F' using [4]:

$$F' = \left(1 + \frac{U_L}{h_p} + \left[\frac{1}{h_p} + \frac{1}{h_{rpg}}\right]^{-1}\right)^{-1} \qquad \text{C38}$$

17. calculate F_R using [4]:

$$F_R = \frac{\dot{m}' c_p}{A_{sur} U_L}\left\{1 - \exp\left[-\frac{U_L F' A_{sur}}{\dot{m}' c_p}\right]\right\} \qquad \text{C37}$$

18. calculate η using [4]:

$$\eta = F_R\left(\alpha_p \tau_g - U_L\left(T'_{fi} - T'_{amb}\right)/E'\right) \qquad \text{C36}$$

19. calculate $\overline{T}'_f$ using [4]:

$$\overline{T}'_f = T'_{fi} + \frac{\eta E'}{U_L F_R}\left(1 - \frac{F_R}{F'}\right) \qquad \text{A20}$$

20. calculate $\overline{T}'_p$ using [4]:

$$\overline{T}'_p = T'_{f,i} + \frac{\eta E'}{U_L F_R}\left(1 - F_R\right) \qquad \text{A21}$$

21. Solving for the temperatures is an iterative procedure. The calculated temperatures replace the initial temperatures used in step 4, and the process repeated until the difference between the initial and the calculated temperatures is less than 0.01^{o}C.

H6 Ho Model for Forced Convection (Ho_{fcad}) [5]

The procedure for the Ho_{fc} model is:

1. Obtain the following data:

- Duct – $\dot{m}$ (kg s^{-1}), W (m), b (m), L (m), ε_g, ε_p, d_g (m), d_b (m), d_e (m), k_g (W m^{-1} K^{-1}), k_{ins} (W m^{-1} K^{-1}), α_p, $SHGC_\theta$ $SHGC_{diff}$
- Meteorological –T'_{amb} (K), $T'_{f,i}$ (K) if different from ambient temperature, T'_{ambr} (K) if different from the front ambient temperature, E_{vdir} (W m^{-2}), E_{vdiff} (W m^{-2}), v - m s^{-1}
- Constants –σ (W m^{-2} K^{-4})

2. Guess the initial temperatures of the glass outer surface ($\overline{T}_{o1}$ - ^{o}C), the glass inner surface ($\overline{T}_g$ - ^{o}C), the solar absorber surface ($\overline{T}_p$ - ^{o}C), the rear surface temperature ($\overline{T}_{o4}$ - ^{o}C) and the fluid temperature (T_f)
3. calculate h_{rpg} using [5]:

$$h_{rpg} = \frac{\sigma\left(T'^2_g + T'^2_p\right)\left(T'_g + T'_p\right)}{\frac{1}{\varepsilon_g} + \frac{1}{\varepsilon_p} - 1} \qquad \text{C28}$$

4. calculate the sky temperature using the HTB2 algorithm described in Section 4.1.12.1 equations 4.13-4.17. The cloud cover for the dates considered has been set to 0.1.

5. calculate h_{rs} using [1]:

$$h_{rs} = \frac{\sigma\varepsilon_1\left(T_g + T_s\right)\left(T_g^2 + T_s^2\right)\left(T_g - T_s\right)}{\left(T_g - T_{amb}\right)} \qquad \text{C30}$$

6. calculate h_w using McAdam's correlation [5]:

$$h_w = 5.7 + 3.8v \qquad \text{C20}$$

7. calculate U_t using [6]:

$$U_t = 1/\left(\frac{1}{h_{rs}} + \frac{d_g}{k_g} + \frac{1}{h_w}\right) \qquad \text{H9}$$

8. calculate U_e using [6]:

$$U_e = 1/\left(\frac{1}{h_{rs}} + \frac{d_e}{k_e} + \frac{1}{h_w}\right) \qquad \text{H10}$$

9. calculate $U_{t\&e}$ using [5]:

$$U_{t\&e} = U_t + \frac{2U_e A_e}{LW} \qquad \text{H11}$$

10. calculate U_b using [6]:

$$U_b = 1/\left(\frac{1}{h_{rs}} + \frac{d_b}{k_b} + \frac{1}{h_w}\right) \qquad \text{H12}$$

11. calculate μ using [3]:

$$\mu = \left[1.846 + 0.00472(\overline{T}'_f - 300)\right]10^{-5} \qquad \text{H18}$$

12. calculate Re using [2] :

$$\text{Re} = \frac{\dot{m}D_h}{A_c\mu} \qquad \text{B5}$$

13. calculate Pr using [2]:

$$\text{Pr} = \frac{c_p\mu}{k} \qquad \text{B6}$$

14. calculate c_p using [3]:

$$c_p = \left[1.007 + 0.00004(\overline{T}'_f - 300)\right]10^3 \qquad \text{H19}$$

15. calculate k using [3]:

$$k = 0.0263 + 0.000074(\overline{T}'_f - 300) \qquad \text{H20}$$

16. calculate Nu using [1]:

$$Nu = 0.036\,\text{Re}^{0.8}\,\text{Pr}^{1/3}\left(\frac{D_h}{L}\right)^{0.055} \qquad \text{C5}$$

17. calculate h_g and h_p using [5]:

$$h_g = h_p = \frac{kNu}{D_h} \qquad \text{C2}$$

18. calculate K using [5]:

$$K = \frac{A_{collector}}{A_{absorber}} \qquad \text{H13}$$

19. calculate P1 using [5]:

$$P_1 = \frac{Kh_{rpg}}{U_{t\&e} + h_g + Kh_{rpg}} - \frac{h_p}{h_{rpg}} - 1 - \frac{U_b}{Kh_{rpg}} \qquad \text{A29}$$

20. calculate P2 using [5]:

$$P_2 = \frac{h_g}{U_{t\&e} + h_g + Kh_{rpg}} + \frac{h_p}{h_{rpg}} \qquad \text{A28}$$

21. calculate P3 using [5]:

$$P_3 = h_g - \frac{Kh_{rpg}P_2}{P_1} \qquad \text{A27}$$

22. calculate P4 using [5]:

$$P_4 = 1 - \frac{Kh_{rpg}}{P_1\left(U_{t\&e} + h_g + Kh_{rpg}\right)} \qquad \text{A26}$$

23. calculate P5 using [5]:

$$P_5 = h_g\left(\frac{P_3}{U_t' + h_g + Kh_{rpg}} - 1\right) - Kh_p\left(\frac{P_2}{P_1} + 1\right) \qquad \text{A25}$$

24. calculate the effective transmittance-absorptance product $E(\tau\alpha)_{e\theta}$ in terms of diffuse and direct solar irradiation with respect to the angle of incidence using:

$$R = E_{vdir} SHGC_\theta R_p R_g \qquad \text{H25}$$

$$E(\tau\alpha)_{e\theta} = \left\lfloor E_{vdir} SHGC_\theta + \left(E_{vdiff} + R\right) SHGC_{diff} \right\rfloor \alpha_p \qquad \text{H26}$$

25. calculate P6 using [5]:

$$P_6 = \frac{U_{t\&e}}{U_{t\&e} + h_g + Kh_{rgp}}\left(P_4 h_g - \frac{Kh_p}{P_1}\right) T_{amb\,f} - \frac{U_b P_2}{P_1} T_{amb\,r} - \frac{P_2}{P_1} E(\tau\alpha)_{e\theta} \qquad \text{A24}$$

26. calculate P7 using [5]:

$$P_7 = \frac{P_5 WL}{\dot{m} c_p} \qquad \text{A23}$$

27. Calculate the air exit temperature (T_{fo}) using [5]:

$$T_{fo} = \left(\frac{P_6}{P_5} + T_{fi} \right) \exp(P_7) - \frac{P_6}{P_5} \qquad \text{H15}$$

28. Calculate the mean air temperature ($\overline{T}_f$) using [5]:

$$\overline{T}_f = \frac{\dot{m} c_p}{2 P_5 WL} \left(\frac{P_6}{P_5} + T_{fi} \right) \left[\exp\left(\frac{P_5 WL}{\dot{m} c_p} \right) - 1 \right] + \frac{1}{2} \left(T_{fi} - \frac{P_6}{P_5} \right) \qquad \text{A31}$$

29. Calculate $\overline{T}_g$ using [5]:

$$\overline{T}_g = \frac{U_b T_a}{P_1 \left(U_{t\&e} + h_g + K h_{rpg} \right)} + \left\{ \frac{h_g}{U_{t\&e} + h_g + K h_{rpg}} - K h_{rpg} \frac{\left[\dfrac{h_g}{U_{t\&e} + h_g + K h_{rpg}} + \dfrac{h_p}{h_{rpg}} \right]}{P_1 \left(U_{t\&e} + h_g + K h_{rpg} \right)} \right\} \overline{T}_f$$

$$+ \left\{ \frac{U_{t\&e}}{U_{t\&e} + h_g + K h_{rpg}} - \frac{K h_{rpg} U_{t\&e}}{P_1 \left(U_{t\&e} + h_g + K h_{rpg} \right)^2} \right\} T_a - \frac{1}{P_1 \left(U_{t\&e} + h_g + K h_{rpg} \right)} E(\tau\alpha)_e \qquad \text{A32}$$

30. Calculate $\overline{T}_p$ using [5]:

$$\overline{T}_p = -\frac{U_b}{K h_{rpg} P_1} T_a - \frac{U_{t\&e}}{\left(U_{t\&e} + h_g + K h_{rpg} \right) P_1} T_a - \frac{1}{P_1} \left[\frac{h_2}{U_{t\&e} + h_g + K h_{rpg}} + \frac{h_p}{h_{rpg}} \right] \overline{T}_f$$

$$- \frac{1}{K h_{rpg} P_1} E(\tau\alpha)_e \qquad \text{A33}$$

31. Calculate $\overline{T}_{o1}$ using [5]:

$$\overline{T}_{o1} = \frac{\dfrac{k_g}{d_g} \overline{T}_g + \left(h_w + h_{rgs} \right) T_{amb}}{h_w + h_{rgs} + \dfrac{k_g}{d_g}} \qquad \text{H16}$$

32. Calculate $\overline{T}_{o4}$ using [5]:

$$\overline{T}_{o4} = \frac{\frac{k_b}{d_b}\overline{T}_p + \left(h_w + h_{rps}\right)T_{amb}}{h_w + h_{rps} + \frac{k_b}{d_b}} \qquad \text{H17}$$

33. Solving for the temperatures is an iterative procedure. The calculated temperatures replace the initial temperatures used in step 2, and the process repeated until the difference between the initial and the calculated temperatures is less than 0.01^oC.

Buoyant Convection – Basic Model

H7 Ong Model for Buoyant Convection (Ong_{bc})

The procedure for the Ong_{bc} model is:

1. Obtain the following data:
   - Duct –W (m), b (m), L (m), ε_g, ε_p, d_b (m), k_{ins} (W m^{-1} K^{-1}), α_g, α_p, τ_g
   - Meteorological –T'_{amb} (K), $T'_{f,i}$ (K) if different from ambient temperature, E_{vg} (W m^{-2}), v (m s^{-1})
   - Constants –σ (W m^{-2} K^{-4}), Coefficient of discharge of air channel (C_d = 0.6), acceleration due to gravity (g - m s^{-2})
2. calculate A_c and D_h (B1)
3. guess the initial mean temperature of the air ($\overline{T}'_f$), glass ($\overline{T}'_g$) and solar absorber ($\overline{T}'_p$). A reasonable first assumption is that they are equal to T'_{amb}+ 1K.
4. calculate the output temperature (T'_{fo}) using [3]:

$$T'_{fo} = \frac{\overline{T}'_f - (1-\gamma)T'_{f_i}}{\gamma} \qquad \text{H27}$$

5. calculate the sky temperature using Swinbank's equation [3]:

$$T'_s = 0.0552T'^{1.5}_{amb} \qquad \text{C31}$$

6. calculate h_w using McAdam's correlation [3]:

$$h_w = 5.7 + 3.8v \qquad \text{C20}$$

7. calculate the air density (ρ) using [3]:

$$\rho = 1.1614 - 0.00353\left(\overline{T}'_f - 300\right) \qquad \text{H28}$$

8. calculate the coefficient of expansion of air (β) using:

$$\beta = \frac{1}{T'_{fo}} \qquad \text{H29}$$

9. calculate μ using [3]:

$$\mu = \left[1.846 + 0.00472(\overline{T}'_f - 300)\right]10^{-5} \qquad \text{H18}$$

10. calculate the Grashof number (Gr) using [2]:

$$Gr = \frac{g\rho^2 \beta \Delta T L^3}{\mu^2} \qquad \text{B9}$$

Where ΔT refers to the air inlet temperature subtracted from the air exit temperature.

11. calculate c_p of the air using [3]:

$$c_p = \left[1.007 + 0.00004(\overline{T}'_f - 300)\right]10^3 \qquad \text{H19}$$

12. calculate k using [3]:

$$k = 0.0263 + 0.000074(\overline{T}'_f - 300) \qquad \text{H20}$$

13. calculate Pr using [2]:

$$\text{Pr} = \frac{c_p \mu}{k} \qquad \text{B6}$$

14. calculate the Rayleigh number using [2]:

$$Ra = Gr\,\text{Pr} \qquad \text{B12}$$

15. calculate h_g and h_p using [2]:

$$h_g = h_p = \frac{kNu}{D_h} \qquad \text{C2}$$

16. Calculate Nu:

- If the Rayleigh number is less than 10^9, the flow is assumed to be laminar, and the Nusselt number is calculated using Incropera and DeWitt's correlation for laminar flow undergoing natural convection [3]:

$$Nu = 0.68 + \frac{0.67Ra^{1/4}}{\left[1 + \left(\frac{0.492}{\text{Pr}}\right)^{9/16}\right]^{4/9}} \qquad \text{C16}$$

- If the Rayleigh number is greater than 10^9, the flow is assumed to be turbulent, and the Nusselt number is calculated using Incropera and DeWitt's correlation for turbulent flow undergoing natural convection [3]:

$$Nu = \left\{ 0.825 + \frac{0.387 Ra^{1/6}}{\left[1 + \left(\frac{0.492}{\mathrm{Pr}} \right)^{9/16} \right]^{8/27}} \right\}^2 \qquad \text{C17}$$

17. calculate h_{rpg} using [3]:

$$h_{rpg} = \frac{\sigma\left(\overline{T}'^2_g + \overline{T}'^2_p\right)\left(\overline{T}'_g + \overline{T}'_p\right)}{\frac{1}{\varepsilon_g} + \frac{1}{\varepsilon_p} - 1} \qquad \text{C28}$$

18. calculate h_{rs} using [3]:

$$h_{rs} = \frac{\sigma\varepsilon_g\left(\overline{T}'_g + T'_s\right)\left(\overline{T}'^2_g + T'^2_s\right)\left(\overline{T}'_g - T'_s\right)}{\left(\overline{T}'_g - T'_{amb}\right)} \qquad \text{C30}$$

19. calculate U_t using [3]:

$$U_t = h_w + h_{rs} \qquad \text{H4}$$

20. calculate U_b using [3]:

$$U_b = \frac{1}{\frac{d_b}{k_b} + \frac{1}{h_w}} \qquad \text{H5}$$

21. calculate S_g using [3]:

$$S_g = \alpha_g E \qquad \text{A15}$$

22. calculate S_p using [3]:

$$S_p = \tau_g \alpha_p E \qquad \text{A16}$$

23. calculate $\dot{m}$ using:

$$\dot{m} = C_d \frac{\rho_{fo} A_o}{\sqrt{1 + A_r}} \sqrt{\frac{2gL\left(\overline{T}'_f - T'_{amb}\right)}{T'_{amb}}} \qquad \text{H30}$$

Where A_o is the area of the air outlet and A_r is the area of the air inlet.

24. calculate M using [3]:

$$M = \frac{\dot{m} c_p}{\gamma W L} \qquad \text{H31}$$

Where $\gamma = 0.75$

25. The temperatures can be found by solving the matrix equation [1]:

$$[T] = [A]^{-1}[B] \qquad \text{A11}$$

where:

$$[T] = \begin{bmatrix} \overline{T}'_g \\ \overline{T}'_f \\ \overline{T}'_p \end{bmatrix}, \quad [A] = \begin{bmatrix} h_g + h_{rpg} + U_t & -h_g & -h_{rpg} \\ h_g & -(h_g + h_p + M) & h_p \\ -h_{rpg} & -h_p & h_p + h_{rpg} + U_b \end{bmatrix}$$

and $[B] = \begin{bmatrix} U_t T'_{amb} + S_g \\ -MT'_{f,i} \\ S_p + U_b T'_{amb} \end{bmatrix}$

26. Solving for the temperatures is an iterative procedure. The calculated temperatures replace the initial temperatures used in step 3, and the process repeated until the difference between the initial and the calculated temperatures is less than 0.01^{o}C.

H8 Yeh Model for Buoyant Convection (Yeh_{bc})

The procedure for the Yeh_{bc} model is:

1. Obtain the following data (please note the required units):

- Duct –W (m), b (m), L (m), ε_g, ε_p, α_p, τ_g, roughness of the duct surface (R – m)
- Meteorological –T'_{amb} (K), $T'_{f,i}$ (K) if different from ambient temperature, E'_{vg} (kJ h^{-1} m^{-2} h^{-1}), v (m s^{-1})
- Constants – σ' (kJ h^{-1} m^{-2} K^{-4}), μ (kg m^{-1} h^{-1}), k (kJh^{-1} m^{-1} K^{-1}), ρ (kg m^{-3}), c_p (kJ kg^{-1} K^{-1}), g (m s^{-2})

2. calculate A_c and D_h (B1)
3. calculate h_w using McAdam's correlation which Yeh adjusted to [4]:

$$h_w = 4.9 + 3.27v \qquad \text{C23}$$

4. Guess $\overline{T}'_f$ and $\overline{T}'_p$. A reasonable first assumption is that they are equal to T'_{amb}+ 1K
5. Guess $\dot{m}$

6. calculate h_{rpg} using [4]:

$$h_{rpg} \approx \frac{4\sigma T'^{3}_{f}}{\frac{1}{\varepsilon_g}+\frac{1}{\varepsilon_p}-1} \qquad \text{C29}$$

7. calculate the coefficient of expansion of air (β) using:

$$\beta = \frac{1}{T'_{fo}} \qquad \text{H29}$$

8. calculate Gr using [2]:

$$Gr = \frac{g\rho^2\beta\Delta TL^3}{\mu^2} \qquad \text{B9}$$

Where ΔT refers to the air inlet temperature subtracted from the air exit temperature.

9. calculate the Prandtl number using [2]:

$$\text{Pr} = \frac{c_p\mu}{k} \qquad \text{B6}$$

10. calculate the Rayleigh number using [2]:

$$Ra = Gr\,\text{Pr} \qquad \text{B12}$$

11. calculate Nu:

- If the Rayleigh number is less than 10^9, the flow is assumed to be laminar, and the Nusselt number is calculated using Incropera and DeWitt's correlation for laminar flow undergoing natural convection [3]:

$$Nu = 0.68 + \frac{0.67Ra^{1/4}}{\left[1+\left(\frac{0.492}{\text{Pr}}\right)^{9/16}\right]^{4/9}} \qquad \text{C16}$$

- If the Rayleigh number is greater than 10^9, the flow is assumed to be turbulent, and the Nusselt number is calculated using Incropera and DeWitt's correlation for turbulent flow undergoing natural convection [3]:

$$Nu = \left\{0.825 + \frac{0.387Ra^{1/6}}{\left[1+\left(\frac{0.492}{\text{Pr}}\right)^{9/16}\right]^{8/27}}\right\}^2 \qquad \text{C17}$$

12. calculate the convective heat transfer coefficient for the surface using [4]:

$$h_p = \frac{kNu}{D_h} \qquad \text{C2}$$

13. calculate the overall top heat loss coefficient (U_t) using [4]:

$$U_t = \left\{ \frac{\frac{\overline{T}'_p}{520}}{\left[\frac{\overline{T}'_p - T'_{amb}}{1+\left(1+0.089h'_w - 0.1166h'_w \varepsilon_p\right)\left(1+0.07866\right)} \right]^{0.43\left(1-\frac{100}{\overline{T}'_p}\right)}} + \frac{1}{h'_w} \right\}^{-1} + \frac{\sigma'\left(\overline{T}'_p + T'_{amb}\right)\left(\overline{T}'^2_p + T'^2_{amb}\right)}{\frac{1}{\varepsilon_p + 0.00591h'_w} + \frac{2+\left(1+0.089h'_w - 0.1166h'_w \varepsilon_p\right)\left(1+0.07866\right)-1+0.133\varepsilon_p}{\varepsilon_g - 1}} \qquad \text{A19}$$

14. calculate U_b using [4]:

$$U_b = \frac{k_{ins}}{d_{ins}} \qquad \text{H7}$$

15. calculate U_L using [4]:

$$U_L = U_t + U_b \qquad \text{H8}$$

16. calculate F' using [4]:

$$F' = \left(1 + \frac{U_L}{h_p} + \left[\frac{1}{h_p} + \frac{1}{h_{rpg}} \right]^{-1} \right)^{-1} \qquad \text{C38}$$

17. calculate F_R using [4]:

$$F_R = \frac{\dot{m}' c_p}{A_{sur} U_L} \left\{ 1 - \exp\left[-\frac{U_L F' A_{sur}}{\dot{m}' c_p} \right] \right\} \qquad \text{C37}$$

18. calculate η using [4]:

$$\eta = F_R\left(\alpha_p \tau_g - U_L\left(T'_{fi} - T'_{amb}\right)/E'\right) \qquad \text{C36}$$

19. calculate $\overline{T}'_f$ using [4]:

$$\overline{T}'_f = T'_{fi} + \frac{\eta E'}{U_L F_R}\left(1 - \frac{F_R}{F'}\right) \qquad \text{A20}$$

20. calculate $\bar{T}'_p$ using [4]:

$$\bar{T}'_p = T'_{f,i} + \frac{\eta E'}{U_L F_R}\left(1 - F_R\right) \qquad \text{A21}$$

21. calculate T'_{fo} using [3]:

$$T'_{fo} = \frac{\bar{T}'_f - (1-\gamma)T'_{f_i}}{\gamma} \qquad \text{H27}$$

22. calculate Re using [2]:

$$\text{Re} = \frac{\dot{m} D_h}{A_c \mu} \qquad \text{B5}$$

23. calculate the friction factor (f) using:

$$f' = 0.11\left(\frac{R}{D_h} + \frac{68}{\text{Re}}\right)^{0.25} \qquad \text{B16}$$

If f' ≥ 0.018: f=f'

If f' < 0.018: f= 0.85*f' + 0.0028

24. calculate the solar irradiation passing through the glazing (q):

$$q = E_{vg} A_g \tau_g$$

25. calculate the velocity of the air flowing through the duct (V) using:

$$V = \left(\frac{gqL^2}{T'_{amb}\, b\rho c_p \left[1.5 + \frac{fL}{D_h}\right]}\right)^{1/3} \qquad \text{A57}$$

26. calculate $\dot{m}$ using:

$$\dot{m} = \rho A_c V$$

27. Solving for the temperatures is an iterative procedure. The calculated temperatures replace the initial temperatures in step 4. The calculated air mass flow replace the initial flow in step 5. The process is repeated until the difference between the initial and the calculated temperatures is less than 0.01^{o}C, and the difference between the initial and calculated air mass flows is less than 0.000001 kg s^{-1}.

H9 Ho Model for Buoyant Convection (Ho_{bc}) [5]

The procedure for the Ho_{bc} model is:

1. Obtain the following data:

- Duct –W (m), b (m), L (m), ε_g, ε_p, d_g (m), d_b (m), d_e (m), k_g (W m^{-1} K^{-1}), k_{ins} (W m^{-1} K^{-1}), α_p, τ_g, R (m)
- Meteorological –T'_{amb} (K), $T'_{f,i}$ (K) if different from ambient temperature, T'_{ambr} (K) if different from the front ambient temperature, E_{vdir} (W m^{-2}), E_{vdiff} (W m^{-2}), v (m s^{-1})
- Constants – σ (W m^{-2} K^{-4}), g (m s^{-2}), μ (kg m^{-1} h^{-1}), k (kJh^{-1} m^{-1} K^{-1}), ρ (kg m^{-3}), c_p (kJ kg^{-1} K^{-1})

2. Guess the initial temperatures of the glass outer surface ($\overline{T}_{o1}$ - ^oC), the glass inner surface ($\overline{T}_g$ - ^oC), the solar absorber surface ($\overline{T}_p$ - ^oC) and the rear surface temperature ($\overline{T}_{o4}$ - ^oC)
3. Guess $\dot{m}$
4. calculate h_{rpg} using [5]:

$$h_{rpg} = \frac{\sigma\left(T'^2_g + T'^2_p\right)\left(T'_g + T'_p\right)}{\frac{1}{\varepsilon_g} + \frac{1}{\varepsilon_p} - 1} \qquad \text{C28}$$

5. calculate h_{rs} using [5]:

$$h_{rs} = \sigma\varepsilon_g\left[T'^{\,2}_{o1} + T'^{\,2}_{amb}\right]\left(T'_{o1} + T'_{amb}\right) \qquad \text{C33}$$

6. calculate h_w using McAdam's correlation [5]:

$$h_w = 5.7 + 3.8v \qquad \text{C20}$$

7. calculate U_t using [6]:

$$U_t = 1/\left(\frac{1}{h_{rs}} + \frac{d_g}{k_g} + \frac{1}{h_w}\right) \qquad \text{H9}$$

8. calculate U_e using [6]:

$$U_e = 1/\left(\frac{1}{h_{rs}} + \frac{d_e}{k_e} + \frac{1}{h_w}\right) \qquad \text{H10}$$

9. calculate $U_{t\&e}$ using [5]:

$$U_{t\&e} = U_t + \frac{2U_e A_e}{LW} \qquad \text{H11}$$

10. calculate U_b using [6]:

$$U_b = 1/\left(\frac{1}{h_{rs}} + \frac{d_b}{k_b} + \frac{1}{h_w}\right) \qquad \text{H12}$$

11. calculate the coefficient of expansion of air (β) using:

$$\beta = \frac{1}{T'_{fo}} \qquad \text{H29}$$

12. calculate Gr using [2]:

$$Gr = \frac{g\rho^2 \beta \Delta T L^3}{\mu^2} \qquad \text{B9}$$

Where ΔT refers to the air inlet temperature subtracted from the air exit temperature.

13. calculate Pr using:

$$\text{Pr} = \frac{c_p \mu}{k} \qquad \text{B6}$$

14. calculate the Ra using [2]:

$$Ra = Gr\,\text{Pr} \qquad \text{B12}$$

15. calculate the Nusselt number:

- If the Rayleigh number is less than 10^9, the flow is assumed to be laminar, and the Nusselt number is calculated using Incropera and DeWitt's correlation for laminar flow undergoing natural convection [3]:

$$Nu = 0.68 + \frac{0.67 Ra^{1/4}}{\left[1 + \left(\frac{0.492}{\text{Pr}}\right)^{9/16}\right]^{4/9}} \qquad \text{C16}$$

- If the Rayleigh number is greater than 10^9, the flow is assumed to be turbulent, and the Nusselt number is calculated using Incropera and DeWitt's correlation for turbulent flow undergoing natural convection [3]:

$$Nu = \left\{ 0.825 + \frac{0.387 Ra^{1/6}}{\left[1 + \left(\frac{0.492}{\mathrm{Pr}} \right)^{9/16} \right]^{8/27}} \right\}^2 \qquad \text{C17}$$

16. calculate h_g and h_p using [5]:

$$h_g = h_p = \frac{kNu}{D_h} \qquad \text{C2}$$

17. calculate K using [5]:

$$K = \frac{A_{collector}}{A_{absorber}} \qquad \text{H13}$$

18. calculate P1 using [5]:

$$P_1 = \frac{Kh_{rpg}}{U_{t\&e} + h_g + Kh_{rpg}} - \frac{h_p}{h_{rpg}} - 1 - \frac{U_b}{Kh_{rpg}} \qquad \text{A29}$$

19. calculate P2 using [5]:

$$P_2 = \frac{h_g}{U_{t\&e} + h_g + Kh_{rpg}} + \frac{h_p}{h_{rpg}} \qquad \text{A28}$$

20. calculate P3 using [5]:

$$P_3 = h_g - \frac{Kh_{rpg} P_2}{P_1} \qquad \text{A27}$$

21. calculate P4 using [5]:

$$P_4 = 1 - \frac{Kh_{rpg}}{P_1 \left(U_{t\&e} + h_g + Kh_{rpg} \right)} \qquad \text{A26}$$

22. calculate P5 using [5]:

$$P_5 = h_g \left(\frac{P_3}{U_t' + h_g + Kh_{rpg}} - 1 \right) - Kh_p \left(\frac{P_2}{P_1} + 1 \right) \qquad \text{A25}$$

23. Calculate the effective transmittance-absorptance product $(\tau\alpha)_e$ of the collector using [5]:

$$(\tau\alpha)_e = \tau_g \alpha_p \qquad \text{H14}$$

24. calculate P6 using [5]:

$$P_6 = \frac{U_{t\&e}}{U_{t\&e} + h_g + Kh_{rgp}} \left(P_4 h_g - \frac{Kh_p}{P_1} \right) T_{amb\,f} - \frac{U_b P_2}{P_1} T_{amb\,r} - \frac{P_2}{P_1} E(\tau\alpha)_e \qquad \text{A24}$$

25. calculate P7 using [5]:

$$P_7 = \frac{P_5 WL}{\dot{m} c_p} \qquad \text{A23}$$

26. Calculate T_{fo} using [5]:

$$T_{fo} = \left(\frac{P_6}{P_5} + T_{fi} \right) \exp(P_7) - \frac{P_6}{P_5} \qquad \text{H15}$$

27. Calculate $\overline{T}_f$ using [5]:

$$\overline{T}_f = \frac{\dot{m} c_p}{2 P_5 WL} \left(\frac{P_6}{P_5} + T_{fi} \right) \left[\exp\left(\frac{P_5 WL}{\dot{m} c_p} \right) - 1 \right] + \frac{1}{2} \left(T_{fi} - \frac{P_6}{P_5} \right) \qquad \text{A31}$$

28. Calculate $\overline{T}_g$ using [5]:

$$\overline{T}_g = \frac{U_b T_a}{P_1 \left(U_{t\&e} + h_g + K h_{rpg} \right)} + \left\{ \frac{h_g}{U_{t\&e} + h_g + K h_{rpg}} - K h_{rpg} \frac{\left[\dfrac{h_g}{U_{t\&e} + h_g + K h_{rpg}} + \dfrac{h_p}{h_{rpg}} \right]}{P_1 \left(U_{t\&e} + h_g + K h_{rpg} \right)} \right\} \overline{T}_f$$

$$+ \left\{ \frac{U_{t\&e}}{U_{t\&e} + h_g + K h_{rpg}} - \frac{K h_{rpg} U_{t\&e}}{P_1 \left(U_{t\&e} + h_g + K h_{rpg} \right)^2} \right\} T_a - \frac{1}{P_1 \left(U_{t\&e} + h_g + K h_{rpg} \right)} E(\tau\alpha)_e \qquad \text{A32}$$

29. Calculate $\overline{T}_p$ using [5]:

$$\overline{T}_p = -\frac{U_b}{K h_{rpg} P_1} T_a - \frac{U_{t\&e}}{\left(U_{t\&e} + h_g + K h_{rpg} \right) P_1} T_a - \frac{1}{P_1} \left[\frac{h_2}{U_{t\&e} + h_g + K h_{rpg}} + \frac{h_p}{h_{rpg}} \right] \overline{T}_f$$

$$- \frac{1}{K h_{rpg} P_1} E(\tau\alpha)_e \qquad \text{A33}$$

30. Calculate $\overline{T}_{o1}$ using [5]:

$$\overline{T}_{o1} = \frac{\dfrac{k_g}{d_g} \overline{T}_g + \left(h_w + h_{rgs} \right) T_{amb}}{h_w + h_{rgs} + \dfrac{k_g}{d_g}} \qquad \text{H16}$$

31. Calculate $\overline{T}_{o4}$ using [5]:

$$\overline{T}_{o4} = \frac{\frac{k_b}{d_b}\overline{T}_p + \left(h_w + h_{rps}\right)T_{amb}}{h_w + h_{rps} + \frac{k_b}{d_b}} \qquad \text{H17}$$

32. calculate the Re using [2]:

$$\text{Re} = \frac{\dot{m}D_h}{A_c\mu} \qquad \text{B5}$$

33. calculate the friction factor (f) using:

$$f' = 0.11\left(\frac{R}{D_h} + \frac{68}{\text{Re}}\right)^{0.25} \qquad \text{B16}$$

If f' ≥ 0.018: f=f'

If f' < 0.018: f= 0.85*f' + 0.0028

34. calculate q using:

$$q = E_{vg}A_g\tau_g$$

35. calculate V using:

$$V = \left(\frac{gqL^2}{T'_{amb}\, b\rho c_p\left[1.5 + \frac{fL}{D_h}\right]}\right)^{1/3} \qquad \text{A57}$$

36. calculate $\dot{m}$ using:

$$\dot{m} = \rho A_c V$$

37. Solving for the temperatures and air mass flow is an iterative procedure. The calculated temperatures replace the initial temperatures in step 2. The calculated air mass flow replaces the initial flow in step 3. The process is repeated until the difference between the initial and the calculated temperatures is less than 0.01°C, and the difference between the initial and calculated air mass flows is less than 0.000001 kg s^{-1}.

H10 Brinkworth Model for Buoyant Convection ($Brink_{bc}$)

The procedure for the $Brinkworth_{bc}$ model is:

1. Obtain the following data:
   - Duct –W (m), b (m), L (m), ε_g, ε_p, α_p, τ_g, R (m)
   - Meteorological –T'_{amb} (K), $T'_{f,i}$ (K) if different from ambient temperature, T'_{ramb} (K), E_{vg} (W m^{-2}), v (m s^{-1})
   - Constants –σ (W m^{-2} K^{-4}), g (m s^{-2}), k (W m^{-1} K^{-1}), the kinematic viscosity of air (ν – m^2 s^{-1}), ρ (kg m^{-3}), c_p (J kg^{-1} K^{-1})
2. calculate A_c and D_h (B1)
3. Guess $\overline{T}'_g$ and $\overline{T}'_p$
4. calculate h_w using McAdam's correlation [5]:

$$h_w = 5.7 + 3.8v \qquad \text{C20}$$

5. Guess ($\dot{m}$)
6. calculate Re using [2]:

$$\mathrm{Re} = \frac{\dot{m} D_h}{A_c \mu} \qquad \text{B5}$$

7. calculate the friction factor (f) using:

$$f' = 0.11\left(\frac{R}{D_h} + \frac{68}{\mathrm{Re}}\right)^{0.25} \qquad \text{B16}$$

   If f' ≥ 0.018: f=f'

   If f' < 0.018: f= 0.85*f' + 0.0028

8. calculate q using:

$$q = E_{vg} A_g \tau_g \alpha_p \qquad \text{H32}$$

9. calculate V using:

$$V = \left(\frac{gqL^2}{T'_{amb}\, b\rho c_p \left[1.5 + \frac{fL}{D_h}\right]}\right)^{1/3} \qquad \text{A57}$$

10. calculate $\dot{m}$) using:

$$\dot{m} = \rho A_c V \qquad \text{H33}$$

11. calculate the coefficient of expansion of air (β) using:

$$\beta = \frac{1}{T'_{fo}} \qquad \text{H29}$$

12. calculate Gr using [2]:

$$Gr = \frac{L^3 \beta g \Delta T}{\nu^2} \qquad \text{B8}$$

13. calculate Pr using [2]:

$$\text{Pr} = \frac{c_p \mu}{k} \qquad \text{B6}$$

14. calculate the dimensionless length (L^+) using [7]:

$$L^+ = \left(\frac{48 \,\text{Pr}}{Gr} \right)^{0.5} \qquad \text{C19}$$

15. calculate the Nu using [8]:

$$N\overline{u} = 5.35 + \frac{0.07}{L^+} \qquad \text{C18}$$

16. calculate the convective heat transfer coefficient for the surface using [5]:

$$h_g = h_p = \frac{kNu}{D_h} \qquad \text{C2}$$

17. calculate the radiative heat loss from the absorbing plate to the glass cover (q_{rpg}) using [8]:

$$q_{rpg} = 4\sigma \left(\frac{\overline{T}_p + \overline{T}_g}{2} + 273.15 \right)^3 \left(\frac{\varepsilon_p}{2 - \varepsilon_p} \right) \left(\overline{T}_p - \overline{T}_g \right) \qquad \text{A58}$$

18. calculate h_{rs} using [5]:

$$h_{rs} = \sigma \varepsilon_c \left[(T_1 + 273)^2 + (T_{amb} + 273)^2 \right] (T_1 + T_{amb} + 546) \qquad \text{C32}$$

19. calculate U_t using [3]:

$$U_t = h_w + h_{rs} \qquad \text{H4}$$

20. calculate the heat transfer coefficient between the glass surface and the air (h_{gf}) as [8]:

$$h_{gf} = \frac{h_g U_t}{h_g + U_t} \qquad \text{H34}$$

21. calculate the sol-air temperature using:

$$T'_{sol} = \frac{q_{rpg}}{U_t} + T_{amb} \qquad \text{H35}$$

NB: T'_{sol} equation has been altered from the reference paper due to the different scenario it is being applied to.

22. calculate the heat transfer coefficient between the absorber surface and the air (h_{pf}) as [8]:

$$h_{pf} = \frac{h_p U_b}{h_p + U_b} \qquad \text{H36}$$

23. calculate the back temperature ($\overline{T}_b$) using [8]:

$$\overline{T}'_b = \frac{\alpha_p \tau_g E_{vg} - q_{rpg}}{U_b} + T_{ramb} \qquad \text{H37}$$

NB: T'_b equation has been altered from the reference paper due to the different scenario it is being applied to.

24. calculate the non-dimensional collector heat transfer parameter (λ) using [8]:

$$\lambda = \frac{h_{gf} A_g + h_{pf} A_p}{\dot{m} c_p} \qquad \text{A64}$$

25. calculate T'_{fo} using [8]:

$$T'_{fo} = T'_{fi} + \left(1 - e^{-\lambda}\right)\left(\frac{h_{gf} A_g \left(T'_{sol} - T'_{fi}\right) + h_{pf} A_p \left(T'_b - T'_{fi}\right)}{h_{gf} A_g + h_{pf} A_p}\right) \qquad \text{A63}$$

26. calculate $\overline{T}'_f$ assuming a linear temperature gradient.

27. calculate $\overline{T}'_g$ using:

$$\overline{T}'_g = \frac{h_{gf}\left(T'_{sol} - \overline{T}'_f\right)}{h_g} + \overline{T}'_f \qquad \text{H38}$$

28. calculate $\overline{T}'_p$ using:

$$\overline{T}'_p = \frac{h_{pf}\left(\overline{T}'_b - \overline{T}'_f\right)}{h_p} + \overline{T}'_f \qquad \text{H39}$$

29. Solving for the temperatures and air mass flow is an iterative procedure. The calculated temperatures replace the initial temperatures in step 3. Similarly the calculated air mass flow replaces the initial guess in step 5. The process is repeated until the difference between the initial and the calculated temperatures is less than 0.01^{o}C, and the difference between the initial and calculated air mass flow is less than 0.000001 kg s^{-1}. The estimated absorber temperature $\overline{T}'_p$ should be adjusted while watching the

effect on the calculated absorber temperature, until the difference between the two is less than 0.01^{o}C.

H11 Stevenson Model for Buoyant Convection ($Steve_{bc}$)

The procedure for the $Brinkworth_{bc}$ model is:

1. Obtain the following data:

- Duct –W (m), b (m), L (m), d_g (m), d_b (m), d_e (m), k_g (W m^{-1} K^{-1}), k_{ins} (W m^{-1} K^{-1}), τ_g, R (m)
- Meteorological –T_{amb} (^{o}C), E_{vg} (W m^{-2}), v (m s^{-1})
- Constants –g (m s^{-2}), μ (kg m^{-1} s^{-1}), ρ (kg m^{-3}), c_p (J kg^{-1} K^{-1})

2. calculate A_c and D_h (B1)
3. calculate h_w using McAdam's correlation [5]:

$$h_w = 5.7 + 3.8v \qquad \text{C20}$$

4. Guess ($\dot{m}$)
5. calculate Re using [2]:

$$\mathrm{Re} = \frac{\dot{m} D_h}{A_c \mu} \qquad \text{B5}$$

6. calculate f using:

$$f' = 0.11\left(\frac{R}{D_h} + \frac{68}{\mathrm{Re}}\right)^{0.25} \qquad \text{B16}$$

If f' ≥ 0.018: f=f'

If f' < 0.018: f= 0.85*f' + 0.0028

7. calculate q using:

$$q = E_{vg} A_g \tau_g \alpha_p \qquad \text{H32}$$

8. calculate V using:

$$V = \left(\frac{gqL^2}{T'_{amb}\, b\rho c_p \left[1.5 + \frac{fL}{D_h}\right]}\right)^{1/3} \qquad \text{A57}$$

9. calculate $\dot{m}$ using:

$$\dot{m} = \rho A_c V \qquad \text{H33}$$

30. calculate U_t using:

$$U_t = 1/\left(\frac{d_g}{k_g} + \frac{1}{h_w}\right) \qquad \text{H40}$$

31. calculate U_e using:

$$U_e = 1/\left(\frac{d_e}{k_e} + \frac{1}{h_w}\right) \qquad \text{H41}$$

32. calculate U_b using:

$$U_b = 1/\left(\frac{d_b}{k_b} + \frac{1}{h_w}\right) \qquad \text{H42}$$

10. calculate $\overline{T}_f$ using:

$$\overline{T}_f = \frac{Q_{in}}{\left(A_g U_g + A_b U_b + 2A_e U_e + c_p \dot{m}\right)} + T_{amb} \qquad \text{H43}$$

11. calculate the exit air temperature using:

$$T_{fo} = \frac{\overline{T}_f - (1-\gamma)T_{f_i}}{\gamma} \qquad \text{H44}$$

Where $\gamma = 0.75$

12. Solving the air mass flow is an iterative procedure. The calculated air mass flow replaces the initial value in step 4. The process is repeated until the difference between the initial and the calculated air mass flow is less than 0.000001 kg s^{-1}.

Buoyant Convection – Modified Model

H12 Ong Model for Buoyant Convection (Ong_{bcad})

The procedure for the Ong_{bcad} model is:

1. Obtain the following data:

- Duct –W (m), b (m), L (m), ε_g, ε_p, d_b (m), k_{ins} (W m^{-1} K^{-1}), α_g, α_p, $SHGC_\theta$, $SHGC_{diff}$

- Meteorological –T'_{amb} (K), $T'_{f,i}$ (K) if different from ambient temperature, E_{vdir} (W m^{-2}), E_{vdiff} (W m^{-2}), v (m s^{-1})
- Constants – σ (W m^{-2} K^{-4}), g (m s^{-2})

2. calculate A_c and D_h (B1)
3. guess $\overline{T}_f$, $\overline{T}_g$ and $\overline{T}_p$. A reasonable first assumption is that they are equal to T'_{amb}+ 1K.
4. calculate T'_{fo} using [3]:

$$T'_{fo} = \frac{\overline{T}'_f - (1-\gamma)T_{f_i}}{\gamma} \qquad \text{H27}$$

Where γ is 0.75

5. calculate the sky temperature using the HTB2 algorithm described in Section 4.1.12.1 equations 4.13-4.17. The cloud cover for 03/07/06 has been set to 0.1.
6. calculate h_w using McAdam's correlation [3]:

$$h_w = 5.7 + 3.8v \qquad \text{C20}$$

7. calculate R1 using:

$$R1 = E_{vdir} SHGC_\theta R_p \qquad \text{H22}$$

8. calculate S_1 using:

$$S_1 = \alpha_{g\theta} E_{vdir} + \alpha_{gdiff}\left(E_{vdiff} + R1\right) \qquad \text{H21}$$

9. calculate R2 using:

$$R2 = R1 R_g \qquad \text{H24}$$

10. calculate S_2 using:

$$S_2 = \left[E_{vdir} SHGC_\theta + \left(E_{vdiff} + R2\right) SHGC_{diff}\right]\alpha_p \qquad \text{H23}$$

11. Guess $\dot{m}$
12. calculate the dynamic viscosity (μ) using [3]:

$$\mu = \left[1.846 + 0.00472(\overline{T}'_f - 300)\right]10^{-5} \qquad \text{H18}$$

13. calculate Re using [2]:

$$\text{Re} = \frac{\dot{m} D_h}{A_c \mu} \qquad \text{B5}$$

14. calculate f using:

$$f' = 0.11\left(\frac{R}{D_h} + \frac{68}{\mathrm{Re}}\right)^{0.25} \qquad \text{B16}$$

If f' ≥ 0.018: f=f'

If f' < 0.018: f= 0.85*f' + 0.0028

15. calculate q using:

$$q = S_2 A_g \qquad \text{H46}$$

16. calculate the air density (ρ) using [3]:

$$\rho = 1.1614 - 0.00353\left(\overline{T}'_f - 300\right) \qquad \text{H28}$$

17. calculate the specific heat capacity (c_p) of the air using [3]:

$$c_p = \left[1.007 + 0.00004(\overline{T}'_f - 300)\right]10^3 \qquad \text{H19}$$

18. calculate V using:

$$V = \left(\frac{gqL^2}{T'_{amb}\, b\rho c_p\left[1.5 + \frac{fL}{D_h}\right]}\right)^{1/3} \qquad \text{A57}$$

19. calculate $\dot{m}$ using:

$$\dot{m} = \rho A_c V \qquad \text{H33}$$

20. calculate the coefficient of expansion of air (β) using:

$$\beta = \frac{1}{T'_{fo}} \qquad \text{H29}$$

21. calculate Gr using [2]:

$$Gr = \frac{g\rho^2 \beta \Delta T L^3}{\mu^2} \qquad \text{B9}$$

Where ΔT refers to the air inlet temperature subtracted from the air exit temperature.

22. calculate the thermal conductivity (k) of the air using [3]:

$$k = 0.0263 + 0.000074(\overline{T}'_f - 300) \qquad \text{H20}$$

23. calculate Pr using [2]:

$$\mathrm{Pr} = \frac{c_p \mu}{k} \qquad \text{B6}$$

24. calculate Ra using [2]:

$$Ra = Gr\,\mathrm{Pr} \qquad \text{B12}$$

25. calculate h_g and h_p using [2]:

$$h_g = h_p = \frac{kNu}{D_h} \qquad \text{C2}$$

26. calculate Nu:

- If the Rayleigh number is less than 10^9, the flow is assumed to be laminar, and the Nusselt number is calculated using Incropera and DeWitt's correlation for laminar flow undergoing natural convection [3]:

$$Nu = 0.68 + \frac{0.67Ra^{1/4}}{\left[1+\left(\frac{0.492}{\mathrm{Pr}}\right)^{9/16}\right]^{4/9}} \qquad \text{C16}$$

- If the Rayleigh number is greater than 10^9, the flow is assumed to be turbulent, and the Nusselt number is calculated using Incropera and DeWitt's correlation for turbulent flow undergoing natural convection [3]:

$$Nu = \left\{0.825 + \frac{0.387Ra^{1/6}}{\left[1+\left(\frac{0.492}{\mathrm{Pr}}\right)^{9/16}\right]^{8/27}}\right\}^2 \qquad \text{C17}$$

27. calculate h_{rpg} using [3]:

$$h_{rpg} = \frac{\sigma\left(\overline{T}'^2_g + \overline{T}'^2_p\right)\left(\overline{T}'_g + \overline{T}'_p\right)}{\frac{1}{\varepsilon_g}+\frac{1}{\varepsilon_p}-1} \qquad \text{C28}$$

28. calculate h_{rs} using [3]:

$$h_{rs} = \frac{\sigma\varepsilon_g\left(\overline{T}'_g + T'_s\right)\left(\overline{T}'^2_g + T'^2_s\right)\left(\overline{T}'_g - T'_s\right)}{\left(\overline{T}'_g - T'_{amb}\right)} \qquad \text{C30}$$

29. calculate U_t using [3]:

$$U_t = h_w + h_{rs} \qquad \text{H4}$$

30. calculate U_b using [3]:

$$U_b = \frac{1}{\frac{d_b}{k_b}+\frac{1}{h_w}} \qquad \text{H5}$$

31. calculate M using [3]:

$$M = \frac{\dot{m} c_p}{\gamma W L} \qquad \text{H31}$$

32. The temperatures can be found by solving the matrix equation [1]:

$$[T] = [A]^{-1}[B] \qquad \text{A11}$$

where:

$$[T] = \begin{bmatrix} \overline{T}'_g \\ \overline{T}'_f \\ \overline{T}'_p \end{bmatrix}, \quad [A] = \begin{bmatrix} h_g + h_{rpg} + U_t & -h_g & -h_{rpg} \\ h_g & -(h_g + h_p + M) & h_p \\ -h_{rpg} & -h_p & h_p + h_{rpg} + U_b \end{bmatrix}$$

and $[B] = \begin{bmatrix} U_t T'_{amb} + S_g \\ -MT'_{f,i} \\ S_p + U_b T'_{amb} \end{bmatrix}$

33. Solving for the temperatures is an iterative procedure. The calculated temperatures replace the initial temperatures in step 3. The calculated air mass flow replaces the initial flow in step 11. The process is repeated until the difference between the initial and the calculated temperatures is less than 0.01^{o}C, and the difference between the initial and calculated air mass flows is less than 0.000001 kg s^{-1}.

H13 Yeh Model for Buoyant Convection (Yeh_{bcad})

The procedure for the Yeh_{bcad} model is:

1. Obtain the following data (please note the required units):

- Duct –W (m), b (m), L (m), ε_g, ε_p, α_p, τ_g, R (m)
- Meteorological –T'_{amb} (K), $T'_{f,i}$ (K) if different from ambient temperature, E'_{vg} (kJ h^{-1} m^{-2} h^{-1}), v (m s^{-1})
- Constants –σ' (kJ h^{-1} m^{-2} K^{-4}), g (m s^{-2})

2. calculate A_c and D_h (B1)
3. calculate the h_w using McAdam's correlation which Yeh adjusted to [4]:

$$h_w = 4.9 + 3.27v \qquad \text{C23}$$

4. Guess $\overline{T}_f$ and $\overline{T}_p$. A reasonable first assumption is that they are equal to T'_{amb}+ 1K.

5. guess ($\dot{m}$)
6. calculate h_{rpg} using [4]:

$$h_{rpg} \approx \frac{4\sigma T'^{3}_{f}}{\frac{1}{\varepsilon_g}+\frac{1}{\varepsilon_p}-1} \qquad \text{C29}$$

7. calculate the air density (ρ) using [3]:

$$\rho = 1.1614 - 0.00353\left(\overline{T}'_{f} - 300\right) \qquad \text{H28}$$

8. calculate β using:

$$\beta = \frac{1}{T'_{fo}} \qquad \text{H29}$$

9. calculate μ using [3]:

$$\mu = \left[1.846 + 0.00472(\overline{T}'_{f} - 300)\right]10^{-5} \qquad \text{H18}$$

Then multiply by 3600 to adapt the units to kg m^{-1} h^{-1}:

10. calculate Gr using [2]:

$$Gr = \frac{g\rho^{2}\beta\Delta T L^{3}}{\mu^{2}} \qquad \text{B9}$$

Where ΔT refers to the air inlet temperature subtracted from the air exit temperature.

11. calculate c_p of the air using [3]:

$$c_p = \left[1.007 + 0.00004(\overline{T}'_{f} - 300)\right]10^{3} \qquad \text{H19}$$

Then divide by 1000 to adapt the units to kJ kg^{-1} K^{-1}

12. calculate k using [3]:

$$k = 0.0263 + 0.000074(\overline{T}'_{f} - 300) \qquad \text{H20}$$

Then multiply by 3600 and divide by 1000 to adapt the units to kJ h^{-1} m^{-1} K^{-1}

13. calculate Pr using [2]:

$$\Pr = \frac{c_p \mu}{k} \qquad \text{B6}$$

14. calculate Ra using [2]:

$$Ra = Gr \Pr \qquad \text{B12}$$

15. calculate Nu using:

- If the Rayleigh number is less than 10^9, the flow is assumed to be laminar, and the Nusselt number is calculated using Incropera and DeWitt's correlation for laminar flow undergoing natural convection [3]:

$$Nu = 0.68 + \frac{0.67 Ra^{1/4}}{\left[1 + \left(\frac{0.492}{\mathrm{Pr}}\right)^{9/16}\right]^{4/9}} \qquad \text{C16}$$

a. If the Rayleigh number is greater than 10^9, the flow is assumed to be turbulent, and the Nusselt number is calculated using Incropera and DeWitt's correlation for turbulent flow undergoing natural convection [3]:

$$Nu = \left\{0.825 + \frac{0.387 Ra^{1/6}}{\left[1 + \left(\frac{0.492}{\mathrm{Pr}}\right)^{9/16}\right]^{8/27}}\right\}^2 \qquad \text{C17}$$

16. calculate h_p using [4]:

$$h_p = \frac{kNu}{D_h} \qquad \text{C2}$$

17. calculate U_t using [4]:

$$U_t = \left\{ \frac{\frac{\overline{T}'_p}{520}}{\left[\frac{\overline{T}'_p - T'_{amb}}{1 + \left(1 + 0.089h'_w - 0.1166h'_w \varepsilon_p\right)\left(1 + 0.07866\right)}\right]^{0.43\left(1 - \frac{100}{\overline{T}'_p}\right)}} + \frac{1}{h'_w} \right\}^{-1} + \frac{\sigma'\left(\overline{T}'_p + T'_{amb}\right)\left(\overline{T}'^2_p + T'^2_{amb}\right)}{\frac{1}{\varepsilon_p + 0.00591h'_w} + \frac{2 + \left(1 + 0.089h'_w - 0.1166h'_w \varepsilon_p\right)\left(1 + 0.07866\right) - 1 + 0.133\varepsilon_p}{\varepsilon_g - 1}} \qquad \text{A19}$$

18. calculate U_b using [4]:

$$U_b = \frac{k_{ins}}{d_{ins}} \qquad \text{H7}$$

19. calculate U_L using [4]:

$$U_L = U_t + U_b \qquad \text{H8}$$

20. calculate F’ using [4]:

$$F' = \left(1 + \frac{U_L}{h_p} + \left[\frac{1}{h_p} + \frac{1}{h_{rpg}}\right]^{-1}\right)^{-1} \qquad \text{C38}$$

21. calculate F_R using [4]:

$$F_R = \frac{\dot{m}' c_p}{A_{sur} U_L}\left\{1 - \exp\left[-\frac{U_L F' A_{sur}}{\dot{m}' c_p}\right]\right\} \qquad \text{C37}$$

22. calculate η using [4]:

$$\eta = F_R\left(\alpha_p \tau_g - U_L\left(T'_{fi} - T'_{amb}\right)/E'\right) \qquad \text{C36}$$

23. calculate $\overline{T}_f$ using [4]:

$$\overline{T}'_f = T'_{fi} + \frac{\eta E'}{U_L F_R}\left(1 - \frac{F_R}{F'}\right) \qquad \text{A20}$$

24. calculate $\overline{T}_p$ the temperature of the solar absorbing surface using [4]:

$$\overline{T}'_p = T'_{f,i} + \frac{\eta E'}{U_L F_R}\left(1 - F_R\right) \qquad \text{A21}$$

34. calculate T'_{fo} using [3]:

$$T'_{fo} = \frac{\overline{T}'_f - (1-\gamma) T'_{f_i}}{\gamma} \qquad \text{H27}$$

25. calculate Re using [2]:

$$\text{Re} = \frac{\dot{m} D_h}{A_c \mu} \qquad \text{B5}$$

26. calculate f using:

$$f' = 0.11\left(\frac{R}{D_h} + \frac{68}{\text{Re}}\right)^{0.25} \qquad \text{B16}$$

If f’ ≥ 0.018: f=f’

If f’ < 0.018: f= 0.85*f’ + 0.0028

27. calculate q using:

$$q = E_{vg} A_g \tau_g$$

28. calculate V using:

$$V = \left(\frac{gqL^2}{T'_{amb}\, b\rho c_p \left[1.5 + \frac{fL}{D_h} \right]} \right)^{1/3} \qquad \text{A57}$$

29. calculate $\dot{m}$ using:

$$\dot{m} = \rho A_c V \qquad \text{B11 (rearranged)}$$

30. Solving for the temperatures is an iterative procedure. The calculated temperatures replace the initial temperatures in step 4. The calculated air mass flow similarly replaces the estimate in step 5. The process is repeated until the difference between the initial and the calculated temperatures is less than 0.01^{o}C, and the difference between the initial and calculated air mass flows is less than 0.000001 kg s^{-1}.

H14 Ho Model for Buoyant Convection (Ho_{bcad}) [5]

The procedure for the Ho_{bcad} model is:

1. Obtain the following data:

- Duct –W (m), b (m), L (m), ε_g, ε_p, d_g (m), d_b (m), d_e (m), k_g (W m^{-1} K^{-1}), k_{ins} (W m^{-1} K^{-1}), α_p, R (m), $SHGC_\theta$ $SHGC_{diff}$
- Meteorological –T'$_{amb}$ (K), T'$_{f,i}$ (K) if different from ambient temperature, T'$_{ambr}$ (K) if different from the front ambient temperature, E_{vdir} (W m^{-2}), E_{vdiff} (W m^{-2}), v (m s^{-1})
- Constants –σ (W m^{-2} K^{-4}), g (m s^{-2})

2. Guess the initial temperatures of the glass outer surface ($\overline{T}_{o1}$ - ^{o}C), the glass inner surface ($\overline{T}_{g}$ - ^{o}C), the solar absorber surface ($\overline{T}_{p}$ - ^{o}C) and the rear surface temperature ($\overline{T}_{o4}$ - ^{o}C)
3. Guess $\dot{m}$
4. calculate h_{rpg} using [5]:

$$h_{rpg} = \frac{\sigma\left(T'^{2}_{g} + T'^{2}_{p}\right)\left(T'_{g} + T'_{p}\right)}{\frac{1}{\varepsilon_g} + \frac{1}{\varepsilon_p} - 1} \qquad \text{C28}$$

5. calculate the sky temperature using the HTB2 algorithm described in Section 4.1.12.1 equations 4.13-4.17. The cloud cover for the dates considered has been set to 0.1.
6. calculate h_{rs} using [1]:

$$h_{rs} = \frac{\sigma\varepsilon_g\left(T_g + T_s\right)\left(T_g^2 + T_s^2\right)\left(T_g - T_s\right)}{\left(T_g - T_{amb}\right)} \qquad \text{C30}$$

7. calculate h_w using McAdam's correlation [5]:

$$h_w = 5.7 + 3.8v \qquad \text{C20}$$

8. calculate U_t using [6]:

$$U_t = 1/\left(\frac{1}{h_{rs}} + \frac{d_g}{k_g} + \frac{1}{h_w}\right) \qquad \text{H9}$$

9. calculate U_e using [6]:

$$U_e = 1/\left(\frac{1}{h_{rs}} + \frac{d_e}{k_e} + \frac{1}{h_w}\right) \qquad \text{H10}$$

10. calculate $U_{t\&e}$ using [5]:

$$U_{t\&e} = U_t + \frac{2U_e A_e}{LW} \qquad \text{H11}$$

11. calculate U_b using [6]:

$$U_b = 1/\left(\frac{1}{h_{rs}} + \frac{d_b}{k_b} + \frac{1}{h_w}\right) \qquad \text{H12}$$

12. calculate ρ using [3]:

$$\rho = 1.1614 - 0.00353\left(\overline{T}'_f - 300\right) \qquad \text{H28}$$

13. calculate μ using [3]:

$$\mu = \left[1.846 + 0.00472(\overline{T}'_f - 300)\right]10^{-5} \qquad \text{H18}$$

14. calculate the coefficient of expansion of air (β) using:

$$\beta = \frac{1}{T'_{fo}} \qquad \text{H29}$$

15. calculate Gr using [2]:

$$Gr = \frac{g\rho^2 \beta \Delta T L^3}{\mu^2} \qquad \text{B9}$$

Where ΔT refers to the air inlet temperature subtracted from the air exit temperature.

16. calculate c_p using [3]:

$$c_p = \left[1.007 + 0.00004(\overline{T}'_f - 300)\right]10^3 \qquad \text{H19}$$

17. calculate k using [3]:

$$k = 0.0263 + 0.000074(\overline{T}'_f - 300) \qquad \text{H20}$$

18. calculate Pr using [2]:

$$\Pr = \frac{c_p \mu}{k} \qquad \text{B6}$$

19. calculate Ra using [2]:

$$Ra = Gr \Pr \qquad \text{B12}$$

20. calculate Nu:

- If the Rayleigh number is less than 10^9, the flow is assumed to be laminar, and the Nusselt number is calculated using Incropera and DeWitt's correlation for laminar flow undergoing natural convection [3]:

$$Nu = 0.68 + \frac{0.67 Ra^{1/4}}{\left[1 + \left(\frac{0.492}{\Pr}\right)^{9/16}\right]^{4/9}} \qquad \text{C16}$$

b. If the Rayleigh number is greater than 10^9, the flow is assumed to be turbulent, and the Nusselt number is calculated using Incropera and DeWitt's correlation for turbulent flow undergoing natural convection [3]:

$$Nu = \left\{0.825 + \frac{0.387 Ra^{1/6}}{\left[1 + \left(\frac{0.492}{\Pr}\right)^{9/16}\right]^{8/27}}\right\}^2 \qquad \text{C17}$$

21. calculate h_g and h_p using [5]:

$$h_g = h_p = \frac{kNu}{D_h} \qquad \text{C2}$$

22. calculate K using [5]:

$$K = \frac{A_{collector}}{A_{absorber}} \qquad \text{H13}$$

23. calculate P1 using [5]:

$$P_1 = \frac{Kh_{rpg}}{U_{t\&e} + h_g + Kh_{rpg}} - \frac{h_p}{h_{rpg}} - 1 - \frac{U_b}{Kh_{rpg}} \qquad \text{A29}$$

24. calculate P2 using [5]:

$$P_2 = \frac{h_g}{U_{t\&e} + h_g + Kh_{rpg}} + \frac{h_p}{h_{rpg}} \qquad \text{A28}$$

25. calculate P3 using [5]:

$$P_3 = h_g - \frac{Kh_{rpg}P_2}{P_1} \qquad \text{A27}$$

26. calculate P4 using [5]:

$$P_4 = 1 - \frac{Kh_{rpg}}{P_1\left(U_{t\&e} + h_g + Kh_{rpg}\right)} \qquad \text{A26}$$

27. calculate P5 using [5]:

$$P_5 = h_g\left(\frac{P_3}{U_t' + h_g + Kh_{rpg}} - 1\right) - Kh_p\left(\frac{P_2}{P_1} + 1\right) \qquad \text{A25}$$

28. Calculate the effective transmittance-absorptance product $E(\tau\alpha)_{e\theta}$ in terms of diffuse and direct solar irradiation with respect to the angle of incidence using:

$$R = E_{vdir} SHGC_\theta R_p R_g \qquad \text{H25}$$

$$E(\tau\alpha)_{e\theta} = \left[E_{vdir} SHGC_\theta + \left(E_{vdiff} + R\right) SHGC_{diff}\right]\alpha_p \qquad \text{H26}$$

29. calculate P6 using [5]:

$$P_6 = \frac{U_{t\&e}}{U_{t\&e} + h_g + Kh_{rgp}}\left(P_4 h_g - \frac{Kh_p}{P_1}\right)T_{amb\,f} - \frac{U_b P_2}{P_1} T_{amb\,r} - \frac{P_2}{P_1} E(\tau\alpha)_e \qquad \text{A24}$$

30. calculate P7 using [5]:

$$P_7 = \frac{P_5 WL}{\dot{m} c_p} \qquad \text{A23}$$

31. Calculate T_{fo} using [5]:

$$T_{fo} = \left(\frac{P_6}{P_5} + T_{fi}\right)\exp(P_7) - \frac{P_6}{P_5} \qquad \text{H15}$$

32. Calculate $\overline{T}_f$ using [5]:

$$\overline{T}_f = \frac{\dot{m}c_p}{2P_5WL}\left(\frac{P_6}{P_5}+T_{fi}\right)\left[\exp\left(\frac{P_5WL}{\dot{m}c_p}\right)-1\right]+\frac{1}{2}\left(T_{fi}-\frac{P_6}{P_5}\right) \quad \text{A31}$$

33. Calculate $\overline{T}_g$ using [5]:

$$\overline{T}_g = \frac{U_bT_a}{P_1\left(U_{t\&e}+h_g+Kh_{rpg}\right)}+\left\{\frac{h_g}{U_{t\&e}+h_g+Kh_{rpg}}-Kh_{rpg}\frac{\left[\dfrac{h_g}{U_{t\&e}+h_g+Kh_{rpg}}+\dfrac{h_p}{h_{rpg}}\right]}{P_1\left(U_{t\&e}+h_g+Kh_{rpg}\right)}\right\}\overline{T}_f$$

$$+\left\{\frac{U_{t\&e}}{U_{t\&e}+h_g+Kh_{rpg}}-\frac{Kh_{rpg}U_{t\&e}}{P_1\left(U_{t\&e}+h_g+Kh_{rpg}\right)^2}\right\}T_a-\frac{1}{P_1\left(U_{t\&e}+h_g+Kh_{rpg}\right)}E(\tau\alpha)_e \quad \text{A32}$$

34. Calculate the solar absorber temperature using [5]:

$$\overline{T}_p = -\frac{U_b}{Kh_{rpg}P_1}T_a-\frac{U_{t\&e}}{\left(U_{t\&e}+h_g+Kh_{rpg}\right)P_1}T_a-\frac{1}{P_1}\left[\frac{h_2}{U_{t\&e}+h_g+Kh_{rpg}}+\frac{h_p}{h_{rpg}}\right]\overline{T}_f$$

$$-\frac{1}{Kh_{rpg}P_1}E(\tau\alpha)_e \quad \text{A33}$$

35. Calculate $\overline{T}_{o1}$ using [5]:

$$\overline{T}_{o1} = \frac{\dfrac{k_g}{d_g}\overline{T}_g+\left(h_w+h_{rgs}\right)T_{amb}}{h_w+h_{rgs}+\dfrac{k_g}{d_g}} \quad \text{H16}$$

36. Calculate $\overline{T}_{o4}$ using [5]:

$$\overline{T}_{o4} = \frac{\dfrac{k_b}{d_b}\overline{T}_p+\left(h_w+h_{rps}\right)T_{amb}}{h_w+h_{rps}+\dfrac{k_b}{d_b}} \quad \text{H17}$$

37. calculate Re using [2] :

$$\text{Re} = \frac{\dot{m}D_h}{A_c\mu} \quad \text{B5}$$

38. calculate f using:

$$f' = 0.11\left(\frac{R}{D_h}+\frac{68}{\text{Re}}\right)^{0.25} \quad \text{B16}$$

If f' ≥ 0.018: f=f'

If f' < 0.018: f= 0.85*f' + 0.0028

39. calculate q using:

$$q = E(\tau\alpha)_{e\theta} A_g$$

40. calculate V using:

$$V = \left(\frac{gqL^2}{T'_{amb}\, b\rho c_p \left[1.5 + \frac{fL}{D_h} \right]} \right)^{1/3} \qquad \text{A57}$$

41. calculate ($\dot{m}$) using:

$$\dot{m} = \rho A_c V \qquad \text{B11 (rearranged)}$$

42. Solving for the temperatures and air mass flow is an iterative procedure. The calculated temperatures replace the initial temperatures in step 2. The calculated air mass flow replaces the initial estimate in step 3. The process is repeated until the difference between the initial and the calculated temperatures is less than 0.01°C, and the difference between the initial and calculated air mass flows is less than 0.000001 kg s^{-1}.

H15 Brinkworth Model for Buoyant Convection (Brink$_{bcad}$)

The procedure for the Brinkworth$_{bcad}$ model is:

1. Obtain the following data:

- Duct –W (m), b (m), L (m), ε_g, ε_p, α_p, R (m), $SHGC_\theta$, $SHGC_{diff}$
- Meteorological –T'_{amb} (K), $T'_{f,i}$ (K) if different from ambient temperature, T'_{ambr} (K) if different from the front ambient temperature, E_{vdir} (W m^{-2}), E_{vdiff} (W m^{-2}), v (m s^{-1})
- Constants –σ (W m^{-2} K^{-4}), g (m s^{-2}), ν (m^2 s^{-1})

2. calculate A_c and D_h (B1)
3. Guess $\overline{T}_g$, $\overline{T}_p$ and $\overline{T}_f$
4. calculate h_w using McAdam's correlation [5]:

$$h_w = 5.7 + 3.8v \qquad \text{C20}$$

5. Guess $\dot{m}$
6. calculate μ using [3]:

$$\mu = \left[1.846 + 0.00472(\overline{T}'_f - 300)\right]10^{-5} \qquad \text{H18}$$

7. calculate Re using [2]:

$$\text{Re} = \frac{\dot{m}D_h}{A_c\mu} \qquad \text{B5}$$

8. calculate f using:

$$f' = 0.11\left(\frac{R}{D_h} + \frac{68}{\text{Re}}\right)^{0.25} \qquad \text{B16}$$

If f' ≥ 0.018: f=f'

If f' < 0.018: f= 0.85*f' + 0.0028

9. calculate ρ using [3]:

$$\rho = 1.1614 - 0.00353\left(\overline{T}'_f - 300\right) \qquad \text{H28}$$

10. calculate c_p of the air using [3]:

$$c_p = \left[1.007 + 0.00004(\overline{T}'_f - 300)\right]10^3 \qquad \text{H19}$$

11. calculate R using:

$$R = E_{vdir}SHGC_\theta R_p R_g \qquad \text{H25}$$

12. calculate q using:

$$q = \left[E_{vdir}SHGC_\theta + \left(E_{vdiff} + R\right)SHGC_{diff}\right]\alpha_p A_g \qquad \text{H44}$$

13. calculate V using:

$$V = \left(\frac{gqL^2}{T'_{amb}\, b\rho c_p\left[1.5 + \frac{fL}{D_h}\right]}\right)^{1/3} \qquad \text{A57}$$

14. calculate $\dot{m}$ using:

$$\dot{m} = \rho A_c V \qquad \text{B11 (rearranged)}$$

15. calculate the coefficient of expansion of air (β) using:

$$\beta = \frac{1}{T'_{fo}} \qquad \text{H29}$$

16. calculate Gr using [2]:

$$Gr = \frac{L^3 \beta g \Delta T}{\nu^2} \quad \text{B8}$$

17. calculate k using [3]:

$$k = 0.0263 + 0.000074(\overline{T}'_f - 300) \quad \text{H20}$$

18. calculate Pr using [2]:

$$\Pr = \frac{c_p \mu}{k} \quad \text{B6}$$

19. calculate the dimensionless length (L^+) using [7]:

$$L^+ = \left(\frac{48 \Pr}{Gr}\right)^{0.5} \quad \text{C19}$$

20. calculate Nu using [8]:

$$N\overline{u} = 5.35 + \frac{0.07}{L^+} \quad \text{C18}$$

21. calculate h_g and h_p using [5]:

$$h_g = h_p = \frac{kNu}{D_h} \quad \text{C2}$$

22. calculate q_{rpg} using [8]:

$$q_{rpg} = 4\sigma\left(\frac{\overline{T}_p + \overline{T}_g}{2} + 273.15\right)^3 \left(\frac{\varepsilon_p}{2 - \varepsilon_p}\right)\left(\overline{T}_p - \overline{T}_g\right) \quad \text{A58}$$

23. calculate h_{rs} using [5]:

$$h_{rs} = \sigma \varepsilon_c \left[(T_1 + 273)^2 + (T_{amb} + 273)^2\right](T_1 + T_{amb} + 546) \quad \text{C32}$$

24. calculate U_t using [1]:

$$U_t = h_w + h_{rs} \quad \text{H4}$$

25. calculate h_{gf} using [8]:

$$h_{gf} = \frac{h_g U_t}{h_g + U_t} \quad \text{H34}$$

26. calculate T'_{sol} using:

$$T'_{sol} = \frac{q_{rpg}}{U_t} + T_{amb} \quad \text{H35}$$

NB: T'_{sol} equation has been altered from the reference paper due to the different scenario it is being applied to.

27. calculate h_{pf} using [8]:

$$h_{pf} = \frac{h_p U_b}{h_p + U_b} \qquad \text{H36}$$

28. calculate T'_b using:

$$T'_b = \frac{\alpha_p \left(E_{vdir} SHGC_\theta + \left(E_{vdiff} + R\right) SHGC_{diff}\right) - q_{rpg}}{U_b} + T_{ramb} \qquad \text{H45}$$

29. calculate λ using [8]:

$$\lambda = \frac{h_{gf} A_g + h_{pf} A_p}{\dot{m} c_p} \qquad \text{A64}$$

30. calculate T'_{fo} using [8]:

$$T'_{fo} = T'_{fi} + \left(1 - e^{-\lambda}\right)\left(\frac{h_{gf} A_g \left(T'_{sol} - T'_{fi}\right) + h_{pf} A_p \left(T'_b - T'_{fi}\right)}{h_{gf} A_g + h_{pf} A_p}\right) \qquad \text{A63}$$

31. calculate $\overline{T}_f$ assuming a linear temperature gradient.

32. calculate $\overline{T}_g$ using:

$$\overline{T}'_g = \frac{h_{gf} \left(T'_{sol} - \overline{T}'_f\right)}{h_g} + \overline{T}'_f \qquad \text{H38}$$

33. calculate $\overline{T}_p$ using:

$$\overline{T}'_p = \frac{h_{pf} \left(\overline{T}'_b - \overline{T}'_f\right)}{h_p} + \overline{T}'_f \qquad \text{H39}$$

34. Solving for the temperatures and air mass flow is an iterative procedure. The calculated temperatures replace the initial temperatures in step 2. The calculated air mass flow replaces the initial estimate in step 5. The process is repeated until the difference between the initial and the calculated temperatures is less than 0.01^{o}C, and the difference between the initial and calculated air mass flows is less than 0.000001 kg s^{-1}. The estimated absorber temperature should be adjusted while watching the effect on the calculated absorber temperature, until the difference between the two is less than 0.01^{o}C.

H16 Stevenson Model for Buoyant Convection (Steve$_{bcad}$)

The procedure for the Brinkworth$_{bc}$ model is:

1. Obtain the following data:

- Duct –W (m), b (m), L (m), d_g (m), d_b (m), d_e (m), k_g (W m^{-1} K^{-1}), k_{ins} (W m^{-1} K^{-1}), R (m), $SHGC_\theta$, $SHGC_{diff}$
- Meteorological –T_{amb} (^oC), E_{vdir} (W m^{-2}), E_{vdir} (W m^{-2}), v (m s^{-1})
- Constants –g (m s^{-2})

2. estimate $\overline{T}_f$
3. calculate A_c and D_h (B1)
4. calculate h_w using McAdam's correlation [5]:

$$h_w = 5.7 + 3.8v \qquad \text{C20}$$

5. guess $\dot{m}$
6. calculate μ using [3]:

$$\mu = \left[1.846 + 0.00472(\overline{T}'_f - 300)\right]10^{-5} \qquad \text{H18}$$

7. calculate Re using [2]:

$$\text{Re} = \frac{\dot{m}D_h}{A_c\mu} \qquad \text{B5}$$

8. calculate f using:

$$f' = 0.11\left(\frac{R}{D_h} + \frac{68}{\text{Re}}\right)^{0.25} \qquad \text{B16}$$

If f' ≥ 0.018: f=f'

If f' < 0.018: f= 0.85*f' + 0.0028

9. calculate ρ using [3]:

$$\rho = 1.1614 - 0.00353\left(\overline{T}'_f - 300\right) \qquad \text{H28}$$

10. calculate c_p using [3]:

$$c_p = \left[1.007 + 0.00004(\overline{T}'_f - 300)\right]10^3 \qquad \text{H19}$$

11. calculate R using:

$$R = E_{vdir}SHGC_\theta R_p R_g \qquad \text{H22}$$

12. calculate q using:

$$q = \left[E_{vdir}SHGC_\theta + \left(E_{vdiff} + R\right)SHGC_{diff}\right]\alpha_p A_g \qquad \text{H44}$$

13. calculate V using:

$$V = \left(\frac{gqL^2}{T'_{amb}\, b\rho c_p \left[1.5 + \frac{fL}{D_h} \right]} \right)^{1/3} \qquad \text{A57}$$

14. calculate $\dot{m}$ using:

$$\dot{m} = \rho A_c V \qquad \text{B11 (rearranged)}$$

15. calculate U_t using:

$$U_t = 1/\left(\frac{d_g}{k_g} + \frac{1}{h_w} \right) \qquad \text{H40}$$

16. calculate U_e using:

$$U_e = 1/\left(\frac{d_e}{k_e} + \frac{1}{h_w} \right) \qquad \text{H41}$$

17. calculate U_b using:

$$U_b = 1/\left(\frac{d_b}{k_b} + \frac{1}{h_w} \right) \qquad \text{H42}$$

18. calculate $\overline{T}_f$ using:

$$\overline{T}_f = \frac{Q_{in}}{\left(A_g U_g + A_b U_b + 2A_e U_e + c_p \dot{m} \right)} + T_{amb} \qquad \text{H43}$$

19. calculate T_{fo} using:

$$T_{fo} = \frac{\overline{T}_f - (1-\gamma) T_{f_i}}{\gamma} \qquad \text{H44}$$

Where $\gamma = 0.75$

20. Solving for the temperatures and air mass flow is an iterative procedure. The calculated temperatures replace the initial temperatures in step 2. The calculated air mass flow replaces the initial flow in step 5. The process is repeated until the difference between the initial and the calculated temperatures is less than 0.01^{o}C, and the difference between the initial and calculated air mass flows is less than 0.000001 kg s^{-1}.

References

1. Ong, K.S., *Thermal performance of solar air heaters: Mathematical model and solution procedure.* Solar Energy, 1995. **55**(2): p. 93-109.
2. ASHRAE, *2005 ASHRAE Handbook: Fundamentals, SI Edition*, ed. R.a.A.C.E. American Society of Heating, Inc. 2005, Atlanta: ASHRAE; 1-931862-71-0.
3. Ong, K.S., *A mathematical model of a solar chimney.* Renewable Energy, 2003. **28**: p. 1047-1060.
4. Yeh, H.-M. and T.-T. Lin, *Efficiency Improvement of Flat-Plate Solar Air Heaters.* Energy, 1996. **21**(6): p. 435-443.
5. Ho, K.T.K. and D.L. Loveday, *Covered profiled steel cladding as an air heating solar collector: laboratory testing, modelling and validation.* Energy and Buildings, 1997. **26**: p. 293-301.
6. British Standards Institution, *Thermal insulation for building equipment and industrial installations - Calculation Rules*, BS EN ISO 12241, 1998, British Standards Institution.
7. Brinkworth, B.J., *A procedure for the routine calculation of laminar free and mixed convection in inclined ducts.* International Journal of Heat and Fluid Flow, 2000. **21**: p. 456-462.
8. Brinkworth, B.J., R.H. Marshall, and Z. Ibarahim, *A Validated Model of Naturally Ventilated PV Cladding.* Solar Energy, 2000. **69**: p. 67-81.

Appendix I - Data relating to Geometry Optimisation

Table I1 Forced Convection: Geometry Parameters with Average Exit Temperature Results.

Length (m)	Width (m)	Depth (m)	Tilt angle (^{o})	20th March (^{o}C)	21st June (^{o}C)	22nd September (^{o}C)	21st December (^{o}C)
0.5	0.1	0.03	40	12.8	19.4	18.2	4.4
12.5	0.1	0.03	40	39.3	55.9	48.0	25.5
0.5	1	0.03	40	20.7	29.5	27.0	10.9
12.5	1	0.03	40	81.1	99.9	89.3	59.7
0.5	0.1	1	40	12.1	18.4	17.5	3.8
12.5	0.1	1	40	23.0	31.5	29.0	11.9
0.5	1	1	40	12.6	18.9	18.0	4.2
12.5	1	1	40	32.0	42.6	38.3	19.9
0.5	0.1	0.03	90	12.4	18.3	17.8	4.6
12.5	0.1	0.03	90	32.4	34.6	39.3	29.4
0.5	1	0.03	90	18.8	23.1	24.3	11.9
12.5	1	0.03	90	66.8	59.7	75.1	68.1
0.5	0.1	1	90	11.9	17.9	17.2	3.9
12.5	0.1	1	90	20.1	24.0	26.6	13.3
0.5	1	1	90	12.4	18.2	17.7	4.4
12.5	1	1	90	28.2	30.4	33.9	23.1
0.5	0.55	0.515	65	13.2	19.3	18.6	5.0
12.5	0.55	0.515	65	39.5	47.0	46.1	30.4
6.5	0.1	0.515	65	21.0	27.8	27.5	12.2
6.5	1	0.515	65	29.6	36.4	35.5	20.8
6.5	0.55	0.03	65	63.2	71.2	72.0	52.5
6.5	0.55	1	65	24.3	30.6	30.3	15.6
6.5	0.55	0.515	40	28.5	38.5	34.7	17.0
6.5	0.55	0.515	90	24.9	28.0	31.6	19.7
6.5	0.55	0.515	65	29.0	35.3	35.1	20.2

Table I2 Forced Convection: Geometry Parameters with Net Power Output for individual ducts.

Length (m)	Width (m)	Depth (m)	Tilt angle (^{o})	20th March (Wh)	21st June (Wh)	22nd September (Wh)	21st December (Wh)
0.5	0.1	0.03	40	184	20	15	11
12.5	0.1	0.03	40	3658	388	314	223
0.5	1	0.03	40	1218	122	104	77
12.5	1	0.03	40	9139	832	732	569
0.5	0.1	1	40	96	10	8	6
12.5	0.1	1	40	1519	141	124	87
0.5	1	1	40	161	15	13	10
12.5	1	1	40	2709	253	217	168
0.5	0.1	0.03	90	141	8	11	13
12.5	0.1	0.03	90	2755	172	227	263
0.5	1	0.03	90	971	57	77	88
12.5	1	0.03	90	7264	426	589	653
0.5	0.1	1	90	73	4	5	7
12.5	0.1	1	90	1144	66	100	101
0.5	1	1	90	132	8	10	12
12.5	1	1	90	2211	130	173	200
0.5	0.55	0.515	65	237	19	19	17
12.5	0.55	0.515	65	3689	298	296	273
6.5	0.1	0.515	65	1266	105	108	90
6.5	1	0.515	65	2384	191	190	177
6.5	0.55	0.03	65	6785	542	558	496
6.5	0.55	1	65	1692	132	137	125
6.5	0.55	0.515	40	2249	213	182	138
6.5	0.55	0.515	90	1772	106	150	166
6.5	0.55	0.515	65	2305	180	185	170

Table I3 Forced Convection: Geometry Parameters with Net Power Output for $10m^2$ Façade Area Results.

Length (m)	Width (m)	Depth (m)	Tilt angle (^{o})	20th March (kWh)	21st June (kWh)	22nd September (kWh)	21st December (kWh)
0.5	0.1	0.03	40	30.5	3.3	2.5	1.9
12.5	0.1	0.03	40	26.5	2.8	2.3	1.6
0.5	1	0.03	40	21.9	2.2	1.9	1.4
12.5	1	0.03	40	7.2	0.7	0.6	0.5
0.5	0.1	1	40	15.8	1.6	1.3	1.0
12.5	0.1	1	40	11.0	1.0	0.9	0.6
0.5	1	1	40	2.9	0.3	0.2	0.2
12.5	1	1	40	2.1	0.2	0.2	0.1
0.5	0.1	0.03	90	23.3	1.4	1.9	2.2
12.5	0.1	0.03	90	20.0	1.2	1.6	1.9
0.5	1	0.03	90	17.5	1.0	1.4	1.6
12.5	1	0.03	90	5.7	0.3	0.5	0.5
0.5	0.1	1	90	12.1	0.7	0.8	1.1
12.5	0.1	1	90	8.3	0.5	0.7	0.7
0.5	1	1	90	2.4	0.1	0.2	0.2
12.5	1	1	90	1.7	0.1	0.1	0.2
0.5	0.55	0.515	65	7.7	0.6	0.6	0.6
12.5	0.55	0.515	65	5.2	0.4	0.4	0.4
6.5	0.1	0.515	65	17.6	1.5	1.5	1.2
6.5	1	0.515	65	3.6	0.3	0.3	0.3
6.5	0.55	0.03	65	18.5	1.5	1.5	1.4
6.5	0.55	1	65	4.6	0.3	0.4	0.4
6.5	0.55	0.515	40	6.1	0.6	0.5	0.4
6.5	0.55	0.515	90	4.8	0.3	0.4	0.5
6.5	0.55	0.515	65	6.3	0.5	0.5	0.5

Table I4 Forced Convection: Geometry Parameters with Air Mass Flow for $10m^2$ Façade Area.

Length (m)	Width (m)	Depth (m)	Tilt angle (^{o})	All Dates (kg s^{-1})
0.5	0.1	0.03	40	1.653
12.5	0.1	0.03	40	0.072
0.5	1	0.03	40	0.180
12.5	1	0.03	40	0.008
0.5	0.1	1	40	1.653
12.5	0.1	1	40	0.072
0.5	1	1	40	0.180
12.5	1	1	40	0.008
0.5	0.1	0.03	90	1.653
12.5	0.1	0.03	90	0.072
0.5	1	0.03	90	0.180
12.5	1	0.03	90	0.008
0.5	0.1	1	90	1.653
12.5	0.1	1	90	0.072
0.5	1	1	90	0.180
12.5	1	1	90	0.008
0.5	0.55	0.515	65	0.325
12.5	0.55	0.515	65	0.014
6.5	0.1	0.515	65	0.139
6.5	1	0.515	65	0.015
6.5	0.55	0.03	65	0.027
6.5	0.55	1	65	0.027
6.5	0.55	0.515	40	0.027
6.5	0.55	0.515	90	0.027
6.5	0.55	0.515	65	0.027

Table I5 Buoyant Convection: Geometry Parameters with Average Exit Temperature Results.

Length (m)	Width (m)	Depth (m)	Tilt angle (^{o})	20th March (^{o}C)	21st June (^{o}C)	22nd September (^{o}C)	21st December (^{o}C)
0.5	0.1	0.03	40	14.0	20.2	18.9	6.1
12.5	0.1	0.03	40	14.9	21.1	19.6	7.1
0.5	1	0.03	40	12.9	19.2	18.0	5.0
12.5	1	0.03	40	13.5	20.0	18.5	5.6
0.5	0.1	1	40	15.9	22.6	20.7	7.8
12.5	0.1	1	40	16.6	23.4	21.3	8.5
0.5	1	1	40	12.5	18.9	17.8	4.5
12.5	1	1	40	12.6	18.9	17.9	4.5
0.5	0.1	0.03	90	13.5	19.0	18.4	6.5
12.5	0.1	0.03	90	14.3	19.5	19.0	7.6
0.5	1	0.03	90	12.6	18.4	17.8	5.2
12.5	1	0.03	90	13.1	18.7	18.1	5.9
0.5	0.1	1	90	15.0	20.1	20.0	8.6
12.5	0.1	1	90	15.5	20.5	20.3	9.4
0.5	1	1	90	12.3	18.3	17.6	4.6
12.5	1	1	90	12.4	18.3	17.7	4.7
0.5	0.55	0.515	65	13.2	19.3	18.4	5.3
12.5	0.55	0.515	65	13.3	19.4	18.5	5.5
6.5	0.1	0.515	65	15.8	21.7	20.6	8.5
6.5	1	0.515	65	12.6	18.7	17.9	4.7
6.5	0.55	0.03	65	13.6	19.4	18.5	6.0
6.5	0.55	1	65	13.5	19.6	18.7	5.6
6.5	0.55	0.515	40	13.2	19.6	18.4	5.1
6.5	0.55	0.515	90	12.9	18.7	18.1	5.4
6.5	0.55	0.515	65	13.2	19.3	18.5	5.4

Table I6 Buoyant Convection: Geometry Parameters with Average Air Mass Flow Results.

Length (m)	Width (m)	Depth (m)	Tilt angle (^{o})	20th March (kg s^{-1})	21st June (kg s^{-1})	22nd September (kg s^{-1})	21st December (kg s^{-1})
0.5	0.1	0.03	40	4.0 E -4	4.2 E -4	3.9 E -4	3.9 E -4
12.5	0.1	0.03	40	0.006	0.006	0.006	0.006
0.5	1	0.03	40	0.009	0.010	0.009	0.009
12.5	1	0.03	40	0.144	0.154	0.143	0.139
0.5	0.1	1	40	0.005	0.005	0.005	0.004
12.5	0.1	1	40	0.087	0.094	0.087	0.085
0.5	1	1	40	0.102	0.108	0.101	0.099
12.5	1	1	40	2.443	2.606	2.424	2.375
0.5	0.1	0.03	90	3.7 E -4	3.3 E -4	3.6 E -4	4.1 E -4
12.5	0.1	0.03	90	0.005	0.005	0.005	0.006
0.5	1	0.03	90	0.008	0.008	0.008	0.009
12.5	1	0.03	90	0.132	0.120	0.131	0.148
0.5	0.1	1	90	0.004	0.004	0.004	0.005
12.5	0.1	1	90	0.081	0.073	0.080	0.090
0.5	1	1	90	0.094	0.086	0.093	0.104
12.5	1	1	90	2.259	2.064	2.235	2.513
0.5	0.55	0.515	65	0.030	0.030	0.029	0.030
12.5	0.55	0.515	65	0.684	0.687	0.678	0.704
6.5	0.1	0.515	65	0.032	0.032	0.032	0.033
6.5	1	0.515	65	0.828	0.831	0.821	0.852
6.5	0.55	0.03	65	0.038	0.038	0.038	0.039
6.5	0.55	1	65	0.580	0.582	0.574	0.596
6.5	0.55	0.515	40	0.363	0.387	0.360	0.353
6.5	0.55	0.515	90	0.336	0.306	0.332	0.373
6.5	0.55	0.515	65	0.367	0.369	0.364	0.378

Table I7 Buoyant Convection: Geometry Parameters with Total Power Output

Length (m)	Width (m)	Depth (m)	Tilt angle (^{o})	20th March (Wh)	21st June (Wh)	22nd September (Wh)	21st December (Wh)
0.5	0.1	0.03	40	1	1	1	1
12.5	0.1	0.03	40	25	29	21	24
0.5	1	0.03	40	17	21	15	17
12.5	1	0.03	40	379	449	320	368
0.5	0.1	1	40	25	32	23	24
12.5	0.1	1	40	558	709	502	528
0.5	1	1	40	142	182	139	127
12.5	1	1	40	3538	4257	3450	3165
0.5	0.1	0.03	90	1	1	1	1
12.5	0.1	0.03	90	19	12	15	30
0.5	1	0.03	90	13	9	11	20
12.5	1	0.03	90	285	186	232	449
0.5	0.1	1	90	18	13	17	29
12.5	0.1	1	90	410	283	366	658
0.5	1	1	90	111	86	107	150
12.5	1	1	90	2768	2132	2664	3740
0.5	0.55	0.515	65	65	66	61	70
12.5	0.55	0.515	65	1590	1619	1499	1734
6.5	0.1	0.515	65	173	171	156	203
6.5	1	0.515	65	1208	1237	1150	1299
6.5	0.55	0.03	65	102	95	86	123
6.5	0.55	1	65	1451	1504	1396	1565
6.5	0.55	0.515	40	803	1016	760	728
6.5	0.55	0.515	90	619	460	578	867
6.5	0.55	0.515	65	832	849	786	906

Table I8 Buoyant Convection: Geometry Parameters with Average Air Mass Flow Results ($10m^2$ Area)

Length (m)	Width (m)	Depth (m)	Tilt angle (^{o})	20th March (kg s^{-1})	21st June (kg s^{-1})	22nd September (kg s^{-1})	21st December (kg s^{-1})
0.5	0.1	0.03	40	0.07	0.07	0.07	0.06
12.5	0.1	0.03	40	0.04	0.05	0.04	0.04
0.5	1	0.03	40	0.16	0.17	0.16	0.16
12.5	1	0.03	40	0.11	0.12	0.11	0.11
0.5	0.1	1	40	0.75	0.80	0.75	0.73
12.5	0.1	1	40	0.63	0.68	0.63	0.61
0.5	1	1	40	1.83	1.95	1.81	1.78
12.5	1	1	40	1.93	2.06	1.91	1.87
0.5	0.1	0.03	90	0.06	0.06	0.06	0.07
12.5	0.1	0.03	90	0.04	0.04	0.04	0.04
0.5	1	0.03	90	0.15	0.14	0.15	0.17
12.5	1	0.03	90	0.10	0.10	0.10	0.12
0.5	0.1	1	90	0.70	0.64	0.69	0.77
12.5	0.1	1	90	0.58	0.53	0.58	0.65
0.5	1	1	90	1.69	1.55	1.67	1.88
12.5	1	1	90	1.78	1.63	1.76	1.99
0.5	0.55	0.515	65	0.96	0.97	0.95	0.99
12.5	0.55	0.515	65	0.97	0.98	0.97	1.00
6.5	0.1	0.515	65	0.45	0.45	0.44	0.46
6.5	1	0.515	65	1.25	1.26	1.24	1.29
6.5	0.55	0.03	65	0.10	0.10	0.10	0.11
6.5	0.55	1	65	1.58	1.59	1.57	1.63
6.5	0.55	0.515	40	0.99	1.06	0.98	0.96
6.5	0.55	0.515	90	0.92	0.84	0.91	1.02
6.5	0.55	0.515	65	1.00	1.00	0.99	1.03

Table I9 Buoyant Convection: Geometry Parameters with Total Power Output for 10m^2 Area Results.

Length (m)	Width (m)	Depth (m)	Tilt angle (^{o})	20th March (kWh)	21st June (kWh)	22nd September (kWh)	21st December (kWh)
0.5	0.1	0.03	40	0.2	0.2	0.2	0.2
12.5	0.1	0.03	40	0.2	0.2	0.2	0.2
0.5	1	0.03	40	0.3	0.4	0.3	0.3
12.5	1	0.03	40	0.3	0.4	0.3	0.3
0.5	0.1	1	40	4.1	5.3	3.7	3.9
12.5	0.1	1	40	4.0	5.1	3.7	3.8
0.5	1	1	40	2.6	3.3	2.5	2.3
12.5	1	1	40	2.8	3.6	2.7	2.5
0.5	0.1	0.03	90	0.2	0.1	0.1	0.2
12.5	0.1	0.03	90	0.1	0.1	0.1	0.2
0.5	1	0.03	90	0.2	0.2	0.2	0.4
12.5	1	0.03	90	0.2	0.1	0.2	0.4
0.5	0.1	1	90	3.0	2.1	2.7	4.8
12.5	0.1	1	90	3.0	2.0	2.6	4.7
0.5	1	1	90	2.0	1.5	1.9	2.7
12.5	1	1	90	2.2	1.7	2.1	3.0
0.5	0.55	0.515	65	2.1	2.1	2.0	2.3
12.5	0.55	0.515	65	2.3	2.3	2.1	2.5
6.5	0.1	0.515	65	2.4	2.4	2.2	2.8
6.5	1	0.515	65	1.8	1.9	1.8	2.0
6.5	0.55	0.03	65	0.3	0.3	0.2	0.3
6.5	0.55	1	65	4.0	4.1	3.8	4.3
6.5	0.55	0.515	40	2.2	2.8	2.1	2.0
6.5	0.55	0.515	90	1.7	1.3	1.6	1.4
6.5	0.55	0.515	65	2.3	2.3	2.1	2.5